

Washington University in St. Louis

## Washington University Open Scholarship

---

Arts & Sciences Electronic Theses and  
Dissertations

Arts & Sciences

---

Spring 5-15-2019

### Siderophore Pathways and Non-traditional Antibiotic Strategies in Multi-drug Resistant *Acinetobacter baumannii*

Tabbatha Bohac

*Washington University in St. Louis*

Follow this and additional works at: [https://openscholarship.wustl.edu/art\\_sci\\_etds](https://openscholarship.wustl.edu/art_sci_etds)

 Part of the [Chemistry Commons](#)

---

#### Recommended Citation

Bohac, Tabbatha, "Siderophore Pathways and Non-traditional Antibiotic Strategies in Multi-drug Resistant *Acinetobacter baumannii*" (2019). *Arts & Sciences Electronic Theses and Dissertations*. 1842.  
[https://openscholarship.wustl.edu/art\\_sci\\_etds/1842](https://openscholarship.wustl.edu/art_sci_etds/1842)

This Dissertation is brought to you for free and open access by the Arts & Sciences at Washington University Open Scholarship. It has been accepted for inclusion in Arts & Sciences Electronic Theses and Dissertations by an authorized administrator of Washington University Open Scholarship. For more information, please contact [digital@wumail.wustl.edu](mailto:digital@wumail.wustl.edu).

WASHINGTON UNIVERSITY IN ST. LOUIS  
Department of Chemistry

Dissertation Examination Committee:  
Timothy A. Wencewicz, Chair  
Jonathan Barnes  
Jeffrey P. Henderson  
Meredith Jackrel  
John-Stephen Taylor

Siderophore Pathways and Non-traditional Antibiotic Strategies in Multi-drug Resistant  
*Acinetobacter baumannii*  
by  
Tabbetha J. Bohac

A dissertation presented to  
The Graduate School  
of Washington University in  
partial fulfillment of the  
requirements for the degree  
of Doctor of Philosophy

May 2019  
St. Louis, Missouri

© 2019, Tabbetha J. Bohac

# Table of Contents

List of Figures .....	v
List of Tables .....	xi
Acknowledgments.....	xii
Abstract of the Dissertation .....	xv
Chapter 1: Introduction – Siderophores of <i>Acinetobacter baumannii</i> .....	1
1.1 Preface.....	2
1.2 Multi-Drug Resistant (MDR) Pathogens.....	2
1.3 Iron Acquisition Pathways .....	3
1.4 Siderophores of <i>A. baumannii</i> .....	8
1.5 Trojan Horse Strategies and Medicinal Applications of Siderophores .....	14
1.6 Figures.....	16
1.7 References .....	27
Chapter 2: Crystal Structure of the Siderophore Binding Protein BauB Bound to an Unusual 2:1 Complex Between Acinetobactin and Ferric Iron .....	37
2.1 Preface.....	38
2.2 Abstract .....	38
2.3 Introduction .....	39
2.4 Results and Discussion.....	41
2.5 Outlook and Conclusions .....	48
2.6 Materials and Methods.....	49
2.7 Figures and Tables .....	55
2.8 References .....	71
Chapter 3: Fimsbactin and Acinetobactin Compete for the Periplasmic Siderophore Binding Protein BauB in Pathogenic <i>Acinetobacter baumannii</i> .....	79
3.1 Preface.....	80
3.2 Abstract .....	80
3.3 Introduction .....	81
3.4 Results and Discussion.....	82
3.5 Outlook and Conclusions .....	96
3.6 Materials and Methods.....	97
3.7 Figures and Tables .....	104
3.8 References .....	140

Chapter 4: Exploring Apparent Redundancy in Siderophore Systems of <i>Acinetobacter baumannii</i>	149
4.1 Preface	150
4.2 Abstract	150
4.3 Introduction	150
4.4 Results and Discussion	151
4.5 Outlook and Conclusions	156
4.6 Materials and Methods	157
4.7 Figures and Tables	163
4.8 References	197
Chapter 5: Rigid Oxazole Acinetobactin Analog Blocks Siderophore Cycling in <i>Acinetobacter baumannii</i>	200
5.1 Preface	201
5.2 Abstract	201
5.3 Introduction	201
5.4 Results and Discussion	203
5.5 Outlook and Conclusions	207
5.6 Materials and Methods	208
5.7 Figures and Tables	228
5.8 References	243
Chapter 6: Iron Binding Proves to be Crucial in Siderophore Cycling Disruption by Oxidized Pre-Acinetobactin in <i>Acinetobacter baumannii</i>	245
6.1 Preface	246
6.2 Abstract	246
6.3 Introduction	247
6.4 Results and Discussion	247
6.5 Outlook and Conclusions	253
6.6 Materials and Methods	253
6.7 Figures and Tables	268
6.8 References	334
Chapter 7: Fimsbactin analogs as mimics of the natural Fimsbactin system	336
7.1 Preface	337
7.2 Abstract	337
7.3 Introduction	337
7.4 Results and Discussion	339

7.5	Outlook and Conclusions .....	342
7.6	Materials and Methods .....	343
7.7	Figures and Tables .....	354
7.8	References .....	382
Chapter 8:	Conclusions and Future Directions .....	386
8.1	Preface .....	387
8.2	Summary of Dissertation.....	387
8.3	Future Directions.....	389
8.4	Acknowledgements .....	396
8.5	Figures .....	398
8.6	References .....	405

# List of Figures

## Chapter 1

Figure 1.1: Iron acquisition from Heme.....	16
Figure 1.2: Iron acquisition from Transferrin and Lactoferrin.....	17
Figure 1.3: Siderophore iron-binding moieties.....	18
Figure 1.4: Generalized siderophore transport pathway.....	19
Figure 1.5: Structures of <i>A. baumannii</i> siderophores .....	19
Figure 1.6: Biosynthetic gene clusters for <i>A. baumannii</i> siderophores .....	20
Figure 1.7: Siderophore biosynthesis in <i>A. baumannii</i> .....	20
Figure 1.8: Synthetic route to PreAcb.....	21
Figure 1.9: Structures of Fimsbactin A-F.....	21
Figure 1.10: Total synthesis of Fimsbactin A .....	22
Figure 1.11: AntiSMASH of siderophore gene clusters.....	25
Figure 1.12: Structures of other natural siderophores.....	26

## Chapter 2

Figure 2.1: Structure of acinetobactin and preacinetobactin.....	55
Figure 2.2: Overlay of two BauB chains.....	55
Figure 2.3: Ribbon representation of BauB bound to Acb2-Fe complex.....	56
Figure 2.4: PROMALS3d structure-based alignment of BauB.....	59
Figure 2.5: Modeling of Acb2-Fe structure into electron density in BauB pocket.....	60
Figure 2.6: Siderophore binding pocket in BauB.....	61
Figure 2.7: Overlay of BauB and CeuE.....	62
Figure 2.8: Structures of Acb2-Fe complex.....	63
Figure 2.9: Structural representation of cis-[Acb <sub>2</sub> Fe] synthetic.....	64
Figure 2.10: Siderophore-dependent fluorescence quenching of C-His <sub>6</sub> -BauB.....	66
Figure 2.11: Overview of acinetobactin pathway in <i>A. baumannii</i> .....	67
Figure 2.12: BauB purification.....	68

## Chapter 3

Figure 3.1: AntiSMASH analysis of Fimsbactin producers.....	106
---	-----

Figure 3.2: Siderophore biosynthesis in <i>A. baumannii</i> .....	107
Figure 3.3: DAD and EICs for Fimsbactin A-F (Trial 1).....	108
Figure 3.4: DAD and EICs for purified Fimsbactin A (Trial 1).....	109
Figure 3.5: DAD and EICs for Fimsbactin A-F (Trial 2) .....	110
Figure 3.6: DAD and EICs for purified Fimsbactin A (Trial 2).....	111
Figure 3.7: HR-MS of Fimsbactin A .....	113
Figure 3.8: <sup>1</sup> H NMR of Fimsbactin A.....	114
Figure 3.9: <sup>13</sup> C NMR of Fimsbactin A .....	115
Figure 3.10: Structures and microbial producers of siderophores.....	116
Figure 3.11: Fimsbactin A titration with Fe(III).....	117
Figure 3.12: Optical absorbance spectrum of <i>holo</i> -FimFe complex.....	118
Figure 3.13: Titration of <i>holo</i> -Acb <sub>2</sub> Fe with <i>apo</i> -Fim.....	121
Figure 3.14: Influence of <i>apo</i> - and <i>holo</i> -siderophores on <i>A. baumannii</i> growth.....	122
Figure 3.15: Dose dependent growth promotion of <i>A. baumannii</i> .....	123
Figure 3.16: Dose dependent growth promotion of <i>A. baumannii</i> with error bars.....	124
Figure 3.17: Influence of <i>apo</i> - and <i>holo</i> -siderophore combinations.....	125
Figure 3.18: Influence of <i>apo</i> - and <i>holo</i> -siderophore combinations full curves.....	129
Figure 3.19: Nucleotide and amino acid sequence of <i>N</i> -His <sub>6</sub> -BauB.....	130
Figure 3.20: SDS-PAGE analysis of Ni-NTA purified <i>N</i> -His <sub>6</sub> -BauB.....	131
Figure 3.21: Siderophore-dependent fluorescence quenching of <i>N</i> -His <sub>6</sub> -BauB.....	132
Figure 3.22: Acb <sub>2</sub> Fe and FimFe compete for BauB binding.....	133
Figure 3.23: Structural comparison of PreAcb <sub>2</sub> Fe, Acb <sub>2</sub> Fe and FimFe complexes.....	134
Figure 3.24: Schematic overview of the iron acquisition pathway in <i>A. baumannii</i> .....	135
Figure 3.25: Structures of Fimsbactin A-F.....	136
Figure 3.26: Antismash analysis of two deposited genomes of <i>A. baumannii</i> .....	137
Figure 3.27: Dose dependent influence of <i>apo</i> -Fim and <i>holo</i> -Fim.....	138
Figure 3.28: Dose dependent influence of <i>apo</i> -Fim and <i>holo</i> -Fim (full curves).....	139

## Chapter 4

Figure 4.1: Siderophores of <i>A. baumannii</i> .....	163
Figure 4.2: Fimsbactin A-F structures.....	163
Figure 4.3: LCMS siderophore extractions.....	164
Figure 4.4: DAD for Fimsbactin A-F.....	165



Figure 4.5: DAD and EIC for Fimsbactin F.....	166
Figure 4.6: DAD and EIC for Fimsbactin F-Fe.....	167
Figure 4.7: HRMS for Fimsbactin F.....	168
Figure 4.8: <sup>1</sup> H NRM of Fimsbactin F.....	169
Figure 4.9A: <sup>13</sup> C NMR of Fimsbactin F.....	170
Figure 4.9B: COSY NMR of Fimsbactin F.....	171
Figure 4.9C: HMBC NMR of Fimsbactin F.....	172
Figure 4.9D: HSQC NMR of Fimsbactin.....	173
Figure 4.10: Dose dependent growth promotion of <i>A. baumannii</i> .....	174
Figure 4.11: Influence of siderophore on <i>A. baumannii</i> growth.....	175
Figure 4.12: Influence of siderophore combinations (FimA/FimF) on growth.....	176
Figure 4.13: Influence of siderophore combinations of growth (FimA/FimF-full curves).....	179
Figure 4.14: Influence of siderophore combinations (Acb/FimF) on growth.....	180
Figure 4.15: Influence of siderophore combinations of growth (Acb/FimF-full curves).....	183
Figure 4.16: Siderophore-dependent fluorescence quenching of <i>N</i> -His <sub>6</sub> -BauB.....	184
Figure 4.17: Optical absorbance spectrum of FimF-Fe complex.....	186
Figure 4.18: Titration of Fimsbactin F with Fe(III).....	186
Figure 4.19: Absorbance of FimF and EDTA over time.....	187
Figure 4.20: Hypothesized relationship between FimA and FimF.....	188
Figure 4.21: Metal titration studies (bar graphs).....	189
Figure 4.22: Metal titration curves for FimA.....	190
Figure 4.23: Metal titration curves for FimF.....	191
Figure 4.24: Metal titration curves for Acb.....	192
Figure 4.25: Metal titration curves for PreAcb.....	193
Figure 4.26: Metal titration curves for PreAcb with Zn.....	194
Figure 4.27: Metal titration curves for OxPreAcb.....	195

## Chapter 5

Figure 5.1: Structures of PreAcb, Acb and OxPreAcb.....	228
Scheme 5.1: Synthesis of precursors to OxPreAcb.....	229
Scheme 5.2: Synthesis of OxPreAcb.....	229
Figure 5.2: OxPreAcb competes with Acb to inhibit growth.....	230
Figure 5.3: OxPreAcb is a potent inhibitor of <i>Acinetobacter baumannii</i> ATCC 19606T.....	231

Figure 5.4: Growth inhibition by OxPreAcb is attenuated by iron.....	232
Figure 5.5: OxPreAcb promotes growth when complexed with iron (III).....	234
Figure 5.6: The antibiotic effect of OxPreAcb is bacteriostatic.....	235
Figure 5.7: OxPreAcb is bacteriostatic towards multiple <i>A. baumannii</i> stains.....	236
Figure 5.8: OxPreAcb forms a 2:1 complex with iron (III).....	237
Figure 5.9: PreAcb, Acb, and OxPreAcb all form colored, high-affinity complexes.....	238
Figure 5.10: OxPreAcb is more rigid than PreAcb.....	239
Figure 5.11: A <sub>1,3</sub> strain induces conformational rigidity.....	239
Figure 5.12: OxPreAcb restricts rotation about the heterocycle-carbonyl bond.....	240
Figure 5.13: Hypothetical model for mechanism of action of OxPreAcb.....	241
Figure 5.14: Structures of siderophores and inhibitors.....	242

## Chapter 6

Figure 6.1: SAR of PreAcb and Acb.....	268
Scheme 6.1: Synthetic route for OxPreAcb and analogs.....	268
Figure 6.2: CAS assay of OxPreAcb and analogs.....	269
Figure 6.3: Importance of hydroxymate group in OxPreAcb.....	270
Figure 6.4: Fluorescence Quenching of BauB by OxPreAcb, PreAcb, Acb apo and holo.....	271
Figure 6.5: Fluorescence Quenching of BauB by OxPreAcb analogs.....	272
Figure 6.6: CDC clinical isolates resistances to current antibiotics.....	273
Figure 6.7: Toxicity data – Alliance Pharma.....	275
Figure 6.8: OxPreAcb-Ga growth studies.....	276
Figure 6.9: OxPreAcb-Ga growth recovery by siderophores (bar graphs).....	277
Figure 6.10: OxPreAcb-Ga growth recovery by siderophores (full growth curves).....	278
Figure 6.11: Fluorescence quenching assay of BauB with OxPreAcb-Ga.....	279
Figure 6.12: OxPreAcb inhibits growth of <i>A. baumannii</i> .....	279
Figure 6.13: UV-Vis spectra of OxPreAcb analogs.....	280

## Chapter 7

Figure 7.1: Structures of Fimsbactin A and synthetic Fimsbactin analogs.....	354
Figure 7.2: Fimsbactin A and three synthetic analogs.....	355
Figure 7.3: Divergent synthesis of Fimsbactin analogs.....	355
Figure 7.4: Influence of <i>apo</i> - and <i>holo</i> -fims analogs on growth (bar graphs).....	356

Figure 7.5: Influence of <i>apo</i> - and <i>holo</i> -fims analogs on growth (full growth curves).....	357
Figure 7.6: Fims analog-Ga inhibition and growth recovery (bar graphs).....	358
Figure 7.7: Fims analog 1-Ga inhibition and growth recovery (full curves).....	359
Figure 7.8: Fims analog 2-Ga inhibition and growth recovery (full curves).....	360
Figure 7.9: Fims analog 3-Ga inhibition and growth recovery (full curves).....	361
Figure 7.10: Fluorescence quenching by Fimsbactin analogs.....	362
Figure 7.11: DFT calculated structures of FimFe and Fims analog 1.....	363
Figure 7.12: UV-Vis spectra of Fims analogs.....	364
Figure 7.13: <sup>1</sup> H NMR of Fim analog 1-OBn.....	365
Figure 7.14: <sup>13</sup> C NMR of Fim analog 1-OBn.....	366
Figure 7.15: <sup>1</sup> H NMR of Fim analog 1.....	367
Figure 7.16: <sup>13</sup> C NMR of Fim analog 1.....	368
Figure 7.17: DAD and EICs for Fim analog 1.....	369
Figure 7.18: HR-MS of Fim analog 1.....	370
Figure 7.19: <sup>1</sup> H NMR of Fim analog 2-OBn.....	371
Figure 7.20: <sup>13</sup> C NMR of Fim analog 2-OBn.....	372
Figure 7.21: <sup>1</sup> H NMR of Fim analog 2.....	373
Figure 7.22: <sup>13</sup> C NMR of Fim analog 2.....	374
Figure 7.23: DAD and EICs for Fim analog 2.....	375
Figure 7.24: HR-MS of Fim analog 2.....	376
Figure 7.25: <sup>1</sup> H NMR of Fim analog 3-OBn/Cbz.....	377
Figure 7.26: <sup>13</sup> C NMR of Fim analog 3-OBn/Cbz.....	378
Figure 7.27: <sup>1</sup> H NMR of Fims analog 3.....	379
Figure 7.28: <sup>13</sup> C NMR of Fims analog 3.....	380
Figure 7.29: DAD and EICs for Fim analog 3.....	381
Figure 7.30: HR-MS of Fim analog 3.....	382

## Chapter 8

Figure 8.1: Proposed synthetic route towards the baumannoferrins.....	398
Figure 8.2: Structures of baumannoferrin A and Acinetoferrin.....	399
Figure 8.3: OxPreAcb sites for future diversification.....	399
Figure 8.4: Potential OxPreAcb click chemistry.....	399
Figure 8.5: Structures of siderophores with oxidizable groups.....	400

Figure 8.6: Anguibactin potential isomerization.....	400
Figure 8.7: Synthetic route towards anguibactin.....	401
Figure 8.8: DAD and EICs of purified anguibactin.....	401
Figure 8.9: Synthetic route towards OxAng.....	402
Figure 8.10: Semi-synthetic route toward OxFimA and OxFimF.....	402
Figure 8.11: Semi-synthetic approach to FimF diversification.....	403
Figure 8.11: Synthetic efforts toward total synthesis of Fim A .....	404

# List of Tables

## **Chapter 2**

Table 2.1: Structural homologs of BauB .....	57
Table 2.2: Structure of Acb analogs and associated properties.....	65
Table 2.3: Summary of BauB crystallization and data collection.....	69
Table 2.4: Date collection and refinement statistics.....	70

## **Chapter 3**

Table 3.1: NMR Characterization for FimA .....	112
Table 3.2: Siderophore Iron Binding Properties.....	119

## **Chapter 4**

Table 4.1: Comparison of <i>A. baumannii</i> siderophore properties .....	185
---	-----

## **Chapter 6**

Table 6.1: MIC, CAS, BauB affinities of OxPreAcb analogs .....	269
Table 6.2: MIC of OxPreACb against CDC clinical isolates of <i>A. baumannii</i> .....	274

## **Chapter 7**

Table 7.1: Iron and BauB binding affinities for FimA and Fimsbactin analogs.....	356
--	-----

# Acknowledgments

This dissertation was made possible by all of Washington University in St. Louis Chemistry Department, in particular my research advisor, Dr. Timothy Wencewicz. I would like to thank Tim for welcoming me into his lab and all his mentorship. I greatly appreciate all the sharing of knowledge, experiences and his contagious optimism. I also would like to thank all of the Chemistry Department amazing staff; they really are the unsung heroes of the department—keeping it running day in and out and always brightening my day.

I thank all the members, past and present, of the Wencewicz group who fought beside me in the trenches each and every day—helping celebrate the successful experimental highs and being there to support during the days the experiments didn't go as planned. While there are too many to name individually, I would like to thank Dr. Justin Shapiro for helping bring me into the lab, teaching me the ropes and being my teammate in team Gram-negative siderophores. He really aided in me jumping right into research. I thank Luting Fang for all the beautiful biology work and growth curves: really couldn't have screened and evaluated all the molecules without her. Additionally, I would like to thank Victoria Banas for hopping right in and aiding in the synthesis and transfer of knowledge. I value all the excitement for chemistry and I'm excited to see where she takes the project! I can't thank Dr. Jana Markley enough for all her support, teaching me all the synthetic organic ways, assistance in proofing and editing my dissertation and her help putting out all the fires (figuratively and literally...). Lastly, I need to thank my day-one Chanez Symister for all her support throughout the years, from classes to lab to living next door, we truly have been through it all and couldn't have done any of it without her.

I thank my thesis committee, Drs. John-Stephen Taylor, Jonathan Barnes, Meredith Jackrel and Jeffrey P. Henderson. I appreciate all your support and insights throughout the years. From questions and suggestions in committee meetings to random chats in the halls to being open to all my random questions I bring to your offices. Thank you for always challenging me, helping me think critically, and bettering me both as a scientist, but more importantly, as a person.

I would not have been able to survive this program, if it wasn't for all my amazing friends and support systems outside the chemistry department. I would be no where if not for the support and encouragement of Dr. Ashley Macrander, aka Dr. Styles. Thank you for all the advice, vent sessions, inspirational speeches, escape rooms, lifetime movies and so much more. So thankful our paths crossed, I look forward to all our future random adventures. I have been privileged to meet and learn from so many wonderful people through graduate student groups. My time with the graduate student senate and the BALSAs group were instrumental shaping my time here and I am extremely thankful for all the skills and friends I've made during my tenure. Additionally, I thank all the friends, teammates and opponents of all the sports teams and running groups that have taken me in upon my arrival in St. Louis, I look forward to continuing these adventures.

Last, but certainly not least, I thank my family for all the continued support. I can't thank my parents enough for always being there for me and for shaping me into the person I am. I'm very thankful for my grandparents for all the visits and phone calls—definitely always a highlight. I thank my brothers for the support and Yvonne Bohac-Allen for being my St. Louis family, for the home-cooked meals and all the adventures.

Tabbatha J. Bohac

*Washington University in St. Louis*

*May 2019*

Dedicated to my parents.



## ABSTRACT OF THE DISSERTATION

Siderophore Pathways and Non-traditional Antibiotic Strategies in Multi-drug Resistant

*Acinetobacter baumannii*

by

Tabbatha J. Bohac

Doctor of Philosophy in Chemistry

Washington University in St. Louis, 2019

Professor Timothy A. Wencewicz, Chair

The rise of antibiotic resistance is driving exploration of non-canonical antibiotic approaches, including neutralization of virulence factors. Multi-drug resistant (MDR) Gram-negative pathogens, including *Acinetobacter baumannii*, are of particular concern because of the small number of clinically useful antibiotics available for use. Here we both expand upon the existing knowledge of two of the siderophores of *A. baumannii*, acinetobactin and fimsbactin, and utilize this knowledge to synthesize novel compounds for the inhibition of pathogenic *A. baumannii* in whole cell assays.

Furthering the current knowledge of the natural siderophore systems of *A. baumannii*, we were able to investigate the interaction of acinetobactin with transport proteins, as well as examine the role of the fimsbactin siderophores in iron acquisition. Specifically, we report a crystal structure of siderophore binding protein BauB bound to *holo*-acinetobactin along with fluorescence quenching assays of acinetobactin and preacinetobactin analogs to BauB. Additionally, we isolate fimsbactin from *A. baumannii* and show the importance of balance between concentrations of siderophores. Further, we explore the cooperative relationship between siderophores fimsbactin A and fimsbactin F.

With this fundamental knowledge in hand, we report a new method for blocking iron acquisition in MDR *A. baumannii* as an antivirulence strategy using rigid oxazole analogs of the known siderophore pre-acinetobactin. In addition, we report the synthesis fimsbactin mimics and confirm utilization of siderophore uptake pathways in model *A. baumannii* systems. Moreover, the fully functional fimsbactin mimics possess a synthetic handle for the coupling of antibiotics allowing for simple incorporation into studies aimed at Trojan horse antibiotic delivery mechanisms.

**Chapter 1: Introduction – Siderophores of**  
***Acinetobacter baumannii***

## 1.1 Preface

This chapter was written by T. Bohac. Section 1.4 was adapted in part from [Bohac, T. J., Fang, L., Giblin, D. E. & Wencewicz, T. A. ACS Chemical Biology, *Manuscript accepted*]. TJB isolated Fimsbactin A, performed characterization, BauB fluorescent quenching binding studies and BauB displacement assays. LF performed all growth curves. DEG performed all DFT calculations. TAW served as principal investigator and oversaw experimental design.

## 1.2 Multi-Drug Resistant (MDR) Pathogens

The Center for Disease Control (CDC) and World Health Organization (WHO) have identified MDR pathogens as a serious threat to the health and well-being of the nation and the World.<sup>1</sup> If not addressed, this threat is predicted to grow, as deaths due to antimicrobial resistance are projected to surpass cancer as the leading cause of death world wide by 2050 and account for the loss of 10 million lives per year.<sup>2</sup> In addition to the physical and emotional costs associate with the loss of lives, by 2050, the total loss in global GDP due to antimicrobial resistance is projected to be greater than \$100 trillion.<sup>2</sup> Even though MDR is projected to have a devastating impact worldwide, many pharmaceutical companies are pulling out of antibiotic research and shutting down whole research divisions due to the lack of profitability in antibiotics. Furthermore, due to the rapid evolution of resistance mechanisms, resistant strains are rendering antibiotics ineffective over shorter periods of time, limiting the profit window. Thus, the burden of research has fallen to academic and non-profit institutions to develop solutions to combat antibiotic resistance through the identification of novel antimicrobial compounds with novel mechanisms of action. This goal serves as the motivation for the work described in this dissertation, which seeks to expand the fundamental knowledge of how pathogenic bacteria function and then utilize this knowledge to synthesize novel potential therapeutic applications to combat the rise in antibiotic resistance.

While resistance amongst pathogenic bacteria seems to be growing globally, there are a handful of pathogens that are multidrug resistant; that is resistant to three or more current antibiotic classes (MDR). These pathogens make up the “ESKAPE” pathogens as they escape from treatment with traditional antibiotics; these pathogens include *Enterococcus faecium*, *Staphylococcus aureus*, *Klebsiella pneumoniae*, *Acinetobacter baumannii*, *Pseudomonas aeruginosa*, and *Enterobacter* species.<sup>3</sup> Over 63% of *A. baumannii* infections (over 7000 annually) are MDR and cause 500 deaths annually in the United States alone.<sup>1</sup> Due to its highly resistant nature of this Gram-negative bacteria, *A. baumannii* will be the focus for the work in this dissertation.

### **1.3 Iron Acquisition Pathways**

Iron is of vital importance for almost all forms of life. The unique chemistry of iron, specifically in the single electron interconversion of ferrous and ferric iron, is instrumental in a plethora of biological processes including, but not limited to, nitrogen fixation, DNA biosynthesis and oxygen transport.<sup>4</sup> Thus, iron is essential for the proliferation of cell growth, which is especially true in the case of an infection where a pathogenic bacteria is attempting to survive, grow, and spread within a host environment. In the instance of an infection, one of the host’s first line of defense is to sequester nutrients, such as iron, away from the pathogen through a process called nutritional immunity, in hopes to starve out the pathogen.<sup>5</sup> This effect is observed in a marked decrease in the concentration of iron in the human serum during times of infection, reaching levels on the order of  $10^{-24}$  M.<sup>6</sup> In order for pathogenic bacteria to survive in host environments, bacteria have evolved numerous acquisition methods for obtaining iron. These methods are highlighted in this section.

#### **Iron Acquisition from Heme**

About 75% of total iron in mammals is bound to heme, thus making heme an attractive target for bacteria from which to acquire iron.<sup>7</sup> To access heme iron, pathogenic bacteria produce small heme-binding proteins called hemophores that are then secreted from the bacteria, where it can then bind heme. Upon successful binding of heme, the hemophore-heme complex is then transferred to specific heme-binding receptor proteins. These proteins differ in Gram-positive and Gram-negative pathogens. Near iron transporter (NEAT) proteins are located on the cell wall of Gram-positive pathogens and are responsible for the transfer of heme through the peptidoglycan and cytoplasmic membrane into the cytosol.<sup>7</sup> However, since this dissertation is focused on the Gram-negative pathogenic bacteria *A. baumannii*, we will focus this section on the iron acquisition from heme by Gram-negative bacteria - specifically heme acquisition system A (HasA)-type hemophores. The HasA/HasR from *S. marcescens* is the most well studied hemophore system of Gram-negative pathogens and, thus, serves as a good model for iron acquisition from heme pathways.<sup>4</sup>

HasA-type hemophores possess the ability to bind heme from a plethora of hemoproteins such as myoglobin, hemoglobin and hemopexin.<sup>8</sup> The iron acquisition pathway from heme in Gram-negative bacteria is depicted in **Figure 1.1**. Upon the binding of heme, HasA-type hemophores then complexes with HasR, a TonB-dependent outer membrane receptor transport protein, and transfers the heme into the periplasm.<sup>9,10</sup> To facilitate transport and acquisition of heme from the periplasm to the cytosol, substrate binding proteins (SBP) aid in trafficking the substrates, in this case heme, to the inner membrane. Most of the common substrate binding proteins that facilitate the transport of heme are characterized as cluster A, class III SBPs.<sup>11</sup> The SBP then docks to inner membrane ABC transporter proteins which facilitate the transport of the heme-iron into the cytosol. Once in the cytosol, the heme-iron complex then binds a heme

oxygenase enzyme, in most cases, a nicotinamide adenine dinucleotide phosphate hydrogen (NADPH)-dependent oxygenase. These enzymes oxidize the heme ring and release iron which is then utilized by the bacteria.<sup>4</sup> The heme is then degraded or effluxed out of the cell by enzymes to prevent toxicity to the bacteria.<sup>7</sup>

### **Transferrin and Lactoferrin Iron Acquisition**

Some pathogenic bacteria may utilize iron from host glycoproteins, transferrin and lactoferrin. One difference being iron acquisition from host glycoproteins, the large size of glycoproteins prohibits their transfer across the outer membrane, and thus iron must be removed directly from the glycoprotein in the extracellular space. The acquisition pathway is depicted in **Figure 1.2**. The pathway commences with the Fur-regulated bipartite system of Ton-B-dependent outer membrane receptor protein TbpA (transferrin)/LbpA (lactoferrin) and surface-associated lipoprotein TbpB (transferrin)/LbpB (lactoferrin).<sup>13,14</sup> While TbpA/LbpA and TbpB/LbpB can both bind holo proteins, it is thought that TbpA/LbpA are also able to bind the apo forms of transferrin/lactoferrin. Therefore, it is hypothesized that a TbpB/LbpB-holo-hTf-TbpA/LbpA complex is formed and responsible for the transport of free iron across the outer membrane, although there currently is no fully elucidated mechanism.<sup>4,14</sup> Once the free iron reaches the periplasm, a periplasmic binding protein (PBP) specifically ferric-binding protein FbpA is responsible for the facilitating of iron(III) across the periplasmic space.<sup>15</sup> FbpA then delivers the iron(III) to ABC transporter, FbpBC, which shuttles the free iron to the cytoplasm for use by the pathogenic bacteria.

### **Free Inorganic Iron Transport**

Many pathogenic bacteria are capable of transporting ferrous iron through a TonB-independent manner using a ferrous iron transport system, Feo.<sup>16</sup> The Feo system possesses a

feoABC operon, comprised of three genes.<sup>4</sup> Once to the periplasm, free elemental iron can be actively transported into the cytoplasm for use by the bacteria. To help facilitate this process, it has been seen that bacteria can secrete reductase enzymes into the extracellular space with the role of converting ferric iron into ferrous which can then be transported.<sup>4</sup>

## Siderophores

An additional mechanism for iron acquisition by pathogenic bacteria, and the focus of this dissertation, is the utilization of small iron-chelating secondary metabolites called siderophores, greek for “iron-carrier”. While there are over 500 siderophores known and characterized, with a plethora more yet to be discovered, all siderophores can be classified into four distinct broad classes based upon their iron-binding moieties: catechols, hydroxamic acids,  $\alpha$ -hydroxy carboxylic acids and mixed ligands siderophores (**Figure 1.3**). Catechol siderophores are produced in both cyclic and linear variants, such as enterobactin, protochelin and vanchrobactin. This class of siderophores has a high iron affinity, as two negatively charged oxygen atoms that can delocalize electron density throughout the aromatic ring. Enterobactin is a well-studied cyclic trimer and one of the strongest known iron chelators, with an extremely high iron affinity of up to  $10^{-52}$ .<sup>17</sup> Hydroxamate bidentate chelating groups can exist in keto or iminol forms. When there is an increased electron density on the carbonyl carbon, in the iminol form, there tends to be a larger iron affinity, this form is stabilized with addition of electron donating groups on the nitrogen.<sup>4</sup> Siderophores comprising this class include Desferrioxamine E, Desferrioxamine B and Cepabactin. While  $\alpha$ -hydroxycarboxylic acid groups are normally found in our mixed ligand siderophore class, there are a few siderophores, such as achromobactin and staphyloferrin, which bind iron solely utilizing  $\alpha$ -hydroxycarboxylic acid groups. Interestingly, these groups can be photoreactive upon coordination to iron (III).<sup>19,20,21</sup> The vast majority of siderophores comprise



the fourth class of mixed-ligand siderophores which possess numerous different variations of the three aforementioned binding moieties. This class includes acinetobactin and amychelin, as well as many others.

Siderophores are biosynthesized via either a multimodular enzyme assembly line called nonribosomal peptide synthetase (NRPSs) or independent of the multimodular NRPS system deemed NRPS-independent siderophore (NIS) synthesis. NRPSs synthesize siderophores in a modular fashion, as each domain facilitates the step for the growing peptide chain with addition of proteinogenic and non-proteinogenic amino acids. These domains include, but are not limited to, activation, adenylation, thioesterase, acyl carrier proteins, condensation, cyclization, dehydration. Examples of NRPS synthesized siderophores include enterobactin and vibriobactin. NRPSs are also responsible for the synthesis of other small molecules, such as peptide-based antibiotics like penicillin and vancomycin.<sup>21</sup> Alternatively, NIS enzymes catalyze the synthesis of nonpeptidic siderophores through the addition of alcohols, carboxylic acids and amines via the formation of ester and amine bonds; this process allows for vast versatility.<sup>22</sup> Most  $\alpha$ -hydroxycarboxylic acid siderophores are synthesized in a NIS manner, including staphyloferrin and aerobactin. Further, there are hybrid siderophores, such as petrobactin, which are synthesized using both NRPS and NIS assembly. Later in this chapter, we will discuss in depth the biosynthesis of the siderophores of interest for this dissertation.

While the exact mechanism of siderophore transport and iron acquisition is siderophore dependent and not fully elucidated, here we will provide a generalized overview of this process. Once the siderophore is biosynthesized, it is then effluxed outside of the bacteria to the extracellular space where it may then bind iron. In Gram-negative pathogens, the siderophore-iron complex is then transported across the outer membrane into the periplasm via a TonB-dependent

protein. Once in the periplasm, periplasmic binding proteins aid in trafficking of the siderophore-iron complex. Some siderophores, like enterobactin, may be reduced in the periplasm, releasing the iron which can then be shuttled across the inner membrane. Other siderophores, like acinetobactin, are shuttled from the periplasmic binding protein to the ABC transport proteins of the inner membrane. Once in the cytoplasm, a reductase enzyme can reduce the iron, and the siderophore may be recycled and effluxed back into the extracellular space, where the cycle can continue. (**Figure 1.4**).

Many pathogenic bacteria synthesize multiple siderophores and while the exact benefit of this structure remains unclear, it is hypothesized that a siderophore cocktail provides unique advantages for the natural producer. *A. baumannii*, the pathogen of interest for this dissertation, is one such pathogen that synthesizes multiple siderophores; these siderophores will be further discussed in the following section.

## **1.4 Siderophores of *A. baumannii***

At least three unique structural families of siderophores (acinetobactin<sup>23</sup>, fimsbactin<sup>24</sup>, and baumannoferrin/acinetoferrin<sup>25,26</sup>) have been detected from clinical isolates of *A. baumannii* and *A. haemolyticus*, **Figure 1.5**. In this section, the biosynthesis (**Figure 1.6**) and chemical synthesis of each of these siderophore families will be presented.

### **Acinetobactin**

Acinetobactin (Acb) is the most studied *A. baumannii* siderophore and is highly conserved in all clinical isolates.<sup>27</sup> Acinetobactins were the first *A. baumannii* siderophore class to be isolated in 1994 and are the most studied class of *A. baumannii* siderophores.<sup>28</sup> Acinetobactin is a nonribosomal peptide (NRP) siderophore that is produced in a pre-acinetobactin (PreAcb) form

featuring hydroxamate and imidazole metal binding motifs derived from L-histidine, along with a phenolate-oxazoline metal chelating group derived from the condensation of 2,3-dihydroxybenzoic acid (2,3-DHB) and L-Thr.<sup>29,30</sup> The nonribosomal peptide synthetase (NRPS) biosynthetic assembly of PreAcb starts with activation of 2,3-DHB and L-Thr as acyl adenylates by adenylation domains A<sub>1</sub> (BasE) and A<sub>2</sub> (BasA), respectively, followed by formation of the aryl acyl carrier protein ArCP (BasF) and peptidyl carrier protein PCP (BasB) thioesters, respectively (**Figure 1.7**). Acylation of the  $\alpha$ -amino group of the L-Thr-PCP thioester by the 2,3-DHB-ArCP-thioester carbonyl is mediated by the condensation C domain (BasB), followed by dehydrative cyclization to the phenolate oxazoline-PCP thioester catalyzed by the cyclization domain Cy (BasD). Nucleophilic attack of *N*-hydroxyhistamine on the phenolate oxazoline-PCP thioester carbonyl releases the mature PreAcb scaffold from the NRPS assembly line. PreAcb spontaneously isomerizes to the isoxazolidinone Acb via nucleophilic attack of the hydroxamate oxygen on the oxazoline-C5' to undergo *5-exo-tet* cyclization with clean stereochemical inversion.<sup>31</sup> Formation of the isoxazolidinone heterocycle masks the hydroxamate metal chelating motif leaving the di-catechol of the 2,3-DHB fragment and the imidazole as the free metal binding groups.<sup>32</sup> Both PreAcb and Acb form stable 2:1 ferric complexes, PreAcb<sub>2</sub>Fe and Acb<sub>2</sub>Fe, respectively, and stimulate *A. baumannii* growth under iron limiting conditions.<sup>33</sup> Isomerization of PreAcb is slow under acidic conditions and chelation of iron(III) prevents isomerization, which has led to speculation that both PreAcb and Acb have a natural role in iron scavenging under acidic infection conditions.<sup>31</sup>

The first total synthesis of acinetobactin was completed in 2010 by Takeuchi and coworkers.<sup>34</sup> The 9 total step synthesis is shown in **Figure 1.8**. Briefly, histamine dihydrochloride is treated with sodium nitrate, followed by substitution with thionyl chloride, to provide the

cholorethyl imidazole hydrochloride salt. S<sub>N</sub>2 reaction with *N*-boc-*O*-benzyloxyamine affords the corresponding *N*-boc-*O*-benzyloxy imidazole, which upon treatment with TFA yields the free amine. At the same time, 2,3 dihydroxybenzaldehyde was converted to the corresponding nitrile through treatment with ammonium hydroxide, sodium formate and formic acid. To the nitrile, acetyl chloride in methanol is added, followed by addition of sodium bicarbonate, to provide the imidate. The imidate is then cyclized with L-threonine benzyl ester to afford the desired oxazoline benzyl ester which yields the free acid upon hydrogenolysis. With the free acid and amine in hand, EDC/HOBt mediated coupling in the presence of facilitating base provides the title compound benzyl protected. Final hydrogenolysis yields pre-acinetobactin, which can then spontaneously isomerize to acinetobactin.

## Fimsbactin

The fimsbactin siderophores, fimsbactin A–F (**Figure 1.9**) were discovered in 2013 and are also derived from an NRPS assembly line resembling the acinetobactin NRPS system, with double heterocyclization domains and a nonmodular gradient organization of condensation domains lacking a type I thioesterase terminating domain.<sup>34,35</sup> Fimsbactin A (Fim) was the primary siderophore in the mixture isolated from *A. baylyi* ADP1, accounting for >85% of the total mass. Fimsbactins B and C are derived from the incorporation of L-Thr instead of L-Ser into the siderophore backbone while fimsbactin D–F are shunt biosynthetic products lacking the cadaverine *N*-hydroxy group, the entire *N*-acetyl-*N*-hydroxy-cadaverine moiety, or seryl-*O*-2,3-DHB ester, respectively. The NRPS phase of Fim biosynthesis is proposed to start with activation of 2,3-DHB and L-Ser as acyl adenylates by adenylation domains A<sub>1</sub> (FbsH) and A<sub>3</sub> (FbsF), respectively, followed by formation of the ArCP (FbsE) and PCP<sub>1</sub> (FbsE) thioesters, respectively (**Figure 1.7**).<sup>24</sup> Acylation of the  $\alpha$ -amino group of the L-Ser-PCP<sub>1</sub> thioester by the 2,3-DHB-ArCP-

thioester carbonyl is presumably mediated by the condensation C domain (FbsF), followed by dehydrative cyclization to the phenolate oxazoline-PCP<sub>1</sub> thioester catalyzed by the Cy domain (FbsE). A second equivalent of L-Ser is activated by the A<sub>3</sub> domain (FbsF) and loaded to PCP<sub>2</sub> (FbsF) as a phosphopantetheinyl thioester. Nucleophilic attack of the  $\alpha$ -amino group of the L-Ser-PCP<sub>2</sub> thioester on the phenolate oxazoline-PCP<sub>1</sub> thioester carbonyl provides the intermediate *N*-acyl-Ser-PCP<sub>2</sub> thioester intermediate. Trans-thioesterification from PCP<sub>2</sub> (FbsF) to PCP<sub>3</sub> (FbsG) and acylation of the Ser free hydroxyl by 2,3-DHB, presumably with catalysis by the C<sub>2</sub> domain (FbsG) provides the penultimate PCP<sub>3</sub>-thioester. The C<sub>3</sub> domain is predicted to mediate cleavage of mature Fim from the NRPS via nucleophilic attack of the PCP<sub>3</sub>-thioester carbonyl by the primary amine of *N*-acetyl-*N*-hydroxy cadaverine. Premature cleavage from the FbsG NRPS module prior to Ser acylation by 2,3-DHB or post-NRPS hydrolysis of fimsbactin A would result in production of fimsbactin F. The remaining fimsbactin analogs can be accounted for by incorporation of L-Thr instead of L-Ser (fimsbactin B and C, respectively), lack of cadaverine oxidation (fimsbactin D), and competing hydrolysis of the penultimate PCP<sub>3</sub> thioester (fimsbactin E).

In 2015, the Kim group successfully synthesized Fimsbactin B, D and F.<sup>36</sup> While they proposed and executed a complete total synthesis of Fimsbactin A (the predicted >90% metabolite of the Fimsbactins)<sup>25</sup>, they failed to isolate pure Fimsbactin A due to epimerization at the final step. Their complete synthesis is depicted in **Figure 1.10**. Briefly, the synthesis of part A commences with an S<sub>N</sub>2 substitution reaction of *N*-Boc-*O*-benzylamine and 4-chlorobutyronitrile. Removal of the Boc-protecting group with TFA followed by *N*-acetylation installs the hydroxamate moiety-benzyl ester protected. Reduction of the terminal nitrile group with hydrogenation using Raney-Ni provides the free amine. EDC/HOBt-mediated coupling in the

presence of facilitating base of the free amine with *N*-Boc-*O*-TBS-L-serine, followed by removal of the Boc-protecting group by TFA yields part A. The synthetic route to part B begins with acid catalyzed esterification of 2,3-dihydroxybenzoic acid followed by reflux with 1,2-bis(bromomethyl)benzene and treatment with acid to provide the *o*-xylyl-protected 2,3-dihydroxybenzoic acid. EDC/HOBt-mediated coupling in the presence of facilitating base of the free carboxylic acid and L-serine-methyl ester, followed by dehydrative oxazoline formation by catalytic MoO<sub>2</sub>(TMHD)<sub>2</sub>, yields part B methyl ester. Final hydrolysis with potassium trimethylsilanolate affords compound part B. With both precursors in hand, free amine part A is coupled with free acid part B using EDC. Removal of TBS-protecting group by HF-pyridine, followed by carbodiimide-promoted esterification with an additional equivalent of part B, affords *o*-benzyl-*o*-xylyl-protected Fimsbactin A. Global deprotection hydrogenolysis provides the title compound.

### **Baumannoferrin**

Baumannoferrin is the most recently characterized *A. baumannii* siderophore, with its' discovery reported in 2015.<sup>25</sup> While there is currently no synthetic route to synthesizing baumannoferrin, it is derived from an NRPS-independent siderophore synthetase (NIS) biosynthetic process.<sup>25</sup> A related NIS siderophore, acinetoferin, has been reported from environmental strains and the opportunistic human pathogen *Acinetobacter haemolyticus*.<sup>26, 37</sup> Baumannoferrin is composed of citrate, 1,3-diaminopropane, 2,4-diaminobutyrate, decenoic acid, and  $\alpha$ -ketoglutarate.<sup>25</sup> The lipophilic nature of the baumannoferrin decenoic acid side chain has led to the proposal that the siderophore might be membrane associated.<sup>38</sup> Baumannoferrin is structurally distinct from the NRPS siderophores PreAcb, Acb, and Fim. The structure contains one hydroxamate and two  $\alpha$ -hydroxy carboxylate metal binding motifs similar to chelating groups

found in other NIS-derived, citrate-based siderophores, such as aerobactin produced by human pathogens including *Klebsiella pneumonia* and uropathogenic *E. coli* (UPEC).<sup>39, 40</sup> PreAcb/Acb and Fim are structurally related by the hydroxamate, catecholate, and phenolate oxazoline metal binding motifs found in common siderophores such as enterobactin<sup>41</sup> and vibriobactin<sup>42</sup>, respectively. Biosynthetic operons for baumannoferrin and PreAcb/Acb are present in all genome-sequenced clinical isolates of *A. baumannii* deposited in the NCBI database (taxid: 470).<sup>27</sup> On the contrary, only 4 unique strains (<10% of sequenced *A. baumannii* strains) contain genes associated with fimsbactin biosynthesis and utilization (**Figure 1.11**). It appears as though human pathogenic strains of *A. baumannii* always retain the capacity for producing at least two siderophores, PreAcb/Acb and baumannoferrin, or occasionally three siderophores, if the Fim biosynthetic operon is present and functional. Since Fim production is optional for pathogenicity, this raises the question as to whether the structural similarity of PreAcb/Acb and Fim is functionally redundant or if the siderophore pathways contribute cooperatively to iron and other metal ion acquisition, leading to increased pathogen virulence.

It is common for pathogenic and environmental microbes to produce multiple siderophores via the presence of multiple biosynthetic gene clusters (as for PreAcb/Acb, Fim, and baumannoferrin in *A. baumannii*), production of shunt/fragment biosynthetic products (as for fimsbactin A–F), precursor-directed biosynthesis (as for fimsbactin incorporation of Thr or Ser), and/or biosynthetic tailoring reactions (as for acyl-enterobactins<sup>43</sup>).<sup>44</sup> Additionally, pathogens often produce siderophore transport proteins for siderophores produced by neighboring bacteria, so called xenosiderophores.<sup>45</sup> Pathogenic *A. baumannii* express the protein FhuD to enable the utilization of hydroxamate-based xenosiderophores including desferrioxamine B, an FDA approved treatment for human iron overload diseases.<sup>46</sup> Potential advantages of utilizing multiple

siderophores<sup>44, 47</sup> include synergistic effects of siderophore combinations on iron acquisition<sup>31</sup>, evasion of immune proteins such as siderocalin<sup>48</sup>, suppression of competing microbial growth<sup>49, 50</sup>, stimulation of cooperative and synergistic microbial growth<sup>51, 52</sup>, expansion of metal uptake beyond iron<sup>53, 54</sup>, quorum sensing and cell signaling<sup>55</sup>, nutritional passivation of necessary but potentially toxic metals<sup>56, 57</sup>, quenching of reactive oxygen species<sup>58, 59</sup>, and induction of metal-dependent cellular responses in the host.<sup>60, 61</sup>

## 1.5 Trojan Horse Strategies and Medicinal Applications of Siderophores

The rise of infections caused by multi-drug resistant (MDR) Gram-negative pathogens, including MDR *Acinetobacter baumannii*, is driving the exploration of nontraditional therapeutic strategies including antivirulence therapies.<sup>62, 63</sup> Blocking virulence pathways such as cellular adhesion, protein secretion, biofilm formation, motility, and nutrient acquisition are presumed to apply less selective pressure for resistance and might work synergistically with traditional antibiotics.<sup>64</sup> Targeting nutrient acquisition pathways is an attractive option since a disproportionate percentage of the pathogen's conditionally essential genome is comprised of genes associated with nutrient scavenging.<sup>65, 66</sup> Fundamental research of siderophores has illuminated a few potential antivirulence therapies that nature itself uses to provide a competitive advantage. Taking a page from nature, researchers aim to implement these techniques into the development of novel potential therapeutics. Herein, we will discuss the use of the Trojan horse antibiotic delivery strategy, as well as the synthesis of structural mimics of known siderophores.

In nature, some pathogenic bacteria synthesize siderophore antibiotic conjugates called sideromycins, such as albomycin and salmycins, which are exported into the extracellular space.<sup>7</sup> Sideromycins then function in a Trojan horse manner, as they can then be imported by competing



bacteria via innate siderophore uptake pathways used to acquire iron. Once transported into the cell, the antibiotic may then be cleaved from the siderophore mimic and can inhibit and kill the competing bacteria. This Trojan horse strategy of synthesizing siderophore-antibiotic conjugates has been of interest to many research groups, including the Miller group which recently reported a synthetic siderophore daptomycin conjugate with potent inhibition (MIC values as low as 0.2  $\mu$ ) against MDR *A. baumannii* strains.<sup>67</sup> While this strategy has been historically limited therapeutically, recently lead compound Cefiderocol of Shionogi, a siderophore cephalosporin conjugate, was reported to have proceeded to phase III clinical trials for the treatment of a range of MDR Gram-negative pathogens.<sup>68</sup>

Another lesson from Nature was discovered by the Henderson group via the isolation of small molecule, escherichelin.<sup>50</sup> The structure of escherichelin is structurally similar to that of known siderophores pyochelin and yersiniabactin, with the largest structural difference being the oxidization of the thiozoline ring to a thiozole (**Figure 1.12**). Interestingly, patients that had a higher concentration of escherichelin in their urine were less likely to contract a UTI.<sup>50</sup> While the exact mechanism of action remains unknown, this phenomenon is hypothesized to be the result of asymptomatic bacteria synthesizing small molecules, like escherichelin, as a protective precaution to aid in out-competing of detrimental pathogens. Escherichelin highlights that a subtle structural change may result in role reversal of a compound, taking a molecule from being a siderophore and growth promoter to an inhibitor.

Trojan horse strategies and inducing subtle structure changes to afford inhibitory properties, while still mimicking the natural system, are just two examples of potential antivirulence approaches to combat the rise in antimicrobial resistance. Chapters 2-4 will focus on expanding the current knowledge base of two of the siderophore families of *A. baumannii*,

acinetobactin and the Fimsbactin (A and F). Then, this knowledge will be applied towards potential therapeutic applications, in Chapters 5-7, as we explore the synthesis of a structural analog of pre-acinetobactin that functions as an inhibitor and the synthesis of a siderophore-linker system of interest to Trojan horse antibiotic delivery.

## 1.6 Figures

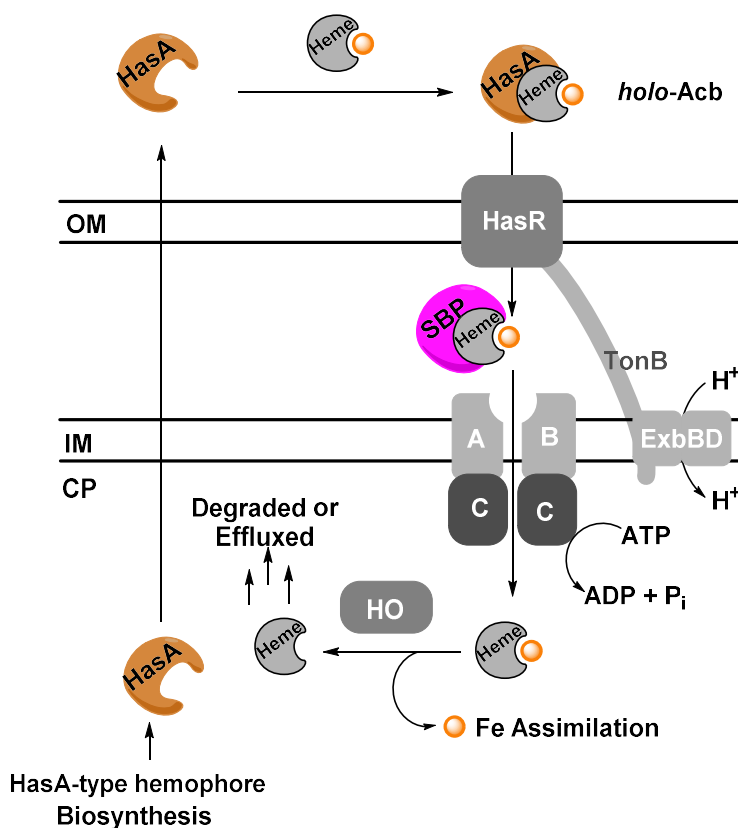


**Figure 1.1:** Iron acquisition from Heme. HasA: Heme acquisition system. SBP: Substrate binding protein. HasR: HasA outer membrane receptor. OM: Outer membrane. IM: Inner membrane. CP: cytoplasm.

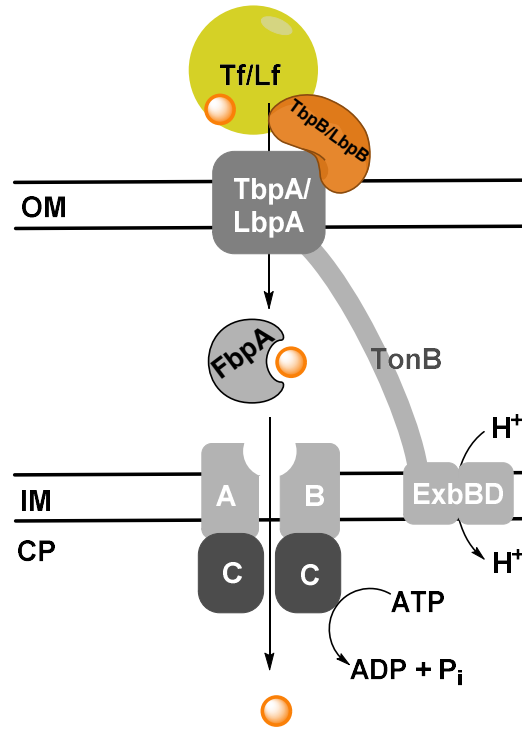


**Figure 1.2:** Iron Acquisition from Transferrin and Lactoferrin. Tf: transferrin. Lf: lactoferrin. TbpA/LbpA: outer membrane receptor protein. TbpB/LbpB: surface-bound lipoprotein. FbpA: periplasmic ferric-binding protein. OM: Outer membrane. IM: Inner membrane. CP: cytoplasm.

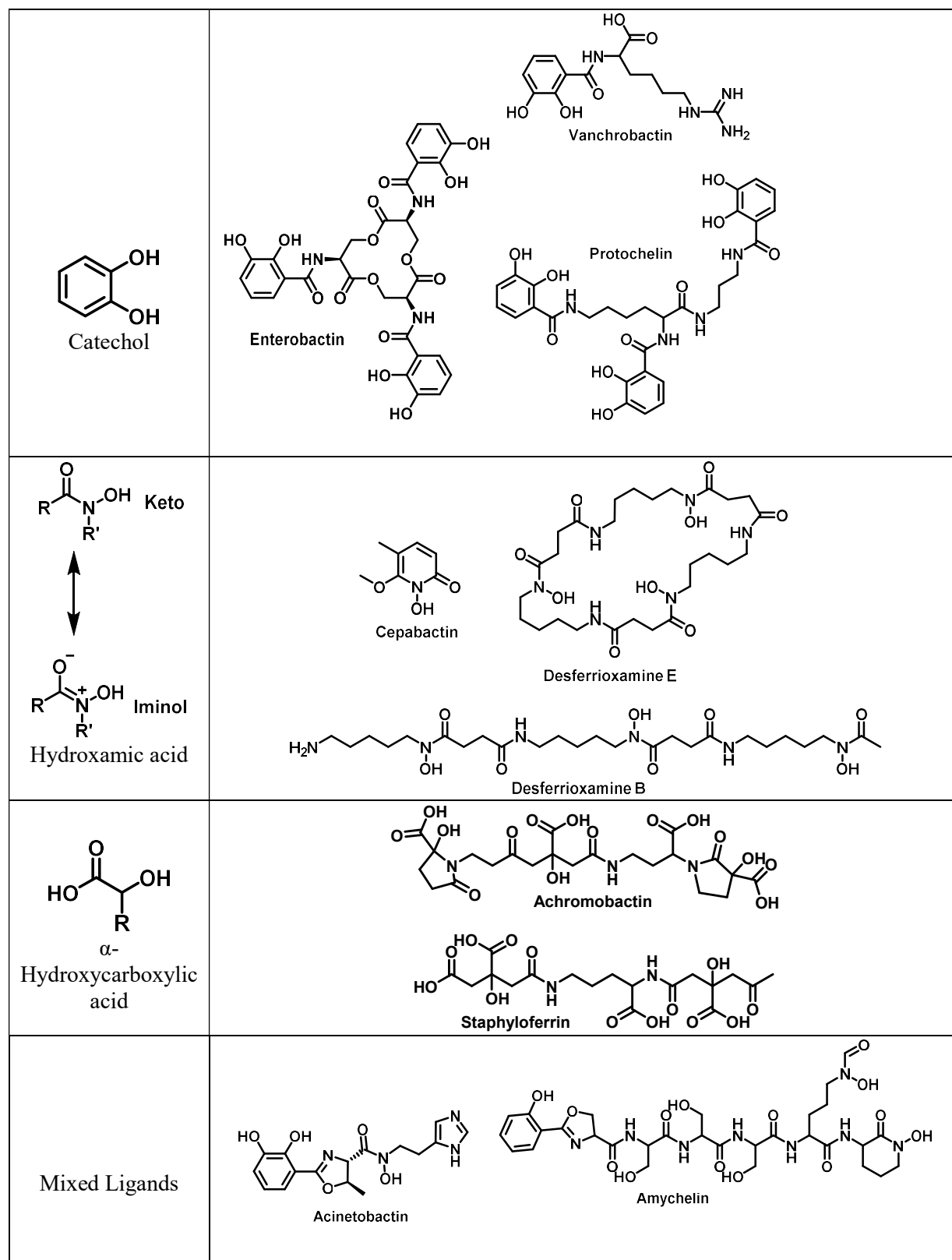


**Figure 1.3:** Siderophore iron-binding moieties and example siderophores

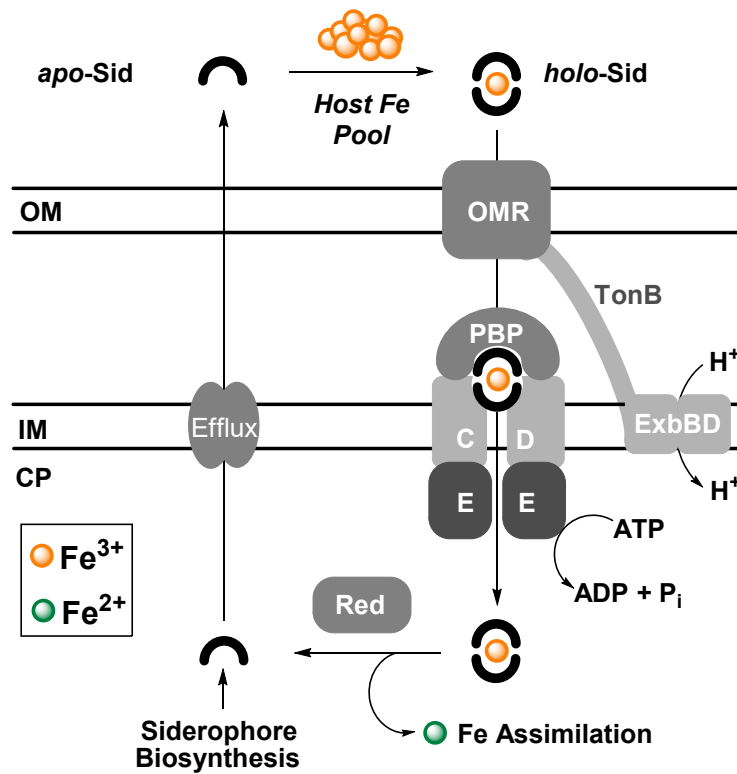


**Figure 1.4:** Generalized Siderophore Transport Pathway. PBP: periplasmic binding protein. Red: reductase enzyme. OM: Outer membrane. IM: Inner membrane. CP: cytoplasm.

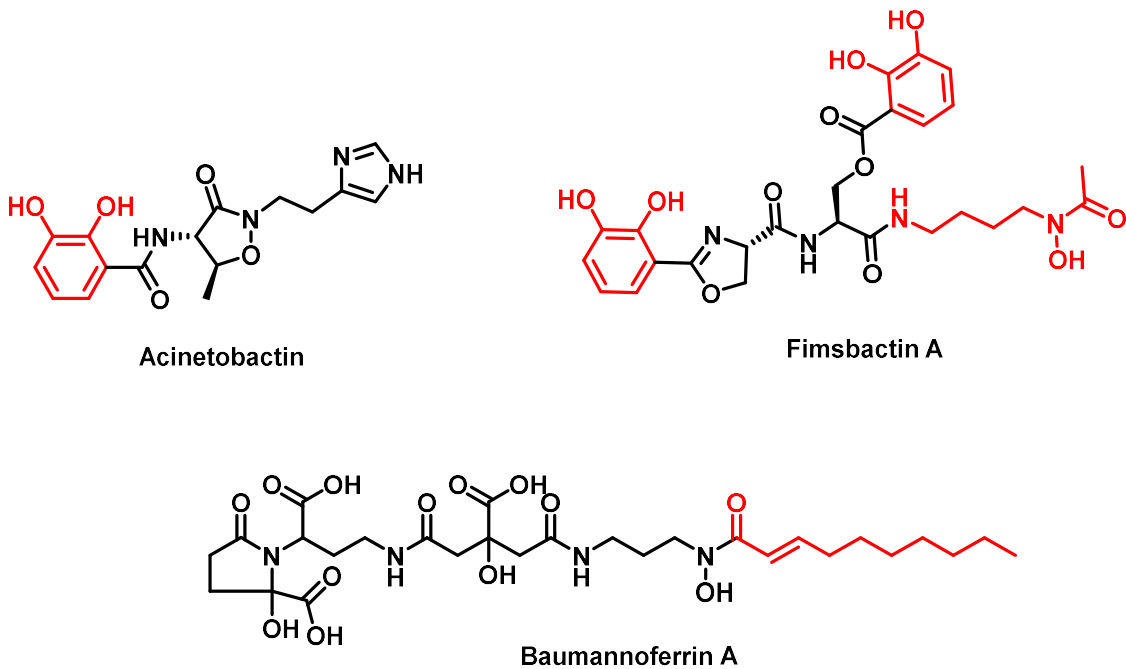


**Figure 1.5:** Structures of *A. baumannii* siderophores.

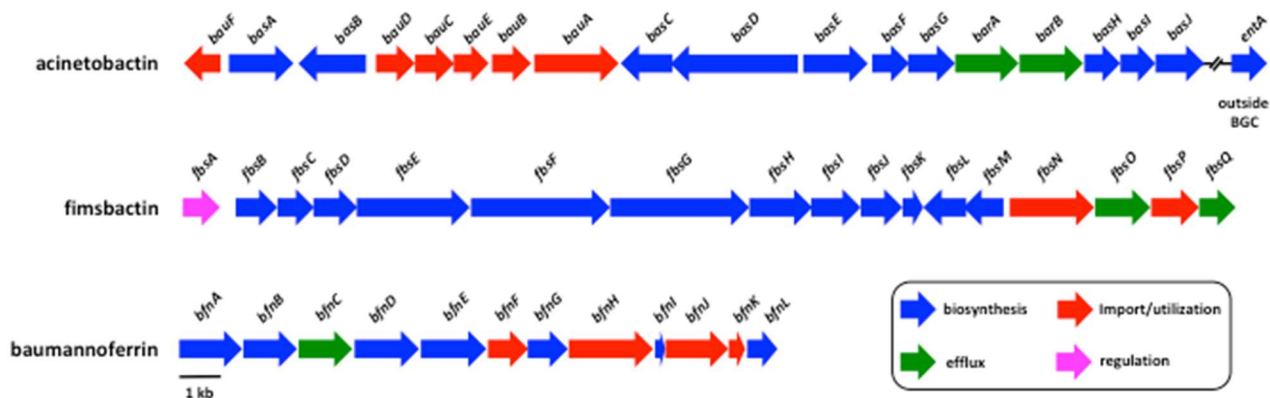


**Figure 1.6.** Biosynthetic gene clusters for acinetobactin<sup>23</sup>, fimsbactin<sup>24</sup>, and baumannoferrin<sup>25</sup> from *A. baumannii* ATCC 17978 along with annotated genes.

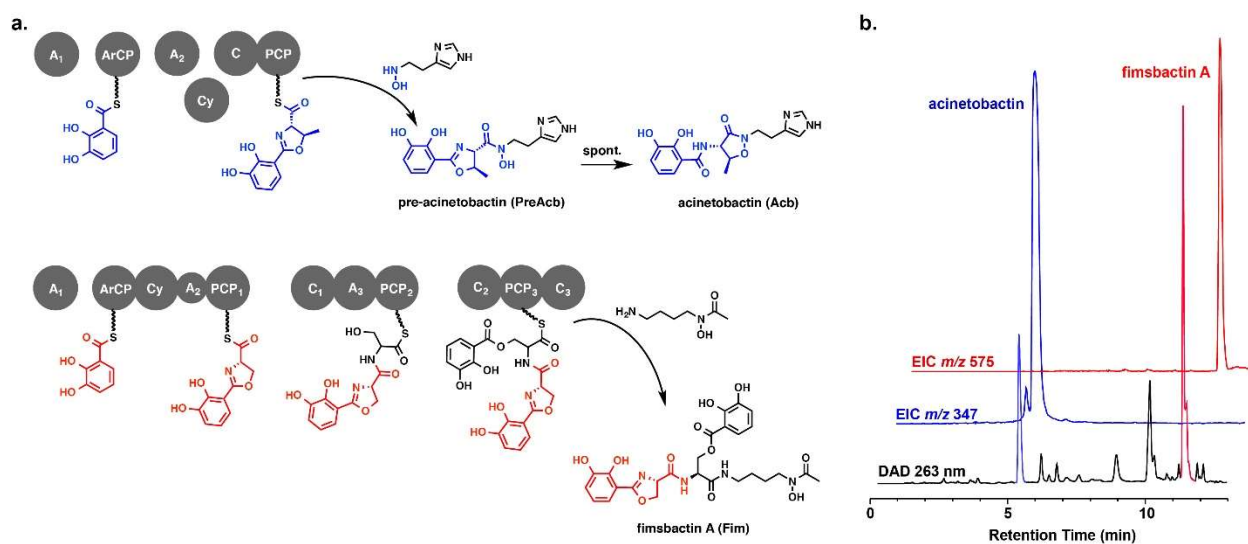


**Figure 1.7:** Siderophore biosynthesis in *A. baumannii*. (a) NRPS assembly lines for acinetobactin (top) and fimsbactin A (bottom) share a common precursor, 2,3-DHB, and a common phenolate oxazoline motif. (b) DAD at 263 nm (black), EIC at  $m/z$  347 (blue), and EIC at  $m/z$  576 (red) chromatograms from LCMS analysis of crude *A. baumannii* ATCC 17978 supernatant after acidification, treatment with XAD-7HP resin, and methanol elution.

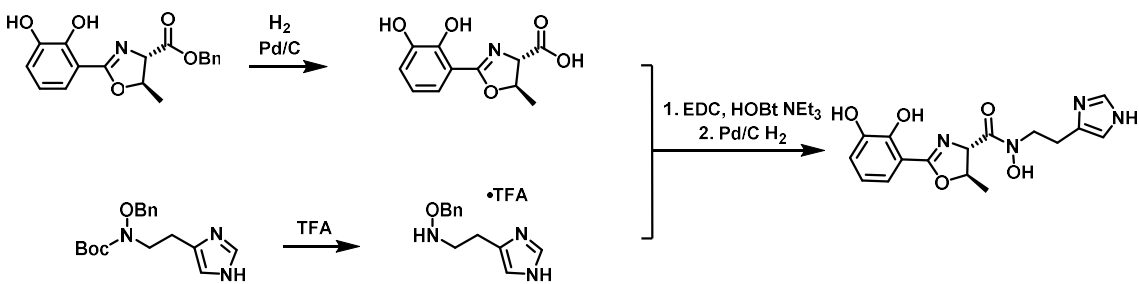
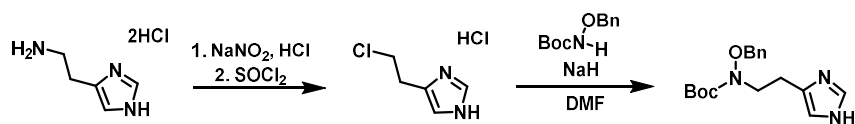
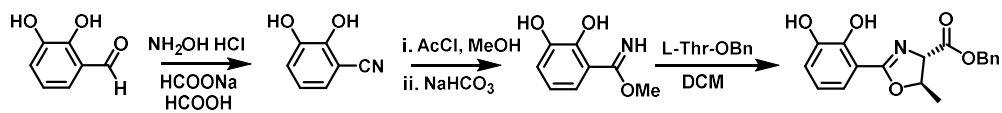


**Figure 1.8:** Synthetic route to PreAcb<sup>34</sup>

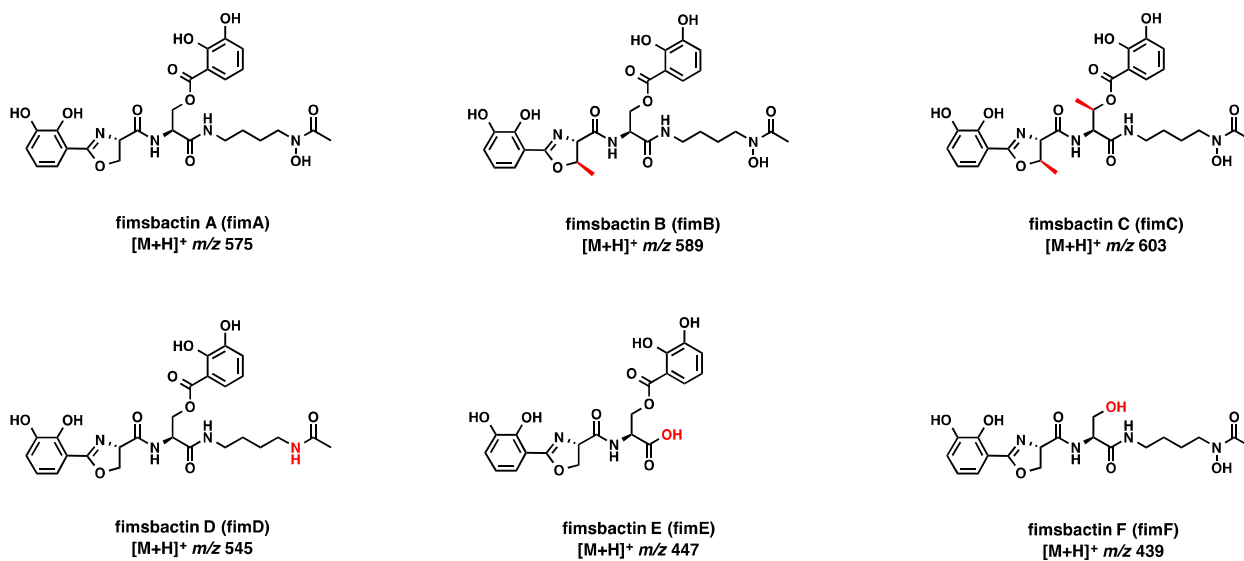


**Figure 1.9.** Structures and  $m/z$  values for  $[M+H]^+$  molecular ions of fimsbactin A–F.<sup>24, 36</sup> Structural differences are highlighted in red.

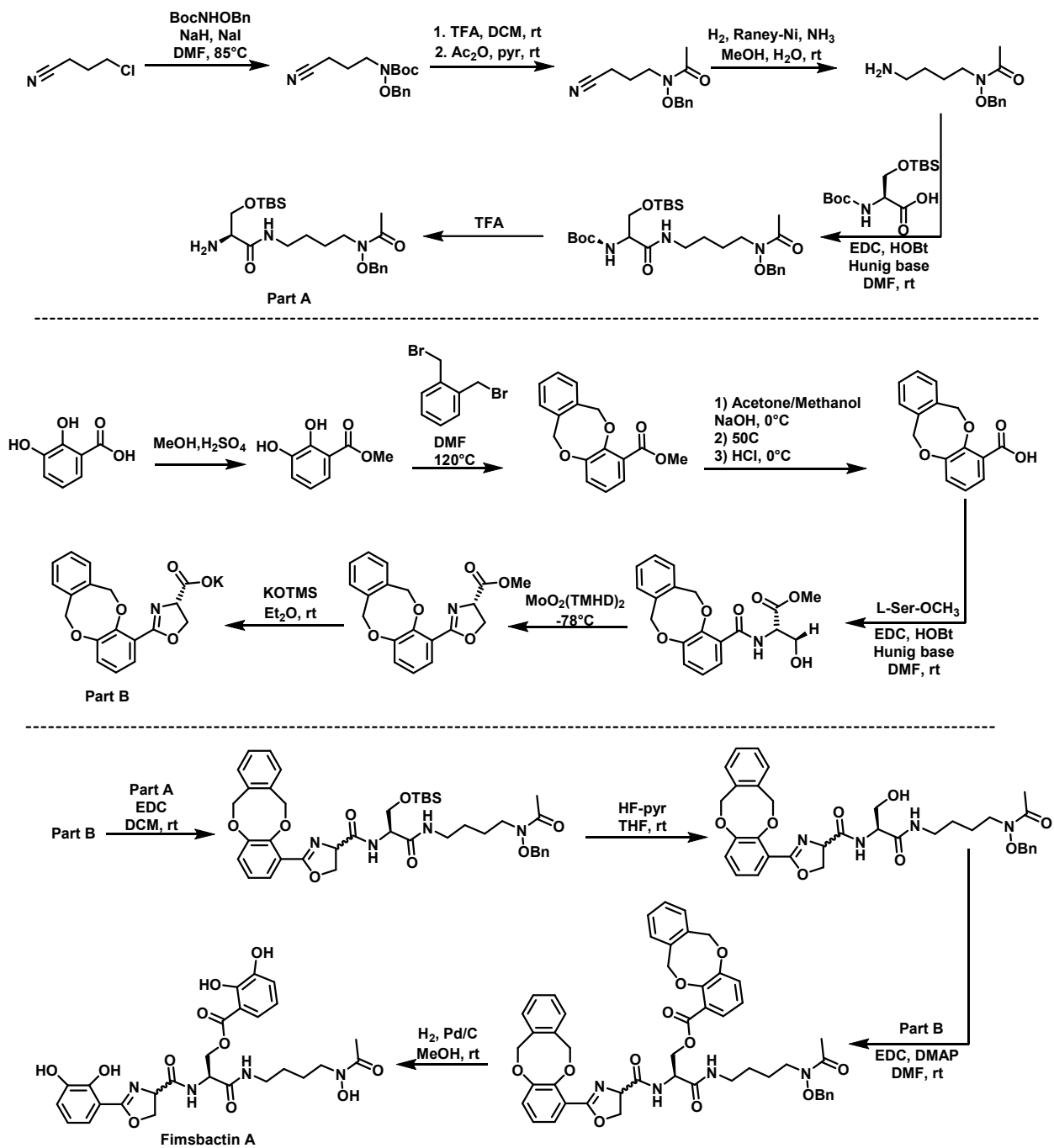


Figure 1.10: Total synthesis of Fimsbactin A<sup>36</sup>



# Fimsbactin Biosynthetic Gene Clusters

AbPK1 (GenBank: GCA\_002753915.1)

Query sequence



BGC0000352: Fimsbactin biosynthetic gene cluster (100% of genes show similarity)



AB042 (GenBank: GCA\_001941765.1)

Query sequence



BGC0000352: Fimsbactin biosynthetic gene cluster (100% of genes show similarity)



D36 (GenBank: GCA\_001399655.1)

Query sequence



BGC0000352: Fimsbactin biosynthetic gene cluster (100% of genes show similarity)



Strain ATCC 17978 (GenBank: GCA\_001593425)

Query sequence



BGC0000352: Fimsbactin biosynthetic gene cluster (100% of genes show similarity)

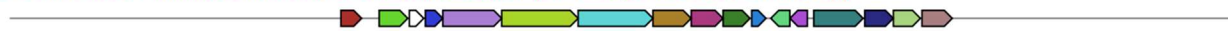


ATCC 17978-mmf (GenBank: GCA\_001077675.1)

Query sequence



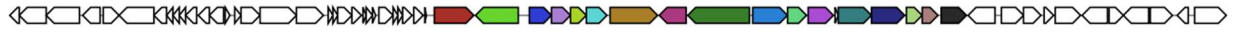
BGC0000352: Fimsbactin biosynthetic gene cluster (94% of genes show similarity)



# Acinetobactin Biosynthetic Gene Clusters

AbPK1 (GenBank: GCA\_002753915.1)

Query sequence



BGC0000294: Acinetobactin biosynthetic gene cluster (78% of genes show similarity)



AB042 (GenBank: GCA\_001941765.1)

Query sequence



BGC0000294: Acinetobactin biosynthetic gene cluster (100% of genes show similarity)



D36 (GenBank: GCA\_001399655.1)

Query sequence



BGC0000294: Acinetobactin biosynthetic gene cluster (100% of genes show similarity)



Strain ATCC 17978 (GenBank: GCA\_001593425)

Query sequence

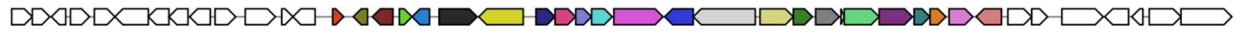


BGC0000294: Acinetobactin biosynthetic gene cluster (100% of genes show similarity)



ATCC 17978-mmf (GenBank: GCA\_001077675.1)

Query sequence



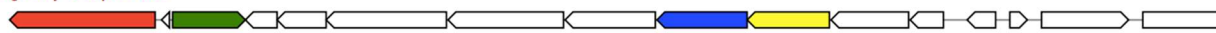
BGC0000294: Acinetobactin biosynthetic gene cluster (100% of genes show similarity)



## Acinetoferrin/Baumannoferrin Biosynthetic Gene Clusters

AbPK1 (GenBank: GCA\_002753915.1)

Query sequence



BGC0000295: Acinetoferrin biosynthetic gene cluster (40% of genes show similarity)



AB042 (GenBank: GCA\_001941765.1)

Query sequence



BGC0000295: Acinetoferrin biosynthetic gene cluster (30% of genes show similarity)



D36 (GenBank: GCA\_001399655.1)

Query sequence

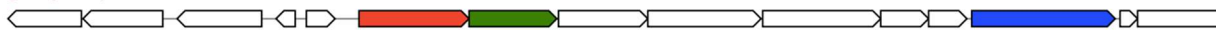


BGC0000295: Acinetoferrin biosynthetic gene cluster (30% of genes show similarity)



Strain ATCC 17978 (GenBank: GCA\_001593425)

Query sequence



BGC0000295: Acinetoferrin biosynthetic gene cluster (30% of genes show similarity)



ATCC 17978-mmf (GenBank: GCA\_001077675.1)

Query sequence



BGC0000295: Acinetoferrin biosynthetic gene cluster (30% of genes show similarity)



**Figure 1.11.** AntiSMASH<sup>69</sup> analysis of putative fimsbactin *A. baumannii* producers identified from BLASTp analysis of *A. baumannii* genomes reveals conservation of acinetobactin and baumannoferrin biosynthetic gene clusters (BGCs). The acinetoferrin BGC is the reference in the antiSMASH database. Acinetoferrin and baumannoferrin BGCs share homology, so comparison for all strains was made to the acinetoferrin BGC.<sup>70</sup>

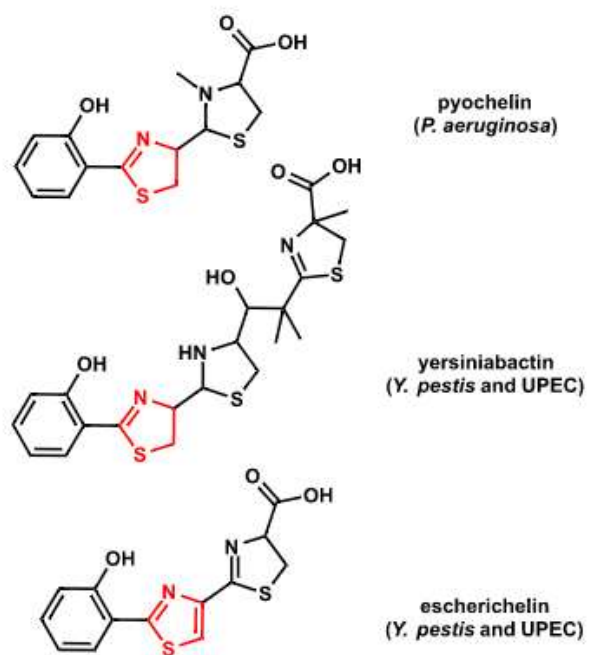


**Figure 1.12:** Structures of natural siderophores, pyochelin and yersiniabactin, and natural siderophore uptake inhibitor, escherichelin<sup>50</sup>

## 1.7 References

- [1] CDC. (2013) Antibiotic Resistance Threats in the United States, 2013, Centers for Disease Control and Prevention, U.S. Department of Health and Human Services, Washington D.C.
- [2] The Review on Antimicrobial Resistance, published from 2014–2016, online source: [www.amr-review.org](http://www.amr-review.org).
- [3] Boucher, H. W.; et al. “Bad Bugs, No Drugs: No ESCAPE! An Update from the ISDA.” *Clin. Infect. Dis.* 2009, 48, 1-12.
- [4] Zane HK, Butler A. 2013. Iron Acquisition (Bacteria). *Comprehensive Inorganic Chemistry II*, 2013, 3, 1-20. (Invited Review), series editors J. Reedijk K Poppelmeier, Vol. 3: Bioinorganic Fundamentals and Applications: Metals in Natural Living Systems and Metals in Toxicology and Medicine; Vol 3 Eds: VL Pecor.
- [5] Weinberg ED (1978) Iron and infection. *Microbiol Rev* 42:45-66
- [6] Braun, V.; Killmann, H., Bacterial solutions to the iron-supply problem. *Trends in biochemical sciences* 1999, 24 (3), 104-9
- [7] Sheldon, J. R., Laakso, H. A. and Heinrichs, D. E. (2016) Iron Acquisition Strategies of Bacterial Pathogens, *Microbiol* 4(2), 1-32.
- [8] Wandersman C, Delepelaire P. (2012). Haemophore functions revisited. *Mol Microbiol* 85, 618–631.
- [9] Izadi-Pruneyre N., Huche F., Lukat-Rodgers G. S., Lecroisey A., Gilli R., Rodgers K. R., Wandersman C., Delepelaire P (2006). The heme transfer from the soluble HasA hemophore to its membrane-bound receptor HasR is driven by protein-protein interaction from a high to a lower affinity binding site. *J Biol Chem* 281, 25541–25550.

- [10] Krieg S., Huche F., Diederichs K., Izadi-Pruneyre N., Lecroisey A., Wandersman C., Delepelaire P., Welte W. (2009). Heme uptake across the outer membrane as revealed by crystal structures of the receptorhemophore complex. *Proc Natl Acad Sci USA* 106, 1045–1050.
- [11] Berntsson RPA., Smits SHJ., Schmitt L., Slotboom D-J., Poolman B. (2010). A structural classification of substrate-binding proteins. *FEBS Lett* 584, 2606–2617.
- [12] Cornelissen C.N., Biswas G.D., Tsai J, Paruchuri D.K., Thompson S.A., Sparling P.F. (1992). Gonococcal transferrin-binding protein 1 is required for transferrin utilization and is homologous to TonB-dependent outer membrane receptors. *J Bacteriol* 174, 5788–5797.
- [13] Anderson J.E., Sparling P.F., Cornelissen C.N. (1994). Gonococcal transferrin-binding protein 2 facilitates but is not essential for transferrin utilization. *J Bacteriol* 176, 3162–3170.
- [14] Noinaj N., Easley N.C., Oke M., Mizuno N., Gumbart J., Boura E., Steere A.N., Zak O., Aisen P., Tajkhorshid E., Evans R.W., Goringe A.R., Mason A.B., Steven A.C., Buchanan S.K. (2012). Structural basis for iron piracy by pathogenic *Neisseria*. *Nature* 483, 53–58.
- [15] Parker Siburt C.J., Mietzner T.A., Crumbliss A.L. (2012). FbpA: a bacterial transferrin with more to offer. *Biochim Biophys Acta* 1820, 379–392.
- [16] Kwok E.Y., Severance S., Kosman D.J. (2006). Evidence for iron channeling in the Fet3p-Ftr1p high-affinity iron uptake complex in the yeast plasma membrane. *Biochemistry* 45, 6317–6327.
- [17] Carrano C.J., Raymond K.N. (1979). Ferric ion sequestering agents. 2. Kinetics and mechanism of iron removal from transferrin by enterobactin and synthetic tricatechols. *J Am Chem Soc* 101,5401–5404.

- [18] Barbeau, K., Rue, E. L., Bruland, K.W, Butler, A. (2001). Photochemical cycling of iron in the surface ocean mediated by microbial iron(III)-binding ligands. *Nature* 413, 409-413.
- [19] Kupper, F. C., Carrano, C.J., Kuhn, J-U., Butler, A. (2006). Photoreactivity of iron(III)-aerobactin: photoproduct structure and iron(III) coordination. *Inorg. Chem* 45, 6028-6033.
- [20] Martin, J.D., Ito, Y., Homann, V.V., Haygood, M.G., Butler, A. (2006). Structure and membrane affinity of new amphiphilic siderophores produced by *Ochrobactrum* sp. SP18. *J. Biol Inorg Chem* 11, 633-641.
- [21] Taylor, G.L., Sheikh, M.A. (2009). Crystal structure of the *Vibrio cholerae* ferric uptake regulator (Fur) reveals insights into metal co-ordination. *Mol Microbiol* 72, 1208-1220.
- [22] Hantke, K. (2001). Iron and metal regulation in bacteria. *Curr Opin Microbiol* 4, 172-177.
- [23] Yamamoto, S., Okujo, N., and Sakakibara, Y. (1994) Isolation and structure elucidation of acinetobactin, a novel siderophore from *Acinetobacter baumannii*, *Archives of microbiology* 162, 249-254.
- [24] Proschak, A., Lubuta, P., Grun, P., Lohr, F., Wilharm, G., De Berardinis, V., and Bode, H. B. (2013) Structure and biosynthesis of fimsbactins A-F, siderophores from *Acinetobacter baumannii* and *Acinetobacter baylyi*, *Chembiochem* 14, 633-638.
- [25] Penwell, W. F., DeGrace, N., Tentarelli, S., Gauthier, L., Gilbert, C. M., Arivett, B. A., Miller, A. A., Durand-Reville, T. F., Joubran, C., and Actis, L. A. (2015) Discovery and Characterization of New Hydroxamate Siderophores, Baumannoferrin A and B, produced by *Acinetobacter baumannii*, *Chembiochem* 16, 1896-1904.
- [26] Okujo, N., Sakakibara, Y., Yoshida, T., and Yamamoto, S. (1994) Structure of acinetoferrin, a new citrate-based dihydroxamate siderophore from *Acinetobacter haemolyticus*, *Biometals* 7, 170-176.

- [27] Antunes, L. C., Imperi, F., Towner, K. J., and Visca, P. (2011) Genome-assisted identification of putative iron-utilization genes in *Acinetobacter baumannii* and their distribution among a genotypically diverse collection of clinical isolates, *Research in microbiology* 162, 279-284.
- [28] Yamamoto, S.; Okujo, N.; Sakakibara, Y., (1994) Isolation and structure elucidation of acinetobactin, a novel siderophore from *Acinetobacter baumannii*. *Archives of microbiology*, 162 (4), 249-54.
- [29] Wuest, W. M., Sattely, E. S., and Walsh, C. T. (2009) Three siderophores from one bacterial enzymatic assembly line, *J Am Chem Soc* 131, 5056-5057.
- [30] Sattely, E. S., and Walsh, C. T. (2008) A latent oxazoline electrophile for N-O-C bond formation in pseudomonine biosynthesis, *J Am Chem Soc* 130, 12282-12284.
- [31] Shapiro, J. A., and Wencewicz, T. A. (2016) Acinetobactin Isomerization Enables Adaptive Iron Acquisition in *Acinetobacter baumannii* through pH-Triggered Siderophore Swapping, *ACS infectious diseases* 2, 157-168.
- [32] Bailey, D. C., Bohac, T. J., Shapiro, J. A., Giblin, D. E., Wencewicz, T. A., and Gulick, A. M. (2018) Crystal Structure of the Siderophore Binding Protein BauB Bound to an Unusual 2:1 Complex Between Acinetobactin and Ferric Iron, *Biochemistry*.
- [33] Shapiro, J. A., and Wencewicz, T. A. (2017) Structure-function studies of acinetobactin analogs, *Metallomics* 9, 463-470.
- [34] Takeuchi, Y.; Ozaki, S.; Satoh, M.; Mimura, K.; Hara, S.; Abe, H.; Nishioka, H.; Harayama, T., (2010). Synthesis of acinetobactin. *Chem. Pharm. Bull.* 52, 1552.
- [35] Wang, H., Fewer, D. P., Holm, L., Rouhiainen, L., and Sivonen, K. (2014) Atlas of nonribosomal peptide and polyketide biosynthetic pathways reveals common occurrence



- of nonmodular enzymes, *Proceedings of the National Academy of Sciences of the United States of America* 111, 9259-9264.
- [36] Ree, H.; Kim, J.; Song, W. Y.; Lee, J. E.; Kim, H. J., (2015) Total Syntheses and Evaluation of the Siderophore Functions of Fimsbactin B and Its Analogs. *Bulletin of the Korean Chemical Society*, 36 (5), 1520-1523.
- [37] Funahashi, T., Tanabe, T., Maki, J., Miyamoto, K., Tsujibo, H., and Yamamoto, S. (2013) Identification and characterization of a cluster of genes involved in biosynthesis and transport of acinetoferrin, a siderophore produced by *Acinetobacter haemolyticus* ATCC 17906T, *Microbiology* 159, 678-690.
- [38] Luo, M., Fadeev, E. A., and Groves, J. T. (2005) Membrane dynamics of the amphiphilic siderophore, acinetoferrin, *J Am Chem Soc* 127, 1726-1736.
- [39] Russo, T. A., Olson, R., Macdonald, U., Metzger, D., Maltese, L. M., Drake, E. J., and Gulick, A. M. (2014) Aerobactin mediates virulence and accounts for increased siderophore production under iron-limiting conditions by hypervirulent (hypermucoviscous) *Klebsiella pneumoniae*, *Infection and immunity* 82, 2356-2367.
- [40] Henderson, J. P., Crowley, J. R., Pinkner, J. S., Walker, J. N., Tsukayama, P., Stamm, W. E., Hooton, T. M., and Hultgren, S. J. (2009) Quantitative Metabolomics Reveals an Epigenetic Blueprint for Iron Acquisition in Uropathogenic *Escherichia coli*, *PLOS Pathogens* 5, e1000305.
- [41] Johnstone, T. C., and Nolan, E. M. (2017) Determination of the Molecular Structures of Ferric Enterobactin and Ferric Enantioenterobactin Using Racemic Crystallography, *Journal of the American Chemical Society* 139, 15245-15250.

- [42] Griffiths, G. L., Sigel, S. P., Payne, S. M., and Neilands, J. B. (1984) Vibriobactin, a siderophore from *Vibrio cholerae*, *The Journal of biological chemistry* 259, 383-385.
- [43] Zane, H. K., Naka, H., Rosconi, F., Sandy, M., Haygood, M. G., and Butler, A. (2014) Biosynthesis of amphi-enterobactin siderophores by *Vibrio harveyi* BAA-1116: identification of a bifunctional nonribosomal peptide synthetase condensation domain, *J Am Chem Soc* 136, 5615-5618.
- [44] McRose, D. L., Seyedsayamdost, M. R., and Morel, F. M. M. (2018) Multiple siderophores: bug or feature?, *Journal of biological inorganic chemistry* 23, 983-993.
- [45] Endicott, N. P., Lee, E., and Wencewicz, T. A. (2017) Structural Basis for Xenosiderophore Utilization by the Human Pathogen *Staphylococcus aureus*, *ACS infectious diseases* 3, 542-553.
- [46] Funahashi, T., Tanabe, T., Mihara, K., Miyamoto, K., Tsujibo, H., and Yamamoto, S. (2012) Identification and characterization of an outer membrane receptor gene in *Acinetobacter baumannii* required for utilization of desferricoprogen, rhodotorulic acid, and desferrioxamine B as xenosiderophores, *Biological & pharmaceutical bulletin* 35, 753-760.
- [47] Johnstone, T. C., and Nolan, E. M. (2015) Beyond iron: non-classical biological functions of bacterial siderophores, *Dalton transactions (Cambridge, England : 2003)* 44, 6320-6339.
- [48] Abergel, R. J., Wilson, M. K., Arceneaux, J. E., Hoette, T. M., Strong, R. K., Byers, B. R., and Raymond, K. N. (2006) Anthrax pathogen evades the mammalian immune system through stealth siderophore production, *Proceedings of the National Academy of Sciences of the United States of America* 103, 18499-18503.

- [49] Bergeron, R. J., Elliott, G. T., Kline, S. J., Ramphal, R., and St James, L., 3rd. (1983) Bacteriostatic and fungostatic action of catecholamide iron chelators, *Antimicrobial agents and chemotherapy* 24, 725-730.
- [50] Ohlemacher, S. I., Giblin, D. E., d'Avignon, D. A., Stapleton, A. E., Trautner, B. W., and Henderson, J. P. (2017) Enterobacteria secrete an inhibitor of Pseudomonas virulence during clinical bacteriuria, *The Journal of clinical investigation* 127, 4018-4030.
- [51] Amin, S. A., Green, D. H., Hart, M. C., Küpper, F. C., Sunda, W. G., and Carrano, C. J. (2009) Photolysis of iron–siderophore chelates promotes bacterial–algal mutualism, *Proceedings of the National Academy of Sciences* 106, 17071.
- [52] Murugappan, R., Karthikeyan, M., Aravinth, A., and Alamelu, M. (2012) Siderophore-mediated iron uptake promotes yeast-bacterial symbiosis, *Applied biochemistry and biotechnology* 168, 2170-2183.
- [53] Song, L., Zhang, Y., Chen, W., Gu, T., Zhang, S.-Y., and Ji, Q. (2018) Mechanistic insights into staphylopin-mediated metal acquisition, *Proceedings of the National Academy of Sciences* 115, 3942.
- [54] Ghssein, G., Brutesco, C., Ouerdane, L., Fojcik, C., Izaute, A., Wang, S., Hajjar, C., Lobinski, R., Lemaire, D., Richaud, P., Voulhoux, R., Espaillet, A., Cava, F., Pignol, D., Borezee-Durant, E., and Arnoux, P. (2016) Biosynthesis of a broad-spectrum nicotianamine-like metallophore in *Staphylococcus aureus*, *Science* 352, 1105-1109.
- [55] McRose, D. L., Baars, O., Seyedsayamdost, M. R., and Morel, F. M. M. (2018) Quorum sensing and iron regulate a two-for-one siderophore gene cluster in *Vibrio harveyi*, *Proceedings of the National Academy of Sciences* 115, 7581.

- [56] Koh, E.-I., Robinson, A. E., Bandara, N., Rogers, B. E., and Henderson, J. P. (2017) Copper import in *Escherichia coli* by the yersiniabactin metallophore system, *Nature Chemical Biology* 13, 1016.
- [57] Chaturvedi, K. S., Hung, C. S., Crowley, J. R., Stapleton, A. E., and Henderson, J. P. (2012) The siderophore yersiniabactin binds copper to protect pathogens during infection, *Nat Chem Biol* 8, 731-736.
- [58] Jin, Z., Li, J., Ni, L., Zhang, R., Xia, A., and Jin, F. (2018) Conditional privatization of a public siderophore enables *Pseudomonas aeruginosa* to resist cheater invasion, *Nature Communications* 9, 1383.
- [59] Chaturvedi, K. S., Hung, C. S., Giblin, D. E., Urushidani, S., Austin, A. M., Dinauer, M. C., and Henderson, J. P. (2014) Cupric yersiniabactin is a virulence-associated superoxide dismutase mimic, *ACS chemical biology* 9, 551-561.
- [60] Qi, B., and Han, M. (2018) Microbial Siderophore Enterobactin Promotes Mitochondrial Iron Uptake and Development of the Host via Interaction with ATP Synthase, *Cell* 175, 571-582.e511.
- [61] Song, E., Ramos, S. V., Huang, X., Liu, Y., Botta, A., Sung, H. K., Turnbull, P. C., Wheeler, M. B., Berger, T., Wilson, D. J., Perry, C. G. R., Mak, T. W., and Sweeney, G. (2018) Holo-lipocalin-2-derived siderophores increase mitochondrial ROS and impair oxidative phosphorylation in rat cardiomyocytes, *Proceedings of the National Academy of Sciences* 115, 1576.
- [62] Harding, C. M., Hennon, S. W., and Feldman, M. F. (2018) Uncovering the mechanisms of *Acinetobacter baumannii* virulence, *Nature reviews. Microbiology* 16, 91-102.

- [63] Lee, C.-R., Lee, J. H., Park, M., Park, K. S., Bae, I. K., Kim, Y. B., Cha, C.-J., Jeong, B. C., and Lee, S. H. (2017) Biology of *Acinetobacter baumannii*: Pathogenesis, Antibiotic Resistance Mechanisms, and Prospective Treatment Options, *Frontiers in cellular and infection microbiology* 7, 55-55.
- [64] Dickey, S. W., Cheung, G. Y. C., and Otto, M. (2017) Different drugs for bad bugs: antivirulence strategies in the age of antibiotic resistance, *Nature Reviews Drug Discovery* 16, 457.
- [65] Gehrke, S. S., Kumar, G., Yokubynas, N. A., Cote, J. P., Wang, W., French, S., MacNair, C. R., Wright, G. D., and Brown, E. D. (2017) Exploiting the Sensitivity of Nutrient Transporter Deletion Strains in Discovery of Natural Product Antimetabolites, *ACS infectious diseases* 3, 955-965.
- [66] Turner, K. H., Wessel, A. K., Palmer, G. C., Murray, J. L., and Whiteley, M. (2015) Essential genome of *Pseudomonas aeruginosa*; in cystic fibrosis sputum, *Proceedings of the National Academy of Sciences* 112, 4110.
- [67] Ghosh, M., Lin, Y. M., Miller, P. A., Mollmann, U., Boggess, W.C., Miller, M. J. (2018) Siderophore Conjugates of Daptomycin are Potent Inhibitors of Carbapenem Resistant Strains of *Acinetobacter baumannii*. *ACS Infect Dis* 4, 1529-1535.
- [68] Business Wire. Shionogi to Present Data on Cefiderocol and Baloxavir Marboxil at IDWeek 2018. (2018) <https://www.businesswire.com/news/home/20180927005497/en/Shionogi-Present-Data-Cefiderocol-Baloxavir-Marboxil-IDWeek>
- [69] Blin, K.; Wolf, T.; Chevrette, M. G.; Lu, X.; Schwalen, C. J.; Kautsar, S. A.; Suarez Durn, H. G.; de los Santos, E. L. C.; Uk Kim, H.; Nave, M.; Dickschat, J. S.; Mitchell, D. A.; Shelest, E.; Breitling, R.; Takano, E.; Yup Lee, S.; Weber, T.; Medema, M. H. (2017) “antiSMASH

4.0–improvements in chemistry prediction and gene cluster boundary identification.”  
*Nucleic Acids Research*, 45, W36–W41.

- [70] Funahashi, T.; Tanabe, T.; Maki, J.; Miyamoto, K.; Tsujibo, H.; Yamamoto, S. (2013)  
“Identification and characterization of a cluster of genes involved in biosynthesis and  
transport of acinetoferrin, a siderophore produced by *Acinetobacter haemolyticus* ATCC  
17906.” *Microbiology*, 159, 678–690.

**Chapter 2: Crystal Structure of the  
Siderophore Binding Protein BauB Bound to  
an Unusual 2:1 Complex Between  
Acinetobactin and Ferric Iron**

## 2.1 Preface

This chapter was adapted in part with permission from [Bailey, D. C., Bohac, T. J., Shapiro, J. A., Giblin, D. E., Wencewicz, T. A. & Gulick, A. M. ACS Biochemistry 47, 6653-6661 (2018)] Copyright ©2018 American Chemical Society. DCB obtained crystal structure and processed diffraction data with structure determination and refinement. TJB synthesized pre-acinetobactin and acinetobactin analogs and performed BauB fluorescent quenching binding studies. JAS expressed and purified BauB and provided initial natural acinetobactin. DEG performed all DFT calculations. TAW and AMG served as principal investigators and oversaw experimental design.

## 2.2 Abstract

The critical role that iron plays in many biochemical processes has led to an elaborate battle between bacterial pathogens and their hosts to acquire and withhold this critical nutrient. Exploitation of iron nutritional immunity is being increasingly appreciated as a potential antivirulence therapeutic strategy, especially against problematic multidrug resistant Gram-negative pathogens such as *Acinetobacter baumannii*. To facilitate iron uptake and promote growth, *A. baumannii* produces a nonribosomally synthesized peptide siderophore called acinetobactin. Acinetobactin is unusual in that it is first biosynthesized in an oxazoline form called preacinetobactin that spontaneously isomerizes to the final isoxazolidinone acinetobactin. Interestingly, both isomers can bind iron and both support growth of *A. baumannii*. To address how the two isomers chelate their ferric cargo and how the complexes are used by *A. baumannii*, structural studies were carried out with the ferric acinetobactin complex and its periplasmic siderophore binding protein BauB. Herein, we present the crystal structure of BauB bound to a bis-tridentate ( $\text{Fe}^{3+}\text{L}_2$ ) siderophore complex. Additionally, we present binding studies that show multiple variants of acinetobactin bind BauB with no apparent change in affinity. These results are



consistent with the structural model that depicts few direct polar interactions between BauB and the acinetobactin backbone. This structural and functional characterization of acinetobactin and its requisite binding protein BauB provides insight that could be exploited to target this critical iron acquisition system and provide a novel approach to treat infections caused by this important multidrug resistant pathogen.

## 2.3 Introduction

In Chapter 1 siderophore biosynthesis and transport was discussed. After export of the siderophore from the cell and subsequent extracellular iron binding, the ferric siderophore must then be transported back into the cell to facilitate nutrient acquisition. In Gram-negative bacteria, siderophore uptake is initiated by a siderophore-selective TonB outer membrane receptor.<sup>1</sup> Once transported into the periplasm, the siderophore is bound by a siderophore binding protein (SBP) that mediates the transfer of the siderophore to an ATP-binding cassette (ABC) transporter for delivery across the inner membrane and into the cytoplasm.<sup>2-4</sup> ABC transporters are transmembrane proteins that are involved in the import and export of a wide variety of molecules. Their cytoplasmic nucleotide binding domains catalyze ATP hydrolysis to drive conformational changes of the transmembrane domain that enable translocation of the ligand. ABC transporters involved in ligand import interact with a variety of substrate binding proteins that capture the ligand in the periplasm. These transfer partners can be soluble periplasmic proteins tethered either to the inner membrane through post-translational lipidation or directly to the ABC transporter.<sup>2,5</sup>

SBPs belong to a larger family of binding proteins that play many roles in transport and uptake of metals, amino acids, and peptides.<sup>6,7</sup> These proteins contain two small  $\alpha/\beta$  domains, each with a central  $\beta$ -sheet that is surrounded by  $\alpha$ -helices. The ligand binding pocket is located between

the two globular domains forming a cradle-like structure. In many members of the family, the relative orientation of the two domains is flexible, resulting from a hinge motion that accompanies substrate binding. A recently updated analysis identifies seven clusters of substrate binding proteins, with the structural motif that spans the two  $\alpha/\beta$  domains forming a distinguishing feature between different groups. SBPs belong to Cluster A, in which a central  $\alpha$ helix forms the bridge between the two smaller domains.<sup>7</sup> This relatively rigid helix limits the hinge motion between the  $\alpha/\beta$  domains and ligand-free and ligand-bound structures adopt very similar conformations regardless of ligand content.<sup>2</sup>

The human pathogen *Acinetobacter baumannii* produces three siderophores. Two siderophores, acinetobactin<sup>8,9</sup> and fimsbactin,<sup>10</sup> are produced through NRPSs, while a third is the NIS-produced baumannoferrin.<sup>11</sup> Of 15 representative *A. baumannii* strains present in the Virulence Factors in Pathogenic Bacteria database,<sup>12</sup> fimsbactin is present in only a single genome (strain ATCC17978). Both acinetobactin **1** and baumannoferrin are present in the other strains. *A. baumannii* SDF, a strain that was isolated from a body louse and which shows many unusual features,<sup>13</sup> lacks all three siderophore clusters. Acinetobactin production has been identified as being an important virulence factor in studies involving both insect and murine infection models.<sup>14</sup> Interestingly, acinetobactin is produced in an oxazoline form known as preacinetobactin **2** that can spontaneously isomerize into the mature isoxazolidinone (**Figure 2.1**). The two forms were found to be favored at acidic and basic pH, respectively, which suggests the single siderophore has evolved for use in multiple environments.<sup>15</sup>

Inhibitors of BasE, an NRPS adenylation domain required for acinetobactin biosynthesis, have been identified by rational design and empiric screening; crystal structures of the most potent inhibitors bound to BasE have been determined.<sup>16,17</sup> While showing promising biochemical

activity, the compounds failed to function with whole cells, likely due to poor cell permeability. An alternative approach to inhibition of siderophore biosynthesis includes targeting ferric-siderophore uptake and transport. A variety of acinetobactin analogues have been synthesized that illustrate that the functional groups required for iron binding are similarly important in the ability to support *A. baumannii* growth in low iron conditions.<sup>18</sup> Additionally, oxidation of the oxazoline ring of preacinetobactin to the oxazole results in an analogue that is able to compete in a dose-dependent manner with the ability of acinetobactin to support of *A. baumannii* growth in low iron conditions.<sup>19</sup> To extend these ongoing studies, we describe herein the liganded structure of the siderophore binding protein BauB from the acinetobactin uptake system. The binding pocket of BauB is populated by a bis-tridentate ferric acinetobactin complex  $[(\text{Acb})_2\text{Fe}]^-$  that is stabilized by iron(III)-coordinating bonds with catechol oxygen and imidazole nitrogen atoms from acinetobactin. This structural model is further supported by functional characterization of BauB/acinetobactin binding, including dissociation constants for BauB with apo- and holo-acinetobactin, as well as a panel of acinetobactin structural analogues that probe the key recognition elements required for binding.

## 2.4 Results and Discussion

### *Structure Determination of BauB.*

The structure of BauB was determined by molecular replacement using YclQ, the siderophore binding protein from petrobactin binding in *Bacillus subtilis*.<sup>20</sup> The model contains two chains in the asymmetric unit, each of which contains residues 39–322, with a single disordered loop. The two chains do not appear to form a dimeric structure, consistent with the monomeric gel filtration results. In chain A, residues 236–238 are disordered, while in chain B, residues 236–240 are disordered. Additionally, beyond the C-terminal Gln322 residues, each chain

contains density for three residues, Leu323-Glu324-His325, derived from the Histag used for purification. In both chains, the N-terminal 17 residues are also disordered, with Glu39 being the first observed residue. The two chains superimpose with an RMS displacement of 0.15 Å over 279 residues (**Figure 2.2**).

BauB adopts the classic two domain conformation seen previously with SBPs of the Cluster A family of substrate binding proteins.<sup>7</sup> The two globular  $\alpha/\beta$  domains are bridged by a central helix formed by residues Glu171-Thr192 (**Figure 2.3**). Use of the DALI structural similarity server identified multiple homologues within the substrate binding protein family.<sup>21</sup> The closest homologues, with sequence identities above 25%, all show RMS displacements of 1.9–3.0 Å over C $\alpha$  positions (**Table 2.1, Figure 2.4**).

#### *Active Site Contents and Structure of Acinetobactin<sub>2</sub>Fe<sup>3+</sup> Complex.*

The siderophore binding pocket of BauB shows clear density for the binding of a complex between two molecules of acinetobactin and a single ferric ion. Each acinetobactin molecule donates both catechol oxygen atoms and one nitrogen atom of the imidazole moiety to form an octahedral arrangement around the central ferric ion. The electron density unambiguously correlates with the molecular structure of the acinetobactin isomer (provided in the crystallization cocktail) and not preacinetobactin (which was not provided). This is consistent with the irreversible nature of the preacinetobactin to acinetobactin isomerization (**Figure 2.5**).

One molecule of acinetobactin is more deeply buried in the substrate binding pocket, while the second is more surface exposed (**Figure 2.6**). Specifically, for the buried molecule, only the 2,3-dihydroxybenzoate (DHB) moiety is solvent accessible while the histamine and isoxazolidinone groups are positioned below the ferric ion against the surface of BauB. In contrast,

the second acinetobactin molecule lies on the surface of the protein, with its peptide backbone exposed to solvent. We note that while the density for both molecules is unequivocal in both chains, the density is marginally more robust for the buried molecule – suggesting that there is perhaps minor flexibility in the binding position of the exposed acinetobactin molecule.

There are no direct polar interactions between the more buried acinetobactin molecule and BauB. The DHB carbonyl oxygen interacts via water molecules with the side chain of Asp83 and the main chain amides of Ile104 and Val105. The methyl group from the heterocycle projects into a hydrophobic pocket formed by Tyr84, Val264, and Tyr301. In contrast, the more exposed acinetobactin molecule makes two polar interactions with the protein. The isoxazolidinone carbonyl oxygen interacts with the side chain of Arg217 through a water molecule, and a hydrogen bond is formed between one catechol oxygen and the side chain of Tyr301. The bound holo-siderophore is presumed to exist as the monoanion  $[(\text{Acb})_2\text{Fe}]^-$ , possibly charge stabilized by a cationic Arg217, with four catecholate oxygens balanced by iron(III) and neutral donation of two imidazole nitrogens to complete the octahedral metal coordination sphere. Interestingly, in both chains, the side chain of Arg282 from a symmetry-related molecule is directed into the binding pocket and interacts with one of the catechol oxygens of the buried acinetobactin molecule to further stabilize the  $[(\text{Acb})_2\text{Fe}]^-$  monoanion. It is also noteworthy that the contribution of the N-terminal globular domain is largely hydrophobic, while the residues from the C-terminal domain are much more polar in nature. In particular, Arg217, Arg261, Tyr301, and potentially His239 all reside on the C-terminal domain.

Conformational flexibility and electrostatics are both important factors contributing to the high-affinity association of siderophore binding proteins with substrate metal complexes, as well as interfacing with membrane-embedded permeases that gate and drive the influx of substrates to

the cytoplasm. Based on the ability of *A. baumannii* to utilize both isomeric forms of acinetobactin, **1** and **2**, a high degree of substrate plasticity for BauB is anticipated.<sup>15</sup> In the homologous SBP CeuE from *Campylobacter jejuni*, the side chains of His227 and Tyr288, the homologue of BauB His239 and Tyr301, form direct interactions with the ferric ion in complexes with catecholbased tetradentate ligands derived from enterobactin fragments that do not complete the octahedral coordination (**Figure 2.7**).<sup>22,23</sup> The conservation of His239 and Tyr301 suggests that BauB is poised to capture ferric complexes with alternate siderophore ligands that do not completely coordinate the central ion, perhaps endowing *A. baumannii* with the ability to interact with other siderophores that it encounters in the environment. Of note, His239 in BauB is positioned on a poorly ordered loop, suggesting an ability to adopt distinct conformations in the presence of different ligands (**Figure 2.7**).

Siderophore binding proteins with strongly anionic or cationic binding pockets are often found to counterbalance the net charge of cognate siderophore-iron complexes (anionic staphyloferrin A-Fe, cationic HtsA; anionic staphyloferrin B-Fe, cationic SirA).<sup>24,25</sup> The base of the *Bacillus subtilis* FeuA SBP, which has been structurally characterized bound to ferric enterobactin, shows a strikingly basic binding pocket with two lysine and two arginine side chains directed into the binding pocket.<sup>26</sup> The 1:1 tricatecholate enterobactin-Fe complex presumably binds as the trianion [EntFe]<sup>3-</sup>, charge stabilized by protonated Lys and Arg residues lining the FeuA siderophore binding pocket. These residues are not conserved in BauB, as has also been observed with other catechol binding SBPs.<sup>26</sup> In contrast, the base of the pocket in BauB is mostly hydrophobic. In particular, Tyr84 and Pro124 in BauB are replaced by lysine residues in FeuA, while Leu203 is replaced by an arginine.

Like BauB, the siderophore binding pocket of FhuD2 does not exhibit the basic nature of FeuA.<sup>27,28</sup> However, the pockets of BauB and FhuD2 are quite different in composition with BauB being much more hydrophobic. The pocket of FhuD2 is polar, with multiple tyrosine, threonine, and tryptophan residues donating hydrogen bonding capabilities to interact with polar hydroxamate ligands such as ferrioxamine B. These polar residues are distributed across the binding pocket from both the N- and C-terminal globular domains.

### ***DFT Calculations of the Acinetobactin<sub>2</sub>Fe<sup>3+</sup> Complex.***

We next explored the ligand complexes using density functional theory (DFT) calculations to assess the stability of the observed 2:1 complex with other potential isomers. The metal coordination mode and ligand/metal stoichiometry observed in the BauB-bound Acb<sub>2</sub>Fe complex is consistent with reported solution-phase fluorescence and optical absorbance spectroscopic titrations.<sup>15,18,19</sup> The presence of stable metal coordinate bonds through two bidentate catecholates is consistent with the broad metal–ligand charge transfer bands at ~570 nm in the optical absorbance spectrum.<sup>15,18,19</sup> The *cis*-[Acb<sub>2</sub>Fe]<sup>−</sup> isomeric form present in the BauB substrate binding site represents one of many possible geometric and optical isomeric forms of the metal complex invoking metal coordinate bonds with the catecholate and imidazole moieties. The distorted octahedron formed at the iron(III) coordination sphere is isomeric with ML<sup>a</sup><sub>4</sub>L<sup>b</sup><sub>2</sub> octahedral complexes, where L<sup>a</sup> represents the catecholate oxygens and L<sup>b</sup> represents the imidazole nitrogens. For ML<sup>a</sup><sub>4</sub>L<sup>b</sup><sub>2</sub> complexes, two isomers, *cis* and *trans*, are possible. The *cis*-[FeO<sub>4</sub>N<sub>2</sub>]<sup>−</sup> orientation is accommodated by the BauB substrate binding pocket; thus, we will refer to the holo-siderophore as *cis*- [Acb<sub>2</sub>Fe]<sup>−</sup> as the apparent BauB substrate.

The siderophore, anguibactin, produced by the fish pathogen *Vibrio anguillarum* is structurally similar the preacinetobactin (**2**) isomeric form with the methyloxazoline replaced by a

thiazoline heterocycle. Anguibactin has been crystallized as the gallium(III) chelate in a  $\text{Ga}_2\text{Anguibactin}_2$  stoichiometry.<sup>29</sup> The  $\text{Ga}_2\text{Anguibactin}_2$  structure is bioctahedral with bridging methanols in the Ga coordination sphere. There are many potential stoichiometric, geometric, and optical isomers for the acinetobactin-Fe complex, including structures related to the  $\text{Ga}_2\text{Anguibactin}_2$  structure that may be present in solution. It is likely that BauB selectively recognizes the *cis*- $[\text{Acb}_2\text{Fe}]^-$  isomeric form. We modeled this isomeric form and others using DFT calculations and found that structures closely related to the *cis*- $[\text{Acb}_2\text{Fe}]^-$  are predicted to be stable in the gas phase (**Figures 2.8, 2.9**). Even if *cis*- $[\text{Acb}_2\text{Fe}]^-$  is not prevalent in solution, it is possible that upon BauB binding the coordination mode is shifted to the experimentally observed *cis*- $[\text{Acb}_2\text{Fe}]^-$ . Such protein-induced shifting of metal coordination mode has been observed for the binding of holo-vibrobactin by human siderocalin, where the phenolate-oxazoline bidentate ligand coordination mode predominates in solution, while the bidentate catecholate mode is favored in the siderocalin substrate binding pocket.<sup>30</sup> Binding of apo-siderophores by periplasmic siderophore binding proteins and siderocalins has also been observed. In the case of human siderocalin, the substrate binding pocket can serve as a template for small dietary catechols to preorganize the ligands for iron sequestration as a strategy for nutritional immunity and possibly iron acquisition.<sup>31</sup>

### ***Binding Studies of Acinetobactin<sub>2</sub>Fe<sup>3+</sup> to BauB.***

To investigate the substrate binding specificity of BauB in solution, we performed intrinsic Trp fluorescence quenching studies in the presence of apo- and holo-acinetobactin. Both forms of the siderophore were bound by BauB with nanomolar affinity, with a slight preference for the holo-siderophore (apparent  $K_d = 160 \pm 80$  nM) over the apo-siderophore (apparent  $K_d = 300 \pm 100$  nM) (**Table 2.2**). We probed key structural features of acinetobactin required for molecular recognition



by BauB, including the site and degree of hydroxylation on the phenyl ring and the presence of the imidazole heterocycle.<sup>18</sup>

***BauB Binds Both the apo and holo Forms of Acinetobactin.***

We therefore chose to use only apo-siderophore variants for comparison since some structural modifications result in loss of iron chelation. We also note that we have obtained diffraction quality crystals of BauB from crystals that were grown in the presence of apo-acinetobactin. We were able to fully resolve the structure, but electron density of the substrate binding pocket did not show full occupancy of an acinetobactin molecule. A peak of ambiguous electron density was observed in the binding pocket that could fit the central isoxazolidinone ring with no density for the flanking DHB and histamine groups. Whether this represents limited occupancy or movement of the aromatic groups in the absence of iron is unclear but it is intriguing to consider the possibility that the apo-acinetobactin core is bound flexibly with iron binding subsequently ordering the histamine and DHB rings.

All of the siderophores caused dose-dependent fluorescence quenching and curve fitting provided apparent  $K_d$  values ranging from 160–520 nM, with no statistical significance between analogues (**Table 2.2, Figure 2.10**). It appears that BauB can bind promiscuously to the acinetobactin scaffold, which is consistent with related periplasmic siderophore binding proteins.<sup>17</sup> Presumably, the outer membrane receptor BauA imparts selectivity for acinetobactin import, mitigating the need for a second level of high specificity filtering in the periplasm (**Figure 2.11**). Although compounds **1**, **1-Fe**, and **3–9** all appear to bind BauB, it is less clear if they share the same binding mode or if all binding modes will lead to influx across the cytoplasmic membrane. The only strong correlation observed for the acinetobactin analogues is that the ability to form a stable complex with iron(III) is required for *A. baumannii* utilization (**Table 2.2**).<sup>18</sup>

## 2.5 Outlook and Conclusions

We report here the structural and functional analysis of BauB, the SBP from the acinetobactin uptake pathway in *A. baumannii*. Our studies show that BauB adopts the typical Class A substrate binding fold, with a central  $\alpha$ -helix spanning the smaller N- and C-terminal domains. The ligand is bound in a central pocket between the two domains that is contributed by mostly hydrophobic residues. The structure of BauB illustrates an unusual  $[\text{Acb}_2\text{Fe}]^-$  complex, in which two acinetobactin molecules each provide two catechol oxygens and an imidazole nitrogen to coordinate the central iron. To our knowledge, this is the first observation of a 2:1 complex of a natural ligand and iron that has been observed in a crystal structure of a siderophore binding protein. These studies continue our ongoing effort to functionally characterize the iron acquisition pathways of *A. baumannii*. The residues of BauB that interact with the ligand include hydrophobic residues that are distributed in sequence across the length of the protein and include few direct interactions with the ligand. The lack of direct interactions enables multiple analogues of acinetobactin to bind BauB with roughly similar affinities and may relate to the ability of bacteria to tune their iron acquisition systems to enable utilization of siderophores produced by other species. The broad substrate binding capability of BauB presents the opportunity for exploiting the acinetobactin transport pathway to develop siderophore-based therapeutics, including antivirulence agents that inhibit the acinetobactin pathway and acinetobactin conjugates including imaging probes for infection diagnostics and antibiotic conjugates for targeted anti-*A. baumannii* therapeutic agents. As noted, we have collected data on the structure of BauB that was crystallized in the presence of acinetobactin in the absence of iron that shows either binding to core of the siderophore or incomplete occupancy. Because of the comparable affinities of BauB for the apo- and holo- forms, we favor the former scenario, in which the apo-ligand binds to the hydrophobic

base of the BauB pocket and the chelating groups adopt a dynamic configuration in the absence of iron. This is further supported by the similar affinity of BauB toward the acinetobactin analogues that we tested. We have additionally attempted to crystallize BauB with the oxazoline pre-Acb but have not yet been able to grow diffraction quality crystals. Continued efforts to crystallize BauB with preAcb or additional acinetobactin variants may provide further clues to the features that enable binding to BauB. While the histamine and isoxazolidinone are buried in one of the two acinetobactin molecules, the DHB moieties are exposed in both molecules within the  $[\text{Acb}_2\text{Fe}]^-$  complex and may provide a locus for attachment of relevant functional groups to achieve these alternate purposes.

## 2.6 Materials and Methods

### *Cloning, Expression, and Purification.*

Multiple protein constructs were designed for use in the structural and functional studies. The 969-bp *bauB* gene from *Acinetobacter baumannii* (Genbank Accession no. AAT52185) was first subcloned into a pET24b expression vector using restriction enzyme-based cloning. Expression of the full-length protein resulted in most of the protein purifying as soluble aggregate, with a small proportion isolated as a folded protein. The soluble protein migrated on analytical gel filtration with an elution volume consistent with a monomer (**Figure 2.12**). Analysis of the fulllength protein construct (1–322) revealed a putative signal peptide (1–22) at the N-terminus directing trafficking to the periplasm.<sup>32,33</sup>

A second expression construct was designed without the putative signal peptide that encoded the mature protein. Following the starting Met residue, the final expression construct contained BauB residues 23–322 and a C-terminal 6 × His tag (···LEHHHHHH). Of note, Cys23 was predicted to be a N-terminal lipidation site<sup>34,35</sup> and the presence of Asp at position 24 suggests

that, upon cleavage of the signal peptide in the periplasm, the protein is natively retained at the periplasmic surface of the cytoplasmic membrane according to the “D+2 Rule”.<sup>36,37</sup>

*E. coli* BL21(DE3) was transformed with the expression plasmid for protein production. Cells were grown to an OD<sub>600</sub> of 0.6–0.8 at 37 °C (250 rpm) and induced to express BauB with the addition of 500 μM IPTG. Following induction, the cells were incubated at 16 °C overnight (≈18 h) before being harvested by centrifugation at  $6 \times 10^3$  g at 4 °C for 15 min. The cell pellet was flash frozen in liquid N<sub>2</sub> and stored at –80 °C.

The frozen cell pellet (≈10 g) was resuspended in 100 mL of lysis buffer (50 mM Tris, 300 mM NaCl, 0.2 mM TCEP, 5% glycerol, 20 mM imidazole, pH 8.0) containing protease inhibitor cocktail, DNase (10 μg/mL), and lysozyme (1 mg/ mL) and incubated at 4 °C for 30 min. Cell lysis was further ensured by sonication (5 × 30 s cycles). The cell slurry was separated by ultracentrifugation at  $185 \times 10^3$  g for 40 min at 4 °C. The supernatant was further clarified via filtration over a 0.45 μm polysulfone membrane. The clarified supernatant was subjected to immobilized metal affinity chromatography (IMAC) by passing it over two 5 mL Ni<sup>2+</sup>-NTA columns in series. Bound proteins were eluted by passing lysis buffer plus 300 mM imidazole over the columns. To remove imidazole, the protein was dialyzed (12 kDa MWCO) overnight at 4 °C in 50 mM Tris, 300 mM NaCl, 0.2 mM TCEP, 0.5 mM EDTA, 5% glycerol, pH 8.0. The dialyzed protein sample was concentrated using a centrifugal filter (10 kDa MWCO) before carrying out preparative size exclusion chromatography (SEC). Protein was eluted over the SEC column (HiLoad 16/60 Superdex 200, GE Healthcare) using a buffer of 50 mM Tris, 150 mM NaCl, 0.2 mM TCEP, pH 8.0 at 1 mL/min (**Figure 2.12**). The desired fractions containing pure BauB as indicated by SDS-PAGE were combined, concentrated to ≈60 mg/mL using a 10 kDa MWCO centrifugal filter, flash frozen in liquid N<sub>2</sub>, and stored at –80 °C.

An N-terminally tagged protein, lacking the signal sequence, was also produced and used in binding studies. N-His6-BauB was expressed from a pET28bTEV plasmid in *E. coli* BL21 (DE3). Briefly, *E. coli* BL21 (DE3) transformed with the BauB expression plasmid were grown in Terrific Broth at 37 °C in a 3 L baffled flask, in the presence of 50 µM kanamycin to an OD<sub>600</sub> of ~0.5. The culture flask was cooled to 20 °C, and BauB expression was induced by the addition of 0.5 mM IPTG (final concentration). Cells were grown overnight (~12 h) at 20 °C. Cells were harvested via centrifugation at 4 °C for 30 min (all remaining steps were carried out at 4 °C). Cells were washed with lysis buffer (50 mM potassium phosphate pH 8.0, 500 mM NaCl, 5 mM BME, 20 mM imidazole, 10% glycerol) and flash frozen in liquid N<sub>2</sub> (40 mL total volume). The frozen cell pellet was thawed and lysed by two passes through an Emulsiflex C5 (Avestin). The lysate was clarified by ultracentrifugation at 50000g for 35 min. The supernatant was passed through NiNTA resin and eluted with 300 mM imidazole in lysis buffer. Elution fractions were analyzed by SDS-PAGE with visualization by Coomassie blue staining. Fractions containing pure N-His6-BauB were combined, dialyzed (50 mM potassium phosphate pH 8.0, 150 mM NaCl, 1 mM DTT, 5% glycerol), and concentrated via centrifugal filtration. Protein purity was analyzed by SDS-PAGE with visualization by Coomassie blue staining. Protein identities were confirmed by ESI-MS. Purified protein was flash frozen in liquid N<sub>2</sub> at 180 µM and stored at -80 °C. The final protein used in the binding studies contained the His6 tag and TEV cleavage site upstream of C23 from the BauB sequence.

### ***Crystallization and X-ray Diffraction Data Collection.***

Two protein crystals were used to collect a complete data set for structure determination. Crystallization and X-ray data collection parameters for both data sets are summarized in **Table 2.3**. Briefly, BauB was exchanged into a minimal crystallization buffer, and ferric acinetobactin

(Acb<sub>2</sub>Fe) in DMSO was added and incubated on ice for 1 h. Acb was isolated from *A. baumannii* ATCC 17978 and purified by RP-C18 prep HPLC as described previously.<sup>15</sup> Acb<sub>2</sub>Fe was prepared by treating Acb with Fe(acac)<sub>3</sub> as described previously.<sup>15</sup> The sample was briefly centrifuged to pellet any precipitate before being crystallized by hanging-drop vapor diffusion. Initial crystallization conditions were identified using an in-house 120-condition screen, in which BauB formed thin needle/platelike crystals in cocktail conditions containing medium to high molecular weight polyethylene glycol (PEG 4K, 8K, or PEG MME 5K) over a relatively wide pH (6.0–9.0) range. Crystals were flash frozen in liquid N<sub>2</sub> and shipped to synchrotron beamlines for remote diffraction data collection.

#### ***Diffraction Data Processing, Structure Determination, and Refinement.***

BauB crystallized in a monoclinic space group P21 with  $\beta = 90^\circ$ . Careful analysis showed that each data set was not twinned nor could higher symmetry be imposed on the data. Scaling the data in the orthorhombic space group P222 resulted in Rmerge values of 0.25, compared to 0.09 determined with the monoclinic space group. The structure of ferric Acb bound BauB was initially solved by molecular replacement to 1.9 Å resolution employing Data Set 1 (**Table 2.3**) using the protein atoms of YclQ35 (PDB 3GFV, 33% sequence identical) as the search model. Due to the thin needle/plate-like morphology of the crystals, it was difficult to achieve a high completeness from a single crystal despite collecting images over an oscillation range of 360°. We therefore merged the data from the initial crystal with data from a second crystal. To do this, the two integrated reflection files from MOSFLM were scaled together with AIMLESS of the CCP4 software suite. Although this second data set was weaker in overall intensity, the increase in completeness was viewed as a reasonable compromise with the resulting poorer merging statistics from combining the two data sets. Processing statistics for the individual (**Table 2.3**) and combined

(Table 2.4) data sets are provided. The merged data set was then used to refine the structure of BauB complexed with Acb2Fe. All data processing and merging was carried out using iMosflm,<sup>38</sup> molecular replacement employing Phaser,<sup>39</sup> automated model building using PHENIX.Autobuild,<sup>40</sup> manual model building and refinement utilizing Coot,<sup>41</sup> and automated refinement employing PHENIX.Refine.<sup>42</sup> Structure-based alignments were performed with PROMALS 3d.<sup>43</sup> The atomic coordinates and structure factors for BauB complexed with ferric Acb have been deposited in the PDB (6MFL).

### ***BauB Binding Studies.***

Acinetobactin (**1**) and analogues (**3–9**) were prepared as described previously.<sup>18</sup> A stock solution of N-His6-BauB, thawed on ice, was prepared at 400 nM in assay buffer (25 mM Tris-HCl, 8 g/L NaCl, 0.2 g/L KCl, pH 7.4). For each experiment, 300  $\mu$ L of the BauB stock solution was transferred to a fluorescence cuvette (HellmaAnalytics High Precision Cell cuvette made of Quartz SUPRASIL; light path 10  $\times$  2 mm) in the presence of substrate (compounds **1**, **1-Fe**, and **3–9**) at variable concentrations ranging from 100–1200 nM. An emission spectrum was taken using a PerkinElmer LS 55 Luminescence Spectrometer (slit width 10 nm; scan speed 400 nm/min) at 300–400 nm using an excitation wavelength of 280 nm. Fluorescence intensity at 320 nm versus substrate concentration (nM) was plotted. The apparent K<sub>d</sub> was calculated by nonlinear regression using a one binding site model in GraphPad Prism v7.0b (**Figure 2.10**). All experiments were performed in duplicate as independent trials.

### ***DFT Calculations.***

For starting geometry of the bimetallic complexes, we chose the crystal structure of the acinetobactin<sub>2</sub>FeIII(S = 5/2) complex bound to BauB. Conformer spaces for complexes were

explored by Monte Carlo/ MMFF molecular mechanics/dynamics, and first step of optimization was performed by using the PM3d semiempirical algorithm (Spartan Linux v10, WaveFunction, Inc.). Using either as an input, we employed DFT (density functional theory, Gaussian 09, Gaussian Inc.) for calculations by using the PBE0 hybrid functional (PBE1PBE in Gaussian parlance) with basis sets Def2-SVP and Def2-TZVP. Minima were optimized at the level PBE0/Def2-SVP, and single-point energies were calculated at level PBE0/Def2-TZVP, with scaled thermal-energy corrections from scaling factors for B3LYP/6-31G(d,p).<sup>44</sup> Solvent-based single-point energies were calculated at the same level by using the CPCM polarizable conductor calculation model for water and using the Universal Force Field for atomic radii.<sup>45</sup> DFT was selected for computational efficiency and integrity.<sup>46,47</sup> Functional and basis sets were chosen for use with the ferric complexes.<sup>48-50</sup>



## 2.7 Figures and Tables

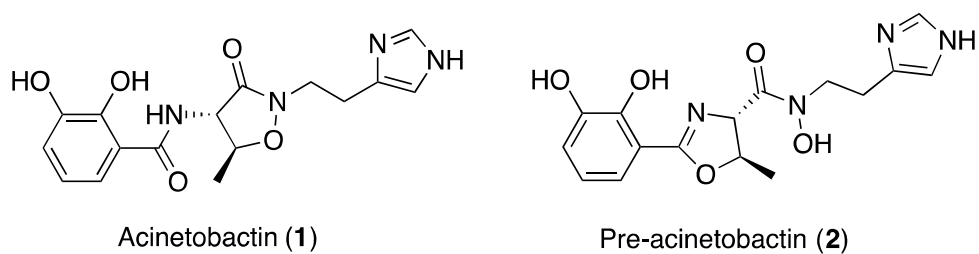


**Figure 2.1.** Chemical structures of acinetobactin (1) and pre-acinetobactin (2) from *A. baumannii*.

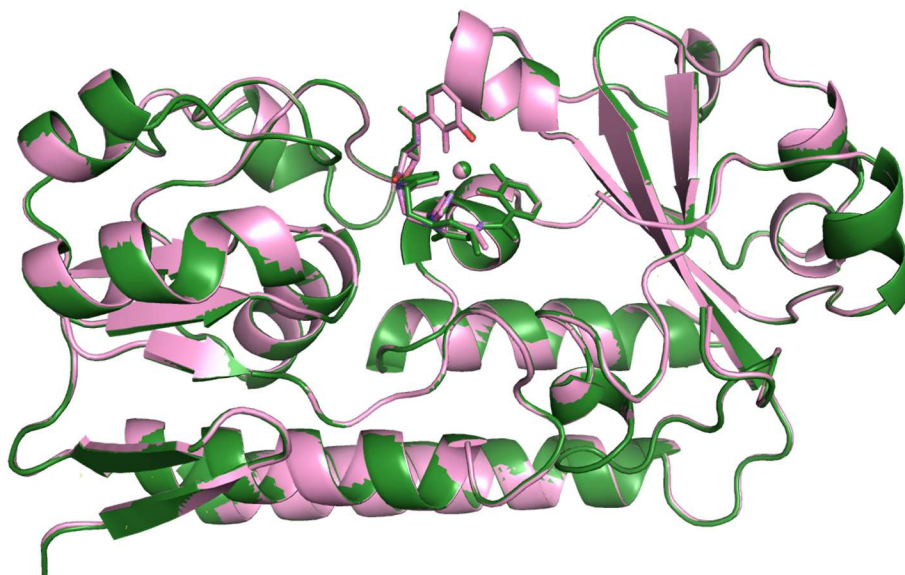


**Figure 2.2.** Overlay of two BauB chains (chain A, pink; chain B, green) superimposed with RMS displacement of 0.15 Å over 279 residues.

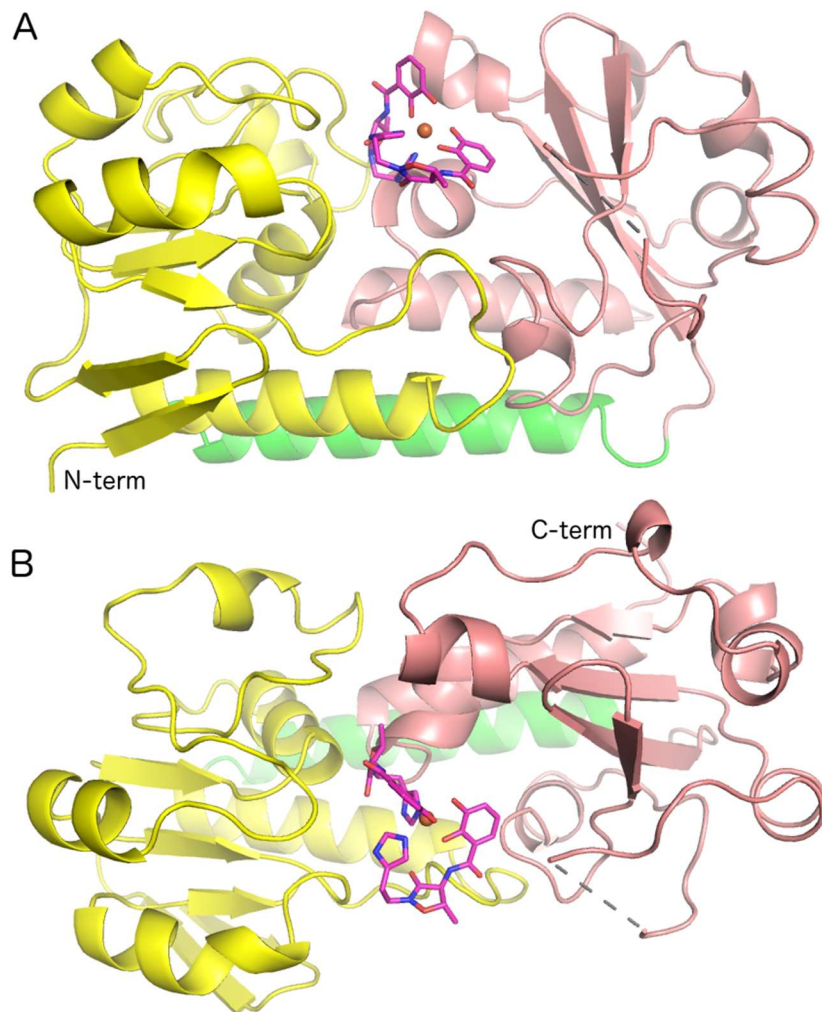


**Figure 2.3.** Ribbon representation of BauB bound to the Acb2•Fe complex. (N-domain, yellow; C-domain pink;  $\alpha$  helix green). Two views are shown, approximately 90° apart rotated around the horizontal axis. The single gap in the protein between residues 235 and 239 is indicated with the dashed line.

PDB	% ID	RMS Disp.	Residues Aligned	Name
3GFV	36	2.0	276/286	<i>B. subtilis</i> YclQ
3TEF	32	2.1	274/279	<i>V. cholerae</i> VctP <i>V. cholera</i>
5AD1	29	2.2	272/290	<i>C. jejuni</i> CeuE
4JCC	29	1.9	270/284	<i>S. pneumoniae</i> PiuA
4MX8	26	2.3	272/302	<i>X. cellulosilytica</i> Periplasmic BP
3MWF	26	3.1	258/292	<i>S. aureus</i> SirA
3TNY	26	3.2	263/280	<i>B. cereus</i> YfiY
2WHY	21	3.2	266/283	<i>B. subtilis</i> FeuA
4FNA	21	3.2	252/278	<i>S. aureus</i> FhuD2

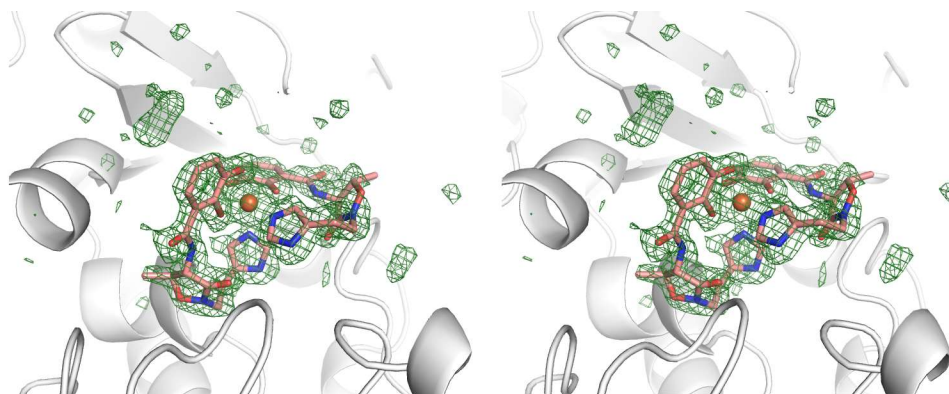
The top hits the search for structural homologs were filtered to remove PDB coordinates for identical proteins with multiple ligands. FeuA and FhuD2 were not among the most highly homologous but are included for comparison with the discussion in the main text.

**Table 2.1.** Structural homologs of BauB

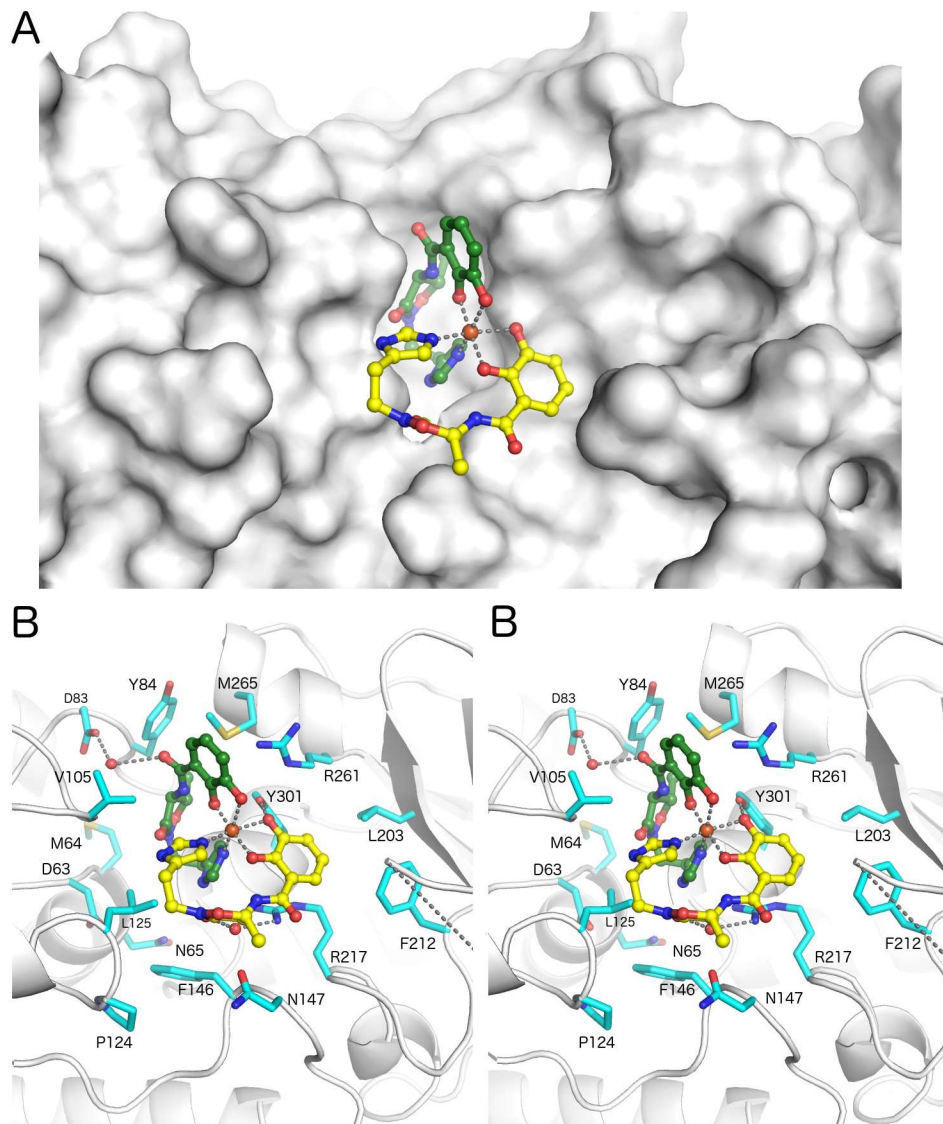
Abaum_BauB	MNWKKKYGGVALIIAAAVTLQACDQKVADTTQASQKLA	EPITVKHAL-----G	48
3MWF SaSirA	MNKVIKMLVVTLAFLLVLGACSGNSNKQSSDRKDKKE	TTSIKHAM-----G	45
3TEF VcVctF	MVLIIVRTLMLRISIKMIPLAYLNHLWKEHMKSRIHCAALGLLAAFAAQA	ETVTIEHRL-----G	60
3GFV BsYclQ	MRSMKKFALLFIALVTAVVISACGNQSTSSKGSDTK	KEQITVKHQL-----D	47
4MX8 XcPBP	MSRTRPIARASMLAVLALTLAACAPSSAGTADDSAETT	PATASYTWRNRTATEEGADPVYE	61
4JCC SpPiuA	MKTSLKLYFTALVASFLLLLGACSTNSSTSQTTETSS	SAPTEVTIKSSL-----D	49
5AD1 CjCeue	MKKS LVFAFFAFLSLILITACNSNSENNASTTKTNTATVKV	LPISMSDEGDSFLVKDSL-----G	62
2WHY BsFeuA	MKKISLTLILLLALTAACGSKNESTASKASGTASEK	KKKIEYLD-----K	46
4FNA SaFhuD2	MKLLLLPLIIMLLVLAACGNQGKKN	NKAETKSYKMDD-----G	38
Abaum_BauB	--TTVIDHLPQR-VAVLDM-NE-ADFLDQLNVP--IMGM-PKDY----	VP-HFLEKYKKAQI-QDLGA-IVQ-	106
3MWF SaSirA	--TTEIKGKPKRVVVTLYQ-GA-TDVAVSLGVKK-PVGA-VESWTQKPKFEEYIKNDL--KDT-KIVGQQEPA-		105
3TEF VcVctF	--KTTLEQKPKR-VVVIQV-GA-LDAIDSFQIE--PVAV-SKFDG---TP-DYLAKYK-SDKY-PSAGS-LFE-		118
3GFV BsYclQ	KNGTKVPKNPKK-VVVFDF-GS-LDTLKLGLDDIVAGL-PKQV----LP-KYLSKFK-DDKY-ADVGS-LKE-		108
4MX8 XcPBP	ETTVEVPVDPQR-IVVFDMAA-LDTIGALGGE--IAGA-PLDS---VP-DYLEEYL-ADDA-FNAGT-LFE-		120
4JCC SpPiuA	-EVLKLSKVPKPKK-IVTFDL-GA-ADTIRALGFKNIVGMMPTKTT---VP-TYLKDLV-GTVKKNVGSMMKEP		108
5AD1 CjCeue	-ENKKIPKNPSK-VVILDLLGI-LDTFDALKLNDKVVGV-PAKN----LPKYLQQQF--KNK-PSVGG-VQQ-		119
2WHY BsFeuA	--TYEVTVPQTK-IAITGSVESMMEDAKLLDVH--PQGA-ISFSGK--FP-DMFKDIT--DKA-EPTGE-KME-		105
4FNA SaFhuD2	-KTVDIPKDKPKR-IAVVAP-TY-AGGLKLGAN--IVAV-NQQV---DQS-KVLKDKFKGV---TKIGD-----		93
Abaum_BauB	PNMERIYALKPD-LILMTP-LHVNQYQE-LSKIAPTIIHYDINFN	NSESNHIGLVKDHM-MTLG-KIFN--KED-	172
3MWF SaSirA	PNLEEISKLKPD-LIVASKVRNEKVYDQQLSKIAPTIVSSTDTV-----FKFKDIT-KLMG-KALG--KEK-		163
3TEF VcVctF	PDFETIYTQKPD-LIVIGP-RASKSYDE-LSKIAPTIVFAAEA---DQGYWESTQQQW-RNLG-KVFA--IEP-		181
3GFV BsYclQ	PDFDKVAELDPD-LIIISA-RQSESYKE-FSKIAPTIIYLGVDTA---KYMESFKSDA-ETIG-KIFD--KED-		170
4MX8 XcPBP	ADLIAIEAQQPD-LIVVGG-RSSGLWAD-LNEIAPTIDLSLRG----SYLDTLEQNT-TFLG-KVLG--AEA-		183
4JCC SpPiuA	PDLEAIAALEPDDLIIASP-RTQKFDKFKKEIAPTIVLFQASKD---DYWTSTKANIEESLA-SAFGETGTQK		171
5AD1 CjCeue	VDFEAINALKPD-LIIISG-RQSKFYDK-LKEIAPTLFVGLDNA---NFLSSFENNV-LSVAKKLYG--LEK-		186
2WHY BsFeuA	PNIEKILEMCPD-VILASTKFPKTLQK-ISTAGTTIPVSHISS-----NWKENMMLLA-QLTG--KEK-		163
4FNA SaFhuD2	GDVEKVAKEKPD-LIIVYS--TDKDIK-YQKVAPTVVVDYNKH-----KYLEQQ-EMLG-KIVG--KED-		150
Abaum_BauB	LARQKVSELDE-QVK-QVQAVTA-----NRPERALVVL--HNN-GAFSNEFIQ-----S-RYGF-IFNNAFGV		227
3MWF SaSirA	EAEDLLKKYDD-KVA-AFQKDAKAKYKDAWPLKASVVN--FRA-DHTRİYAG-----G-YAGE-IL-NDLGF		222
3TEF VcVctF	AVEAKIEQVDA-QFK-SIMQYNQ-----QHKSDAMLVN--SSG-GNLTTFGAN-----S-RFSS-VY-KDFGF		236
3GFV BsYclQ	KVKDELANIDHHSIADDVKKTAE-----KLNKNGLVIM--AND-GKISAFGPK-----S-RYGL-IH-DVFGV		225
4MX8 XcPBP	EAESVLAELEA-GIA-EAKAAVT-----EASGTGLGIM--VSG-GQLSALSPNTGNDPRGARGGL-IY-DVFGV		243
4JCC SpPiuA	KAKEELAKLDE-SIQ-EVATKNE-----SSDKKALAIL--LNE-GKMAAFGAK-----SRFFSF-LY-QTLKF		226
5AD1 CjCeue	EALEKISDIKN-EIE-KAKSIV-----DEKDKKALIIILLTNSNKNKISAFGPQ-----S-RFGI-IH-DVLGI		235

2WHY BsFeuA	KAKKI <b>IADYEQ</b> -DLK-ETKTKIN---DKAKDSKAL <b>VIR</b> --IRQ-GNIYI <b>YPEQ</b> -----V-YFNST <b>LY</b> -GDLGL	222
4FNA SaFhuD2	KVKAWKKD <b>WEE</b> -TTA-KDGKEIKKAI--GQDATV <b>S</b> LFD--EFD-KKLY <b>TY</b> GDN-----WGRGGE <b>VLY</b> -QAFGL	210
Abaum_BauB	KPASG-----VVD <b>TSL</b> <b>H</b> Q <b>P</b> ISSE-FI <b>I</b> KKAD <b>P</b> D <b>I</b> LY <b>V</b> DR <b>T</b> AV <b>M</b> EH-RPNINAAS <b>VE</b> -NPL--LRQ <b>T</b> KA <b>W</b> KNG	290
3MWF SaSirA	KRNKDLQKQVDNGKD-IIQLTS <b>K</b> E-S <b>I</b> PLMN-AD <b>H</b> IF <b>V</b> VKSDPN <b>A</b> KD-AALV <b>K</b> KT <b>ES</b> E <b>W</b> TSS <b>K</b> EW <b>K</b> NLD <b>A</b> V <b>K</b> NN	292
3TEF VcVctF	SETVPV----SK <b>ES</b> S- <b>H</b> GD <b>L</b> IS <b>F</b> E-Y <b>I</b> REHN- <b>P</b> KT <b>L</b> L <b>V</b> VD <b>R</b> DK <b>V</b> V <b>T</b> K-GETN <b>I</b> RQ <b>T</b> F <b>E</b> -NDL--V <b>K</b> AT <b>T</b> A <b>Y</b> K <b>N</b> G	299
3GFV BsYclQ	APADQN----IKAST <b>H</b> Q <b>Q</b> SV <b>S</b> Y <b>E</b> -Y <b>I</b> SK <b>T</b> N- <b>P</b> D <b>Y</b> L <b>F</b> V <b>I</b> DR <b>G</b> T <b>A</b> IG <b>E</b> --TS <b>S</b> T <b>K</b> Q <b>V</b> VE-NDY--V <b>K</b> N <b>V</b> N <b>A</b> V <b>K</b> N <b>G</b>	287
4MX8 XcPBP	QP <b>V</b> LED----IKAA-T <b>H</b> GE <b>P</b> IS <b>F</b> E-F <b>L</b> LE <b>H</b> D- <b>P</b> Q <b>W</b> L <b>V</b> W <b>V</b> DR <b>D</b> AAT <b>G</b> A <b>E</b> G <b>A</b> Q <b>A</b> K <b>V</b> L <b>D</b> - <b>N</b> E <b>I</b> --V <b>N</b> R <b>T</b> A <b>A</b> T <b>E</b> D	307
4JCC SpPiuA	K <b>P</b> T <b>D</b> T <b>K</b> ----F <b>E</b> D <b>S</b> R <b>H</b> Q <b>Q</b> EV <b>S</b> F <b>ES</b> SV <b>K</b> E <b>I</b> N- <b>P</b> D <b>I</b> L <b>F</b> V <b>I</b> N <b>R</b> T <b>L</b> A <b>I</b> G <b>D</b> N <b>S</b> S <b>S</b> N <b>D</b> G <b>V</b> L <b>E</b> - <b>N</b> A <b>L</b> -- <b>I</b> A <b>E</b> T <b>P</b> A <b>A</b> K <b>N</b> G	289
5AD1 CjCeuE	NAV <b>D</b> EN----IK <b>V</b> GT- <b>H</b> G <b>K</b> S <b>I</b> N <b>S</b> E-F <b>I</b> L <b>E</b> K <b>N</b> N <b>P</b> D <b>Y</b> I <b>F</b> V <b>V</b> DR <b>N</b> V <b>I</b> L <b>G</b> N-K <b>E</b> R <b>A</b> Q <b>Q</b> G <b>I</b> L <b>D</b> - <b>N</b> A <b>L</b> --V <b>A</b> K <b>T</b> K <b>A</b> A <b>Q</b> N <b>K</b>	297
2WHY BsFeuA	KAPNE <b>V</b> KA---AK <b>A</b> Q-ELLIS <b>L</b> E <b>K</b> L <b>L</b> SE <b>M</b> N- <b>P</b> D <b>H</b> IF <b>V</b> Q <b>F</b> S <b>D</b> -DEN <b>A</b> D <b>K</b> P <b>D</b> AL <b>K</b> D <b>L</b> E <b>K</b> - <b>N</b> P <b>I</b> -- <b>W</b> K <b>S</b> L <b>K</b> A <b>V</b> K <b>E</b> D	284
4FNA SaFhuD2	K <b>M</b> Q <b>P</b> E <b>Q</b> Q <b>K</b> --L <b>T</b> A <b>K</b> A-G <b>W</b> A <b>E</b> V <b>K</b> Q <b>E</b> - <b>E</b> I <b>E</b> K <b>Y</b> A- <b>G</b> D <b>Y</b> I <b>V</b> S <b>T</b> SE <b>G</b> K-----P <b>T</b> P <b>G</b> Y <b>E</b> S-T <b>N</b> M-- <b>W</b> K <b>N</b> L <b>K</b> A <b>T</b> K <b>E</b> G	268
Abaum_BauB	R <b>V</b> I-F <b>V</b> D <b>A</b> D <b>A</b> W <b>H</b> T <b>T</b> - <b>A</b> A <b>S</b> P <b>T</b> S <b>L</b> --K <b>I</b> V <b>M</b> E <b>D</b> -V <b>K</b> K <b>G</b> Y <b>Q</b>	322
3MWF SaSirA	Q <b>V</b> S <b>D</b> D <b>L</b> D <b>E</b> I <b>T</b> W <b>N</b> L <b>A</b> -G <b>G</b> Y <b>K</b> S <b>S</b> --L <b>K</b> L <b>I</b> D <b>D</b> D <b>L</b> Y <b>E</b> K <b>L</b> N <b>N</b> I <b>E</b> K <b>Q</b> S <b>K</b>	330
3TEF VcVctF	H <b>I</b> A-Y <b>L</b> D <b>V</b> N <b>A</b> W <b>H</b> I <b>A</b> -I <b>S</b> G <b>V</b> K <b>A</b> T--E <b>Q</b> M <b>V</b> A <b>D</b> -M <b>K</b> A <b>S</b> V <b>G</b> M <b>Q</b>	333
3GFV BsYclQ	H <b>V</b> I-Y <b>L</b> D <b>S</b> A <b>T</b> W <b>H</b> L <b>S</b> -G <b>G</b> G <b>L</b> E <b>S</b> M <b>T</b> -Q <b>Q</b> M <b>I</b> K <b>E</b> -V <b>K</b> D <b>G</b> L <b>E</b> K	320
4MX8 XcPBP	H <b>V</b> L-Y <b>L</b> N <b>P</b> T <b>A</b> W <b>H</b> I <b>V</b> F <b>F</b> G <b>G</b> V <b>E</b> E <b>T</b> -R <b>I</b> M <b>I</b> D <b>D</b> -V <b>L</b> Q-VA <b>A</b> R	340
4JCC SpPiuA	K <b>K</b> I <b>I</b> Q <b>L</b> T <b>P</b> D <b>L</b> W <b>H</b> L <b>S</b> -G <b>G</b> G <b>L</b> E <b>S</b> T <b>K</b> K <b>L</b> M <b>M</b> I <b>E</b> D- <b>I</b> Q <b>K</b> A <b>L</b> K	321
5AD1 CjCeuE	K <b>I</b> I-Y <b>L</b> D <b>P</b> E <b>Y</b> W <b>H</b> L <b>A</b> S <b>G</b> N <b>G</b> L <b>E</b> S <b>L</b> --K <b>T</b> M <b>I</b> L <b>E</b> - <b>I</b> K <b>N</b> A <b>V</b> K	330
2WHY BsFeuA	H <b>V</b> Y-V <b>N</b> S <b>V</b> D <b>P</b> L <b>A</b> Q--G <b>G</b> T <b>A</b> W <b>S</b> K <b>V</b> -V <b>R</b> F <b>L</b> K <b>A</b> - <b>A</b> A <b>E</b> K <b>L</b> T <b>Q</b> N <b>K</b> L <b>T</b> Q <b>N</b>	317
4FNA SaFhuD2	H <b>I</b> V-K <b>V</b> D <b>A</b> G <b>T</b> Y <b>W</b> ---Y <b>N</b> D <b>P</b> Y <b>T</b> L--D <b>F</b> M <b>R</b> K <b>D</b> -L <b>K</b> E <b>K</b> L <b>I</b> K <b>A</b> A <b>K</b>	302

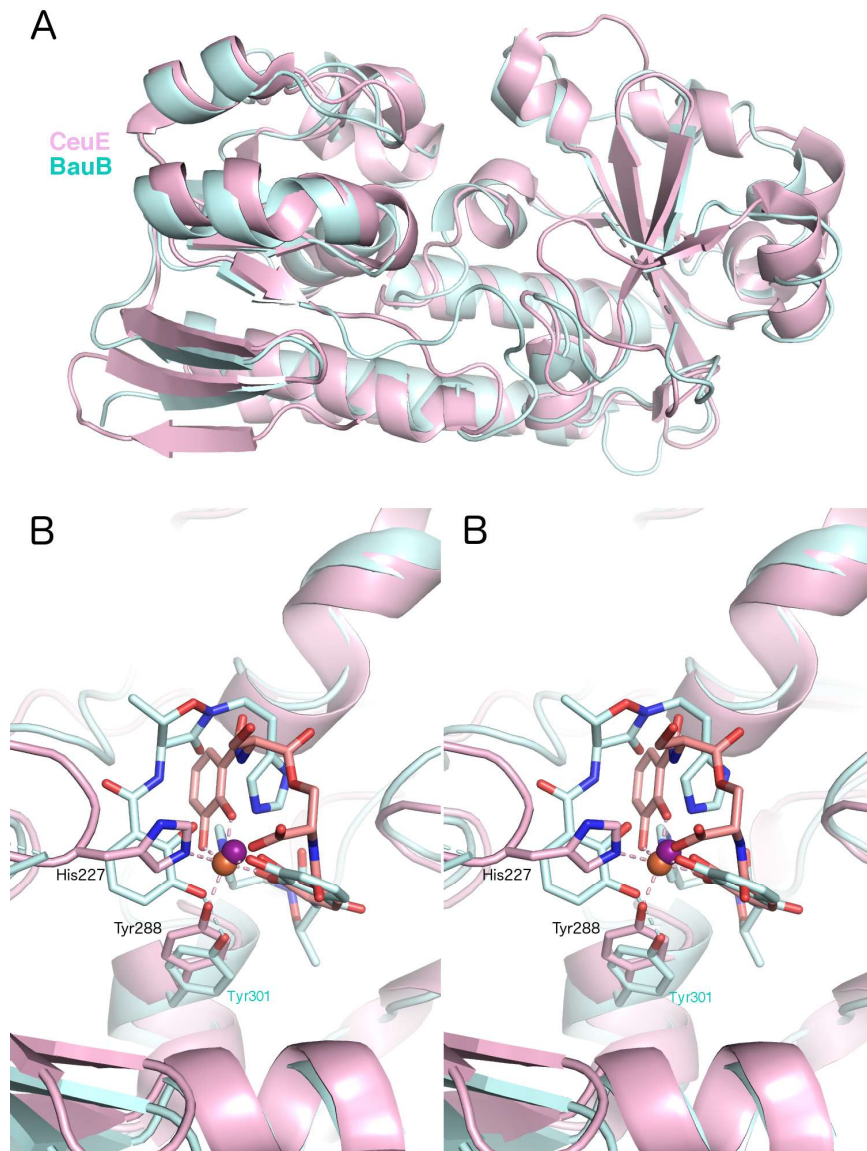
**Figure 2.4.** PROMALS3d structure-based alignment of BauB with homologous siderophore binding proteins. Sequences are identified by PDB code as described in Table 2.1. Conserved sequences are identified in red, while homologous residues are identified in blue. His239 and Tyr301 of BauB are highlighted in green. BauB residues in Figure 2.6B are highlighted in yellow. Disordered residues are shown in orange.



**Figure 2.5.** Modeling of acinetobactin<sub>2</sub>Fe structure into the electron density in the BauB substrate binding pocket. Stereorepresentation of the final model of ligands bound to BauB. Omit map electron density, contoured at  $2.5 \sigma$ , was calculated with coefficients of the form  $F_o - F_c$  using the final model from which the ligands were removed and subjected to a round of simulated annealing refinement.

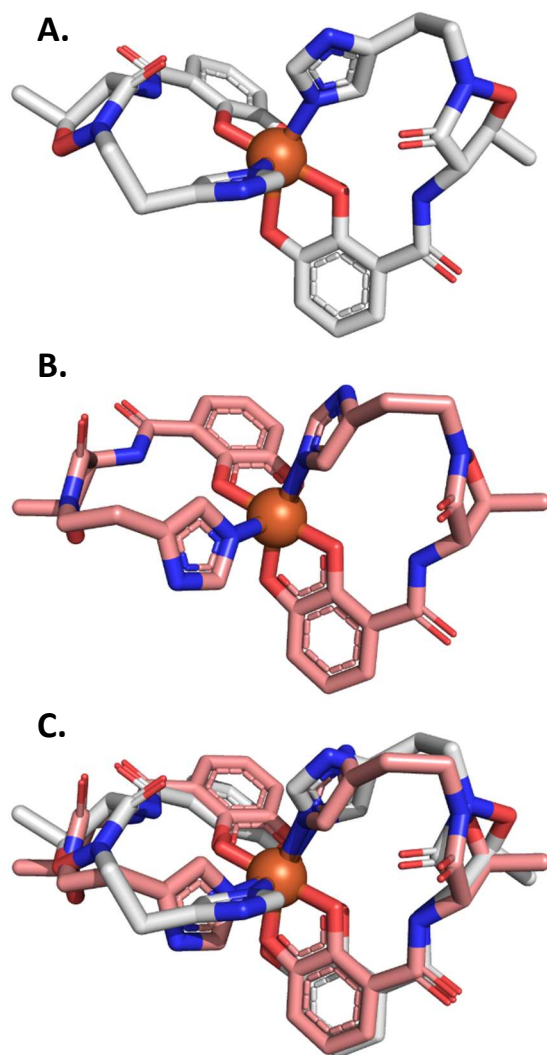


**Figure 2.6.** Siderophore binding pocket in BauB. (A) The Acb<sub>2</sub>Fe ligand is shown with buried (green) and exposed (yellow) acinetobactin molecules with a surface representation of BauB. (B) Stereorepresentation of the residues that form the binding pocket.

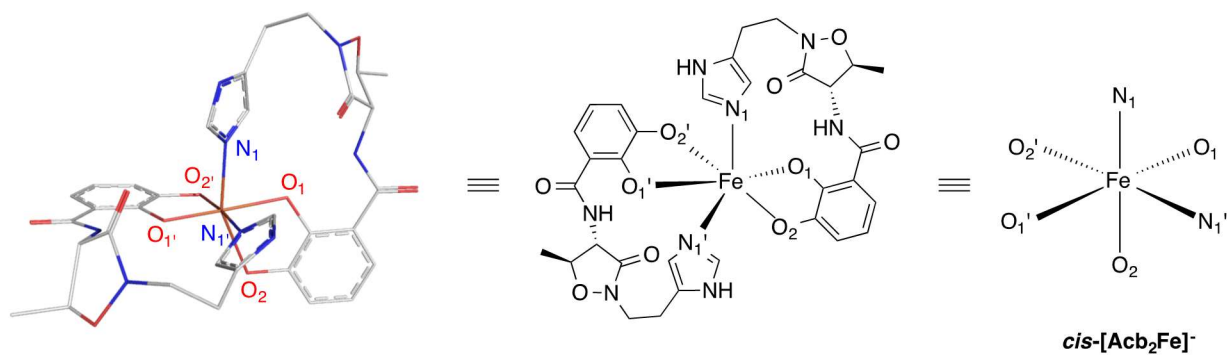


**Figure 2.7.** Overlay of BauB and CeuE. A. Ribbon diagram showing BauB (6MFL, cyan) and CeuE (5ADW, pink). B. Stereorepresentation of the siderophore binding pocket of BauB bound to [Acb<sub>2</sub>:Fe]<sup>-1</sup> anion superimposed with CeuE bound to bis-(2,3-dihydroxybenzoyl-L-Ser). His227 and Tyr288 from CeuE directly coordinate the ferric ion. Tyr301 of BauB interacts with a catechol oxygen of the more exposed acinetobactin molecule. The side chain of His239 in BauB is adjacent to a disordered loop and no density is present for the side chain.

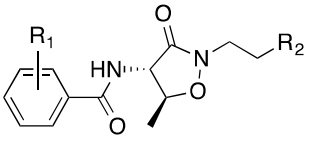




**Figure 2.8.** Structures of  $(\text{Acb})_2\text{Fe}$  from (A) experimental fitting into the electron density of the BauB substrate binding pocket and (B) DFT calculated lowest energy structure for the monoanionic  $[(\text{Acb})_2\text{Fe}]^-$  metal complex (PBE0/Def2-SVP; PBE0/Def2-TZVP; PBE1PBE = PBE0 in Gaussian). (C) Overlay of  $(\text{Acb})_2\text{Fe}$  structures from experimental (grey) and DFT (salmon) modeling.



**Figure 2.9.** Structural representations of the experimentally observed *cis*-[Acb<sub>2</sub>Fe]<sup>-</sup> geometric and optical isomer. The *cis*-[Acb<sub>2</sub>Fe]<sup>-</sup> structure is isomeric with ML<sub>4</sub><sup>a</sup>L<sub>2</sub><sup>b</sup> octahedral metal complexes where L<sup>a</sup> is oxygen and L<sup>b</sup> is nitrogen represented as [FeO<sub>4</sub>N<sub>2</sub>]<sup>-</sup>.

	CAS (+/-) <sup>1</sup>	<i>A. baumannii</i> Growth Promotion (+/-) <sup>1</sup>	BauB Apparent $K_d$ (nM) <sup>2</sup>
<b>1</b> , R <sub>1</sub> = 2,3-OH; R <sub>2</sub> = Im	+	++	300 ± 100
<b>1-Fe</b> , R <sub>1</sub> = 2,3-OH; R <sub>2</sub> = Im	NA	+++	160 ± 80
<b>3</b> , R <sub>1</sub> = 2,3-OH; R <sub>2</sub> = CH <sub>2</sub> Im	+	+	320 ± 130
<b>4</b> , R <sub>1</sub> = 2-OH; R <sub>2</sub> = Im	-	-	520 ± 270
<b>5</b> , R <sub>1</sub> = 3-OH; R <sub>2</sub> = Im	-	-	250 ± 70
<b>6</b> , R <sub>1</sub> = 4-OH; R <sub>2</sub> = Im	-	-	250 ± 70
<b>7</b> , R <sub>1</sub> = 2,3-OMe; R <sub>2</sub> = Im	-	-	270 ± 70
<b>8</b> , R <sub>1</sub> = H; R <sub>2</sub> = Im	-	-	520 ± 220
<b>9</b> , R <sub>1</sub> = 2,3-OH; R <sub>2</sub> = Me	+	+	320 ± 130

<sup>1</sup>Results from CAS assay and *A. baumannii* growth promotion were reported previously.<sup>27</sup> For the CAS assay, + indicates a positive result correlating to Fe binding and a - indicates no apparent Fe binding. For the growth promotion of *A. baumannii*, a +/++/+++ indicates positive promotion of growth with more '+' symbols correlating to more relative growth. <sup>2</sup>Experiments were performed in duplicate as independent trials. Error represents standard deviation from the mean. <sup>3</sup>NA = not applicable.

**Table 2.2.** Structure of acinetobactin analogs and associated properties.

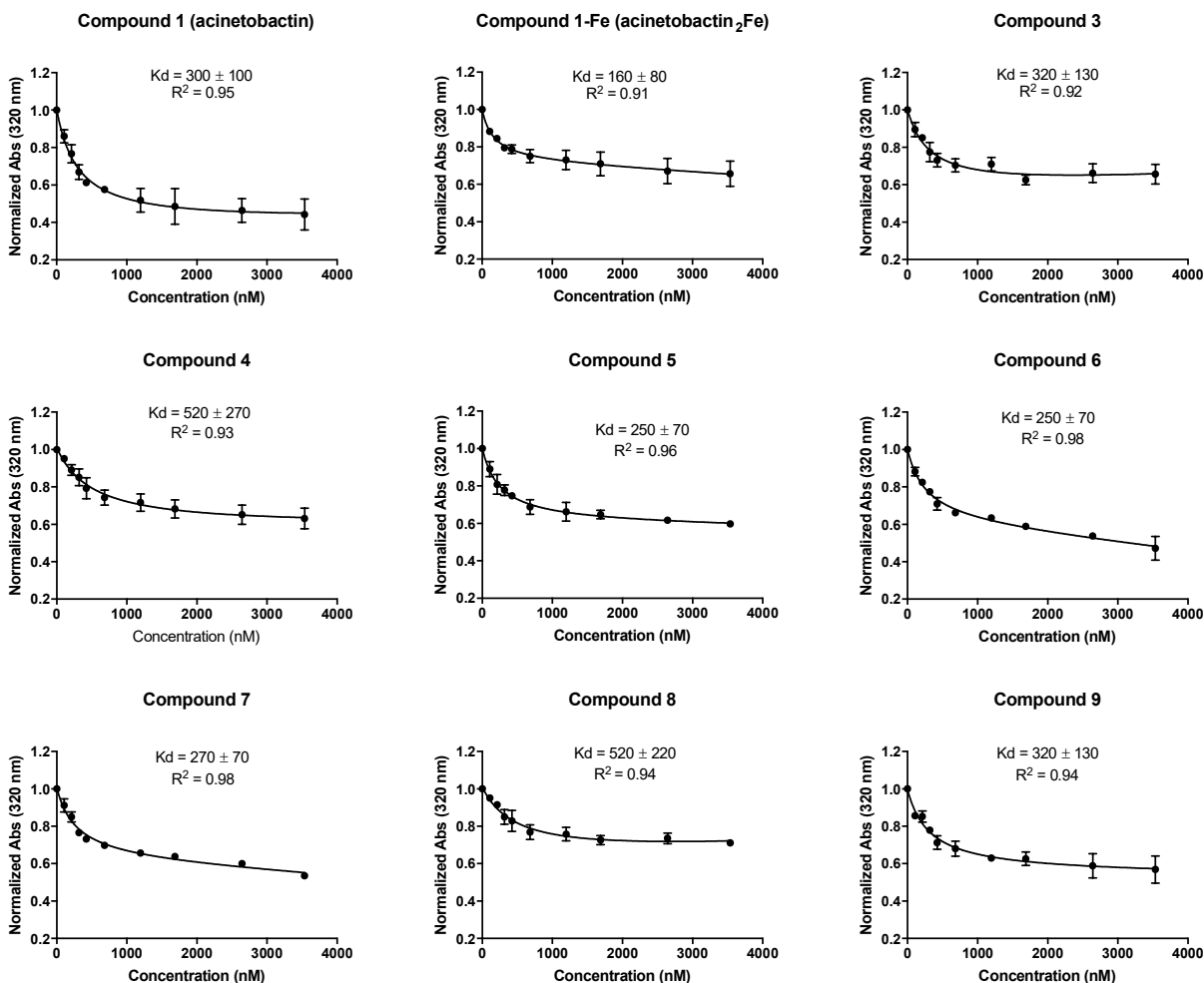


**Figure 2.10.** Siderophore-dependent fluorescence quenching of *C*-His<sub>6</sub>-BauB. Graphs depict intrinsic tryptophan fluorescence quenching (y-axis;  $\lambda_{\text{excitation}} = 280 \text{ nm}$ ;  $\lambda_{\text{emission}} = 340 \text{ nm}$ ) of *C*-His<sub>6</sub>-BauB in the presence of variable siderophore concentrations (x-axis). Apparent  $K_d$  values were calculated using a single-binding mode curve fitting model in GraphPad Prism version 7.0b.

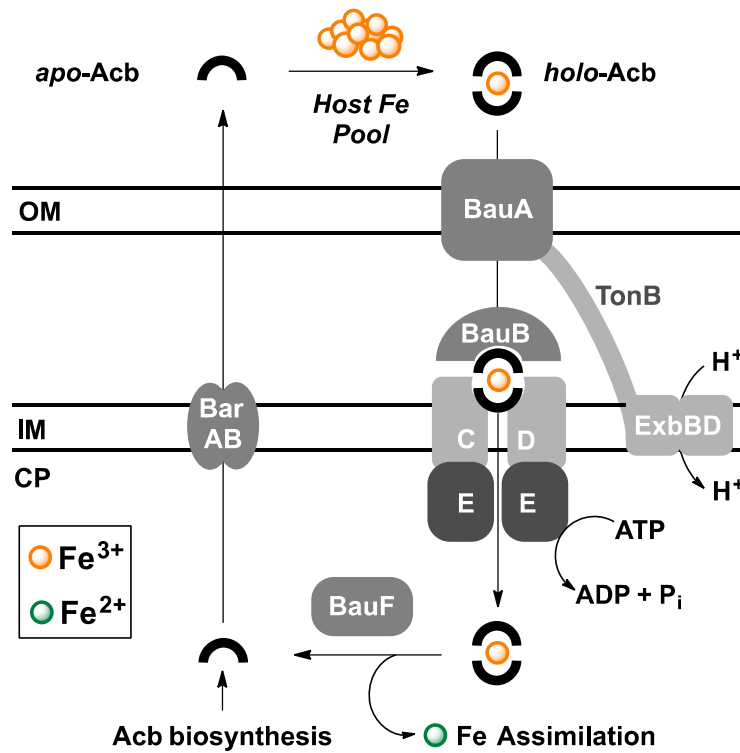


**Figure 2.11.** Overview of the acinetobactin pathway in *A. baumannii*. BarAB is a putative efflux pump for cytoplasmic apo-Acb. Once formed, the holo-Acb ferric complex is imported to the periplasm by the TonB-dependent outer membrane protein BauA. Presumably, BauA is selective for importing various forms of Acb. Periplasmic holo-Acb is delivered to the inner membrane permease BauCDE by the SBP BauB (the focus of this work). Once imported to the cytoplasm, the holo-Acb ferric complex is likely reduced giving ferrous iron and apo-Acb, which is recycled.

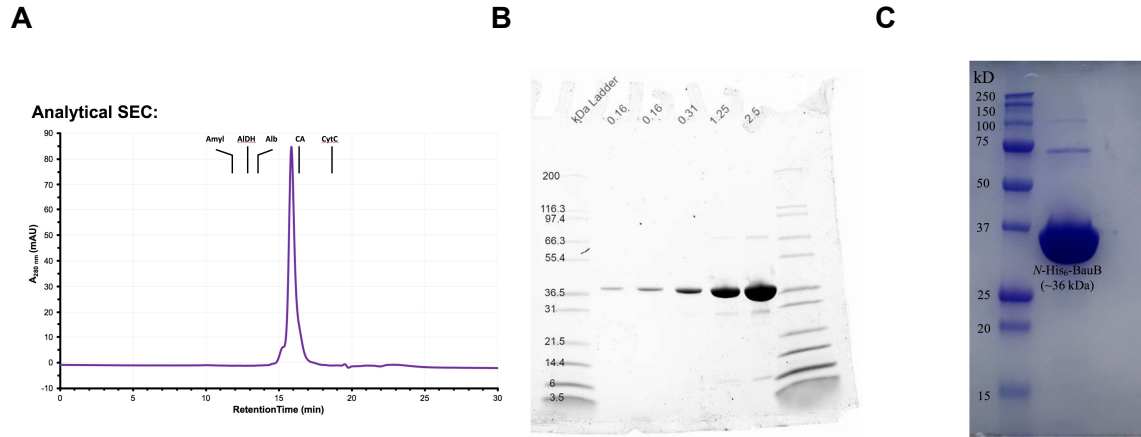


**Figure 2.12. BauB purification.** (A) Analytical gel filtration of full length BauB showing monomeric status in solution. Retention times for  $\beta$ -Amylase (200 kD), Alcohol Dehydrogenase (150 kD), Albumin (66 kD), Carbonic Anhydrase (29 kD) and Cytochrome C (12.4 kD) standards are indicated. (B) SDS-PAGE gel recombinant C-His<sub>6</sub>-BauB purified from *E. coli* BL21. Molecular weight markers and mass of protein loaded are labeled. (C) SDS-PAGE analysis of Ni-NTA purified N-His<sub>6</sub>-BauB (~36.1 kDa).

<b>Data Set Entry</b>	<b>1</b>	<b>2</b>
<b>Crystal Identifier</b>	BB_41	BB_5
<b>Protein</b>	CHis_BauB-SS (50 mg/mL) + ferric Acb (3 mM)	
<b>Protein Buffer</b>	10 mM Tris, 30 mM NaCl, 0.04 mM TCEP, pH 8.0	50 mM Tris, 150 mM NaCl, 0.2 mM TCEP, pH 8.0
<b>Crystallization Cocktail</b>	25% PEG MME 5k, 50 mM MES pH 6.0 (14 °C)	34% PEG 4k, 100 mM EPPS pH 8.0 (14 °C)
<b>Cryoprotection</b>	Serial transfer through 8,16,20% ethylene glycol in cocktail	
<b>Beamline</b>	SSRL 12-2	APS GM/CA 23ID-D
<b>Detector Distance (mm)</b>	375	325
<b>Oscillation Range (°)</b>	360	180
<b>Oscillation Angle (°)</b>	0.25	0.20
<b>No. of Images</b>	1,440	900
<b>Exposure Time (s)</b>	0.5	0.2
<b>Beam size (w × h, μm)</b>	100 × 100	200 × 100
<b>Wavelength (Å)</b>	0.9795	1.0332
<b>Data Collection</b>		
<b>Resolution range (Å)</b>	68.6 – 1.9 (2.0 – 1.9)	45.6 – 2.0 (2.04 – 2.0)
<b>Space group</b>	P 2 <sub>1</sub>	P 2 <sub>1</sub>
<b>Unit cell a, b, c (Å)</b>	37.6, 137.3, 56.3	37.9, 136.8, 56.3
<b>α, β, γ (°)</b>	90.0, 90.0, 90.0	90.0, 90.1, 90.0
<b>Total Observations</b>	260338	123410
<b>Unique reflections</b>	39102	38149
<b>Multiplicity</b>	6.7	3.2
<b>Completeness (%)</b>	87.3 (90.5)	97.7 (91.1)
<b>Mean I/sigma(I)</b>	11.8 (6.7)	3.2 (3.0)
<b>R<sub>MERGE</sub></b>	0.09 (0.17)	0.19 (0.58)
<b>R<sub>MEAS</sub></b>	0.11 (0.20)	0.26 (0.80)
<b>CC1/2</b>	0.99 (0.97)	0.94 (0.42)

**Table 2.3.** Summary of BauB crystallization and data collection.

	<b>BauB-Acb<sub>2</sub>-Fe<sup>3+</sup></b>
<b>PDB ID</b>	<b>6MFL</b>
<b>Data Collection</b>	
Resolution range (Å)	68 – 1.9 (1.94-1.90)
Space group	P 2 <sub>1</sub>
Unit cell a, b, c (Å) $\alpha, \beta, \gamma$ (°)	37.8, 137.1, 56.2, 90, 90.0, 90
Number Crystals	2
Total Observations	347119 (22375)
Unique reflections	44580 (2908)
Multiplicity	7.8
Completeness (%)	99.2 (99.6)
Mean I/sigma(I)	11.6 (5.6)
R <sub>MERGE</sub>	0.178 (0.570)
R <sub>MEAS</sub>	0.204 (0.662)
CC1/2	0.970 (0.679)
<b>Structure Refinement</b>	
Reflections used in refinement	44255
Reflections used for R <sub>FREE</sub>	2140
R <sub>WORK</sub>	16.9
R <sub>FREE</sub>	21.4
Number of non-hydrogen atoms	
macromolecules	4928
Ligands	102
Solvent	372
Wilson B-factor (Å <sup>2</sup> )	13.8
Average B-factor (Å <sup>2</sup> )	
Chain A (main, side)	14.8, 20.5
Chain B (main, side)	13.9, 20.4
Acb <sub>2</sub> Fe	18.0
Water	23.3
Ethylene glycol	34.7
RMSD bond lengths (Å)	0.01
RMSD bond angles (°)	1.12
Ramachandran analysis	
favored (%)	97.0
allowed (%)	3.0
outliers (%)	0.0
Rotamer outliers (%)	0.8
MolProbity Clashscore	2.9

**Table 2.4.** Data collection and refinement statistics



## 2.8 References

- (1) Chu, B. C., Garcia-Herrero, A., Johanson, T. H., Krewulak, K. D., Lau, C. K., Peacock, R. S., Slavinskaya, Z., and Vogel, H. J. (2010) Siderophore uptake in bacteria and the battle for iron with the host; a bird's eye view. *BioMetals* 23, 601–611.
- (2) Lewinson, O., and Livnat-Levanon, N. (2017) Mechanism of Action of ABC Importers: Conservation, Divergence, and Physiological Adaptations. *J. Mol. Biol.* 429, 606–619.
- (3) Tanaka, K. J., Song, S., Mason, K., and Pinkett, H. W. (2018) Selective substrate uptake: The role of ATP-binding cassette (ABC) importers in pathogenesis. *Biochim. Biophys. Acta, Biomembr.* 1860, 868–877.
- (4) Yang, M., Livnat Levanon, N., Acar, B., Aykac Fas, B., Masrati, G., Rose, J., Ben-Tal, N., Haliloglu, T., Zhao, Y., and Lewinson, O. (2018) Single-molecule probing of the conformational homogeneity of the ABC transporter BtuCD. *Nat. Chem. Biol.* 14, 715–722.
- (5) Locher, K. P. (2016) Mechanistic diversity in ATP-binding cassette (ABC) transporters. *Nat. Struct. Mol. Biol.* 23, 487–493.
- (6) Berntsson, R. P., Smits, S. H., Schmitt, L., Slotboom, D. J., and Poolman, B. (2010) A structural classification of substrate-binding proteins. *FEBS Lett.* 584, 2606–2617.
- (7) Scheepers, G. H., Lycklama a Nijeholt, J. A., and Poolman, B. (2016) An updated structural classification of substrate-binding proteins. *FEBS Lett.* 590, 4393–4401.
- (8) Dorsey, C. W., Tolmasky, M. E., Crosa, J. H., and Actis, L. A. (2003) Genetic organization of an *Acinetobacter baumannii* chromosomal region harbouring genes related to siderophore biosynthesis and transport. *Microbiology* 149, 1227–1238.

- (9) Dorsey, C. W., Tomaras, A. P., Connerly, P. L., Tolmasky, M. E., Crosa, J. H., and Actis, L. A. (2004) The siderophore-mediated iron acquisition systems of *Acinetobacter baumannii* ATCC 19606 and *Vibrio anguillarum* 775 are structurally and functionally related. *Microbiology* 150, 3657–3667.
- (10) Proschak, A., Lubuta, P., Grun, P., Lohr, F., Wilharm, G., De Berardinis, V., and Bode, H. B. (2013) Structure and biosynthesis of fimsbactins A-F, siderophores from *Acinetobacter baumannii* and *Acinetobacter baylyi*. *ChemBioChem* 14, 633–638.
- (11) Penwell, W. F., DeGrace, N., Tentarelli, S., Gauthier, L., Gilbert, C. M., Arivett, B. A., Miller, A. A., Durand-Reville, T. F., Joubran, C., and Actis, L. A. (2015) Discovery and Characterization of New Hydroxamate Siderophores, Baumannoferrin A and B, produced by *Acinetobacter baumannii*. *ChemBioChem* 16, 1896–1904.
- (12) Chen, L., Zheng, D., Liu, B., Yang, J., and Jin, Q. (2016) VFDB 2016: hierarchical and refined dataset for big data analysis–10 years on. *Nucleic Acids Res.* 44, D694–697.
- (13) Vallenet, D., Nordmann, P., Barbe, V., Poirel, L., Mangenot, S., Bataille, E., Dossat, C., Gas, S., Kreimeyer, A., Lenoble, P., Oztas, S., Poulain, J., Segurens, B., Robert, C., Abergel, C., Claverie, J. M., Raoult, D., Medigue, C., Weissenbach, J., and Cruveiller, S. (2008) Comparative analysis of *Acinetobacters*: three genomes for three lifestyles. *PLoS One* 3, No. e1805.
- (14) Gaddy, J. A., Arivett, B. A., McConnell, M. J., Lopez-Rojas, R., Pachon, J., and Actis, L. A. (2012) Role of acinetobactin-mediated iron acquisition functions in the interaction of *Acinetobacter baumannii* strain ATCC 19606T with human lung epithelial cells, *Galleria mellonella* caterpillars, and mice. *Infect. Immun.* 80, 1015–1024.

- (15) Shapiro, J. A., and Wencewicz, T. A. (2016) Acinetobactin Isomerization Enables Adaptive Iron Acquisition in *Acinetobacter baumannii* through pH-Triggered Siderophore Swapping. *ACS Infect. Dis.* 2, 157–168.
- (16) Neres, J., Engelhart, C. A., Drake, E. J., Wilson, D. J., Fu, P., Boshoff, H. I., Barry, C. E., 3rd, Gulick, A. M., and Aldrich, C. C. (2013) Non-nucleoside inhibitors of BasE, an adenyating enzyme in the siderophore biosynthetic pathway of the opportunistic pathogen *Acinetobacter baumannii*. *J. Med. Chem.* 56, 2385–2405.
- (17) Drake, E. J., Duckworth, B. P., Neres, J., Aldrich, C. C., and Gulick, A. M. (2010) Biochemical and structural characterization of bisubstrate inhibitors of BasE, the self-standing nonribosomal peptide synthetase adenyate-forming enzyme of acinetobactin synthesis. *Biochemistry* 49, 9292–9305.
- (18) Shapiro, J. A., and Wencewicz, T. A. (2017) Structure-function studies of acinetobactin analogs. *Metallomics* 9, 463–470.
- (19) Bohac, T. J., Shapiro, J. A., and Wencewicz, T. A. (2017) Rigid Oxazole Acinetobactin Analog Blocks Siderophore Cycling in *Acinetobacter baumannii*. *ACS Infect. Dis.* 3, 802–806.
- (20) Zawadzka, A. M., Kim, Y., Maltseva, N., Nichiporuk, R., Fan, Y., Joachimiak, A., and Raymond, K. N. (2009) Characterization of a *Bacillus subtilis* transporter for petrobactin, an anthrax stealth siderophore. *Proc. Natl. Acad. Sci. U. S. A.* 106, 21854–21859.
- (21) Holm, L., and Laakso, L. M. (2016) Dali server update. *Nucleic Acids Res.* 44, W351–355.

- (22) Raines, D. J., Moroz, O. V., Wilson, K. S., and Duhme-Klair, A. K. (2013) Interactions of a periplasmic binding protein with a tetradentate siderophore mimic. *Angew. Chem., Int. Ed.* 52, 4595–4598.
- (23) Raines, D. J., Moroz, O. V., Blagova, E. V., Turkenburg, J. P., Wilson, K. S., and Duhme-Klair, A. K. (2016) Bacteria in an intense competition for iron: Key component of the *Campylobacter jejuni* iron uptake system scavenges enterobactin hydrolysis product. *Proc. Natl. Acad. Sci. U. S. A.* 113, 5850–5855.
- (24) Grigg, J. C., Cooper, J. D., Cheung, J., Heinrichs, D. E., and Murphy, M. E. (2010) The *Staphylococcus aureus* siderophore receptor HtsA undergoes localized conformational changes to enclose staphyloferrin A in an arginine-rich binding pocket. *J. Biol. Chem.* 285, 11162–11171.
- (25) Grigg, J. C., Cheung, J., Heinrichs, D. E., and Murphy, M. E. (2010) Specificity of Staphyloferrin B recognition by the SirA receptor from *Staphylococcus aureus*. *J. Biol. Chem.* 285, 34579–34588.
- (26) Peuckert, F., Ramos-Vega, A. L., Miethke, M., Schworer, C. J., Albrecht, A. G., Oberthur, M., and Marahiel, M. A. (2011) The siderophore binding protein FeuA shows limited promiscuity toward exogenous triscatecholates. *Chem. Biol.* 18, 907–919.
- (27) Endicott, N. P., Lee, E., and Wencewicz, T. A. (2017) Structural Basis for Xenosiderophore Utilization by the Human Pathogen *Staphylococcus aureus*. *ACS Infect. Dis.* 3, 542–553.
- (28) Podkowa, K. J., Briere, L. A., Heinrichs, D. E., and Shilton, B. H. (2014) Crystal and solution structure analysis of FhuD2 from *Staphylococcus aureus* in multiple unliganded conformations and bound to ferrioxamine-B. *Biochemistry* 53, 2017–2031.

- (29) Hossain, M. B., Jalal, M. A. F., and van der Helm, D. (1998) Gallium-complex of anguibactin, a siderophore from fish pathogen *Vibrio anguillarum*. *J. Chem. Crystallogr.* 28, 57–60.
- (30) Allred, B. E., Correnti, C., Clifton, M. C., Strong, R. K., and Raymond, K. N. (2013) Siderocalin outwits the coordination chemistry of vibriobactin, a siderophore of *Vibrio cholerae*. *ACS Chem. Biol.* 8, 1882–1887.
- (31) Shields-Cutler, R. R., Crowley, J. R., Miller, C. D., Stapleton, A. E., Cui, W., and Henderson, J. P. (2016) Human Metabolome-derived Cofactors Are Required for the Antibacterial Activity of Siderocalin in Urine. *J. Biol. Chem.* 291, 25901–25910.
- (32) Nielsen, H. (2017) Predicting Secretory Proteins with SignalP. *Methods Mol. Biol.* 1611, 59–73.
- (33) Kall, L., Krogh, A., and Sonnhammer, E. L. (2007) Advantages of combined transmembrane topology and signal peptide prediction—the Phobius web server. *Nucleic Acids Res.* 35, W429–432.
- (34) Braun, V., and Wu, H. C. (1994) Lipoproteins, structure, function, biosynthesis and model for protein export. In *New Compr. Biochem.* (Ghuysen, J. M., and Hakenbeck, R., Eds.), pp 319–341, *Elsevier*.
- (35) Juncker, A. S., Willenbrock, H., Von Heijne, G., Brunak, S., Nielsen, H., and Krogh, A. (2003) Prediction of lipoprotein signal peptides in Gram-negative bacteria. *Protein Sci.* 12, 1652–1662.

- (36) Seydel, A., Gounon, P., and Pugsley, A. P. (1999) Testing the '+2 rule' for lipoprotein sorting in the Escherichia coli cell envelope with a new genetic selection. *Mol. Microbiol.* 34, 810–821.
- (37) Yamaguchi, K., Yu, F., and Inouye, M. (1988) A single amino acid determinant of the membrane localization of lipoproteins in E. coli. *Cell* 53, 423–432.
- (38) Battye, T. G., Kontogiannis, L., Johnson, O., Powell, H. R., and Leslie, A. G. (2011) iMOSFLM: a new graphical interface for diffraction-image processing with MOSFLM. *Acta Crystallogr, Sect.D: Biol. Crystallogr.* 67, 271–281.
- (39) McCoy, A. J., Grosse-Kunstleve, R. W., Adams, P. D., Winn, M. D., Storoni, L. C., and Read, R. J. (2007) Phaser crystallographic software. *J. Appl. Crystallogr.* 40, 658–674.
- (40) Terwilliger, T. C., Grosse-Kunstleve, R. W., Afonine, P. V., Moriarty, N. W., Zwart, P. H., Hung, L. W., Read, R. J., and Adams, P. D. (2008) Iterative model building, structure refinement and density modification with the PHENIX AutoBuild wizard. *Acta Crystallogr., Sect. D: Biol. Crystallogr.* 64, 61–69.
- (41) Emsley, P., and Cowtan, K. (2004) Coot: model-building tools for molecular graphics. *Acta Crystallogr. Sect. D: Biol. Crystallogr.* 60, 2126–2132.
- (42) Afonine, P. V., Grosse-Kunstleve, R. W., Echols, N., Headd, J. J., Moriarty, N. W., Mustyakimov, M., Terwilliger, T. C., Urzhumtsev, A., Zwart, P. H., and Adams, P. D. (2012) Towards automated crystallographic structure refinement with phenix.refine. *Acta Crystallogr., Sect. D: Biol. Crystallogr.* 68, 352–367.

- (43) Pei, J., and Grishin, N. V. (2014) PROMALS3D: multiple protein sequence alignment enhanced with evolutionary and three dimensional structural information. *Methods Mol. Biol.* 1079, 263–271.
- (44) Pople, J. A., Scott, A. P., Wong, M. W., and Radom, L. (1993) Scaling factors for obtaining fundamental vibrational frequencies and zero-point energies from Hf/6-31G\* and Mp2/6-31G\* Harmonic Frequencies. *Isr. J. Chem.* 33, 345–350.
- (45) Cossi, M., Rega, N., Scalmani, G., and Barone, V. (2003) Energies, structures, and electronic properties of molecules in solution with the C-PCM solvation model. *J. Comput. Chem.* 24, 669–681.
- (46) Shephard, M. J., and Paddonrow, M. N. (1995) Gas-Phase structure of the bicyclo[2.2.1]heptane (Norbornane) cation-radical – a combined ab-initio MO and density-functional study. *J. Phys. Chem.* 99, 3101–3108.
- (47) Zhao, Y., and Truhlar, D. G. (2008) Density functionals with broad applicability in chemistry. *Acc. Chem. Res.* 41, 157–167.
- (48) Rydberg, P., and Olsen, L. (2009) The accuracy of geometries for iron porphyrin complexes from density functional theory. *J. Phys. Chem. A* 113, 11949–11953.
- (49) Ansbacher, T., Srivastava, H. K., Martin, J. M., and Shurki, A. (2010) Can DFT methods correctly and efficiently predict the coordination number of copper(I) complexes? A case study. *J. Comput. Chem.* 31, 75–83.

(50) Weigend, F., and Ahlrichs, R. (2005) Balanced basis sets of split valence, triple zeta valence and quadruple zeta valence quality for H to Rn: Design and assessment of accuracy. *Phys. Chem. Chem. Phys.* 7, 3297–3305.



**Chapter 3: Fimsbactin and Acinetobactin**  
**Compete for the Periplasmic Siderophore**  
**Binding Protein BauB in Pathogenic**  
***Acinetobacter baumannii***

## 3.1 Preface

This chapter was adapted in part from [Bohac, T. J., Fang, L., Giblin, D. E. & Wencewicz, T. A. ACS Chemical Biology, *Manuscript accepted* DOI: 10.1021/acscchembio.8b01051]. TJB isolated Fimsbactin A, performed characterization, BauB fluorescent quenching binding studies and BauB displacement assays. LF performed all growth curves. DEG performed all DFT calculations. TAW served as principal investigator and oversaw experimental design.

## 3.2 Abstract

Environmental and pathogenic microbes produce siderophores as small iron-binding molecules to scavenge iron from natural environments. It is common for microbes to produce multiple siderophores to gain a competitive edge in mixed microbial environments. Human pathogenic *Acinetobacter baumannii* produces up to three siderophores: acinetobactin, baumannoferrin, and fimsbactin. Production of acinetobactin and baumannoferrin is highly conserved amongst clinical isolates, while fimsbactin production appears to be less common. Fimsbactin is structurally related to acinetobactin through the presence of catecholate and phenolate oxazoline metal binding motifs, and both are derived from non-ribosomal peptide assembly lines with similar catalytic domain orientations and identities. Here we report on the chemical, biochemical, and microbiological investigation of fimsbactin and acinetobactin alone and in combination. We show that fimsbactin forms a 1:1 complex with iron(III) that is thermodynamically more stable than the 2:1 acinetobactin ferric complex. Alone, both acinetobactin and fimsbactin stimulate *A. baumannii* growth, but in combination the two siderophores appear to compete for uptake and collectively inhibit bacterial growth. We show that fimsbactin directly competes with acinetobactin for binding the periplasmic siderophore binding protein BauB, suggesting a possible biochemical mechanism for the phenomenon where

siderophore build up in the periplasm leads to iron starvation. We propose an updated model for siderophore utilization and cooperativity in *A. baumannii* that frames the molecular, biochemical, and cellular interplay of multiple iron acquisition systems in a multi-drug resistant Gram-negative human pathogen.

### 3.3 Introduction

We sought to investigate the interplay of two high-affinity *A. baumannii* siderophore-based iron acquisition systems; the PreAcb/Acb and Fim pathways. Here, we show that Acb and Fim alone stimulate *A. baumannii* growth under iron deficient conditions. Both siderophores promote growth more efficiently in the *holo*, iron-bound forms. Surprisingly, we found that *apo*-Fim is antagonistic towards *holo*-Acb, leading us to hypothesize that Acb and Fim have competing transport pathways. We recently reported the x-ray crystal structure of the periplasmic siderophore binding protein BauB bound to a stable Acb<sub>2</sub>Fe complex which provided the template for understanding siderophore molecular recognition in *A. baumannii*.<sup>1</sup> In this work, we show that both isomers of acinetobactin, PreAcb and Acb, and Fim bind to BauB with nanomolar affinity. Intrinsic fluorescence quenching and direct binding via an immobilized BauB-LCMS competition experiment validated meaningful BauB binding to *apo*- and *holo*-forms of PreAcb, Acb, and Fim. The promiscuity of BauB is explained using density functional theory (DFT) calculated structures of the PreAcb<sub>2</sub>Fe and FimFe complexes against the BauB•Acb<sub>2</sub>Fe crystal structure which reveals how the three *A. baumannii* siderophores fulfill the octahedral iron(III) coordination sphere using ligands derived from the common 2,3-DHB-Thr/Ser phenolate oxazoline, catechol, and imidazole/hydroxamate motifs that display identical stereochemistry about the ferric metal center and overlapping electron density in the ligand coordination sphere. Pathway competition between

Acb and Fim might explain, in part, why it is rare to find clinical isolates of pathogenic *A. baumannii* harboring biosynthetic operons for both siderophores.

### 3.4 Results and Discussion

#### *Purification of Acb and Fim from A. baumannii ATCC 17978.*

The fimsbactin siderophores were originally isolated from the environmental strain *A. baylyi* ADP1.<sup>2</sup> Up to this point, Fim had not been isolated from any pathogenic strains of *A. baumannii*, although comparative genomics predicts the presence of the Fim operon in at least 4 unique strains of *A. baumannii* in the NCBI database (**Figure 3.1**). One of these strains is human pathogenic *A. baumannii* ATCC 17978, a clinical isolate that is predicted to be a producer of Acb, Fim, and baumannoferrin.<sup>3</sup> We isolated crude Acb and fimsbactin A–F from *A. baumannii* ATCC 17978 grown in iron deficient M9 minimal medium at 37 °C. LC-MS analysis of the crude fermentation broths from two separate trials showed the presence of Acb and all of the fimsbactin isomers, fimsbactin A–F, with fimsbactin A providing the largest signal in the optical absorbance and extracted ion chromatogram (EIC) traces (**Figure 3.2-3.6**). This validates coproduction of Acb and Fim by a human pathogenic strain of *A. baumannii*. Acb and fimsbactin A were purified via RP-C18 prep-HPLC allowing for isolation of both siderophores from a single fermentation. Acb was isolated in >95% purity by LCMS at a mass recovery after purification of 31 mg/L averaged over two trials. No PreAcb was observed, which is consistent with the instability of PreAcb during extended fermentations at physiological pH and previous failed isolation attempts. However, PreAcb is readily available in our group through total synthesis.<sup>4</sup> Fimsbactin A was isolated as a mixture of fimsbactin A (>90%) and fimsbactins B, C, and F (≤10%) according to LCMS and NMR analysis. We validated that fimsbactin A is the primary component by HRMS and comparison of the 1D (<sup>1</sup>H, <sup>13</sup>C) NMR spectra against the literature reported values (**Table 3.1**,

**Figures 3.7-3.9).**<sup>2</sup> The mass recovery of Fim after purification was 5 mg/L averaged over two independent trials. The greater mass production of Acb over Fim is consistent with the observations for siderophore production in *A. baylyi*.<sup>2</sup> We were unable to detect any positively charged ions corresponding to *apo*- or *holo*- baumannoferrin in the *A. baumannii* ATCC 17978 supernatants, despite the predicted biosynthetic capacity for this siderophore (**Figure 3.1**).<sup>5</sup> It is possible that the baumannoferrins remain membrane associated or have a low ionization potential in positive mode electrospray ionization (ESI) due to the anionic carboxylate/hydroxamate metal chelating groups, thus, proving to be undetectable by the low-resolution single quadrupole mass spectrometer employed in this study.<sup>6</sup> We utilized synthetic PreAcb, natural Acb, and natural Fim (>90% fimsbactin A) for all studies in this work.

### ***Iron-Binding properties of fimsbactin A.***

Fimsbactin A is a mixed ligand biscatecholate-monohydroxamate siderophore that is structurally related to other NRPS siderophores including heterobactin A<sup>7</sup>, JBIR-16<sup>8</sup>, vibriobactin<sup>9</sup>, vulnibactin<sup>10</sup>, fluvibactin<sup>11</sup>, agrobactin<sup>12</sup>, parabactin<sup>13,14</sup>, and protochelin<sup>15</sup> (**Figure 3.10**). All of these related siderophores are hexadentate metal chelators with three bidentate ligands (either catecholates, phenolate oxazolines, and/or hydroxamates) branching from three arms of a tetrahedral atom, either nitrogen or carbon, creating a tripodal ferric coordination template. Vibriobactin, vulnibactin, fluvibactin, agrobactin, and parabactin are all spermidine-based with a tetrahedral nitrogen at the apex of the tripod, while protochelin and heterobactin are lysine-based using the  $\alpha$ -carbon of L-Lys as the tetrahedral branch point for the three metal chelating ligands. Fimsbactin A is most similar to protochelin and heterobactin in that the tetrahedral branching atom for the three metal chelating ligands is the  $\alpha$ -carbon of L-Ser. Additionally, the 2,3-DHB catechol

moiety is attached via ester linkage to the Ser hydroxyl group as opposed to amide linkages in the related siderophores.

The structure of fimsbactin A is unique and resembles a cross between the metal chelating groups found in heterobactin A<sup>7</sup>, produced by *Rhodococcus erythropolis*, and agrobactin<sup>12</sup>, from plant pathogenic *Agrobacterium tumefaciens* (**Figure 3.10**). Fimsbactin A is composed of hydroxamate, phenolate oxazoline, and catecholate metal chelating groups derived from *N*-acetyl-*N*-hydroxy-cadaverine, serine-2,3-DHB oxazoline, and 2,3-DHB, respectively.<sup>2</sup> Heterobactin A contains hydroxamate, phenolate oxazoline, and catecholate ligands derived from cyclized *N*-hydroxy-ornithine, 2,5-dihydroxy-5-amino-benzoate and 2,3-DHB, respectively.<sup>7</sup> The phenolate oxazoline group of heterobactin A is distinct from that found in fimsbactin in that metal coordination between the oxazoline nitrogen and phenolate oxygen is not possible in heterobactin A. Instead, metal chelation for this ligand arrangement probably occurs through the amide carbonyl oxygen and either the phenolate oxygen or the oxazoline nitrogen. Agrobactin contains two catecholates from 2,3-DHB and one phenolate oxazoline derived from cyclized L-Thr-2,3-DHB methyl oxazolines.<sup>12</sup> Both heterobactin A and agrobactin form stable 1:1 complexes with unique ligand-to-metal charge transfer bands in the optical absorbance spectra appearing at 560 nm and 520 nm, respectively, for the ferric *holo*-siderophores.<sup>7,12,16</sup> For comparison, the well known 1:1 enterobactin tris-catecholate ferric complex has a characteristic ligand-to-metal charge transfer band at 498 nm.<sup>17</sup> The unique optical absorbance bands arise from metal:ligand charge transfer and reflect the unique metal:ligand geometry and speciation of the soluble ferric siderophore complexes. We sought to investigate the iron binding properties of fimsbactin A in comparison to PreAcb and Acb to better understand metal chelation dynamics of the mixed siderophore system in *A. baumannii*.

The ferric *holo*-siderophore complexes of PreAcb, Acb, and Fim were prepared by treatment with Fe(acac)<sub>3</sub> using a method reported previously by our group.<sup>4,18,19,20</sup> Titration of Fim with Fe(acac)<sub>3</sub> in MeOH monitored by fluorescence quenching ( $\lambda_{\text{excitation}} = 330 \text{ nm}$ ;  $\lambda_{\text{emission}} = 380 \text{ nm}$ ) was consistent with the formation of a stable ferric complex of Fim (**Figure 3.11**). At low iron concentrations, the titration curve appears to indicate formation of 2:1 Fim<sub>2</sub>Fe complexes that eventually convert to the 1:1 FimFe complex with added iron. These observations are consistent with previous studies of mixed ligand siderophores, including heterobactin A, where iron chelation geometry and metal:ligand stoichiometry of *holo*-siderophores was shown to vary with metal/ligand concentrations and pH.<sup>16</sup> LCMS analysis of FimFe was also consistent with the formation of a 1:1 siderophore:iron complex. Using ESI in positive ion mode, FimFe ionized as the [M+H]<sup>+</sup> ion with an observed  $m/z = 627$ . Both PreAcb and Acb form 2:1 siderophore:iron complexes, PreAcb<sub>2</sub>Fe and Acb<sub>2</sub>Fe, respectively, that lose iron upon ionization by ESI in positive ion mode to give [M+H]<sup>+</sup> ions with  $m/z = 347$ .<sup>4</sup> This difference in ionization modes reflects the increased relative stability of a 1:1 siderophore:iron complex, FimFe, compared to 2:1 siderophore:iron complexes, PreAcb<sub>2</sub>Fe and Acb<sub>2</sub>Fe, towards ESI.

The optical absorbance spectrum of FimFe shows a broad ligand-to-metal charge transfer absorbance band at 445 nm (**Figure 3.12**). PreAcb<sub>2</sub>Fe and Acb<sub>2</sub>Fe show ligand-to-metal charge transfer absorbance bands at 515 and 570 nm, respectively, in the optical absorbance spectra. The red spectral shift for FimFe ( $\lambda_{\text{max}} = 445 \text{ nm}$ ) compared to PreAcb<sub>2</sub>Fe ( $\lambda_{\text{max}} = 515 \text{ nm}$ ) and Acb<sub>2</sub>Fe ( $\lambda_{\text{max}} = 570 \text{ nm}$ ) implies that there are greater interactions between ferric iron and stronger-field ligands in the FimFe complex. We also measured the apparent iron(III) affinity ( $\log K_{\text{Fe}}$ ) of FimFe to be  $27.1 \pm 0.2$  using an EDTA competition assay (**Table 3.2; Equations 3.1**). The FimFe complex appears to be more stable than the PreAcb<sub>2</sub>Fe (apparent  $\log K_{\text{Fe}} = 27.4 \pm 0.2$ ) and Acb<sub>2</sub>Fe

(apparent  $\log K_{\text{Fe}} = 26.2 \pm 0.1$ ).<sup>4</sup> This is consistent with the relative stability of mycobactin (more stable; phenolate oxazoline, bis-hydroxamate) and exochelin (less stable; imidazole-containing bis-hydroxamate) ferric siderophores from *Mycobacterium tuberculosis*.<sup>21</sup> We confirmed that apparent  $K_{\text{Fe}}$  for FimFe was greater than Acb<sub>2</sub>Fe through a competitive iron exchange assay. Treatment of Acb<sub>2</sub>Fe with an equimolar amount of apo-Fim resulted in formation of the FimFe complex. The exchange of iron(III) from Acb<sub>2</sub>Fe to Fim was confirmed by optical absorbance spectroscopy and LCMS. The iron exchange was slow, but after 20 hours nearly full exchange was observed, suggesting that the 1:1 FimFe was thermodynamically more stable than the 2:1 Acb<sub>2</sub>Fe complex (**Figure 3.13**). The relevance of iron exchange between siderophores is unknown but could play a role in the overall iron acquisition process through a metal shuttle.<sup>22</sup> The potential for siderophore cooperativity via iron exchange between Fim and PreAcb/Acb involvement is discussed further in the following sections of this chapter. Collectively, these observations support 1:1 stoichiometry and metal chelation through the phenolate oxazoline ligand for the soluble FimFe complex at pH 7.4.

***Fimsbactin A stimulates A. baumannii growth under iron-deficient conditions.***

Formation of stable ferric complexes is the first requirement for siderophore-mediated iron acquisition.<sup>23</sup> The second requirement is import of the *holo*-siderophore across the bacterial cell envelope. To investigate the ability of *A. baumannii* to utilize FimFe as an iron source, we performed kinetic growth recovery assays in M9 minimal medium supplemented with 2,2'-dipyridyl (DIP). We used the model strain *A. baumaunnii* ATCC 17978, a natural producer of Fim and PreAcb/Acb, and fine tuned DIP concentrations, as previously described<sup>4,18,20</sup>, to where only weak growth is observed unless an iron supplement is added to the medium (**Figure 3.14**). As a positive control we showed that both Acb and Acb<sub>2</sub>Fe recover the growth of *A. baumaunnii* ATCC



17978 in a dose-dependent manner (**Figure 3.14a,c, 3.15, 3.16**). As expected from our previous work<sup>4</sup>, Acb<sub>2</sub>Fe stimulates growth at lower concentrations and to a higher final cell density, as measure by optical density at 600 nm (OD<sub>600</sub>) for liquid cultures incubated at 37 °C up to 48 hours. A similar trend was observed for Fim and FimFe, where both promote *A. baumannii* growth in a time- and dose-dependent manner with FimFe, providing faster and more enhanced growth recovery (**Figure 3.14b,d, 3.15, 3.16**). Clearly, pre-loading Acb and Fim with iron(III) is beneficial for growth promotion under these growth conditions. Since Acb<sub>2</sub>Fe and FimFe were both prepared as pure ferric complexes with removal of all residual iron, the potent growth stimulating effects must be attributed to utilization of the siderophore ferric complexes as an iron source. These results show for the first time that FimFe can serve as a true iron source for *A. baumannii* ATCC 17978 and support the role of the fimsbactins as natural siderophore substrates.<sup>24</sup>

***apo-Fim antagonizes the growth promoting effects of [Fe(Acb)<sub>2</sub>].***

After establishing the individual roles of Fim and PreAcb/Acb as siderophores, we sought to probe the more challenging question of why *A. baumannii* produces multiple siderophores in the first place. More specifically, we thought it curious why all pathogenic *A. baumannii* maintain the ability to produce and utilize PreAcb/Acb while <10% produce Fim. We hypothesized that siderophore competition, as opposed to cooperativity, might have led to evolutionary selection of PreAcb/Acb over Fim. To test for siderophore competition between Acb and Fim, we performed checkerboard kinetic growth recovery assays using combinations of Acb, Fim, Acb<sub>2</sub>Fe, and FimFe against *A. baumannii* ATCC 17978 under the same iron restrictive growth conditions described previously (**Figure 3.17-3.18**). We were surprised to discover that combinations of *apo*-siderophores Acb and Fim were growth inhibitory (**Figure 3.17a**) compared to each *apo*-siderophore alone (**Figure 3.14**). Increasing the concentration of Acb from 3.9 μM to 62.5 μM in

the presence of 3.9  $\mu\text{M}$  Fim slightly recovered growth. Increasing the concentration of Fim to 62.5  $\mu\text{M}$  in the presence of 62.5  $\mu\text{M}$  Acb returned the antagonistic effect on Acb-promoted growth. The addition of *holo*-siderophores recovered *A. baumannii* growth, but increasing the concentration of *apo*-siderophores could still antagonize growth slightly. **Figure 3.17b** shows that 15.6  $\mu\text{M}$  Acb<sub>2</sub>Fe can recover *A. baumannii* growth in the presence of 3.9  $\mu\text{M}$  or 62.5  $\mu\text{M}$  Fim. However, Acb<sub>2</sub>Fe at 0.5  $\mu\text{M}$  was not capable of recovering growth in the presence of Fim at 3.9 or 62.5  $\mu\text{M}$ . The addition of *apo*-Acb at 62.5  $\mu\text{M}$  was also slightly antagonistic towards FimFe at 0.5 and 15.6  $\mu\text{M}$  in the growth recovery assay (**Figure 3.17c**), although to a lesser extent than the effect of *apo*-Fim on Acb<sub>2</sub>Fe (**Figure 3.17b**).

The discovery that Fim and Acb appear to be antagonistic adds to the complexity of understanding the delicate balance of metals and siderophores in pathogenic *A. baumannii*. This phenomenon is consistent with our hypothesis that Acb and Fim competition drove natural selection of the Acb pathway found in all *A. baumannii* clinical isolates. In natural environments siderophore competition plays a critical role in microbial population dynamics.<sup>25,26</sup> Siderophore producers often produce siderophore cocktails and express siderophore transport and utilization proteins for xenosiderophores in order to gain a competitive advantage.<sup>19</sup> Some siderophores are inhibitory towards competing bacteria by withholding metals from the extracellular and/or intracellular environment.<sup>27</sup> Some siderophores are attached to antibiotics, so called sideromycins, to deliver a toxic payload into susceptible competitor cells.<sup>28</sup> Some siderophores are thought to directly compete for uptake at the receptor level through endogenous pathways.<sup>20,29</sup> Thus, we turned our attention to probing for pathway competition between Acb and Fim in *A. baumannii* to gain further insight on the underlying cause of the antagonistic siderophore relationship.

### ***Fim, PreAcb, and Acb binding to BauB.***

Bioinformatic analysis of the fimsbactin biosynthetic operon revealed some potential gaps in the uptake pathway, including no dedicated periplasmic siderophore binding protein (SBP) and no inner membrane permease. (A more detailed discussion of the PreAcb/Acb and Fim transport pathways is provided in a later section.) Outer membrane receptors (OMRs) are often highly selective for binding cognate substrates, while SBPs can be broader in terms of binding small molecules.<sup>19,23,28,30</sup> Thus, we hypothesized that the SBP responsible for binding PreAcb/Acb might also bind Fim, which shares structural homology to PreAcb/Acb through the phenolate oxazoline and catecholate moieties. We turned our focus towards BauB, the highly conserved periplasmic SBP responsible for binding PreAcb/Acb and shuttling the corresponding *holo*-siderophores to the membrane permease, BauCDE, to facilitate import to the cytoplasm. We hypothesized that Fim might compete with PreAcb/Acb for BauB binding and inhibit the import of ferric siderophore complexes to the cytoplasm. To test this hypothesized, we pursued *in vitro* reconstitution of BauB and evaluated the ability of *apo*- and *holo*-forms of PreAcb, Acb, and Fim to compete for binding.

The gene encoding for BauB (GenBank AAT52185) contains a *N*-terminal signal sequence (residues 1–22), indicating that BauB is exported from the cytoplasm and localized to the periplasm. The full length *bauB* gene was codon optimized for expression in *E. coli*, and the genetic region encoding for residues 23–322 of BauB was subcloned into a pET28 vector encoding for an *N*-terminal hexahistidine tag and including a TEV protease cleavable site (**Figure 3.19**). After expression in *E. coli* BL21 (DE3) and purification by Ni-NTA affinity chromatography the *N*-His<sub>6</sub>-BauB was used in siderophore binding studies with the intact hexahistidine tag (**Figure 3.20**). We first confirmed binding of BauB to authentic PreAcb and Acb using an intrinsic tryptophan fluorescence quenching assay.<sup>1</sup> We observed dose-dependent fluorescence quenching for both the *apo*- and *holo*-forms of both acinetobactin isomers. The binding of both *apo*- and *holo*-

siderophores by outer membrane siderophore receptors and periplasmic siderophore binding proteins is common.<sup>19,31</sup> The apparent  $K_d$  values for *apo*-PreAcb and *holo*-PreAcb<sub>2</sub>Fe were  $380 \pm 110$  nM and  $750 \pm 160$  nM, respectively (**Table 3.2**). While the apparent  $K_d$  for *holo*-PreAcb<sub>2</sub>Fe appeared to be greater than *apo*-PreAcb, it is noteworthy that the degree of fluorescence quenching was greater for the ferric complex (**Figure 3.21**). In fact, the degree of BauB fluorescence quenching by *holo*-PreAcb<sub>2</sub>Fe was greater than all of the siderophores in the study possibly indicating a unique binding mode. The apparent  $K_d$  values for *apo*-Acb and *holo*-Acb<sub>2</sub>Fe were  $300 \pm 100$  nM and  $160 \pm 80$  nM, respectively (**Table 3.2**). The apparent trend in binding affinities of *apo*- $K_d < \textit{holo}$ - $K_d$  for Acb appear to be reversed for the measurements obtained for PreAcb where *apo*- $K_d > \textit{holo}$ - $K_d$ . Treatment of BauB with *apo*- and *holo*-forms of Fim resulted in dose dependent fluorescence quenching with curve shapes and apparent  $K_d$  values falling within the margin of error for those observed for Acb (**Table 3.2**). The apparent  $K_d$  values for *apo*-Fim and *holo*-FimFe were  $360 \pm 140$  nM and  $240 \pm 90$  nM, respectively. All apparent  $K_d$  values were calculated using a one-site binding model to fit the binding stoichiometry observed in the BauB•Acb<sub>2</sub>Fe crystal structure.<sup>1</sup> These results are consistent with our hypothesis that PreAcb, Acb, and Fim compete for binding to BauB. We next turned to investigating the nature of this binding competition using a siderophore displacement assay with resin-immobilized BauB.

### ***Fimsbactin A and acinetobactin directly compete for binding to BauB.***

To validate that Fim binding to BauB is authentic we performed a competitive binding experiment with Acb<sub>2</sub>Fe and FimFe using resin-immobilized BauB. Our group previously has reported this type of binding assay on the study of ferrioxamine siderophore competition for binding FhuD2, the xenosiderophore receptor displayed on the cell surface of pathogenic *Staphylococcus aureus*.<sup>32</sup> We started by preparing a resin-immobilized BauB column by saturating

Ni-NTA resin with *N*-His<sub>6</sub>-BauB. Column saturation and quantity of immobilized BauB was determined by SDS-PAGE analysis of column flowthrough from the protein-loading step. Treatment of the BauB resin with a solution of Acb<sub>2</sub>Fe resulted in a decrease of ion counts in the EIC trace for *m/z* 347, corresponding to the [M+H]<sup>+</sup> ion for Acb (this is the dominate ion in the MS spectrum of Acb<sub>2</sub>Fe). Treatment of the BauB•Acb<sub>2</sub>Fe resin with a solution of FimFe recovered ion counts for Acb<sub>2</sub>Fe, indicating that the excess FimFe displaced Acb<sub>2</sub>Fe from the resin resulting in BauB•FimFe resin and elution of Acb<sub>2</sub>Fe (**Figure 3.22a**). Similarly, treatment of the BauB resin with FimFe resulted in a decrease of ion counts in the EIC trace for *m/z* 627, corresponding to the [M+H]<sup>+</sup> ion for FimFe (this is the dominate ion in the MS spectrum of FimFe) after washing the column with buffer. Treatment of the BauB•FimFe resin with a solution of Acb<sub>2</sub>Fe recovered ion counts for FimFe in the elution, indicating that the excess Acb<sub>2</sub>Fe displaced FimFe from the resin resulting in BauB•Acb<sub>2</sub>Fe resin and elution of FimFe (**Figure 3.22b**). We also found that the BauB resin could be cycled between treatment with Acb<sub>2</sub>Fe and FimFe multiple times with reversible siderophore displacement. These competition experiments validate that BauB binds to tightly and reversible to both Acb<sub>2</sub>Fe and FimFe. Since BauB binding is reversible, the delicate balance between concentrations of *apo*-siderophores PreAcb, Acb, Fim, and corresponding *holo* ferric complexes will ultimately determine which siderophore species dominates the BauB binding equilibrium. Our results here show that Fim antagonizes *A. baumannii* growth promotion by Acb<sub>2</sub>Fe, suggesting that occupancy of BauB in the periplasm by Fim might exclude import of Acb<sub>2</sub>Fe to the cytoplasm. This suggests that concentrations of Acb are kept higher than concentrations of Fim during growth of *A. baumannii* ATCC 17978 under iron deficient minimal medium conditions to balance siderophore cooperativity and pathway competition allowing for efficient iron scavenging.

### ***Structural similarity of FimFe, PreAcb<sub>2</sub>Fe, and Acb<sub>2</sub>Fe ferric complexes.***

In order to bind BauB, the molecular volume, stereochemistry, and geometrical orientation of ligands around the ferric metal center must be similar for PreAcb<sub>2</sub>Fe, Acb<sub>2</sub>Fe, and FimFe. We investigated these properties using density functional theory (DFT) calculations to create energy minimized structural models of PreAcb<sub>2</sub>Fe and FimFe using the experimentally observed geometry of the Acb<sub>2</sub>Fe complex recently reported for the BauB•Acb<sub>2</sub>Fe crystal structure (**Figure 3.23**).<sup>1</sup> We assumed that PreAcb<sub>2</sub>Fe, Acb<sub>2</sub>Fe, and FimFe exist as the mono anions in the ferric complexes. BauB appears to recognize one enantiomer of the *cis*-[Acb<sub>2</sub>Fe]<sup>-</sup> isomeric form. The DFT-computed energy minimized structures of [FimFe]<sup>-</sup> (**Figure 3.23a**) and *cis*-[PreAcb<sub>2</sub>]<sup>-</sup> (**Figure 3.23b**) were strikingly similar to the experimentally observed *cis*-[Acb<sub>2</sub>Fe]<sup>-</sup> complexed to BauB (**Figure 3.23c**). An overlay of the three structures revealed how the common phenolate oxazoline fragment aligns nicely and the L-Ser stereochemistry enables [FimFe]<sup>-</sup> to map the hydroxamate and catecholate ligands to the same ferric binding sites as the imidazole and catecholate ligands of *cis*-[Acb<sub>2</sub>Fe]<sup>-</sup>, respectively. As shown in **Figure 3.23e**, BauB binds one half of the *cis*-[Acb<sub>2</sub>Fe]<sup>-</sup> complex through hydrophobic interactions with one of the Acb ligands while the second Acb ligand remains largely solvent exposed. The computed structures of *cis*-[PreAcb<sub>2</sub>Fe]<sup>-</sup> and [FimFe]<sup>-</sup> would appear to fit this same binding mode to BauB and might explain how all three siderophores can compete for binding to periplasmic BauB. Since FimFe is the only stable 1:1 complex, this could indicate that BauB cannot facilitate transport of 1:1 siderophore:iron complexes across the inner membrane through the associated membrane permease BauCDE hinting at a potential shuttling mechanism for 2:1 PreAcb/Acb:iron complexes.<sup>22,33,34</sup>

### ***A new model for siderophore cooperativity in A. baumannii.***

Our findings have been largely consistent with the current understanding of PreAcb/Acb biosynthesis and utilization in pathogenic *A. baumannii* (**Figure 3.24**). PreAcb is the kinetic biosynthetic product of the biosynthetic enzymes BasA–J, while Acb is formed via non-enzymatic isomerization of PreAcb as the thermodynamic biosynthetic end product.<sup>35,36</sup> Both PreAcb and Acb can reach the extracellular space, presumably via efflux mediated in part by BarAB.<sup>4</sup> The TonB-dependent OMR BauA has been shown to be essential for PreAcb/Acb utilization, presumably providing import of *holo*-siderophores to the periplasm.<sup>37,38</sup> The periplasmic SBP BauB, which might be membrane anchored although this has not been experimentally confirmed<sup>1</sup>, is then thought to shuttle *holo*-siderophores to the ABC-type membrane permease BauCDE<sub>2</sub> where import to the cytoplasm is driven by ATP hydrolysis. BauF is a putative flavin-dependent oxidoreductase responsible for reduction of the ferric *holo*-siderophore complexes to release ferrous for incorporation into protein scaffolds such as the iron-sulfur cluster generating protein SufU.<sup>39,40,41</sup> The *apo*-siderophores, PreAcb and/or Acb, can then reenter the transport cycle.

Our findings provide new insight into the role of PreAcb, Acb, and Fim in overall siderophore-mediated iron acquisition by *A. baumannii*. The Fim biosynthetic operon contains genes encoding for an efflux pump FbsOQ, a TonB-dependent OMR FbsN, and a putative reductase FbsP. The reductase FbsP is predicted to be secreted to the periplasm due to the presence of an *N*-terminal signal sequence, similar to the siderophore-interacting periplasmic reductases YqjH and FpvC in *E. coli* and *P. aeruginosa*, respectively.<sup>40,42</sup> We propose that Fim is exported in part by FbsOQ after biosynthesis in the cytoplasm. Extracellular FimFe is presumably imported to the periplasm by FbsN where periplasmic reduction by FbsN releases Fim that reenters the transport cycle and ferrous iron for direct import to the periplasm via the endogenous ferrous transport system FeoABC.<sup>43,44</sup> This transport model is analogous to the well-studied utilization

pathway for the siderophore pyoverdine in pathogenic *P. aeruginosa*.<sup>45</sup> Furthermore, *P. aeruginosa* balances the use of multiple siderophores for adaptive iron acquisition during infection where some siderophores stay in the periplasm (pyoverdine) and some enter the cytoplasm (pyochelin).<sup>46</sup> Analogously, *A. baumannii* might utilize Fim as the periplasmic siderophore and PreAcb/Acb as the cytoplasmic siderophore. This model suggests that Fim never makes it to the cytoplasm, which is consistent with the observation that fimsbactin analogs conjugated to antibiotics with periplasmic targets (beta-lactams, daptomycin, vancomycin) show potent, iron-dependent growth inhibitory activity against *A. baumannii* while the same siderophores conjugated to antibiotics with cytoplasmic targets (fluoroquinolones) show no antibacterial activity.<sup>47</sup> One unique structural feature of fimsbactin A is the presence of an L-Ser-2,3-DHB ester, which resembles a fragment of the L-Ser-2,3-DHB tri-lactone scaffold of enterobactin.<sup>48</sup> Similar to enterobactin, it is possible that hydrolysis of the L-Ser-2,3-DHB ester in the periplasm may play a role in iron release.<sup>49</sup> The product of fimsbactin A hydrolysis is fimsbactin F, which is the second most concentrated member of the fimsbactin mixture present in *A. baumannii* ATCC 17978 supernatants (**Figures 3.3-3.6, 3.25**).

If fimsbactins accumulate in the periplasm, this would create a scenario for competition between Fim and PreAcb/Acb to bind BauB that is consistent with our current findings. A build up of excess Fim in the periplasm could shift the BauB equilibrium towards BauB•Fim and inhibit the import of PreAcb/Acb leading to the growth inhibitory effect that we observed for the siderophore combinations. It is also possible that Fim, PreAcb, and Acb compete for iron and form mixed siderophore ferric complexes that act as transport inhibitors. A crystal structure of the *A. baumannii* outer membrane siderophore receptor, BauA, bound to a mixed (PreAcb)(Acb)Fe ferric complex was recently deposited in the protein data bank (PDB 6H7F). The



BauA•(PreAcb)(Acb)Fe structure shows complexation of the iron by the PreAcb ligand through phenolate oxazoline, hydroxamate, and imidazole filling four of the six coordination sites in the octahedral ferric center. The final two coordination sites are apparently filled by the 2,3-DHB catecholate of the Acb ligand. The structure suggests that BauA only interacts with the PreAcb ligand while the Acb dangles outside of the binding pocket. Our group recently reported a competitive inhibitor of siderophore uptake based on an oxidized analog of PreAcb that induces an iron-dependent growth inhibitory effect on *A. baumannii* that is similar to the effect of *apo-Fim*.<sup>20</sup> The oxidized PreAcb features an aromatic oxazole in place of the PreAcb oxazoline that stabilizes the PreAcb structure and prevents isomerization to Acb. The BauA•(PreAcb)(Acb)Fe structure suggests that *apo-* and *holo-* variants of the oxazole PreAcb and/or fimsbactin A might also bind to BauA in a similar manner, although this requires experimental validation.

Our work suggests that competition for periplasmic BauB is possible, but it is not entirely clear whether competition for BauA plays a role in the growth inhibitory effect of *apo-fimsbactin A*. We tested the effect of excess *apo-Fim* on the growth of *A. baumannii* ATCC 19606T, a strain that does not produce the fimsbactins, but does produce PreAcb/Acb and is predicted to produce baumannoferrin (**Figure 3.26**).<sup>5,37</sup> Treatment of wild type *A. baumannii* ATCC 19606T and mutant variants s1 (insertional mutant in *basD*, deficient in PreAcb/Acb biosynthesis), t6 (insertional mutation in *bauA*, deficient in PreAcb/Acb import to periplasm), and t7 (insertional mutation in *bauD*, deficient in PreAcb/Acb import to cytoplasm) with *apo-Fim* under iron deficient minimal medium conditions produced the same growth inhibited phenotype in the kinetic growth studies (**Figures 3.27-3.28**). Addition of *holo-FimFe* recovered the growth of wild type and mutant *A. baumannii* strains suggesting that FimFe can serve as an iron source in the absence of the dedicated Fim utilization proteins FbsOQNP. It is possible that FimFe can be imported through BauA and/or

some of the other ~20 TonB-dependent outer membrane receptors<sup>50</sup> present in pathogenic strains of *A. baumannii* through direct import or siderophore shuttling with PreAcb/Acb.<sup>22,51</sup> These results suggest that fimsbactin A bioactivity is independent of BauA and BauD consistent with the hypothesis for periplasmic accumulation of toxic levels of Fim. A recent study in *Mycobacterium tuberculosis* showed that a siderophore efflux mutant accumulated toxic concentrations of mycobactin siderophores supporting the idea that maintaining the appropriate balance of intracellular siderophores is critical to balance metal homeostasis.<sup>52</sup> The same appears to be true for *A. baumannii*. Regardless of the underlying cause of *apo*-fimsbactin toxicity, the growth studies with *A. baumannii* ATCC 19606T confirm that pathway competition between PreAcb, Acb, and Fim is important even for non-producers of the fimsbactins, including the majority of *A. baumannii* clinical isolates.

### 3.5 Outlook and Conclusions

Pathogenic bacteria often produce multiple siderophores to enhance iron acquisition, expand capacity for metal scavenging, evade the human immune system, and gain a competitive edge in mixed microbial environments. All genome sequenced clinical isolates of the MDR Gram-negative pathogen *A. baumannii* produce the siderophores PreAcb, Acb, and baumannoferrin. PreAcb and Acb both enhance iron acquisition and contribute to pathogen virulence, while the role of baumannoferrin has not yet been investigated. A small percentage (<10%) of *A. baumannii* clinical isolates produce a third family of siderophores known as the fimsbactins. We have shown that *A. baumannii* ATCC 17978 produces Acb in greater quantities than Fim and both siderophores can be purified from culture supernatants. Here, we show that fimsbactin A, the primary component of the fimsbactin siderophore mixture, competes directly with Acb/Acb<sub>2</sub>Fe for import across the *A. baumannii* cell envelope. The two siderophores compete directly for binding to the

periplasmic siderophore binding protein BauB and possibly to other proteins in the Acb pathway. This competition might explain why the majority of *A. baumannii* clinical isolates have lost the ability to produce the fimsbactins but have maintained genes for Acb biosynthesis and expression in a highly conserved manner. Due to the structural similarities of Fim, PreAcb, and Acb, sharing common NRPS-derived fragments from phenolate oxazolines and catecholates from 2,3-DHB, we propose that the fimsbactin scaffold serves as an ideal template for designing new siderophore-antibiotic conjugates that can outcompete native siderophores for cell entry under infection conditions; however, this antibiotic delivery strategy should be reserved for antibiotics with periplasmic targets, since our current understanding of the fimsbactin pathway suggests import is limited to the periplasm.<sup>47,53,54</sup> The inherent growth inhibitory effect of *apo*-Fim towards *A. baumannii* also presents the opportunity to design competitive inhibitors of siderophore uptake that might serve as antivirulence agents to starve the pathogen of iron.<sup>20,27</sup> Our findings suggest that if concentrations of the fimsbactin are kept low, we hypothesize that Acb and Fim can function cooperatively to enhance iron acquisition in *A. baumannii*; but if the concentration of Fim exceeds Acb, the presence of multiple siderophores becomes counter productive. Further studies on the effects of natural siderophore combinations are needed to reveal the subtle details of cooperativity and competition at the molecular, protein, and cellular level of bacterial iron acquisition.

## 3.6 Materials and Methods

### *Strains, Materials, and Instrumentation.*

Growth studies were conducted using *A. baumannii* ATCC 17978 and ATCC 19606T. The s1, t6, and t7 mutant strains of *A. baumannii* ATCC 19606T were obtained from Prof. Luis Actis (Miami University).<sup>37</sup> Pre-cultures and 96-well plate *A. baumannii* growth assays were performed in filter-sterilized M9 minimal media. M9 minimal media was prepared for all experiments as

previously described.<sup>4,18,20</sup> Samples for LC-MS were prepared in 0.45  $\mu$ M PTFE mini-UniPrep vials from Agilent. All preparatory HPLC was performed using a Beckman Coulter SYSTEM GOLD 127P solvent module and 168 detector with a Phenomenex Luna 10u C18(2) 100A column, 250  $\times$  21.20 mm, 10  $\mu$ m with guard column. Prep HPLC was performed with a mobile phase of 5 mM ammonium acetate in (A) water and (B) acetonitrile, and data were processed using 32 Karat software, v7.0. LC-MS was performed on an Agilent 6130 quadrupole LC-MS with G1313 autosampler, G1315 diode array detector, and 1200 series solvent module. A Phenomenex Gemini C18 column, 50  $\times$  2 mm, 5  $\mu$ m with guard column was used for all LC-MS separations. LC-MS mobile phases were 0.1% formic acid in (A) water and (B) acetonitrile, and data were processed using G2710 ChemStation software. NMR was performed on a Varian Unity Inova-600 MHz instrument with a cold probe. Bacterial growth studies were performed using polystyrene 96-well plates with polystyrene lids. OD<sub>600</sub> measurements were taken on a Molecular Devices SpectraMax Plus 384 plate reader.

### ***Isolation and purification of Acb and Fim.***

Acinetobactin (Acb) and fimsbactin A (Fim) was isolated and purified from *A. baumannii* ATCC 17978 cultures using a modified literature procedure.<sup>4,55</sup> PreAcb was synthesized as described previously by our group.<sup>4</sup> Briefly, 1 L cultures of *A. baumannii* ATCC 17978 were grown overnight in M9 minimal media. Cells were pelleted and the supernatant was adjusted to pH ~6 using citric acid. XAD-7HP resin was added to the supernatant and the mixture was shaken gently. The mixture was filtered and the resin was washed with methanol. The methanol washings were combined and concentrated via rotary evaporation under reduced pressure. Acb (retention time 12 min, 31 mg/L) and Fim (retention time 15 min, 5 mg/L) were purified from the crude residue by preparatory HPLC (gradient of 0% B to 95% B over 17 min, then 95% B to 100% B

over 8 min). Fim represents a mixture of fimsbactin A (>90%) and fimsbactins B,C,F (≤10%) as judged by NMR and LC-MS analysis (**Figures 3.3-3.9**). The *holo*-siderophores were prepared by mixing PreAcb, Acb, and Fim with excess Fe(acac)<sub>3</sub> in methanol following by concentration and trituration with Et<sub>2</sub>O to provide the pure PreAcb<sub>2</sub>Fe, Acb<sub>2</sub>Fe, and FimFe complexes.<sup>4,18</sup>

#### ***A. baumannii* Growth Studies.**

Stock solutions of Acb, Fim, Acb<sub>2</sub>Fe, and FimFe were prepared in M9 media at 250 μM (up to 2.5% final DMSO v/v). Each well of a 96-well plate was filled with 50 μL of M9 media. 50 μL of the 250 μM test compound stock solutions were added to the first row of a 96 well plate. Compounds were serially diluted down the plate to 3.9 μM. An inoculum was made by adding 100 μL of 0.5 McFarland standard (*A. baumannii* ATCC 17978 or ATCC 19606T-wt, s1, t6, and t7 mutants) to 4.0 mL of M9 minimal media supplemented with 350 μM 2,2'-dipyridyl (DIP). Inoculum (50 μL) was added to each well for a final concentration of 175 μM DIP per well and a serial dilution of test compounds at 62.5-1.95 μM. Growth promotion was determined at 37 °C by measuring OD<sub>600</sub> using a microplate reader (Molecular Devices SpectraMax Plus 384 plate reader). Control growth curves were performed in M9 media with 175 μM DIP and no test compounds. DIP concentrations were optimized prior to each experiment by serial dilution against *A. baumannii* under the growth conditions described in this section. All experiments were performed in triplicate as independent trials.

For the biological evaluation of combinations of Acb, Fim, and corresponding ferric complexes, a 96-well plate was filled with 40 μL of M9 minimal media per well, 5 μL of each of the compounds of interest, a final concentration of 175 μM DIP per well and 50 μL of the inoculum. To explore the combination of Acb/Fim, the following concentrations were tested in duplicate in all possible combinations: 3.9 μM, 15.6 μM, 62.5 μM. For the combination of Acb/FimFe the

following concentrations were tested in duplicate in all possible combinations: Acb 3.9  $\mu\text{M}$ , 15.6  $\mu\text{M}$ , 62.5  $\mu\text{M}$ ; FimFe 0.5  $\mu\text{M}$ , 3.9  $\mu\text{M}$ , 15.6  $\mu\text{M}$ . For the combination of Acb<sub>2</sub>Fe/Fim the following concentrations were tested in duplicate in all possible combinations: Acb<sub>2</sub>Fe 0.5  $\mu\text{M}$ , 3.9  $\mu\text{M}$ , 15.6  $\mu\text{M}$ ; Fim 3.9  $\mu\text{M}$ , 15.6  $\mu\text{M}$ , 62.5  $\mu\text{M}$ . Growth promotion was determined at 37 °C by measuring OD<sub>600</sub> using a microplate reader (Molecular Devices SpectraMax Plus 384 plate reader). Control growth curves were performed in M9 media with 175 DIP and no test compounds. All experiments were performed in duplicate as independent trials.

#### ***Determination of FimFe Complex Stoichiometry.***

A solution of 570  $\mu\text{M}$  Fim in methanol was prepared. A fluorescence emission spectrum was recorded ( $\lambda_{\text{excitation}} = 330 \text{ nm}$ ;  $\lambda_{\text{emission}} = 380 \text{ nm}$ ). To determine stoichiometry of the complex between Fim and Fe(III), aliquots of a methanolic solution of Fe(acac)<sub>3</sub> were added 0.044 equivalents at a time via Hamilton syringe and emission spectra were recorded after each addition. Peak fluorescence (Abs<sub>380nm</sub>) was plotted against Fe(III) equivalents to reveal a 1:1 FimFe stoichiometry (**Figure 3.11**).

#### ***Determination of Apparent $K_{\text{Fe}}$ for FimFe.***

A stock solution of 100  $\mu\text{M}$  FimFe was prepared in 10 mM HEPES buffer (10 mM HEPES, 600 mM NaCl, 100 mM KCl, pH 7.4) and an optical absorbance spectrum was obtained from  $\lambda = 300\text{--}700 \text{ nm}$  (**Figure 3.12**). While continuously monitoring optical absorbance at 500 nm, EDTA was added at a final concentration of 120  $\mu\text{M}$  (1.2 equivalents relative to FimFe). The apparent iron-binding affinity ( $K_{\text{Fe}}$ ) was determined based on the change in optical absorbance at 500 nm after 800 min for two independent trials using the equations provided in the supplementary information.

### ***N-His<sub>6</sub>-BauB Expression and Purification.***

The *bauB* gene from *Acinetobacter baumannii* (Genbank Accession Number AAT52185) was codon optimized for expression in *E. coli* and cloned into a pET28b vector by GenScript Biotech Corporation. The *bauB* gene was then subcloned into a pET28bTEV vector using restriction enzyme-based cloning (**Figure 3.19**).<sup>1</sup> BauB was expressed as the *N*-terminal hexahistidine fusion, *N*-His<sub>6</sub>-BauB, in *E. coli* BL21 (DE3). Briefly, *E. coli* BL21 (DE3) transformed with the BauB expression plasmid were grown in 1 L of terrific broth at 37 °C in a 3 L baffled flask, in the presence of 50 µg/mL kanamycin to an OD<sub>600</sub> of ~0.5. The culture flask was cooled to 20 °C and BauB expression was induced by the addition of 0.5 mM IPTG (final concentration). Cells were grown overnight (~12 h) at 20 °C. Cells were harvested via centrifugation at 4 °C for 30 min (all remaining steps were carried out at 4 °C). Cells were washed with lysis buffer (50 mM potassium phosphate pH 8.0, 500 mM NaCl, 5 mM BME, 20 mM imidazole, 10% glycerol) and flash frozen in liquid N<sub>2</sub> (40 mL total volume). The frozen cell pellet was thawed and lysed by two passes through an Emulsiflex C5 (Avestin). The lysate was clarified by ultra-centrifugation at 50000g for 35 min. The supernatant was passed through Ni-NTA resin and eluted with 300 mM imidazole in lysis buffer. Elution fractions were analyzed by SDS-PAGE with visualization by Coomassie blue staining. Fractions containing pure *N*-His<sub>6</sub>-BauB were combined, dialyzed (50 mM potassium phosphate pH 8.0, 150 mM NaCl, 1 mM DTT, 5% glycerol), and concentrated via centrifugal filtration. Protein purity was analyzed by SDS-PAGE with visualization by Coomassie blue staining (**Figure 3.20**). Protein mass were confirmed by ESI-MS. Purified protein was flash frozen in liquid N<sub>2</sub> at 180 µM and stored at -80 °C.

### ***Determination of Apparent $K_d$ Values for BauB.***

*N*-His<sub>6</sub>-BauB was recovered on ice from a -80 °C freezer stock. A 400 nM BauB stock solution was prepared in assay buffer (25 mM Tris-HCl, 8 g/L NaCl, 0.2 g/L KCl, pH 7.4). For each measurement, 300 µL of the BauB stock solution was transferred to a fluorescence cuvette (HellmaAnalytics High Precision Cell cuvette made of Quartz SUPRASIL; light path 10 x 2 mm) in the presence of substrate (PreAcb, PreAcb<sub>2</sub>Fe, Acb, Acb<sub>2</sub>Fe, Fim, FimFe) at concentrations ranging from 100–1200 nM. Emission spectra were recorded at  $\lambda_{\text{emission}} = 300\text{--}400$  nm using a PerkinElmer LS 55 Luminescence Spectrometer (slit width 10 nm; scan speed 400 nm/min) at  $\lambda_{\text{excitation}} = 280$  nm. Fluorescence intensity at 320 nm was plotted versus substrate concentration (nM) and apparent  $K_d$  was calculated using nonlinear regression and a one binding site model in GraphPad Prism v7.0b (**Figure 3.21**).<sup>1</sup> All experiments were performed in duplicate as independent trials.

### ***Siderophore Competition Studies with Immobilized BauB.***

*N*-His<sub>6</sub>-BauB was immobilized on Ni-NTA resin following a literature protocol for performing siderophore-affinity chromatography.<sup>32</sup> Saturation of the Ni-NTA resin (2.3 cm x 1 cm resin volume) with BauB was confirmed by SDS-PAGE analysis of the column flowthrough. The Ni-NTA-BauB column was washed thoroughly with phosphate buffer (50 mM potassium phosphate pH 8.0, 150 mM NaCl, 1 mM BME, 5% glycerol). A solution of Acb<sub>2</sub>Fe (5 mL, 0.1 mg/mL) was loaded onto the column and column was rocked gently for 30 min at 4 °C. Column flowthrough was collected and the resin was washed with excess phosphate buffer (5 x 5 mL). FimFe (5 mL, 0.1 mg/mL) was then loaded and the column was gently rocked for 30 min at 4 °C. The flowthrough was collected and the resin was washed with excess phosphate buffer (5 x 5 mL). Acb<sub>2</sub>Fe (5 mL, 0.1 mg/mL) was then added back onto the column and after rocking for 30 min the flowthrough was collected. Aliquots of the column loading solutions and elutions were analyzed



by LCMS for the presence of Acb<sub>2</sub>Fe and FimFe. For Acb<sub>2</sub>Fe, the extracted ion chromatogram (EIC) for  $m/z = 347$ , corresponding to the  $[M+H]^+$  for *apo*-Acb, was plotted. For FimFe, the EIC for  $m/z = 627$  corresponding to the  $[M+H]^+$  for *holo*-FimFe was plotted.

### ***DFT Calculations.***

Stable *holo*-siderophore complexes with ferric iron were calculated using density functional theory<sup>56,57</sup> (DFT) in a similar manner as described previously.<sup>1</sup> We used the crystal structure of the Acb<sub>2</sub>FeIII(S=5/2) complex bound to BauB (PDB 6FML) as starting geometry of the PreAcb<sub>2</sub>Fe and FimFe ferric complexes. Monte Carlo/MMFF molecular mechanics/dynamics was used to explore conformer spaces. Initial structure optimization was performed by using the PM3d semi-empirical algorithm (Spartan Linux v10, WaveFunction, Inc.). We employed DFT (Density Functional Theory, Gaussian 09, Gaussian Inc.) for calculations using the PBE0 hybrid functional (PBE1PBE in Gaussian parlance) with basis sets Def2-SVP and Def2-TZVP. Minima were optimized at the level PBE0/Def2-SVP and single-point energies were calculated at level PBE0/Def2-TZVP, with scaled thermal-energy corrections from B3LYP/6-31G(d,p).<sup>58</sup> Solvent-based single-point energies were calculated at the same level using the CPCM polarizable conductor calculation model for water and the Universal Force Field for atomic radii.<sup>59</sup> DFT functionals and basis sets were chosen for efficiency and compatibility with ferric complexes.<sup>60,61,62</sup>

## 3.7 Figures and Tables

### Fimsbactin Biosynthetic Gene Clusters

AbPK1 (GenBank: GCA\_002753915.1)

Query sequence



BGC0000352: Fimsbactin biosynthetic gene cluster (100% of genes show similarity)



AB042 (GenBank: GCA\_001941765.1)

Query sequence



BGC0000352: Fimsbactin biosynthetic gene cluster (100% of genes show similarity)



D36 (GenBank: GCA\_001399655.1)

Query sequence



BGC0000352: Fimsbactin biosynthetic gene cluster (100% of genes show similarity)



Strain ATCC 17978 (GenBank: GCA\_001593425)

Query sequence



BGC0000352: Fimsbactin biosynthetic gene cluster (100% of genes show similarity)

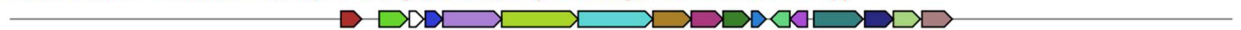


ATCC 17978-mmf (GenBank: GCA\_001077675.1)

Query sequence



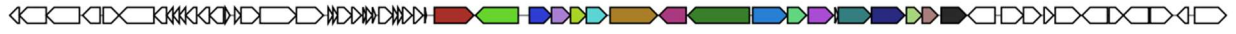
BGC0000352: Fimsbactin biosynthetic gene cluster (94% of genes show similarity)



# Acinetobactin Biosynthetic Gene Clusters

AbPK1 (GenBank: GCA\_002753915.1)

Query sequence



BGC0000294: Acinetobactin biosynthetic gene cluster (78% of genes show similarity)



AB042 (GenBank: GCA\_001941765.1)

Query sequence



BGC0000294: Acinetobactin biosynthetic gene cluster (100% of genes show similarity)



D36 (GenBank: GCA\_001399655.1)

Query sequence



BGC0000294: Acinetobactin biosynthetic gene cluster (100% of genes show similarity)



Strain ATCC 17978 (GenBank: GCA\_001593425)

Query sequence

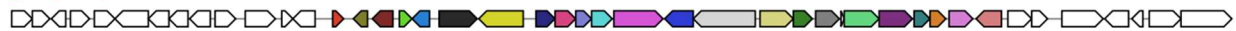


BGC0000294: Acinetobactin biosynthetic gene cluster (100% of genes show similarity)



ATCC 17978-mmf (GenBank: GCA\_001077675.1)

Query sequence



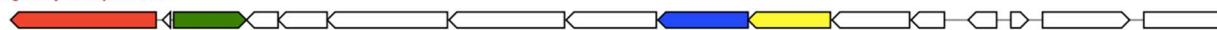
BGC0000294: Acinetobactin biosynthetic gene cluster (100% of genes show similarity)



## Acinetoferrin/Baumannoferrin Biosynthetic Gene Clusters

AbPK1 (GenBank: GCA\_002753915.1)

Query sequence

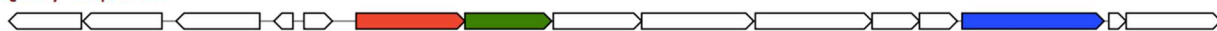


BGC0000295: Acinetoferrin biosynthetic gene cluster (40% of genes show similarity)



AB042 (GenBank: GCA\_001941765.1)

Query sequence



BGC0000295: Acinetoferrin biosynthetic gene cluster (30% of genes show similarity)



D36 (GenBank: GCA\_001399655.1)

Query sequence

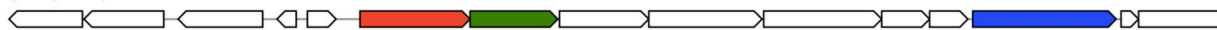


BGC0000295: Acinetoferrin biosynthetic gene cluster (30% of genes show similarity)



Strain ATCC 17978 (GenBank: GCA\_001593425)

Query sequence



BGC0000295: Acinetoferrin biosynthetic gene cluster (30% of genes show similarity)



ATCC 17978-mmf (GenBank: GCA\_001077675.1)

Query sequence



BGC0000295: Acinetoferrin biosynthetic gene cluster (30% of genes show similarity)



**Figure 3.1.** AntiSMASH<sup>63</sup> analysis of putative fimsbactin *A. baumannii* producers identified from BLASTp analysis of *A. baumannii* genomes reveals conservation of acinetobactin and baumannoferrin biosynthetic gene clusters (BGCs). The acinetoferrin BGC is the reference in the antiSMASH database. Acinetoferrin and baumannoferrin BGCs share homology, so comparison for all strains was made to the acinetoferrin BGC.<sup>64</sup>

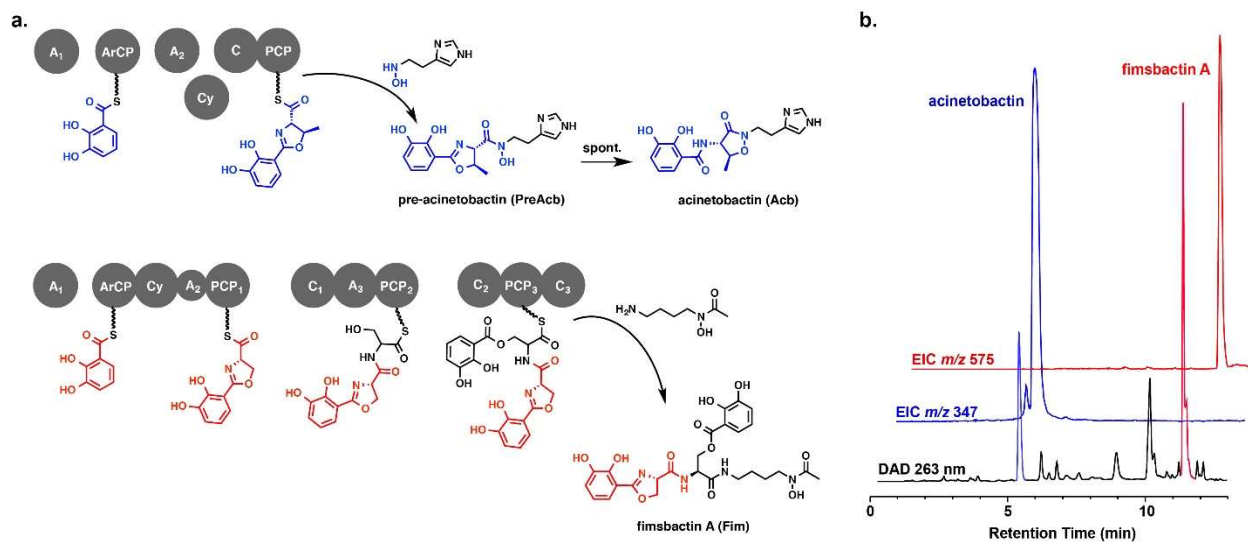


**Figure 3.2:** Siderophore biosynthesis in *A. baumannii*. (a) NRPS assembly lines for acinetobactin (top) and fimsbactin A (bottom) share a common precursor, 2,3-DHB, and a common phenolate oxazoline motif. (b) DAD at 263 nm (black), EIC at  $m/z$  347 (blue), and EIC at  $m/z$  576 (red) chromatograms from LCMS analysis of crude *A. baumannii* ATCC 17978 supernatant after acidification, treatment with XAD-7HP resin, and methanol elution. Same as **Figure 1.7**.

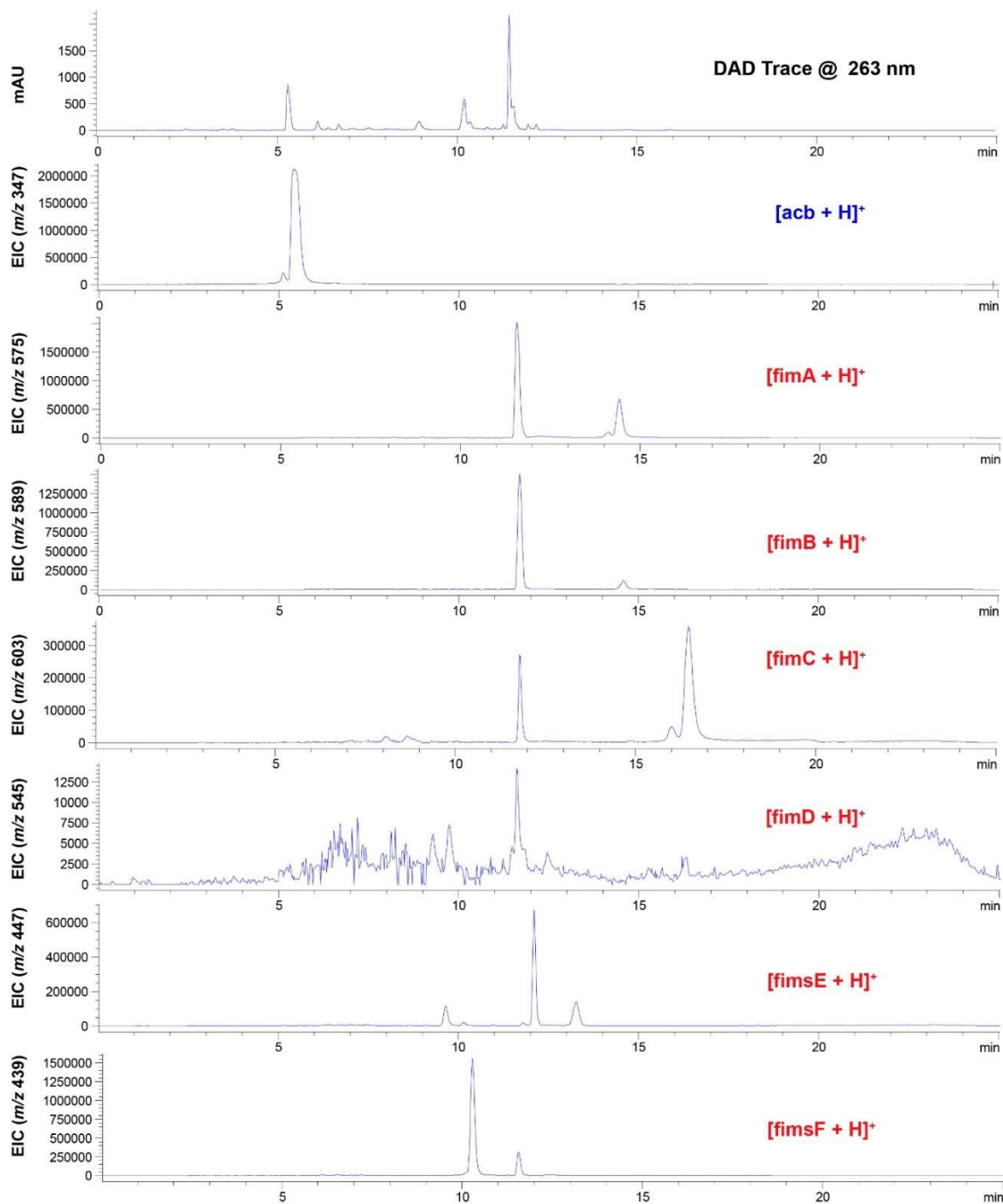


**Figure 3.3.** Diode array optical absorbance detection (DAD) and extracted ion chromatograms (EICs) for fimsbactin A–F  $[M+H]^+$  ions from LCMS analysis of *A. baumannii* ATCC 17978 culture supernatant extractions (**Trial #1**) using ESI ionization in positive ion mode. The x-axis represents retention time (min) for all chromatograms.

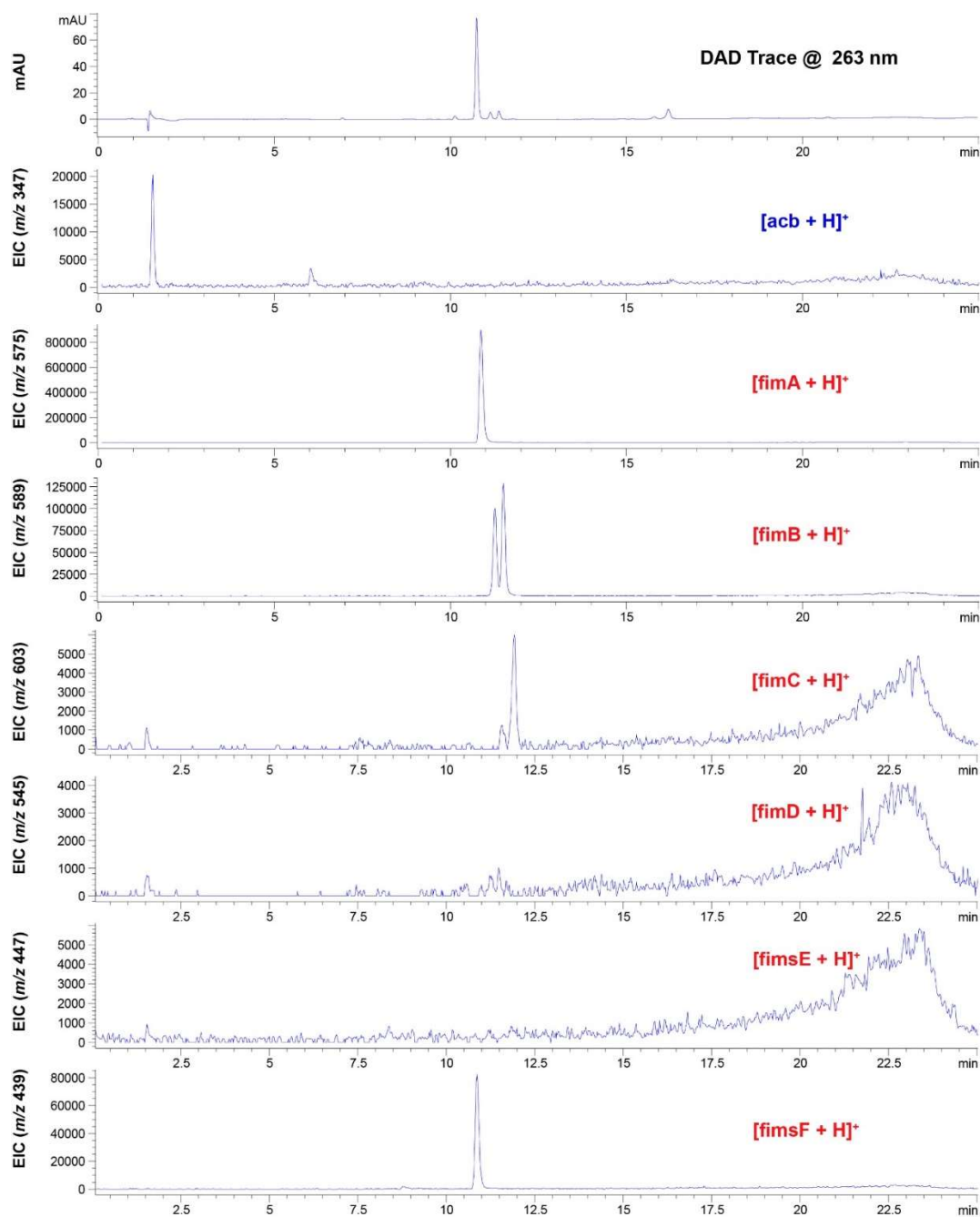


**Figure 3.4.** Diode array optical absorbance detection (DAD) and extracted ion chromatograms (EICs) for fimsbactin A–F  $[M+H]^+$  ions from LCMS analysis of HPLC-purified fimsbactin A from *A. baumannii* ATCC 17978 (**Trial #1**) using ESI ionization in positive ion mode. The x-axis represents retention time (min) for all chromatograms.

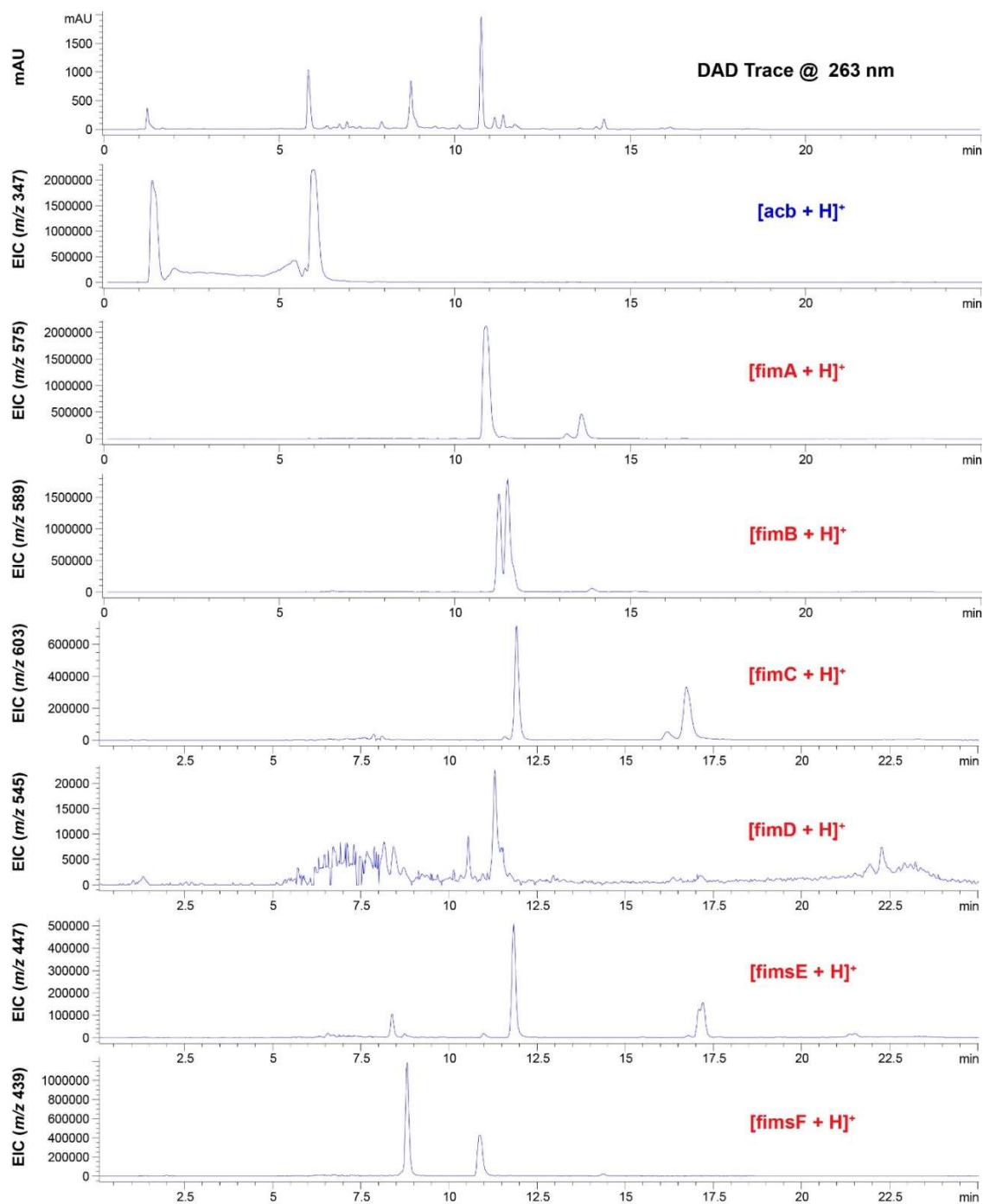


**Figure 3.5.** Diode array optical absorbance detection (DAD) and extracted ion chromatograms (EICs) for fimsbactin A–F  $[M+H]^+$  ions from LCMS analysis of *A. baumannii* ATCC 17978 culture supernatant extractions (**Trial #2**) using ESI ionization in positive ion mode. The x-axis represents retention time (min) for all chromatograms.



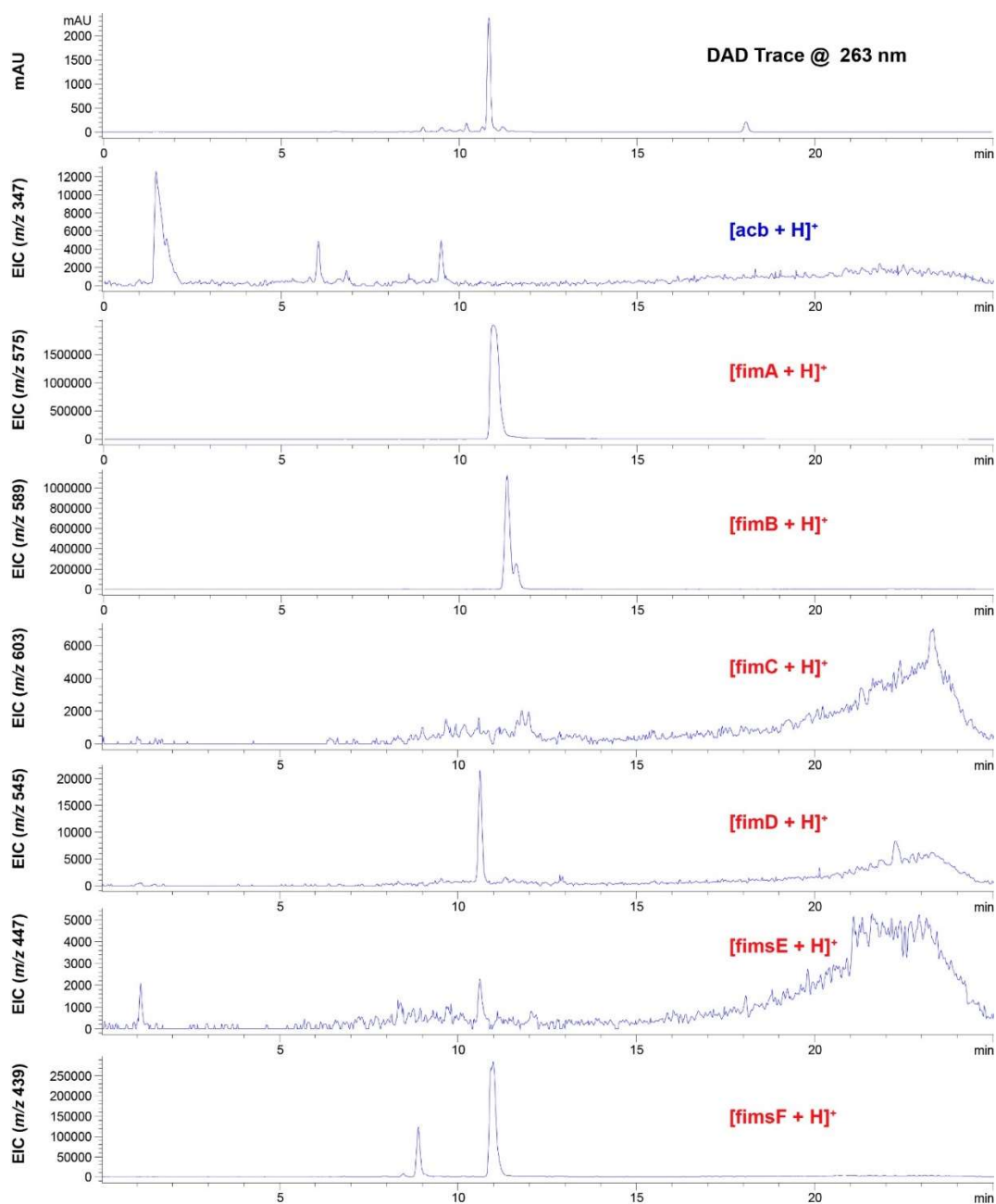
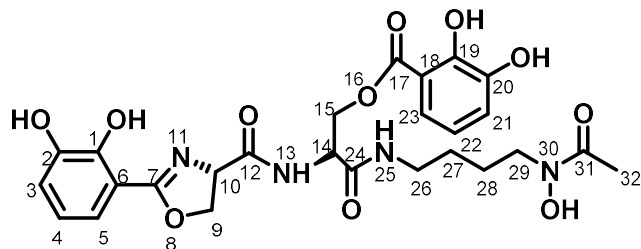


**Figure 3.6.** Diode array optical absorbance detection (DAD) and extracted ion chromatograms (EICs) for fimsbactin A–F  $[M+H]^+$  ions from LCMS analysis of HPLC-purified fimsbactin A from *A. baumannii* ATCC 17978 (**Trial #2**) using ESI ionization in positive ion mode. The x-axis represents retention time (min) for all chromatograms.



	$^{13}\text{C} - \text{Reported}^2$	$^{13}\text{C} - \text{Observed}$	$^1\text{H} - \text{Reported}^2$	$^1\text{H} - \text{Observed}$
1	148.2	148.2		
2	145.7	145.7		
3	119.3	119.5	6.968 (dd)	6.97 (dt)
4	118.6	118.7	6.74 (t)	6.74 (t)
5	117.7	117.9	7.08 (dd)	7.07 (dd)
6	110.1	110.1		
7	166.3	163.6		
9	69.1	69.3	4.52 (dd)	4.52 (dd)
			4.61 (dd)	4.60 (m)
10	66.9	67.2	5.06 (dd)	5.06 (dd)
11				
12	169.9	168.9		
13			8.72 (dd)	8.74 (d)
14	51.5	51.7	4.72 (m)	4.72 (m)
15	64.3	64.5	4.39 (m)	4.39 (dd)
			4.61 (m)	4.60 (m)
17	168.7	167.9		
18	112.8	112.8		
19	149.5	149.5		
20	146.0	146.0		
21	120.7	120.9	6.97 (dd)	6.97 (dt)
22	118.6	118.8	6.59 (t)	6.59 (t)
23	119.6	119.8	7.15 (dd)	7.15 (dd)
24	167.7	166.5		
25			8.23 (dt)	8.26 (t)
26	38.3	38.5	3.10 (m)	3.09 (m)
27	25.9	26.4	1.38 (m)	1.38 (m)
28	23.5	23.7	1.49 (m)	1.49 (m)
29	46.3	46.5	3.45 (t)	3.45 (t)
31	170.1	170.1		
32	20.1	20.3	1.96 (s)	1.96 (s)

**Table 3.1.** NMR characterization data for purified fimsbactin A from this work compared with previously reported data from the original isolation and characterization of fimsbactin A.<sup>2</sup>

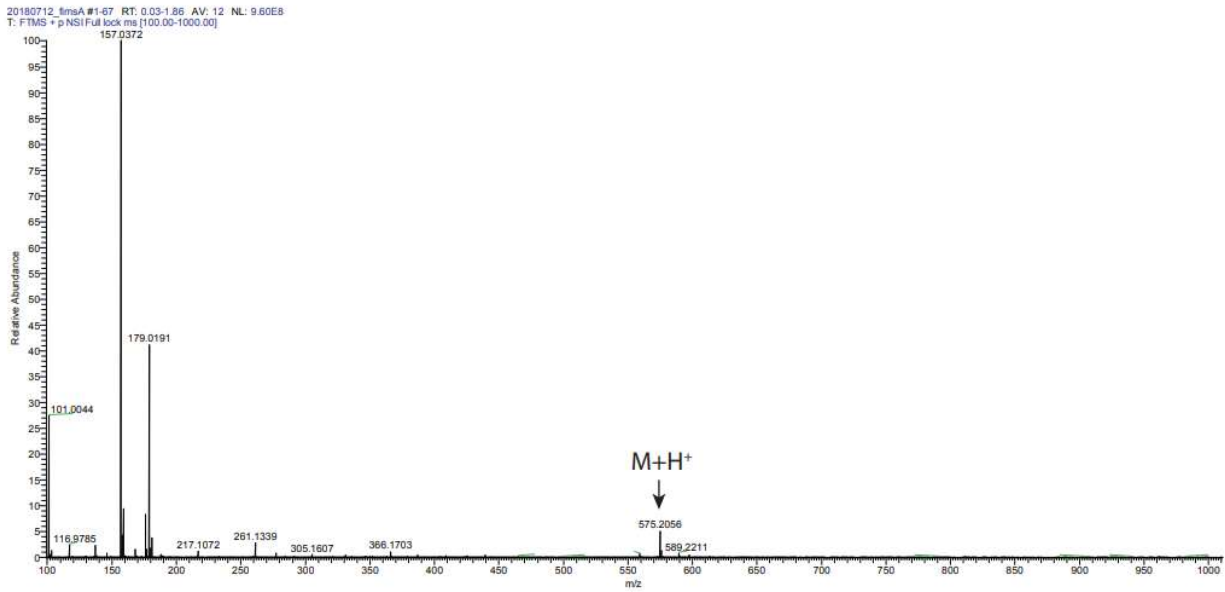


**Figure 3.7.** High-resolution ESI MS (positive ion mode) of fimsbactin A purified by prep-HPLC from *A. baumannii* ATCC 17978 culture supernatant (**Trial #1**). Expected  $[M+H]^+$  for  $C_{26}H_{31}N_4O_{11}$  575.1984, found 575.2056.

<sup>1</sup>H NMR – 600 MHz  
DMSO – d<sub>6</sub>  
Fimsbactin A

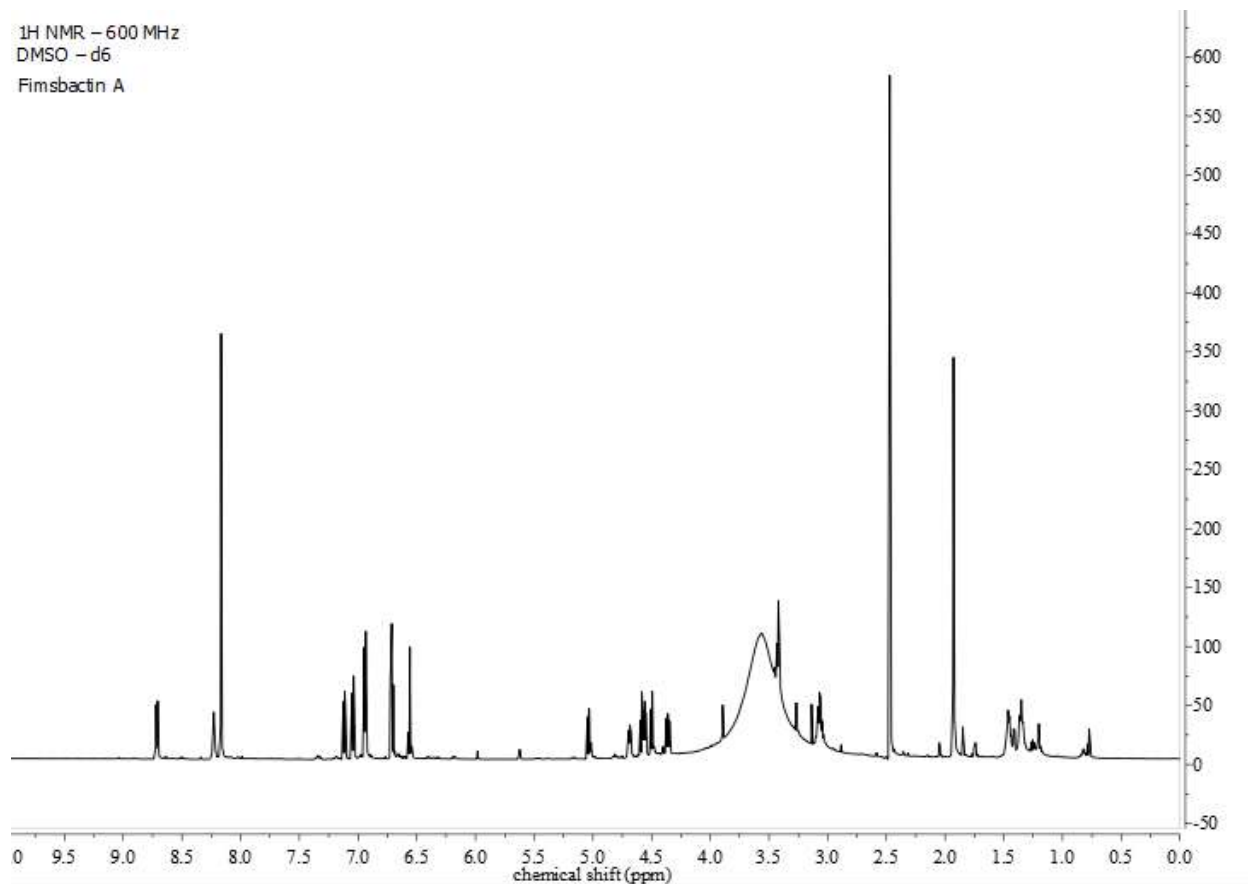


**Figure 3.8.** <sup>1</sup>H-NMR (600 MHz, DMSO-*d*<sub>6</sub>) spectrum of purified fimsbactin A purified by prep-HPLC from *A. baumannii* ATCC 17978. The x-axis is chemical shift given in parts per million (ppm). The y-axis is arbitrary peak intensity.

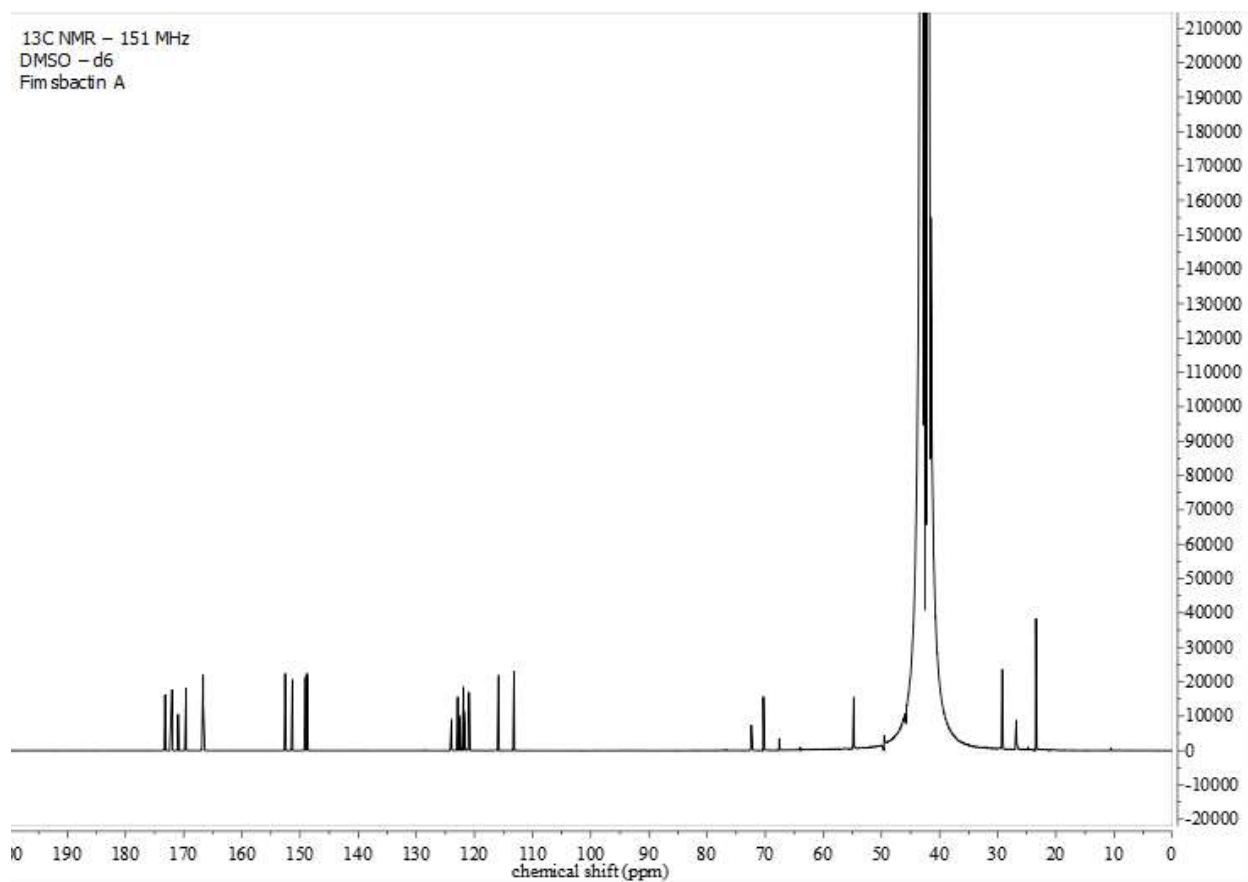
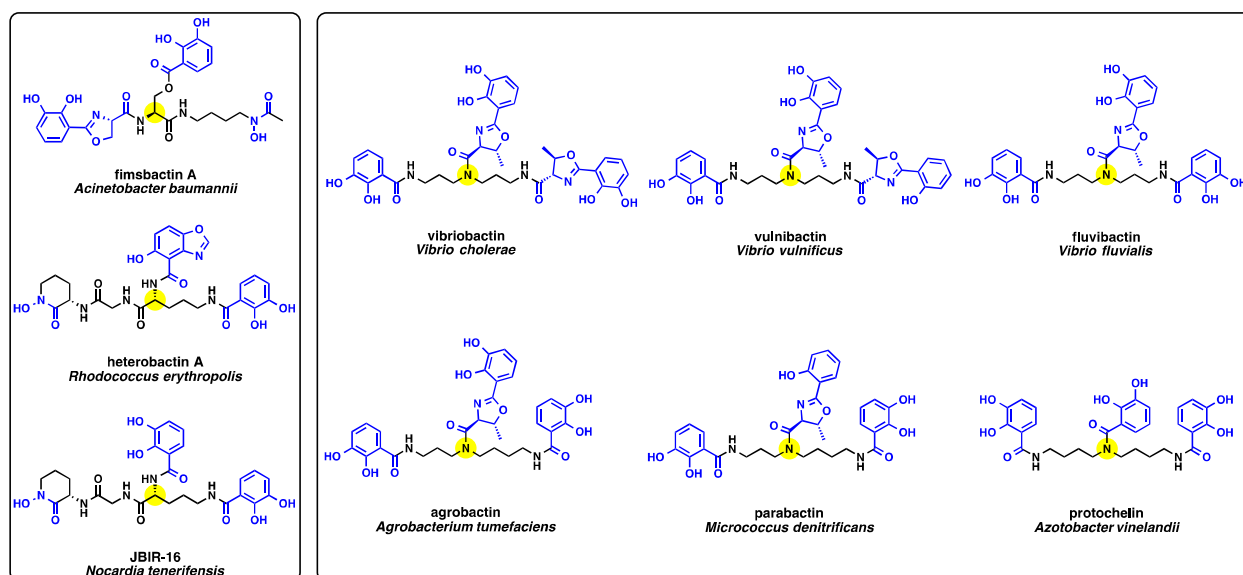


**Figure 3.9.** <sup>13</sup>C-NMR (151 MHz, DMSO-*d*<sub>6</sub>) spectrum of purified fimsbactin A purified by prep-HPLC from *A. baumannii* ATCC 17978. The x-axis is chemical shift given in parts per million (ppm). The y-axis is arbitrary peak intensity.



AMINO ACID SCAFFOLD

SPERMIDINE SCAFFOLD

**Figure 3.10.** Structures and microbial producers of amino acid-based siderophores fimsbactin A<sup>2</sup>, heterobactin A<sup>7</sup>, and JBIR-16<sup>8</sup> and spermidine-based siderophores vibriobactin<sup>9</sup>, vulnibactin<sup>10</sup>, fluvibactin<sup>11</sup>, agrobactin<sup>12</sup>, parabactin<sup>13,14</sup>, and protochelin<sup>15</sup>. Iron chelating groups are shown in blue. The tetrahedral branch point for metal chelating ligands is highlighted by a yellow circle.

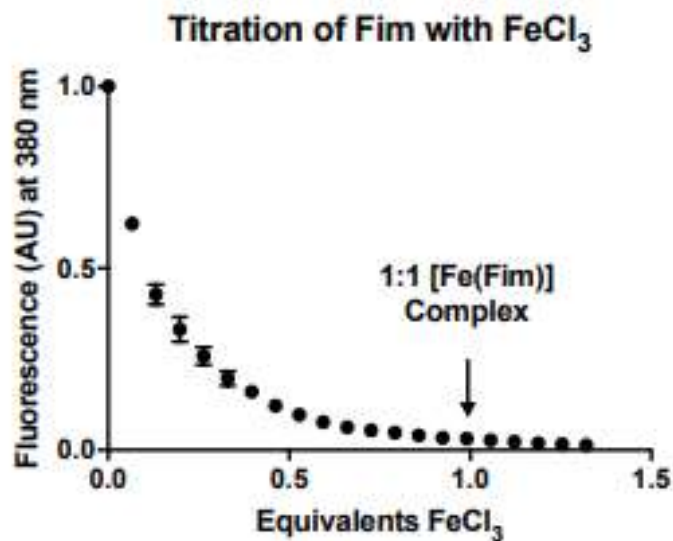


**Figure 3.11.** Fimsbactin A forms a 1:1 complex with Fe(III). Graph depicts fluorescence ( $\lambda_{\text{excitation}} = 330 \text{ nm}$ ;  $\lambda_{\text{emission}} = 380 \text{ nm}$ ) vs equivalents of FeCl<sub>3</sub> showing a titration end point correlating with 1:1 stoichiometry. Was performed as two independent trials. Error bars represent standard deviation from the mean.

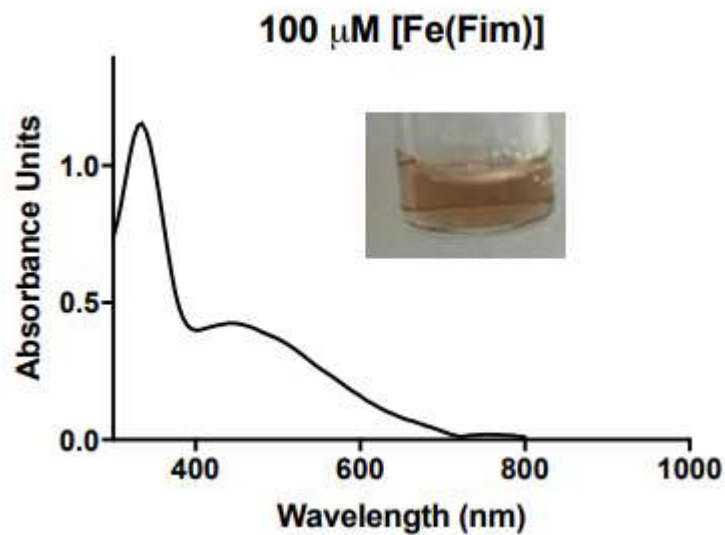


**Figure 3.12.** Optical absorbance spectrum of the *holo*-FimFe complex at 100  $\mu$ M in phosphate buffer (50 mM potassium phosphate pH 8.0, 150 mM NaCl, 1 mM DTT, 5% glycerol). Molar extinction coefficient ( $\epsilon$ ) of *holo*-[Fe(Fim)] was determined to be  $4255 \text{ M}^{-1} \text{ cm}^{-1}$  at 445 nm. The inset shows the visible color of the [Fe(Fim)] solution at 100  $\mu$ M.



Siderophore	Siderophore:Fe(III) Stoichiometry <sup>a</sup>	Metal:Ligand Charge Transfer Band ( $\lambda_{\text{abs}}$ )	Apparent $\log K_{\text{Fe}}$ <sup>b</sup>	Apparent BauB $K_d$ (nM) <sup>c</sup>
<b>PreAcb</b>	2:1	515 nm	$27.4 \pm 0.2$	$380 \pm 110$ ( $750 \pm 160$ )
<b>Acb</b>	2:1	570 nm	$26.2 \pm 0.1$	$300 \pm 100$ ( $160 \pm 80$ )
<b>Fim</b>	1:1	445 nm	$27.1 \pm 0.2$	$360 \pm 140$ ( $240 \pm 90$ )

<sup>a</sup>Siderophore:Fe stoichiometry was measured by titration of siderophores with  $\text{Fe}(\text{acac})_3$  monitored by quenching of intrinsic siderophore fluorescence. <sup>b</sup>Apparent  $\log K_{\text{Fe}}$  values for PreAcb<sub>2</sub>Fe and Acb<sub>2</sub>Fe are literature values.<sup>4</sup> <sup>c</sup>Values in parentheses are for the ferric *holo*-siderophore complexes. The apparent  $K_d$  for Acb and Acb<sub>2</sub>Fe are literature values.<sup>1</sup> Data is reported as mean  $\pm$  standard deviation from the mean for at least two independent trials.

**Table 3.2.** Siderophore iron binding properties and apparent BauB dissociation constants ( $K_d$ ).

### Equations 3.1

As described in the experimental methods section of the main text, an EDTA competition experiment was used to measure the apparent  $K_{Fe}$  for FimFe at pH 7.4. The following equations were used to calculate apparent  $K_{Fe}$  based on the change in optical absorbance observed at 500 nm for FimFe in the presence of 1.2 equivalents of EDTA. A  $K_{Fe}$  value of  $10^{25.1}$  was used for EDTA at pH 7.4 in final calculations.<sup>64</sup>

$$(1) \quad K_L = \frac{[FeL]}{[Fe^{3+}][L]} \quad \text{for the following equilibrium;} \quad [Fe^{3+}] + [L] \rightleftharpoons [FeL]$$

$$(2) \quad K_{FeEDTA} = \frac{[FeEDTA]}{[Fe^{3+}][EDTA]} \quad \text{for the following equilibrium;} \quad [Fe^{3+}] + [EDTA] \rightleftharpoons [FeEDTA]$$

$$(3) \quad K_{Exchange} = \frac{K_L}{K_{FeEDTA}} \quad \text{for the following equilibrium;} \quad [FeEDTA] + [L] \rightleftharpoons [FeL] + [EDTA]$$

$$(4) \quad K_{Exchange} = \frac{[FeL][EDTA]}{[FeEDTA][L]}$$

$$(5) \quad \Delta = \frac{Abs_{FeL} - Abs_{FeL+EDTA}}{\epsilon_L}$$

$$(6) \quad K_L = K_{FeEDTA} \times \frac{[FeL][EDTA]}{[FeEDTA][L]}$$

$$(7) \quad [FeL] = \frac{Abs_{FeL}}{\epsilon_L}$$

$$(8) \quad [EDTA] = [EDTA]_T - \Delta \quad \text{where} \quad [EDTA]_T = \text{total EDTA added}$$

$$(9) \quad [FeEDTA] = \Delta$$

$$(10) \quad [L] = \Delta$$

$$(11) \quad K_{Fe} = \text{apparent } K_L$$

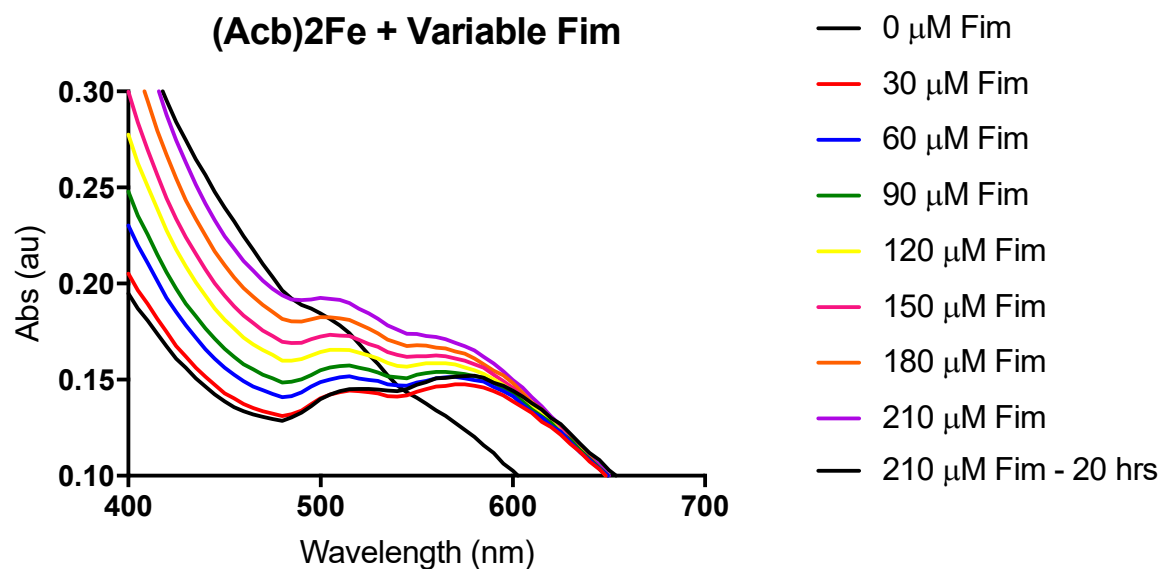


**Figure 3.13.** Titration of *holo-Acb<sub>2</sub>Fe* with *apo-Fim* reveals slow exchange of iron leading to apparent complete formation of *holo-FimFe*. Optical absorbance spectra were collected for each concentration after 20 min in phosphate buffer (50 mM potassium phosphate pH 8.0, 150 mM NaCl, 1 mM DTT, 5% glycerol). The final optical absorbance spectrum with 210  $\mu\text{M}$  *apo-Fim* added was measured after 20 hours.

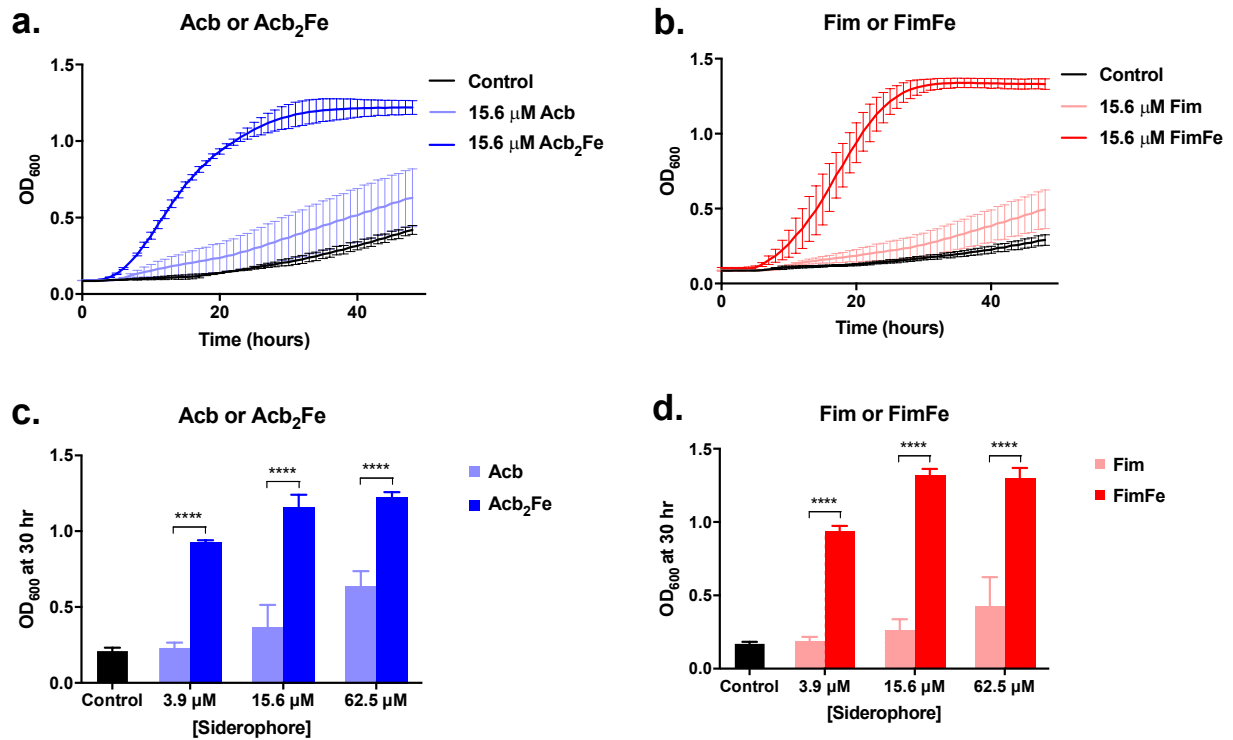


**Figure 3.14.** Influence of *apo*- and *holo*-siderophores on *A. baumannii* growth. Line graphs depict the growth of *A. baumannii* ATCC 17978 determined by measuring the optical density at 600 nm (OD<sub>600</sub>) as a function of time in the presence of (a) Acb or Acb<sub>2</sub>Fe and (b) Fim or FimFe. Bar graphs depict the comparison of OD<sub>600</sub> values after 30 hours in the presence of variable concentrations of (c) Acb or Acb<sub>2</sub>Fe and (d) Fim or FimFe. Error bars represent standard deviations from the mean for three independent trials. \*\*\*\*p < 0.0001

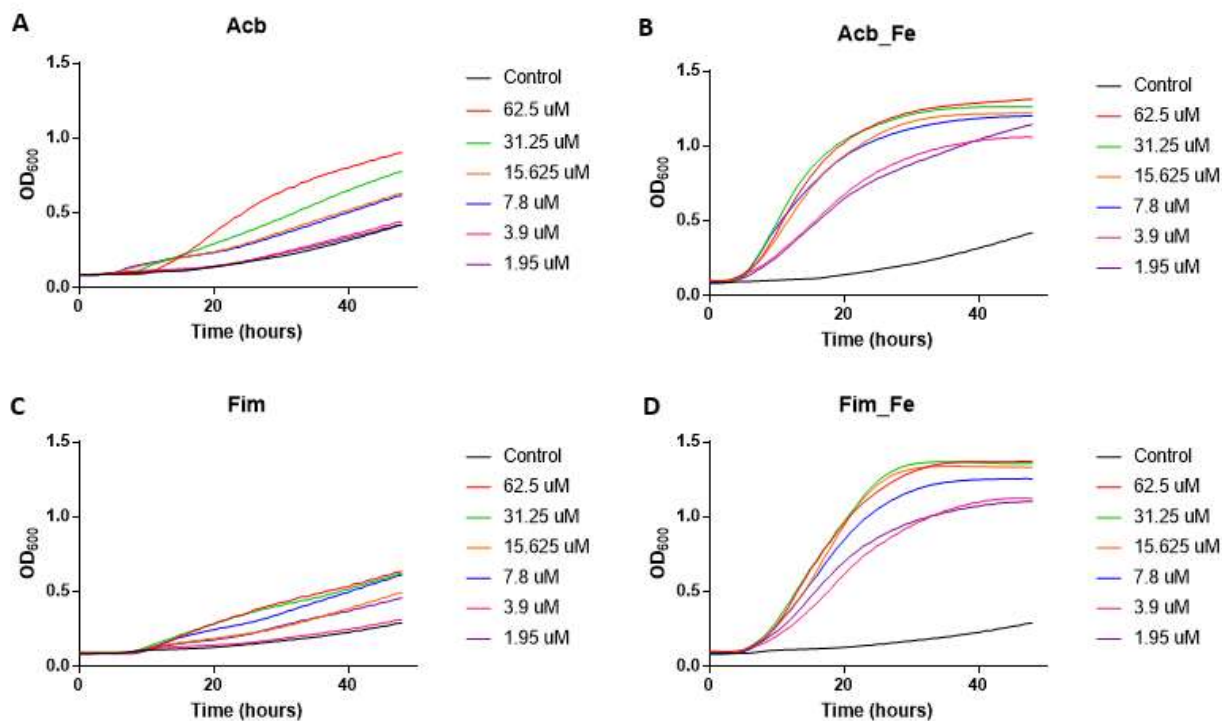


**Figure 3.15.** Dose dependent growth promotion of *A. baumannii* ATCC 17978 by (A) apo-acinetobactin (Acb), (B) holo-acinetobactin (Acb\_Fe), (C) apo-fimsbactin (Fim), and (D) holo-fimsbactin (Fim\_Fe). Line graphs depict the growth of *A. baumannii* ATCC 17978 in M9 minimal medium supplemented with 175  $\mu$ M 2,2'-dipyridyl (DIP) determined by measuring the optical density at 600 nm ( $OD_{600}$ ) as a function of time in the presence of variable siderophore concentrations. All experiments were performed in triplicate. Error bars are shown in **Figure 3.16**. Data from these plots were used to create the line and bar graphs shown in **Figure 3.14**

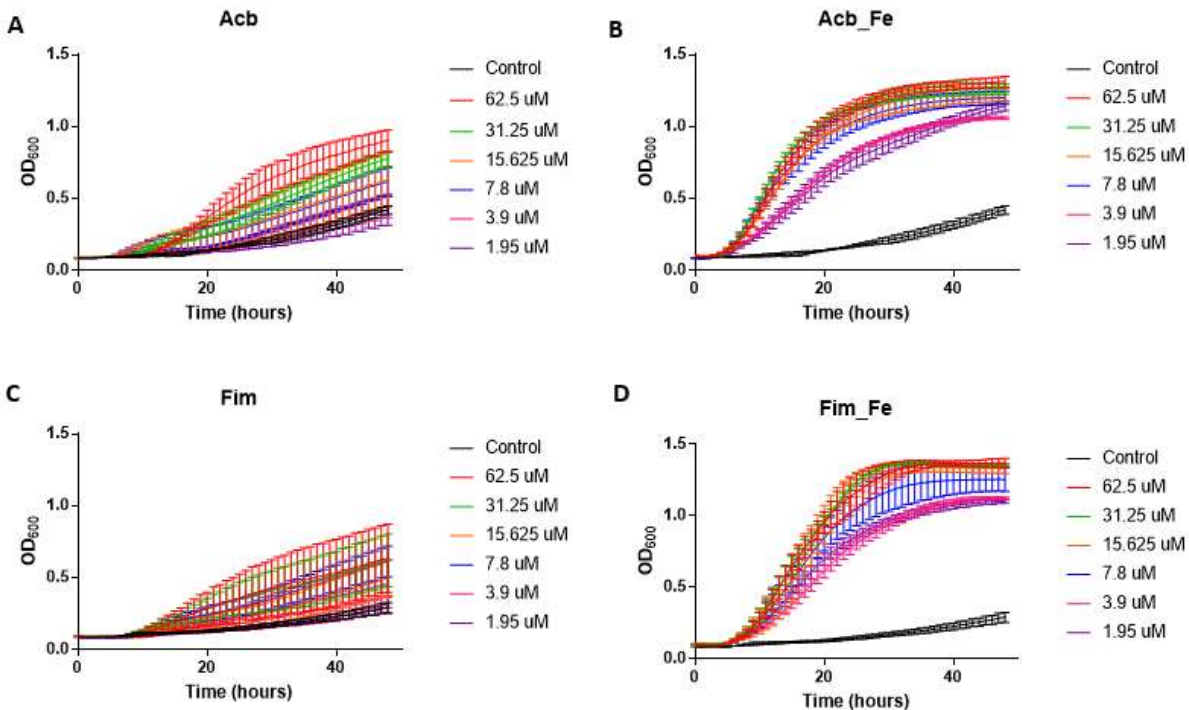


**Figure 3.16.** Dose dependent growth promotion of *A. baumannii* ATCC 17978 by (A) apo-acinetobactin (Acb), (B) holo-acinetobactin (Acb\_Fe), (C) apo-fimsbactin (Fim), and (D) holo-fimsbactin (Fim\_Fe). Line graphs depict the growth of *A. baumannii* ATCC 17978 in M9 minimal medium supplemented with 175  $\mu\text{M}$  2,2'-dipyridyl (DIP) determined by measuring the optical density at 600 nm ( $\text{OD}_{600}$ ) as a function of time in the presence of variable siderophore concentrations. Error bars represent standard deviations from the mean for three independent trials. Line graphs are shown without error bars for clarity in **Figure 3.15**. Data from these plots were used to create the line and bar graphs shown in **Figure 3.14**.

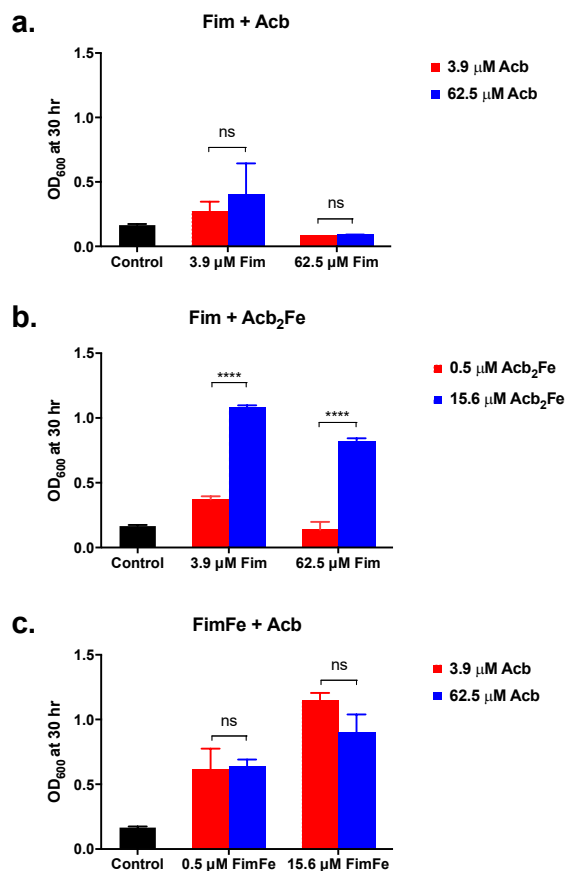
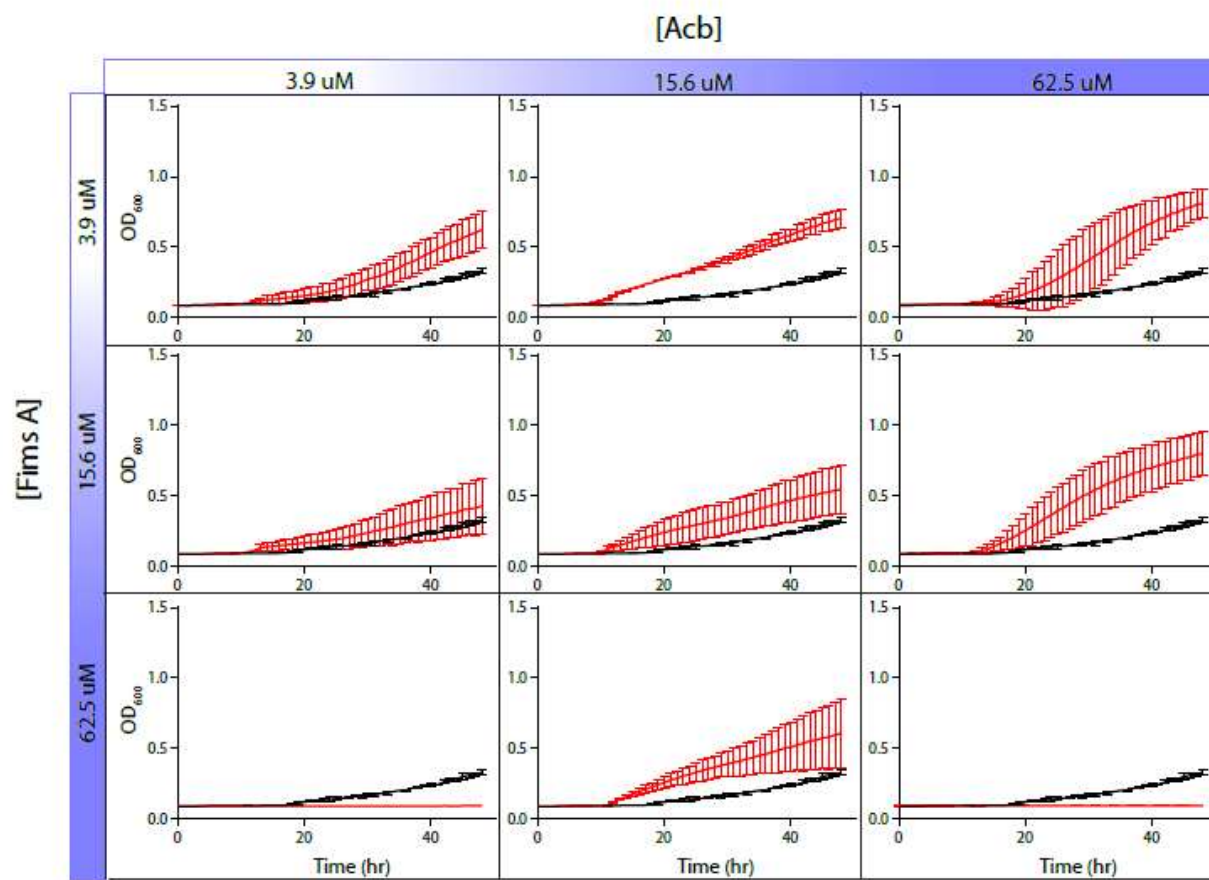


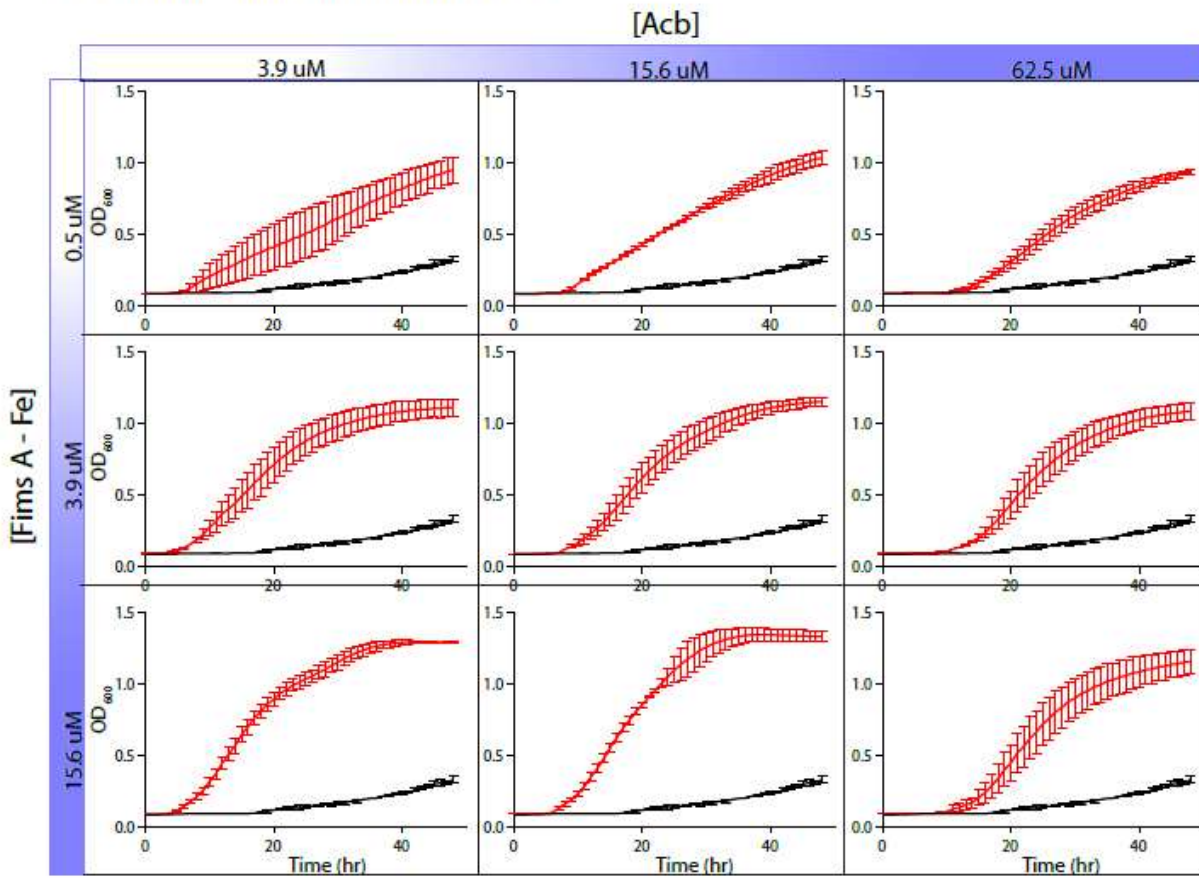
**Figure 3.17.** Influence of *apo*- and *holo*-siderophore combinations on *A. baumannii* growth. Bar graphs depict the comparison of *A. baumannii* ATCC 17978 growth measured by optical density at 600 nm ( $OD_{600}$ ) values after 30 hours in the presence of variable concentrations of (a) Fim and Acb, (b) Fim and Acb<sub>2</sub>Fe, and (c) FimFe and Acb. Error bars represent standard deviations from the mean for two independent trials. \*\*\*\*  $p < 0.0001$ ; ns = not significant

### A. Acinetobactin + Fimsbactin A



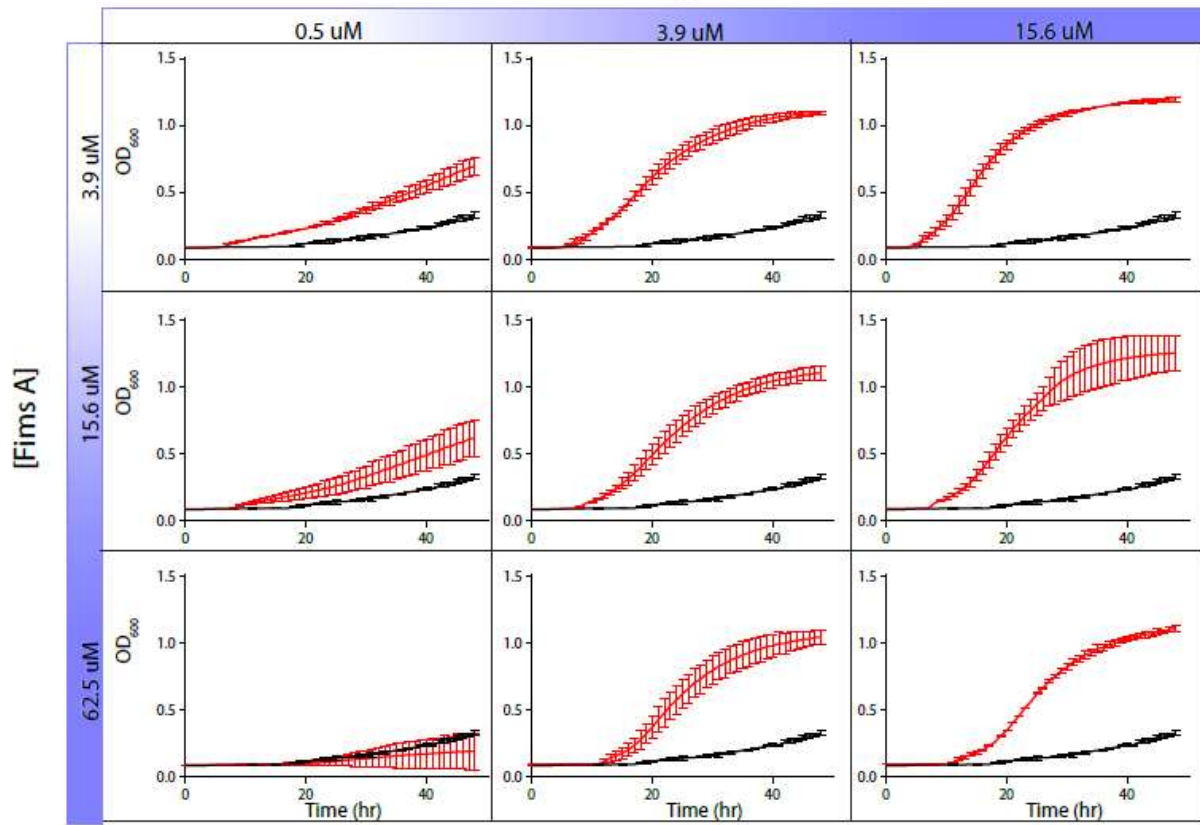


B. Acinetobactin + Fimsbactin A - Fe



C. Acinetobactin - Fe + Fimsbactin A

[Acb<sub>2</sub>-Fe]



D. Fimsbactin A-Fe + Fimsbactin A

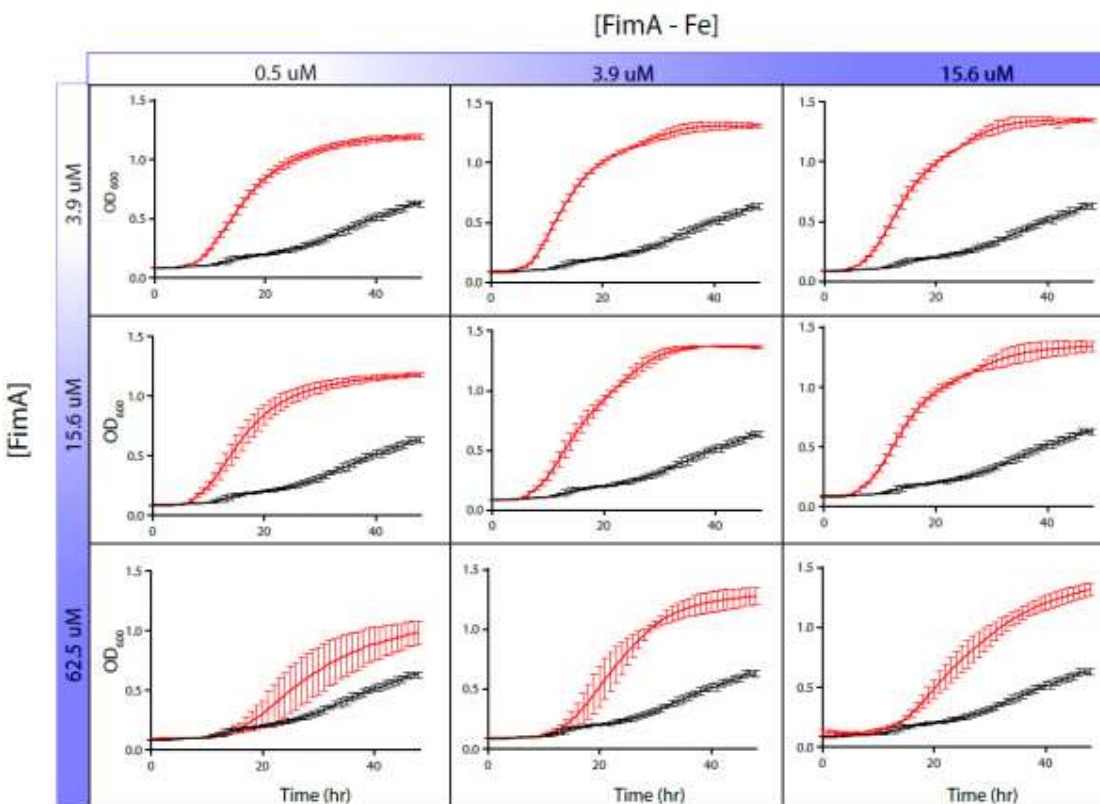


**Figure 3.18.** Influence of *apo*- and *holo*-siderophore combinations on the growth of *A. baumannii* ATCC 17978. Line graphs depict the growth of *A. baumannii* ATCC 17978 in M9 minimal medium supplemented with 175  $\mu$ M 2,2'-dipyridyl (DIP) determined by measuring the optical density at 600 nm ( $OD_{600}$ ) as a function of time in the presence of variable concentrations of siderophore mixtures. For all graphs, siderophore concentration gradients are provide on the x-axis and y-axis of the checkerboard. The black line graph represents bacterial growth without addition of siderophores. The red line graph represents bacterial growth in the presence of variable concentrations of (A) *apo*-Fim and *apo*-Acb, (B) *holo*-FimFe and *apo*-Acb, (C) *apo*-Fim and *holo*-Acb<sub>2</sub>Fe or (D) *apo*-Fim and *holo*-FimFe. Error bars represent standard deviations from the mean for two independent trials. Data from these plots were used to create bar graphs shown in **Figure 3.17**

***N*-His<sub>6</sub>-BauB in pET28bTEV (cleavable *N*-term His-tag):**

Nucleotide:

AAGGAGATATACCATGGGCAGCAGCCATCATCATCATCACAGCAGCGGC<sup>↓</sup>GAAACCTGTATTTTCAG<sup>↓</sup>GGCC  
ATATGTGCGACCAAAAAGTTGCGGATACCACCCAGGCGAGCCAAAAGTGGCGGAGCCGATTACCGTTAAGCAC  
GCGCTGGGCACCACCGTGATCGACCACCTGCCGAGCGTGTGGCGGTTCTGGATATGAACGAAGCGGACTTCCTG  
GATCAACTGAACGTTCCGATTATGGGCATGCCGAAAGACTACGTGCCGCACTTTCTGGAGAAGTATAAAAAGGAC  
GCGCAGATTCAAGATCTGGGTGCGATCGTTACGCCAACATGGAACGTATTTATGCGCTGAAACCGGATCTGATC  
CTGATGACCCCGCTGCACGTGAACCAAGTACCAAGAGCTGAGCAAGATCGCGCCGACCATTCACTATGACATCAACT  
TCAACAACAGCGAAAGCAACCACATTGGCCTGGTTAAAGATCACATGATGACCCTGGGTAAAATCTTTAACAAAG  
AGGACCTGGCGCGTCAGAAAGTGAGCGAGCTGGATGAACAAGTGAAGCAGGTTCAAGCGGTGACCGCGAACCG  
TCCGGAACGTGCGCTGGTTGTGCTGCACAACAACGGTTCGTTTACGCAACTTTGGCATTCAAGAGCCGTTACGGTTTC  
ATCTTTAACGCGTTCGCGCTTAAGCCGGCGAGCGGTGTGGTTGACACCAGCCTGCACGGTCAACCGATTAGCAGC  
GAGTTTATCAAAAAGCGGACCCGGATATCCTGTATATTGTTGATCGTACCGCGGTGATGGAGCACCGTCCGAAC  
ATCAACGCGGCGAGCGTGGAAAACCGCTGCTGCTCAGACCAAAGCGTGGAAAGAACGGCCGTGTTATTTTCGTT  
GATGCGGATGCGTGGTACACCACCGCGGCGAGCCGACCAGCCTGAAGATCGTTATGGAAGACGTGAAAAAGG  
TTATCAATAAAAGCTT

Amino Acid:

GSSHHHHHHSSGENLYFQ<sup>↓</sup>GHMCDQKVADTTQASQKLAEPITVKHALGTTVIDHLPQRVA  
VLDMNEADFLDQLNVPIMGMPKDYVPHFLEKYKKDAQIQDLGAIVQPNMERIYALKPDLI  
LMTPLHVNQYQELSKIAPTIHYDINFNSESNHIGLVKDHMMTLGKIFNKEDLARQKVSE  
LDEQVKQVQAVTANRPERALVVLHNNGAFSNFGIQSRYGFIFNAFGVKPASGVVDTSLHG  
QPISSEFIKKADPDILYIVDRTAVMEHRPNINAASVENPLLRQTKAWKNGRVIFVDADAW  
YTTAASPTSLKIVMEDVKKGYQ

**Figure 3.19.** Nucleotide and amino acid sequence of *N*-His<sub>6</sub>-BauB in pET28bTEV (TEV-cleavable *N*-term hexahistidine-tag). Start and stop codons are underlined. The TEV cleavage site is indicated by an arrow<sup>↓</sup>. The 969-bp *bauB* gene from *Acinetobacter baumannii* (Genbank Accession Number AAT52185) was used as the sequence template for subcloning.

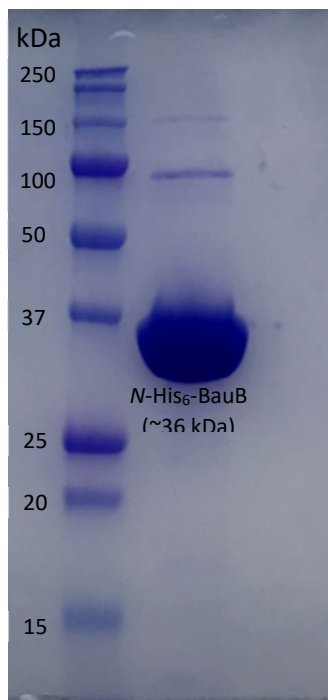


**Figure 3.20.** SDS-PAGE analysis of Ni-NTA purified *N*-His<sub>6</sub>-BauB (~36.1 kDa). Gel was stained using Coomassie blue dye. This image was also used in the supplementary information for our manuscript describing the x-ray crystal structure of BauB.<sup>1</sup>

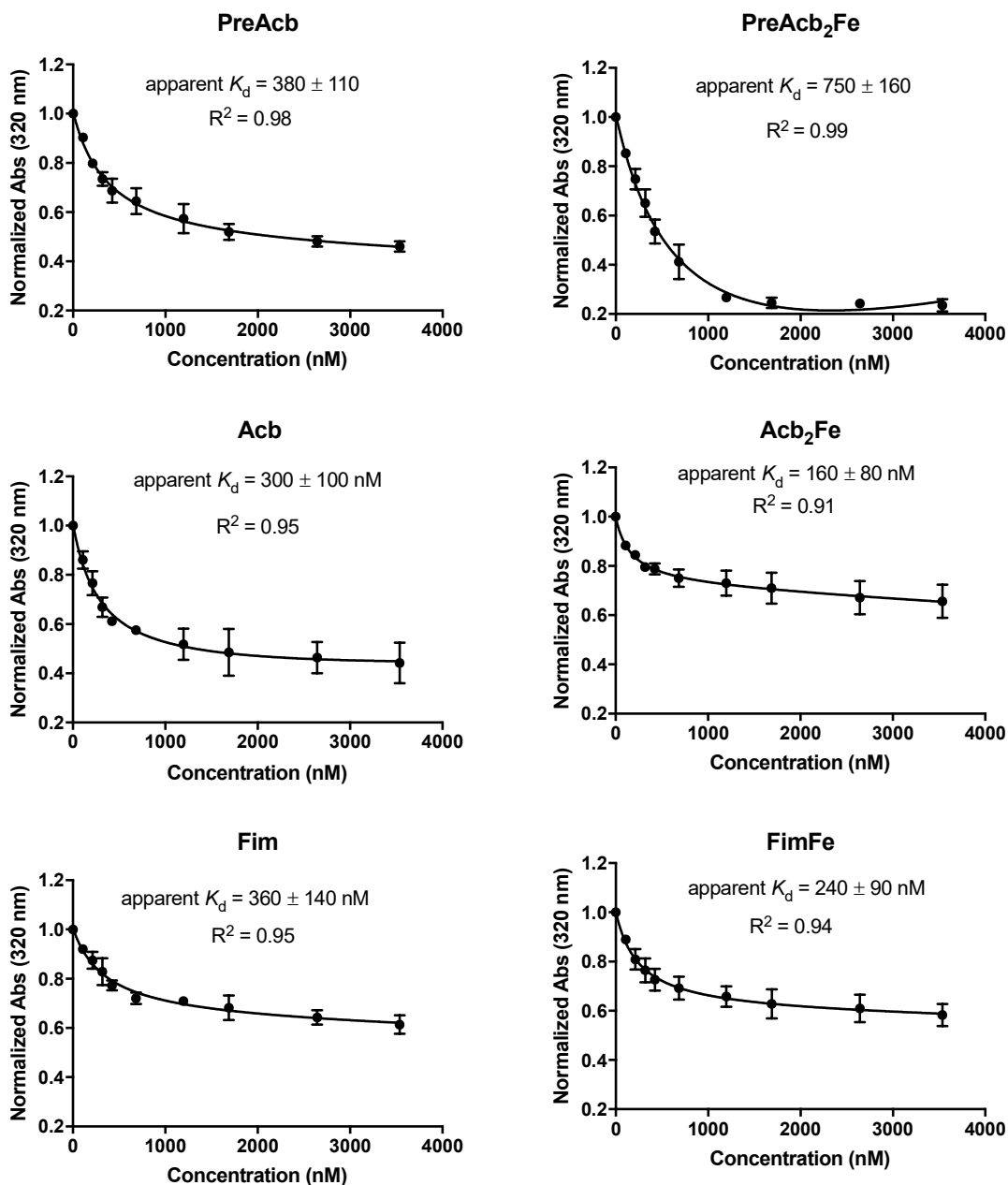


**Figure 3.21.** Siderophore-dependent fluorescence quenching of *N*-His<sub>6</sub>-BauB. Graphs depict intrinsic tryptophan fluorescence quenching (y-axis;  $\lambda_{\text{excitation}} = 280$  nm;  $\lambda_{\text{emission}} = 340$  nm) of 400 nM *N*-His<sub>6</sub>-BauB in the presence of variable siderophore concentrations (x-axis). Apparent  $K_d$  values were calculated using a single-binding mode curve-fitting model in GraphPad Prism version 7.0b. Error bars represent standard deviations for two independent trials.

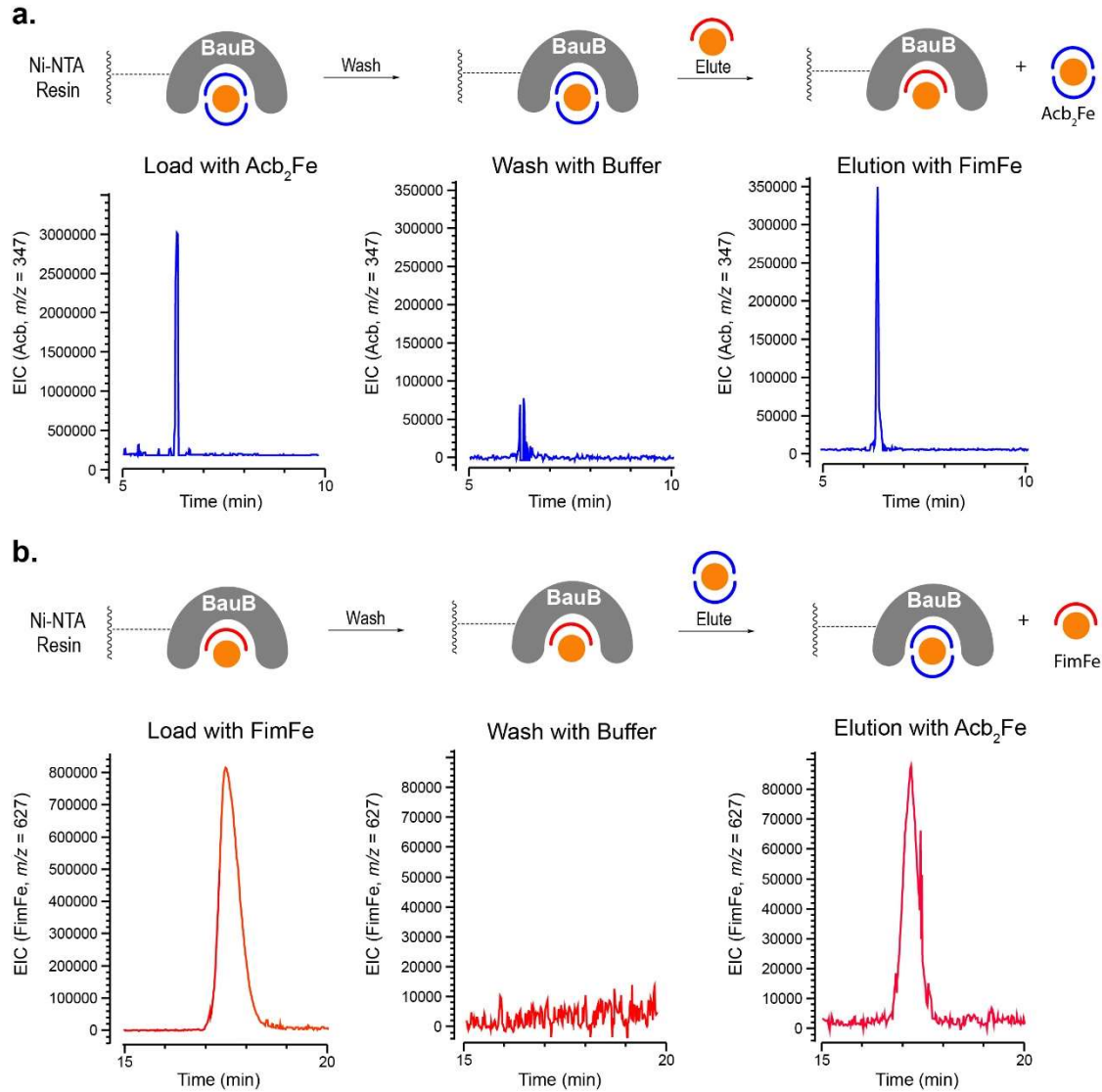


**Figure 3.22.** Acb<sub>2</sub>Fe and FimFe compete for BauB binding. *N*-His<sub>6</sub>-BauB was immobilized on Ni-NTA resin and loaded with (a) Acb<sub>2</sub>Fe or (b) FimFe, washed with phosphate buffer, and eluted with a competing *holo*-siderophore. Column elutions were analyzed by LCMS for Acb<sub>2</sub>Fe ( $m/z = 347$ ) and FimFe ( $m/z = 627$ ) after each step. Extracted ion chromatograms (EIC) are shown for the initially bound *holo*-siderophore. EICs are representative for two independent trials.

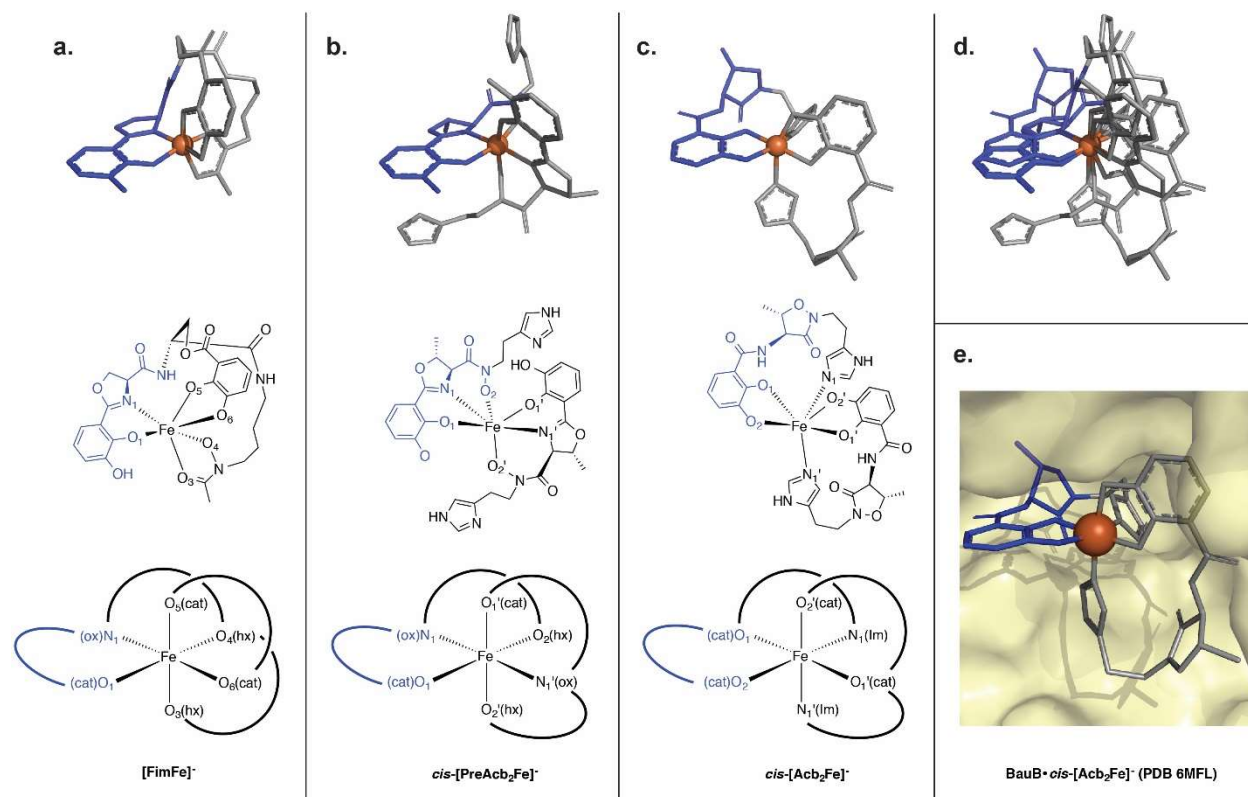


**Figure 3.23.** Structural comparison of PreAcb<sub>2</sub>Fe, Acb<sub>2</sub>Fe, and FimFe complexes. DFT calculated structures of the monoanionic (a) 1:1 [FimFe]<sup>-</sup> and (b) 2:1 *cis*-[PreAcb<sub>2</sub>Fe]<sup>-</sup> complexes (see experimental methods for DFT parameters). (c) Experimentally observed structure of the monoanionic *cis*-[Acb<sub>2</sub>Fe]<sup>-</sup> complex bound to the siderophore binding protein BauB (PDB 6MFL). (d) Overlay of all three structures highlighting similarity of geometry and placement of ligands (ox, oxazoline; cat, catecholate; hx, hydroxamate; im, imidazole) around the ferric iron center. (e) Surface view of the siderophore binding pocket of BauB occupied by *cis*-[Acb<sub>2</sub>Fe]<sup>-</sup> (PDB 6MFL).



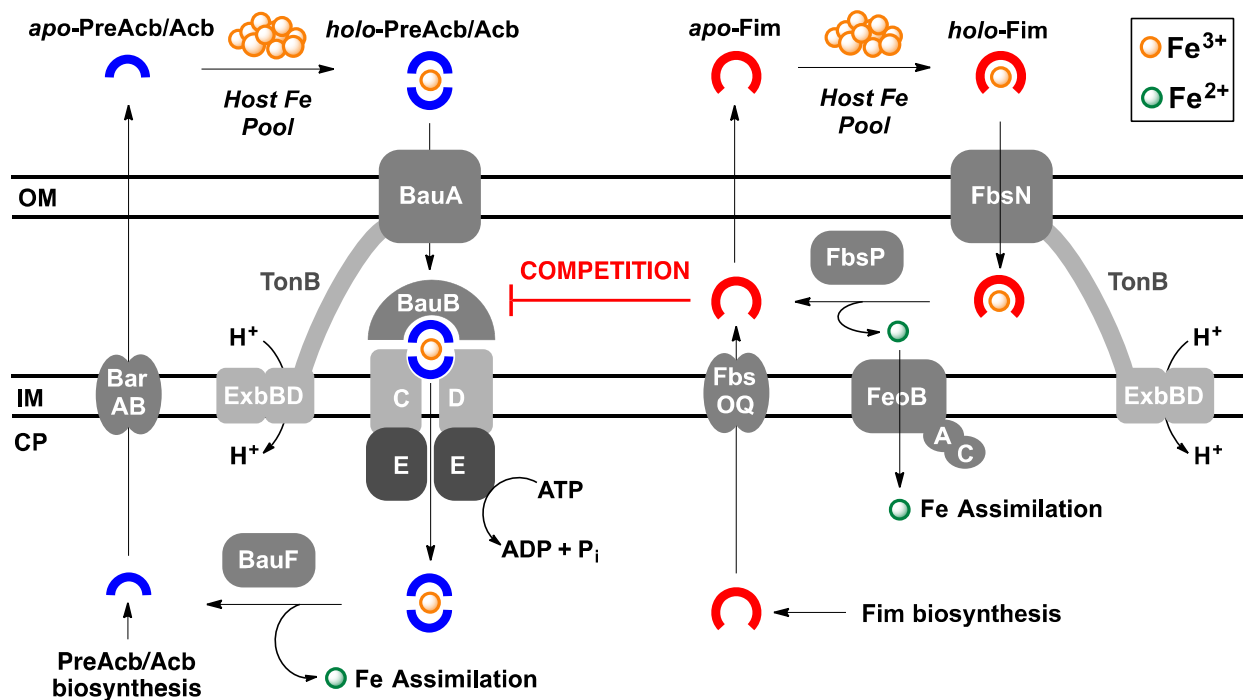


**Figure 3.24.** Schematic overview of the PreAcb/Acb and Fim iron acquisition pathways in *A. baumannii*. The Fim pathway has not been experimentally characterized and is hypothesized based on homology to related pathways in Gram-negative bacteria. Periplasmic BauB is highlighted to show interactions with both PreAcb/Acb and Fim connecting the two pathways through competition for the periplasmic siderophore-binding protein.

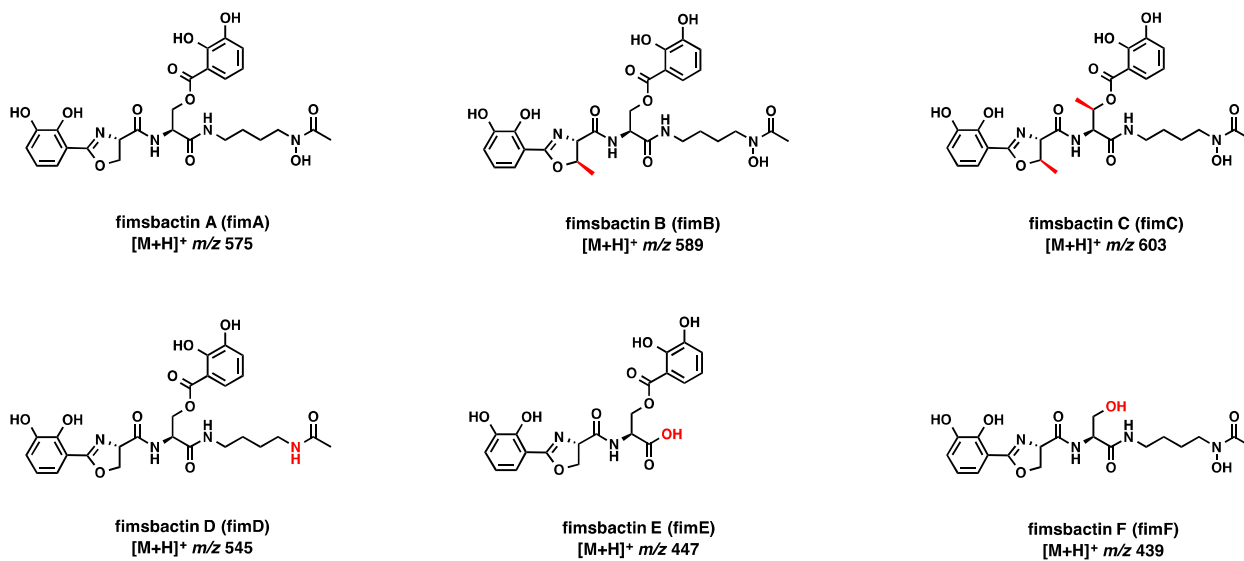


**Figure 3.25.** Structures and  $m/z$  values for  $[M+H]^+$  molecular ions of fimsbactin A–F.<sup>2</sup> Structural differences are highlighted in red.

## Acinetobactin BGCs

ATCC 19606 (GenBank: GCA\_000162295.1)

Query sequence



BGC0000294: Acinetobactin biosynthetic gene cluster (100% of genes show similarity)



ATCC 19606 (GenBank: GCA\_002811175.1)

Query sequence



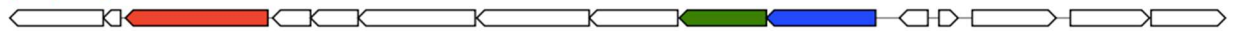
BGC0000294: Acinetobactin biosynthetic gene cluster (100% of genes show similarity)



## Acinetoferrin/Baumannoferrin BGCs

ATCC 19606 (GenBank: GCA\_000162295.1)

Query sequence

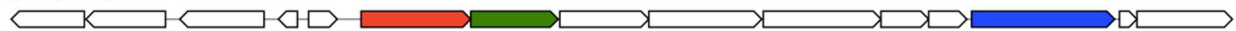


BGC0000295: Acinetoferrin biosynthetic gene cluster (30% of genes show similarity)



ATCC 19606 (GenBank: GCA\_002811175.1)

Query sequence



BGC0000295: Acinetoferrin biosynthetic gene cluster (30% of genes show similarity)



**Figure 3.26.** Antismash analysis of two deposited genomes of *A. baumannii* ATCC 19606 turned up acinetobactin and acinetoferrin/baumannoferrin as the only siderophore BGCs present in the genome. No fimsbactin BGCs were detected.

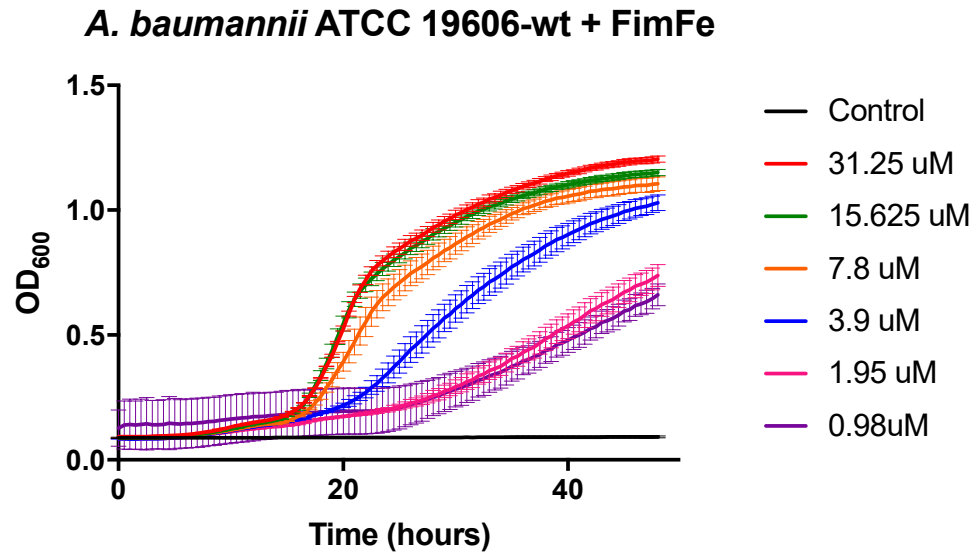
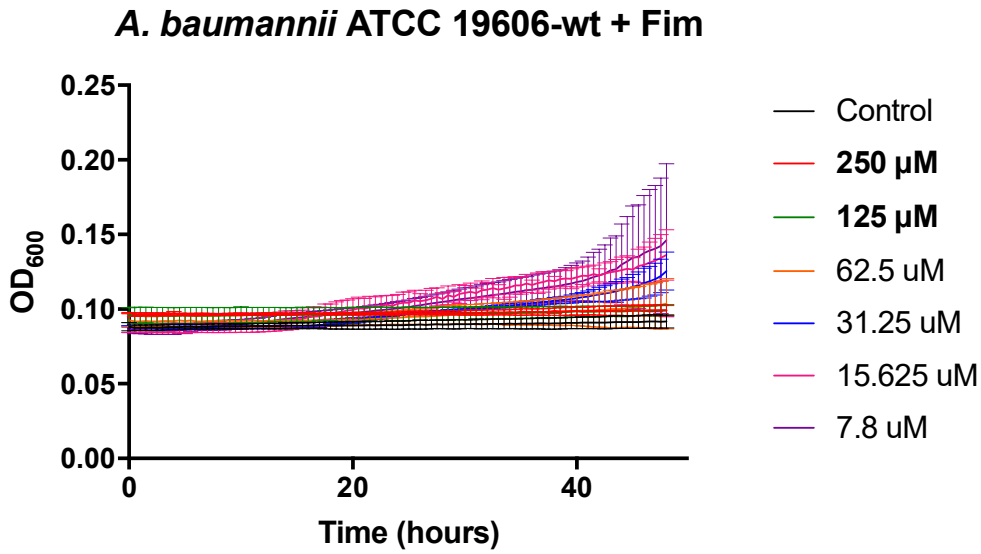


**Figure 3.27.** Dose dependent influence of *apo*-Fim and *holo*-FimFe on *A. baumannii* ATCC 19606 growth. Line graphs depict the growth of wild-type *A. baumannii* ATCC 19606 in M9 minimal medium supplemented with 175  $\mu$ M 2,2'-dipyridyl (DIP) determined by measuring the optical density at 600 nm (OD<sub>600</sub>) as a function of time in the presence of variable siderophore concentrations. Error bars represent standard deviations from the mean for three independent trials.

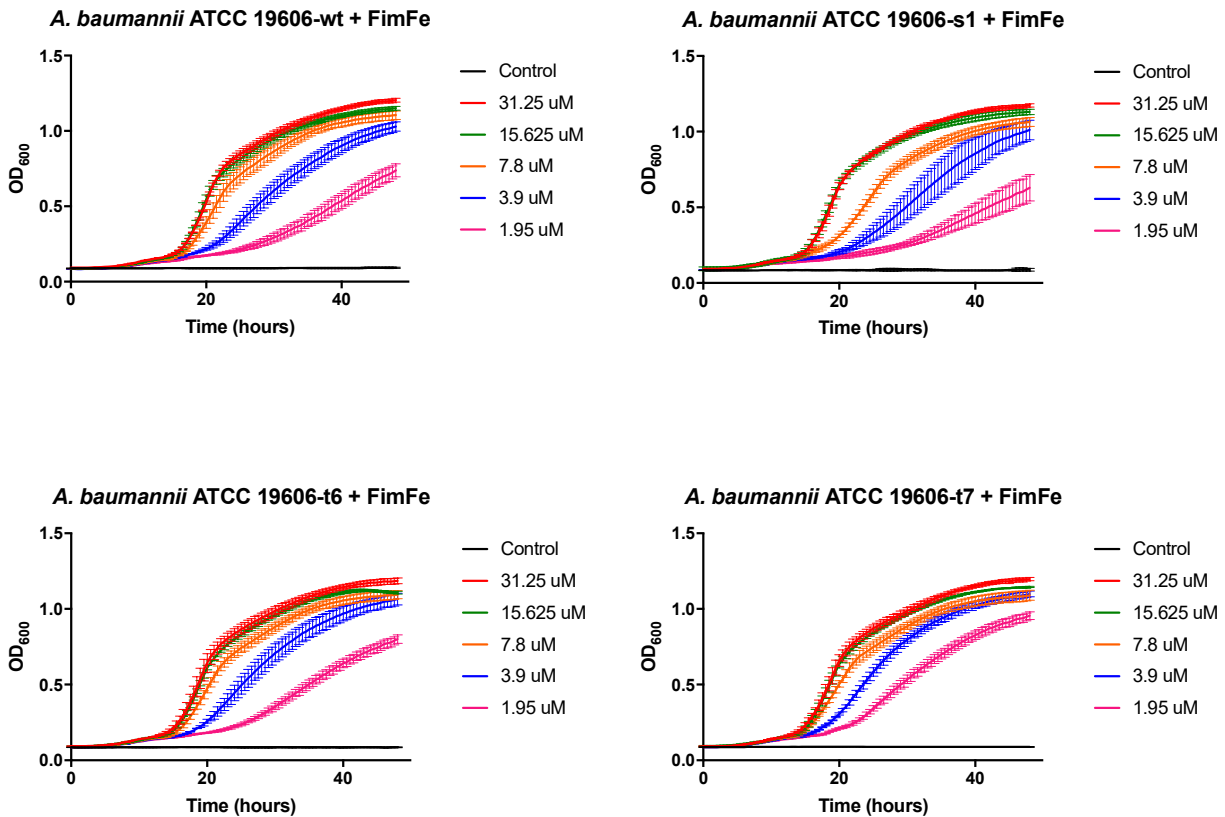


**Figure 3.28.** Dose dependent growth promotion of *A. baumannii* ATCC 19606 strains by *holo*-FimFe. Line graphs depict the growth of wild-type (wt), s1-mutant (insertional mutant in *basD*, deficient in PreAcb/Acb biosynthesis), t6-mutant (insertional mutation in *bauA*, deficient in PreAcb/Acb import to periplasm), and t7-mutant (insertional mutation in *bauD*, deficient in PreAcb/Acb import to cytoplasm) strains of *A. baumannii* ATCC 19606 in M9 minimal medium supplemented with 175  $\mu$ M 2,2'-dipyridyl (DIP) determined by measuring the optical density at 600 nm ( $OD_{600}$ ) as a function of time in the presence of variable siderophore concentration. Error bars represent standard deviations from the mean for three independent trials.

### 3.8 References

- [1] Bailey, D. C., Bohac, T. J., Shapiro, J. A., Giblin, D. E., Wencewicz, T. A., and Gulick, A. M. (2018) Crystal Structure of the Siderophore Binding Protein BauB Bound to an Unusual 2:1 Complex Between Acinetobactin and Ferric Iron, *Biochemistry*.
- [2] Proschak, A., Lubuta, P., Grun, P., Lohr, F., Wilharm, G., De Berardinis, V., and Bode, H. B. (2013) Structure and biosynthesis of fimsbactins A-F, siderophores from *Acinetobacter baumannii* and *Acinetobacter baylyi*, *Chembiochem* 14, 633-638.
- [3] Smith, M. G., Gianoulis, T. A., Pukatzki, S., Mekalanos, J. J., Ornston, L. N., Gerstein, M., and Snyder, M. (2007) New insights into *Acinetobacter baumannii* pathogenesis revealed by high-density pyrosequencing and transposon mutagenesis, *Genes & Development* 21, 601-614.
- [4] Shapiro, J. A., and Wencewicz, T. A. (2016) Acinetobactin Isomerization Enables Adaptive Iron Acquisition in *Acinetobacter baumannii* through pH-Triggered Siderophore Swapping, *ACS infectious diseases* 2, 157-168.
- [5] Penwell, W. F., DeGrace, N., Tentarelli, S., Gauthier, L., Gilbert, C. M., Arivett, B. A., Miller, A. A., Durand-Reville, T. F., Joubran, C., and Actis, L. A. (2015) Discovery and Characterization of New Hydroxamate Siderophores, Baumannoferrin A and B, produced by *Acinetobacter baumannii*, *Chembiochem* 16, 1896-1904.
- [6] Bollinger, J. G., Naika, G. S., Sadilek, M., and Gelb, M. H. (2013) LC/ESI-MS/MS detection of FAs by charge reversal derivatization with more than four orders of magnitude improvement in sensitivity, *Journal of lipid research* 54, 3523-3530.

- [7] Carrano, C. J., Jordan, M., Drechsel, H., Schmid, D. G., and Winkelmann, G. (2001) Heterobactins: A new class of siderophores from *Rhodococcus erythropolis* IGTS8 containing both hydroxamate and catecholate donor groups, *Biometals* 14, 119-125.
- [8] Mukai, A., Komaki, H., Takagi, M., and Shin-ya, K. (2009) Novel siderophore, JBIR-16, isolated from *Nocardia tenerifensis* NBRC 101015, *The Journal of antibiotics* 62, 601-603.
- [9] Griffiths, G. L., Sigel, S. P., Payne, S. M., and Neilands, J. B. (1984) Vibriobactin, a siderophore from *Vibrio cholerae*, *The Journal of biological chemistry* 259, 383-385.
- [10] Okujo, N., Saito, M., Yamamoto, S., Yoshida, T., Miyoshi, S., and Shinoda, S. (1994) Structure of vulnibactin, a new polyamine-containing siderophore from *Vibrio vulnificus*, *Biometals* 7, 109-116.
- [11] Yamamoto, S., Okujo, N., Fujita, Y., Saito, M., Yoshida, T., and Shinoda, S. (1993) Structures of two polyamine-containing catecholate siderophores from *Vibrio fluvialis*, *Journal of biochemistry* 113, 538-544.
- [12] Ong, S. A., Peterson, T., and Neilands, J. B. (1979) Agrobactin, a siderophore from *Agrobacterium tumefaciens*, *The Journal of biological chemistry* 254, 1860-1865.
- [13] Tait, G. H. (1975) The identification and biosynthesis of siderochromes formed by *Micrococcus denitrificans*, *The Biochemical journal* 146, 191-204.
- [14] Peterson, T., and Nielands, J. B. (1979) Revised structure of a catecholamide spermidine siderophore: From *Paracoccus denitrificans*, *Tetrahedron Letters* 20, 4805-4808.
- [15] Cornish, A. S., and Page, W. J. (1995) Production of the triacetate siderophore protochelin by *Azotobacter vinelandii*, *Biometals* 8, 332-338.
- [16] Bergeron, R. J., Singh, S., and Bharti, N. (2011) Synthesis of Heterobactins A and B and *Nocardia* Heterobactin, *Tetrahedron* 67, 3163-3169.

- [17] Bao, G., Clifton, M., Hoette, T. M., Mori, K., Deng, S.-X., Qiu, A., Viltard, M., Williams, D., Paragas, N., Leete, T., Kulkarni, R., Li, X., Lee, B., Kalandadze, A., Ratner, A. J., Pizarro, J. C., Schmidt-Ott, K. M., Landry, D. W., Raymond, K. N., Strong, R. K., and Barasch, J. (2010) Iron traffics in circulation bound to a siderocalin (Ngal)-catechol complex, *Nature chemical biology* 6, 602-609.
- [18] Shapiro, J. A., and Wencewicz, T. A. (2017) Structure-function studies of acinetobactin analogs, *Metallomics* 9, 463-470.
- [19] Endicott, N. P., Lee, E., and Wencewicz, T. A. (2017) Structural Basis for Xenosiderophore Utilization by the Human Pathogen *Staphylococcus aureus*, *ACS infectious diseases* 3, 542-553.
- [20] Bohac, T. J., Shapiro, J. A., and Wencewicz, T. A. (2017) Rigid Oxazole Acinetobactin Analog Blocks Siderophore Cycling in *Acinetobacter baumannii*, *ACS infectious diseases* 3, 802-806.
- [21] McQueen, C. F., and Groves, J. T. (2018) A reevaluation of iron binding by Mycobactin J, *Journal of biological inorganic chemistry* 23, 995-1007.
- [22] Stintzi, A., Barnes, C., Xu, J., and Raymond, K. N. (2000) Microbial iron transport via a siderophore shuttle: A membrane ion transport paradigm, *Proceedings of the National Academy of Sciences* 97, 10691.
- [23] Hider, R. C., and Kong, X. (2010) Chemistry and biology of siderophores, *Natural product reports* 27, 637-657.
- [24] Ree, H., Kim, J., Song, W. Y., Lee, J. E., and Kim, H. J. (2015) Total Syntheses and Evaluation of the Siderophore Functions of Fimsbactin B and Its Analogs, *Bulletin of the Korean Chemical Society* 36, 1520-1523.



- [25] McRose, D. L., Seyedsayamdost, M. R., and Morel, F. M. M. (2018) Multiple siderophores: bug or feature?, *Journal of biological inorganic chemistry* 23, 983-993.
- [26] McRose, D. L., Baars, O., Seyedsayamdost, M. R., and Morel, F. M. M. (2018) Quorum sensing and iron regulate a two-for-one siderophore gene cluster in *Vibrio harveyi*, *Proceedings of the National Academy of Sciences* 115, 7581.
- [27] Bergeron, R. J., Elliott, G. T., Kline, S. J., Ramphal, R., and St James, L., 3rd. (1983) Bacteriostatic and fungostatic action of catecholamide iron chelators, *Antimicrobial agents and chemotherapy* 24, 725-730.
- [28] Wencewicz, T. A., and Miller, M. J. (2018) Sideromycins as Pathogen-Targeted Antibiotics, In *Antibacterials: Volume II* (Fisher, J. F., Mobashery, S., and Miller, M. J., Eds.), pp 151-183, Springer International Publishing, Cham.
- [29] Ohlemacher, S. I., Giblin, D. E., d'Avignon, D. A., Stapleton, A. E., Trautner, B. W., and Henderson, J. P. (2017) Enterobacteria secrete an inhibitor of *Pseudomonas* virulence during clinical bacteriuria, *The Journal of clinical investigation* 127, 4018-4030.
- [30] Krewulak, K. D., and Vogel, H. J. (2008) Structural biology of bacterial iron uptake, *Biochimica et Biophysica Acta (BBA) - Biomembranes* 1778, 1781-1804.
- [31] Hoegy, F., Celia, H., Mislin, G. L., Vincent, M., Gallay, J., and Schalk, I. J. (2005) Binding of iron-free siderophore, a common feature of siderophore outer membrane transporters of *Escherichia coli* and *Pseudomonas aeruginosa*, *The Journal of biological chemistry* 280, 20222-20230.
- [32] Rivera, G. S. M., Beamish, C. R., and Wencewicz, T. A. (2018) Immobilized FhuD2 Siderophore-Binding Protein Enables Purification of Salmycin Sideromycins from *Streptomyces violaceus* DSM 8286, *ACS infectious diseases* 4, 845-859.

- [33] Fukushima, T., Allred, B. E., Sia, A. K., Nichiporuk, R., Andersen, U. N., and Raymond, K. N. (2013) Gram-positive siderophore-shuttle with iron-exchange from Fe-siderophore to apo-siderophore *Bacillus cereus*; YxeB, *Proceedings of the National Academy of Sciences* *110*, 13821.
- [34] Fukushima, T., Allred, B. E., and Raymond, K. N. (2014) Direct Evidence of Iron Uptake by the Gram-Positive Siderophore-Shuttle Mechanism without Iron Reduction, *ACS chemical biology* *9*, 2092-2100.
- [35] Wuest, W. M., Sattely, E. S., and Walsh, C. T. (2009) Three siderophores from one bacterial enzymatic assembly line, *J Am Chem Soc* *131*, 5056-5057.
- [36] Sattely, E. S., and Walsh, C. T. (2008) A latent oxazoline electrophile for N-O-C bond formation in pseudomonine biosynthesis, *J Am Chem Soc* *130*, 12282-12284.
- [37] Dorsey, C. W., Tomaras, A. P., Connerly, P. L., Tolmasky, M. E., Crosa, J. H., and Actis, L. A. (2004) The siderophore-mediated iron acquisition systems of *Acinetobacter baumannii* ATCC 19606 and *Vibrio anguillarum* 775 are structurally and functionally related, *Microbiology* *150*, 3657-3667.
- [38] Gaddy, J. A., Arivett, B. A., McConnell, M. J., López-Rojas, R., Pachón, J., and Actis, L. A. (2012) Role of Acinetobactin-Mediated Iron Acquisition Functions in the Interaction of *Acinetobacter baumannii* Strain ATCC 19606T with Human Lung Epithelial Cells, *Galleria mellonella* Caterpillars, and Mice, *Infection and Immunity* *80*, 1015.
- [39] Miethke, M. (2013) Molecular strategies of microbial iron assimilation: from high-affinity complexes to cofactor assembly systems, *Metallomics* *5*, 15-28.

- [40] Miethke, M., Hou, J., and Marahiel, M. A. (2011) The Siderophore-Interacting Protein YqjH Acts as a Ferric Reductase in Different Iron Assimilation Pathways of *Escherichia coli*, *Biochemistry* 50, 10951-10964.
- [41] Li, K., Chen, W.-H., and Bruner, S. D. (2015) Structure and Mechanism of the Siderophore-Interacting Protein from the Fuscachelin Gene Cluster of *Thermobifida fusca*, *Biochemistry* 54, 3989-4000.
- [42] Ganne, G., Brillet, K., Basta, B., Roche, B., Hoegy, F., Gasser, V., and Schalk, I. J. (2017) Iron Release from the Siderophore Pyoverdine in *Pseudomonas aeruginosa* Involves Three New Actors: FpvC, FpvG, and FpvH, *ACS chemical biology* 12, 1056-1065.
- [43] Álvarez-Fraga, L., Vázquez-Ucha, J. C., Martínez-Gutián, M., Vallejo, J. A., Bou, G., Beceiro, A., and Poza, M. (2018) Pneumonia infection in mice reveals the involvement of the *feoA* gene in the pathogenesis of *Acinetobacter baumannii*, *Virulence* 9, 496-509.
- [44] Lau, C. K., Krewulak, K. D., and Vogel, H. J. (2016) Bacterial ferrous iron transport: the Feo system, *FEMS microbiology reviews* 40, 273-298.
- [45] Schalk, I. J., and Guillon, L. (2013) Pyoverdine biosynthesis and secretion in *Pseudomonas aeruginosa*: implications for metal homeostasis, *Environmental microbiology* 15, 1661-1673.
- [46] Cornelis, P., and Dingemans, J. (2013) *Pseudomonas aeruginosa* adapts its iron uptake strategies in function of the type of infections, *Frontiers in cellular and infection microbiology* 3, 75-75.
- [47] Wencewicz, T. A., and Miller, M. J. (2013) Biscatecholate-monohydroxamate mixed ligand siderophore-carbacephalosporin conjugates are selective sideromycin antibiotics that target *Acinetobacter baumannii*, *Journal of medicinal chemistry* 56, 4044-4052.

- [48] Johnstone, T. C., and Nolan, E. M. (2017) Determination of the Molecular Structures of Ferric Enterobactin and Ferric Enantioenterobactin Using Racemic Crystallography, *Journal of the American Chemical Society* 139, 15245-15250.
- [49] Perraud, Q., Moynie, L., Gasser, V., Munier, M., Godet, J., Hoegy, F., Mely, Y., Mislin, G. L. A., Naismith, J. H., and Schalk, I. J. (2018) A Key Role for the Periplasmic PfeE Esterase in Iron Acquisition via the Siderophore Enterobactin in *Pseudomonas aeruginosa*, *ACS chemical biology* 13, 2603-2614.
- [50] Antunes, L. C., Imperi, F., Towner, K. J., and Visca, P. (2011) Genome-assisted identification of putative iron-utilization genes in *Acinetobacter baumannii* and their distribution among a genotypically diverse collection of clinical isolates, *Research in microbiology* 162, 279-284.
- [51] Funahashi, T., Tanabe, T., Mihara, K., Miyamoto, K., Tsujibo, H., and Yamamoto, S. (2012) Identification and characterization of an outer membrane receptor gene in *Acinetobacter baumannii* required for utilization of desferricoprogen, rhodotorulic acid, and desferrioxamine B as xenosiderophores, *Biological & pharmaceutical bulletin* 35, 753-760.
- [52] Jones, C. M., Wells, R. M., Madduri, A. V. R., Renfrow, M. B., Ratledge, C., Moody, D. B., and Niederweis, M. (2014) Self-poisoning of *Mycobacterium tuberculosis* by interrupting siderophore recycling, *Proceedings of the National Academy of Sciences* 111, 1945.
- [53] Ghosh, M., Lin, Y. M., Miller, P. A., Mollmann, U., Boggess, W. C., and Miller, M. J. (2018) Siderophore Conjugates of Daptomycin are Potent Inhibitors of Carbapenem Resistant Strains of *Acinetobacter baumannii*, *ACS infectious diseases* 4, 1529-1535.

- [54] Ghosh, M., Miller, P. A., Mollmann, U., Claypool, W. D., Schroeder, V. A., Wolter, W. R., Suckow, M., Yu, H., Li, S., Huang, W., Zajicek, J., and Miller, M. J. (2017) Targeted Antibiotic Delivery: Selective Siderophore Conjugation with Daptomycin Confers Potent Activity against Multidrug Resistant *Acinetobacter baumannii* Both in Vitro and in Vivo, *Journal of medicinal chemistry* 60, 4577-4583.
- [55] Yamamoto, S., Okujo, N., and Sakakibara, Y. (1994) Isolation and structure elucidation of acinetobactin, a novel siderophore from *Acinetobacter baumannii*, *Archives of microbiology* 162, 249-254.
- [56] Shephard, M. J., and Paddon-Row, M. N. (1995) Gas Phase Structure of the Bicyclo[2.2.1]heptane (Norbornane) Cation Radical: A Combined ab Initio MO and Density Functional Study, *The Journal of Physical Chemistry* 99, 3101-3108.
- [57] Zhao, Y., and Truhlar, D. G. (2008) Density functionals with broad applicability in chemistry, *Accounts of chemical research* 41, 157-167.
- [58] Pople, J. A., Scott, A. P., Wong, M. W., and Radom, L. (1993) Scaling Factors for Obtaining Fundamental Vibrational Frequencies and Zero-Point Energies from HF/6-31G\* and MP2/6-31G\* Harmonic Frequencies, *Israel Journal of Chemistry* 33, 345-350.
- [59] Cossi, M., Rega, N., Scalmani, G., and Barone, V. (2003) Energies, structures, and electronic properties of molecules in solution with the C-PCM solvation model, *Journal of Computational Chemistry* 24, 669-681.
- [60] Rydberg, P., and Olsen, L. (2009) The Accuracy of Geometries for Iron Porphyrin Complexes from Density Functional Theory, *The Journal of Physical Chemistry A* 113, 11949-11953.

- [61] Ansbacher, T., Srivastava, H. K., Martin, J. M., and Shurki, A. (2010) Can DFT methods correctly and efficiently predict the coordination number of copper(I) complexes? A case study, *J Comput Chem* 31, 75-83.
- [62] Weigend, F., and Ahlrichs, R. (2005) Balanced basis sets of split valence, triple zeta valence and quadruple zeta valence quality for H to Rn: Design and assessment of accuracy, *Physical Chemistry Chemical Physics* 7, 3297-3305.
- [63] Blin, K.; Wolf, T.; Chevrette, M. G.; Lu, X.; Schwalen, C. J.; Kautsar, S. A.; Suarez Durn, H. G.; de los Santos, E. L. C.; Uk Kim, H.; Nave, M.; Dickschat, J. S.; Mitchell, D. A.; Shelest, E.; Breitling, R.; Takano, E.; Yup Lee, S.; Weber, T.; Medema, M. H. “antiSMASH 4.0—improvements in chemistry prediction and gene cluster boundary identification.” *Nucleic Acids Research* 2017, 45, W36–W41.
- [64] Funahashi, T.; Tanabe, T.; Maki, J.; Miyamoto, K.; Tsujibo, H.; Yamamoto, S. “Identification and characterization of a cluster of genes involved in biosynthesis and transport of acinetoferrin, a siderophore produced by *Acinetobacter haemolyticus* ATCC 17906.” *Microbiology* 2013, 159, 678–690.

**Chapter 4: Exploring Apparent Redundancy**  
**in Siderophore Systems of**  
***Acinetobacter baumannii***

## 4.1 Preface

This chapter was written by TJB. TJB, LF, DEG and TAW contributed to the work in this chapter. TJB isolated Fimsbactin F, performed characterization, BauB fluorescent quenching binding studies and metal titration assays. LF performed all growth curves and protein expression and purification. DEG performed all DFT calculations. TAW served as principal investigator and oversaw experimental design.

## 4.2 Abstract

Exploring the concept of siderophore redundancy in pathogenic bacteria has been one of interest in recent decades. Understanding the inter-workings of the relationship of the production of siderophores in a “siderophore cocktail”, is an area we sought to help elucidate. Herein, we report the production, isolation, characterization and protein interactions of a previously underexplored Fimsbactin isomer, Fimsbactin F. We investigate the relationship between Fimsbactin F and other two other *A. baumannii* siderophores, acinetobactin and Fimsbactin A, through competition assays. Furthermore, we sought to understand the metal preference and selectivity of these siderophores. This was achieved through the titrations of four known *A. baumannii* siderophores (Acb, PreAcb, FimA and FimF) and one synthetic siderophore mimic (OxPreAcb) with six metal chloride solutions (iron, copper, nickel, cobalt, zinc and magnesium). We observed the ability of these small molecules to bind a wide range of metals and set the stage for further explore of the role of PreAcb in zinc homeostasis particularly.

## 4.3 Introduction

In Chapter 1, and then again in Chapter 3, we introduced the concept of apparent siderophore redundancy as a potential evolutionary advantage for bacterial virulence. In this



chapter, we sought to further investigate the need or purpose for pathogenic bacteria to synthesize and utilize multiple siderophore scaffolds to acquire essential nutrients. Though there is often uneven production of each individual siderophore in most siderophore cocktails, many pathogenic bacteria produce multiple siderophores of their own—including *E. coli*, *M. tuberculosis* and the focus of this dissertation, *A. baumannii*.<sup>1,2,3</sup> Additionally, pathogens like *S. aureus* can utilize xenosiderophores, or siderophores produced by other bacteria, as a means to gain competitive over neighboring colonies.

As highlighted numerous times throughout this dissertation, *A. baumannii* synthesizes a siderophore cocktail comprised of three classes of siderophores—acinetobactin, the fimbactins, and the baumannoferrins **Figure 4.1**. In chapter 3, we explored Fimsbactin A and the relationship between acinetobactin (Acb) and Fimsbactin A (FimA). We highlighted the importance of balance in the relative concentrations of siderophores in the ability to provide a competitive advantage. Herein, we aim to explore the apparent siderophore redundancy of the Fimsbactin siderophore class. This class is comprised of Fimsbactin isomers A-F, **Figure 4.2**, which contain multiple iron chelating groups including hydroxamates and catechols.<sup>4</sup> In particular, we were interested in the relationship between FimA and Fim F— a shunt biosynthetic product lacking the seryl-O-2,3-DHB ester, and we hypothesized that an enzymatic interconversion between FimA and FimF might result in a single biologically relevant siderophore entity. The following chapter outlines a series of studies aimed at elucidating the apparent siderophore redundancies in pathogenic *A. baumannii*, particularly as it relates to the complete Fimsbactin-iron acquisition pathway.

## 4.4 Results and Discussion

*Purification of Acb, FimA and FimF from A. baumannii ATCC 17978.*

In Chapter 3, the isolation, purification and evaluation of Fimsbactin A was discussed in depth. Herein, we highlight the isolation and evaluation of isomer Fimsbactin F. In this regard, we isolated crude Acb and Fimsbactins A and F from *A. baumannii* ATCC 17978 grown in M9 minimal media supplement with 2,2'-dipyridyl (DIP). LC-MS analysis of crude supernatant broth, seen in **Figures 4.3** and **4.4**, identified Acb as the most produced siderophore, followed by Fimsbactin A and Fimsbactin F, respectively. Preparatory HPLC of the crude mixtures allowed for separation, isolation and purification of these three siderophores (Acb: 31 mg/L, FimA: 5 mg/L and FimF: 2 mg/L), and the full characterization of Fimsbactin F is highlighted in **Figures 4.5-4.9**.

### ***Iron-Binding properties of FimF***

Similarly to that previously described for acinetobactin and fimsbactin A, we determined the iron binding affinity of FimF using a competitive binding assay carried out in the presence of EDTA. The iron-binding affinity of FimF was consistent with those previously reported for Acb and FimA ( $\text{LogK}_{\text{Fe}} = 25.9$  for FimF compared to 27.4, 26.2 and 27.1 for PreAcb, Acb and FimA, respectively), suggesting no significant iron-binding advantage for the production of any one siderophore (**Table 4.1**). In addition to iron binding, we sought to investigate the dose-dependent influence of FimF on the whole cell growth of *A. baumannii*. We observed dose-dependent growth promotion of whole cell *A. baumannii* cultured in the presence of Fimsbactin F, with an enhanced effect observed for the *holo*-variant (**Figure 4.10** and **4.11**). These findings are consistent with previous siderophores growth studies, which demonstrate increased growth promotion of siderophores doped in the metal-bound form.

### ***Siderophore competition assays***

Our previous work highlighted the necessity for balance in siderophore combinations, as we saw an inhibitory effect on whole cell growth of *A. baumannii* at high concentrations of FimA,

in the presence of both low and high concentrations of Acb. Thus, to explore possible new relationships, we conducted checkerboard-combination growth studies with purified FimF in combination with Acb or FimA. We first examined the effect that combinations of FimA and FimF in both *apo*- and *holo*-forms had on the whole cell growth of *A. baumannii*. Interestingly, we observed an inhibitory effect at high concentrations of FimA that was strikingly similar to the observations gathered in our prior work on FimA and Acb cooperativity. Notably, this inhibition can be mitigated by the addition of *holo*-siderophore to the *apo*-FimA populated environment (**Figures 4.12 and 4.13**). However, in combinations of Acb and FimF, no inhibitory effect was observed; instead, higher concentrations of siderophore led to increased growth promotion across the board, suggesting a cooperative, as oppose to competitive, relationship between Acb and FimF (**Figure 4.14 and 4.15**).

### ***Siderophore binding to BauB***

In addition to metal binding, siderophore competition cocktails, and effects on whole cell growth, we were particularly interested in the ability of FimF to bind to periplasmic protein BauB—since we previously demonstrated a direct competition between Acb and FimA for BauB through fluorescence quenching assays.<sup>5</sup> Thus, through intrinsic tryptophan fluorescence quenching assays, we identified siderophore-dependent quenching and were able to calculate apparent  $K_d$  values for BauB binding of both the *apo*- as well as the *holo*- siderophores to be 297.4 nM and 360.3 nM, respectively, using a single-binding mode curve-fitting model in GraphPad Prism (**Figure 4.16, Table 4.1**). These values indicate BauB binding of both FimF and FimF-Fe— with a higher affinity observed for the iron-bound form. These dissociation constants are consistent with the BauB binding affinities observed for other *A. baumannii* siderophores, suggesting

potential competition for the siderophore transport pathway involved in the acquisition of iron required for bacterial virulence.

### ***Fimsbactin A potential cleavage by esterase enzymes***

Through studies of Trojan horse siderophore-antibiotic conjugates, work by Wencewicz et al. suggests Fimsbactin A fails to transverse the inner membrane to reach the cytoplasm of the cell.<sup>6</sup> It must be noted, however, that the fimsbactin mimic utilized in the studies by Wencewicz et al are not able to be hydrolyzed; this ability to be hydrolyzed might be required to enter into the cytoplasm. Our studies in this chapter draw a parallel between *A. baumannii* siderophores Acb and FimF—as both siderophores possess similar iron affinities, bind in 2:1 siderophore-iron complexes, and behave similarly in combination growth studies. However, in order to help elucidate apparent siderophore redundancies, we sought to investigate if FimA can be cleaved by an esterase to afford FimF—a molecule that might be able to cross the inner membrane. To test this hypothesis, we are currently expressing and purifying FbsM—a thioesterase enzyme encoded for in the Fimsbactin gene cluster.<sup>4</sup> Additionally, our lab is expressing and purifying BesA—a common ferri-bacillibactin esterase which could also potentially hydrolyze the FimA ester to afford FimF.<sup>7</sup> With these enzymes in hand, future efforts will explore possible cleavage of the FimA ester in an *in vitro* assay coupled to LCMS detection. However, based upon our current understanding of the siderophore cocktail cooperativity, our updated working model of the transport uptake pathways of the siderophore cocktail of *A. baumannii* is shown in **Figure 4.20**.

According to this working model, Fimsbactin A is biosynthesized in the cytoplasm and effluxed out of the cell, where the siderophore can then bind what would otherwise be bio-unavailable iron. The *holo*-siderophore is then imported into the periplasm via outer-membrane transport protein FbsN. Once in the periplasm, an esterase enzyme may facilitate the conversion

of FimA to FimF, at which time the iron may be reduced by FbsP from Fe(III) to Fe(II) and pass into the cytoplasm through inner membrane FeoAB transporters. The now *apo*-FimF might then bind with BauB (as shown to be possible by our fluorescence quenching assays), potentially forming a 2:1 complex with PreAcb or Acb and iron, and be transported through inner-membrane transport protein BauCDE. Once in the cytoplasm, FimF might then be recycled into FimA through FimA biosynthesis, and the cycle would repeat.

### ***Siderophore metal binding assays***

While the vast majority of the work with and studies of siderophores have centered on iron binding, metal binding specificity and metal affinities may distinguish these seemingly redundant siderophores as multifunctional collections of multipurpose small molecule metal chelators with important implications in metal homeostasis beyond iron. In this light, aiming to explore metal chelation selectivity, we conducted fluorescence titration assays of four siderophores of *A. baumannii* (PreAcb, Acb, FimA and FimF), along with one synthetic analog and growth inhibitor (OxPreAcb—discussed at length in Chapters 5 and 6), with a panel of six metals (iron, copper, nickel, cobalt, zinc and magnesium). Across the board, iron promoted quenching was most pronounced, indicating a distinct preference for iron binding (or iron is just a better quencher), with FimA possessing the highest preference (**Figures 4.21-4.27**). In addition, we were able to observe siderophore-metal binding with copper, nickel and cobalt, as well, which supports the potential role of siderophores in maintaining metal homeostasis in pathogenic bacteria. Interestingly, we observed a small fluorescence enhancement with addition of magnesium to siderophores in solution and a large enhancement upon the addition of zinc; notably, PreAcb-zinc binding produced a large fluorescence response, reaching maximum detection limits upon the addition of less than 0.2 equivalents of zinc. While we are still working to better understand this

result, we hypothesize unique interactions between zinc and the metal chelating functional groups present in the siderophores of *A. baumannii* are responsible for the unusual increase in fluorescence upon metal binding—as other small molecule siderophores, such as pyoverdine, containing hydroxamate and catecholate metal binding motifs are known to be of vital importance for optimal growth in the presence of zinc in *Pseudomonas aeruginosa*.<sup>8</sup> It must be noted, however, that fluorescence quenching was observed in the case of zinc titration with siderophore analog OxPreAcb. We hypothesize that this structurally rigidified synthetic molecule may allow for unique metal binding modes which differs from the natural PreAcb/Acb siderophore systems. Current efforts with our collaborator Dr. Daryl Giblin are ongoing to investigate metal preference via DFT calculations of these metal complexes.

## 4.5 Outlook and Conclusions

In conclusion, we isolated, purified and characterized a previously under-studied *A. baumannii* siderophore, Fimsbactin F. We demonstrated the ability of FimF to promote growth, as well as bind iron, and we determined both siderophore-iron binding stoichiometry and BauB binding affinity for the truncated FimA analog (FimF). Current efforts in our laboratory are aimed at investigating the relationship between FimA and FimF through purification of esterase and thioesterase enzymes to probe the apparent redundancy of fimsbactin production in *A. baumannii*. In addition, in this chapter, we sought to explore the metal preference of *A. baumannii* siderophores (PreAcb, Acb, FimA and FimF) and synthetic inhibitor (OxPreAcb) in an effort to better understand the role of siderophore cocktails in bacterial metal homeostasis. We discovered a distinct preference for siderophore iron-binding but identified the ability of the screened siderophores and siderophore analog to bind other metals such as copper and cobalt. Most notably,

there appears to be a unique relationship between PreAcb and zinc which we believe warrants further study. .

## 4.6 Materials and Methods

### *Strains, Materials, and Instrumentation.*

Growth studies were conducted using *A. baumannii* ATCC 17978 and ATCC 19606T. Pre-cultures and 96-well plate *A. baumannii* growth assays were performed in filter-sterilized M9 minimal media. M9 minimal media was prepared for all experiments as previously described.<sup>9,10,11</sup> Samples for LC-MS were prepared in 0.45  $\mu$ M PTFE mini-UniPrep vials from Agilent. All preparatory HPLC was performed using a Beckman Coulter SYSTEM GOLD 127P solvent module and 168 detector with a Phenomenex Luna 10u C18(2) 100A column, 250  $\times$  21.20 mm, 10  $\mu$ m with guard column. Prep HPLC was performed with a mobile phase of 5 mM ammonium acetate in (A) water and (B) acetonitrile, and data were processed using 32 Karat software, v7.0. LC-MS was performed on an Agilent 6130 quadrupole LC-MS with G1313 autosampler, G1315 diode array detector, and 1200 series solvent module. A Phenomenex Gemini C18 column, 50  $\times$  2 mm, 5  $\mu$ m with guard column was used for all LC-MS separations. LC-MS mobile phases were 0.1% formic acid in (A) water and (B) acetonitrile, and data were processed using G2710 ChemStation software. NMR was performed on a Varian Unity Inova-600 MHz instrument with a cold probe. Bacterial growth studies were performed using polystyrene 96-well plates with polystyrene lids. OD<sub>600</sub> measurements were taken on a Molecular Devices SpectraMax Plus 384 plate reader.

### *Isolation and purification of Acb, FimA and FimF.*

Acinetobactin (Acb), Fimsbactin A (FimA) and Fimsbactin F were isolated and purified from *A. baumannii* ATCC 17978 cultures using a modified literature procedure.<sup>9,12</sup> PreAcb and

OxPreAcb were synthesized as described previously by our group.<sup>5,9</sup> Briefly, 1 L cultures of *A. baumannii* ATCC 17978 were grown overnight in M9 minimal media. Cells were pelleted and the supernatant was adjusted to pH ~6 using citric acid. XAD-7HP resin was added to the supernatant and the mixture was shaken gently. The mixture was filtered and the resin was washed with methanol. The methanol washings were combined and concentrated via rotary evaporation under reduced pressure. Acb (retention time 12 min, 31 mg/L), FimA (retention time 15 min, 5 mg/L) and FimF (retention time 13 min, 2 mg/L) were purified from the crude residue by preparatory HPLC (gradient of 0% B to 95% B over 17 min, then 95% B to 100% B over 8 min). The *holo*-siderophores were prepared by mixing PreAcb, Acb, FimA and FimF with excess Fe(acac)<sub>3</sub> in methanol following by concentration and trituration with Et<sub>2</sub>O to provide the pure PreAcb<sub>2</sub>Fe, Acb<sub>2</sub>Fe, FimAFe and FimF<sub>2</sub>Fe complexes.<sup>9,10</sup>

#### ***A. baumannii* Growth Studies.**

Stock solutions of FimF and FimFFe were prepared in M9 media at 250 μM (up to 2.5% final DMSO v/v). Each well of a 96-well plate was filled with 50 μL of M9 media. 50 μL of the 250 μM test compound stock solutions were added to the first row of a 96 well plate. Compounds were serially diluted down the plate to 3.9 μM. An inoculum was made by adding 100 μL of 0.5 McFarland standard (*A. baumannii* ATCC 17978) to 4.0 mL of M9 minimal media supplemented with 350 μM 2,2'-dipyridyl (DIP). Inoculum (50 μL) was added to each well for a final concentration of 175 μM DIP per well and a serial dilution of test compounds at 62.5-1.95 μM. Growth promotion was determined at 37 °C by measuring OD<sub>600</sub> using a microplate reader (Molecular Devices SpectraMax Plus 384 plate reader). Control growth curves were performed in M9 media with 175 μM DIP and no test compounds. DIP concentrations were optimized prior to



each experiment by serial dilution against *A. baumannii* under the growth conditions described in this section. All experiments were performed in triplicate as independent trials.

For the biological evaluation of combinations of FimA, FimF, and corresponding ferric complexes, a 96-well plate was filled with 40  $\mu\text{L}$  of M9 minimal media per well, 5  $\mu\text{L}$  of each of the compounds of interest, a final concentration of 175  $\mu\text{M}$  DIP per well and 50  $\mu\text{L}$  of the inoculum. To explore the combination of FimA/FimF, the following concentrations were tested in duplicate in all possible combinations: 3.9  $\mu\text{M}$ , 15.6  $\mu\text{M}$ , 62.5  $\mu\text{M}$ . For the combination of FimAFe/FimF the following concentrations were tested in duplicate in all possible combinations: FimAFe 0.5  $\mu\text{M}$ , 3.9  $\mu\text{M}$ , 15.6  $\mu\text{M}$ ; FimF 3.9  $\mu\text{M}$ , 15.6  $\mu\text{M}$ , 62.5  $\mu\text{M}$ . For the combination of FimA/FimFFe the following concentrations were tested in duplicate in all possible combinations: FimA 3.9  $\mu\text{M}$ , 15.6  $\mu\text{M}$ , 62.5  $\mu\text{M}$ ; FimFFe 0.5  $\mu\text{M}$ , 3.9  $\mu\text{M}$ , 15.6  $\mu\text{M}$ . Growth promotion was determined at 37  $^{\circ}\text{C}$  by measuring  $\text{OD}_{600}$  using a microplate reader (Molecular Devices SpectraMax Plus 384 plate reader). Control growth curves were performed in M9 media with 175  $\mu\text{M}$  DIP and no test compounds. All experiments were performed in duplicate as independent trials.

For the biological evaluation of combinations of FimF, Acb, and corresponding ferric complexes, a 96-well plate was filled with 40  $\mu\text{L}$  of M9 minimal media per well, 5  $\mu\text{L}$  of each of the compounds of interest, a final concentration of 175  $\mu\text{M}$  DIP per well and 50  $\mu\text{L}$  of the inoculum. To explore the combination of FimF/Acb, the following concentrations were tested in duplicate in all possible combinations: 3.9  $\mu\text{M}$ , 15.6  $\mu\text{M}$ , 62.5  $\mu\text{M}$ . For the combination of FimFFe/Acb the following concentrations were tested in duplicate in all possible combinations: FimFFe 0.5  $\mu\text{M}$ , 3.9  $\mu\text{M}$ , 15.6  $\mu\text{M}$ ; Acb 3.9  $\mu\text{M}$ , 15.6  $\mu\text{M}$ , 62.5  $\mu\text{M}$ . For the combination of FimF/Acb<sub>2</sub>Fe the following concentrations were tested in duplicate in all possible combinations: FimF 3.9  $\mu\text{M}$ , 15.6  $\mu\text{M}$ , 62.5  $\mu\text{M}$ ; Acb<sub>2</sub>Fe 0.5  $\mu\text{M}$ , 3.9  $\mu\text{M}$ , 15.6  $\mu\text{M}$ . Growth promotion was determined at 37  $^{\circ}\text{C}$  by

measuring OD<sub>600</sub> using a microplate reader (Molecular Devices SpectraMax Plus 384 plate reader). Control growth curves were performed in M9 media with 175  $\mu$ M DIP and no test compounds. All experiments were performed in duplicate as independent trials.

#### ***Determination of FimFFe Complex Stoichiometry.***

A solution of 570  $\mu$ M FimF in methanol was prepared. A fluorescence emission spectrum was recorded ( $\lambda_{\text{excitation}} = 330 \text{ nm}$ ;  $\lambda_{\text{emission}} = 380 \text{ nm}$ ). To determine stoichiometry of the complex between Fim and Fe(III), aliquots of a methanolic solution of Fe(acac)<sub>3</sub> were added 0.044 equivalents at a time via Hamilton syringe and emission spectra were recorded after each addition. Peak fluorescence (Abs<sub>380nm</sub>) was plotted against Fe(III) equivalents to reveal a 2:1 FimFFe stoichiometry (**Figure 4.18**).

#### ***Determination of Apparent $K_{\text{Fe}}$ for FimFFe.***

A stock solution of 100  $\mu$ M FimFFe was prepared in 10 mM HEPES buffer (10 mM HEPES, 600 mM NaCl, 100 mM KCl, pH 7.4) and an optical absorbance spectrum was obtained from  $\lambda = 300\text{--}700 \text{ nm}$  (**Figure 4.17**). While continuously monitoring optical absorbance at 500 nm, EDTA was added at a final concentration of 120  $\mu$ M (1.2 equivalents relative to FimFFe). The apparent iron-binding affinity ( $K_{\text{Fe}}$ ) was determined based on the change in optical absorbance at 500 nm after 800 min for two independent trials using the equations provided in the supplementary information.

#### ***N-His<sub>6</sub>-BauB Expression and Purification.***

The *bauB* gene from *Acinetobacter baumannii* (Genbank Accession Number AAT52185) was codon optimized for expression in *E. coli* and cloned into a pET28b vector by GenScript Biotech Corporation. The *bauB* gene was then subcloned into a pET28bTEV vector using

restriction enzyme-based cloning.<sup>14</sup> BauB was expressed as the *N*-terminal hexahistidine fusion, *N*-His<sub>6</sub>-BauB, in *E. coli* BL21 (DE3) as described in Chapter 3. Protein purity was analyzed by SDS-PAGE with visualization by Coomassie blue staining. Protein mass were confirmed by ESI-MS. Purified protein was flash frozen in liquid N<sub>2</sub> at 180 μM and stored at –80 °C.

#### ***Determination of Apparent $K_d$ Values for BauB.***

*N*-His<sub>6</sub>-BauB was recovered on ice from a –80 °C freezer stock. A 400 nM BauB stock solution was prepared in assay buffer (25 mM Tris-HCl, 8 g/L NaCl, 0.2 g/L KCl, pH 7.4). For each measurement, 300 μL of the BauB stock solution was transferred to a fluorescence cuvette (HellmaAnalytics High Precision Cell cuvette made of Quartz SUPRASIL; light path 10 x 2 mm) in the presence of *apo*- and *holo*-FimBactinF at concentrations ranging from 100–1200 nM. Emission spectra were recorded at  $\lambda_{\text{emission}} = 300\text{--}400$  nm using a PerkinElmer LS 55 Luminescence Spectrometer (slit width 10 nm; scan speed 400 nm/min) at  $\lambda_{\text{excitation}} = 280$  nm. Fluorescence intensity at 320 nm was plotted versus substrate concentration (nM) and apparent  $K_d$  was calculated using nonlinear regression and a one binding site model in GraphPad Prism v7.0b (Figure 4.16, Table 4.1).<sup>14</sup> All experiments were performed in duplicate as independent trials.

#### ***Metal Titration Studies.***

A 500 μM stock solution of *apo*-small molecule (PreAcb, Acb, FimA, FimF or OxPreAcb) was prepared in methanol. 300 μL of the small molecule stock solution was transferred to a fluorescence cuvette (HellmaAnalytics High Precision Cell cuvette made of Quartz SUPRASIL; light path 10 x 2 mm). An emission spectra was recorded at  $\lambda_{\text{emission}} = 300\text{--}400$  nm using a PerkinElmer LS 55 Luminescence Spectrometer (slit width 10 nm; scan speed 400 nm/min) at  $\lambda_{\text{excitation}} = 280$  nm. 10 mM metal chloride stock solutions were prepared (Fe<sup>3+</sup>, Ni<sup>2+</sup>, Zn<sup>2+</sup>, Cu<sup>2+</sup>,

Co<sup>2+</sup> and Mg<sup>2+</sup>). 1  $\mu$ L portions of the 10 mM metal chloride stock solutions were added to the 300  $\mu$ L 500  $\mu$ M small molecule solution. Following each addition, the solution was gently mixed and an emission spectra was recorded. In the case of PreAcb and Zinc, absorption maxed out the detector limits following less than 0.2 equivalents added. To obtain a more accurate view of the absorption from the addition of Zinc, experiment was re-ran using 0.0066 equivalent additions of zinc chloride. Fluorescence intensity at 460 nm was plotted versus equivalents of metal ion in GraphPad Prism v7.0b (**Figures 4.21-4.27, Table 4.1**). All experiments were performed in duplicate as independent trials.

## 4.7 Figures and Tables

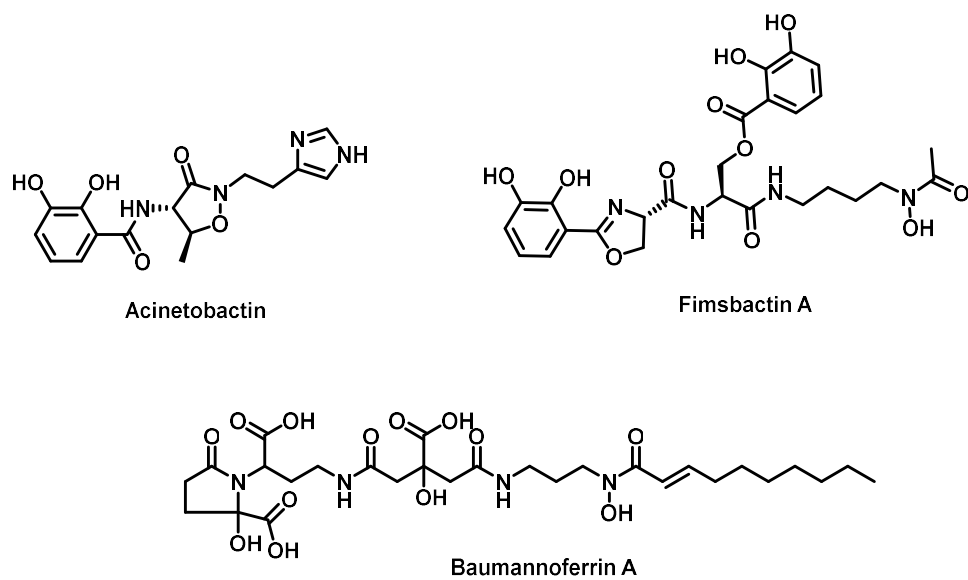


**Figure 4.1:** Siderophores of *Acinetobacter baumannii*.

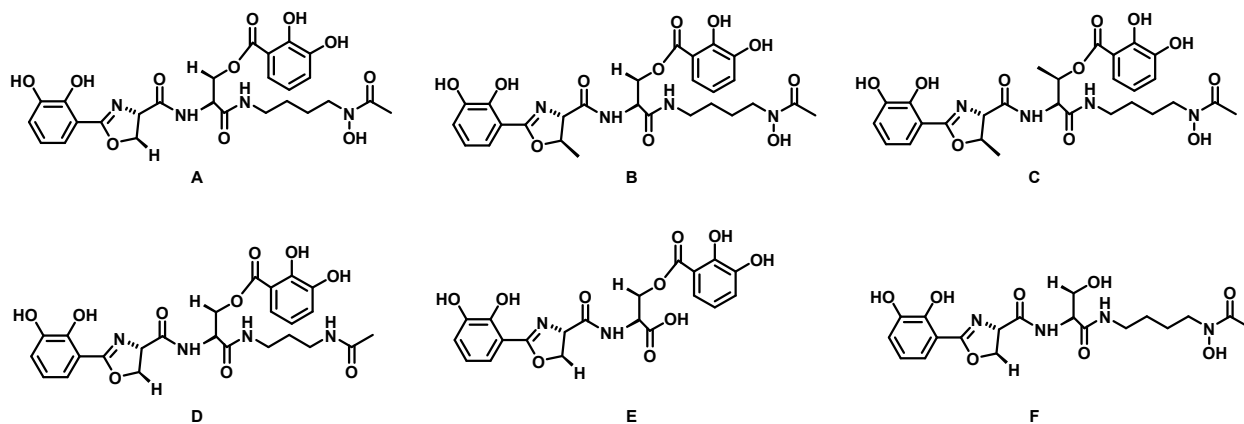


**Figure 4.2:** Fimsbactin siderophores A-F.

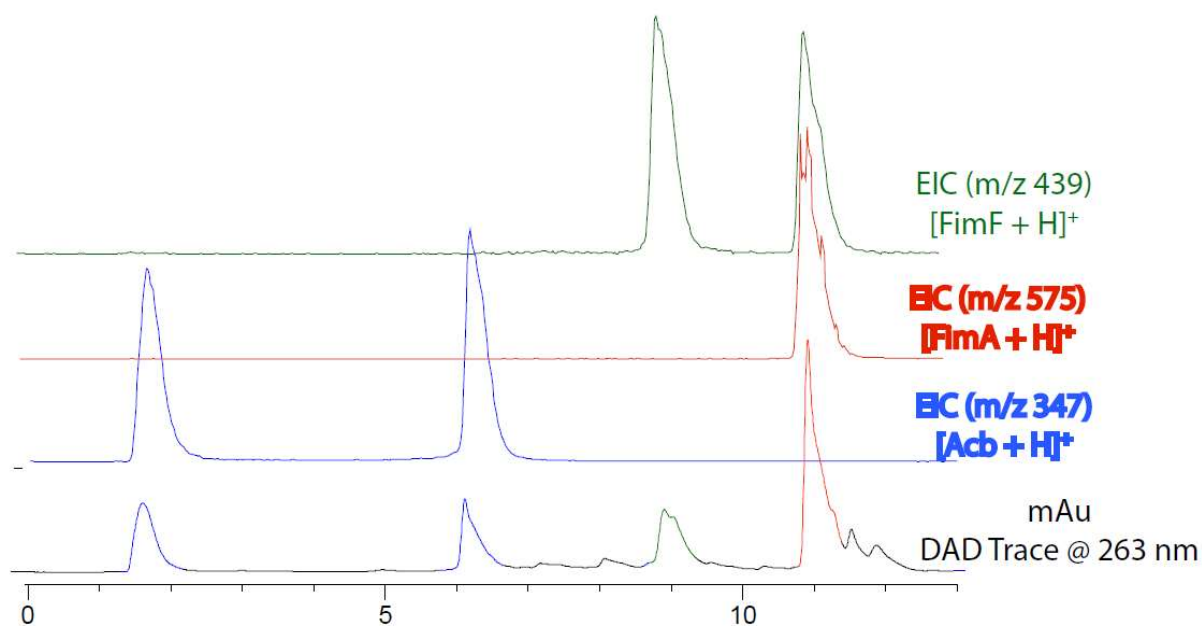


**Figure 4.3:** DAD at 263 nm (black), EIC at  $m/z$  347 (blue), EIC at  $m/z$  576 (red), and EIC at  $m/z$  439 (green) chromatograms from LCMS analysis of crude *A. baumannii* ATCC 17978 supernatant after acidification, treatment with XAD-7HP resin, and methanol elution.

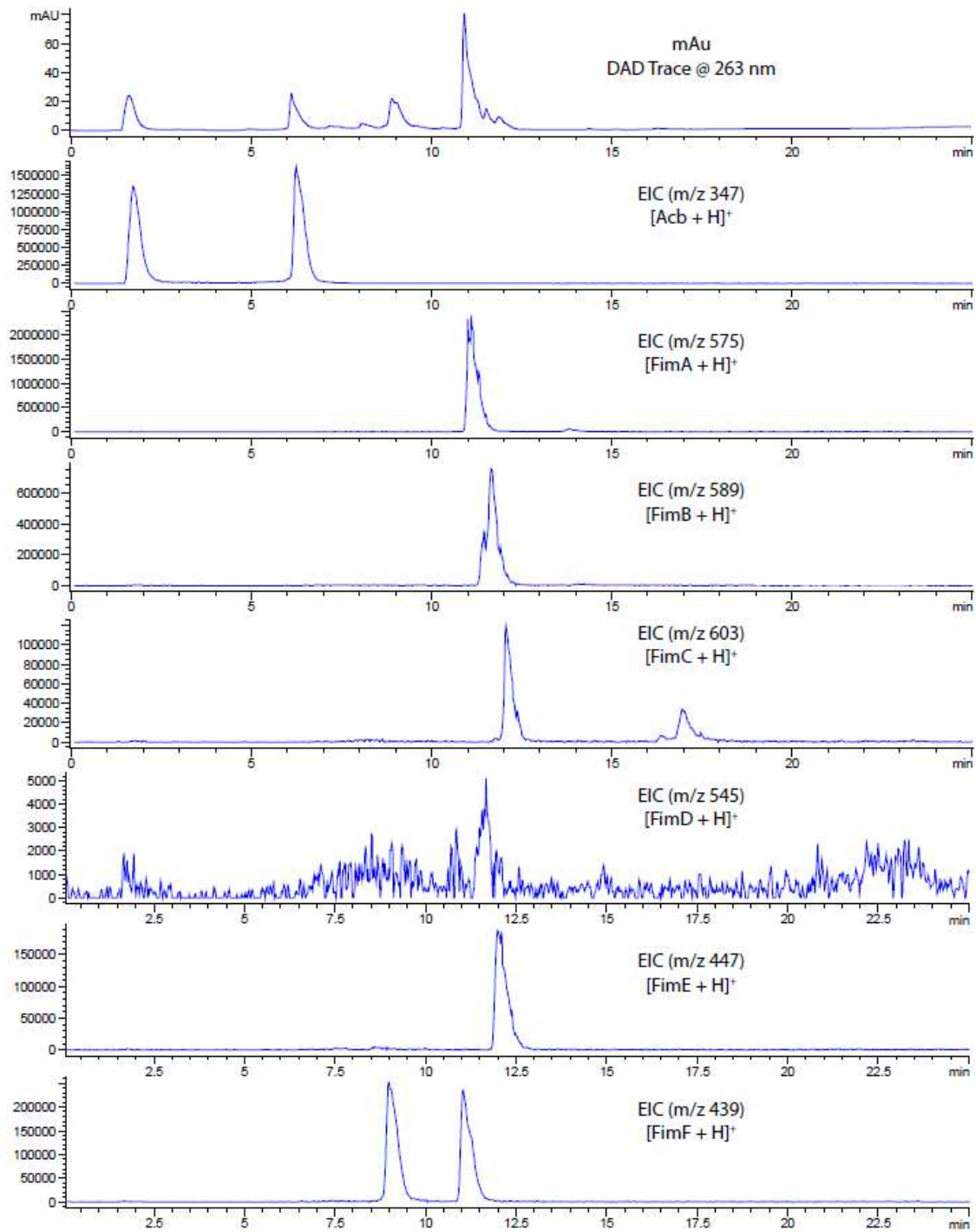


**Figure 4.4:** Diode array optical absorbance detection (DAD) and extracted ion chromatograms (EICs) for fimsbactin A–F  $[M+H]^+$  ions from LCMS analysis of culture supernatant extraction from *A. baumannii* ATCC 17978 using ESI ionization in positive ion mode. The x-axis represents retention time (min) for all chromatograms.

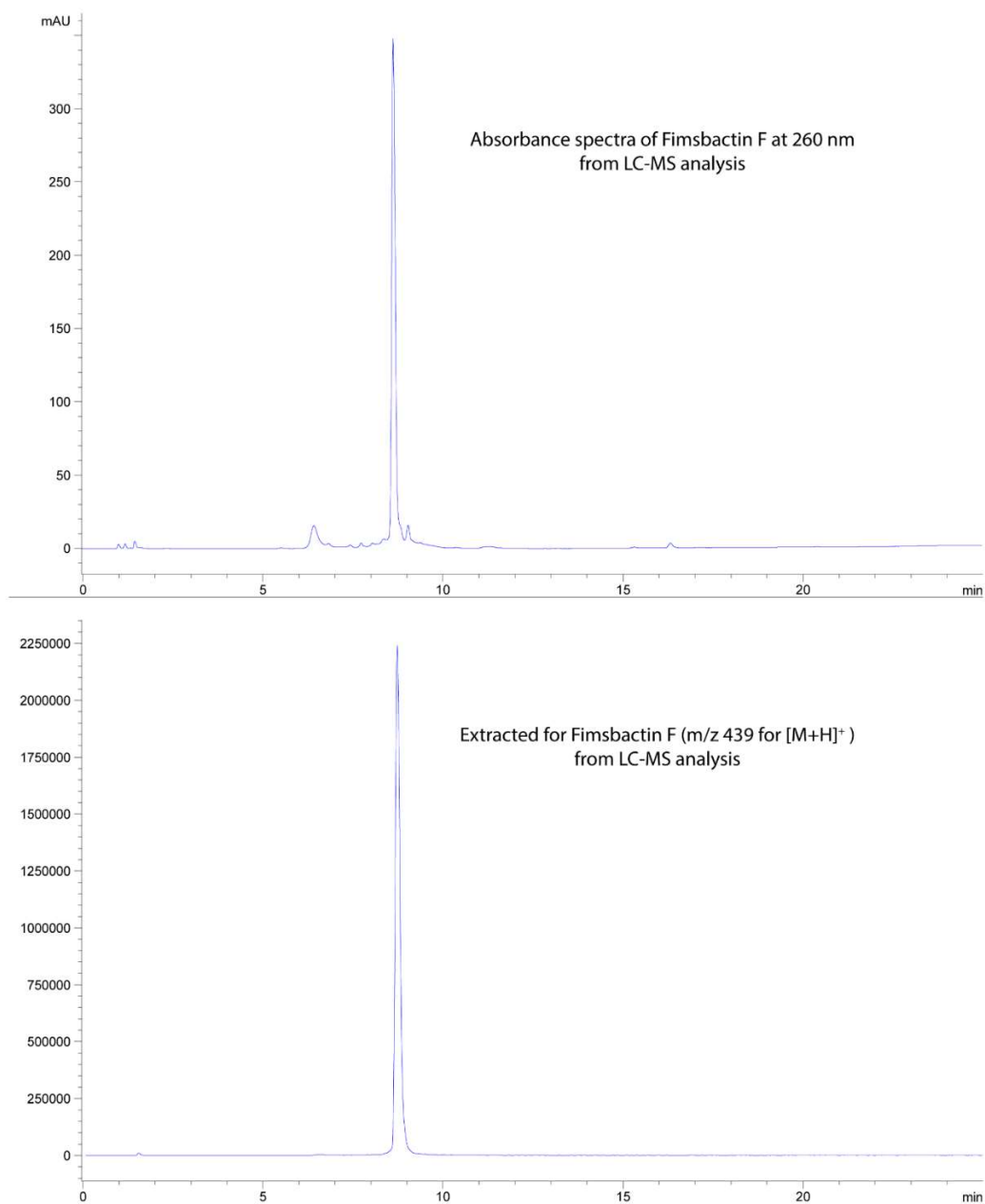


**Figure 4.5:** Diode array optical absorbance detection (DAD) and extracted ion chromatograms (EICs) for Fimsbactin F  $[M+H]^+$  ions from LCMS analysis using positive ion mode of *A. baumannii* ATCC 17978 culture supernatant HPLC-Prep purified. The x-axis represents retention time (min) for all chromatograms



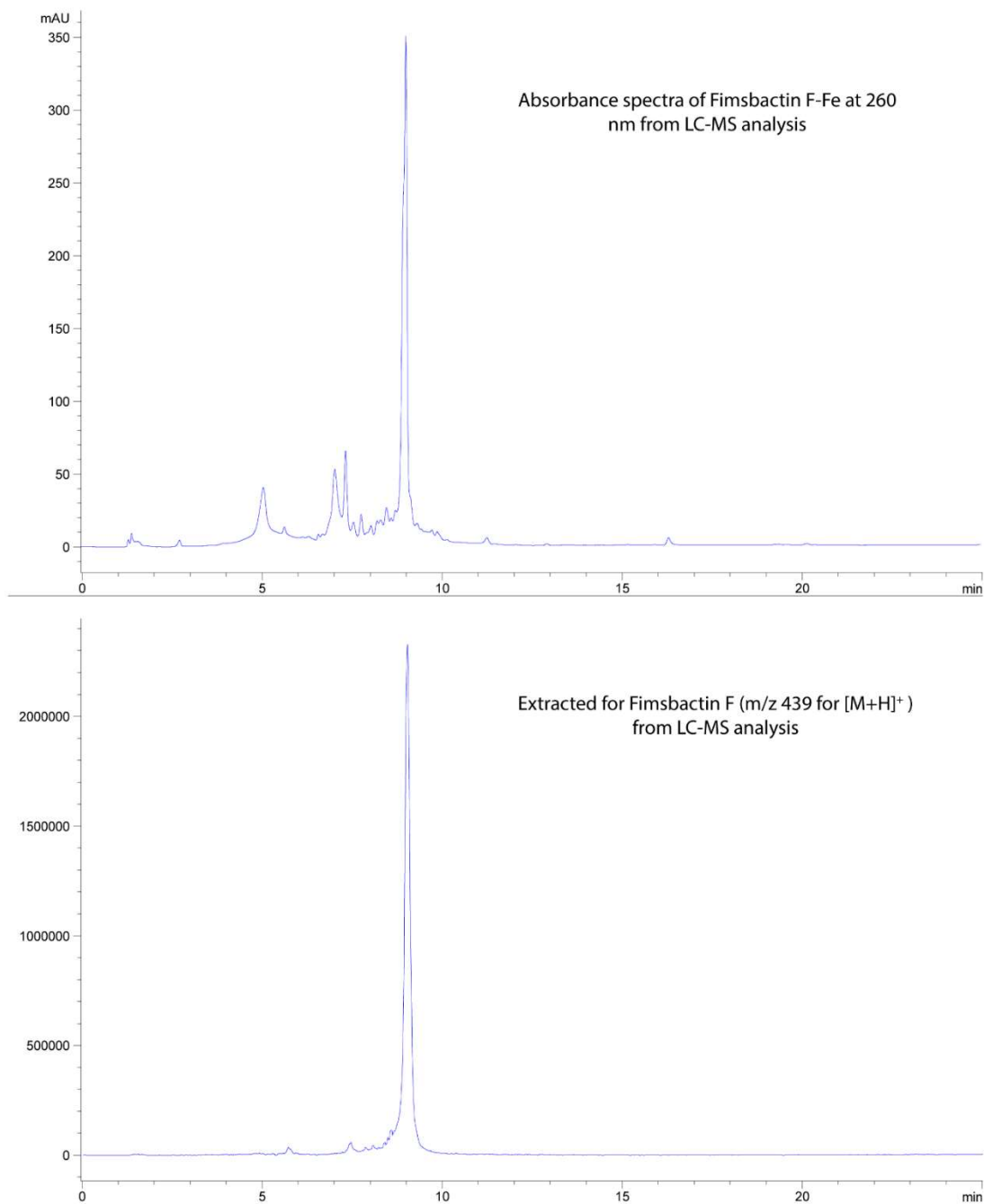


**Figure 4.6:** Diode array optical absorbance detection (DAD) and extracted ion chromatograms (EICs) for Fimsbactin-F  $[M+H]^+$  ions from LCMS analysis using positive ion mode of *A. baumannii* ATCC 17978 culture supernatant HPLC-Prep purified. Fimsbactin F-Fe ionizes as Fimsbactin-F ion  $[M+H]^+$  The x-axis represents retention time (min) for all chromatograms

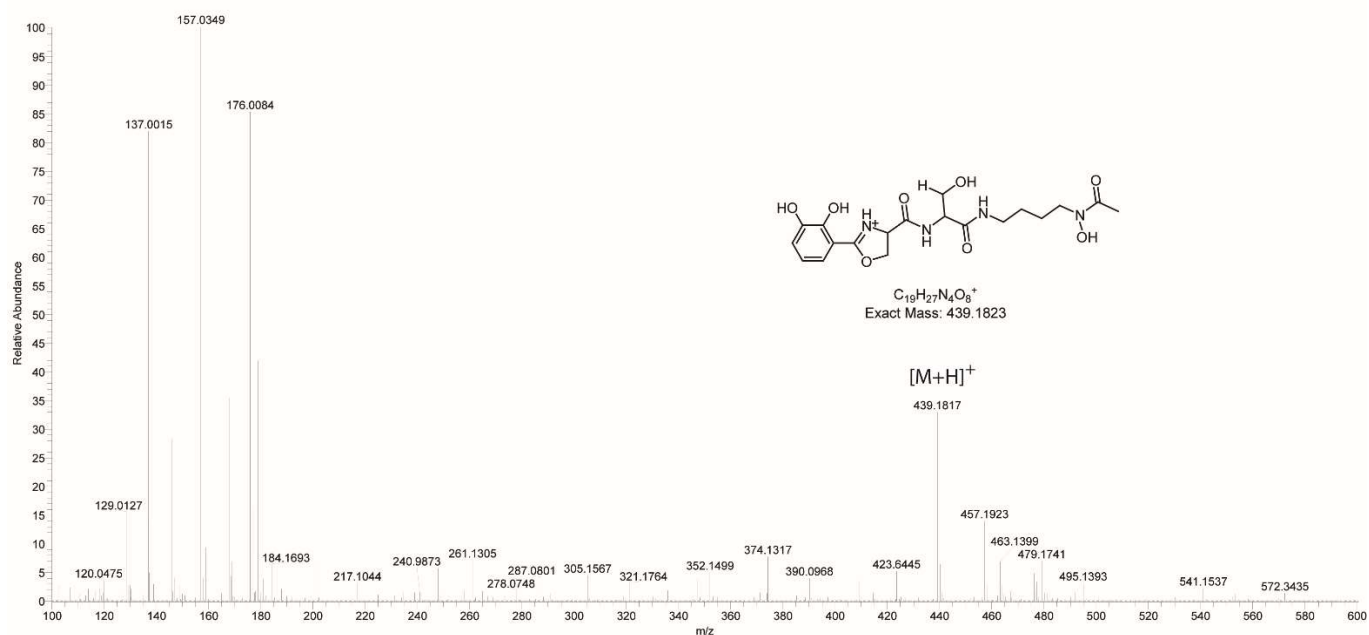


**Figure 4.7:** High-resolution ESI MS (positive ion mode) of Fimsbactin F purified by prep-HPLC from *A. baumannii* ATCC 17978 culture supernatant. Expected  $[M+H]^+$  for  $C_{19}H_{27}N_4O_8$  439.1823, found 439.1817.

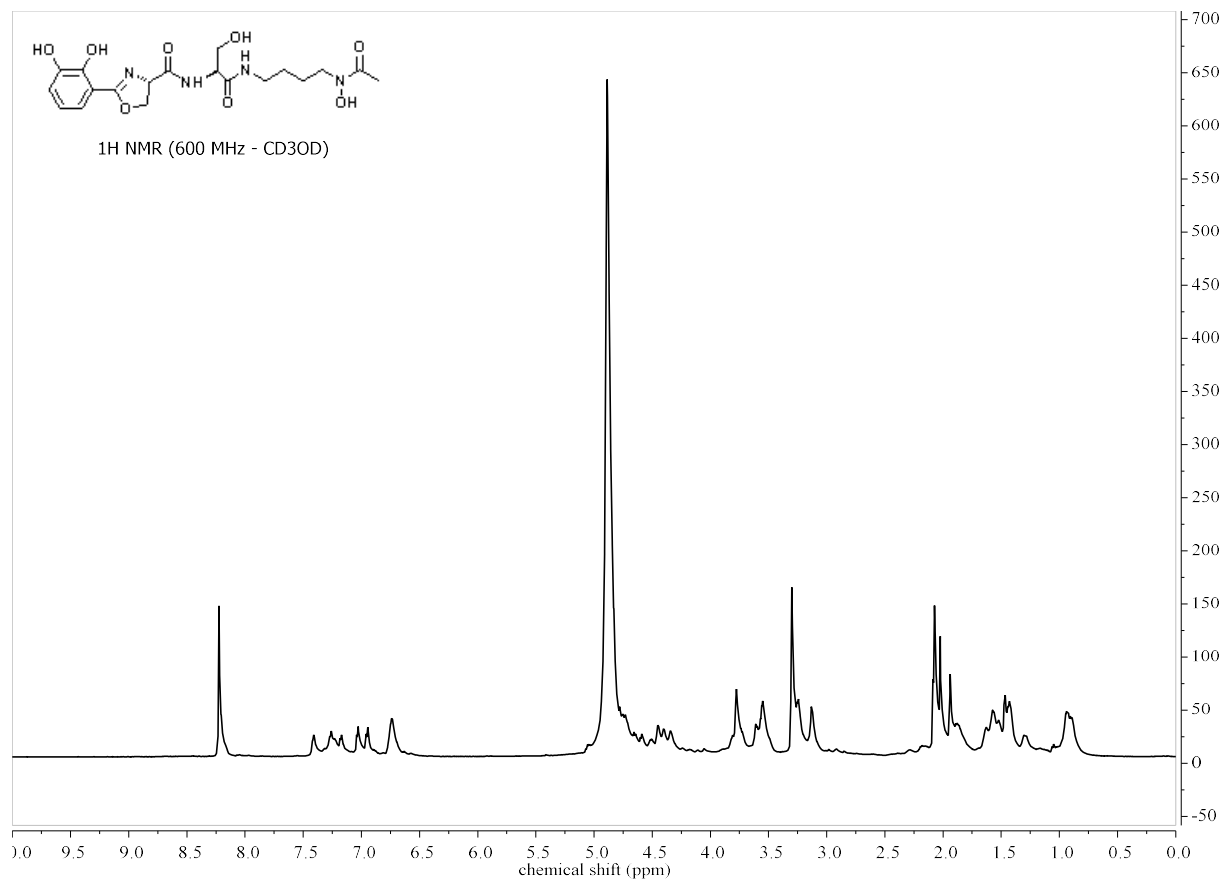


**Figure 4.8:**  $^1\text{H}$ -NMR (600 MHz,  $\text{CD}_3\text{OD}$ ) spectrum of purified Fimsbactin F purified by prep-HPLC from *A. baumannii* ATCC 17978. The x-axis is chemical shift given in parts per million (ppm). The y-axis is arbitrary peak intensity.

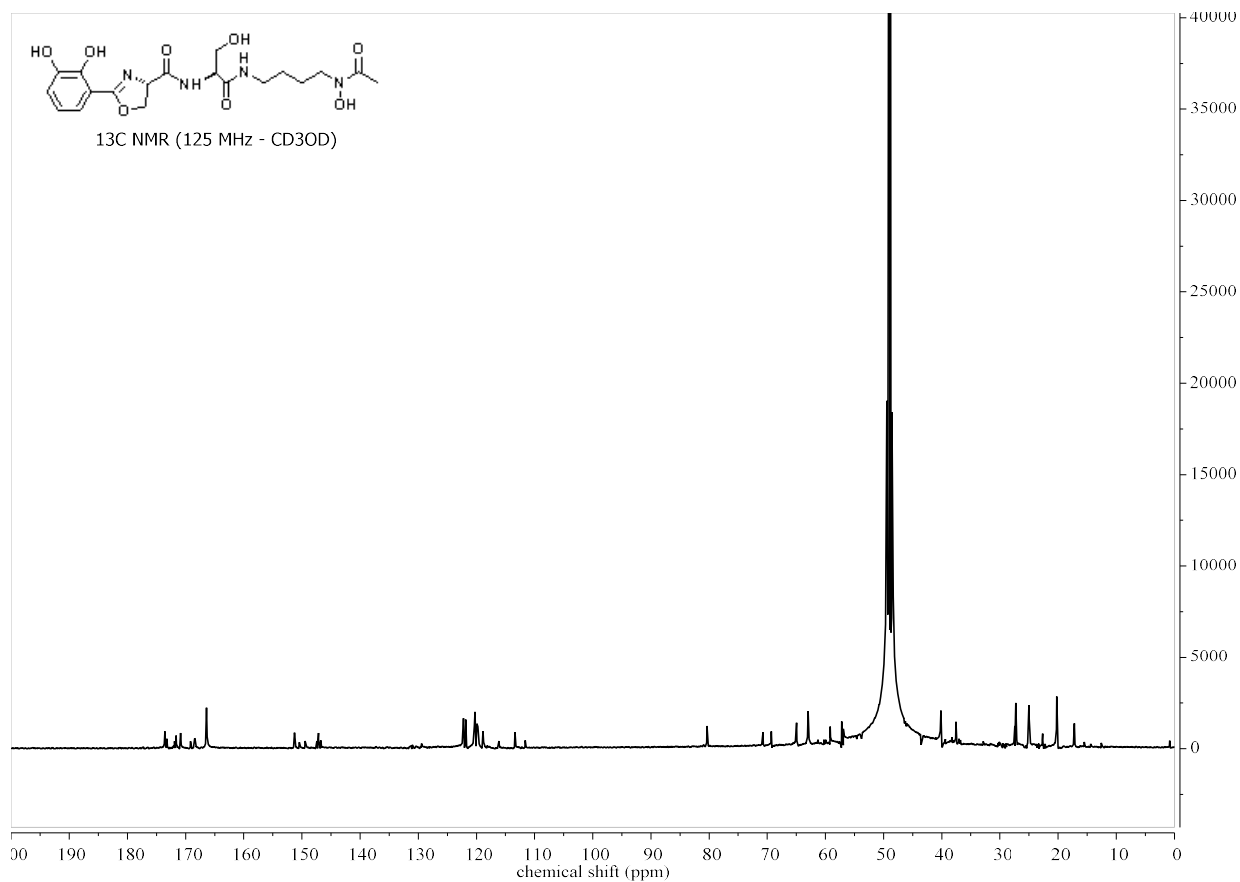


**Figure 4.9A:**  $^{13}\text{C}$ -NMR (151 MHz,  $\text{CD}_3\text{OD}$ ) spectrum of purified Fimsbactin F purified by prep-HPLC from *A. baumannii* ATCC 17978. The x-axis is chemical shift in parts per million (ppm). The y-axis is arbitrary peak intensity.

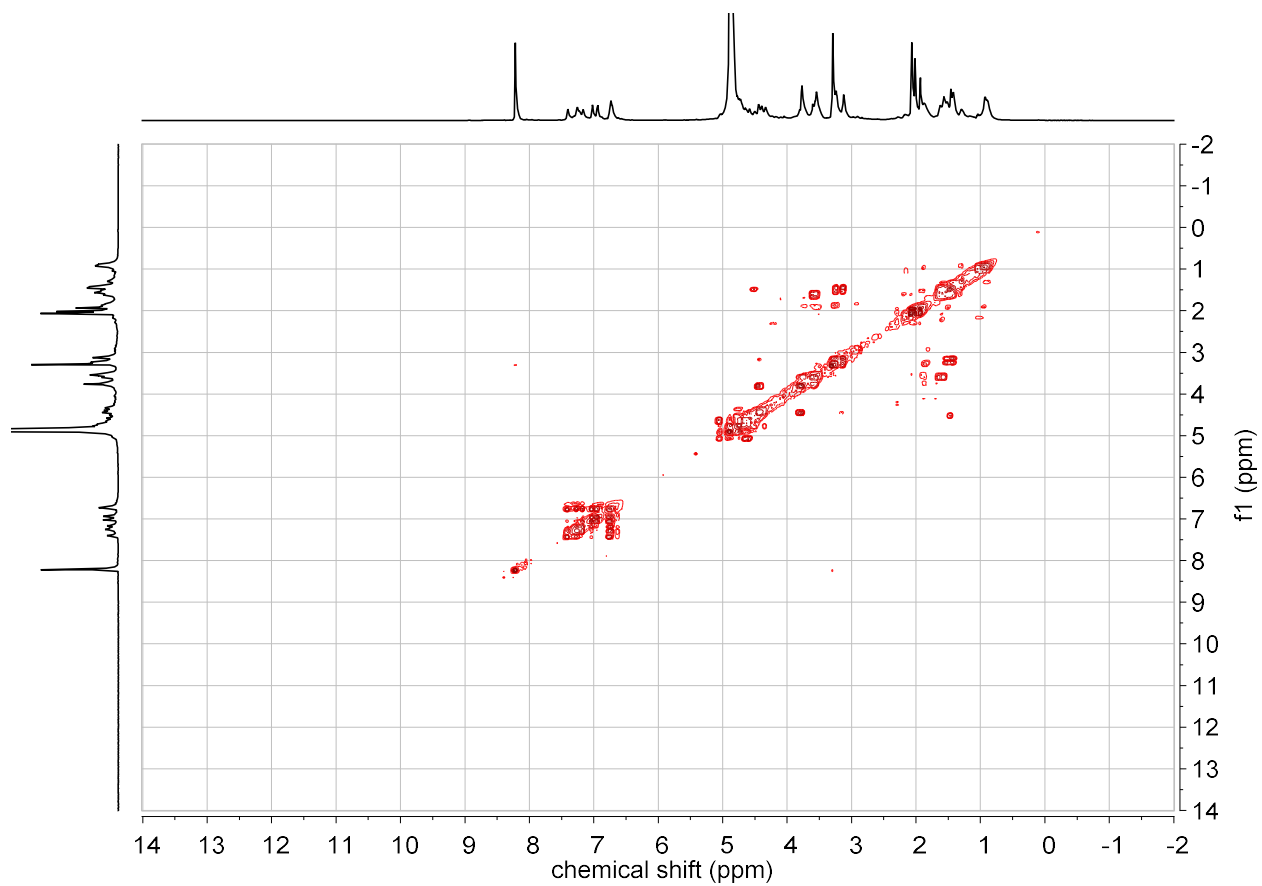


**Figure 4.9B:** COSY-NMR ( $\text{CD}_3\text{OD}$ ) spectrum of purified Fimsbactin F purified by prep-HPLC from *A. baumannii* ATCC 17978.

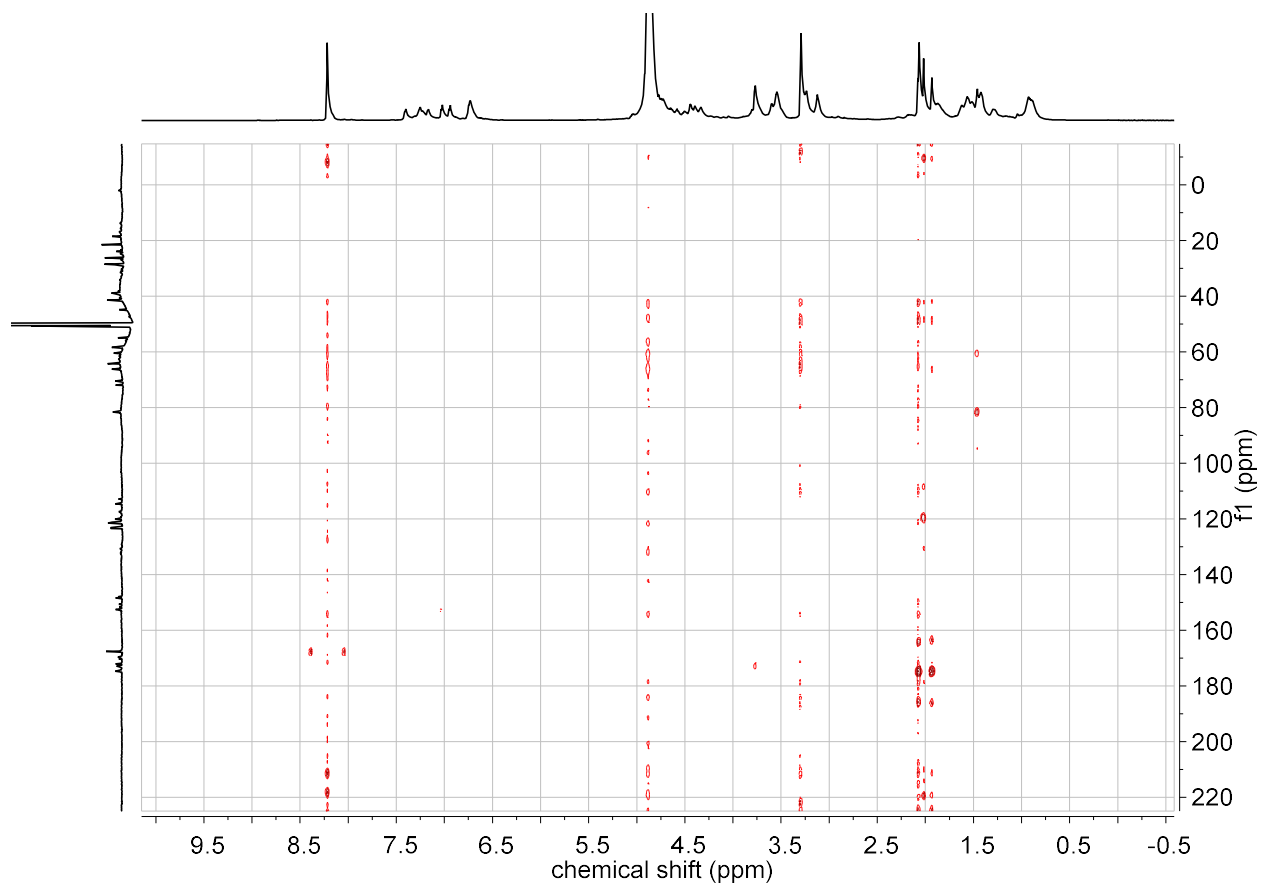


**Figure 4.9C:** HMBC-NMR (CD<sub>3</sub>OD) spectrum of purified Fimsbactin F purified by prep-HPLC from *A. baumannii* ATCC 17978.

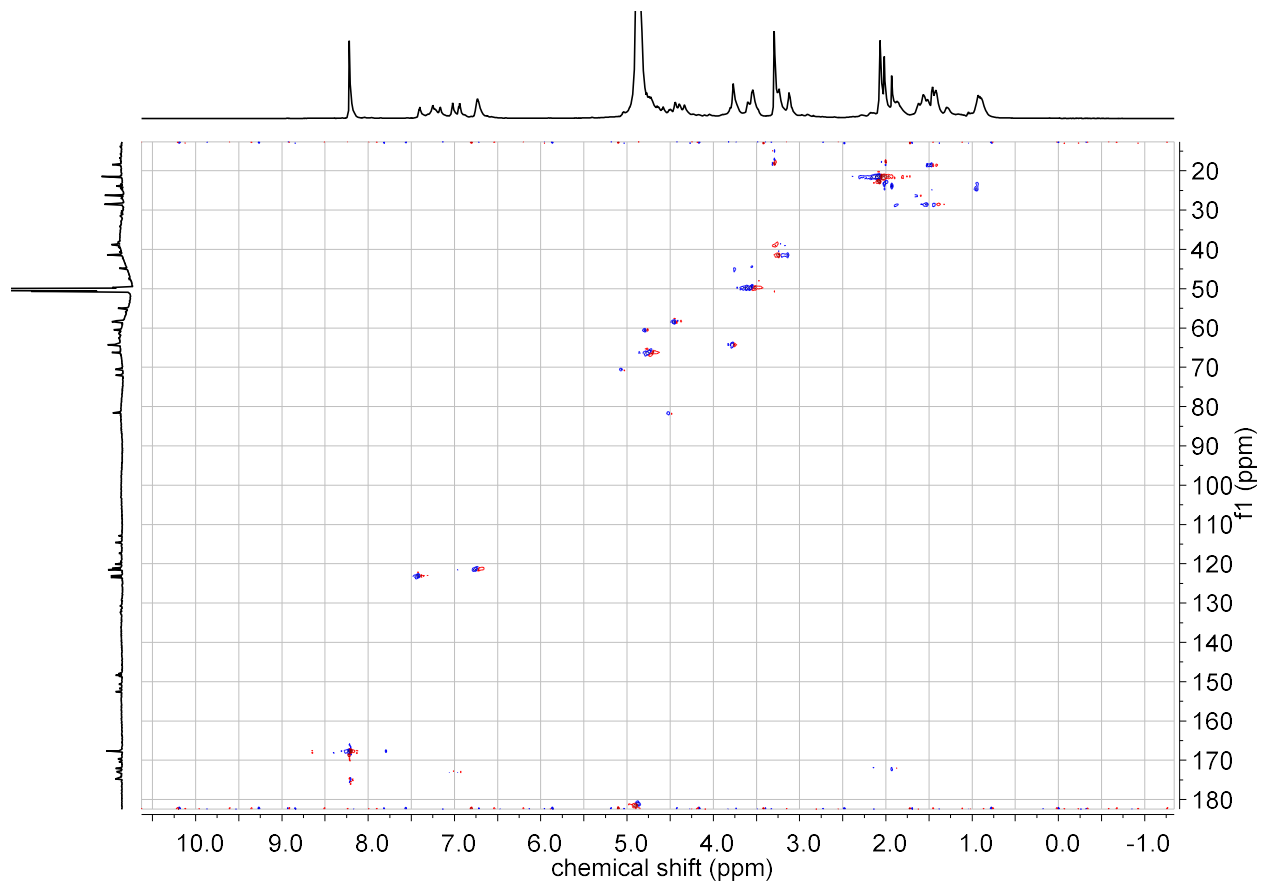


**Figure 4.9D:** HSQC-NMR ( $\text{CD}_3\text{OD}$ ) spectrum of purified Fimsbactin F purified by prep-HPLC from *A. baumannii* ATCC 17978.

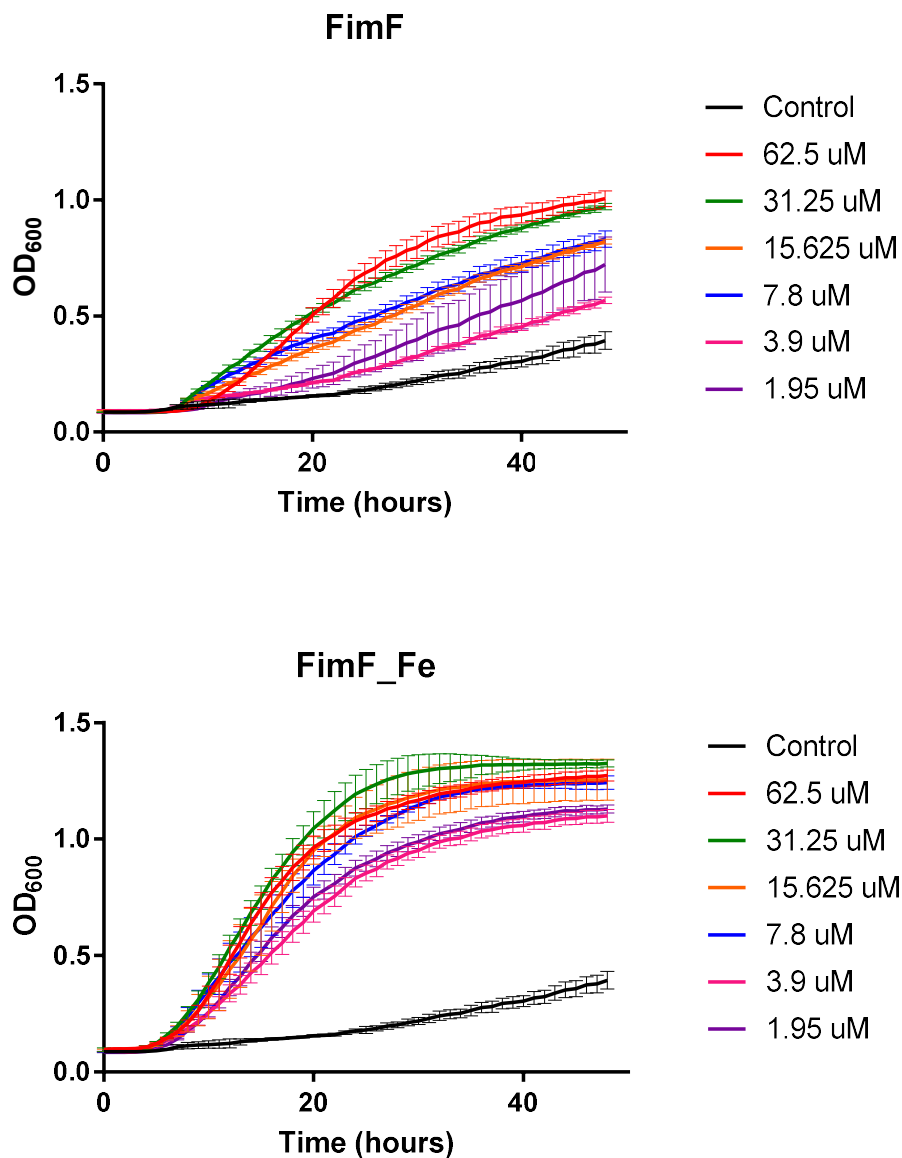


**Figure 4.10:** Dose dependent growth promotion of *A. baumannii* ATCC 17978 by *apo*-Fimsbactin F and *holo*-Fimsbactin F. Line graphs depict the growth of *A. baumannii* ATCC 17978 in M9 minimal media supplemented with 175  $\mu$ M 2,2'-dipyridyl (DIP) determined by measuring the optical density at 600 nm (OD<sub>600</sub>) as a function of time in the presence of variable siderophore concentrations. All experiments were performed in triplicate. Data from these plots were used to create the bar graphs in **Figure 4.11**.



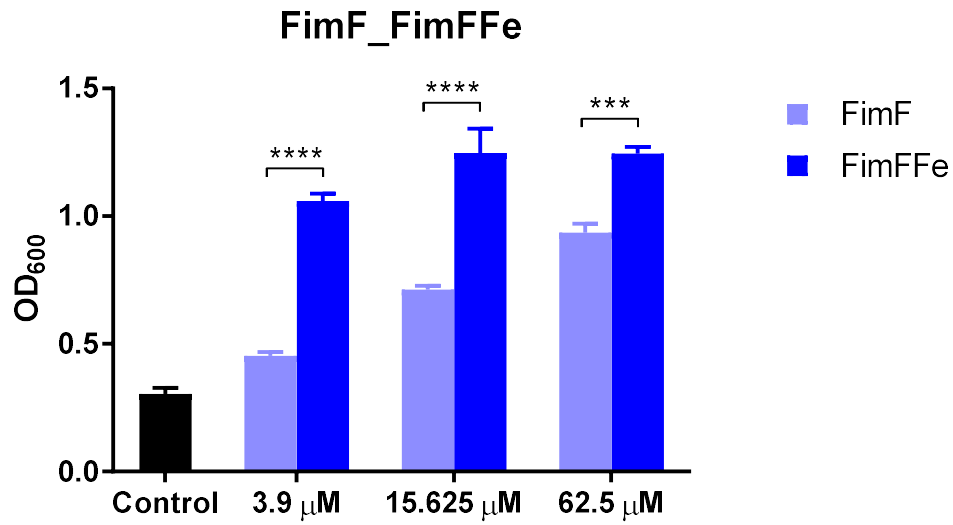


**Figure 4.11:** Influence of *apo*- and *holo*-siderophore on *A. baumannii* growth depicting the comparison of OD<sub>600</sub> values after 30 hours in the presence of variable concentrations of FimF and FimF<sub>2</sub>Fe. Error bars represent standard deviations from the mean for three independent trials.

\*\*\*\*p<0.0001, \*\*\*p<0.001.

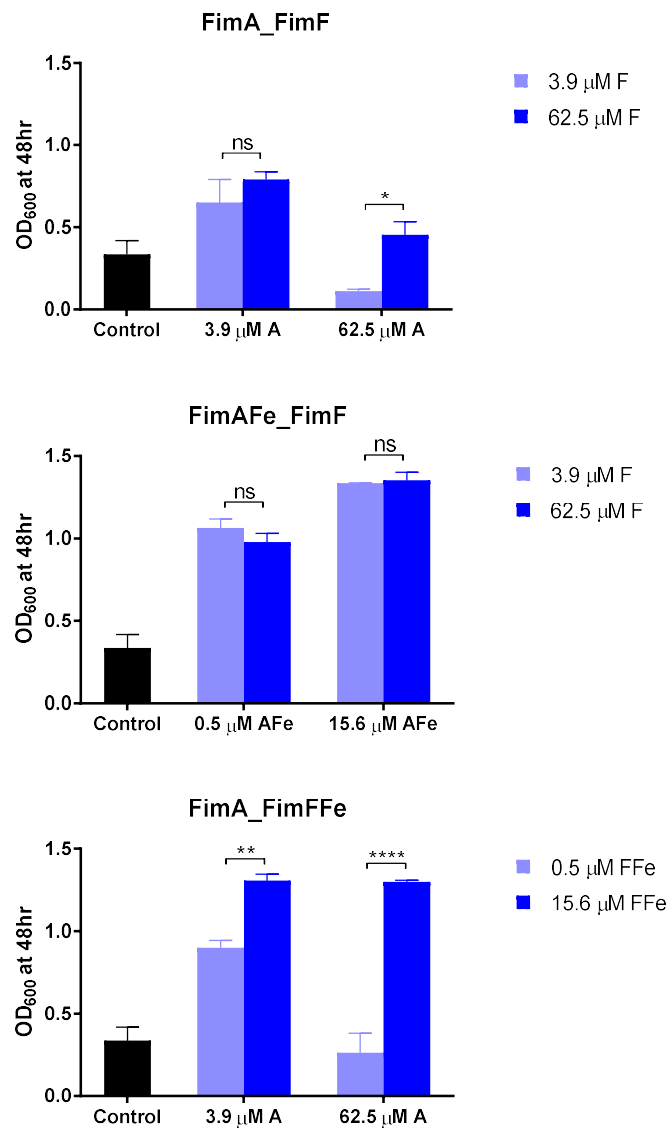
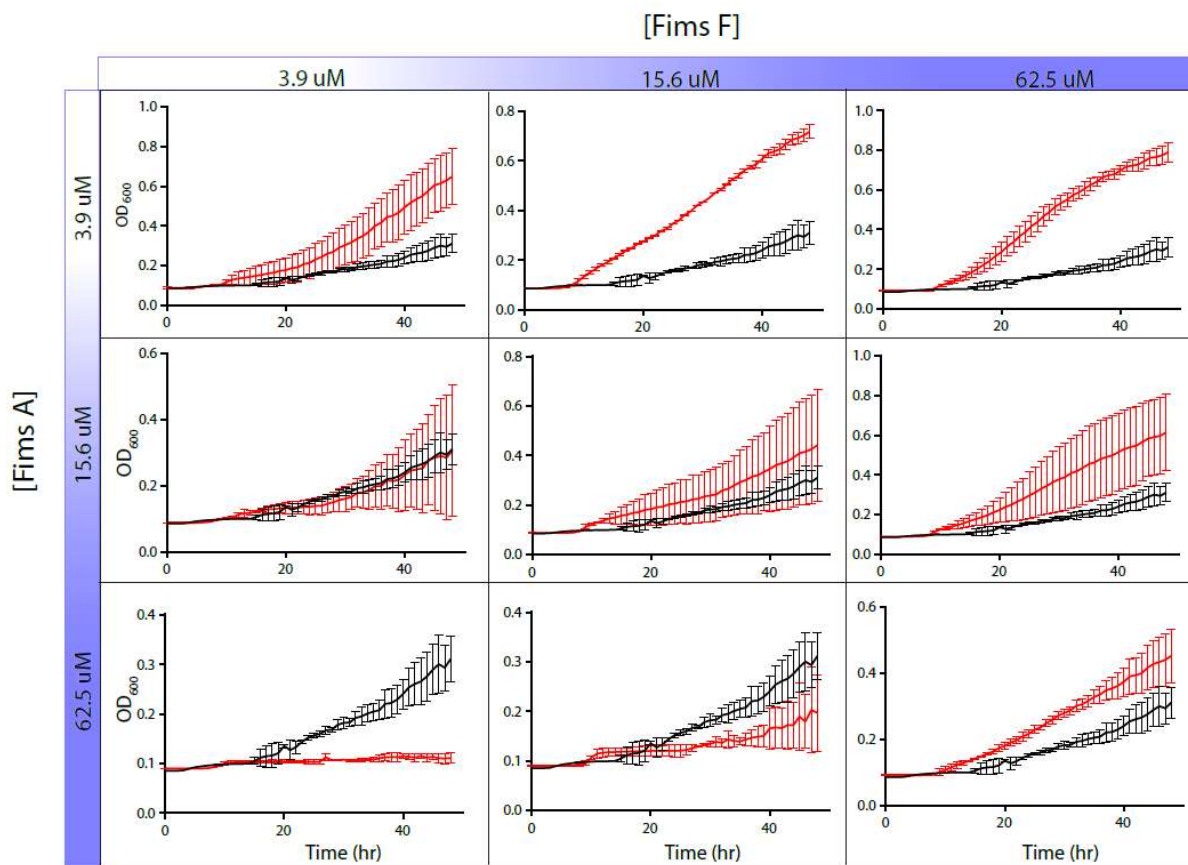
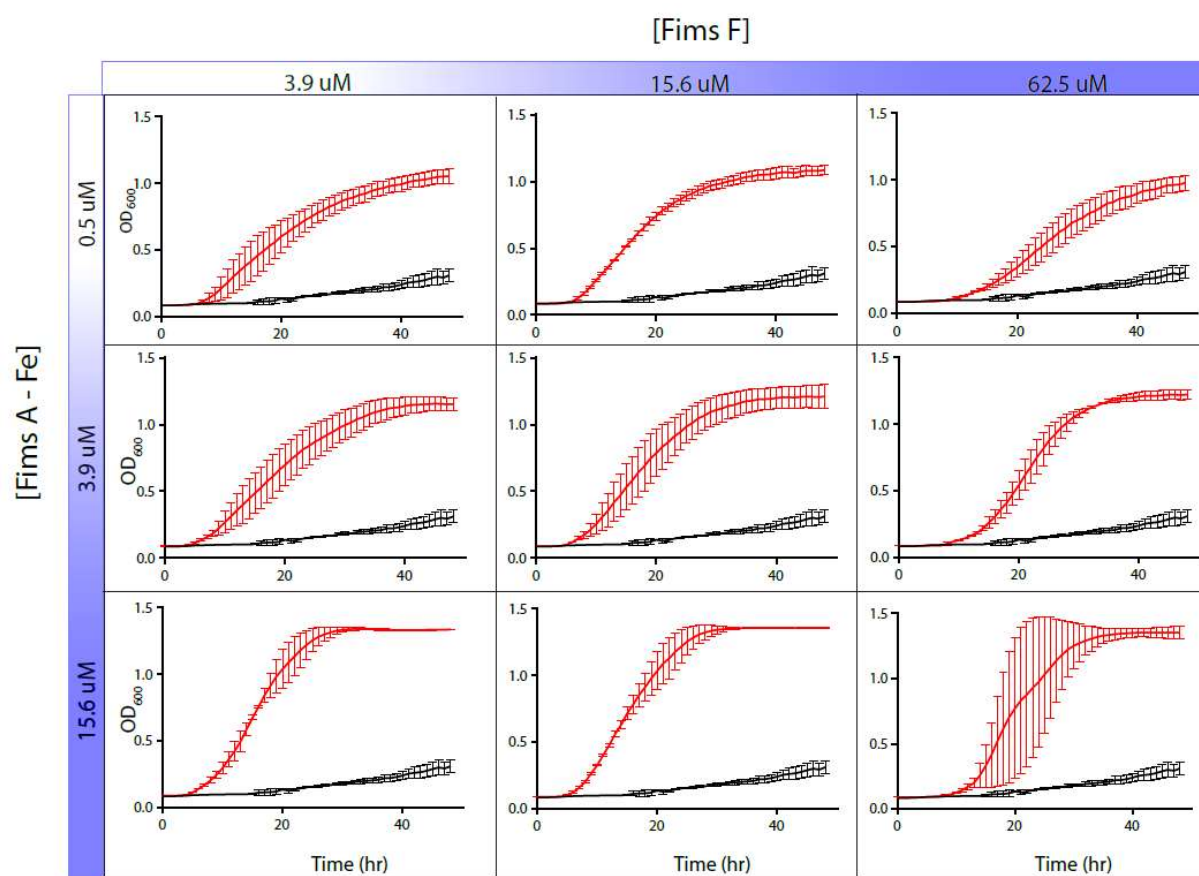


**Figure 4.12:** Influence of *apo*- and *holo*-siderophore combinations on *A. baumannii* growth. Bar graphs depict the comparison of *A. baumannii* ATCC 17978 growth measured by optical density at 600 nm ( $OD_{600}$ ) values after 30 hours in the presence of variable concentrations of (a) FimA and FimF, (b) FimAFe and FimF, and (c) FimA and FimF<sub>2</sub>Fe. Error bars represent standard deviations from the mean for two independent trials. \*\*\*\* $p < 0.0001$ ; \*\* $p < 0.01$ ; \* $p < 0.1$ ; ns = not significant. **Figure 4.13** shows full growth curve data.

A. Fimsbactin F + Fimsbactin A



B. Fimsbactin F + Fimsbactin A-Fe



### C. Fimsbactin F-Fe + Fimsbactin A

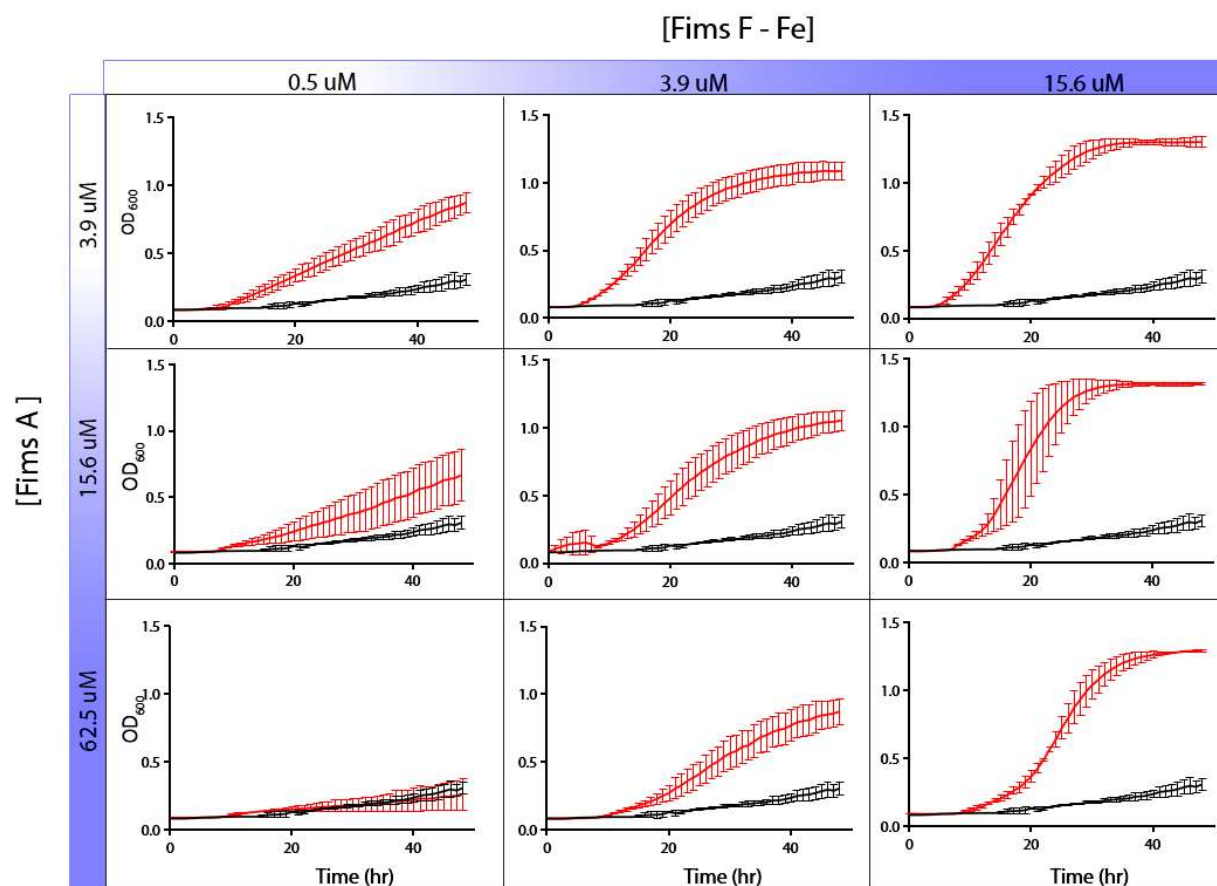


**Figure 4.13:** Influence of *apo*- and *holo*-siderophore combinations on the growth of *A. baumannii* ATCC 17978. Line graphs depict the growth of *A. baumannii* ATCC 17978 in M9 minimal media supplemented with 175 μM 2,2'-dipyridyl (DIP) determined by measuring the optical density at 600 nm (OD<sub>600</sub>) as a function of time in the presence of variable concentrations of siderophore mixtures. For all graphs, siderophore concentration gradients are provide on the x-axis and y-axis of the checkerboard. The black line graph represents bacterial growth without addition of siderophores. The red line graph represents bacterial growth in the presence of variable concentrations of (A) *apo*-FimA and *apo*-FimF, (B) *holo*-FimAFe and *apo*-FimF, or (C) *apo*-FimA and *holo*-FimF<sub>2</sub>Fe. Error bars represent standard deviations from the mean for two independent trials. Data from these plots were used to create bar graphs shown in **Figure 4.12**

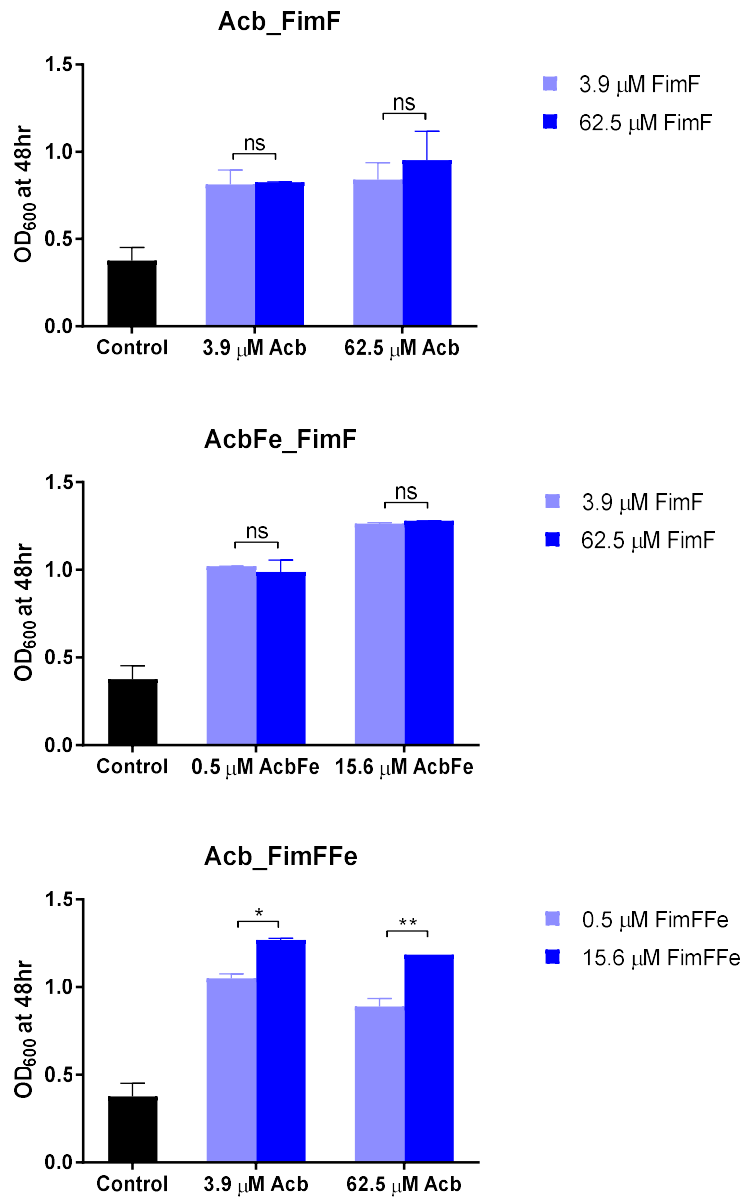
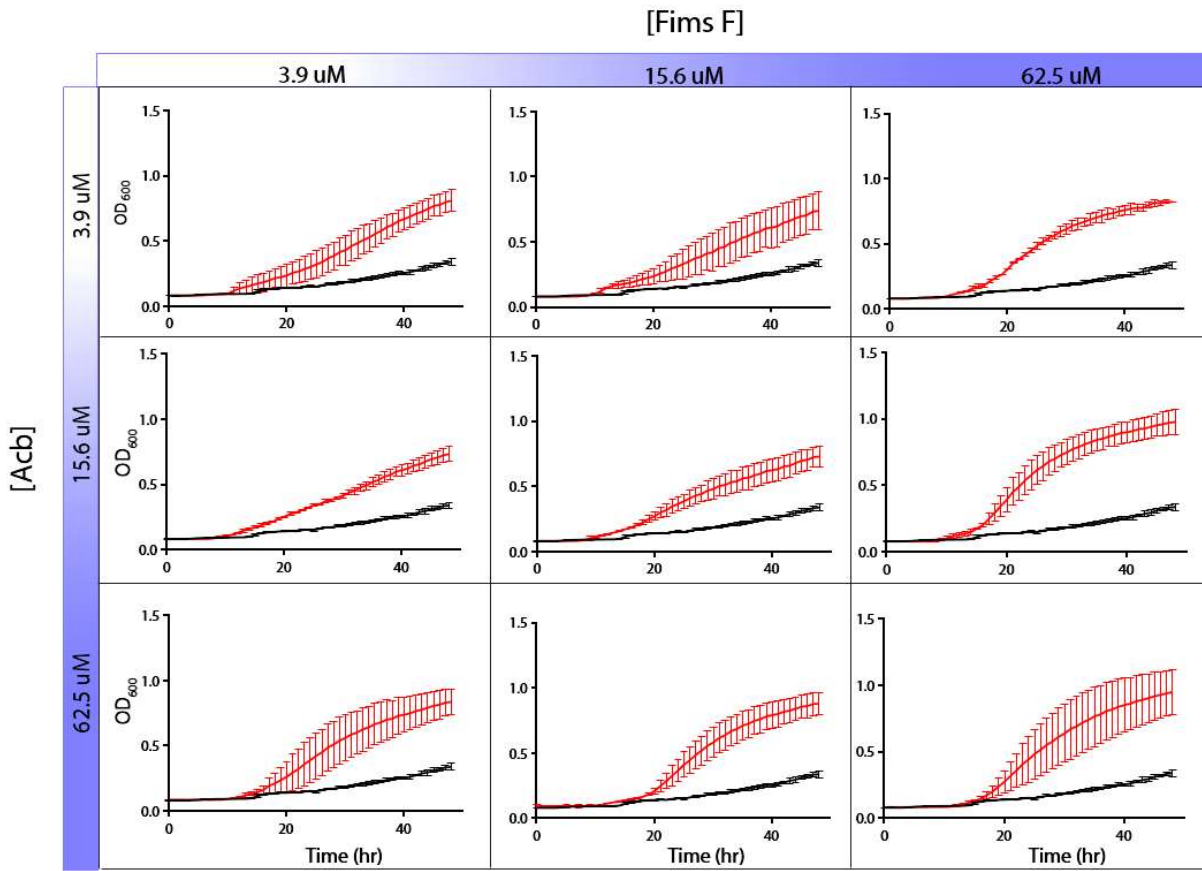
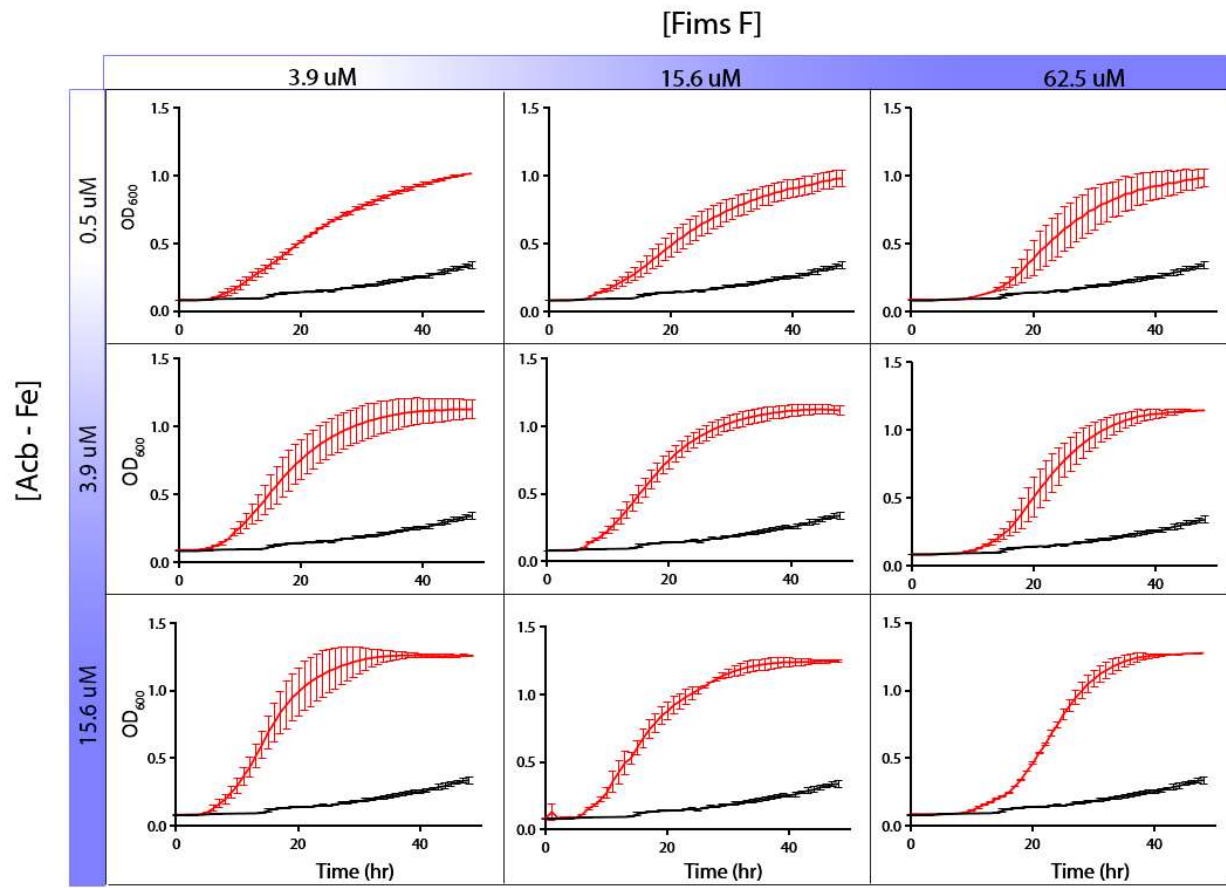


**Figure 4.14:** Influence of *apo*- and *holo*-siderophore combinations on *A. baumannii* growth. Bar graphs depict the comparison of *A. baumannii* ATCC 17978 growth measured by optical density at 600 nm ( $OD_{600}$ ) values after 30 hours in the presence of variable concentrations of (a) Acb and FimF, (b) Acb<sub>2</sub>Fe and FimF, and (c) Acb and FimF<sub>2</sub>Fe. Error bars represent standard deviations from the mean for two independent trials. \*\* $p < 0.01$ ; \* $p < 0.1$ ; ns = not significant. **Figure 4.15** shows full growth curve data.

A. Fimsbactin F + Acb



B. Fimsbactin F + Acb-Fe





### C. Fimsbactin F-Fe + Acb

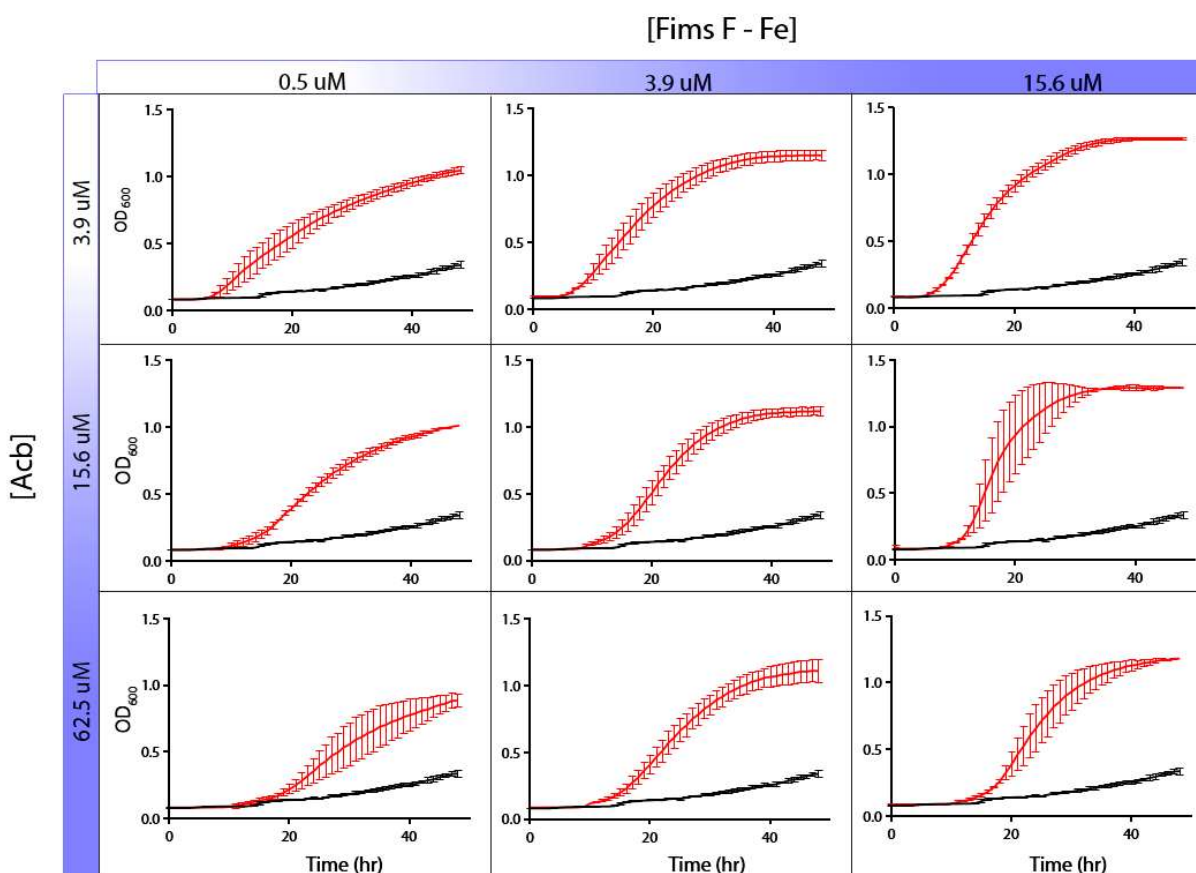
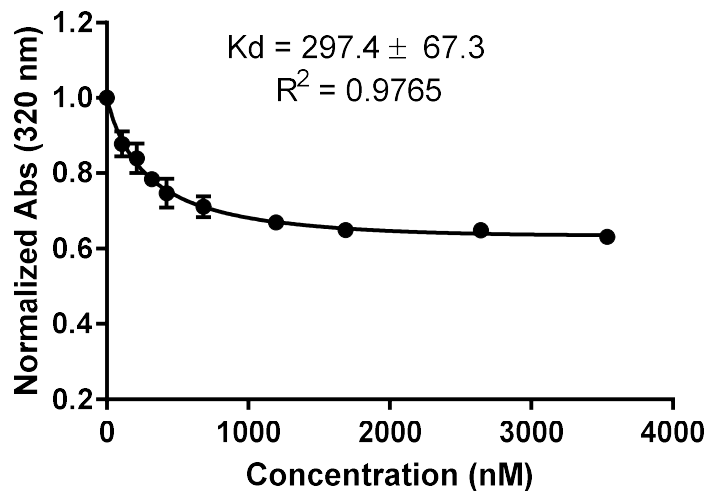


**Figure 4.15:** Influence of *apo*- and *holo*-siderophore combinations on the growth of *A. baumannii* ATCC 17978. Line graphs depict the growth of *A. baumannii* ATCC 17978 in M9 minimal media supplemented with 175  $\mu$ M 2,2'-dipyridyl (DIP) determined by measuring the optical density at 600 nm ( $OD_{600}$ ) as a function of time in the presence of variable concentrations of siderophore mixtures. For all graphs, siderophore concentration gradients are provide on the x-axis and y-axis of the checkerboard. The black line graph represents bacterial growth without addition of siderophores. The red line graph represents bacterial growth in the presence of variable concentrations of (A) *apo*-Acb and *apo*-FimF, (B) *holo*-Acb<sub>2</sub>Fe and *apo*-FimF, or (C) *apo*-Acb and *holo*-FimF<sub>2</sub>Fe. Error bars represent standard deviations from the mean for two independent trials. Data from these plots were used to create bar graphs shown in **Figure 4.14**

### Fluorescence Quenching of BauB by FimF



### Fluorescence Quenching of BauB by FimF - Fe

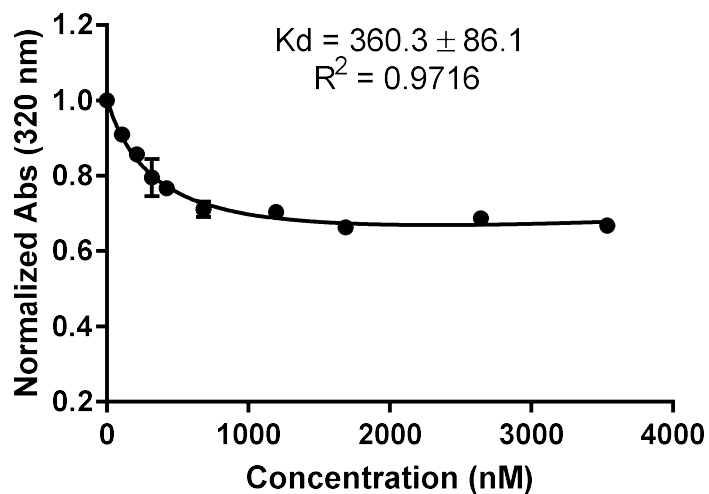


**Figure 4.16:** Siderophore-dependent fluorescence quenching of *N*-His<sub>6</sub>-BauB. Graphs depict intrinsic tryptophan fluorescence quenching (y-axis:  $\lambda_{\text{excitation}} = 280 \text{ nm}$ ;  $\lambda_{\text{emission}} = 340 \text{ nm}$ ) of 400 nm *N*-His<sub>6</sub>-BauB in the presence of variable siderophore concentrations (x-axis). Apparent  $K_d$  values were calculated using a single-binding mode curve-fitting model in GraphPad Prism version 7.0b. Error bars represent standard deviations for two independent trials.

Compound	BauB Binding	LogK <sub>Fe</sub>	Fe Binding
	Affinity (apo/holo)		Ratio
<b>FimA</b> <sup>5</sup>	354.8 ± 139.3/	27.1 ± 0.2	1:1
	244.4 ± 93.3		
<b>PreAcb</b> <sup>9,10,14</sup>	382.8 ± 106.1/	27.4 ± 0.2	2:1
	754.4 ± 155.4		
<b>Acb</b> <sup>9,10,14</sup>	302.5 ± 105.1/	26.2 ± 0.1	2:1
	162.3 ± 81.4		
<b>FimF</b>	297.4 ± 67.3/	25.9 ± 0.1	2:1
	360.3 ± 86.1		

**Table 4.1.** Comparison of *A. baumannii* siderophore periplasmic siderophore binding protein, BauB, iron affinity and iron stoichiometry.

### UV-Vis Spectra Fimsbactin F

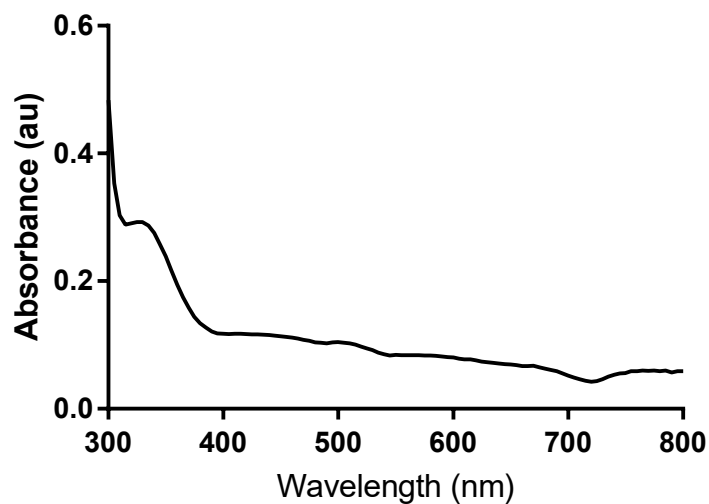


**Figure 4.17:** Optical absorbance spectrum of the *holo*-FimF<sub>2</sub>Fe complex at 100  $\mu$ M in phosphate buffer (50 mM potassium phosphate at pH 8.0, 150 mM NaCl, 1 mM DTT, 5% glycerol).

### Titration of Fimsbactin F with Fe (III) - Normalize Abs

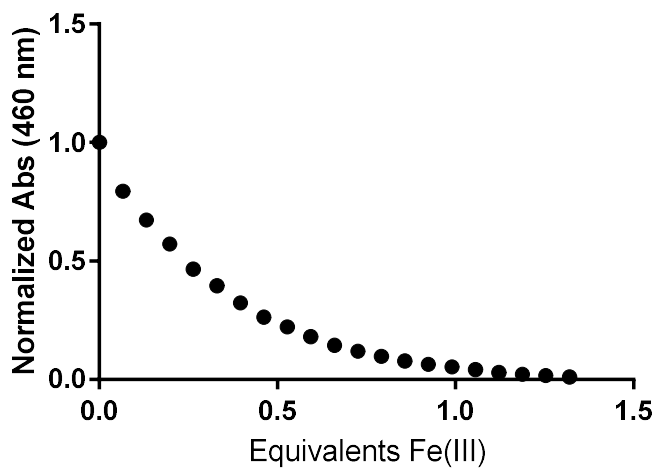


**Figure 4.18:** Fimsbactin F forms a 2:1 complex with Fe(III). Graph depicts fluorescence ( $\lambda_{\text{excitation}} = 330$  nm;  $\lambda_{\text{emission}} = 380$  nm) vs equivalents of Fe(acac)<sub>3</sub> showing a titration end point correlating with 2:1 stoichiometry.

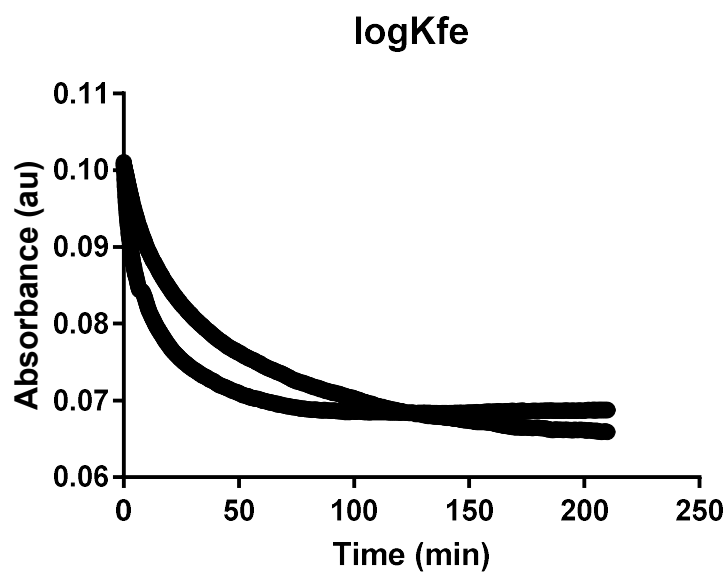
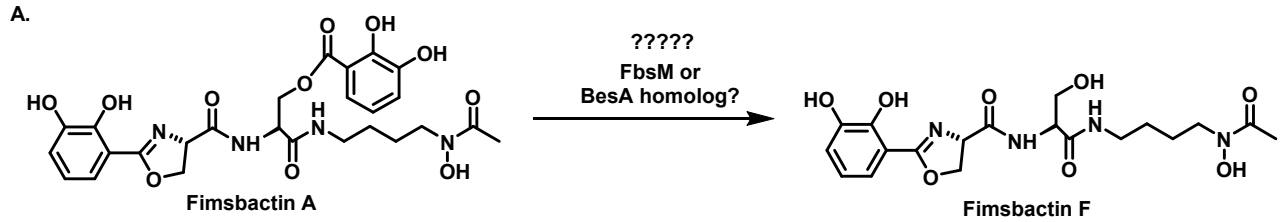


**Figure 4.19:** Absorbance over time of FimF in 10 mM HEPES following addition of EDTA. Data from this figure was used to calculate the apparent  $K_{Fe}$  of FimsF



B.

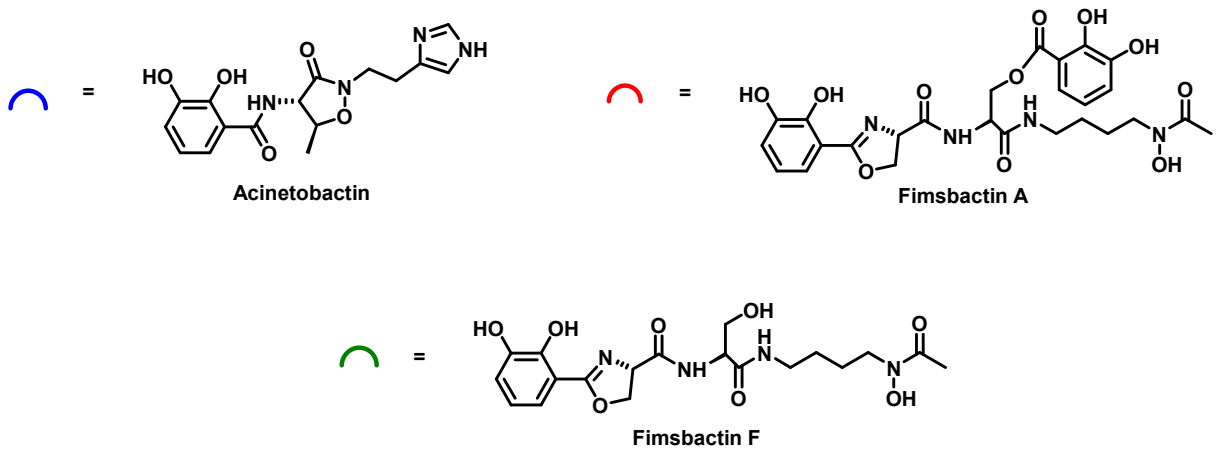
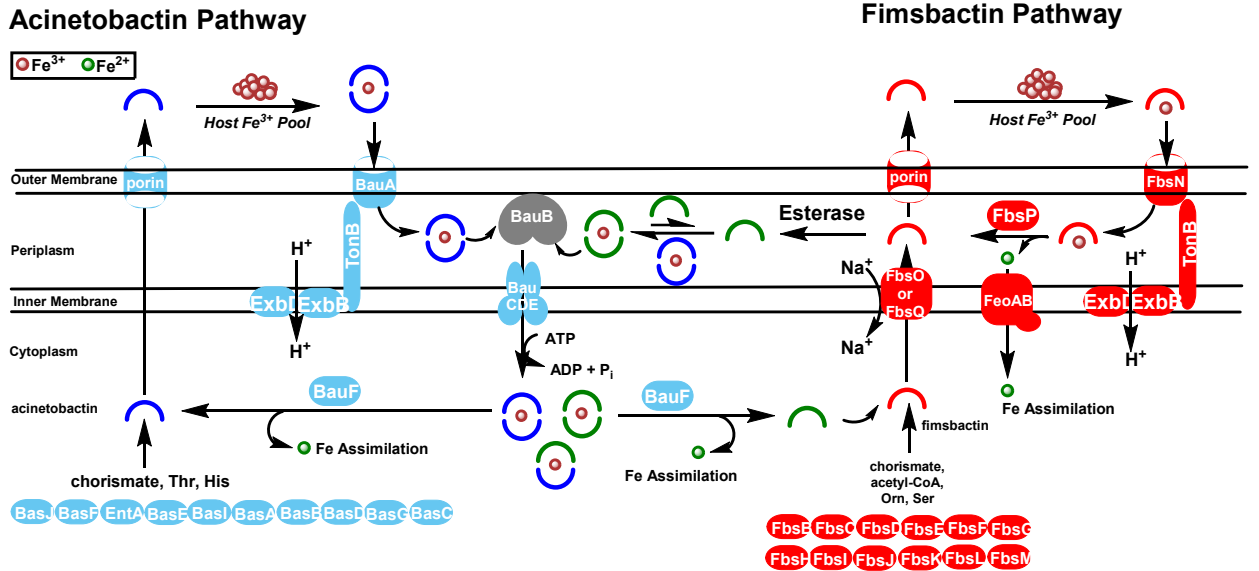


**Figure 4.20:** Hypothesized potential relationship between FimA and FimF. We hypothesize Fimsbactin can compete with some acinetobactin transport proteins, as we already demonstrated a competition for siderophore binding protein, BauB.

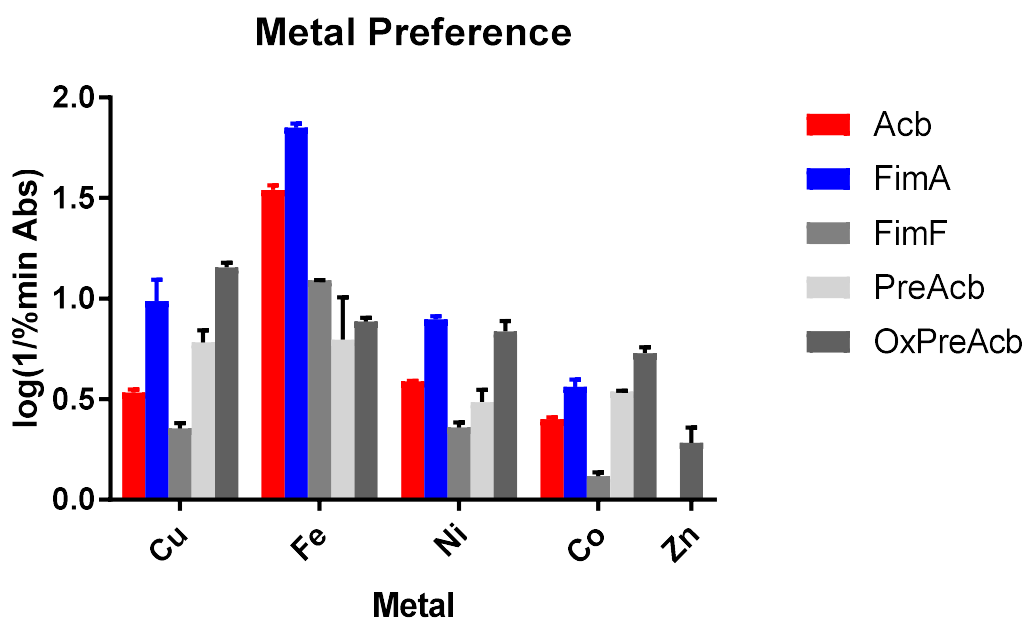
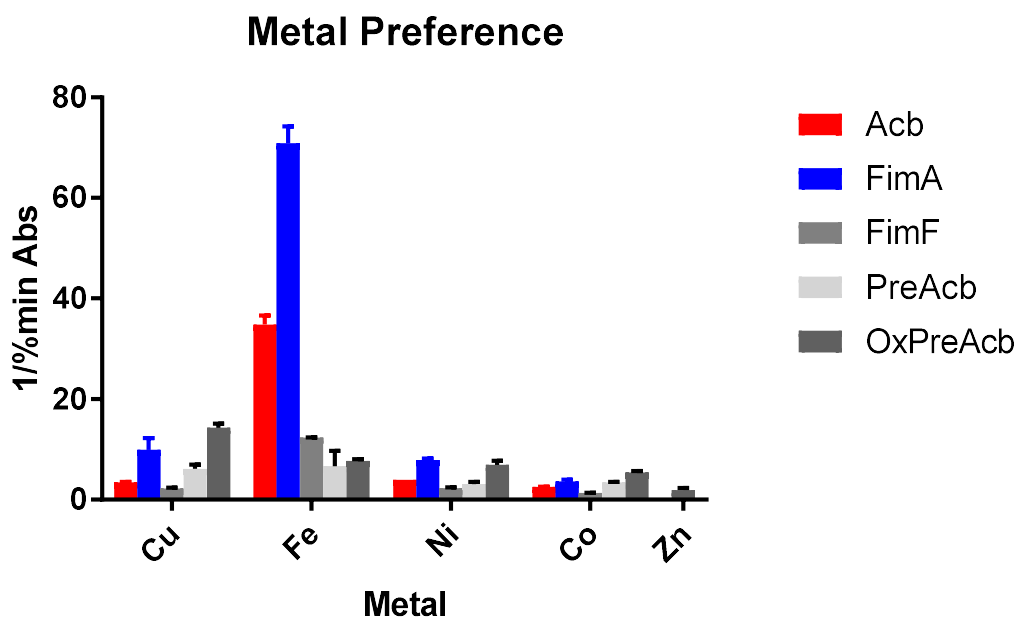


**Figure 4.21:** Metal titration studies with Copper, iron, nickel, cobalt and zinc chloride with Acb, PreAcb, FimA, FimF and OxPreAcb. Top graph x-axis:  $1/[(\text{min abs at } 460 \text{ nm} / \text{starting abs at } 460 \text{ nm}) \times 100]$ . Bottom graph x-axis:  $\log(1/[(\text{min abs at } 460 \text{ nm} / \text{starting abs at } 460 \text{ nm}) \times 100])$ .

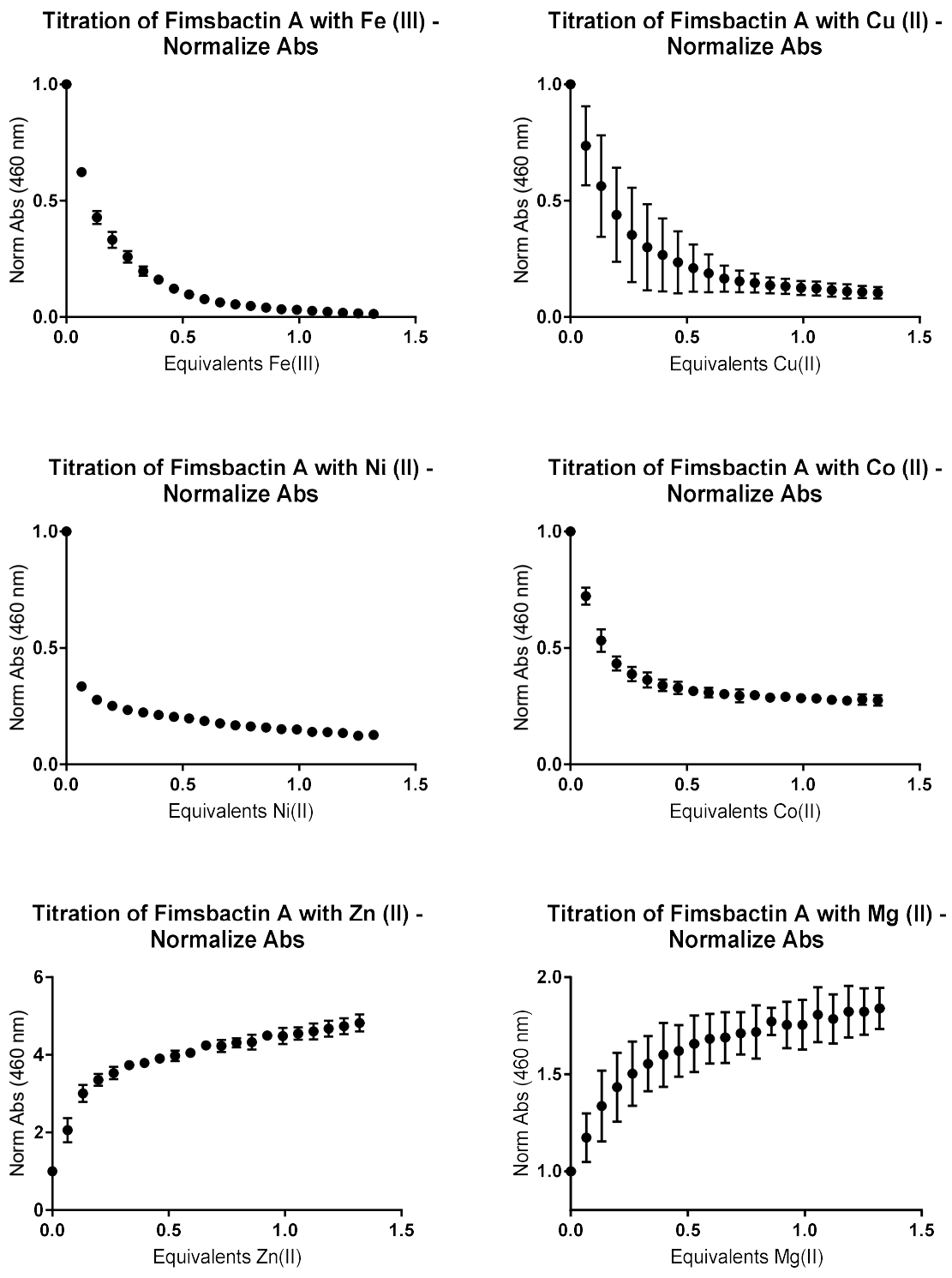


**Figure 4.22:** Metal titration curves for Fima



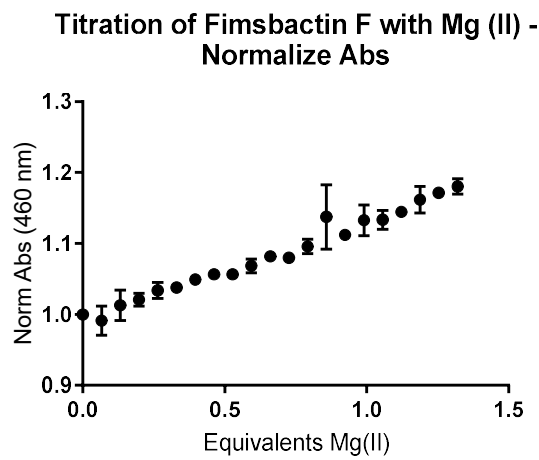
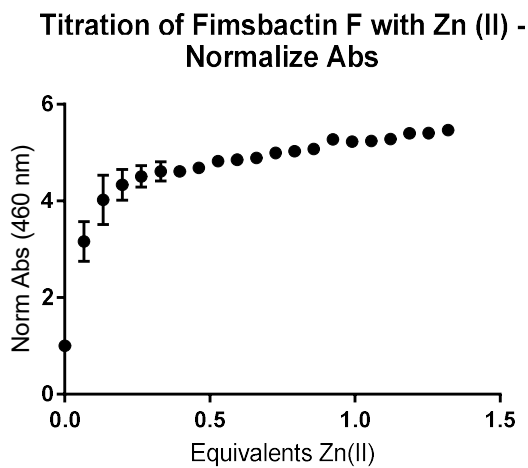
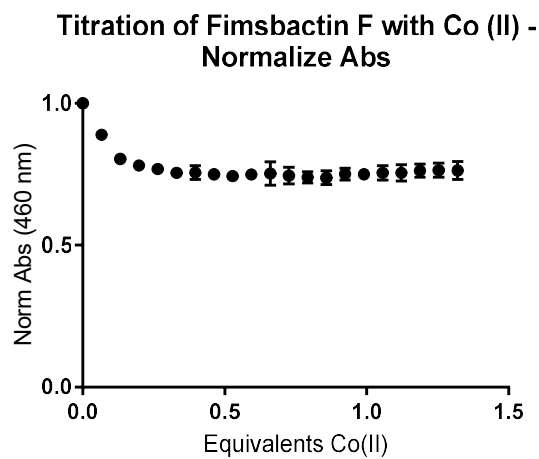
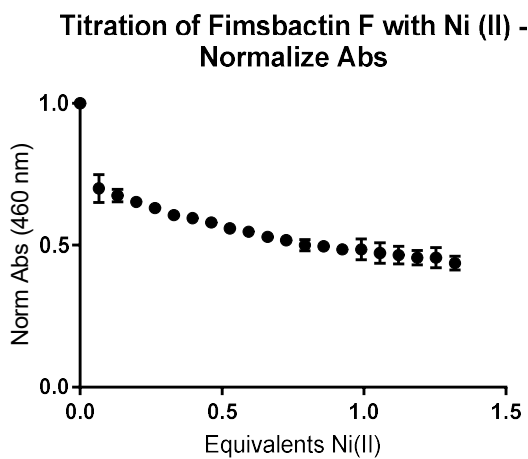
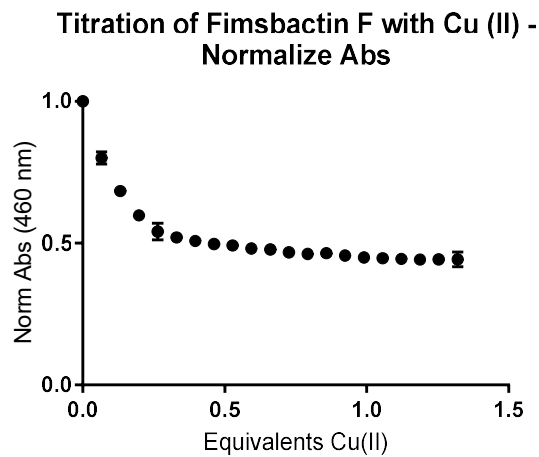
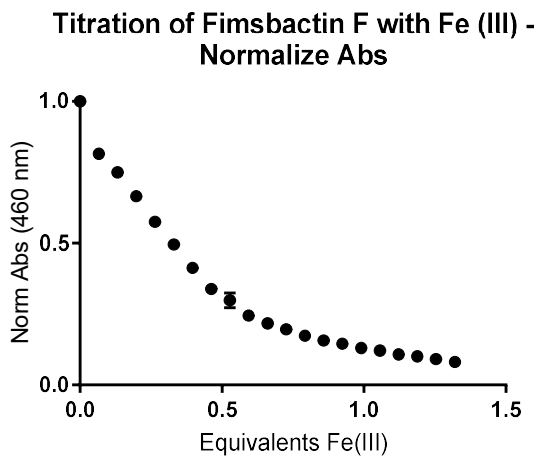


**Figure 4.23:** Metal titration curves for FimF

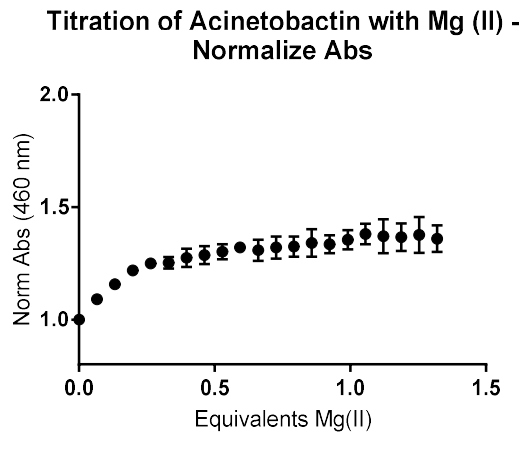
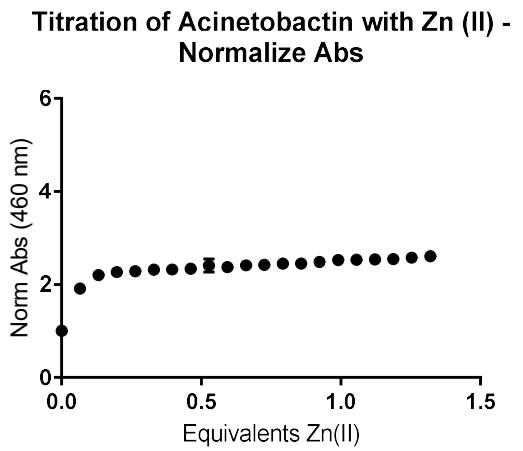
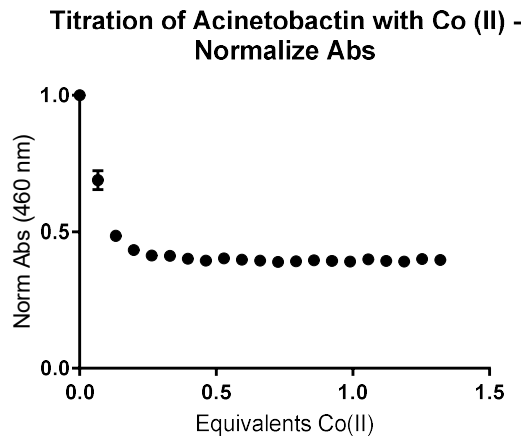
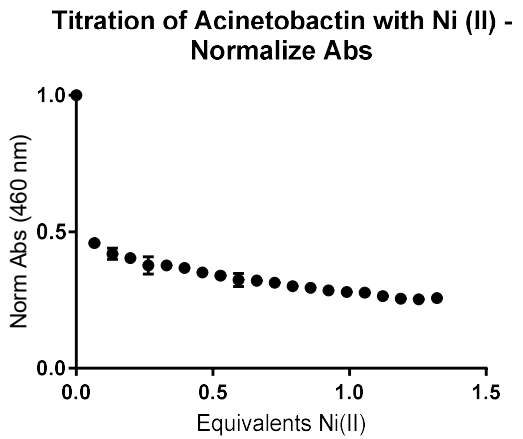
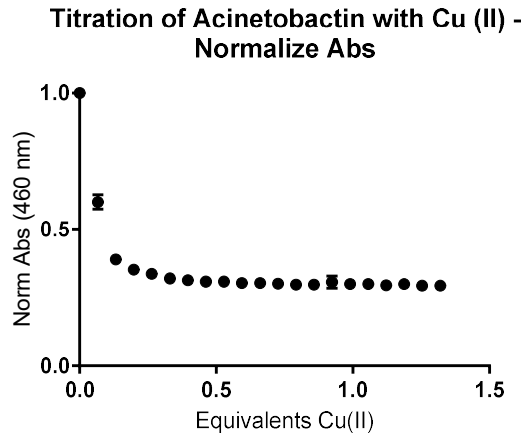
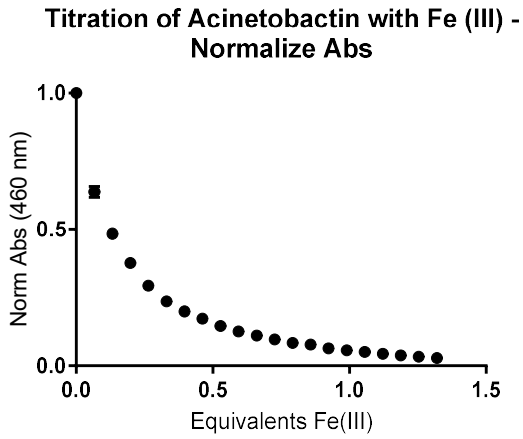


**Figure 4.24:** Metal titration curves for Acb

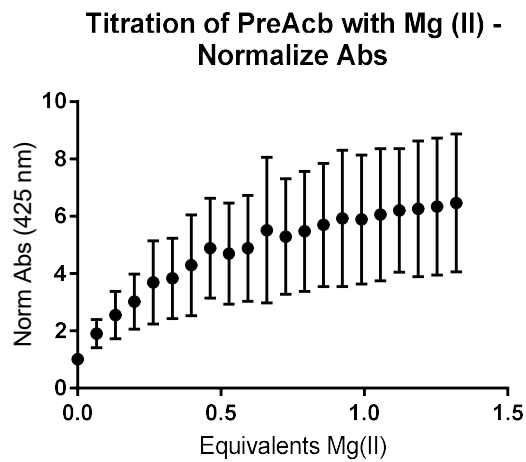
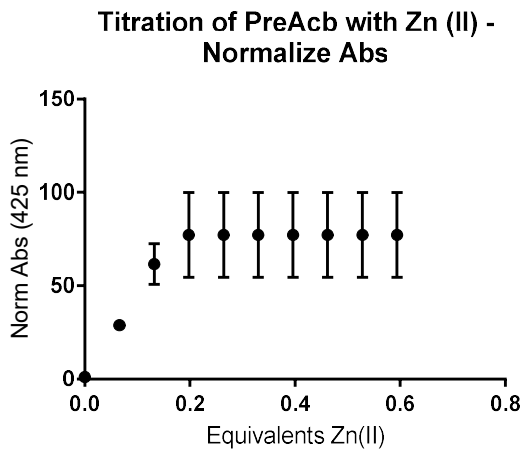
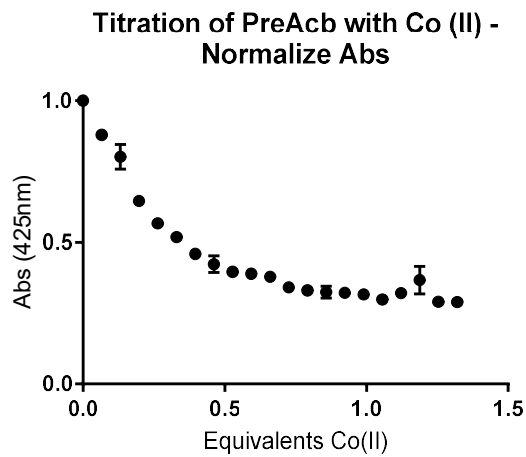
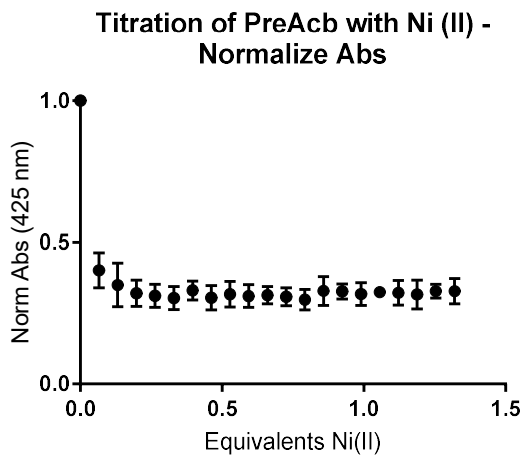
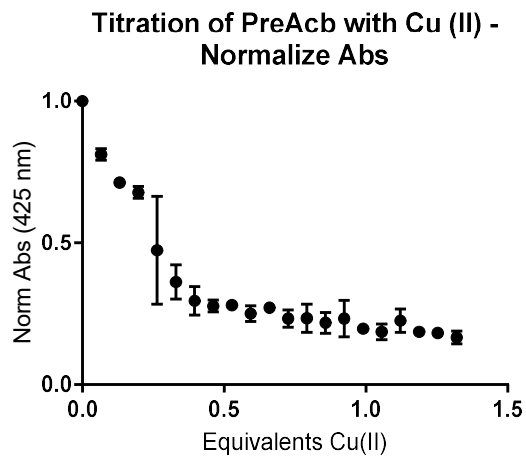
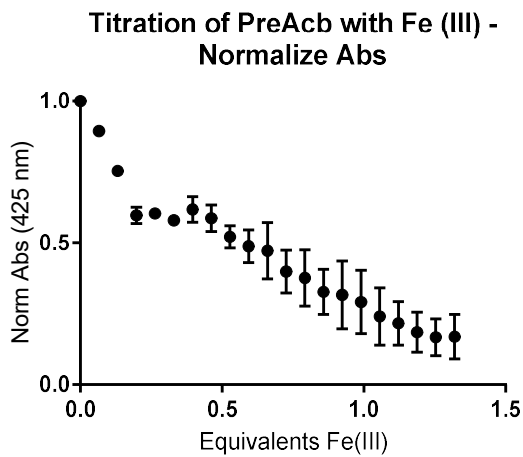
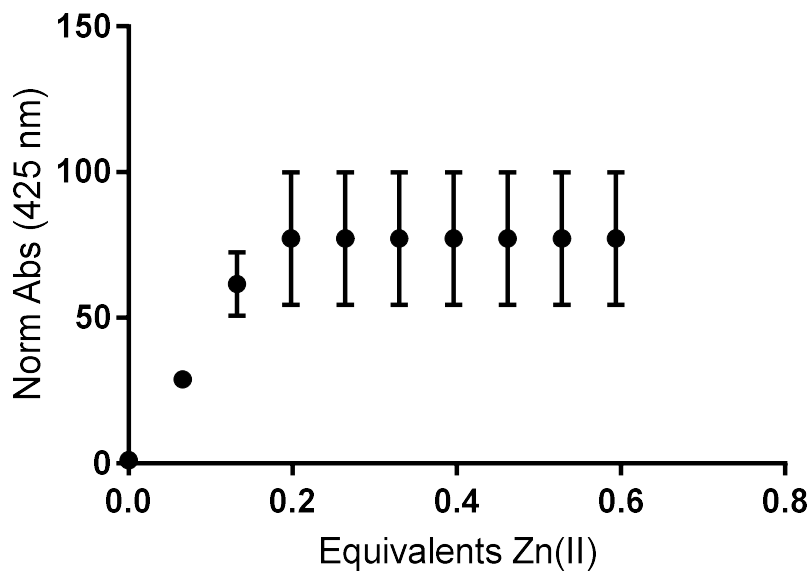


**Figure 4.25:** Metal titration curves for PreAcb

### Titration of PreAcb with Zn (II) - Normalize Abs



### PreAcb ZnCl<sub>2</sub> dilute

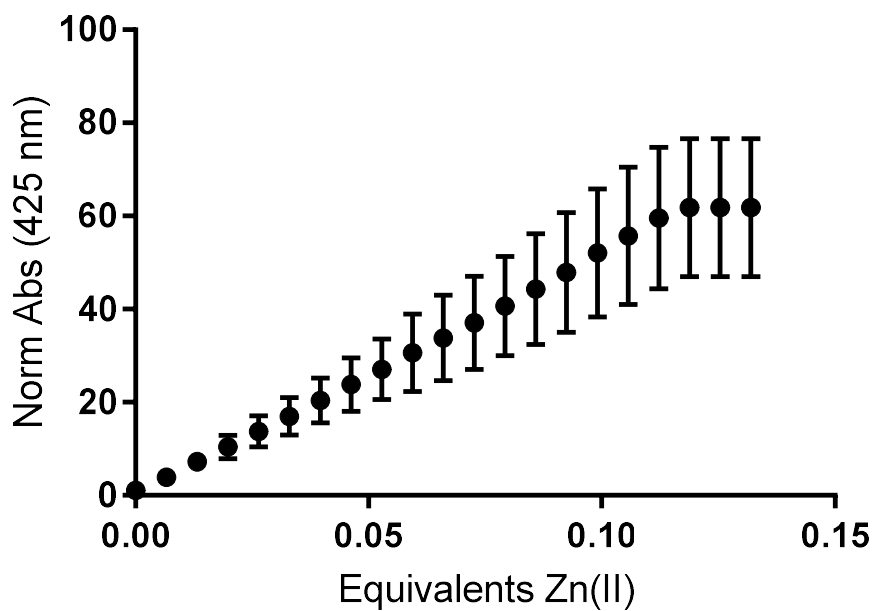


**Figure 4.26:** Metal titration curve for PreAcb titrated with Zn, maxed out the detector at less than 0.2 equivalents.

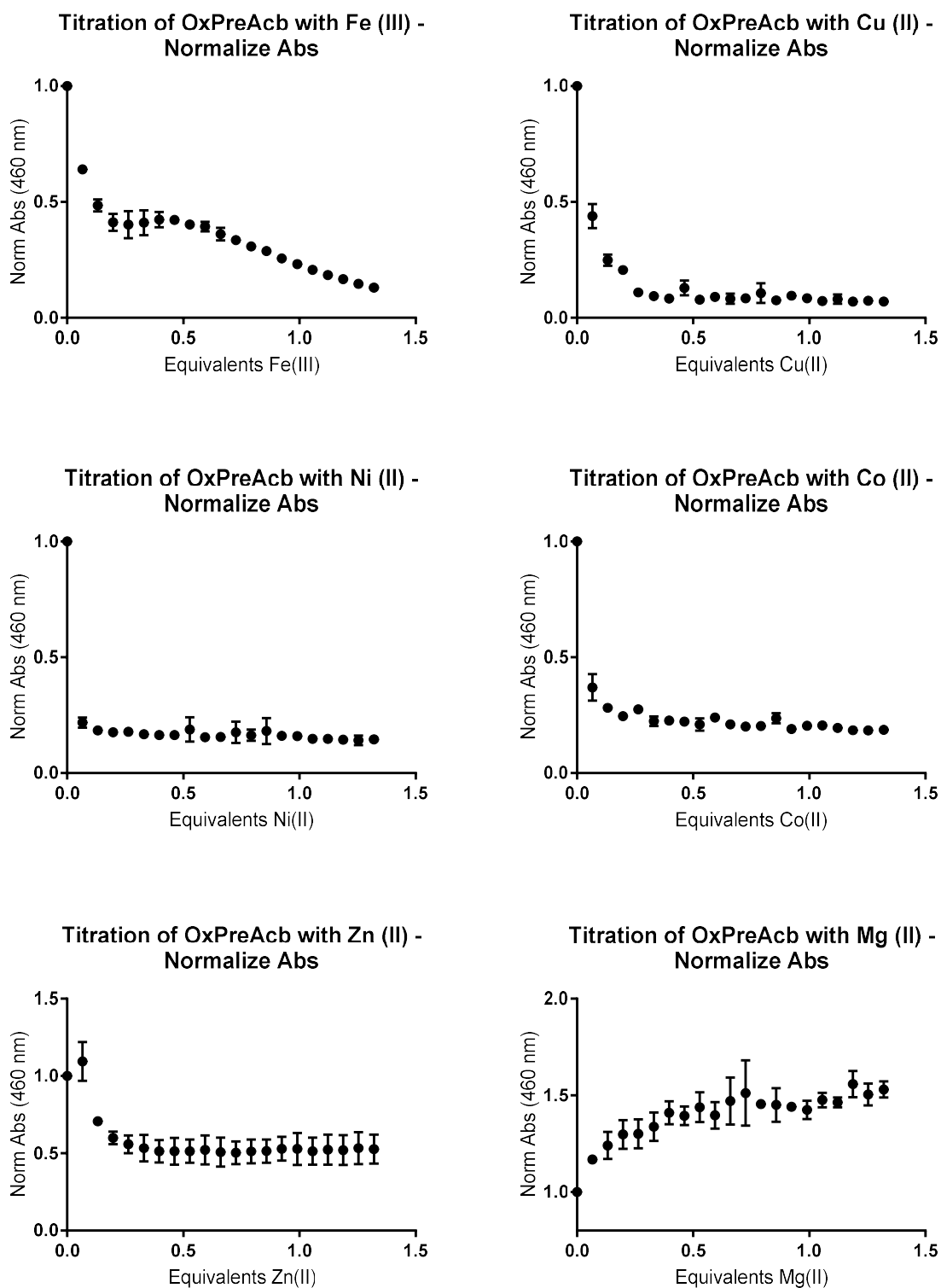


**Figure 4.27:** Metal titration curves for OxPreAcb

## Equations 4.1

As described in the experimental methods section of the main text, an EDTA competition experiment was used to measure the apparent  $K_{Fe}$  for  $FimF_2Fe$  at pH 7.4. The following equations were used to calculate apparent  $K_{Fe}$  based on the change in optical absorbance observed at 500 nm for  $FimF_2Fe$  in the presence of 1.2 equivalents of EDTA. A  $K_{Fe}$  value of  $10^{25.1}$  was used for EDTA at pH 7.4 in final calculations.<sup>15</sup>

$$(1) \quad K_L = \frac{[FeL]}{[Fe^{3+}][2L]} \quad \text{for the following equilibrium;} \quad [Fe^{3+}] + [2L] \rightleftharpoons [FeL_2]$$

$$(2) \quad K_{FeEDTA} = \frac{[FeEDTA]}{[Fe^{3+}][EDTA]} \quad \text{for the following equilibrium;} \quad [Fe^{3+}] + [EDTA] \rightleftharpoons [FeEDTA]$$

$$(3) \quad K_{Exchange} = \frac{K_L}{K_{FeEDTA}} \quad \text{for the following equilibrium;} \quad [FeEDTA] + [2L] \rightleftharpoons [FeL_2] + [EDTA]$$

$$(4) \quad K_{Exchange} = \frac{[FeL_2][EDTA]}{[FeEDTA][2L]}$$

$$(5) \quad \Delta = \frac{Abs_{FeL} - Abs_{FeL+EDTA}}{\epsilon_L}$$

$$(6) \quad K_L = K_{FeEDTA} \times \frac{[FeL][EDTA]}{[FeEDTA][2L]}$$

$$(7) \quad [FeL_2] = \frac{Abs_{FeL}}{\epsilon_L}$$

$$(8) \quad [EDTA] = [EDTA]_T - \Delta \quad \text{where} \quad [EDTA]_T = \text{total EDTA added}$$

$$(9) \quad [FeEDTA] = \Delta$$

$$(10) \quad [2L] = \Delta$$

$$(11) \quad K_{Fe} = \text{apparent } K_L$$

## 4.8 References

- [1] McRose, D. L., Seyedsayamdost, M.R., and Morel, F.M.M. (2018) Multiple siderophores: bug or feature?, *Journal of Biological Inorganic Chemistry*. 23:983-993.
- [2] Ratledge, C., Ewing, M. (1996) The occurrence of carboxymycobactin, the siderophore of pathogenic mycobacteria, as a second extracellular siderophore in *Mycobacterium smegmatis*, *Microbiology*. 142, 2207-2212.
- [3] Gobin, J., Horwitz, M.A. (1996) Exochelins of *Mycobacterium tuberculosis* remove iron from human iron-binding proteins and donate iron to mycobactins in the *M. tuberculosis* cell wall, *Journal of Experimental Medicine*. 183 (4): 1527.
- [4] Proschak, A., Lubuta, P., Grun, P., Lohr, F., Wilharm, G., De Berardinis, V., and Bode, H. B. (2013) Structure and biosynthesis of fimsbactins A-F, siderophores from *Acinetobacter baumannii* and *Acinetobacter baylyi*, *Chembiochem* 14, 633-638.
- [5] Bohac, T.J., Fang, L., Giblin, D.E., and Wencewicz, T.A. (2019). Fimsbactin and Acinetobactin compete for the periplasmic siderophore binding protein BauB in Pathogenic *Acinetobacter baumannii*. *ACS Chemical Biology*. Manuscript accepted DOI: 10.1021/acscchembio.8b01051.
- [6] Wencewicz, T. A., and Miller, M. J. (2013) Biscatecholate-monohydroxamate mixed ligand siderophore-carbacephalosporin conjugates are selective sideromycin antibiotics that target *Acinetobacter baumannii*, *Journal of medicinal chemistry* 56, 4044-4052.
- [7] Mlethke, M., Klotz, O., Linne, U., May, J.J., Becjering, C.L., and Marahiel, M. (2006) Ferri-bacillibactin uptake and hydrolysis in *Bacillus subtilis*, *Molecular Microbiology* 61(6), 1413-1427.

- [8] Hofte, M., Buysens, S., Koedam, N., and Cornelis, P. (1993) Zinc affects siderophore-mediated high affinity iron uptake systems in the rhizosphere *Pseudomonas aeruginosa* 7NSK2, *BioMetals* 6, 85-91.
- [9] Shapiro, J. A., and Wencewicz, T. A. (2016) Acinetobactin Isomerization Enables Adaptive Iron Acquisition in *Acinetobacter baumannii* through pH-Triggered Siderophore Swapping, *ACS infectious diseases* 2, 157-168.
- [10] Shapiro, J. A., and Wencewicz, T. A. (2017) Structure-function studies of acinetobactin analogs, *Metallomics* 9, 463-470.
- [11] Bohac, T. J., Shapiro, J. A., and Wencewicz, T. A. (2017) Rigid Oxazole Acinetobactin Analog Blocks Siderophore Cycling in *Acinetobacter baumannii*, *ACS infectious diseases* 3, 802-806.
- [12] Yamamoto, S., Okujo, N., and Sakakibara, Y. (1994) Isolation and structure elucidation of acinetobactin, a novel siderophore from *Acinetobacter baumannii*, *Archives of microbiology* 162, 249-254.
- [13] Smith, M. G., Gianoulis, T. A., Pukatzki, S., Mekalanos, J. J., Ornston, L. N., Gerstein, M., and Snyder, M. (2007) New insights into *Acinetobacter baumannii* pathogenesis revealed by high-density pyrosequencing and transposon mutagenesis, *Genes & Development* 21, 601-614.
- [14] Bailey, D. C., Bohac, T. J., Shapiro, J. A., Giblin, D. E., Wencewicz, T. A., and Gulick, A. M. (2018) Crystal Structure of the Siderophore Binding Protein BauB Bound to an Unusual 2:1 Complex Between Acinetobactin and Ferric Iron, *Biochemistry*.
- [15] Funahashi, T.; Tanabe, T.; Maki, J.; Miyamoto, K.; Tsujibo, H.; Yamamoto, S. "Identification and characterization of a cluster of genes involved in biosynthesis and transport of



acinetoferrin, a siderophore produced by *Acinetobacter haemolyticus* ATCC 17906.”  
*Microbiology* 2013, 159, 678–690.

**Chapter 5: Rigid Oxazole Acinetobactin**  
**Analog Blocks Siderophore Cycling in**  
***Acinetobacter baumannii***

## 5.1 Preface

This chapter was adapted in part with permission from [Bohac, T. J., Shapiro, J. A. & Wencewicz, T. A. ACS Infect. Dis.3, 802-806 (2017)] Copyright ©2017 American Chemical Society. All authors contributed to writing of the manuscript. TJB synthesized all compounds and performed Spartan computational work. JAS performed biological evaluation of compounds. TAW served as principal investigator and oversaw experimental design.

## 5.2 Abstract

The emergence of multi-drug resistant (MDR) Gram-negative bacterial pathogens has raised global concern. Non-traditional therapeutic strategies, including antivirulence approaches, are gaining traction as a means of applying less selective pressure for resistance *in vivo*. Here, we show that rigidifying the structure of the siderophore pre-acinetobactin from MDR *Acinetobacter baumannii* via oxidation of the phenolate-oxazoline moiety to a phenolate-oxazole results in a potent inhibitor of siderophore transport and imparts a bacteriostatic effect at low micromolar concentrations under infection-like conditions.

## 5.3 Introduction

As discussed in prior chapters, our laboratory seeks to understand the PreAcb pathway in great molecular detail.<sup>1</sup> The PreAcb pathway starts when the siderophore scaffold is assembled on an NRPS biosynthetic template.<sup>2</sup> After formation of the phenolate oxazoline moiety, the penultimate thioester is cleaved from the NRPS peptidylcarrier domain by N-hydroxyhistamine releasing PreAcb (**1**) (**Figure 5.1**). Upon release from the NRPS, PreAcb is effluxed to the extracellular space where it isomerizes to the isooxazolidinone acinetobactin (Acb, **2**) (**Figure 5.1**).<sup>2</sup> The 5-exo-tet cyclization proceeds with clean stereochemical inversion at C5' and shows a distinct pH-rate-dependent profile.<sup>1</sup> The isomerization is slow at acidic pH and fast at neutral and

basic pH. Both forms of the siderophore, **1** and **2**, promote the growth of *A. baumannii* ATCC 17978 under iron-restrictive conditions and use the same transport proteins. Given that most sites of *A. baumannii* infection are acidic, we hypothesize that both PreAcb and Acb will be present and functional as iron-sequestering virulence factors, providing a growth advantage under an expanded pH range. Consistent with this hypothesis, PreAcb accumulates in *A. baumannii* supernatants in acidic media, while only Acb is detectable in neutral media. Both PreAcb and Acb form stable, 2:1 complexes with iron(III). Structure-function studies of PreAcb and Acb analogs showed that iron(III) chelation is required for growth promotion of *A. baumannii* in iron-restrictive media.<sup>3</sup> Structural analogs incapable of promoting growth might competitively inhibit the Acb pathway.

Subtle structural changes in a siderophore scaffold can dramatically influence function. A single carbon epimer of mycobactin was shown to block siderophore cycling in *M. tuberculosis* leading to high intracellular accumulation of siderophores that induced a lethal phenotype.<sup>4</sup> Mutasynthesis of pyochelin analogs by feeding substituted salicylate precursors to *P. aeruginosa* decreases the efficiency of iron uptake.<sup>5</sup> The modified pyochelin analogs are potential competitive inhibitors that block pyochelin uptake. Furthermore, oxidation of the thiazoline in pyochelin to the corresponding aromatic thiazole was shown to block transport of ferric pyochelin in *P. aeruginosa*.<sup>6</sup> Oxidized des-methyl pyochelin binds tightly to the pyochelin outer membrane transporter FptA and blocks uptake, but not binding, of ferric pyochelin. Computational docking and molecular dynamics simulations showed that oxidized pyochelin is more rigid than pyochelin, which might limit its ability to form stable metal complexes and increase stability of the FptA complex. The des-methyl phenolate-bis-thiazoline precursor to pyochelin is also a known intermediate in yersiniabactin biosynthesis.<sup>7</sup> Recently, Henderson and coworkers showed that yersiniabactin-producing Enterobacteriaceae also excrete oxidized des-methyl pyochelin, a

compound now identified as escherichelin, to block virulence of opportunistic *P. aeruginosa* during clinical bacteriuria.<sup>8</sup> Escherichelin-producing Enterobacteriaceae have potential as probiotic treatments for urinary tract infections and purified escherichelin might also be useful as an antivirulence agent. Similar to escherichelin blocking siderophore transport in pyochelin-utilizing pathogens, we hypothesize that oxidation of the PreAcb oxazoline to the corresponding aromatic oxazole (**3**) might rigidify the siderophore backbone, block isomerization to Acb, and result in inhibition of PreAcb/Acb uptake (**Figure 5.1**).

## 5.4 Results and Discussion

The synthesis of oxidized pre-acinetobactin (OxPreAcb, **3**) commenced with two precursors, *N*-Boc-*O*-benzylhydroxy-histamine **6** and oxazole benzyl ester **8** (**Scheme 5.1**). Hydroxyhistamine **6** was synthesized starting from histamine, as previously reported.<sup>1,9</sup> Diazotization/halogenation of histamine dihydrochloride **4** with sulfuric acid and potassium bromide, followed by addition of sodium nitrite, provided the corresponding bromo- and chloro-ethylimidazoles **5** in 52% yield, as a ~3:1 bromo-/chloro-mixture. SN2 displacement of halo-mixture **5** with the sodium salt of *N*-boc-*O*-benzylhydroxamine afforded *N*-Boc-*O*-benzylhydroxyhistame **6** in good yield. Oxazole **8** was synthesized in a one-pot, two- step synthesis adapted from Graham,<sup>10</sup> via the condensation of 2,3-dihydroxybenzaldehyde with Bn-protected L-Thr and subsequent oxidation of the intermediate aminal with BrCCl<sub>3</sub>. Hydrogenolytic debenylation of **8** and TFA-mediated Boc-removal of **6** generated the free acid **9** and amine **10**, respectively (**Scheme 5.2**). EDC/HOBt coupling of **9** and **10** provided *O*-benzyl protected *N*-hydroxyamide **11**. Hydrogenolysis of **11** yielded OxPreAcb **3** to complete the synthesis in 5 longest linear steps (LLS) and 7 total steps.

OxPreAcb is stable and does not spontaneously isomerize in aqueous buffer as observed for the oxazoline to isooxazolidinone isomerization from PreAcb and Acb.<sup>1</sup> Thus, OxPreAcb is structurally “locked” in the PreAcb-like form via aromatization to the phenolate-oxazole heterocycle. We investigated the effect of Acb and OxPreAcb on the growth of *A. baumannii* ATCC 19606T in M9 minimal medium under iron-restrictive (125  $\mu$ M 2,2'-dipyridyl) conditions. We chose Acb over PreAcb because we have shown in previous work that both isomers have equivalent growth promoting effects at pH 7, and Acb is easier to isolate from *A. baumannii* cultures.<sup>1</sup> As expected, Acb promoted the growth of *A. baumannii* ATCC 19606T in a dose-dependent manner (**Figure 5.2A**). In striking contrast, OxPreAcb strongly inhibited growth at all concentrations tested (0.78-50  $\mu$ M) (**Figure 5.2B**). Furthermore, growth inhibition by OxPreAcb was competitive and dose-dependent in the presence of 10  $\mu$ M Acb (**Figure 5.2C**). Antagonism of OxPreAcb growth inhibitory activity by Acb supports competition for the same biological target or transport pathway. OxPreAcb activity was confirmed on two separate synthetic lots to confirm the observed biological activity (**Figure 5.3**). In medium supplemented with 100  $\mu$ M 2,2'-dipyridyl, OxPreAcb inhibited *A. baumannii* ATCC 19606T growth with an MIC of 1.56  $\mu$ M.

To probe the iron-dependence of OxPreAcb activity, wild-type *A. baumannii* ATCC 19606T and a biosynthesis deficient ATCC 19606T s1 mutant were grown in M9 media in the presence of variable OxPreAcb with and without supplemented 10  $\mu$ M Fe(acac)<sub>3</sub> (**Figure 5.4**). Ciprofloxacin was included as a control antibiotic with activity that is not strongly affected by iron concentration.<sup>11</sup> As expected, ciprofloxacin activity against *A. baumannii* ATCC 19606T and the s1 mutant was not affected by iron concentration. However, the growth inhibitory activity of OxPreAcb was strongly antagonized by iron supplementation. The amount of OxPreAcb required to fully inhibit growth of wild-type ATCC 19606T and ATCC 19606T s1 was 50  $\mu$ M (**Figure**

**5.4AC**). Upon supplementation with 10  $\mu\text{M}$   $\text{Fe}(\text{acac})_3$ , the concentration of Ox-PreAcb required to fully inhibit growth increased to 200  $\mu\text{M}$  (**Figure 5.4BD**). PreAcb biosynthesis is under the transcriptional control of ferric uptake repressors (FURs).<sup>2</sup> FUR proteins repress transcription when bound to Fe(II) and allow transcription when no metal is bound. This level of transcriptional control ensures that expression of proteins in costly siderophore pathways remain reserved for times of iron restriction when the metal is needed most. Iron-dependence is commonly observed for SACs and other antibiotics that rely on siderophore-binding proteins for cell entry.<sup>12</sup> Thus, OxPreAcb might be entering cells via the Acb pathway.

To investigate the role of Acb transport proteins on the growth inhibiting activity of OxPreAcb we performed growth studies in M9 medium using gene insertion mutants of *A. baumannii* ATCC 19606T t6 and t7, which are deficient in the outer membrane receptor protein BauA and inner-membrane transport protein BauD, respectively (**Figure 5.5**).<sup>1</sup> Wild type ATCC 19606T and the t7 mutant showed similar levels of growth, while the s1 and t6 mutants showed reduced growth across multiple concentrations of OxPreAcb (**Figure 5.5A**). Interestingly, when OxPreAcb was pre-complexed with Fe(III) prior to growth studies, the growth of wild type *A. baumannii* ATCC 19606T and the s1, t6, and t7 mutants was promoted suggesting that the OxPreAcb-Fe(III) complex can be used as a source of iron and only the metal-free form of OxPreAcb has growth inhibitory activity (**Figure 5.5B**). Disrupting Acb biosynthesis and transport systems does not strongly affect the growth inhibitory activity of OxPreAcb. The activity of OxPreAcb is antagonized by supplementing growth medium with Fe(III). Thus, it remains unclear whether complexation of OxPreAcb truly abolishes the growth inhibitory effect or if that added Fe(III) is simply having the same antagonistic effect as supplementation with  $\text{Fe}(\text{acac})_3$ . During human infections, iron is a limiting nutrient so OxPreAcb would be presumably be metal free and

growth inhibitory towards *A. baumannii* pathogens.<sup>13</sup> The overall growth inhibitory effect of OxPreAcb on *A. baumannii* appears to be bacteriostatic (**Figure 5.6**).

We tested the antibiotic activity of OxPreAcb against two additional clinical isolates of *A. baumannii* (ATCC 17978 and ATCC 19961), the non-pathogenic strain *Acinetobacter baylyi* ATCC 33305, and pathogenic *E. coli* ATCC 29522 (**Figure 5.7**). The iron-restrictive M9 medium supplemented with DIP was optimized specifically for *A. baumannii* ATCC 19606T. To ensure growth of all the strains the M9 media was not supplemented with DIP, which reduces the potency of OxPreAcb for inhibiting bacterial growth (similar to supplementing Fe(acac)<sub>3</sub>). OxPreAcb inhibited the growth of all the Gram-negative bacteria at 100–200 μM. This could indicate that a more general mechanism than siderophore disruption, such as metal withholding or metalloenzyme targeting, is at play. All of the *Acinetobacter* strains produce Acb, and *E. coli* is known to transport catecholate siderophores, so a siderophore-based inhibition mechanism is still possible.

The conversion of OxPreAcb from a growth inhibitor to a growth promoter upon iron(III) chelation inspired us to study the iron(III) binding properties. We used a fluorescence quenching assay to titrate OxPreAcb with iron(III) showing that a stable 2:1 (OxPreAcb)<sub>2</sub>Fe(III) complex forms (**Figure 5.8**). PreAcb and Acb also form stable 2:1 complexes with iron(III).<sup>3</sup> We used an EDTA competition assay to measure the apparent stability constants ( $K_{Fe}$ ) of the (PreAcb)<sub>2</sub>Fe(III), (Acb)<sub>2</sub>Fe(III), and (OxPreAcb)<sub>2</sub>Fe(III) complexes (**Figure 5.9**). Apparent  $K_{Fe}$  values were  $27.4 \pm 0.2$ ,  $26.2 \pm 0.1$ , and  $26.5 \pm 0.3$  for (PreAcb)<sub>2</sub>Fe(III), (Acb)<sub>2</sub>Fe(III), and (OxPreAcb)<sub>2</sub>Fe(III), respectively. Based on similarity of the apparent  $K_{Fe}$  values we predict that OxPreAcb will be competitive with PreAcb and Acb for iron(III) in a biological setting.



## 5.5 Outlook and Conclusions

The mechanistic basis for the growth inhibitory activity of OxPreAcb against Gram-negative bacteria remains unknown. Simple oxidation of the PreAcb oxazoline to the OxPreAcb oxazole is predicted to increase rigidity of the siderophore backbone. Energy minimization of the metal-free PreAcb and OxPreAcb structures revealed significant differences in 3D-orientations of the phenolate-oxazoline and phenolate-oxazole moieties, respectively (**Figure 5.10**). Both the phenolate-oxazoline and phenolate-oxazole systems are relatively flat, with the trans-oxazoline of PreAcb slightly puckered and the oxazole of OxPreAcb appearing in plane with the phenyl ring. In the gas phase, a stable H-bond was predicted between the 2-hydroxyl group of the phenyl ring with the oxazoline nitrogen of PreAcb, which presumably stabilizes the planar structure and restricts rotation around the oxazoline C1 to phenyl C1' bond. The same type of H-bonding interaction was found in the OxPreAcb energy minimized structure except the H-bond was formed between the oxazole nitrogen and the hydroxyl group of the hydroxamic acid. PreAcb is capable of this same H-bonding interaction, but it was not found during energy minimization. The origin for this difference in H-bonding modes might be the relative rotational barriers about the oxazoline/oxazole C4 to hydroxamate carbonyl carbon bond. The trans-orientation of the oxazoline methyl and hydroxamate substituents decreases steric clash in rotational isomers. The cis-planar orientation of the oxazole methyl and hydroxamate substituents introduces A<sub>1,3</sub>-strain. Computational analysis of the energy landscape for rotational isomers about the oxazoline/oxazole C4 to hydroxamate carbonyl carbon bond of PreAcb and OxPreAcb supported this model (**Figure 5.11, 5.12**). The sterically smaller carbonyl group of the hydroxamate prefers to eclipse the oxazole methyl group to minimize the A<sub>1,3</sub>-strain, which puts the bulky *N*-alkyl-*N*-hydroxy group closer to the oxazole nitrogen. Restricted rotation in the rigid phenolate-oxazole ligand set of OxPreAcb is

predicted to limit the accessible number of theoretical modes for iron(III) chelation compared to the more flexible PreAcb and Acb structures. In medicinal chemistry, rigidity is often used to increase the affinity of a ligand for a protein target.<sup>14</sup> Escherichelin, a rigid pyochelin analog, was shown to tightly bind the outer membrane receptor FptA and block transport of ferric pyochelin.<sup>6</sup> A similar phenomenon might be taking place in *A. baumannii* for OxPreAcb in the presence of Acb. Like escherichelin<sup>8</sup>, OxPreAcb might be effective at blocking virulence of *A. baumannii* by disrupting siderophore utilization, which is required for growth during infection (**Figure 5.13**).<sup>14</sup> Here, the importance of molecular recognition is revealed by subtle structural changes (**Figure 5.14**). A more detailed understanding of siderophore receptor binding and membrane transport paradigms in *A. baumannii* are required to fully appreciate how OxPreAcb competes with Acb for cellular uptake.<sup>15</sup> It also remains unclear whether the net growth inhibitory effect of OxPreAcb is due exclusively to blocking siderophore cycling or if inhibition of metalloenzymes or disruption of metal homeostasis are contributing factors.<sup>16</sup> Phenolate-oxazolines and phenolate-thiazolines are common motifs in many siderophore scaffolds, including siderophores associated with virulence in bacterial pathogens.<sup>17</sup> Simple oxidation of the oxazolines/thiazolines found in bacterial siderophores might be a general strategy for preparing rigid siderophore analogs as antivirulence agents that competitively block siderophore utilization in producing pathogens.

## 5.6 Materials and Methods

### *Strains, Materials, and Instrumentation*

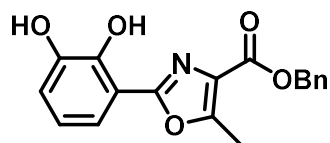
Growth studies were conducted using *A. baumannii* ATCC 19606TT and derivatives t6 (bauA::EZ::TN<R6Kcori/KAN-2>), t7 (bauD::EZ::TN<R6Kcori/KAN-2>), and s1 (basD::aph) provided by Dr. Luis Actis. Precultures and 96-well plate *A. baumannii* growth assays were performed in filter-sterilized M9 minimal media. Samples for LC-MS were prepared in 0.45  $\mu$ M

PTFE mini-UniPrep vials from Agilent. All preparatory HPLC was performed using a Beckman Coulter SYSTEM GOLD 127P solvent module and 168 detector with a Phenomenex Luna 10u C18(2) 100A column, 250 × 21.20 mm, 10 μm with guard column. Prep HPLC was performed with a mobile phase of 5 mM ammonium acetate in (A) water and (B) acetonitrile, and data were processed using 32 Karat software, version 7.0. All LC-MS was performed on an Agilent 6130 quadrupole LC-MS with G1313 autosampler, G1315 diode array detector, and 1200 series solvent module. A Phenomenex Gemini C18 column, 50 × 2 mm, 5 μm with guard column was used for all LC-MS separations. LC-MS mobile phases were 0.1% formic acid in (A) water and (B) acetonitrile, and data were processed using G2710 ChemStation software. NMR was performed on a Varian Unity Inova-600 MHz instrument with a cold probe. Bacterial growth studies were performed using polystyrene 96-well plates with polystyrene lids. OD600 measurements were taken on a Molecular Devices SpectraMax Plus 384 plate reader.

### ***Acinetobactin Isolation***

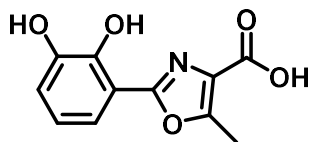
Natural acintobactin was isolated and purified from *A. baumannii* cultures as previously reported.<sup>1</sup> Briefly, liter cultures of *A. baumannii* ATCC 17978 were grown overnight in M9 minimal media. The cultures were centrifuged down and the supernatant was adjusted to pH 6. XAD-7HP resin was added and the supernatant was shaken. The resin was washed with methanol. The methanol extract was concentrated and preparatory HPLC purified to yield pure acinetobactin.

## Compound Synthesis

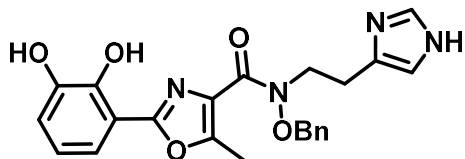


**Benzyl 2-(2,3-dihydroxyphenyl)-5-methyloxazole-4-carboxylate (8).** The synthesis of **8** was adapted from a previously reported, one-pot synthesis of oxazoles.<sup>10</sup> To a clean, dry round bottom flask equipped with a stirbar and argon inlet was added *L*-threonine benzyl ester oxalate (1.0 g, 3.34 mmol), potassium carbonate (0.92 g, 6.68 mmol), and *N,N'*-dimethylacetamide (8.3 mL) (Note: a white, cloudy solution was formed). To the resultant mixture was added 2,3-dihydroxybenzaldehyde (0.46 g, 3.34 mmol) [solid, in one portion], which resulted in the formation of a bright yellow solution which stirred at room temperature, under argon, for 12 hrs. After 12 hrs, the reaction was cooled to 0°C, and bromotrichloromethane (0.99 mL, 10.02 mmol) and 1,8-diazabicyclo[5.4.0]undec-7-ene (1.50 mL, 10.02 mmol) were added. The resulting deep orange solution was stirred at 0°C for 2 hrs, at which point the reaction was removed from the ice bath and warmed to rt. The mixture stirred at rt for an additional 10 hrs [monitored by LC-MS]. The reaction was diluted with DD-H<sub>2</sub>O (3x original volume) and extracted with MTBE (3 x 15 mL) and EtOAc (3 x 15 mL). The organic layers were combined, washed with brine, and dried over Na<sub>2</sub>SO<sub>4</sub>. The product was concentrated by rotary evaporation to yield a dark orange sticky solid (0.92 g, 85% crude yield). The crude product was then purified as needed by prep HPLC (gradient of 0% B to 95% B for 17 min then hold at 100% B for 8 minutes) to provide the title compound as a pale yellow oil (5 mg per injection, yielded 3.5 mg of pure compound). <sup>1</sup>H NMR (600 MHz, Chloroform-*d*) δ 7.46 (d, *J* = 7.1 Hz, 2H), 7.43 – 7.33 (m, 4H), 7.31 (d, *J* = 8.0 Hz, 1H), 7.03 (d, *J* = 7.9 Hz, 1H), 6.86 (t, *J* = 7.9 Hz, 1H), 5.38 (s, 2H), 2.70 (s, 3H). <sup>13</sup>C NMR (151

MHz, Chloroform-*d*)  $\delta$  161.5, 159.5, 155.4, 145.3, 144.7, 135.7, 128.8, 128.6, 128.4, 127.0, 120.0, 117.6, 116.9, 110.2, 66.8, 12.3. LC-MS calcd for C<sub>18</sub>H<sub>16</sub>NO<sub>5</sub> (M + H)<sup>+</sup> 326.1028; found 326.1.

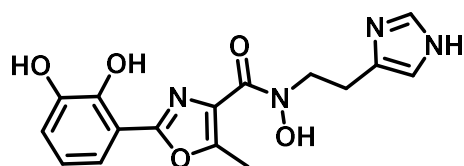


**2-(2,3-dihydroxyphenyl)-5-methyloxazole-4-carboxylic acid (9).** To a solution of oxazole **8** (20 mg, 0.06 mmol) in MeOH (2 mL) was added 10% P/C (2 mg) at rt. The vial was purged with H<sub>2</sub> and allowed to stir under H<sub>2</sub> atm (1 atm) for 1 hr [monitored by LC-MS]. Once complete, as judged by LC-MS, the solid catalyst was removed via syringe filtration, and the solution was concentrated under reduced pressure to provide pure carboxylic acid **9** as a clear colorless oil (99% yield). <sup>1</sup>H NMR (600 MHz, Methanol-*d*<sub>4</sub>)  $\delta$  7.33 (d, *J* = 7.9 Hz, 1H), 6.94 (d, *J* = 7.9 Hz, 1H), 6.83 (t, *J* = 7.9 Hz, 1H), 2.72 (s, 3H). <sup>13</sup>C NMR (151 MHz, Methanol-*d*<sub>4</sub>)  $\delta$  164.8, 160.8, 156.7, 147.2, 146.8, 128.5, 120.8, 119.4, 117.6, 111.7, 12.0. LC-MS calcd for C<sub>11</sub>H<sub>10</sub>NO<sub>5</sub> (M + H)<sup>+</sup> 236.0559; found 236.1.



**N-(2-(1H-imidazol-4-yl)ethyl)-N-(benzyloxy)-2-(2,3-dihydroxyphenyl)-5-methyloxazole-4-carboxamide (11).** To a clean, dry round bottom flask equipped with a stirbar and argon inlet was added carboxylic acid **9** (60 mg, 0.25 mmol), DMF (8 mL), and hydroxyhistamine **7** (82 mg, 0.38 mmol). To the stirring solution was added EDC (198 mg, 1.28 mmol) and HOBt (172 mg, 1.28 mmol), and Et<sub>3</sub>N was added to the reaction dropwise until a pH of ~9 was obtained. The reaction stirred under argon for 12 hrs (monitored by LC-MS), at which point the reaction mixture was concentrated by rotary evaporation and purified by prep HPLC (gradient of 0% B to 95% B in 17

minutes, 95% B to 100% B in 2 minutes, hold 100% B for 8 minutes) to yield title compound **11** as a pale yellow oil (64 mg, 58% yield). <sup>1</sup>H NMR (600 MHz, DMSO-*d*<sub>6</sub>) δ 7.49 (s, 1H), 7.38 – 7.26 (m, 5H), 7.20 (dd, *J* = 7.9, 1.6 Hz, 1H), 6.92 (d, *J* = 7.8 Hz, 1H), 6.79 (s, 1H), 6.75 (t, *J* = 7.8 Hz, 1H), 4.95 (s, 2H), 4.06 (t, *J* = 7.2 Hz, 2H), 2.87 (t, *J* = 7.2 Hz, 2H), 2.42 (s, 3H). <sup>13</sup>C NMR (151 MHz, DMSO-*d*<sub>6</sub>) δ 172.0, 161.4, 157.9, 146.1, 145.1, 134.8, 129.3, 129.1, 128.6, 128.3, 119.6, 118.2, 116.5, 111.1, 75.6, 25.0, 21.1, 11.4. HRMS calcd for C<sub>23</sub>H<sub>23</sub>N<sub>4</sub>O<sub>5</sub> (M + H)<sup>+</sup> 435.1663; found 435.1669



*N*-(2-(1*H*-imidazol-4-yl)ethyl)-2-(2,3-dihydroxyphenyl)-*N*-hydroxy-5-methyloxazole-4-carboxamide (**3**). *O*-benzyl-oxidized-pre-acinetobactin **11** (12 mg, 0.05 mmol) was stirred in MeOH with ~1/10 mass equivalent of 10% Pd/C under H<sub>2</sub> atmosphere (1 atm). Upon confirmation of reaction completion by LC-MS (~1 hr), the solid catalyst was removed through syringe filtration and the solution was concentrated by rotary evaporation to provide oxidized preacinetobactin **3** as a colorless oil. <sup>1</sup>H NMR (600 MHz, DMSO-*d*<sub>6</sub>) δ 7.54 (s, 1H), 7.23 (dd, *J* = 7.9, 1.6 Hz, 1H), 6.95 – 6.92 (m, 1H), 6.86 (s, 1H), 6.80 (t, *J* = 7.9 Hz, 1H), 3.93 (s, br, 2H), 2.88 (t, *J* = 7.3 Hz, 2H), 2.50 (s, 3H, under DMSO residual solvent peak). <sup>13</sup>C NMR (151 MHz, DMSO-*d*<sub>6</sub>) δ 157.8, 151.4, 146.2, 145.3, 134.8, 128.0, 119.5, 118.2, 116.1, 110.7, 48.6, 11.4. HRMS calcd for C<sub>16</sub>H<sub>17</sub>N<sub>4</sub>O<sub>5</sub> (M + H)<sup>+</sup> 345.1199; found 345.1193.

## ***Biological Studies***

M9 minimal media was prepared for all experiments as previously described.<sup>1</sup>

For biological assessment of acinetobactin **2** and oxidized pre-acinetobactin **3** under iron-restrictive conditions, stock solutions of 800  $\mu\text{M}$  **2** and **3** were prepared in M9 minimal media and filter sterilized. A 96-well plate was filled with 50  $\mu\text{L}$  of M9 minimal media per well. Into the first column, 50  $\mu\text{L}$  of either acinetobactin stock or oxidized pre-acinetobactin stock was added, and columns were serially diluted down to 1.56  $\mu\text{M}$ . An inoculum was made by adding 200  $\mu\text{L}$  of 0.5 McFarland standard (*A. baumannii* ATCC 19606TT s1) to 29.8 mL of M9 minimal media supplemented with 250  $\mu\text{M}$  2,2'-dipyridyl. Inoculum (50  $\mu\text{L}$ ) was added to each well for a final concentration of 125  $\mu\text{M}$  2,2'-dipyridyl and a serial dilution of 200-0.78  $\mu\text{M}$  acinetobactin and oxidized pre-acinetobactin. Growth promotion or inhibition was determined as compared to a control with 125  $\mu\text{M}$  2,2'-dipyridyl, 0  $\mu\text{M}$  acinetobactin and 0  $\mu\text{M}$  oxidized pre-acinetobactin. All experiments were performed in triplicate. For confirmation of biological activity of re-purified compound, procedure was reproduced but with 200  $\mu\text{M}$  2,2'-dipyridyl inoculum for a final concentration of 100  $\mu\text{M}$  2,2'-dipyridyl.

For biological assessment of competition between acinetobactin **2** and oxidized pre-acinetobactin **3**, a stock solution of 800  $\mu\text{M}$  **3** was prepared in M9 minimal media and filter sterilized. A 96-well plate was filled with 50  $\mu\text{L}$  of M9 minimal media per well. Into the first column, 50  $\mu\text{L}$  of oxidized pre-acinetobactin stock was added, and columns were serially diluted down to 1.56  $\mu\text{M}$ . An inoculum was made by adding 200  $\mu\text{L}$  of 0.5 McFarland (*A. baumannii* ATCC 19606TT s1) to 29.8 mL of M9 minimal media supplemented with 200  $\mu\text{M}$  2,2'-dipyridyl and 20  $\mu\text{M}$  acinetobactin. Inoculum (50  $\mu\text{L}$ ) was added to each well for a final concentration of 100  $\mu\text{M}$  2,2'-dipyridyl, 10  $\mu\text{M}$  acinetobactin, and a serial dilution of 200-0.78  $\mu\text{M}$  oxidized pre-

acinetobactin. Growth promotion or inhibition was determined as compared to a control with 100  $\mu\text{M}$  2,2'-dipyridyl, 10  $\mu\text{M}$  acinetobactin, and 0  $\mu\text{M}$  oxidized pre-acinetobactin. All experiments were performed in triplicate.

For the biological evaluation of the  $\text{Fe}^{3+}$ -complex of oxidized pre-acinetobactin, 200  $\mu\text{M}$  stocks of acinetobactin- $\text{Fe}^{3+}$  and oxidized pre-acinetobactin- $\text{Fe}^{3+}$  were prepared in M9 minimal media and filter sterilized. A 96-well plate was filled with 50  $\mu\text{L}$  of M9 minimal media per well. Into the first column, 50  $\mu\text{L}$  of either acinetobactin- $\text{Fe}^{3+}$  stock or oxidized pre-acinetobactin- $\text{Fe}^{3+}$  stock was added, and columns were serially diluted down to 0.39  $\mu\text{M}$ . An inoculum was made by adding 200  $\mu\text{L}$  of 0.5 McFarland standard (*A. baumannii* ATCC 19606TT s1) to 29.8 mL of M9 minimal media supplemented with 300  $\mu\text{M}$  2,2'-dipyridyl. Inoculum (50  $\mu\text{L}$ ) was added to each well for a final concentration of 150  $\mu\text{M}$  2,2'-dipyridyl and a serial dilution of 50-0.19  $\mu\text{M}$  acinetobactin and oxidized pre-acinetobactin. Growth promotion was determined as compared to a control with 125  $\mu\text{M}$  2,2'-dipyridyl, 0  $\mu\text{M}$  acinetobactin- $\text{Fe}^{3+}$  and 0  $\mu\text{M}$  oxidized pre-acinetobactin- $\text{Fe}^{3+}$ . All experiments were performed in triplicate.

For MIC evaluation of oxidized pre-acinetobactin, stock solutions of 800  $\mu\text{M}$  oxidized pre-acinetobactin and ciprofloxacin were prepared in M9 minimal media and filter sterilized. Eight 96-well plates were filled with 50  $\mu\text{L}$  of M9 minimal media per well. For the first column of each plate, 50  $\mu\text{L}$  of either oxidized pre-acinetobactin stock or ciprofloxacin stock was added, and columns were serially diluted down to 1.56  $\mu\text{M}$ . Seven separate inocula were prepared by diluting 200  $\mu\text{L}$  of appropriate 0.5 McFarland standard (*E. coli* ATCC 25922, *A. baumannii* ATCC 19606TT, *A. baumannii* ATCC 19606T t6, *A. baumannii* ATCC 19606T t7, or *A. baumannii* ATCC 19606T s1) in either plain M9 minimal media (all bacterial strains) or M9 minimal media supplemented with 20  $\mu\text{M}$   $\text{Fe}(\text{acac})_3$  (just *A. baumannii* ATCC 19606T and *A. baumannii* ATCC



19606T s1). Inocula (50  $\mu$ L) were added to each well of separate plates for a final concentration of either 0  $\mu$ M or 10  $\mu$ M  $\text{Fe}^{3+}$  and a serial dilution of 200-0.78  $\mu$ M oxidized pre-acinetobactin and ciprofloxacin. Growth was measured by endpoint  $\text{OD}_{600}$ . All experiments were performed in triplicate.

### ***Determination of $K_{Fe}$***

Stock solutions of 100  $\mu\text{M}$  pre-acinetobactin **1**, acinetobactin **2**, and oxidized pre-acinetobactin **3** were prepared in 10 mM HEPES buffer and a UV-Vis scan was recorded. Next 120  $\mu\text{M}$  EDTA was added and absorbance at 500 nm was measured over 800 minutes. Iron-binding affinity ( $K_{Fe}$ ) was determined using the following calculations.

$$(1) \quad K_L = \frac{[FeL_2]}{[Fe^{3+}][L]^2} \quad \text{for the following equilibrium;} \quad [Fe^{3+}] + 2[L] \rightleftharpoons [FeL_2]$$

$$(2) \quad K_{FeEDTA} = \frac{[FeEDTA]}{[Fe^{3+}][EDTA]} \quad \text{for the following equilibrium;} \quad [Fe^{3+}] + [EDTA] \rightleftharpoons [FeEDTA]$$

$$(3) \quad K_{Exchange} = \frac{K_L}{K_{FeEDTA}} \quad \text{for the following equilibrium;} \quad [FeEDTA] + 2[L] \rightleftharpoons [FeL_2] + [EDTA]$$

$$(4) \quad K_{Exchange} = \frac{[FeL_2][EDTA]}{[FeEDTA][L]^2}$$

$$(5) \quad \Delta = \frac{Abs_{FeL_2} - Abs_{FeL+EDTA}}{\epsilon_L}$$

$$(6) \quad K_L = K_{FeEDTA} \times \frac{[FeL_2][EDTA]}{[FeEDTA][L]^2}$$

$$(7) \quad [FeL_2] = \frac{Abs_{FeL_2}}{\epsilon_L}$$

$$(8) \quad [EDTA] = [EDTA]_T - \Delta \quad \text{where} \quad [EDTA]_T = \text{total EDTA added}$$

$$(9) \quad [FeEDTA] = \Delta$$

$$(10) \quad [L] = 2\Delta$$

$$(11) \quad K_{Fe} = \text{apparent } K_L$$

### ***Fluorescence Quenching Titration***

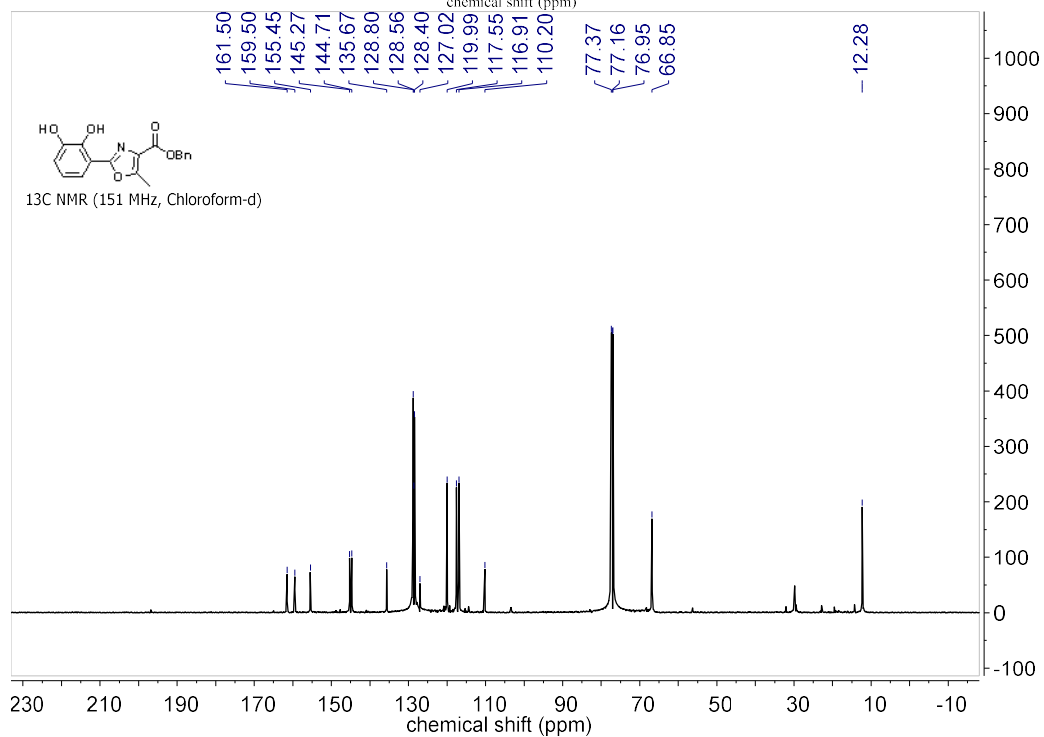
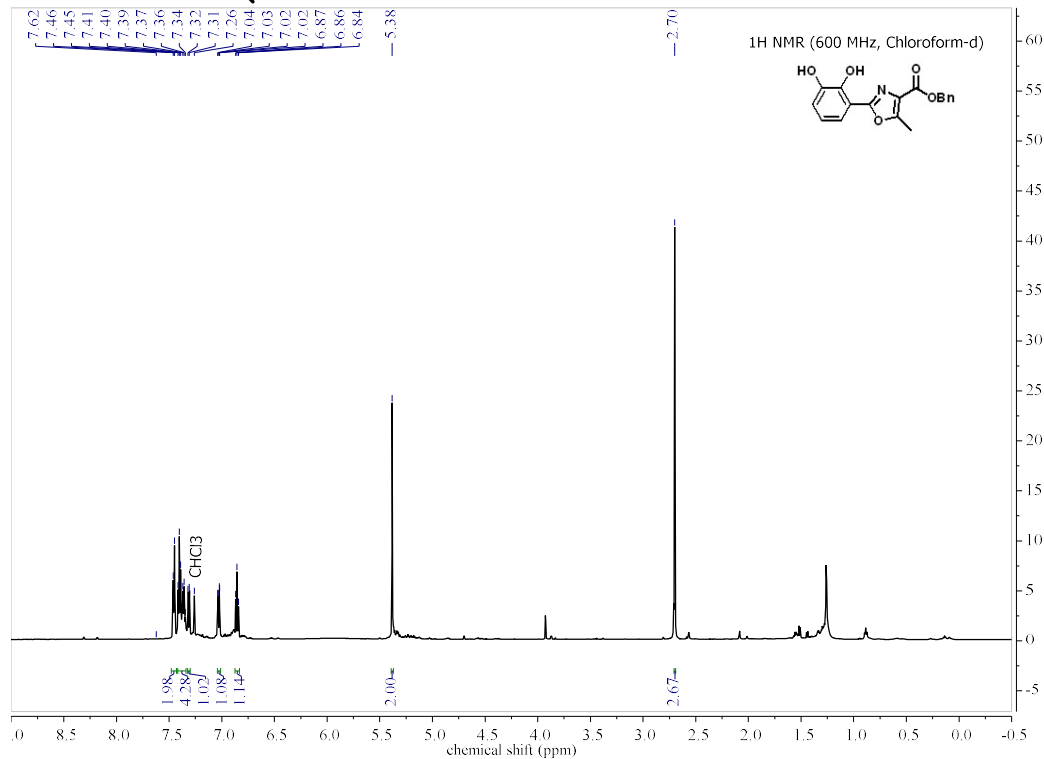
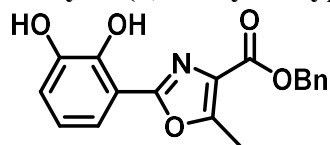
A solution of 570  $\mu\text{M}$  oxidized pre-acinetobactin **3** in methanol was prepared and a fluorescence emission spectra was recorded ( $\lambda_{\text{excitation}} = 330 \text{ nm}$ ). To determine stoichiometry of the complex between **3** and iron (III),  $\text{Fe}(\text{acac})_3$  was added 0.0438 equivalents at a time (1  $\mu\text{L}$  of 10  $\mu\text{M}$   $\text{Fe}(\text{acac})_3$  added by Hamilton syringe) and emission spectra were recorded at 380 nm after each addition. Peak fluorescence ( $\text{Abs}_{380\text{nm}}$ ) was plotted against iron (III) equivalents.

### ***Computational Studies***

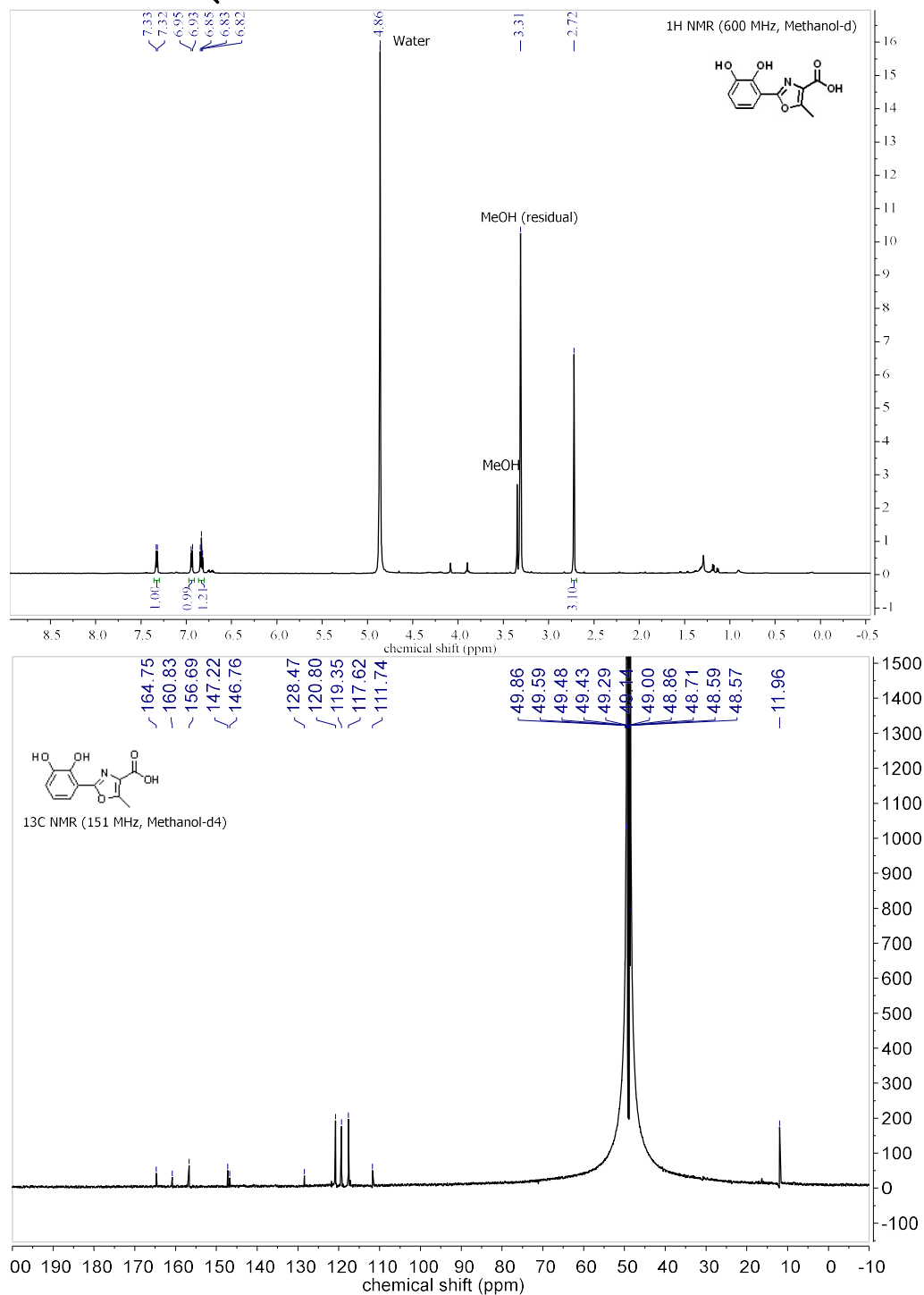
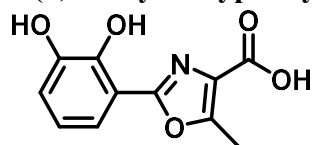
All calculations were performed using Spartan '16. Oxidized pre-acinetobactin **3** and pre-acinetobactin **1** were modeled in Spartan. The lowest energy conformations were obtained using the minimize energy function. The 3'-4'-9-8 dihedral (see **Table 5.1** for atom numbers) was constrained in both molecules as the energy profile was created investigating the rotation around the oxazole-carbonyl bond. The energy profile was run at ground state in the gas state with molecular mechanics MMFF. The energy was calculated in kJ/mol as the heterocycle-carbonyl bond rotated 360 degrees over 25 steps. The energy was plotted as against the 25 conformations.

### ***Compound Characterization***

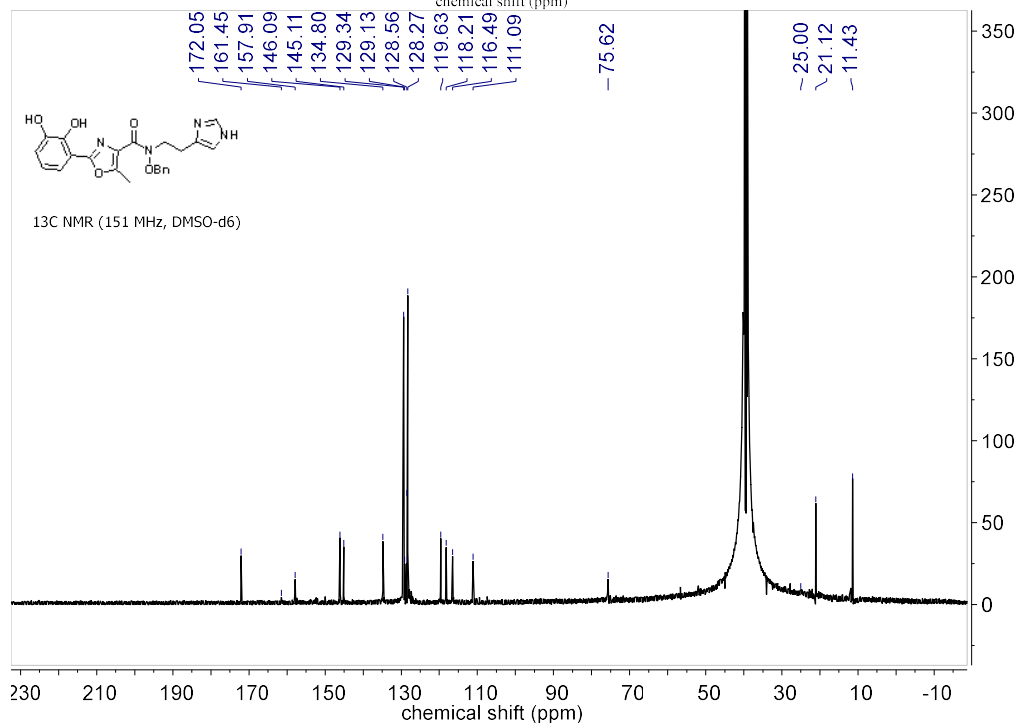
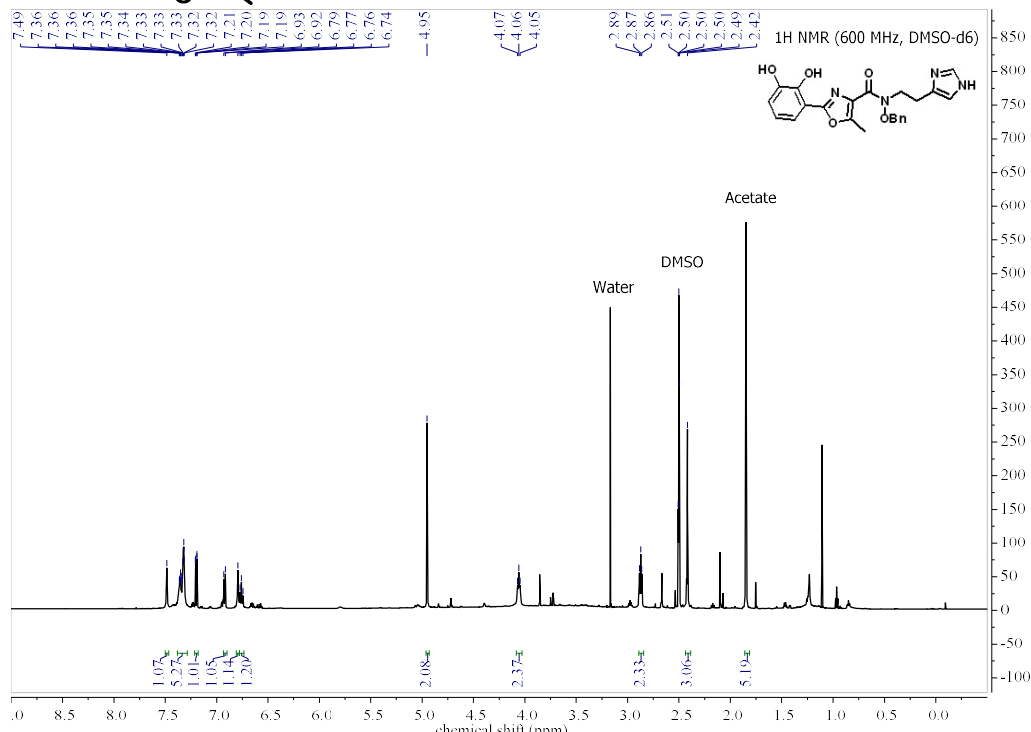
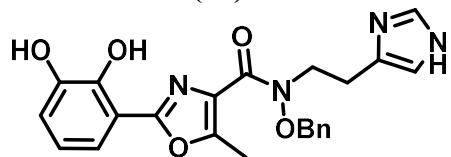
### Benzyl 2-(2,3-dihydroxyphenyl)-5-methyloxazole-4-carboxylate (8)

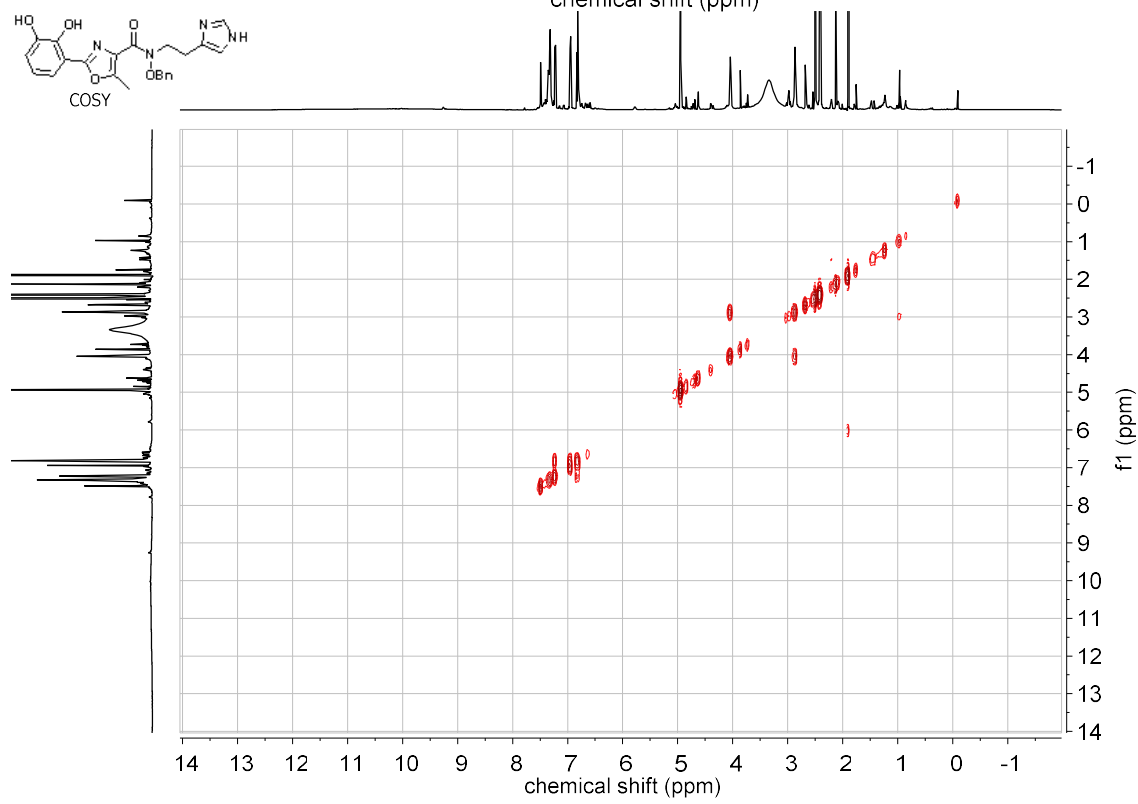
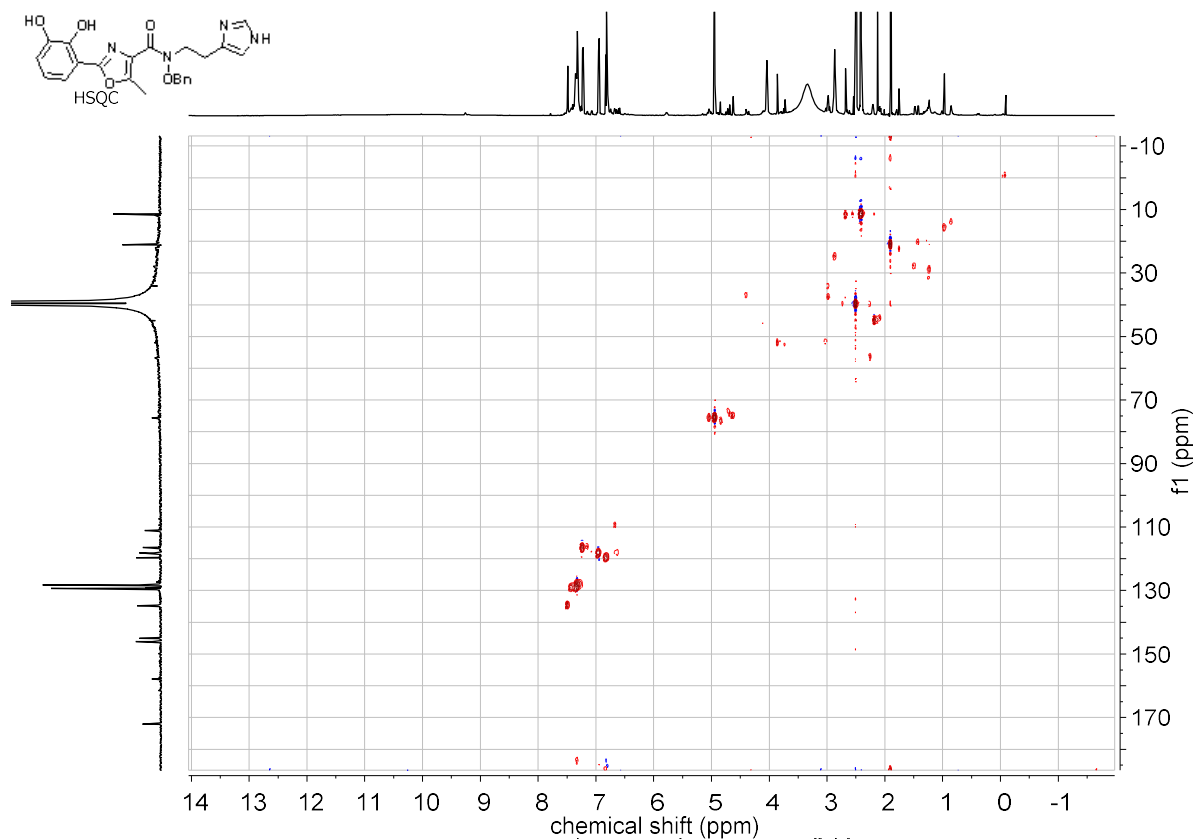


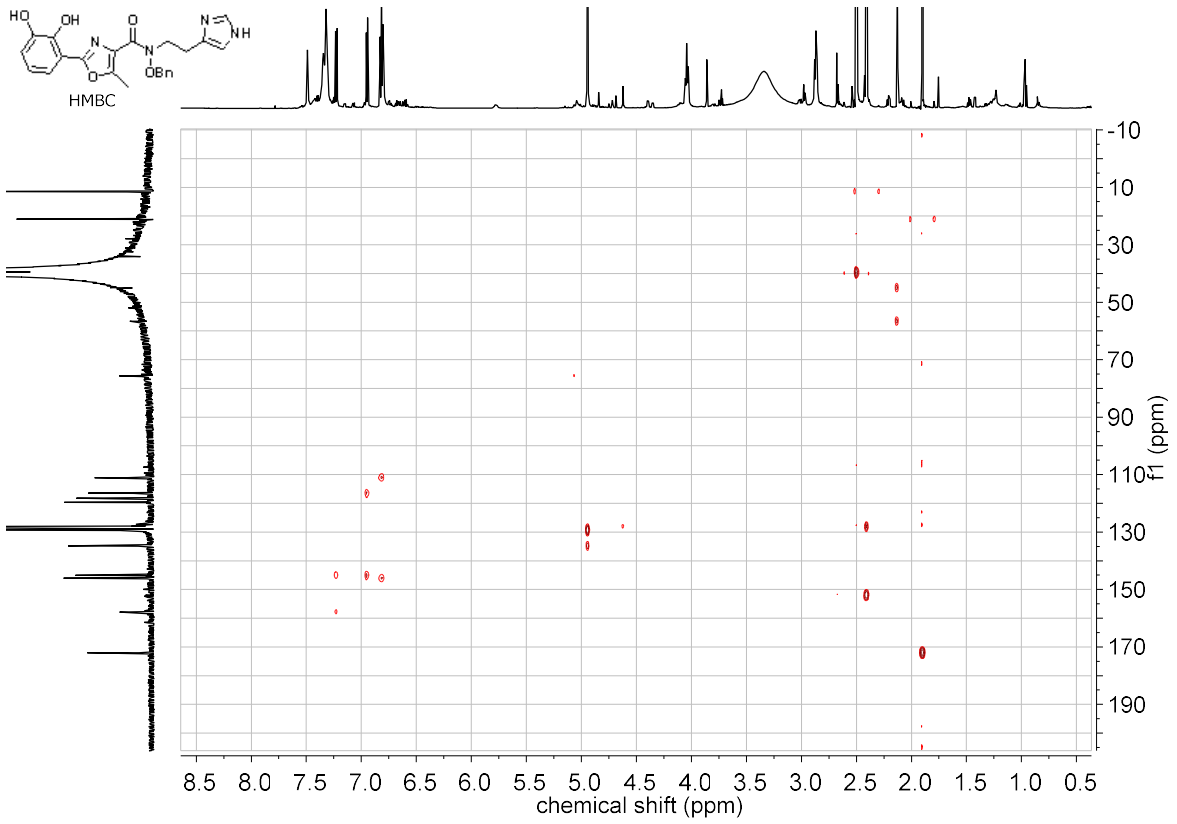
## 2-(2,3-dihydroxyphenyl)-5-methyloxazole-4-carboxylic acid (9)



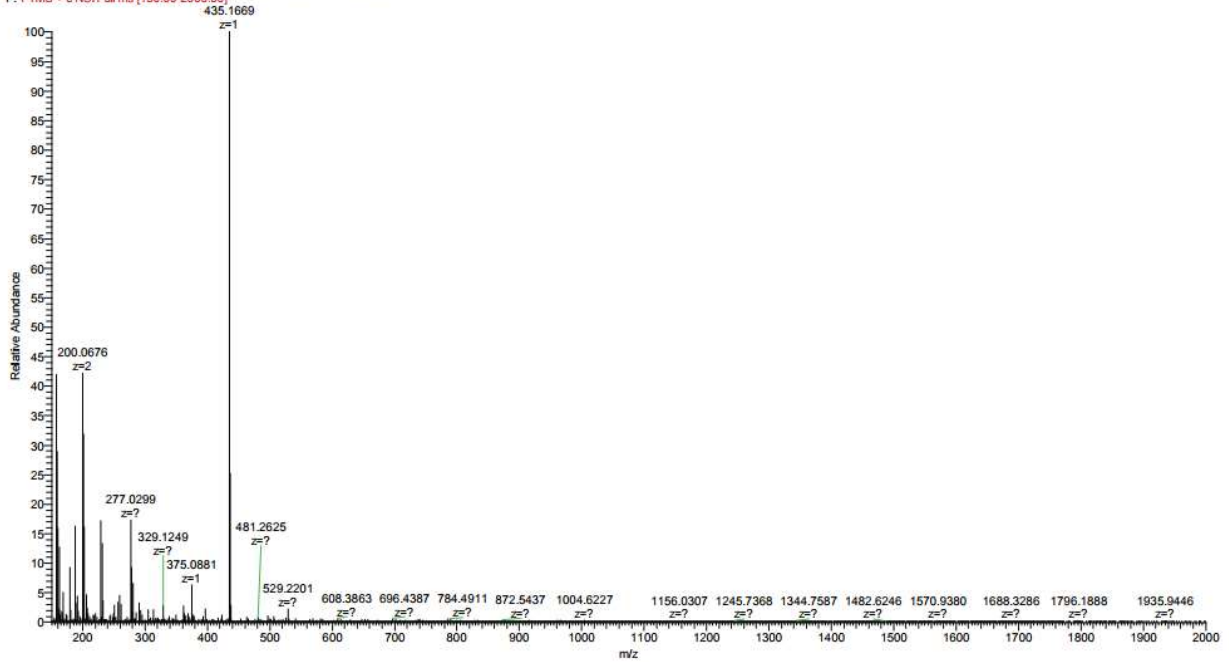
**N-(2-(1H-imidazol-4-yl)ethyl)-N-(benzyloxy)-2-(2,3-dihydroxyphenyl)-5-methyloxazole-4-carboxamide (11)**





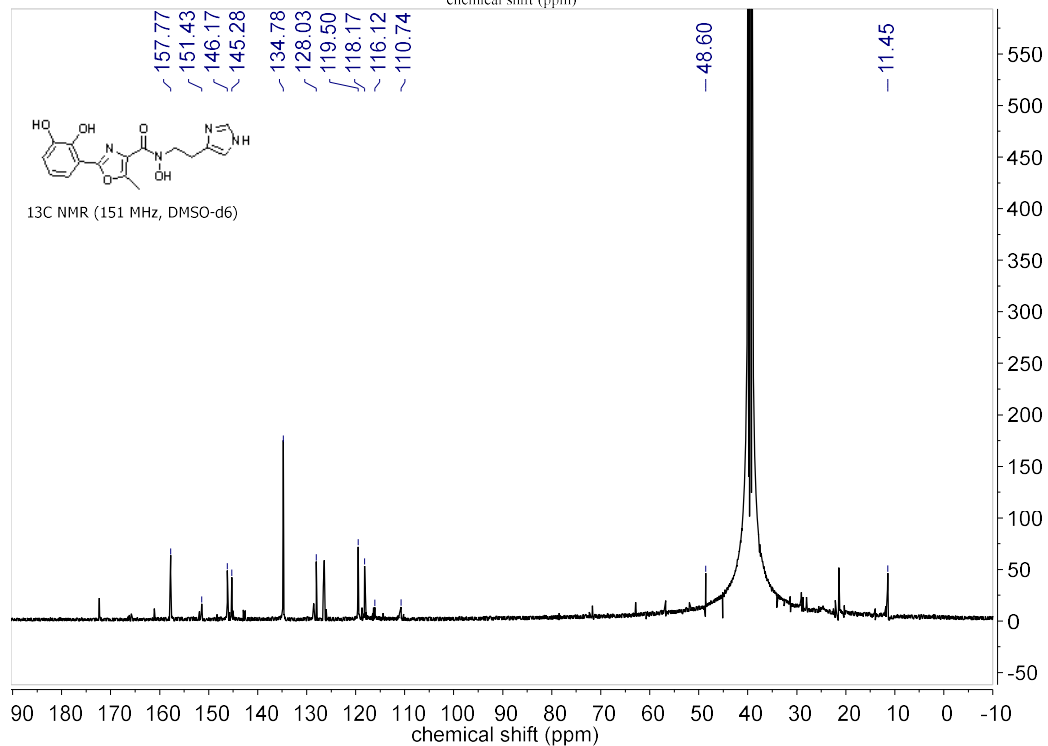
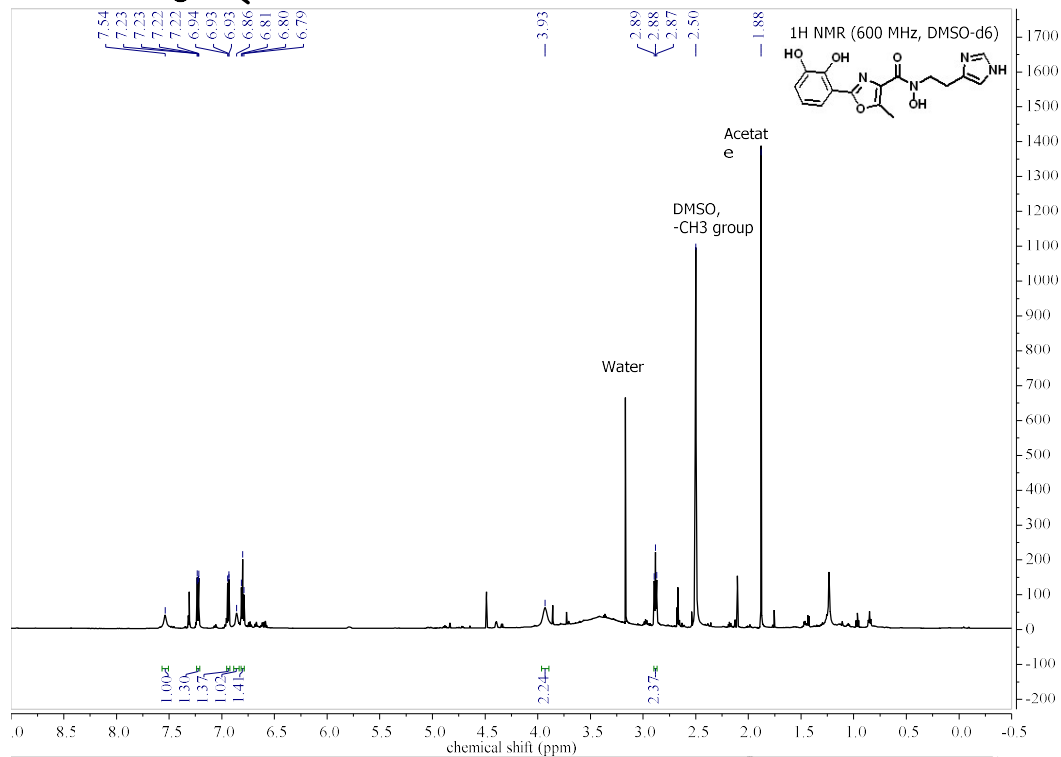
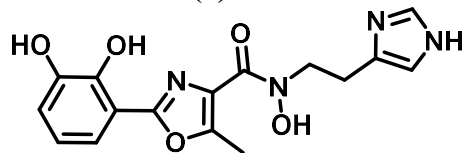


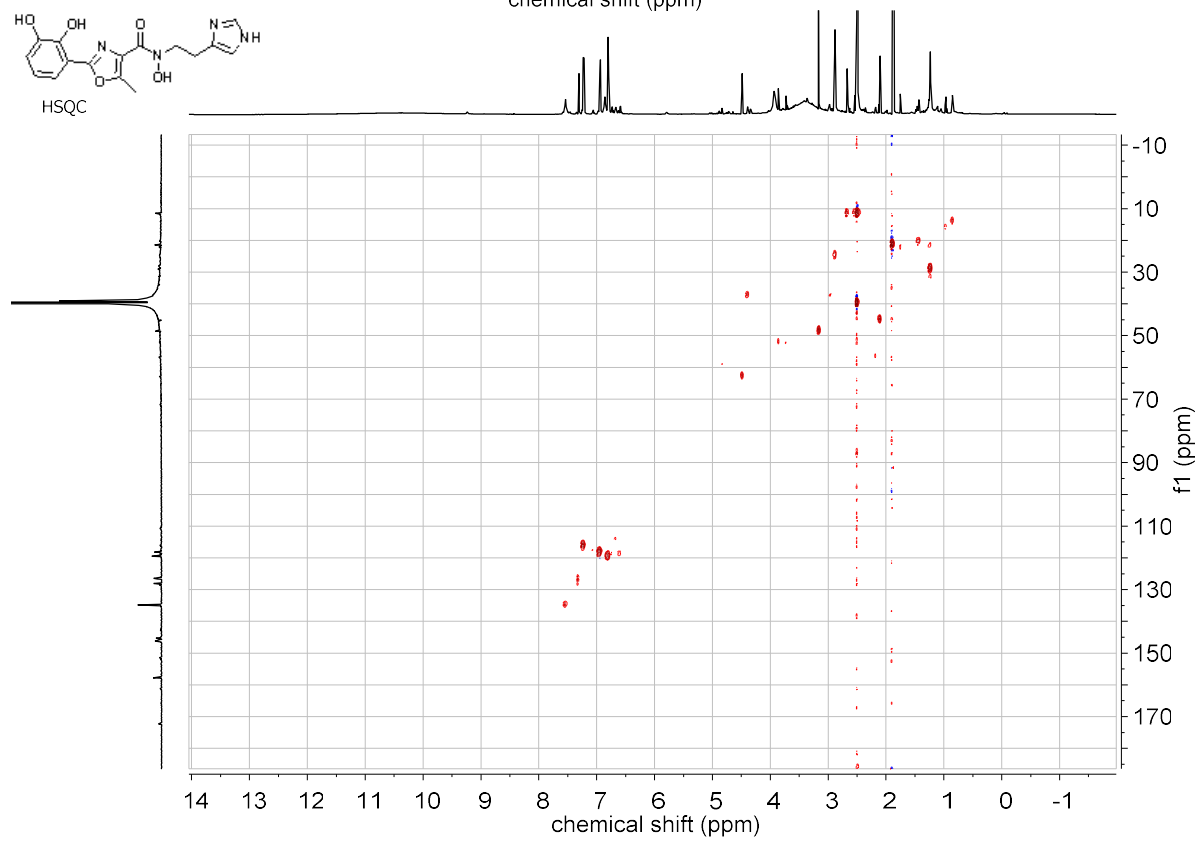
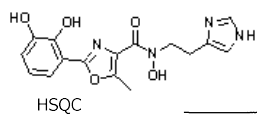
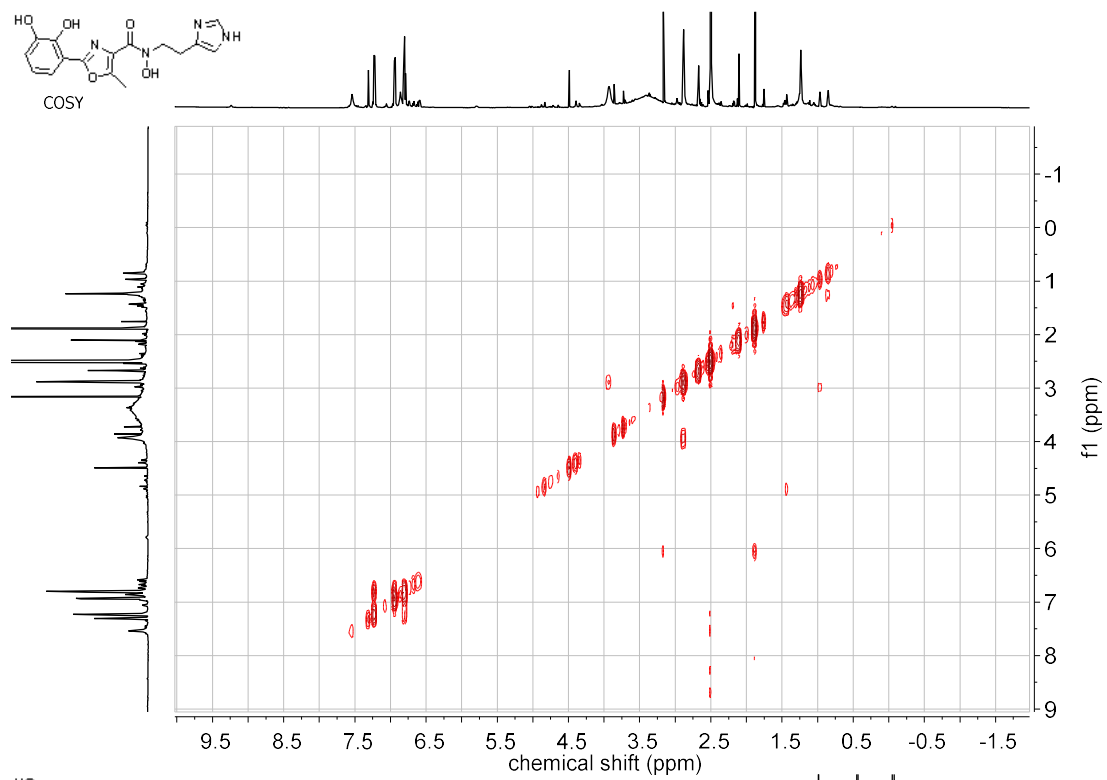
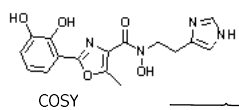
20170725\_TJB\_ex\_acine\_OBn#1-9 RT: 0.0-0.2 AV: 9 NL: 1.71E6  
 F: FTMS - c NSI Full ms [150.00-2000.00]

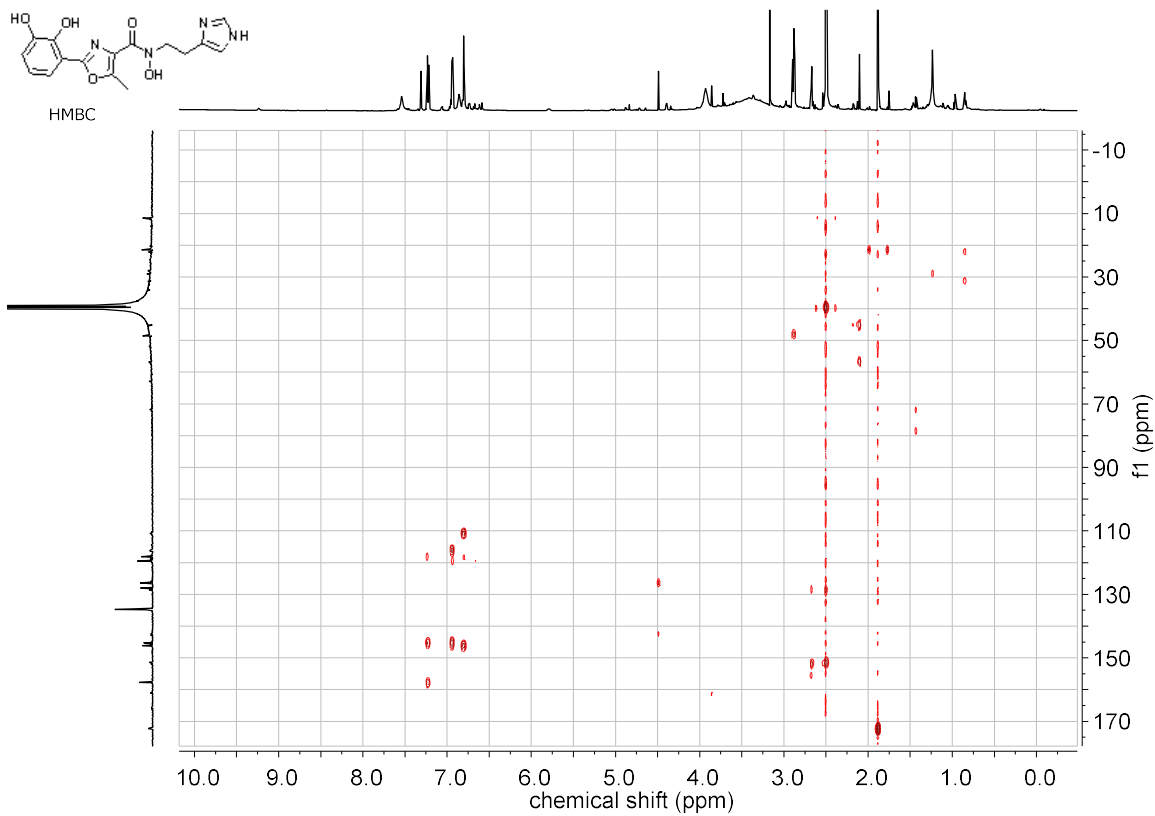




**N-(2-(1H-imidazol-4-yl)ethyl)-2-(2,3-dihydroxyphenyl)-N-hydroxy-5-methyloxazole-4-carboxamide (3)**







### HRMS – OxPreA (3)

XIC for 345.1194 @ 2ppm tolerance

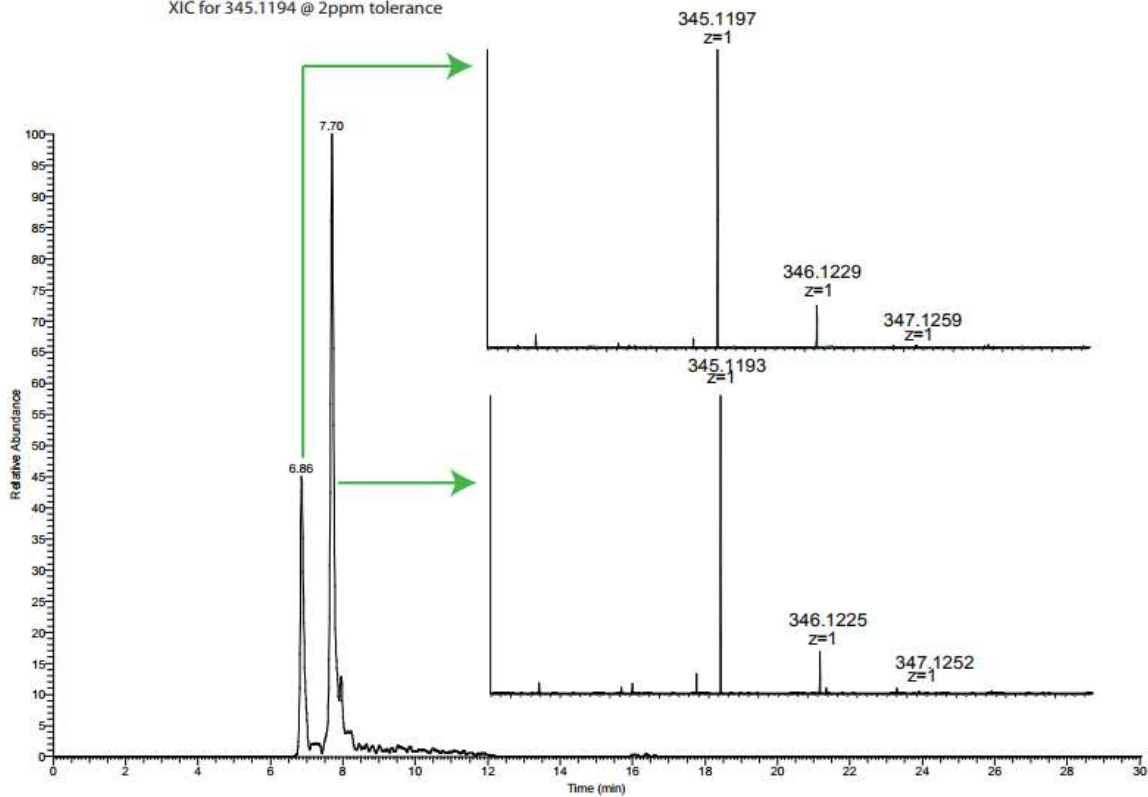
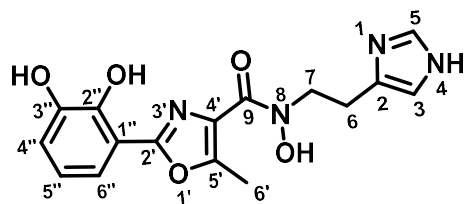


**Table 5.1.** 2D NMR characterization data of oxidized pre-acinetobactin (**3**) in DMSO-d<sub>6</sub>.

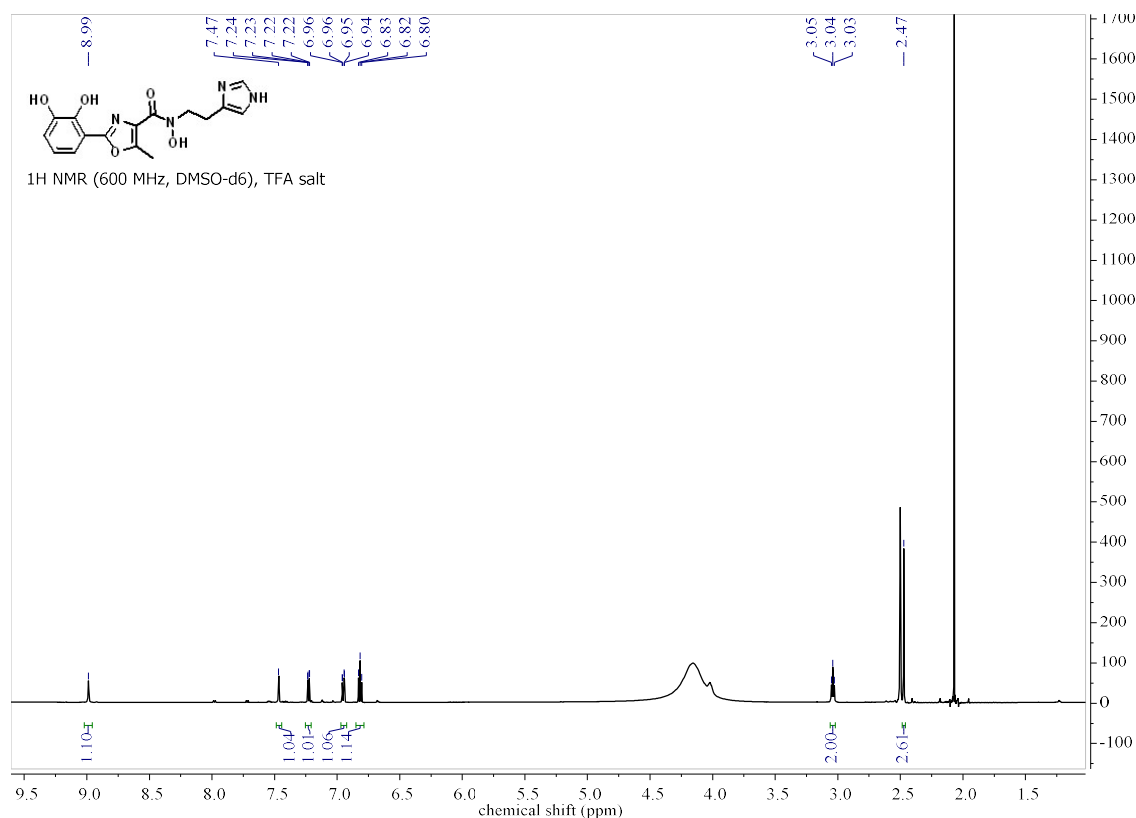


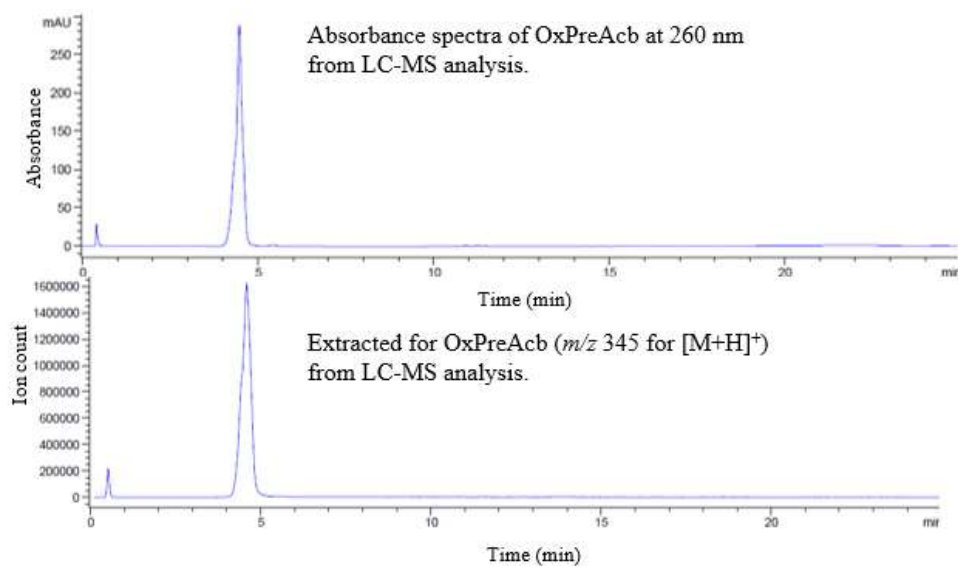
Oxidized Pre-Acinetobactin (**3**)

Atom	<sup>13</sup> C (ppm)	<sup>1</sup> H (ppm), Multiplets in Hz	COSY 1H-1H 3 bond	HMBC 1H-13C 2-3 bond	HSQC
2					
3		6.86 (s, 1H)	-	-	-
5	134.8	7.54 (s, 1H)	-	-	5
6	24.9	2.88 (t, 2H)	7	7	6
7	48.1	3.93 (s(br), 2H)	6	-	-
9			-	-	-
2'	157.8		-	-	-
4'	128.0		-	-	-
5'	151.5		-	-	-
6'	11.5	2.50 (s, 3H)	-	5'	6'
1''	110.7		-	-	-
2''	145.3		-	4'',6''	-
3''	146.2		-	5''	-
4''	118.2	6.92-6.95 (m, 1H)	5''	2'',5''	4''
5''	119.6	6.80 (t, 1H)	6''	3'',4''	5''
6''	116.1	7.23 (dd, 1H)	5''	2'',2'',4''	6''

## OxPreAcb (TFA salt)

OxPreAcb (**3**) was re-purified by preparatory HPLC upon reviewer request. Prep HPLC was performed with a mobile phase of 0.1% trifluoroacetic acid in (A) water and (B) acetonitrile (gradient of 0% B to 95% B in 17 min, 95% B to 100% B in 2 min, hold 100% B for 8 min). See <sup>1</sup>H NMR and LC-MS below. This batch of OxPreA was higher purity and reproduced the iron-dependent growth inhibitory effects on *A. baumannii* (**Figure 5.3**).





## 5.7 Figures and Tables

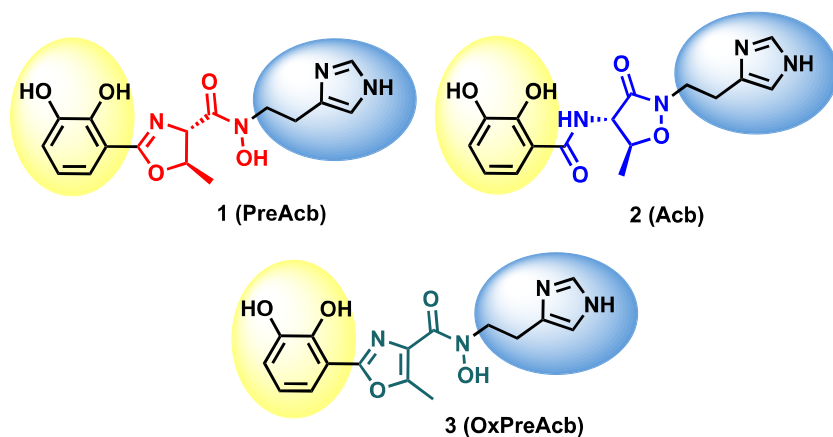
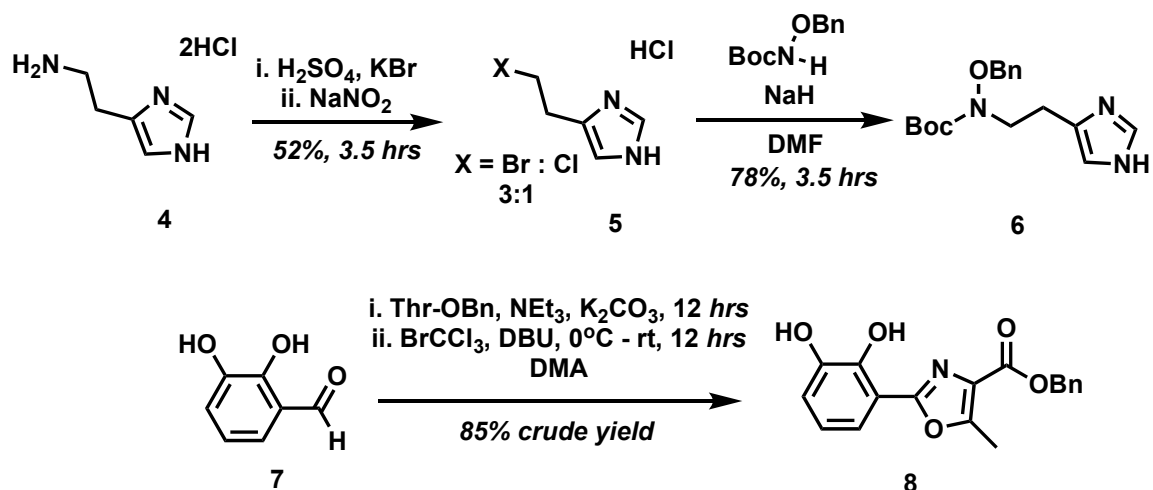
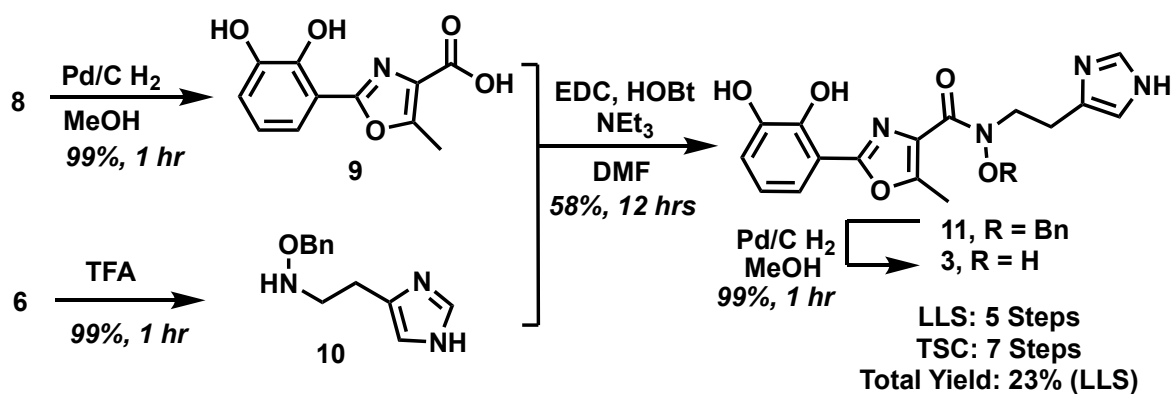


**Figure 5.1.** Structures of pre-acinetobactin (PreAcb, **1**), acinetobactin (Acb, **2**), and oxidized pre-acinetobactin (OxPreAcb, **3**).



Scheme 5.1: Synthesis of precursors to OxPreAcb (3)



Scheme 5.2: Synthesis of OxPreAcb (3)

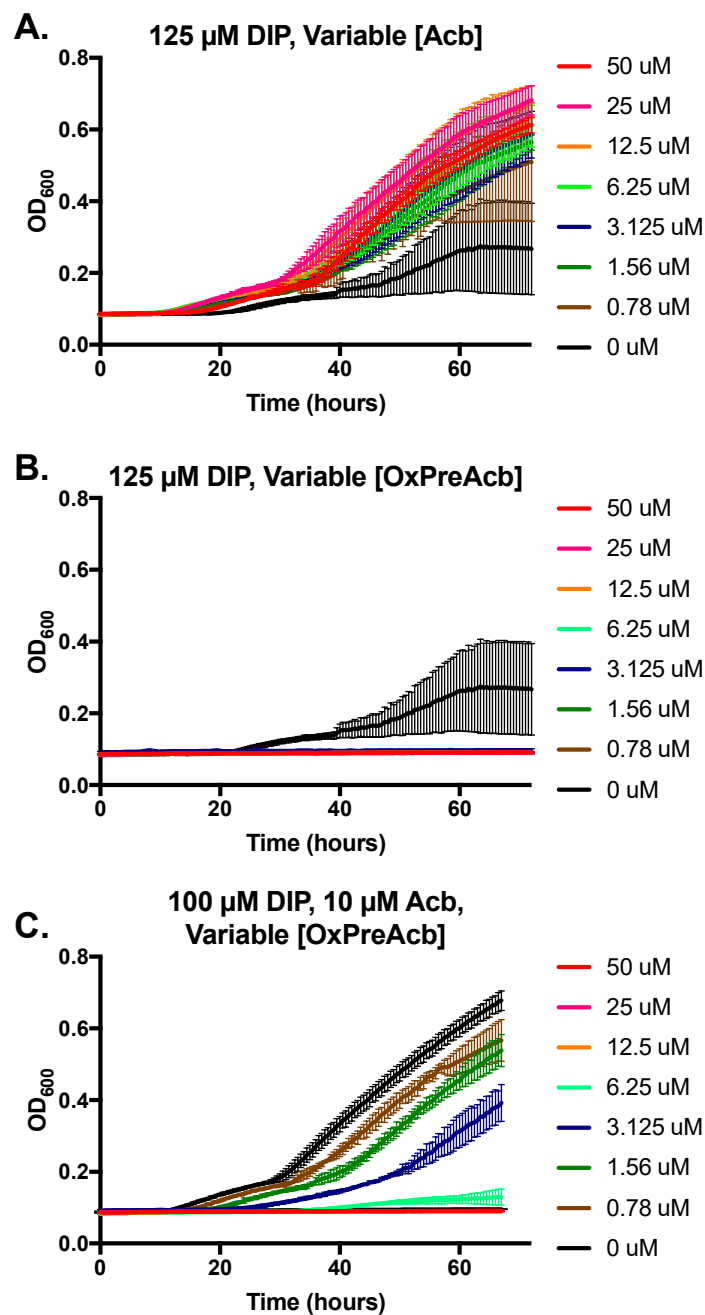


**Figure 5.2.** OxPreAcb (3) competes with Acb (2) to inhibit *A. baumannii* growth. Growth curves of *A. baumannii* ATCC 19606T in M9 minimal medium supplemented with 125 μM 2,2'-dipyridyl (DIP) and gradient concentrations of Acb (A.), 125 μM DIP and gradient concentrations of OxPreAcb (B.), 100 μM DIP, 10 μM Acb, and gradient concentrations of OxPreAcb (C.). Error bars represent s.d. for three independent trials.



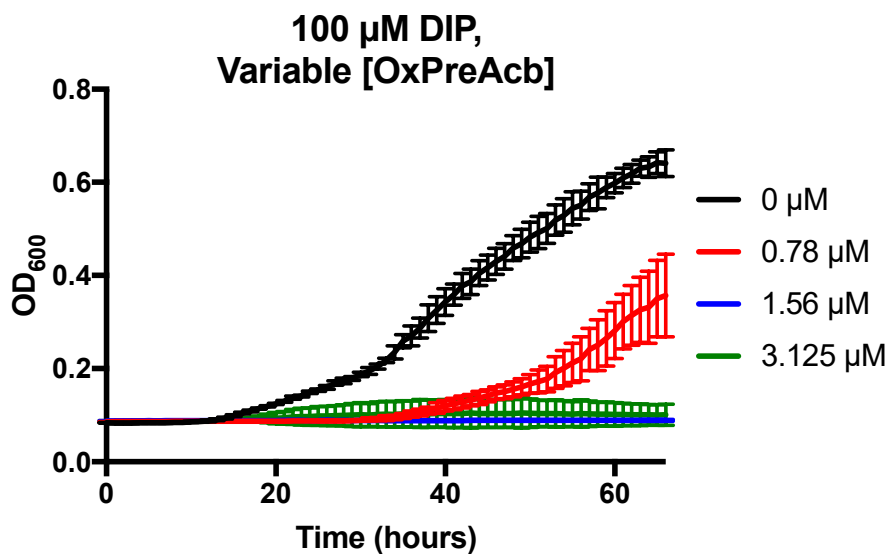


**Figure 5.3. Oxidized pre-acinetobactin (3) is a potent inhibitor of *Acinetobacter baumannii* ATCC 19606T growth in iron (III) controlled M9 minimal media.** By reviewer request, the target compound was isolated to a greater degree of purity to ensure that extra signals from the NMR were not responsible for biological activity. Re-purified compound was then tested under new conditions to give an MIC<sub>90</sub> reading. Compound **3** totally inhibited growth at 1.56  $\mu$ M under these conditions.

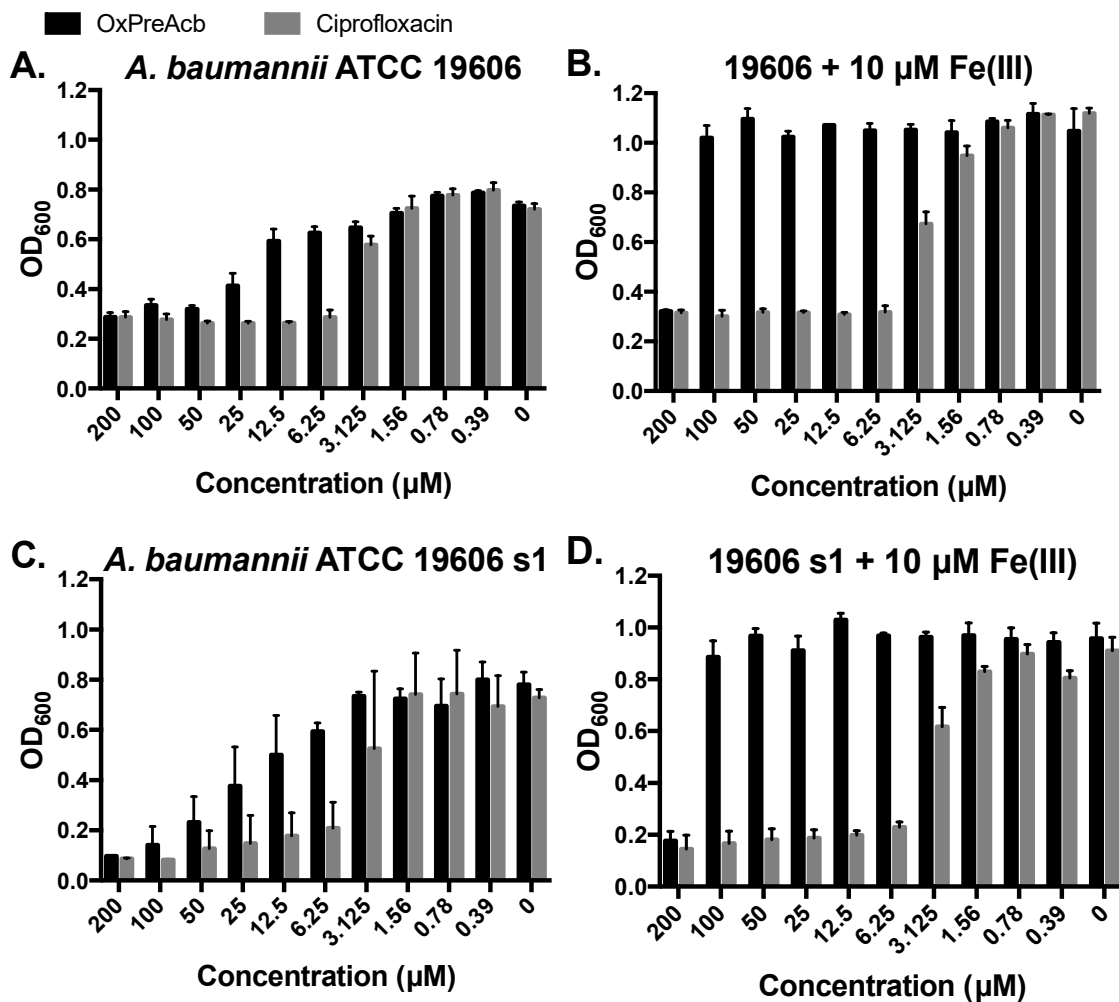
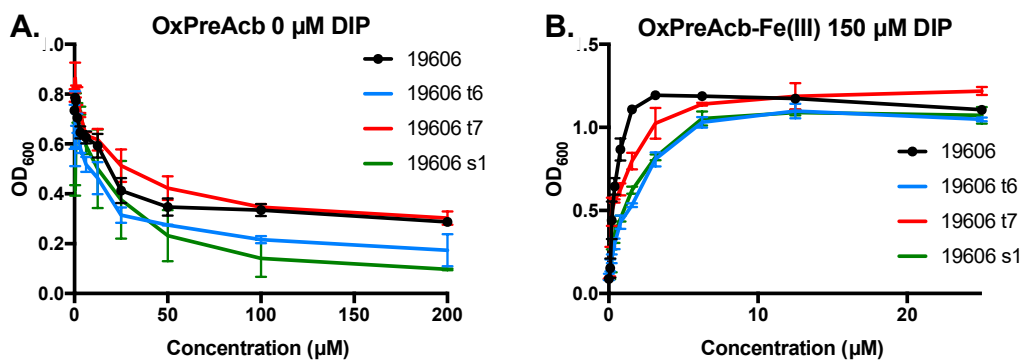


**Figure 5.4.** Growth inhibition by OxPreAcb (3) is attenuated by iron. OD<sub>600</sub> taken at 42 hrs of *A. baumannii* ATCC 19606T and 19606T s1 (Acb biosynthesis mutant) grown in M9 minimal medium supplemented with gradient concentrations of either OxPreAcb (3) (black bars) or ciprofloxacin (grey bars). No DIP was added to the media. (A.) Wild-type *A. baumannii* ATCC 19606T. (B.) Wild-type ATCC 19606T supplemented with 10 μM Fe(acac)<sub>3</sub>. (C.) ATCC 19606T s1. (D.) ATCC 19606T s1 supplemented with 10 μM Fe(acac)<sub>3</sub>. Error bars represent s.d. for three independent trials.



Concentration OxPreAcb (µM)	p-value (t6)	p-value (t7)	p-value (s1)
200	0.4929*	0.4452	0.0001***
100	0.002**	0.4935	0.0127*
50	0.0213*	0.0871*	0.1401
25	0.0450*	0.1042	0.7185
12.5	0.0474*	0.5530	0.3827
6.25	0.0084**	0.6228	0.2429
3.125	0.0252*	0.0095**	0.0068**
1.56	0.4204	0.0211*	0.4948
0.78	0.0053**	0.0941	0.2769
0.39	0.2244	0.0837	0.0001***
0	0.1018	0.0006***	0.2460

Concentration OxPreAcb-Fe(III) (µM)	p-value (t6)	p-value (t7)	p-value (s1)
25	0.0015**	0.0017**	0.3074
12.5	0.0495*	0.7924	0.004**
6.25	0.0016**	0.0112*	0.0072**
3.125	0.0001***	0.0363*	0.0001***
1.56	0.0001***	0.0005***	0.001**
0.78	0.0006***	0.0052**	0.0005***
0.39	0.0006***	0.0432*	0.0023**
0.195	0.0256*	0.5659	0.0033**
0.98	0.7008	0.5602	0.1355
0	0.2917	0.6997	0.1963

All p-values are relative to the wild type strain at equal concentration of added molecule.

\* indicates a difference that is statistically significant.

\*\* indicates a difference that is very statistically significant.

\*\*\* indicates a difference that is extremely statistically significant.

**Figure 5.5. OxPreAcb (3) promotes the growth of *A. baumannii* when complexed with iron (III).**

Endpoint OD<sub>600</sub> measurements taken of bacterial growth of wild-type and mutants of *A. baumannii* ATCC 19606T in M9 minimal media. (A.) Media supplemented with gradient concentrations of oxidized pre-acinetobactin (3). Media contains 0 μM 2,2'-Dipyridyl. Measurements taken at 42 hours. (B.) Media supplemented with gradient concentrations of oxidized pre-acinetobactin (3) Fe(III)-Complex. Media contains 150 μM 2,2'-Dipyridyl. Measurements taken at 48 hours. Error bars represent standard deviations for three independent trials. All p-values and statistical significance are provided below in table format.

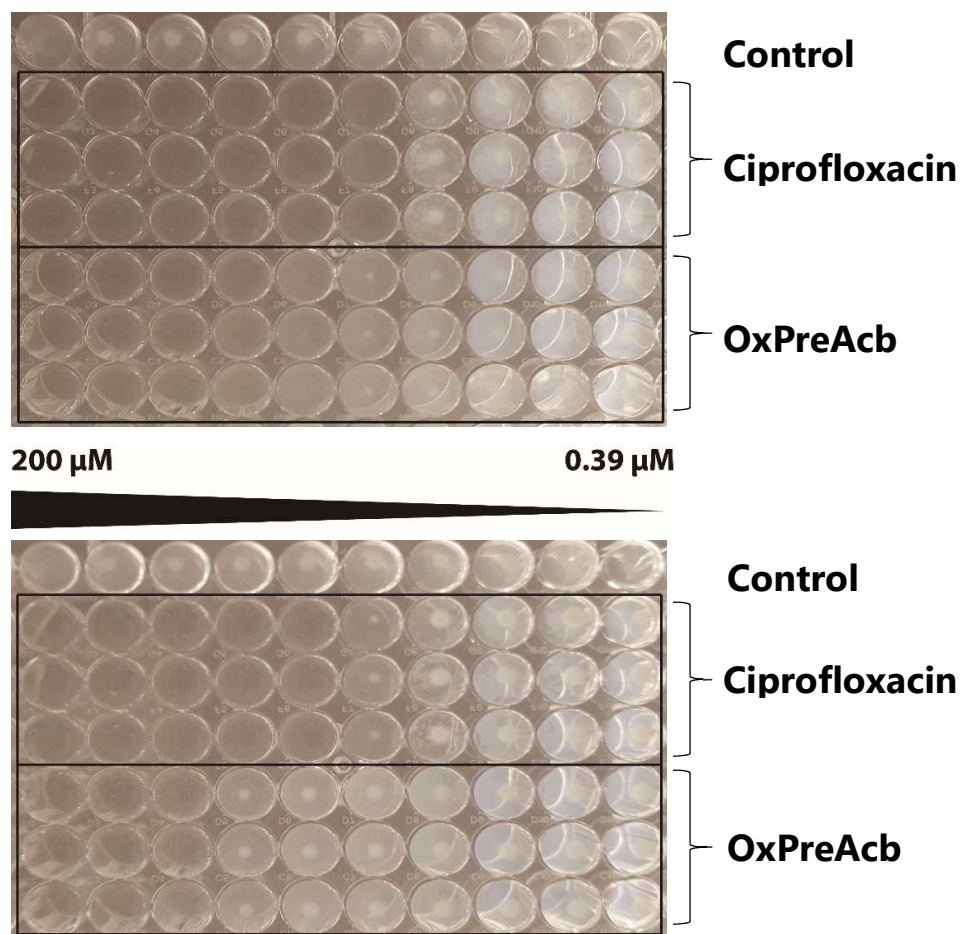


**Figure 5.6. The antibiotic effect of oxidized pre-acinetobactin (3) is bacteriostatic.** Images of 96 well microplates at 42 hours (top) and 72 hours (bottom) showing dose dependent and bacteriostatic antibiotic effect of serially diluted oxidized pre-acinetobactin (3) against *A. baumannii* ATCC 19606T with a ciprofloxacin control. Wells in control rows contain no ciprofloxacin and no oxidized pre-acinetobactin. Growth curve analysis and regrowth studies of cells treated with OxPreAcb suggest no loss of viable *A. baumannii* cells upon treatment with OxPreAcb.

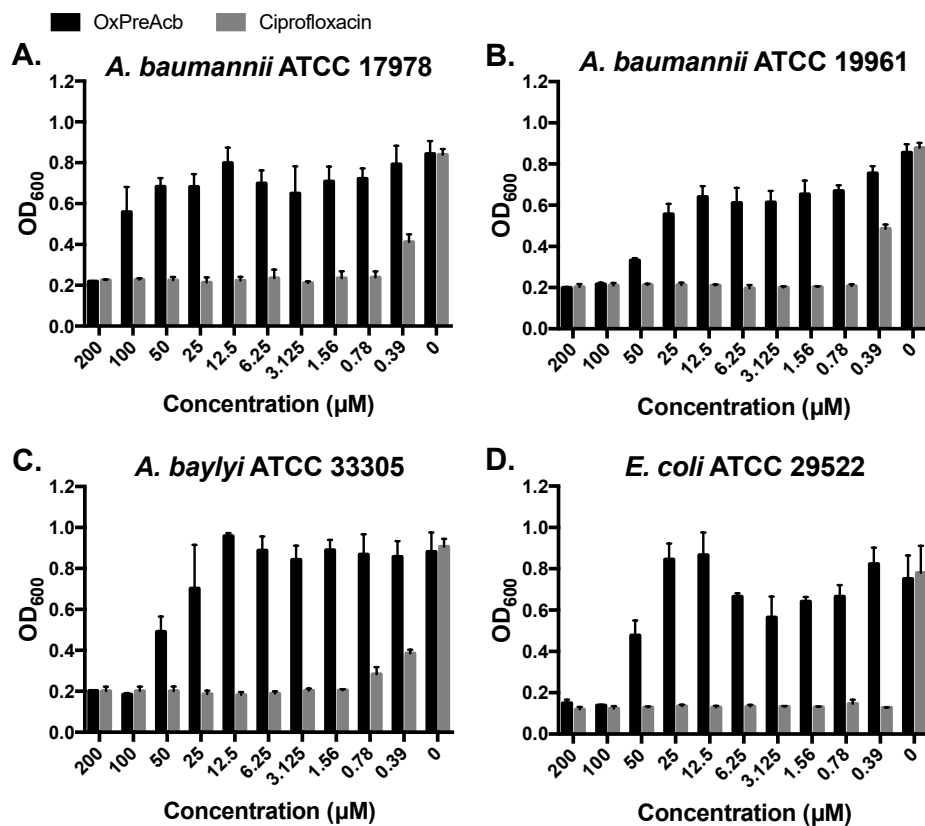


**Figure 5.7. Oxidized pre-acinetobactin (3) is bacteriostatic towards multiple strains of pathogenic *A. baumannii*, as well as environmental *Acinetobacter* and pathogenic *E. coli*.** Endpoint OD<sub>600</sub> measurements taken of bacterial growth in M9 minimal media supplemented with gradient concentrations of either oxidized pre-acinetobactin (3) or ciprofloxacin. (A.) *Acinetobacter baumannii* ATCC 17978. (B.) *Acinetobacter baumannii* ATCC 19961. (C.) *Acinetobacter baylyi* ATCC 33305. (D.) *Escherichia coli* ATCC 29522.

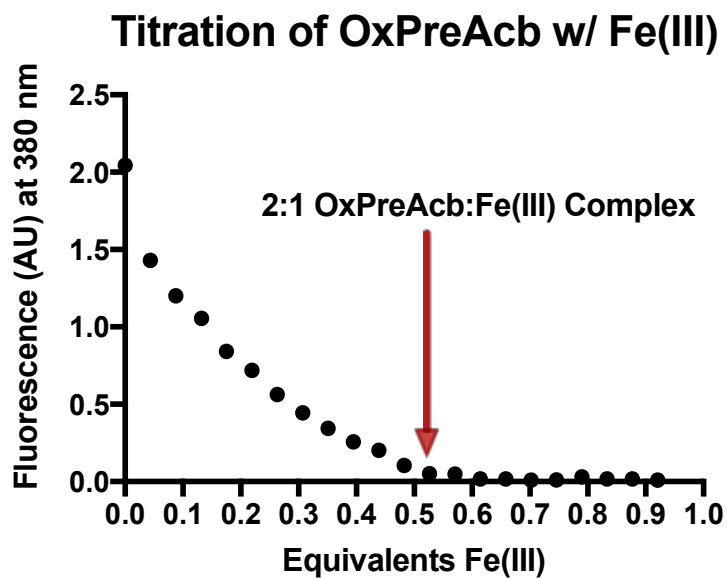


**Figure 5.8. Oxidized pre-acinetobactin (3) forms a stable 2:1 complex with iron (III).** Graph shows the peak absorbance at 380 nm of emission spectra ( $\lambda_{\text{ex}} = 330 \text{ nm}$ ) of **3** ( $570 \mu\text{M}$ ) with increasing quantities of  $\text{Fe}(\text{acac})_3$ .

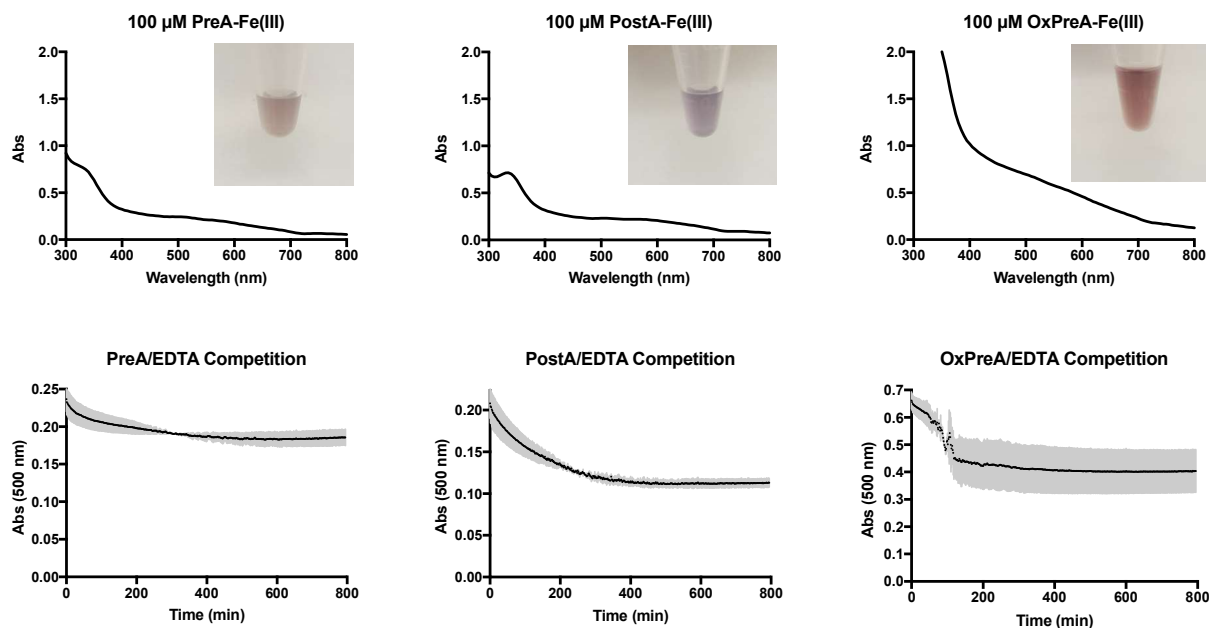


**Figure 5.9. Pre-acinetobactin, acinetobactin, and oxidized pre-acinetobactin all form colored, high-affinity complexes with iron(III).** (A.) UV-Vis spectra of 100 μM pre-acinetobactin (**1**) complexed with iron (III) in 10 μM HEPES buffer. (B.) UV-Vis spectra of 100 μM oxidized pre-acinetobactin (**3**) complexed with iron (III) in 10 μM HEPES buffer. (C.) Kinetic single-wavelength (500 nm) scan of 100 μM pre-acinetobactin (**1**) complexed with iron (III) in HEPES supplemented with 120 μM EDTA. Black line represents average of two independent measurements and grey area represents standard deviation.  $\text{Log}(K_{\text{Fe}})$  calculations provided in Equations 1–11. (D.) Kinetic single-wavelength (500 nm) scan of 100 μM oxidized pre-acinetobactin (**3**) complexed with iron (III) in HEPES supplemented with 120 μM EDTA. Black line represents average of two independent measurements and grey area represents standard deviation.  $\text{Log}(K_{\text{Fe}})$  calculations provided in Equations 1–11. The apparent  $K_{\text{Fe}}$  values for the 2:1 PreAcb, Acb, and OxPreAcb iron(III) complexes were  $27.4 \pm 0.2$ ,  $26.2 \pm 0.1$ , and  $26.5 \pm 0.3$ , respectively.



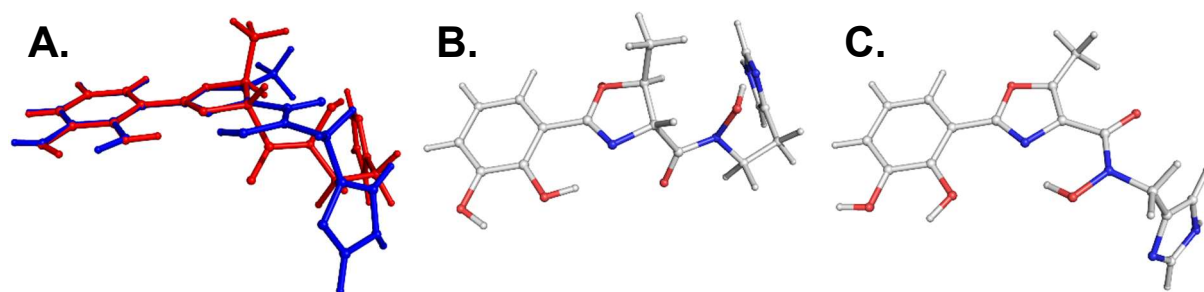


**Figure 5.10. Oxidized pre-acinetobactin is more rigid than pre-acinetobactin.** Gas phase minimum energy calculation structures of (A.) pre-acinetobactin (red) overlaid with oxidized pre-acinetobactin (blue), (B.) pre-acinetobactin, and (C.) oxidized pre-acinetobactin. Pre-acinetobactin forms a stable intramolecular H-bond between the C2-hydroxyl group of the phenyl ring with the oxazoline nitrogen. Oxidized pre-acinetobactin forms a stable H-bond between the hydroxyl group of the hydroxamic acid and the oxazole nitrogen.

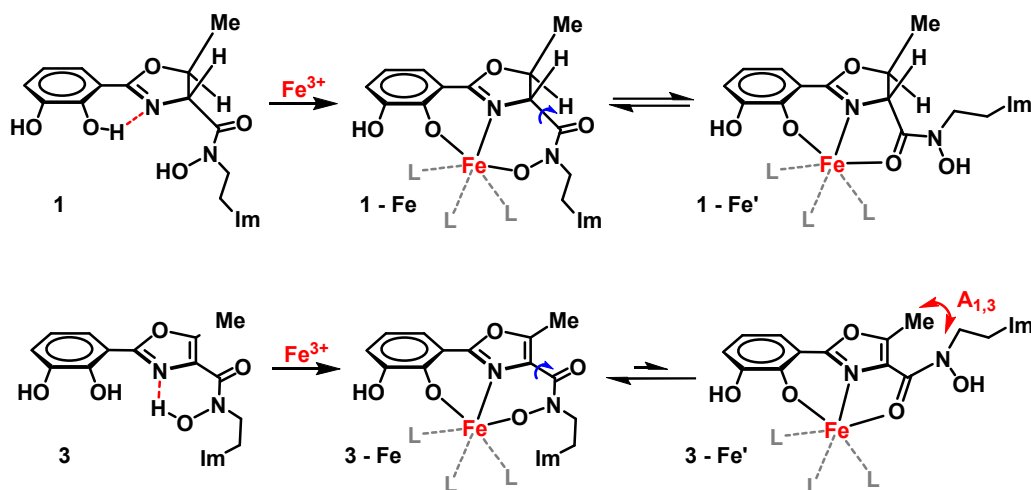


**Figure 5.11. A<sub>1,3</sub> strain induces conformational rigidity.** Energy minimization shows OxPreAcb adopts a planar geometry causing reduced flexibility, which may contribute to antibiotic properties.

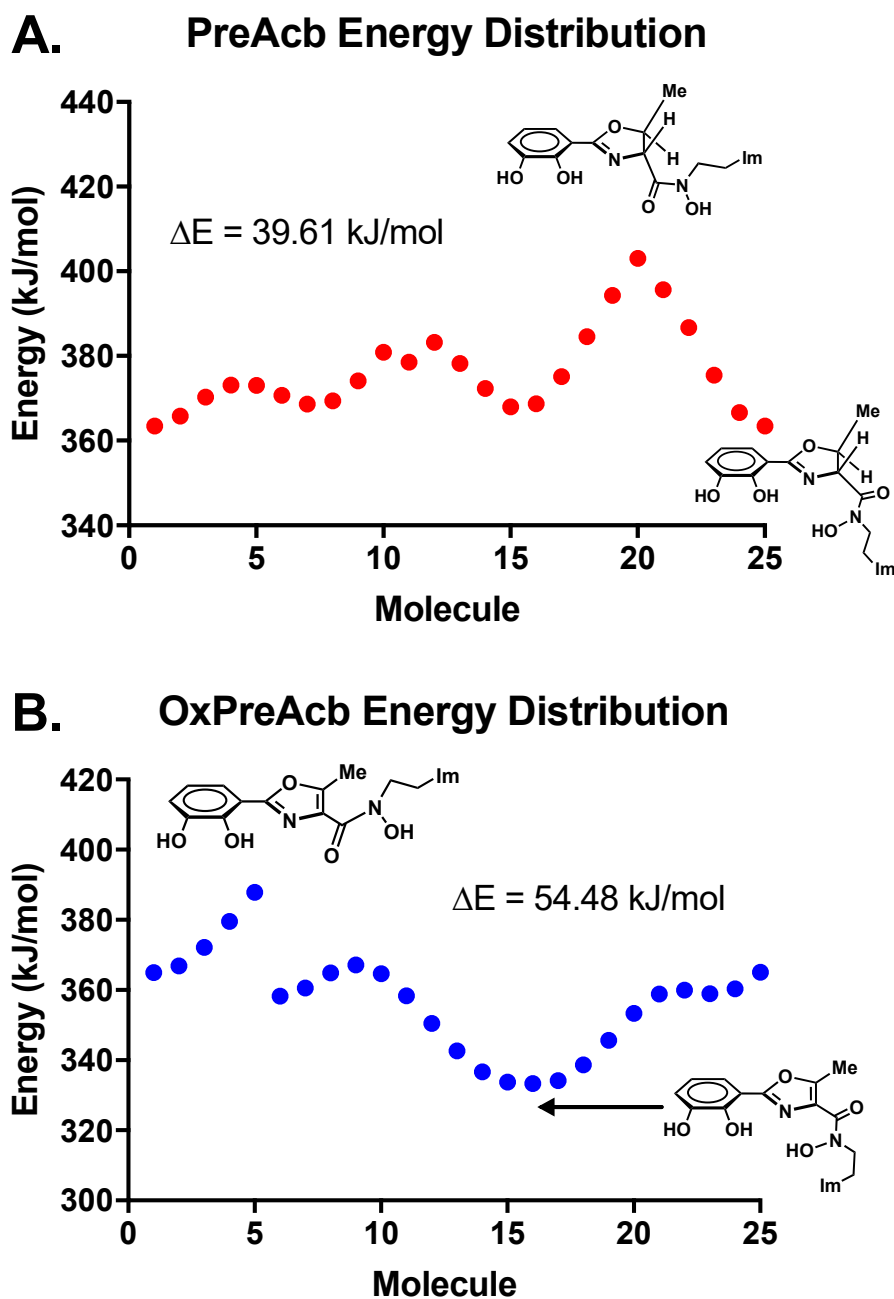


**Figure 5.12. Oxidation of pre-acinetobactin oxazoline to the corresponding oxazole restricts rotation about the heterocycle-carbonyl bond through the introduction of A<sub>1,3</sub> strain. (A.) Energy coordinate diagram for rotation around the oxazoline-carbonyl bond in pre-acinetobactin 1. (B.) Energy coordinate diagram for rotation around the oxazole-carbonyl bond in oxidized pre-acinetobactin 3.**

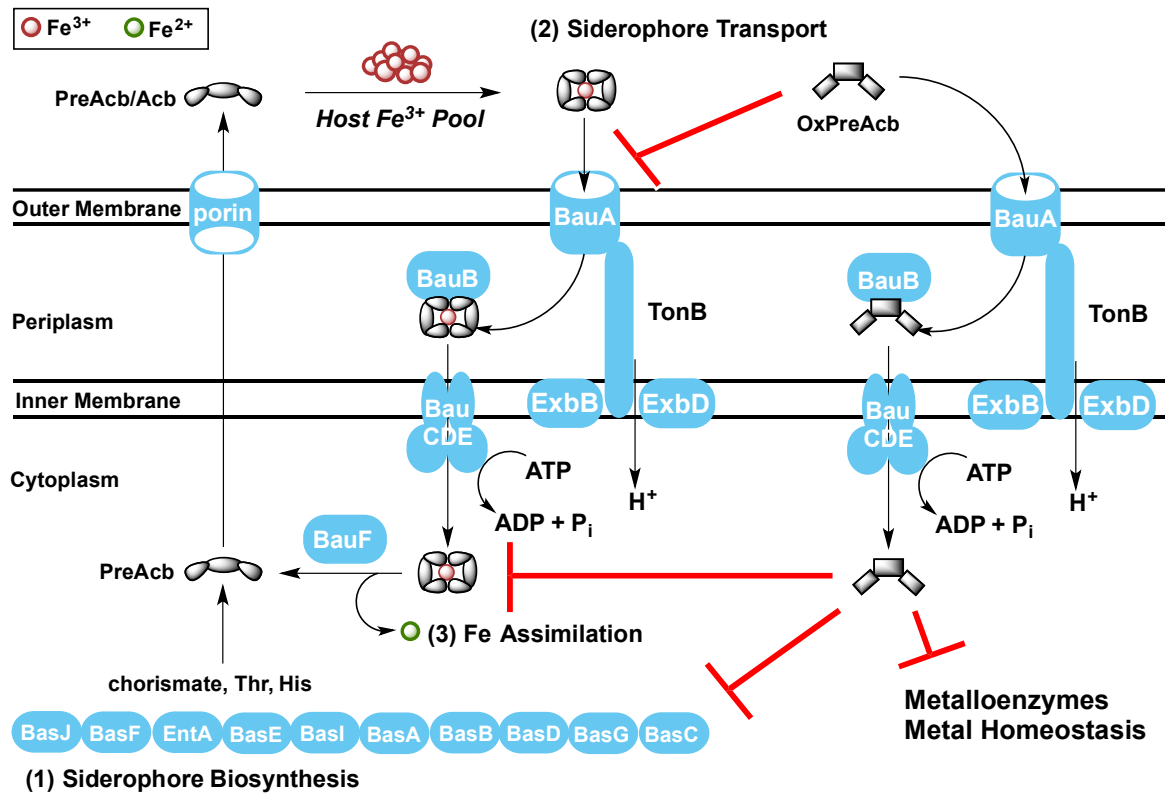


**Figure 5.13. Hypothetical model for the mechanism of action of OxPreAcb growth inhibition of *A. baumannii*.** Biosynthesis of PreAcb takes place in the cytoplasm. Efflux of PreAcb to the extracellular space provides a mixture of PreAcb and Acb after isomerization spontaneously occurs. PreAcb and Acb form stable complexes (PreAcb)<sub>2</sub>Fe(III) and (Acb)<sub>2</sub>Fe(III), respectively, that are transported to the periplasmic space by the outer membrane receptor BauA with assistance of the ExbB/ExbD/TonB complex. The periplasmic binding protein BauB shuttles (PreAcb)<sub>2</sub>Fe(III) and (Acb)<sub>2</sub>Fe(III) to the ABC-transporter BauCDE for transport to the cytoplasm. The flavin reductase BauF is predicted to reduce Fe(III) to Fe(II) and provide PreAcb/Acb for the next siderophore cycle. OxPreAcb is competitive with Acb and inhibits the growth of *A. baumannii*. The mechanism of competition with Acb and growth inhibition is unknown. Competition for transport could take place at the level of BauA on the outside of the cell or BauB on the inside of the cell. Raymond proposed a shuttle mechanism for siderophore transport in

Gram-negative bacteria that argues for the involvement of both an iron-bound siderophore and an iron-free siderophore that undergo metal swapping.<sup>15</sup> The iron-free OxPreAcb might interfere with this siderophore shuttle process, but more fundamental studies of this membrane transport paradigm are required to test this hypothesis. Additionally, OxPreAcb might inhibit siderophore biosynthesis or iron assimilation processes by a competitive mechanism resulting from the structural similarity of OxPreAcb to PreAcb and Acb. Lastly, OxPreAcb was shown to strongly chelate iron(III) so a general mechanism of metalloenzyme inhibition or disruption of metal homeostasis might be at play. This type of more general mechanism might account for the growth inhibitory activity of OxPreAcb against non-Acb producing bacteria like *E. coli*.<sup>16</sup>

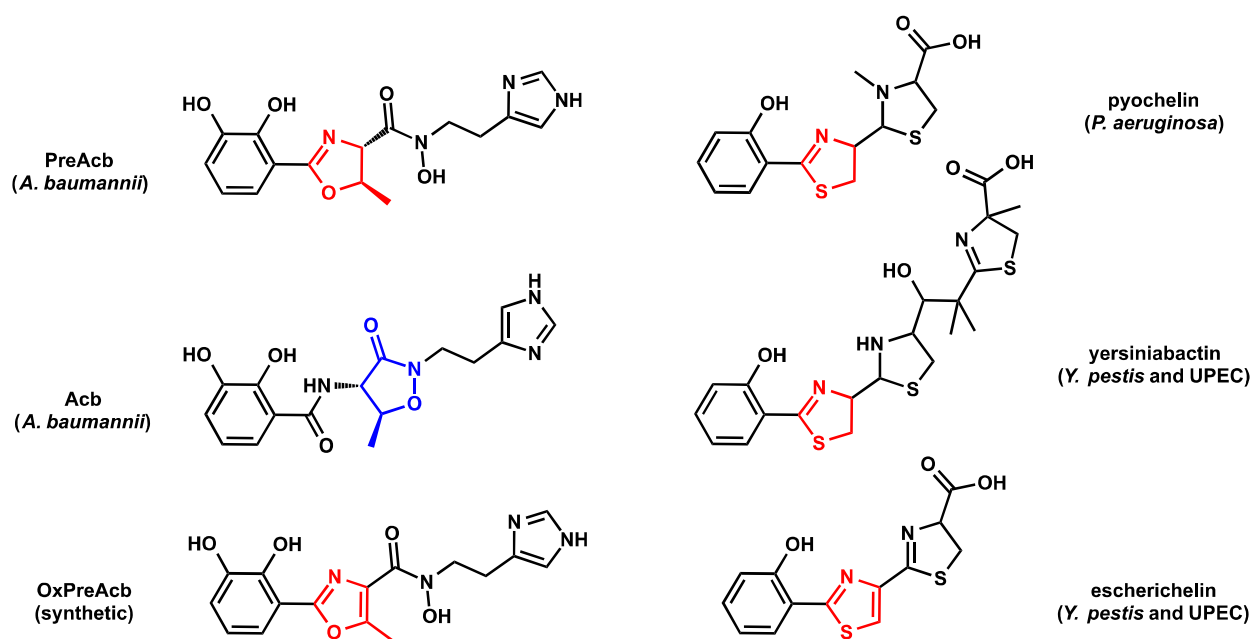


**Figure 5.14. Structures of pre-acinetobactin (PreAcb), acinetobactin (Acb), OxPreAcb, pyochelin, yersiniabactin, and escherichelin.** OxPreAcb and escherichelin both contain rigid aromatic heterocycles and inhibit the growth of pathogenic bacteria producing structurally similar siderophores with non-aromatic heterocycles.

## 5.8 References

- (1) Shapiro J.A.; Wencewicz T.A. *ACS Infect. Dis.* 2016, 2, 157-168. doi: 10.1021/acsinfecdis.5b00145
- (2) Wuest W.M.; Sattely E.S.; Walsh C.T. *J. Am. Chem. Soc.* 2009, 131, 5056-5057. doi: 10.1021/ja900815w
- (3) (a.) Shapiro J. A.; Wencewicz T.A. *Metallomics.* 2017, 9, 463-470. doi: 10.1039/c7mt00064b (b.) Song W.Y.; Jeong D.; Kim J; Lee M.W.; Oh M.H.; Kim K.J. *Org Lett.* 2017 19, 500-503. doi: 10.1021/acs.orglett.6b03671 (c.) Balado M.; Segede Y; Rey D.; Osorio C.R.; Rodriguez J.; Lemos M.L.; Jiménez C. *ACS Chem Biol* 2017, 12, 479-493 doi: 10.1021/acschembio.6b00805
- (4) Liu, Z.; Liu, F.; Aldrich, A. *J. Org. Chem.* 2015, 80, 6545-6552. doi: 10.1021/acs.joc.5b00455
- (5) Mislin, G.; Burger, A.; Abdallah, M. *Tetrahedron.* 2004, 60, 12139-12145. doi: 10.1016/j.tet.2004.10.030
- (6) Mislin, G.; Hoegy, F.; Cobessi, D.; Poole, K.; Rognan, D.; Schalk, I. *J. Mol. Biol.* 2006, 357, 1437-1448. doi: 10.1016/j.jmb.2006.01.080
- (7) Miller D.A.; Luo L.; Hillson N.; Keating T.A.; Walsh C.T. *Chem Biol.* 2002, 9, 333-44. doi: 10.1021/bi002905v
- (8) Ohlemacher, S. I.; Giblin, D. E.; d'Avignon, D. A.; Staple-ton, A. E.; Trautner, B. W.; Henderson, J. P. *J. Clin. Invest.* 2017, Epub ahead of print. doi: 10.1172/JCI92464

- (9) Takeuchi, Y.; Ozaki, S.; Satoh, M.; Mimure, K.; Hara, S.; Abe, H.; Nishioka, H.; Harayama, T. *Chem. Pharm. Bull.* 2010, 58, 1552-1553. doi: 10.1248/cpb.58.1552
- (10) Graham, T. *Org. Lett.* 2010, 12, 3614-3617. doi: 10.1021/ol101346w
- (11) Motoya, T.; Miyashita, M.; Kawachi, A.; Yamada, L. *JPP* 2000, 52, 397-401.
- (12) de Carvalho, C.; Fernandes, P. *Front. Microbiol.* 2014, 5, 1-3.
- (13) Mortensen B.L.; Skaar E.P. *Front. Cell Infect. Microbiol.* 2013, 3, 95. doi: 10.3389/fcimb.2013.00095
- (14) Huggins, D.; Sherman, W.; Tidor, B. *J. Med. Chem.* 2012, 55, 1424-1444. doi: 10.1021/jm2010332
- (15) Stintzi, A.; Barnes, C.; Xu, J.; Raymond, K. *N. Proc. Natl. Acad. Sci. U.S.A.* 2000, 97, 10691-10696. doi: 10.1073/pnas.200318797
- (16) Chan, A. N.; Shiver, L. S.; Wever, W. J.; Razvi, S. Z. A.; Traxler, M. F.; Li, B. *Proc. Natl. Acad. Sci. U.S.A.* 2017, 10, 2717-2722. doi: 10.1073/pnas.1612810114
- (17) Hider, R. C.; Kong, X. *Nat. Prod. Rep.* 2010, 27, 637-657. doi: 10.1039/b906679a

**Chapter 6: Iron Binding Proves to be Crucial  
in Siderophore Cycling Disruption by Oxidized  
Pre-Acinetobactin in Acinetobacter baumannii**

## 6.1 Preface

The abstract of this chapter was adapted in part from [Bohac, T. J., Shapiro, J. A., Wencewicz, T. A.] abstract for ACS national meeting Boston, August 2018. This chapter was adapted in part from manuscript in preparation [Bohac, T. J., Shapiro, J. A., Fang, F, Giblin, D. E. & Wencewicz, T. A.]. TJB synthesized all compounds and performed all compound characterization. JAS performed MIC evaluation of compounds. LF performed growth studies with gallium complex. DEG performed DTF computational work. TAW served as principal investigator and oversaw experimental design and completion.

## 6.2 Abstract

The rise of antibiotic resistance is driving exploration of non-canonical antibiotic approaches, including neutralization of virulence factors. Multi-drug resistant (MDR) Gram-negative pathogens, including *Acinetobacter baumannii*, are of particular concern because of the small number of clinically useful antibiotics available for use. We have previously reported a new method for blocking iron acquisition in MDR *A. baumannii* as an antivirulence strategy using rigid oxazole analogs of the siderophore acinetobactin. All genome sequenced clinical isolates of MDR *A. baumannii* to date possess the capacity for acinetobactin biosynthesis and utilization. Acinetobactin is a primary iron scavenging molecule for *A. baumannii* that is found in two isomeric forms, pre-acinetobactin and acinetobactin, composed of either an oxazoline or isooxazolidinone core, respectively. By oxidizing the oxazoline of pre-acinetobactin to an oxazole, we stabilized this isomeric form providing a molecule that is still capable of forming high affinity 2:1 siderophore:iron(III) complexes and gains cell entry via the acinetobactin uptake pathway. Here we report a comprehensive investigation of acinetobactin structure-function relationships for the oxazoline, oxazole, and isooxazolidinone isomeric forms and show that iron chelation and receptor



binding are critical for biological activity. The oxazole acinetobactin analog is a potent growth inhibitor (MIC values as low as 1  $\mu$ M) of the CDC panel of MDR *A. baumannii* clinical isolates and represents a new lead antivirulence molecule for disrupting siderophore-mediated iron acquisition in this deadly pathogen.

## 6.3 Introduction

Previously, as discussed in Chapter 5, we have synthesized oxidized pre-acinetobactin (OxPreAcb) by conversion of the phenolate-oxazoline moiety to a phenolate-oxazole.<sup>1</sup> We showed that this small structural change resulted in a drastic change in bioactivity, from a growth promotor as PreAcb to a growth inhibitor as OxPreAcb. We hypothesized that this planar structure would be more rigid due to A<sub>1,3</sub> strain and that this rigidity may contribute to the antibiotic properties demonstrated by OxPreAcb. There have been few reports of oxidized siderophore-variants as potential antimicrobials<sup>2</sup>—particularly as it relates to *A. baumannii*. Therefore, studies probing specific structure-activity relationships of these interesting small molecules are of great interest. In this study, we shed light on how OxPreAcb functions and what moieties are critical to inhibitory function. This work establishes structure activity relationships of OxPreAcb that are crucial to further optimization of the drug-like properties of OxPreAcb. We report the synthesis and biological evaluation of a library of OxPreAcb analogs. These analogs demonstrate a direct correlation between iron binding and the ability to inhibit growth.

## 6.4 Results and Discussion

Previous work by our group investigated the structure activity relationship of analogs of pre-acinetobactin and acinetobactin.<sup>3, 4</sup> A panel of ten pre-acinetobactin and nine corresponding acinetobactin analogs were synthesized. These analogs explored the effect of hydroxyl group

positioning on the aromatic catechol on the left hand side of the molecule, the chain length and influence of the imidazole group on the right hand side of the molecule, and the role of the hydroxamate hydroxyl group on bioactivity and iron binding. The features of these analogs probed the ability of the compound to bind iron, the ability to promote growth and the rate of isomerization. The findings of this study highlighted the necessity of the 2'-hydroxyl group for both iron (III) binding as well as growth promotion in the pre-acinetobactin form, while the hydroxamate hydroxyl group and the presence of the imidazole ring were seen to influence the rate of isomerization. In the acinetobactin form, both the 2'- and 3'- hydroxyl groups were crucial in iron (III) binding and growth promotion ability of the compound (**Figure 6.1**).

Equipped with the knowledge from our SAR studies on pre-acinetobactin and acinetobactin, we aimed to investigate OxPreAcb in a similar manner. The three parts of the OxPreAcb molecule that were of interest to us were: (1) the necessity and positioning of the hydroxyl groups on the aromatic ring of OxPreAcb, (2) the necessity of the imidazole ring, and (3) the necessity of the hydroxamate hydroxyl group. We probed the role of these moieties through the synthesis of OxPreAcb and 8 structural analogs generated from various commercially available substituted benzaldehydes (**Scheme 6.1**). The modularity and convergent nature of the synthesis allows for ease of diversification, as starting with various commercially available benzaldehydes provides diversification around the left hand aromatic ring, while compounding of various amines affords diversification on the right hand side of the molecule. Starting with the corresponding benzaldehyde, the addition of L-threonine benzyl ester, followed by the oxidation of the intermediate oxazoline, provided the corresponding oxazole benzyl esters. Hydrogenolysis of the benzyl ester afforded the corresponding carboxylic acids that when exposed to EDC, HOBt coupling with various amines, in the presence of facilitating base, afforded compound **2**, along

with the benzyl protected OxPreAcb **1** and compounds **3-9**. Final deprotection of these intermediates with H<sub>2</sub> and Pd/C delivered title compounds **1, 3-9** in good yield (38-63%).

It has been hypothesized that OxPreAcb utilizes the Acb uptake pathway and that the ability of OxPreAcb to bind iron (III) is instrumental to the mode of action. Therefore, with the panel of analogs in hand, the ability of each analog to bind iron (III) was explored through a chrome azurol S assay (CAS) (**Figure 6.2**). Compounds **1** and **3-6** demonstrated iron binding ability. As compound **3** lacks the imidazole group on the right hand side of the molecule, and is instead replaced with a butane group, its ability to bind iron(III) demonstrates that the presence of the imidazole group is not necessary for metal chelation. Compounds **3-6** each contain a hydroxyl group in the 2'- position, while compounds **5** and **6** contain an additional hydroxyl group in the 5'- or 4'- position respectively. The ability for all three of these compound to bind iron(III) indicated the necessity for the 2'- hydroxyl group, while the presence or position of an additional hydroxyl group seems no have no influence on metal bonding (**Table 6.1**). Taken collectively, all the compounds with iron binding capabilities contained both a 2'-hydroxyl group, as well as the hydroxamate hydroxyl group, deeming these groups crucial for metal chelation ability. These results complement our group's previous finding that the oxidized system of OxPreAcb adopts a planar geometry and was predicted to bind iron with these two hydroxyl moieties. We hypothesized that this binding mode was favored over binding iron through the 2'-hydroxyl and the carbonyl oxygen due to A<sub>1,3</sub> strain induced between the methyl group and the hydroxamate substituents (hydroxyl group or imidazole ring) (**Figure 6.3**). This A<sub>1,3</sub> strain is not as severe in the natural pre-acinetobactin siderophore due to the *trans* orientation between the methyl and hydroxamate groups.

To test the inhibitory effect of our analogs, MIC<sub>90</sub> values were obtained through growth studies in iron restricted minimal media. Briefly, OxPreAcb analogs were serially diluted in M9 media supplemented with 100µM DIP. MIC<sub>90</sub> values were read as the lowest concentration at which no visible growth was observed. Compounds **2** and **7-9** all provided MIC values >200; analog **2** does not contain the hydroxymate hydroxyl group, while analogs **7-9** are the 3'-OH, benzyl and 2,3-dimethoxy analogs, respectively. Interestingly, these four analogs are all of the analogs with a negative CAS result and inability to bind iron(III) (**Table 6.1**). This finding indicates that iron binding is crucial to the mode of action leading to growth inhibition. Compounds **1** and **3-6** all inhibited growth with MIC values as low as 0.78 µM, again correlating directly with the ability of the molecule to chelate metal. Compound **3** demonstrated that the presence of the imidazole ring is not required for iron binding (positive CAS result) nor for growth inhibition (MIC value 1.56µM), signifying the right hand side of the molecule as a potential site for further derivatization.

With these compounds in hand, we sought to explore the ability of these analogs to utilize and interact with the siderophore uptake pathway. Preacintobactin and acinetobactin are known to be transported through TonB-dependent outer membrane transport protein, BauA. Recently, Naismith and coworkers resolved an interesting crystal structure of a holo-PreAcb/Acb complex bound to BauA.<sup>5</sup> Once in the periplasm, periplasmic siderophore binding protein, BauB, directs the siderophore-iron complex to the inner membrane ABC-transport protein, BauCDE. As discussed in Chapter 2, a crystal structure of Acb<sub>2</sub>Fe-BauB complex highlighted the binding mode of Acb-iron and matched that was predicted by DFT calculations.<sup>6</sup> With expressed and purified BauB in hand, we performed fluorescence quenching assays of the small molecule to BauB to determine BauB binding affinities for the natural compound along with the analogs (**Figures 6.4,**

**6.5 & Table 6.1).** All molecules possessing a substituent in the 2'- position of the ring on the right hand side of the molecule were able to bind BauB with nM affinities; notably, molecules **7** and **8** which lack a 2'- substituent failed to bind BauB. This finding indicates the necessity of a substituent (hydroxyl or methyl ester) to be the 2'- position of the right hand catechol ring, which is likely needed for hydrogen bonding to the protein binding site. We determined the binding affinities for both the iron free (apo) and iron bound (holo) forms of the natural siderophores Acb and Fims, in addition to OxPreAcb and analogs, as relevant references to natural BauB binding. In the holo form, OxPreAcb has the lowest BauB binding affinity, suggesting that OxPreAcb can interact with and can potentially outcompete with the natural siderophores for the siderophore pathway.

With lead compound OxPreAcb in hand, we sought to investigate the how effective this compound inhibited the growth of clinically relevant bacterial strains; thus, we performed growth studies of OxPreAcb against 13 clinical strains of *A. baumannii* obtained from the CDC AR-BANK. These clinical isolates have various number of resistances genes (5-14 antibiotic genes) and serve as a representation of clinically relevant multidrug resistant *A. baumannii*. The MIC<sub>90</sub>'s and susceptible – intermediate – resistant (S-I-R) interpretation of these isolates against 21 common antibiotics are obtained by the CDC and listed in **Figure 6.6**. OxPreAcb showed inhibition of all 13 strains as low as 1.56µM at 17 hours and as low as 6.25µM at 40 hours (**Table 6.2**), demonstrating the potential for OxPreAcb to treat clinical multidrug resistant infections. The increase in MIC<sub>90</sub> values at 17 hours to 40 hours and the growth recovery over time is consistent with our previous hypothesis that OxPreAcb works in a bacteriostatic manner.

We determined the relative cytotoxicity using a lactose dehydrogenase (LDH) release assay of OxPreAcb to healthy stable cell type, mammalian cells, and found OxPreAcb to be non-

cytotoxic, with LDH release of 1.379% at 100 $\mu$ M concentration OxPreAcb (**Figure 6.7**). Cytotoxicity was determined through average lactate dehydrogenase release in madin-darby canine kidney cells. This low toxicity is encouraging and serves as grounds to warrant further investigation and optimization of OxPreAcb and oxidized siderophore scaffolds as a general ant virulence approach.

To help elucidate the mechanism of action of OxPreAcb, we sought to determine whether disruption of the siderophore is in fact the target or if OxPreAcb plays a role in general disruption of metal homeostasis or metalloenzyme inhibition within the cell. In order to explore this possibility, the OxPreAcb-Ga complex was synthesized. Gallium has been reported to have antibacterial activity when conjugated to both protoporphyrin IX (potent activity against Gram-negative and Gram-positive bacteria)<sup>7</sup> as well as siderophores such as deferoxamine mesylate (activity against *P. aeruginosa*).<sup>8</sup> Further, as gallium serves as a mimic of iron, gallium fails to be reduced in cells and therefore upon reaching the cytoplasm, siderophore-gallium conjugates would fail to be reduced, thus preventing release of free metal and recycling of the siderophore. Initial growth studies of OxPreAcb-Ga against *A. baumannii* ATCC17978 in M9 minimal media with supplemented DIP showed complete growth inhibition at all concentrations (**Figure 6.8**). This inhibition of activity by OxPreAcb-Ga, however, can be recovered in a dose-dependent manner upon the addition of Fim-Fe, Acb<sub>2</sub>-Fe or OxPreAcb-Fe. This growth recovery upon siderophore addition indicates that OxPreAcb-Ga was not merely a general toxic effect from the presence of Ga but instead points to pathway competition of OxPreAcb-Ga and *A. baumannii* siderophore and supports the theory that OxPreAcb disrupts the siderophore pathway, as opposed to disrupting metal homeostasis (**Figure 6.9 & 6.10**). Further evidence that OxPreAcb utilizes the siderophore

pathway is shown in the ability of OxPreAcb-Ga binding to BauB with similar affinity to that of the natural siderophores (**Figure 6.11**).

## 6.5 Outlook and Conclusions

In summary, we generated, characterized, and evaluated eight structural analogs of previously reported OxPreAcb to identify structure-activity-relationships related to iron binding, growth inhibition, and periplasmic binding protein affinity (BauB). Studies show a direct correlation between inhibition and ability to bind iron. Additionally, the right hand portion of the molecule was identified as a potential site for further diversification, as the presence of the imidazole tail did not have an effect on iron binding ability nor growth inhibition ability. Moreover, growth inhibitions studies with (OxPreAcb)<sub>2</sub>-Ga and corresponding growth recovery promoted by known, iron-bound *A. baumannii* siderophores suggests a competition of OxPreAcb with the natural system (**Figure 6.12**). BauB binding assays highlight the ability of OxPreAcb analogs to bind to this protein, provided the analog possesses a substituent (hydroxyl or methoxy) in the 2'-position. In conclusion, through the presented studies, we have identified promising candidates, with low cytotoxicity and potent inhibitory activity across a panel of highly resistant *A. baumannii* clinical isolates, which merit further study and evaluation as lead compounds for the treatment of MDR *A. baumannii* infections.

## 6.6 Materials and Methods

### *Strains, Materials, and Instrumentation*

Growth studies for the oxidized pre-acinetobactin analog panel were conducted using *A. baumannii* ATCC 19606<sup>T</sup> provided by Dr. Luis Actis. Growth studies for oxidized pre-acinetobactin against clinical strains were conducted using *A. baumannii* AR-BANK #0273,

#0275, #0278, #0284, #0287, #0290, #0293, #0296, #0299, #0302, #0305, #0308, #0311 from the Antimicrobial Resistance Bank (collected by the CDC and FDA), provided to us by Dr. Gautam Dantas. Precultures and 96-well plate *A. baumannii* growth assays were performed in filter-sterilized M9 minimal media. Samples for LC-MS were prepared in 0.45  $\mu$ M PTFE mini-UniPrep vials from Agilent. All preparatory HPLC was performed using a Beckman Coulter SYSTEM GOLD 127P solvent module and 168 detector with a Phenomenex Luna 10u C18(2) 100A column, 250  $\times$  21.20 mm, 10  $\mu$ m with guard column. Prep HPLC was performed with a mobile phase of 5 mM ammonium acetate in (A) water and (B) acetonitrile, and data were processed using 32 Karat software, version 7.0. All LC-MS was performed on an Agilent 6130 quadrupole LC-MS with G1313 autosampler, G1315 diode array detector, and 1200 series solvent module. A Phenomenex Gemini C18 column, 50  $\times$  2 mm, 5  $\mu$ m with guard column was used for all LC-MS separations. LC-MS mobile phases were 0.1% formic acid in (A) water and (B) acetonitrile, and data were processed using G2710 ChemStation software. NMR was performed on a Varian Unity Inova-600 MHz instrument with a cold probe. Bacterial growth studies were performed using polystyrene 96-well plates with polystyrene lids.

### ***CAS Assay***

CAS agar plates were prepared as described previously.<sup>1,3,4</sup> Wells were made in the solid agar, and 50  $\mu$ L each of 100  $\mu$ M solutions of oxidized pre-acinetobactin analogs in M9 minimal media (diluted from calibrated DMSO-d<sub>6</sub> stocks) were pipetted into the wells. Color change was observed after 4 hours.

### ***A. baumannii Growth Studies in Minimal Media***

M9 minimal media was made as described previously.<sup>3</sup>

### **Analog Panel:**



Solutions of 800  $\mu\text{M}$  oxidized pre-acinetobactin analogs in M9 media were filter sterilized. 96-well plates were filled with 50  $\mu\text{L}$  of M9 minimal media per well. Into the first column, 50  $\mu\text{L}$  of analog was added and columns were serially diluted down to 0.39  $\mu\text{M}$ . An inoculum was made by adding 200  $\mu\text{L}$  of a 0.5 McFarland standard of *A. baumannii* ATCC 19606<sup>T</sup> to 29.8  $\mu\text{L}$  of 200  $\mu\text{M}$  2,2'-dipyridyl in M9 minimal media. Inoculum (50  $\mu\text{L}$ ) was added to each well for a final concentration of 100  $\mu\text{M}$  2,2'-dipyridyl and a serial dilution of 200  $\mu\text{M}$ -0.39  $\mu\text{M}$  analog. An MIC<sub>90</sub> was read visually as the concentration at which no growth was observed and recorded at 72 hours.

#### **Clinical Strain Panel:**

A solution of 800  $\mu\text{M}$  oxidized pre-acinetobactin in M9 media was filter sterilized. 96-well plates were filled with 50  $\mu\text{L}$  of M9 minimal media per well. Into the first column, 50  $\mu\text{L}$  of oxidized pre-acinetobactin was added and columns were serially diluted down to 0.39  $\mu\text{M}$ . For each AR-BANK strain described in the above section, an inoculum was made by adding 200  $\mu\text{L}$  of a 0.5 McFarland standard to 29.8  $\mu\text{L}$  of 200  $\mu\text{M}$  2,2'-dipyridyl in M9 minimal media. Inoculum (50  $\mu\text{L}$ ) was added to each well for a final concentration of 100  $\mu\text{M}$  2,2'-dipyridyl and a serial dilution of 200  $\mu\text{M}$ -0.39  $\mu\text{M}$  analog. An MIC<sub>90</sub> was read visually as the concentration at which no growth was observed and recorded at 17 hours and 40 hours.

#### **OxPreAcb-Ga growth studies in *A. baumannii* ATCC 17978:**

For biological assessment of OxPreAcb-Ga under iron-restrictive conditions, stock solutions of 10 mM of OxPreAcb-Ga were prepared in DMSO. A 96-well plate was filled with 50  $\mu\text{L}$  of M9 minimal media per well. These stock solution were diluted adding 20  $\mu\text{L}$  of 10 mM OxPreAcb-Ga stock to 180  $\mu\text{L}$  of M9 minimal media, affording a 1 mM stock solutions. 50  $\mu\text{L}$  of OxPreAcb-Ga 1 mM stock solutions were added to the first row of a 96 well plate. Compound was serially diluted down the plate to 7.8  $\mu\text{M}$ . An inoculum was made by adding 100  $\mu\text{L}$  of 0.5

McFarland standard (*A. baumannii* ATCC 17978) to 4.0 mL of M9 minimal media supplemented with 350  $\mu\text{M}$  2,2'-dipyridyl. Inoculum (50  $\mu\text{L}$ ) was added to each well for a final concentration of 175  $\mu\text{M}$  2,2'-dipyridyl and a serial dilution of 250-7.8  $\mu\text{M}$  OxPreAcb-Ga. Growth promotion was determined as compared to a control with 175  $\mu\text{M}$  2,2'-dipyridyl, 0  $\mu\text{M}$  OxPreAcb-Ga. All experiments were performed in triplicate.

#### **Combination studies of OxPreAcb-Ga and Fim-Fe, Acb-Fe or OxPreAcb-Fe:**

For the biological evaluation of combinations of OxPreAcb-Ga and Fim-Fe, Acb-Fe or OxPreAcb-Fe, a 96-well plate was filled with 50  $\mu\text{L}$  of M9 minimal media per well. 2.5  $\mu\text{L}$  of 10 mM OxPreAcb-Fe or Fim-Fe was added into 197.5  $\mu\text{L}$  M9 minimal media to make 125  $\mu\text{M}$  stock solution. For Acb-Fe, 3.3  $\mu\text{L}$  of 7.6 mM Acb-Fe was added into 196.7  $\mu\text{L}$  M9 minimal media to make 125  $\mu\text{M}$  stock solution. 50  $\mu\text{L}$  of Fim-Fe, Acb-Fe or OxPreAcb-Fe was added to the first row of a 96 cell plate. Compounds were serially diluted down the plate to 0.975  $\mu\text{M}$ . 4.68  $\mu\text{L}$  of 10 mM OxPreAcb-Ga was added to 115.32  $\mu\text{L}$  M9 minimal media to make 0.39  $\mu\text{M}$  stock solution. 2  $\mu\text{L}$  of 0.39  $\mu\text{M}$  OxPreAcb stock solution was added to each well of 96-well plate. An inoculum was made by adding 100  $\mu\text{L}$  of 0.5 McFarland standard (*A. baumannii* ATCC 17978) to 4.0 mL of M9 minimal media supplemented with 350  $\mu\text{M}$  2,2'-dipyridyl. Inoculum (50  $\mu\text{L}$ ) was added to each well for a final concentration of 175  $\mu\text{M}$  2,2'-dipyridyl, 7.8  $\mu\text{M}$  OxPreAcb-Ga and a serial dilution of 31.25-0.975  $\mu\text{M}$  iron compounds. Growth promotion was determined as compared to a control with 175  $\mu\text{M}$  2,2'-dipyridyl, 0  $\mu\text{M}$  OxPreAcb-Ga. All experiments were performed in triplicate.

#### ***BauB Fluorescence Quenching Studies***

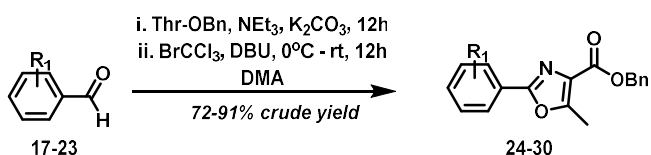
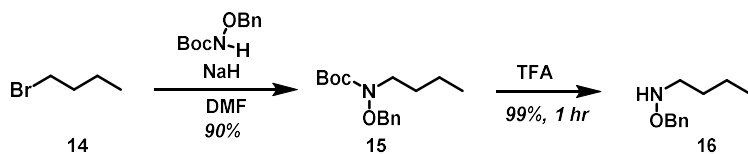
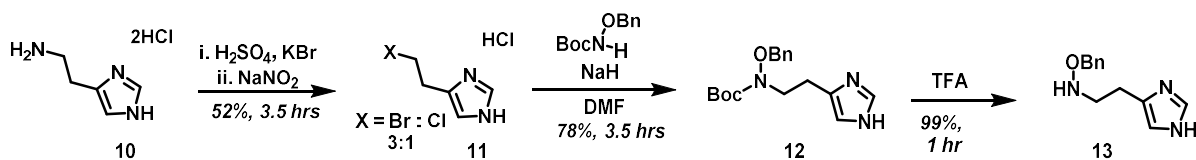
BauB fluorescence quenching experiments were performed as previously reported.<sup>6</sup> Briefly, a 183  $\mu\text{M}$  bead of protein BauB-ss was thawed and diluted ten-fold in TBS buffer to afford

a 18.3  $\mu\text{M}$  stock solution. This stock solution was then diluted again to provide a 400 nM stock solution. 300  $\mu\text{L}$  of the 400 nM stock solution was transferred to a fluorescence cuvette. A stock solution of 400 nM protein and 16  $\mu\text{M}$  small molecule was made.

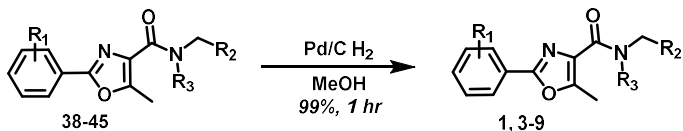
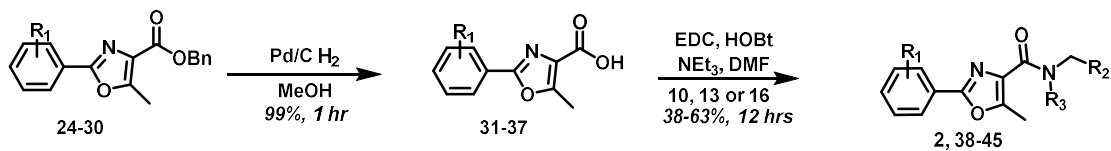
An emission spectrum was taken at each concentration as an average of 3 scans. Excitation wavelength of 280 nm, fluorescence observed between 300 and 400 nm. Slit width was set to 10 nm with a scan speed of 400. Fluorescence at 320 nm was tracked as a function of small molecule concentration. All measurements were performed in duplicate.

Fluorescence spectra were taken of 400 nM protein with the following concentrations of small molecule: 0 nM, 106.8 nM, 212.8 nM, 318.0 nM, 422.4 nM, 684.0 nM, 1196.0 nM, 1688.0 nM, 2644.0 nM and 3536.0 nM.

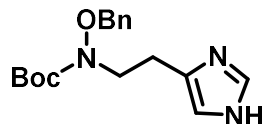
## Compound Synthesis



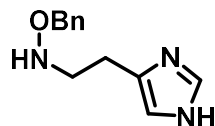
Compound	R <sub>1</sub>
17, 24, 31	2,3-di-OH
18, 25, 32	2-OH
19, 26, 33	2,5-di-OH
20, 27, 34	2,4-di-OH
21, 28, 35	4-OH
22, 29, 36	H
23, 30, 37	2,3-di-OMe



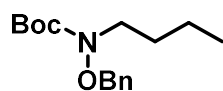
Compound	R <sub>1</sub>	R <sub>2</sub>	R <sub>3</sub>
38	2,3-di-OH		OBn → OH (OxPreA, 1)
2	2,3-di-OH		H (2)
39	2,3-di-OH		OBn → OH (3)
40	2-OH		OBn → OH (4)
41	2,5-di-OH		OBn → OH (5)
42	2,4-di-OH		OBn → OH (6)
43	4-OH		OBn → OH (7)
44	H		OBn → OH (8)
45	2,3-di-OMe		OBn → OH (9)



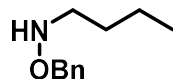
**Compound 12** was synthesized and characterized as previously reported by our group.<sup>3</sup>



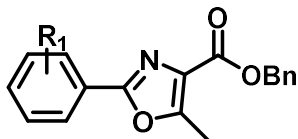
**Compound 13** was synthesized through the *N*-Boc removal of *N*-Boc-*O*-benzylhydroxylamine (**12**). 20mg of **12** was dissolved in 5 mL of neat TFA. Reaction stirred for 1 hr, monitored by LC-MS. Upon verification of completion, TFA was removed by rotary evaporation under reduced pressure to afford the TFA salt of *O*-benzylhydroxylamine **13** in quantitative yield. Compound **13** was used without purification or characterization.



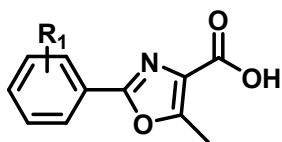
**Compound 15** was synthesized and characterized as previously reported by our group.<sup>4</sup>



**Compound 16** was synthesized through the *N*-Boc removal of *N*-Boc-*O*-benzylhydroxylamine (**15**). 20mg of **15** was dissolved in 5 mL of neat TFA. Reaction stirred for 1 hr, monitored by LC-MS. Upon verification of completion, TFA was removed by rotary evaporation under reduced pressure to afford the TFA salt of *O*-benzylhydroxylamine **16** in quantitative yield. Compound **16** was used without purification or characterization.

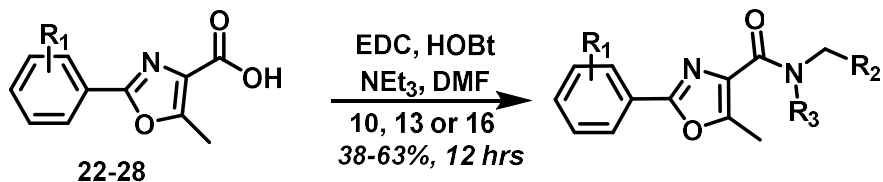


**General Procedure A.** The synthesis of oxazole benzyl esters **24-30** was adapted from a previously reported, one-pot synthesis of oxazoles.<sup>9</sup> Briefly, *L*-threonine benzyl ester oxalate (3.34 mmol), potassium carbonate (6.68 mmol), and *N,N*'-dimethylacetamide (8.3 mL) were stirred under argon. To the resultant mixture was added various benzaldehyde (3.34 mmol), the solution stirred at room temperature, under argon, for 12 hrs. After 12 hrs, the reaction was cooled to 0°C, and bromotrichloromethane (10.02 mmol) and 1,8-diazabicyclo[5.4.0]undec-7-ene (10.02 mmol) were added. The solution stirred at 0°C for 2 hrs, at which point the reaction was removed from the ice bath and warmed to rt. The mixture stirred at rt for an additional 10 hrs [monitored by LC-MS]. The reaction was diluted with DD-H<sub>2</sub>O (3x original volume) and extracted with MTBE (3 x 15 mL) and EtOAc (3 x 15 mL). The organic layers were combined, washed with brine, and dried over Na<sub>2</sub>SO<sub>4</sub>. The product was concentrated by rotary evaporation to yield desired compound. The crude product was then purified as needed by prep HPLC (gradient of 0% B to 95% B for 17 min then hold at 100% B for 8 minutes) to provide the title compound. NMR matched previous reports.<sup>1</sup>

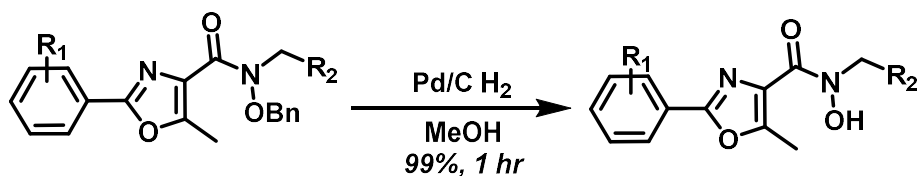


**General Procedure B.** Oxazole carboxylic acids **31-37** were synthesized through the hydrogenation of oxazole benzyl esters **24-30**. Briefly, oxazole benzyl esters **24-30** (20 mg) were dissolved in MeOH (2 mL) 10% P/C (2 mg) was added at rt. The vial was purged with H<sub>2</sub> and allowed to stir under H<sub>2</sub> atm (1 atm) for 1 hr [monitored by LC-MS]. Once complete, as judged by LC-MS, the solid catalyst was removed via syringe filtration, and the solution was concentrated

under reduced pressure to provide pure carboxylic acids **31-37** in quantitative yield. These compounds were used without purification or characterization.

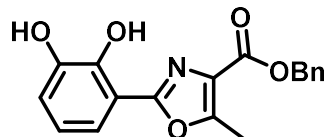


**General Procedure C.** Compounds **2**, **38-45** were synthesized through the coupling of oxazole carboxylic acids **31-37** and amines **10**, **13** and **16**. Carboxylic acids **31-37** (0.25 mmol) were dissolved in DMF (8 mL) under argon. Amines **10**, **13** or **16** (0.38 mmol) were added. To the stirring solution was added EDC (1.28 mmol) and HOBT (1.28 mmol). Et<sub>3</sub>N was added to the reaction dropwise until a pH of ~9 was obtained. The reaction stirred under argon for 12 hrs (monitored by LC-MS), at which point the reaction mixture was concentrated by rotary evaporation and purified by prep HPLC (gradient of 0% B to 95% B in 17 minutes, 95% B to 100% B in 2 minutes, hold 100% B for 8 minutes) to yield title compound **2**, **38-45**. Compound **2** was characterized by HRMS and 2D-NMR.

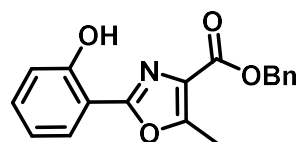


**General Procedure D.** OxPreA and analogs (**1-9**) were synthesized through hydrogenation of oxazole amides **38-45**. Oxazole amides **38-45** was stirred in MeOH with ~1/10 mass equivalent of 10% Pd/C under H<sub>2</sub> atmosphere (1 atm). Upon confirmation of reaction completion by LC-MS (~1 hr), the solid catalyst was removed through syringe filtration and the solution was concentrated by

rotary evaporation to afford desired compounds **1-9** in quantitative yield. Characterized by HRMS and 2D-NMR.

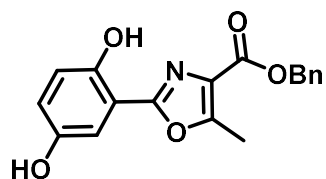


**Compound 17** was synthesized and characterized as previously reported in our group.<sup>1</sup>



**Compound 18** was synthesized by general procedure **A** starting with 2-hydroxybenzaldehyde.

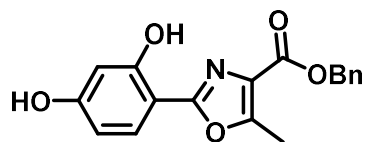
<sup>1</sup>H NMR (600 MHz, Chloroform-*d*)  $\delta$  10.82 (s, 1H), 7.77 (dd,  $J = 7.9, 1.7$  Hz, 1H), 7.46 (d, 2H), 7.40 (t,  $J = 7.5$  Hz, 2H), 7.36 (d, 2H), 7.07 (d,  $J = 8.4, 0.8$  Hz, 1H), 6.94 (t,  $J = 8.0, 7.4, 0.9$  Hz, 1H), 5.37 (s, 2H), 2.70 (s, 3H). <sup>13</sup>C NMR (151 MHz, Chloroform-*d*)  $\delta$  161.5, 159.4, 157.4, 155.3, 135.7, 132.8, 128.8, 128.5, 128.3, 127.0, 126.0, 119.5, 117.5, 110.4, 66.7, 12.2. LC-MS calcd for C<sub>18</sub>H<sub>16</sub>NO<sub>4</sub> (M + H)<sup>+</sup> 310.1074; found 310.1



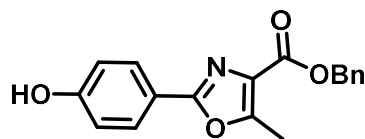
**Compound 19** was synthesized by general procedure **A** starting with 2,5-dihydroxybenzaldehyde. <sup>1</sup>H NMR (600 MHz, DMSO-*d*<sub>6</sub>)  $\delta$  10.03 (s, 1H), 9.25 (s, 1H), 7.47 (d,  $J = 7.2$  Hz, 2H), 7.42 (t,  $J = 7.4$  Hz, 2H), 7.38 – 7.34 (m, 1H), 7.16 (d,  $J = 2.7$  Hz, 1H), 6.91 – 6.84 (m, 2H), 5.36 (s, 2H), 2.67 (s, 3H). <sup>13</sup>C NMR (151 MHz, DMSO-*d*<sub>6</sub>)  $\delta$  160.8, 158.6, 155.9, 150.1,



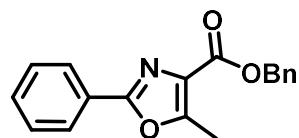
149.2, 135.8, 128.6, 128.2, 128.1, 126.3, 120.7, 117.9, 111.4, 110.2, 66.1, 11.9. LC-MS calcd for  $C_{18}H_{16}NO_5$  ( $M + H$ )<sup>+</sup> 325.1023; found 326.1



**Compound 20** was synthesized by general procedure **A** starting with 2,4-dihydroxybenzaldehyde. <sup>1</sup>H NMR (600 MHz, Chloroform-*d*)  $\delta$  7.65 (d,  $J = 8.7$  Hz, 1H), 7.45 (d, 2H), 7.39 (t,  $J = 7.3$  Hz, 2H), 7.35 (d,  $J = 7.3$  Hz, 1H), 6.52 (d,  $J = 2.3$  Hz, 1H), 6.45 (dd,  $J = 8.6$ , 2.3 Hz, 1H), 5.37 (s, 2H), 2.68 (s, 3H). <sup>13</sup>C NMR (151 MHz, Chloroform-*d*)  $\delta$  161.8, 159.7, 159.7, 159.7, 159.3, 154.7, 135.8, 128.8, 128.5, 127.7, 126.8, 107.9, 103.7, 66.8, 12.2. LC-MS calcd for  $C_{18}H_{16}NO_5$  ( $M + H$ )<sup>+</sup> 326.1023; found 326.1

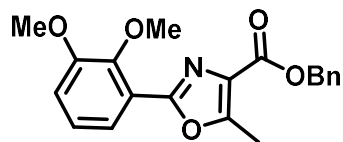


**Compound 21** was synthesized by general procedure **A** starting with 4-hydroxybenzaldehyde. <sup>1</sup>H NMR (600 MHz, Chloroform-*d*)  $\delta$  7.90 (d,  $J = 8.9$  Hz, 1H), 7.43 (d,  $J = 6.9$  Hz, 1H), 7.38 – 7.28 (m, 4H), 6.87 (d,  $J = 8.9$  Hz, 1H), 5.37 (s, 2H), 2.66 (s, 2H). <sup>13</sup>C NMR (151 MHz, Chloroform-*d*)  $\delta$  162.5, 160.2, 158.6, 158.4, 156.0, 135.9, 139.9, 128.7, 128.7, 128.6, 128.4, 116.0, 66.8, 12.4. LC-MS calcd for  $C_{18}H_{16}NO_4$  ( $M + H$ )<sup>+</sup> 310.1074; found 310.1

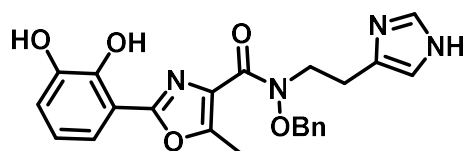


**Compound 22** was synthesized by general procedure **A** starting with benzaldehyde. <sup>1</sup>H NMR (600 MHz, Chloroform-*d*)  $\delta$  8.09 – 8.00 (m, 2H), 7.52 – 7.46 (m, 2H), 7.45 – 7.40 (m, 3H), 7.38 (t,  $J = 7.2$  Hz, 2H), 7.35 – 7.30 (m, 1H), 5.41 (s, 2H), 2.68 (s, 3H). <sup>13</sup>C NMR (151 MHz,

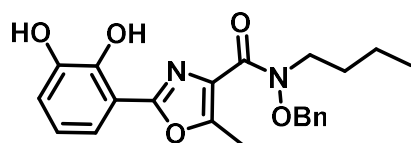
Chloroform-*d*)  $\delta$  162.4, 159.8, 156.5, 135.9, 130.8, 128.8, 128.7, 128.7, 128.5, 128.4, 126.7, 66.7, 12.4. LC-MS calcd for  $C_{18}H_{16}NO_3$  ( $M + H$ )<sup>+</sup> 294.1125; found 294.1



**Compound 23** was synthesized by general procedure **A** starting with 2,3 dimethoxybenzaldehyde. <sup>1</sup>H NMR (600 MHz, Chloroform-*d*)  $\delta$  7.55 (dd,  $J = 7.9, 1.5$  Hz, 1H), 7.47 (d,  $J = 7.4$  Hz, 2H), 7.37 (t,  $J = 7.3$  Hz, 2H), 7.35 – 7.30 (m, 1H), 7.11 (t,  $J = 8.0$  Hz, 1H), 7.02 (dd,  $J = 8.2, 1.5$  Hz, 1H), 5.40 (s, 2H), 3.92 (s, 3H), 3.90 (s, 3H), 2.69 (s, 3H). <sup>13</sup>C NMR (151 MHz, Chloroform-*d*)  $\delta$  162.5, 158.4, 156.8, 153.7, 148.0, 136.1, 128.7, 128.5, 128.5, 128.4, 124.4, 122.1, 121.6, 114.9, 66.6, 61.5, 56.2, 12.5. LC-MS calcd for  $C_{20}H_{20}NO_5$  ( $M + H$ )<sup>+</sup> 354.1336; found 354.1

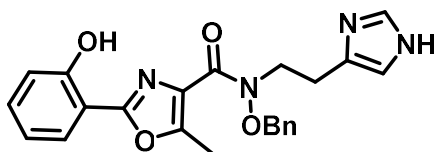


**Compound 38** was synthesized and characterized as previously reported by our group.<sup>1</sup>



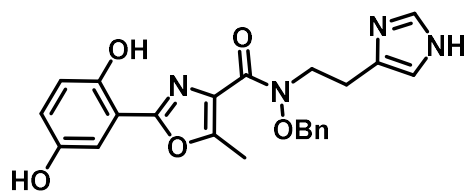
**Compound 39** was synthesized by general procedure **C** through EDC/HOBt mediated couple of oxazole carboxylic acid **31** and *O*-benzylehydroxylamine **16** in the presence of facilitating base. <sup>1</sup>H NMR (600 MHz, DMSO-*d*<sub>6</sub>)  $\delta$  7.95 (s, 1H), 7.42 (s, 2H), 7.31 (s, 3H), 7.24 (dd,  $J = 7.9, 1.6$  Hz, 1H), 6.95 (dd,  $J = 7.9, 1.5$  Hz, 1H), 6.82 (t,  $J = 7.9$  Hz, 1H), 4.99 (s, 1H), 4.94 (s, 1H), 3.88 – 3.72 (m, 2H), 1.69 – 1.54 (m, 2H), 1.38 – 1.24 (m, 2H), 0.94 – 0.76 (m, 3H). <sup>13</sup>C NMR (151 MHz, DMSO-*d*<sub>6</sub>)  $\delta$  158.1, 146.0, 145.1, 133.7, 129.4, 129.13, 129.02, 128.6, 128.6, 128.3, 119.7, 118.3,

118.1, 116.4, 76.6, 19.3, 19.0, 13.6, 13.4. LC-MS calcd for C<sub>22</sub>H<sub>25</sub>N<sub>2</sub>O<sub>5</sub> (M + H)<sup>+</sup> 397.1758; found 397.2



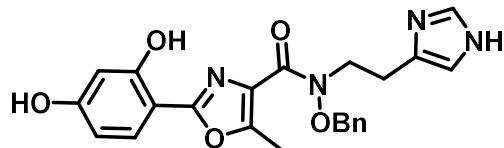
**Compound 40** was synthesized by general procedure C through EDC/HOBt mediated couple of oxazole carboxylic acid **32** and *O*-benzylehydroxylamine **13** in the presence of facilitating base.

<sup>1</sup>H NMR (600 MHz, DMSO-*d*<sub>6</sub>) δ 7.78 (dd, *J* = 7.8, 1.7 Hz, 1H), 7.50 (s, 1H), 7.44 – 7.39 (m, 1H), 7.35 (s, 2H), 7.31 (s, 3H), 7.06 (dd, *J* = 8.3, 1.1 Hz, 1H), 7.02 – 6.97 (m, 1H), 6.80 (s, 1H), 4.95 (s, 2H), 4.05 (t, *J* = 7.2 Hz, 2H), 2.88 (t, *J* = 7.2 Hz, 2H), 2.43 (s, 3H). <sup>13</sup>C NMR (151 MHz, DMSO-*d*<sub>6</sub>) δ 172.1, 161.6, 157.2, 156.1, 152.2, 135.0, 134.8, 132.6, 129.3, 128.5, 128.4, 128.3, 126.9, 119.7, 118.1, 117.0, 111.0, 75.6, 25.1, 11.5. LC-MS calcd for C<sub>23</sub>H<sub>22</sub>N<sub>4</sub>O<sub>4</sub> (M + H)<sup>+</sup> 418.1641; found 418.2



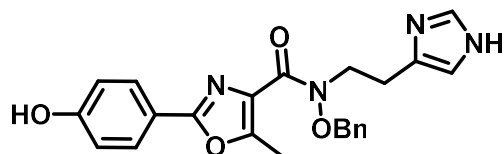
**Compound 41** was synthesized by general procedure C through EDC/HOBt mediated couple of oxazole carboxylic acid **33** and *O*-benzylehydroxylamine **13** in the presence of facilitating base.

<sup>1</sup>H NMR (600 MHz, DMSO-*d*<sub>6</sub>) δ 7.49 (s, 1H), 7.36 – 7.28 (m, 5H), 7.15 (d, *J* = 2.8 Hz, 1H), 6.88 (d, *J* = 8.7 Hz, 1H), 6.86 (dd, *J* = 8.9, 2.8 Hz, 1H), 6.80 (s, 1H), 5.79 (s, 1H), 4.94 (s, 2H), 4.03 (t, *J* = 7.2 Hz, 2H), 2.86 (t, *J* = 7.2 Hz, 2H), 2.41 (s, 3H). <sup>13</sup>C NMR (151 MHz, DMSO-*d*<sub>6</sub>) δ 158.0, 157.6, 150.0, 149.0, 134.8, 129.3, 128.5, 128.4, 128.3, 120.3, 117.9, 111.4, 110.5, 56.6, 45.0, 27.9, 15.7. LC-MS calcd for C<sub>23</sub>H<sub>22</sub>N<sub>4</sub>O<sub>5</sub> (M + H)<sup>+</sup> 434.1590; found 434.2



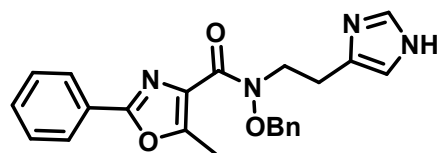
**Compound 42** was synthesized by general procedure **C** through EDC/HOBt mediated couple of oxazole carboxylic acid **34** and *O*-benzylehydroxylamine **13** in the presence of facilitating base.

$^1\text{H}$  NMR (600 MHz,  $\text{DMSO-}d_6$ )  $\delta$  7.59 (d,  $J = 8.5$  Hz, 1H), 7.49 (s, 1H), 7.36 – 7.28 (m, 5H), 6.79 (s, 1H), 6.43 (dd,  $J = 8.6, 2.2$  Hz, 1H), 6.41 (d,  $J = 2.3$  Hz, 1H), 5.78 (s, 2H), 4.93 (s, 2H), 4.02 (t,  $J = 7.3$  Hz, 2H), 2.86 (t,  $J = 7.3$  Hz, 2H), 2.39 (s, 3H).  $^{13}\text{C}$  NMR (151 MHz,  $\text{DMSO-}d_6$ )  $\delta$  161.6, 158.2, 158.0, 157.9, 134.8, 129.3, 128.5, 128.3, 127.9, 108.3, 102.8, 102.6, 56.7, 45.6, 28.0, 15.7. LC-MS calcd for  $\text{C}_{23}\text{H}_{22}\text{N}_4\text{O}_5$  ( $\text{M} + \text{H}$ ) $^+$  434.1590; found 434.2



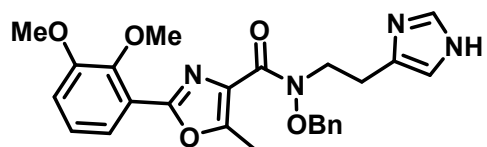
**Compound 43** was synthesized by general procedure **C** through EDC/HOBt mediated couple of oxazole carboxylic acid **35** and *O*-benzylehydroxylamine **13** in the presence of facilitating base.

$^1\text{H}$  NMR (600 MHz,  $\text{DMSO-}d_6$ )  $\delta$  7.76 (d,  $J = 8.7$  Hz, 2H), 7.49 (s, 1H), 7.41 (s, 1H), 7.34 (s, 2H), 6.88 (d,  $J = 8.7$  Hz, 2H), 5.77 (d,  $J = 6.4$  Hz, 3H), 5.04 (s, 2H), 4.09 (s, 2H), 2.89 – 2.83 (m, 2H), 2.44 (s, 3H).  $^{13}\text{C}$  NMR (151 MHz,  $\text{DMSO-}d_6$ )  $\delta$  160.0, 158.1, 158.0, 134.7, 129.0, 128.4, 128.3, 127.8, 117.3, 116.0, 56.8, 37.6, 28.0, 15.7. LC-MS calcd for  $\text{C}_{23}\text{N}_2\text{N}_4\text{O}_4$  ( $\text{M} + \text{H}$ ) $^+$  418.1641; found 418.2



**Compound 44** was synthesized by general procedure **C** through EDC/HOBt mediated couple of oxazole carboxylic acid **36** and *O*-benzylehydroxylamine **13** in the presence of facilitating base.

$^1\text{H}$  NMR (600 MHz,  $\text{DMSO-}d_6$ )  $\delta$  7.96 – 7.92 (m, 2H), 7.55 – 7.49 (m, 3H), 7.50 (s, 1H), 7.41 (s, 2H), 7.33 (s, 3H), 6.81 (s, 1H), 5.06 (s, 2H), 4.11 (s, 2H), 2.89 (t, 2H), 2.47 (s, 3H).  $^{13}\text{C}$  NMR (151 MHz,  $\text{DMSO-}d_6$ )  $\delta$  135.3, 134.7, 131.0, 130.8, 129.2, 129.2, 129.1, 128.4, 128.3, 126.4, 126.1, 126.0, 125.9, 75.7, 51.7, 24.9, 11.6. LC-MS calcd for  $\text{C}_{23}\text{H}_{22}\text{N}_4\text{O}_3$  ( $\text{M} + \text{H}$ ) $^+$  402.1692; found 402.2



**Compound 45** was synthesized by general procedure **C** through EDC/HOBt mediated couple of oxazole carboxylic acid **37** and *O*-benzylehydroxylamine **13** in the presence of facilitating base.

$^1\text{H}$  NMR (600 MHz,  $\text{DMSO-}d_6$ )  $\delta$  7.48 (s, 1H), 7.43 – 7.36 (m, 2H), 7.36 – 7.31 (m, 3H), 7.23 (dd,  $J = 8.2, 1.8$  Hz, 1H), 7.19 (t,  $J = 7.9$  Hz, 1H), 6.79 (s, 1H), 5.79 (s, 1H), 5.03 (s, 2H), 4.13 (s, 2H), 3.86 (s, 3H), 3.78 (s, 3H), 2.87 (t,  $J = 7.5$  Hz, 2H), 2.47 (s, 3H).  $^{13}\text{C}$  NMR (151 MHz,  $\text{DMSO-}d_6$ )  $\delta$  162.1, 158.0, 155.9, 153.4, 147.0, 135.4, 134.7, 129.1, 128.4, 128.3, 124.6, 121.0, 120.8, 115.1, 60.7, 56.8, 51.7, 28.0, 15.7. LC-MS calcd for  $\text{C}_{25}\text{H}_{27}\text{N}_4\text{O}_5$  ( $\text{M} + \text{H}$ ) $^+$  463.1976; found 463.2

## 6.7 Figures and Tables

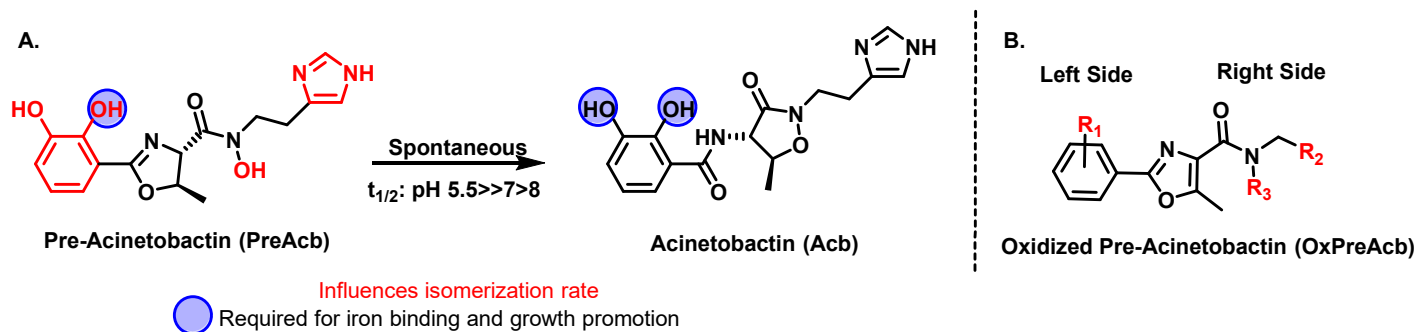
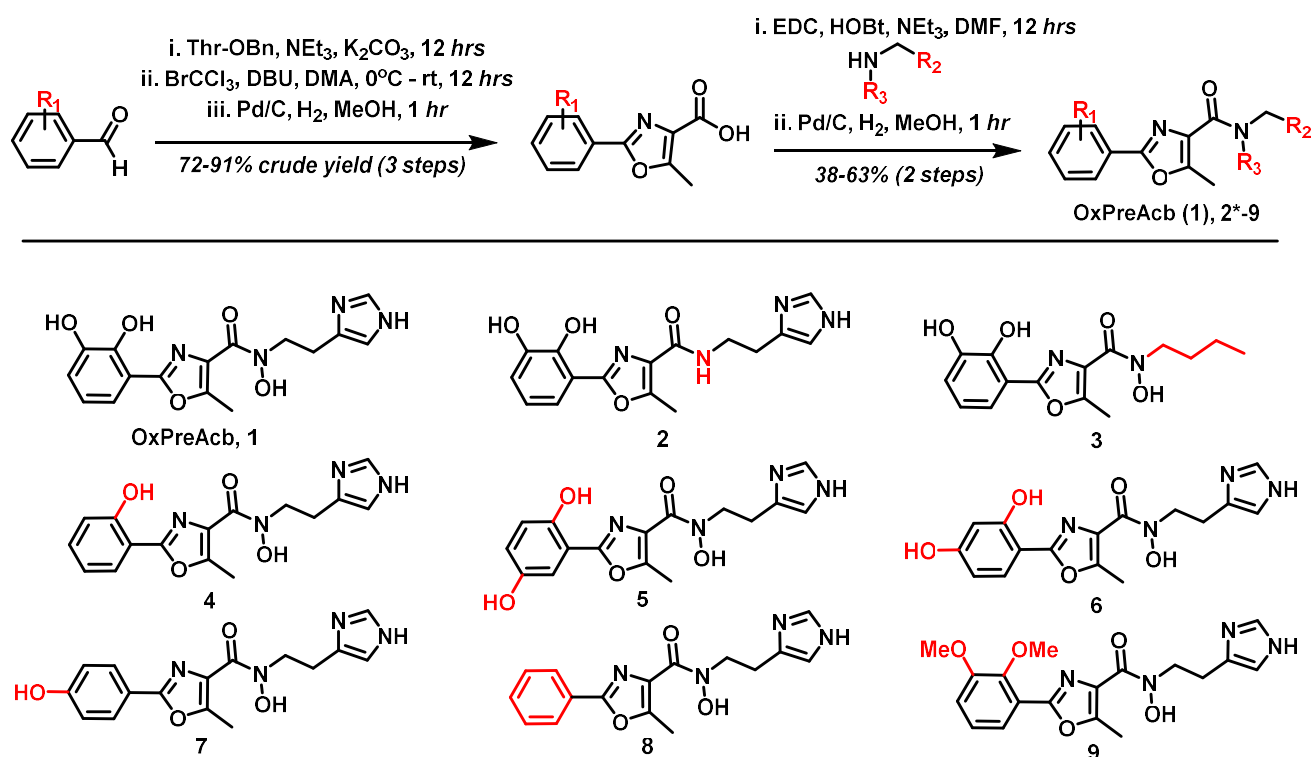


**Figure 6.1:** SAR analysis of pre-acinetobactin and acinetobactin<sup>2</sup>



**Scheme 6.1:** Synthetic route for OxPreAcb and analogs. \*note: compound 2 lacks a hydroxymethyl hydroxyl group and thus does not require a final de-protection step

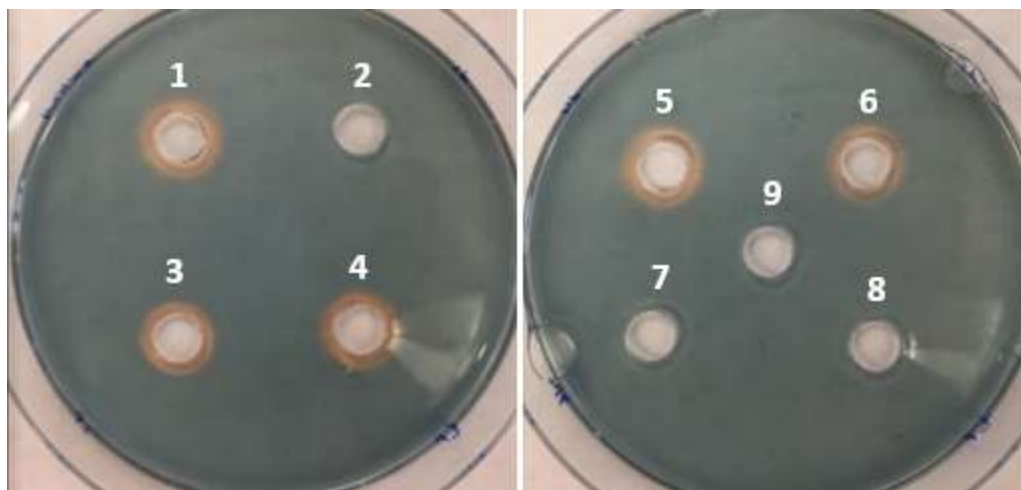


**Figure 6.2:** CAS assay determination of iron binding ability of OxPreAcb and analogs

COMPOUND	MIC	CAS	BAUB BINDING AFFINITY
<b>Acb</b>	>200	+	302 ± 105
<b>Acb-Fe</b>	>200	+	162 ± 81
<b>PreAcb</b>	>200	+	383 ± 106
<b>PreAcb-Fe</b>	>200	+	754 ± 155
<b>FimsA</b>	>200	+	355 ± 139
<b>FimsA-Fe</b>	>200	+	244 ± 93
<b>OxPreAcb, 1</b>	1.56	+	198 ± 78
<b>OxPreAcb-Fe</b>	>200	+	317 ± 172
<b>OxPreAcb-Ga</b>	<0.78	+	293 ± 172
<b>2</b>	>200	-	183 ± 112
<b>3</b>	1.56	+	218 ± 126
<b>4</b>	0.78	+	217 ± 212
<b>5</b>	0.78	+	260 ± 129
<b>6</b>	0.78	+	206 ± 138
<b>7</b>	>200	-	No fit
<b>8</b>	>200	-	No fit
<b>9</b>	>200	-	143 ± 60

**Table 6.1:** MIC<sub>90</sub> values (μM), CAS assay and BauB affinities for natural siderophores and OxPreAcb derivatives

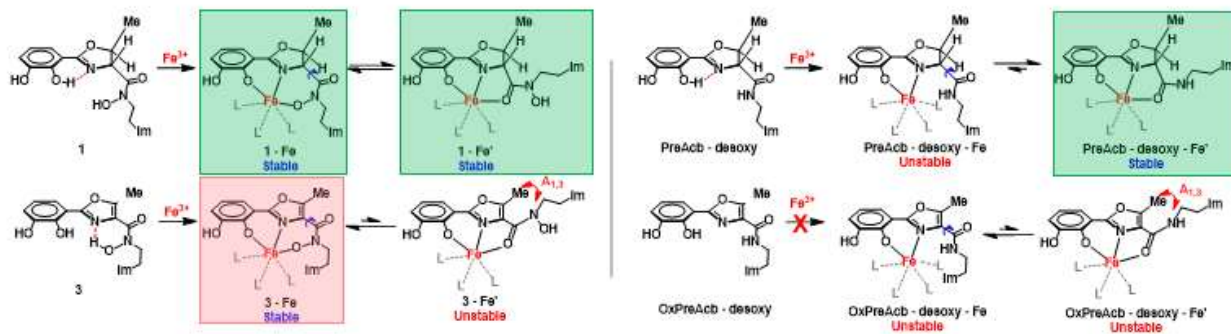


**Figure 6.3:** The presence of the hydroxymate group in OxPreAcb is necessary for OxPreAcb inhibition



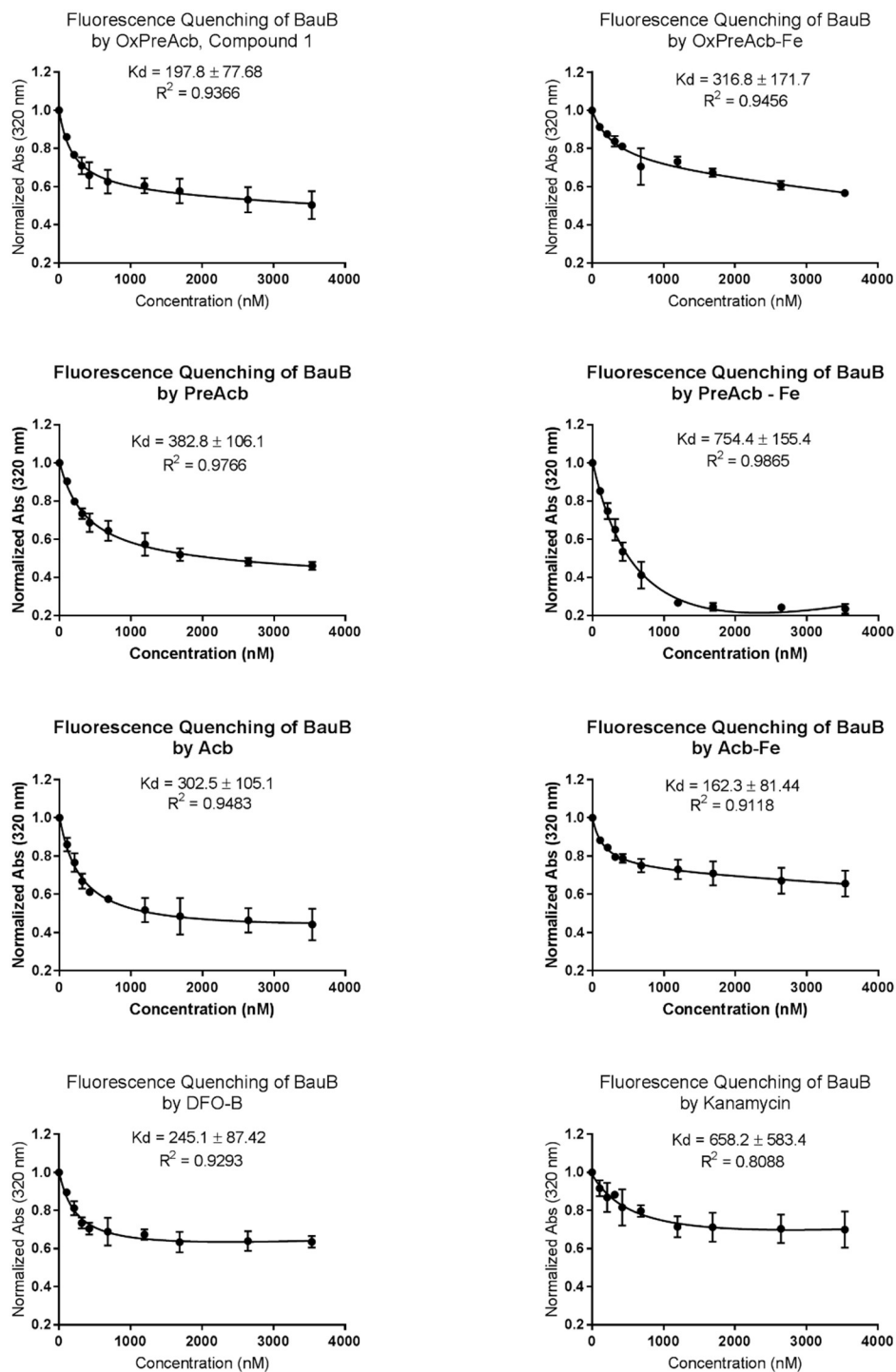


**Figure 6.4:** Fluorescence Quenching of BauB by OxPreAcb, OxPreAcb-Fe, PreAcb, PreAcb-Fe, Acb, Acb-Fe, DFO-B and Kanamycin

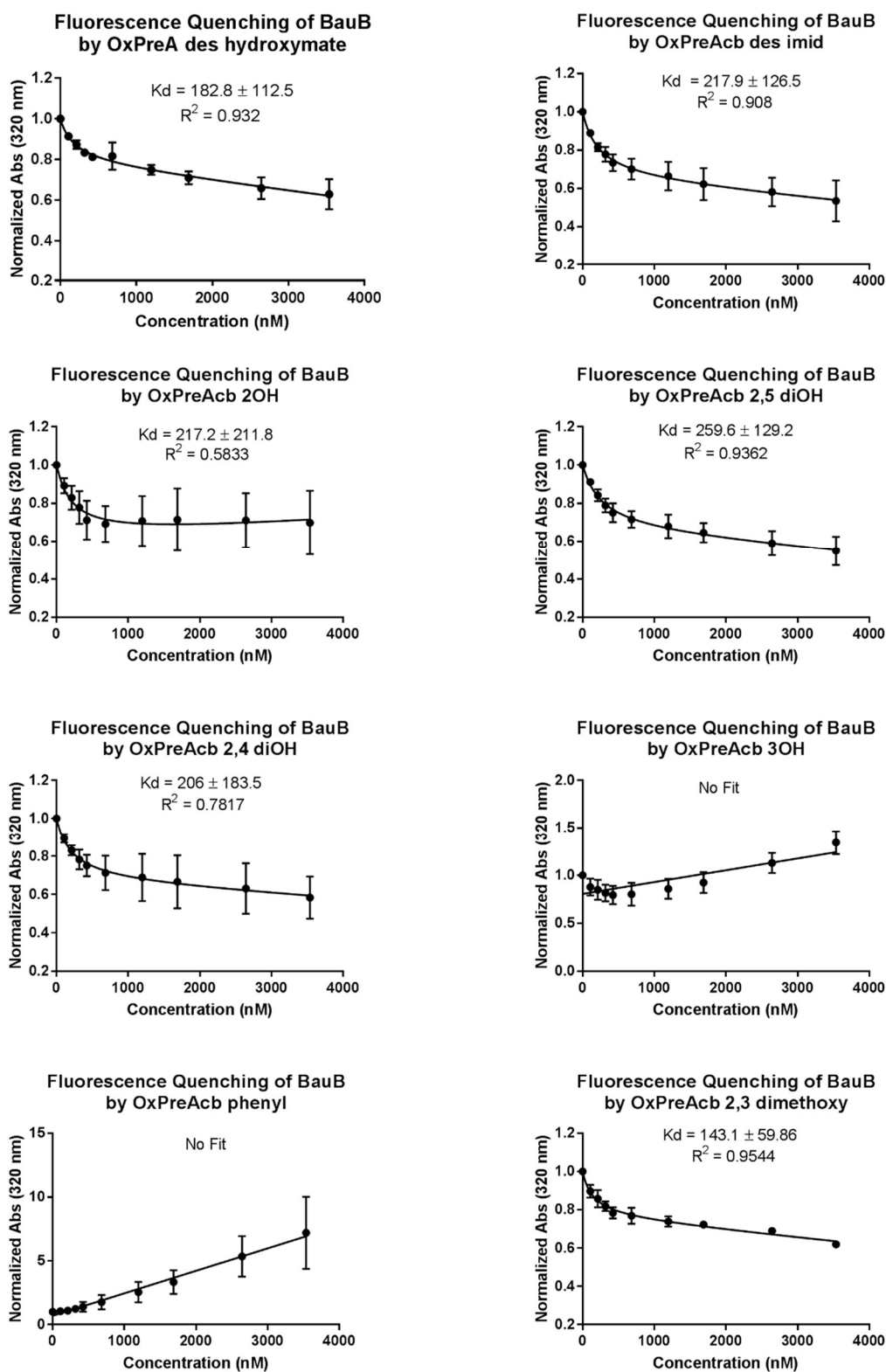


**Figure 6.5:** Fluorescence Quenching of BauB by OxPreAcb analogs

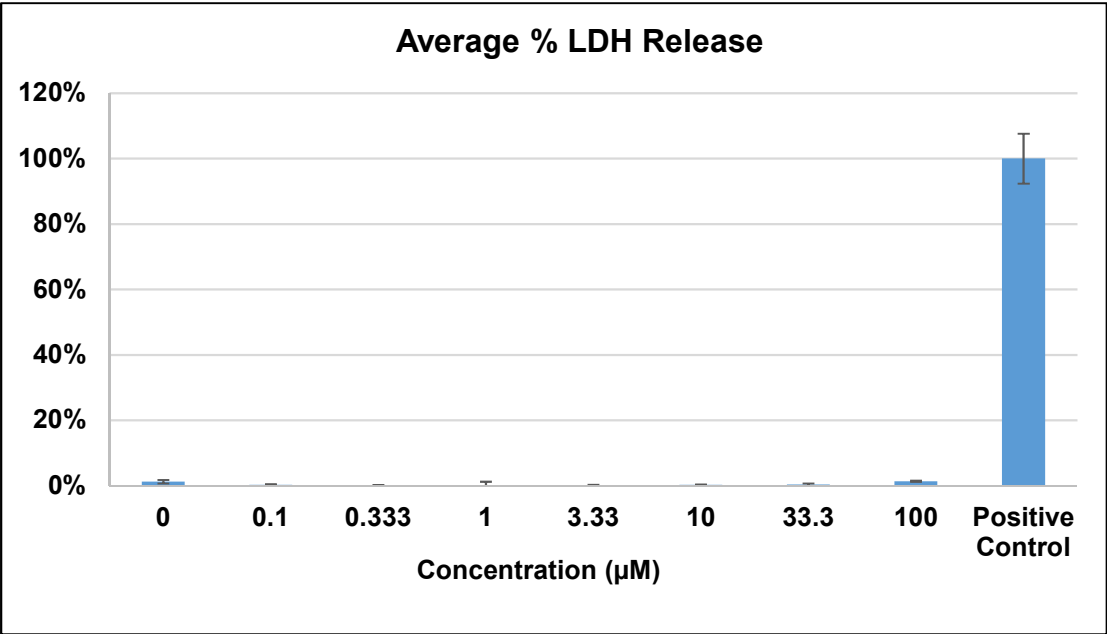
AR-BANK #	Total # of AR Genes	Amikacin	Ampicillin/sulbactam	Cefepime	Cefotaxime	Ceftriaxone	Ciprofloxacin	Colistin	Doripenem	Gentamicin	Imipenem	Imipenem+Chelators	Levofloxacin	Meropenem	Minocycline	Piperacillin/tazobactam	Polymyxin B	Tetracycline	Tigecycline	Tobramycin	Trimethoprim/sulfamethoxazole
0273	9	R	R	R	R	R	R	S	R	R	R	.	R	R	I	R	S	R	.	R	R
0275	11	R	R	R	R	R	R	S	R	R	R	.	R	R	I	R	S	R	.	R	R
0278	14	R	R	R	R	R	R	S	R	R	R	.	R	R	I	R	S	R	.	R	R
0284	7	R	R	R	R	R	R	S	R	R	R	.	R	R	S	R	S	R	.	R	R
0287	6	I	R	R	R	R	R	S	R	S	R	.	R	R	S	R	S	R	.	R	R
0290	13	R	R	R	R	R	R	S	R	R	R	.	R	R	I	R	S	R	.	R	R
0293	5	I	R	R	R	R	R	S	R	R	R	.	I	R	I	R	S	R	.	R	S
0296	6	R	R	R	R	R	R	S	R	R	R	.	R	R	S	R	S	R	.	R	R
0299	14	R	R	R	R	R	R	S	R	R	R	.	R	R	S	R	S	R	.	R	R
0302	9	R	R	R	R	R	R	S	R	R	R	.	R	R	I	R	S	R	.	R	R
0305	7	I	I	R	R	R	R	S	R	R	R	.	R	R	S	R	S	S	.	R	R
0308	10	R	R	R	R	R	R	R	R	R	R	.	R	R	R	R	R	R	.	R	R
0311	11	R	R	R	R	R	R	S	R	R	R	.	R	R	S	R	S	R	.	R	R

Figure 6.6: CDC clinical isolates resistances to current antibiotics (S - susceptible, I – intermediate, R - resistant)

<i>CDC Isolate Strain</i>	<i>MIC<sub>90</sub> (17 hrs)</i> <i>μm</i>	<i>MIC<sub>90</sub> (40 hrs)</i> <i>μm</i>
0273	1.56	6.25
0275	3.125	6.25
0278	3.125	6.25
0284	12.5	25
0287	3.125	6.25
0290	6.25	25
0293	0.78	6.25
0296	6.25	25
0299	No growth	12.5
0302	6.25	25
0305	3.125	12.5
0308	6.25	25
0311	6.25	25

**Table 6.2:** MIC<sub>90</sub> values of OxPreAcb against CDC clinical isolates of *A. baumannii*

Cytotoxicity (MDCK, LDH Release, n=3)			
Positive Control	LDH Lysis Buffer		
Test Compound	Concentration ( $\mu\text{M}$ )	Average LDH Release (%)	SD
OxPreAcb	0	1.238%	0.535%
	0.1	0.298%	0.222%
	0.333	0.094%	0.094%
	1	0.157%	1.102%
	3.33	0.016%	0.267%
	10	0.235%	0.163%
	33.3	0.345%	0.380%
	100	1.379%	0.190%
Positive Control	NA	100.000%	7.636%



**Figure 6.7:** Toxicity data Alliance Pharma

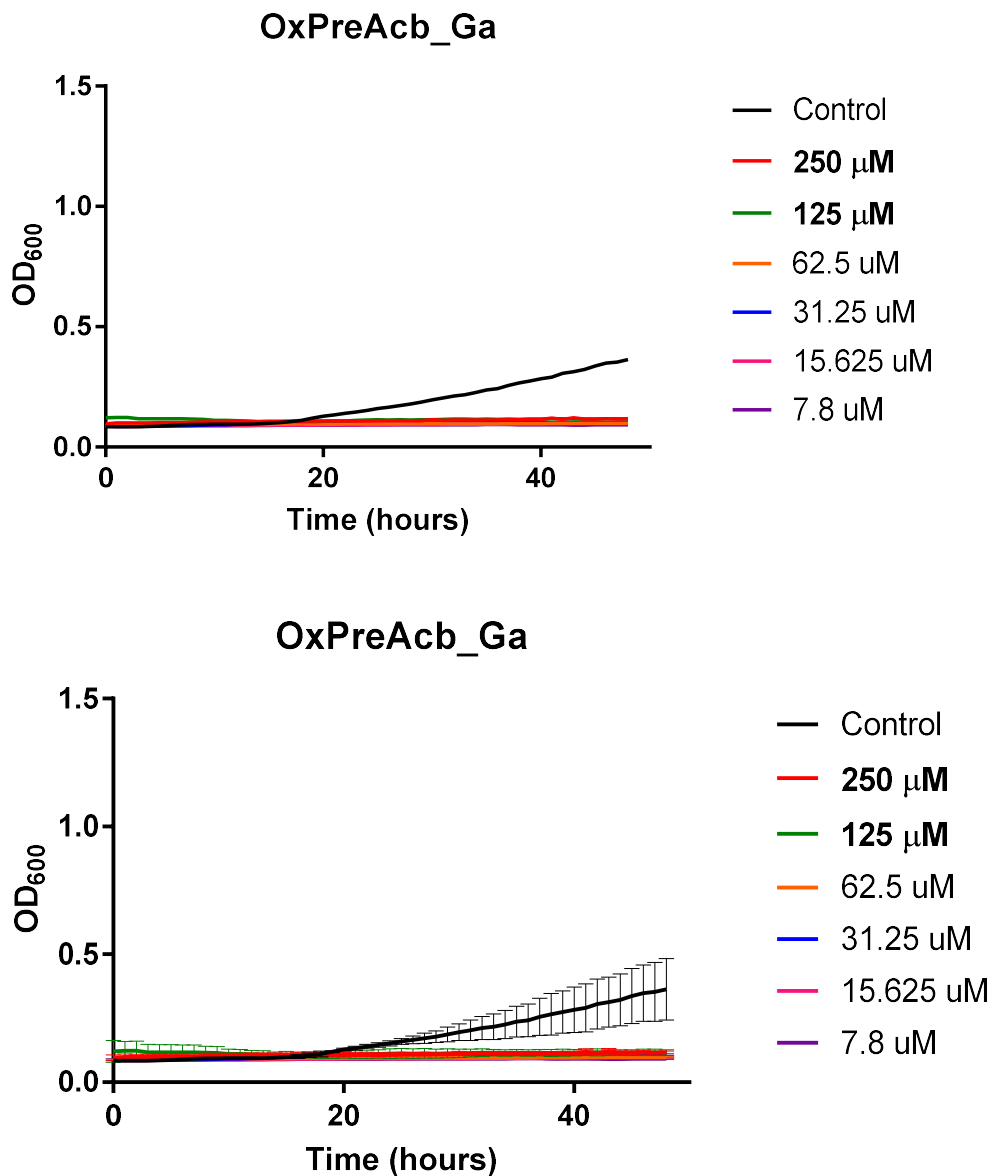


**Figure 6.8:** OxPreAcb<sub>2</sub>Ga inhibits *A. baumannii* ATCC17978 growth. Growth curves of *A. baumannii* in M9 minimal medium supplemented with 125  $\mu\text{M}$  2,2'-dipyridyl (DIP) and gradient concentrations of OxPreAcb<sub>2</sub>Ga (A.), without error bars (B.) with error bars. Error bars represent s.d. for three independent trials.

### Growth Studies with *A. baumannii* ATCC17978

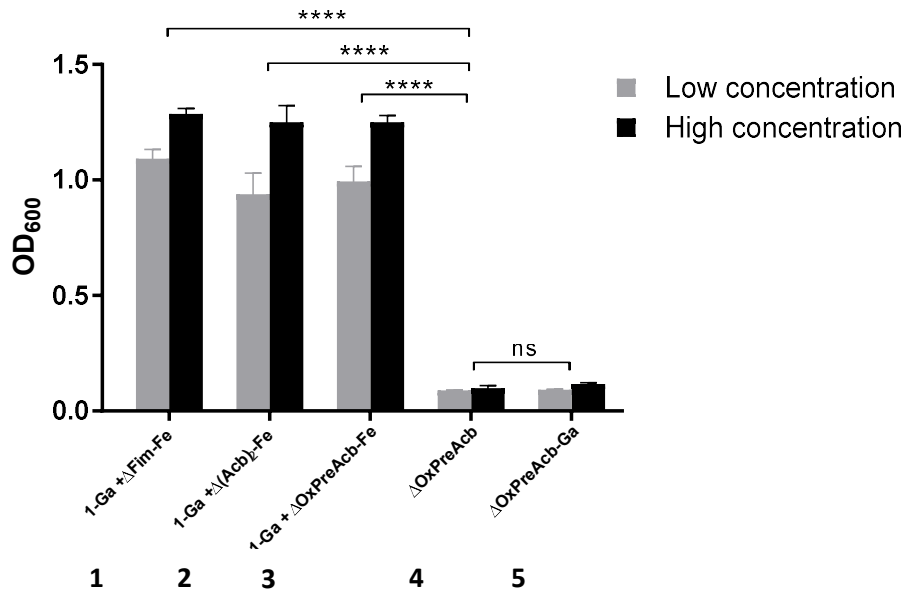


**Figure 6.9:** Growth studies of *A. baumannii* ATCC17978 in the presences of 1. OxPreAcb-Ga (7.8 μM) and Fims-Fe (31.25 μM, 0.975 μM) 2. OxPreAcb-Ga (7.8 μM) and (Acb)<sub>2</sub>-Fe (31.25 μM, 0.975 μM) 3. OxPreAcb-Ga (7.8 μM) and OxPreAcb-Fe (31.25 μM, 0.975 μM) 4. OxPreAcb (250 μM, 6.25 μM). 5. OxPreAcb-Ga (250 μM, 7.8 μM)

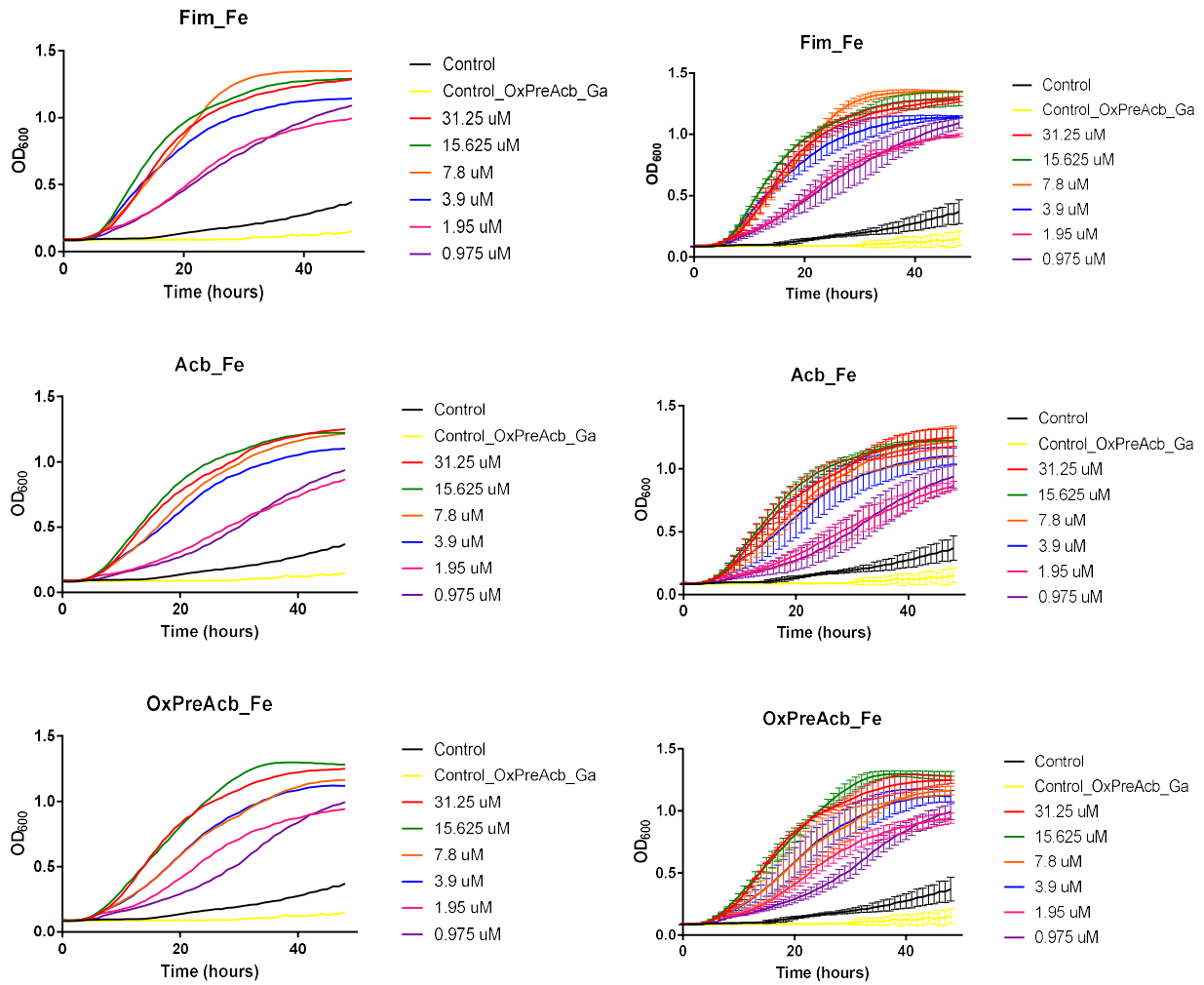


**Figure 6.10:** 7.8  $\mu\text{M}$  OxPreAcb-Ga with variable Fims-Fe, Acb-Fe and OxPreAcb-Fe growth studies against *A. baumannii* ATCC17978. Growth in M9 minimal medium supplemented with DIP. Error bars represent s.d. for three independent trials.



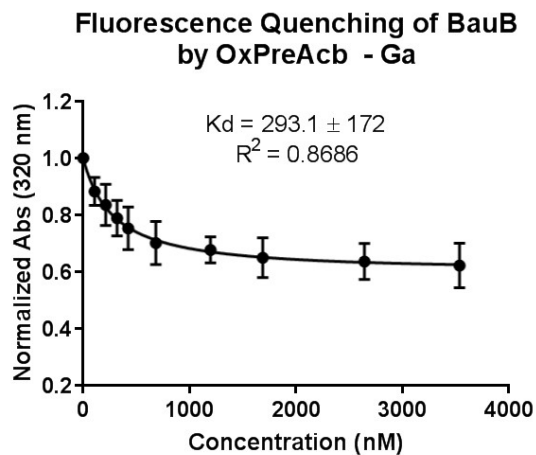


**Figure 6.11:** Fluorescence quenching assay of BauB with OxPreAcb-Ga

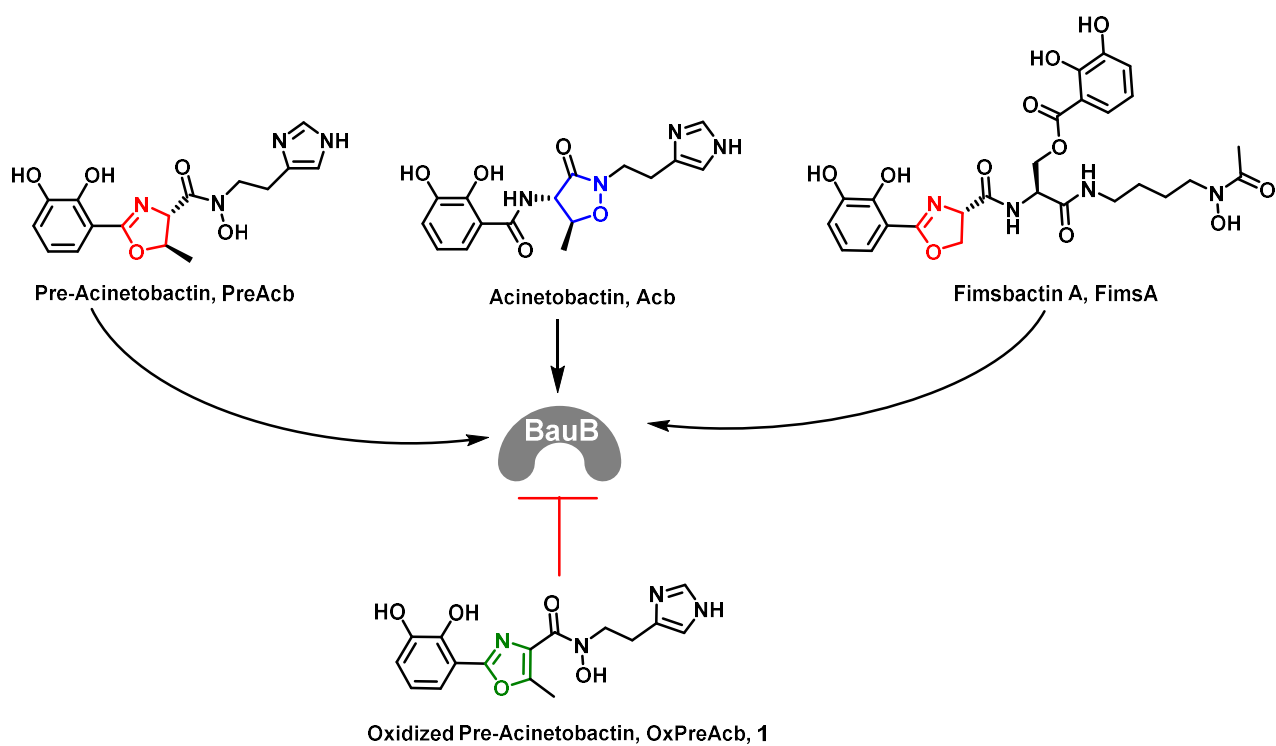


**Figure 6.12:** OxPreAcb inhibits growth of *A. baumannii* by disruption of the siderophore pathway, as shown by the ability of OxPreAcb to bind periplasmic siderophore binding protein, BauB.

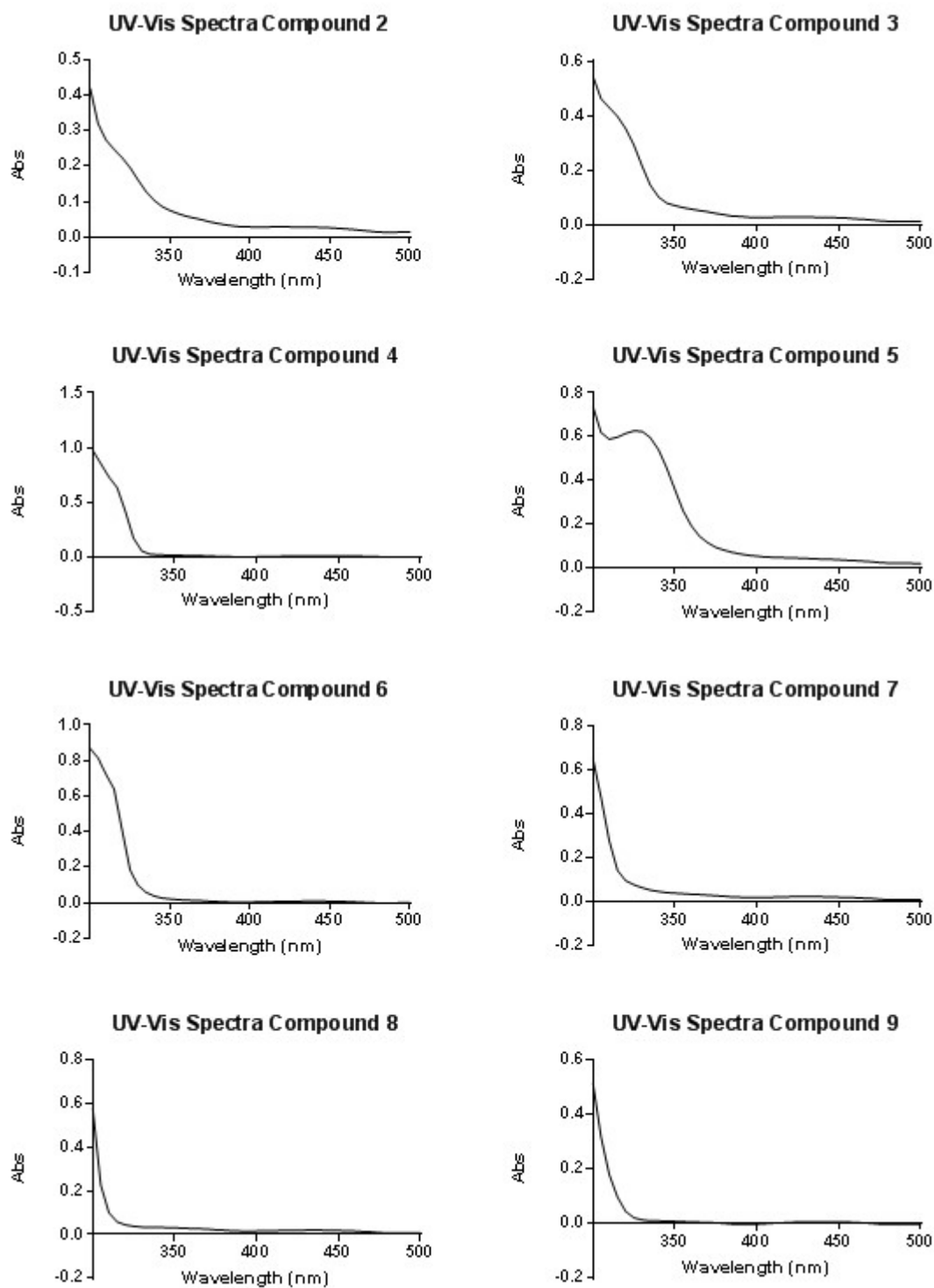
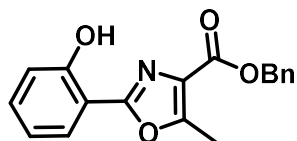
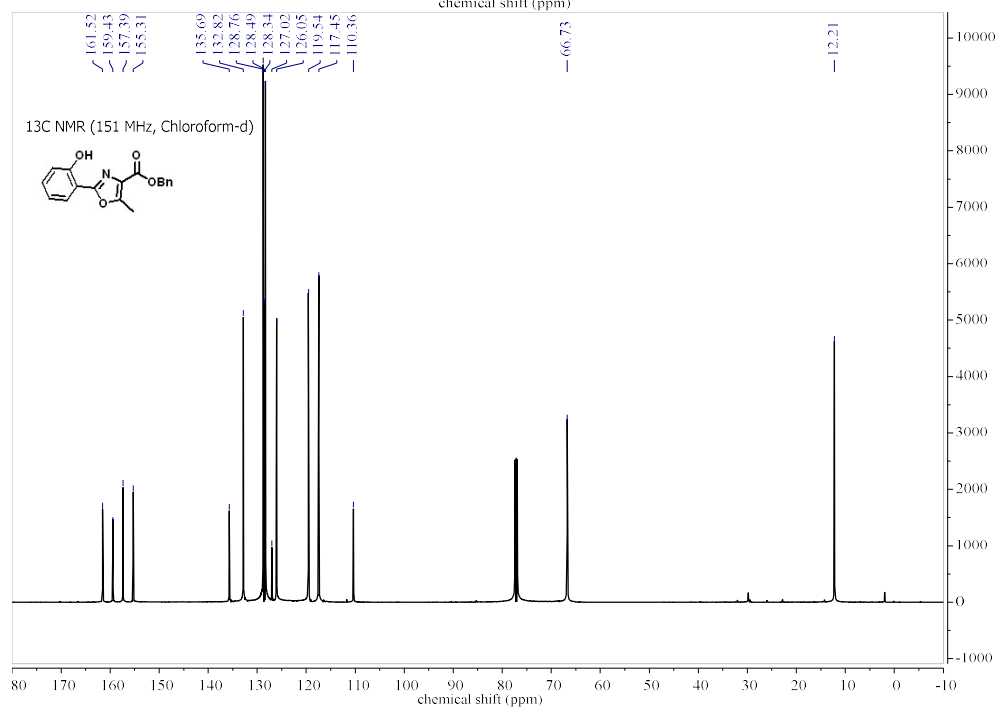
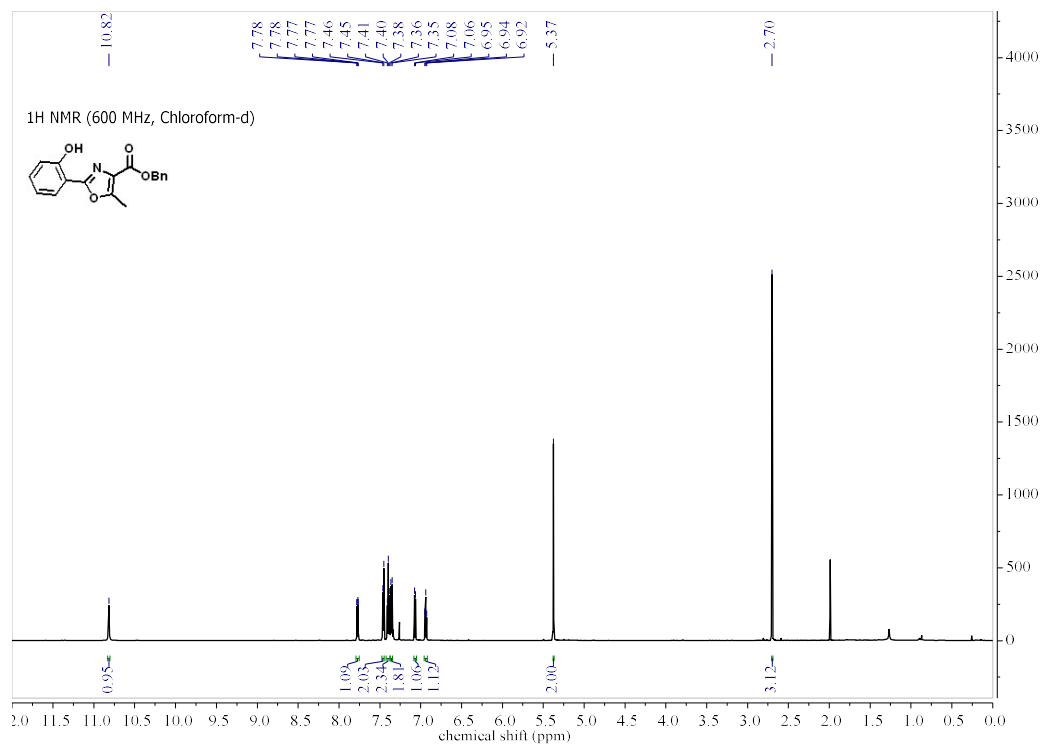


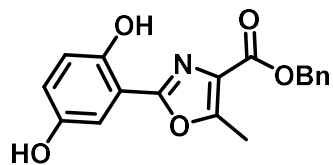
**Figure 6.13:** UV-Vis spectra for *apo*-OxPreAcb analogs

**Compound Characterization Data**

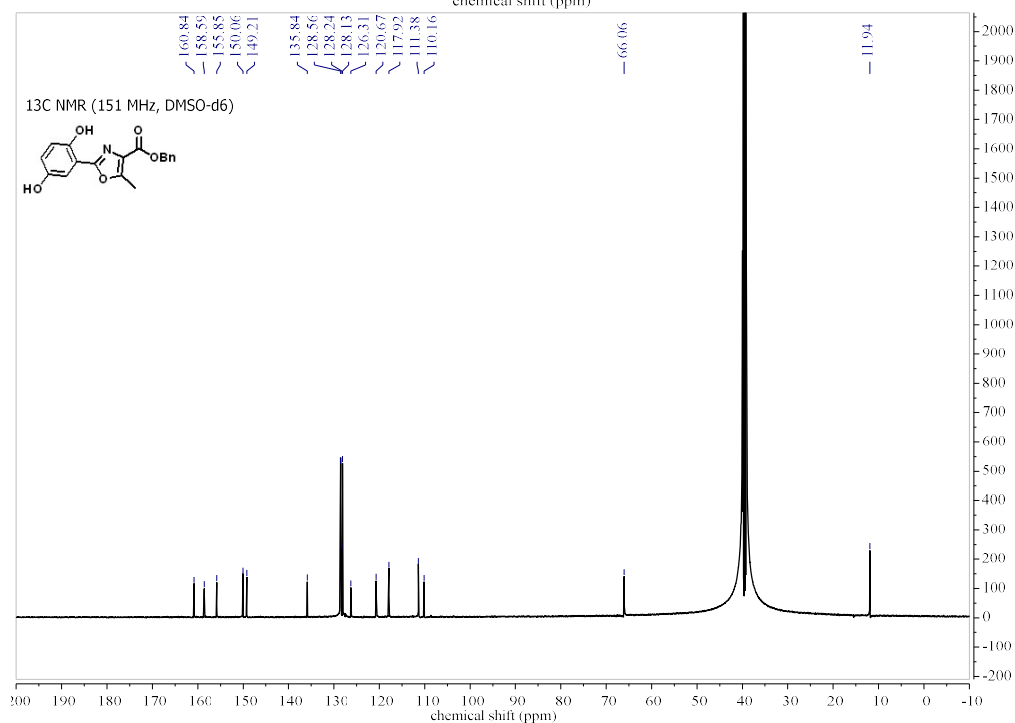
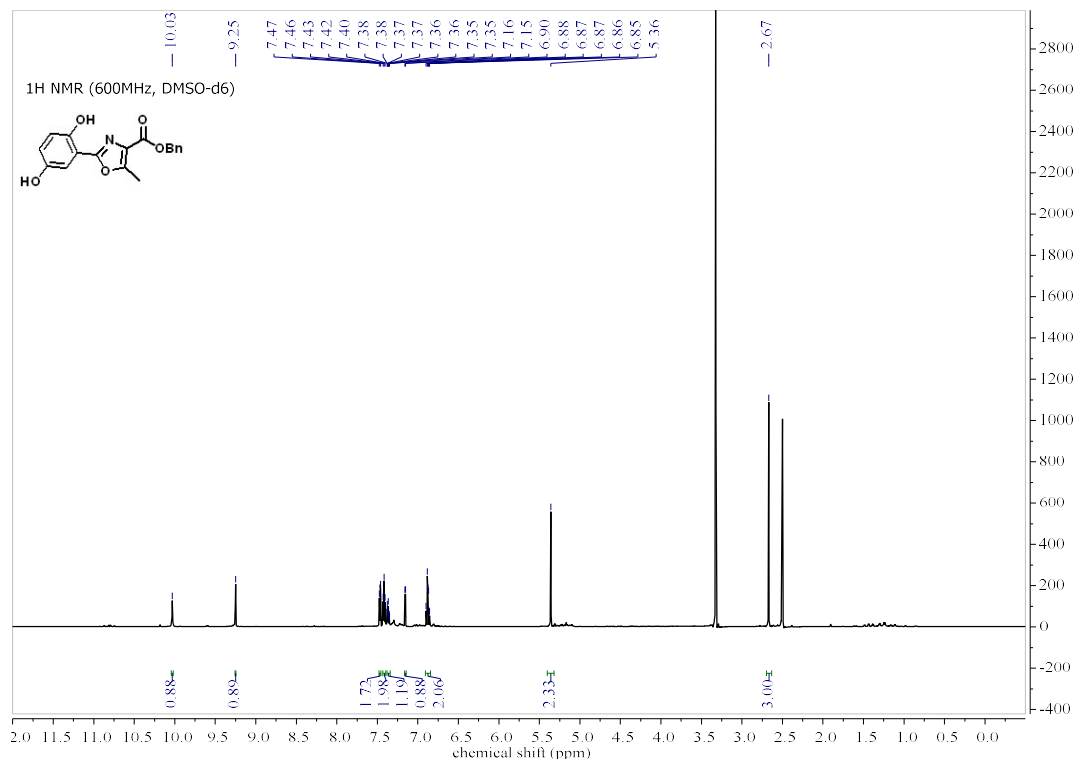


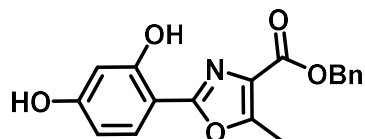
benzyl 2-(2-hydroxyphenyl)-5-methyloxazole-4-carboxylate (18)



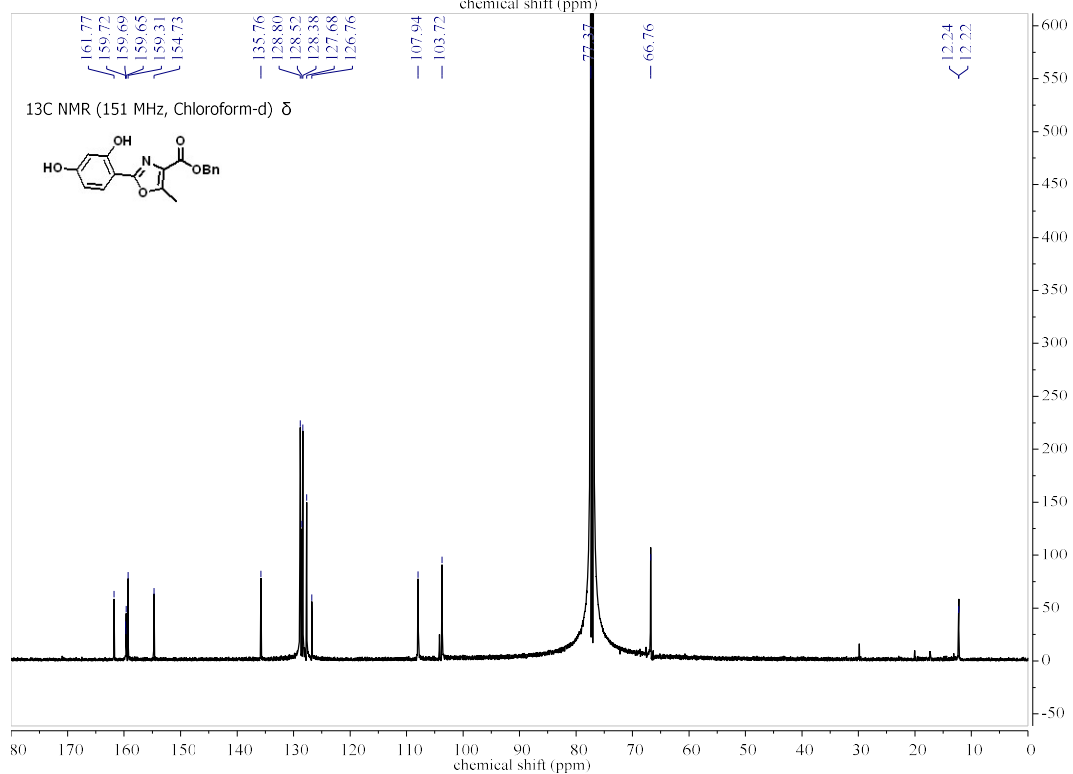
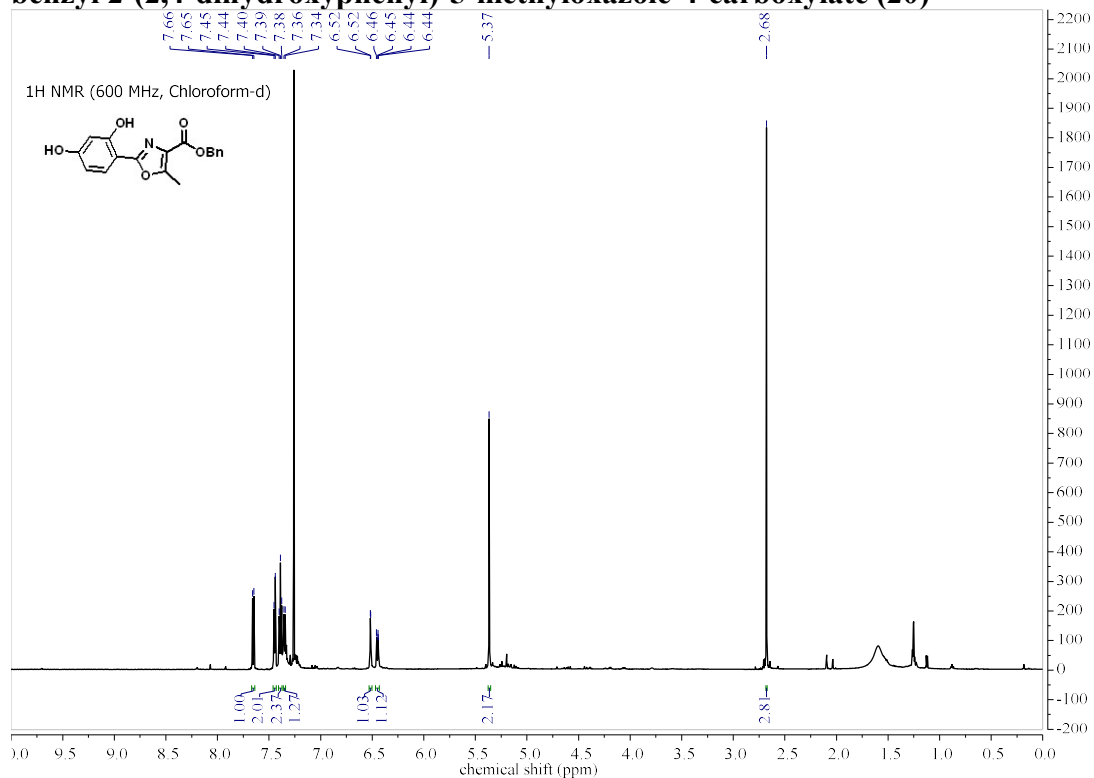


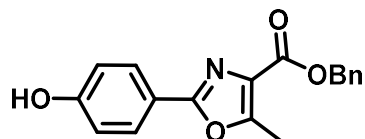
benzyl 2-(2,5-dihydroxyphenyl)-5-methyloxazole-4-carboxylate (19)



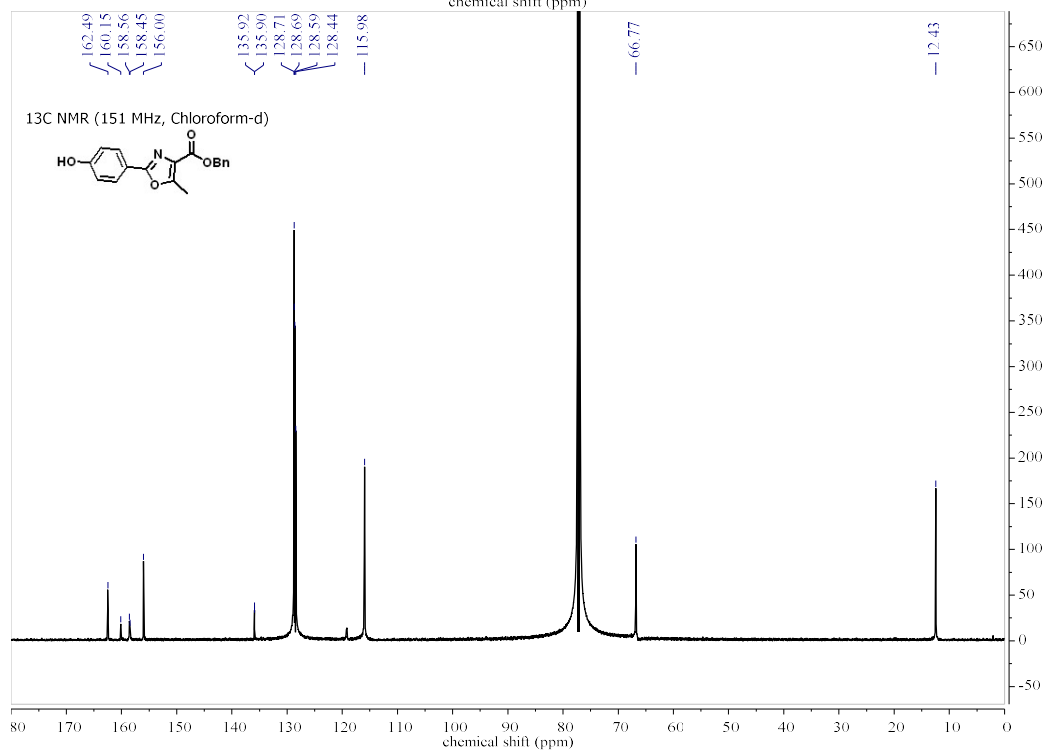
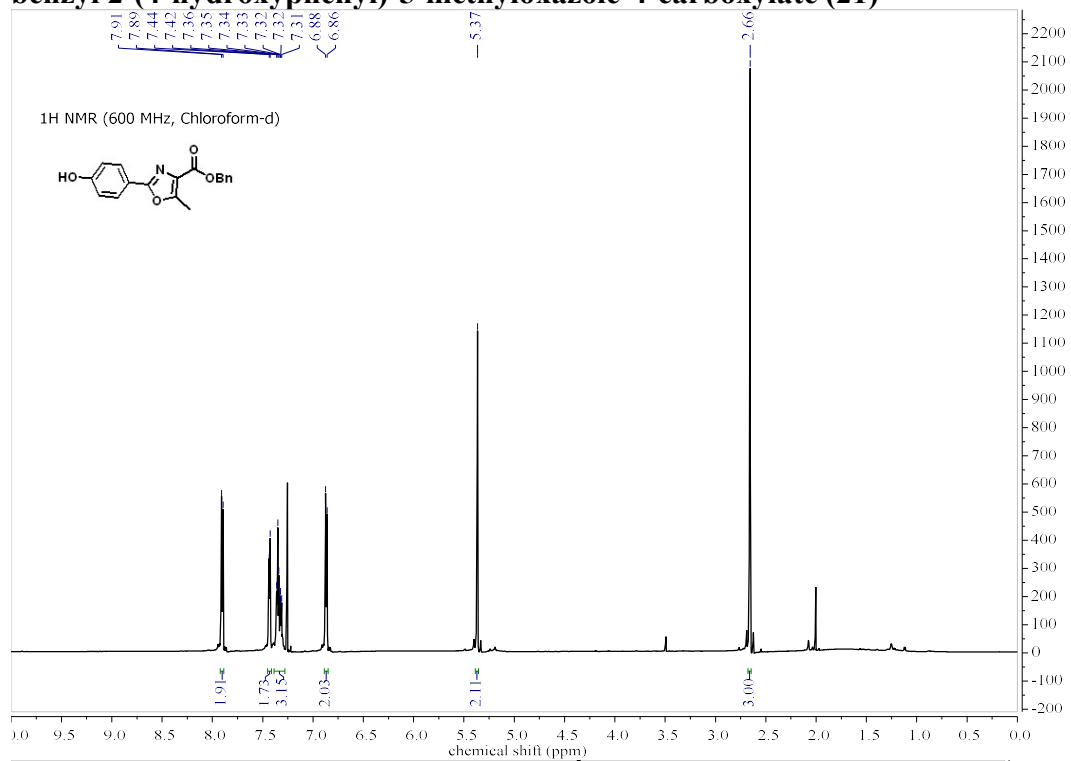


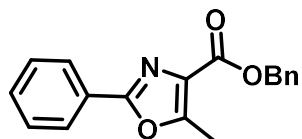
benzyl 2-(2,4-dihydroxyphenyl)-5-methyloxazole-4-carboxylate (20)



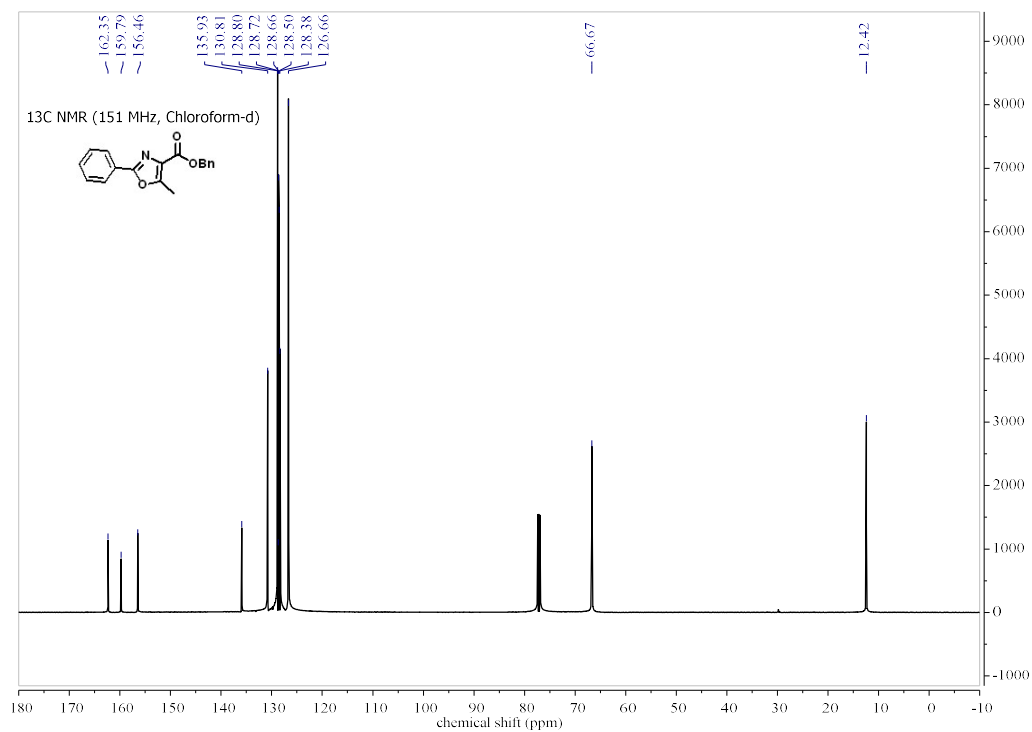
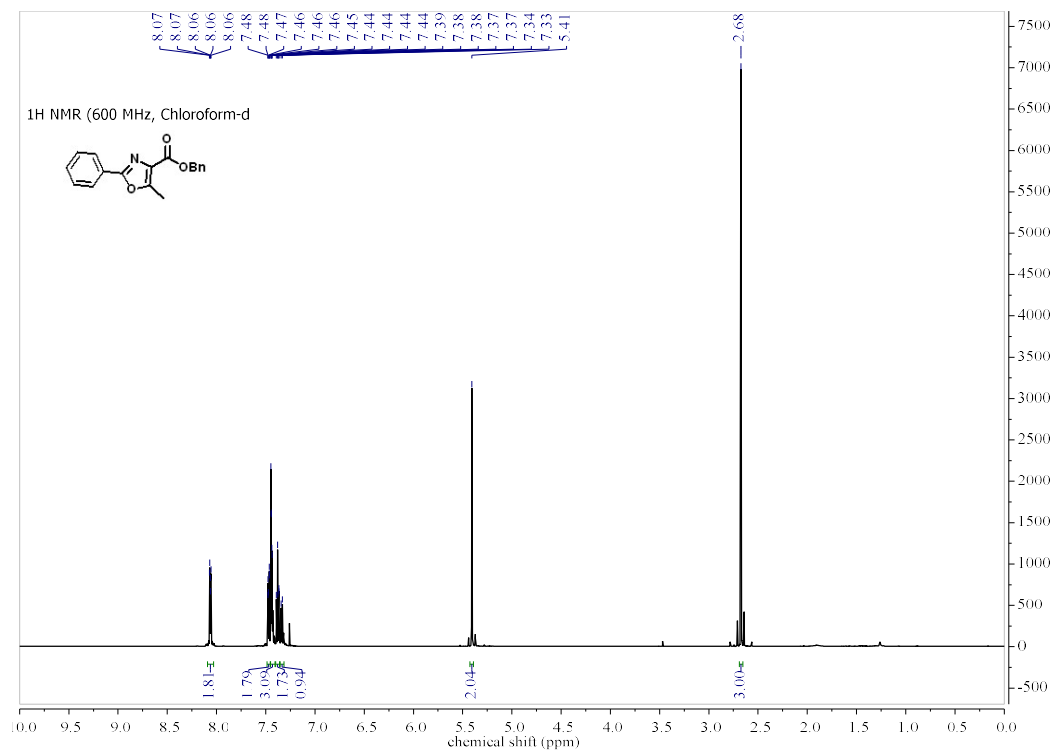


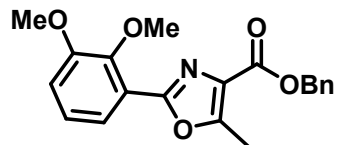
benzyl 2-(4-hydroxyphenyl)-5-methyloxazole-4-carboxylate (21)



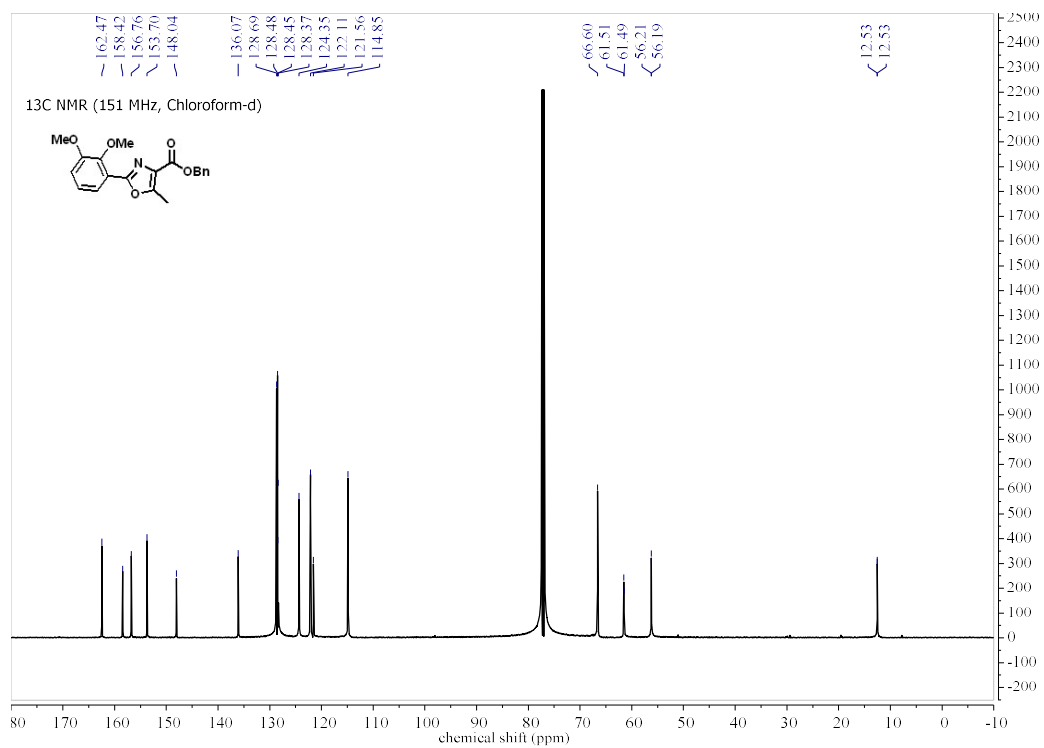
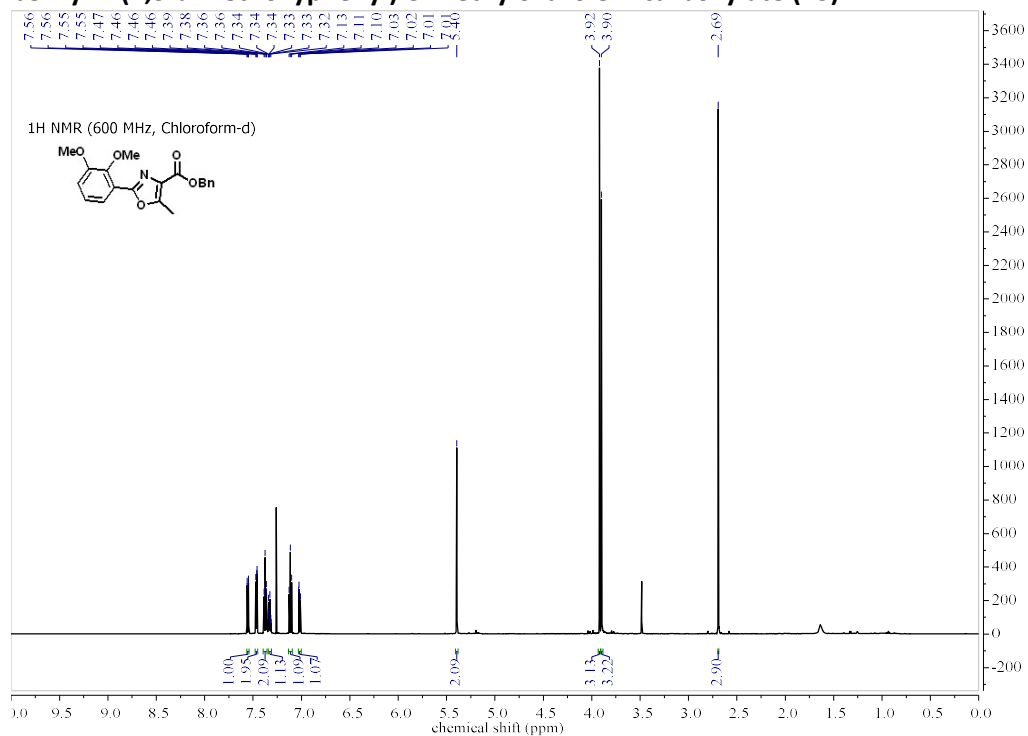


benzyl 5-methyl-2-phenyloxazole-4-carboxylate (22)

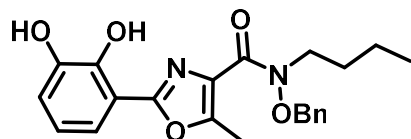




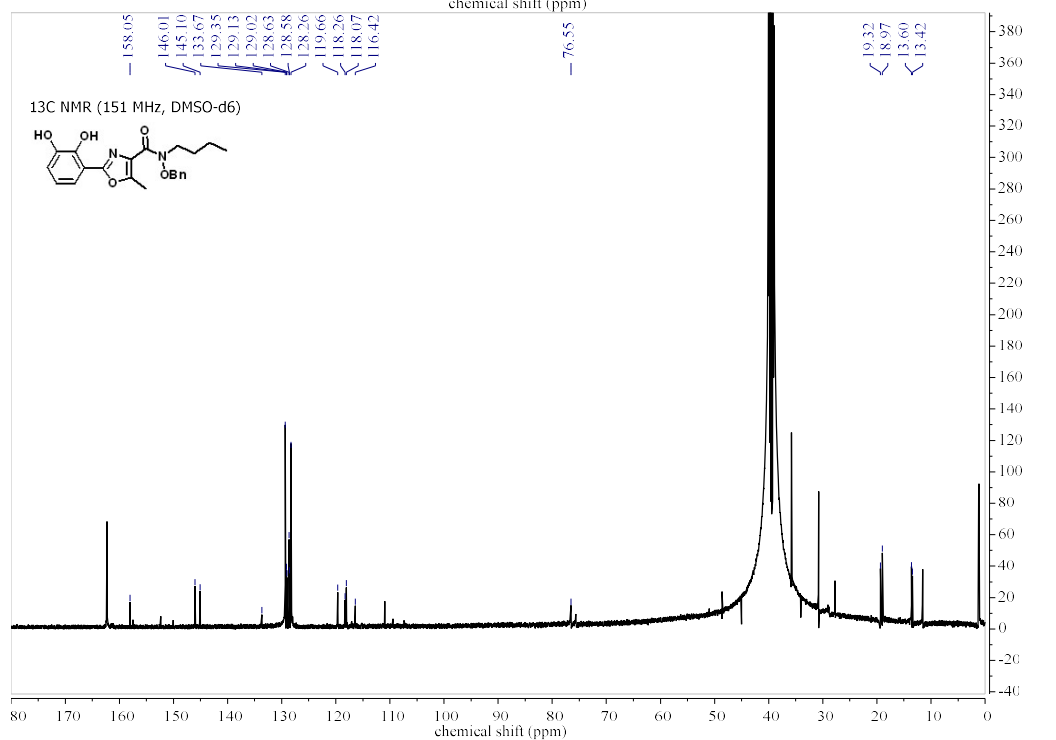
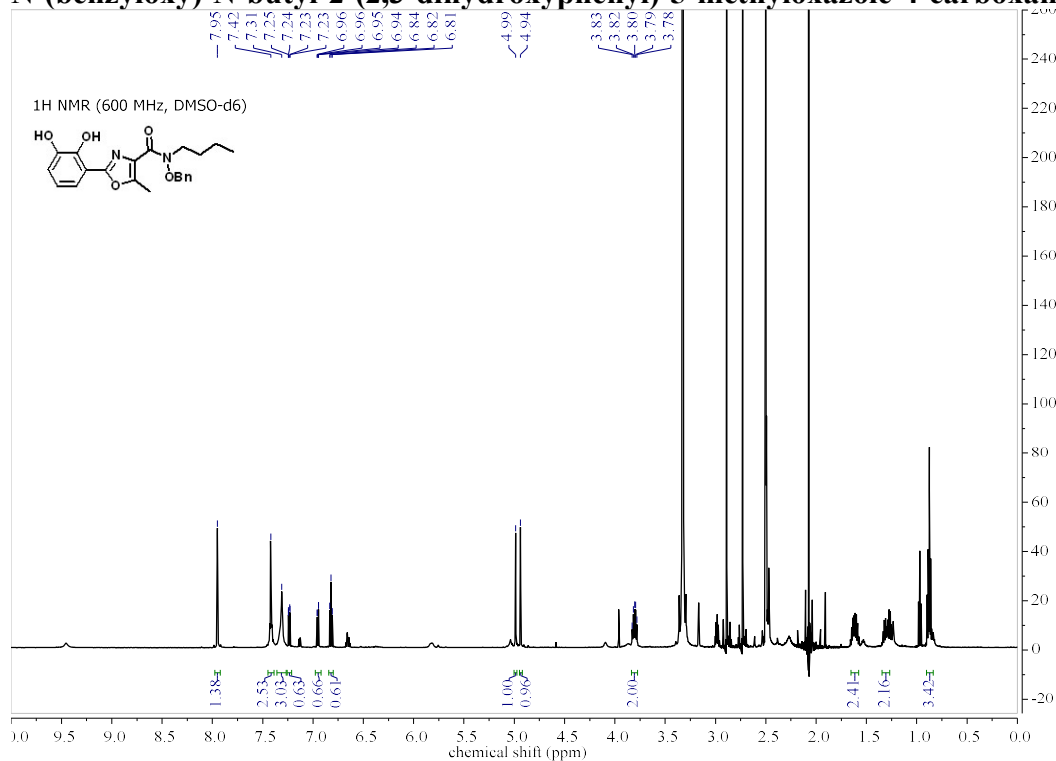
benzyl 2-(2,3-dimethoxyphenyl)-5-methyloxazole-4-carboxylate (23)

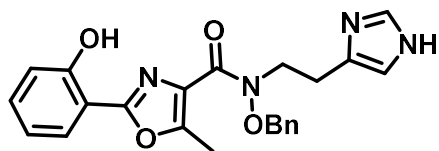




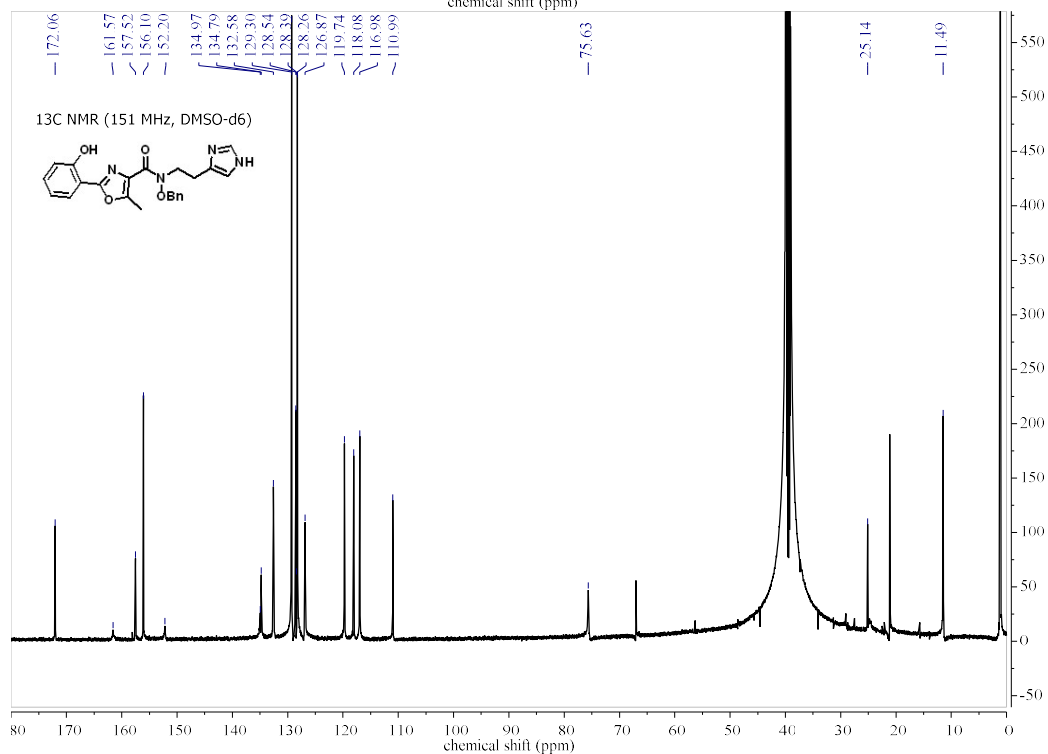
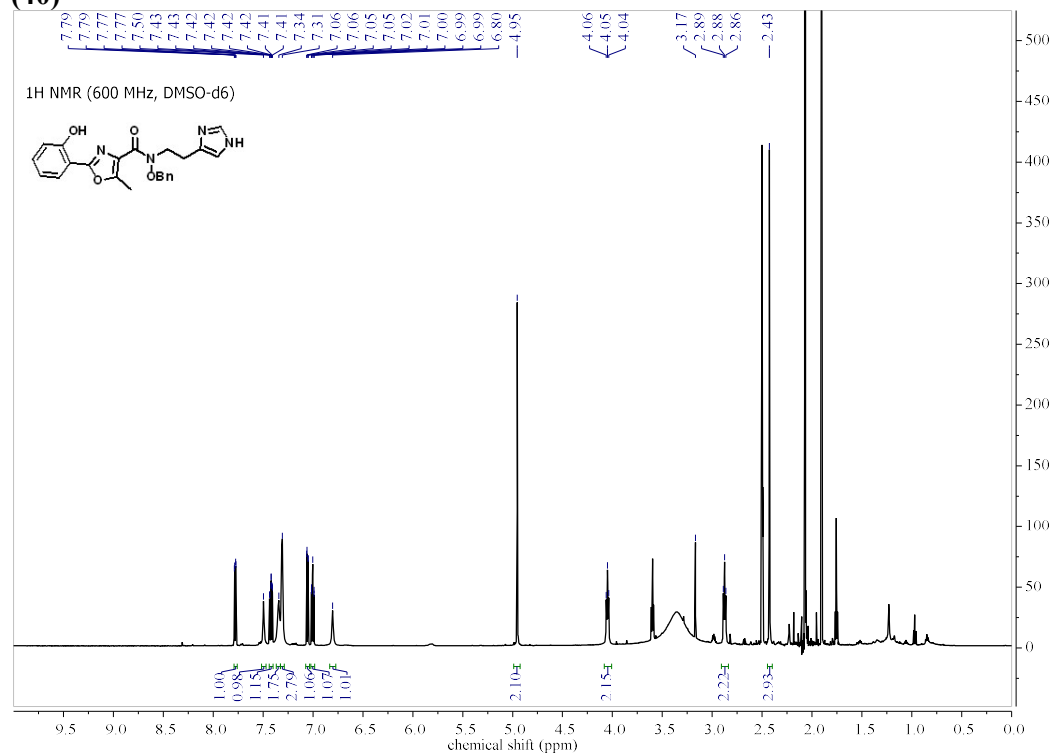


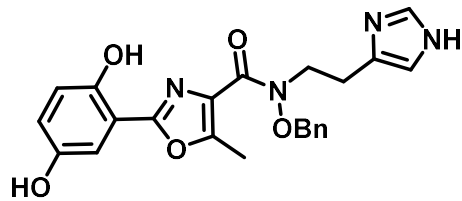
**N-(benzyloxy)-N-butyl-2-(2,3-dihydroxyphenyl)-5-methyloxazole-4-carboxamide (39)**



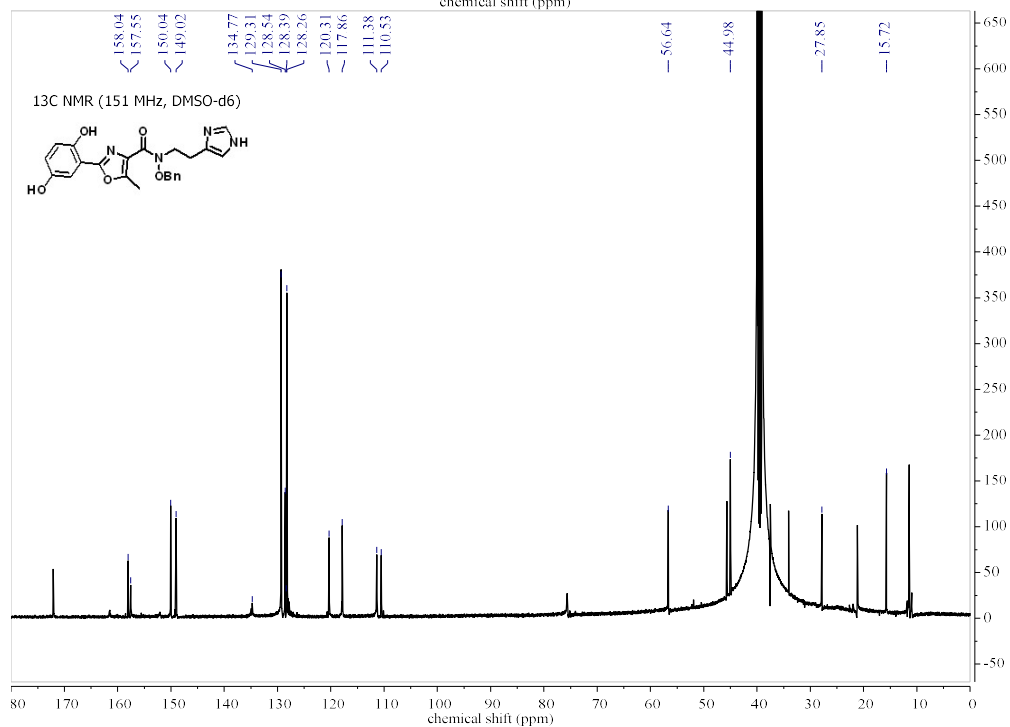
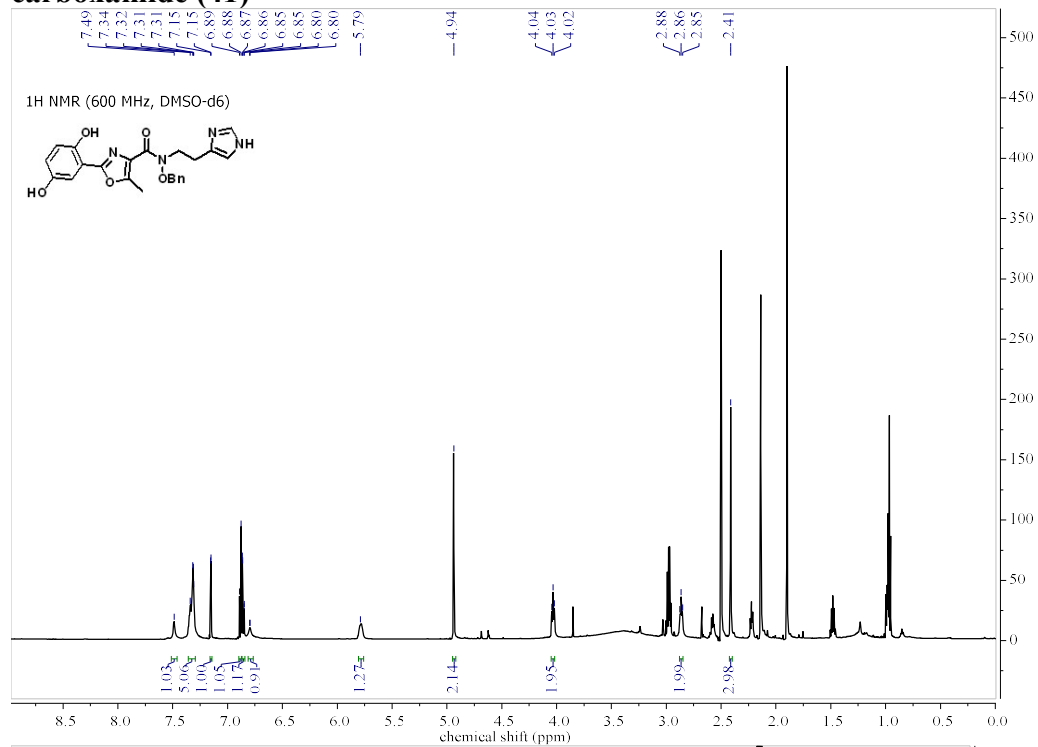


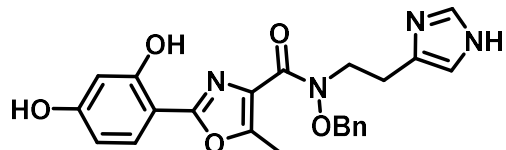
**N-(2-(1H-imidazol-4-yl)ethyl)-N-(benzyloxy)-2-(2-hydroxyphenyl)-5-methyloxazole-4-carboxamide (40)**



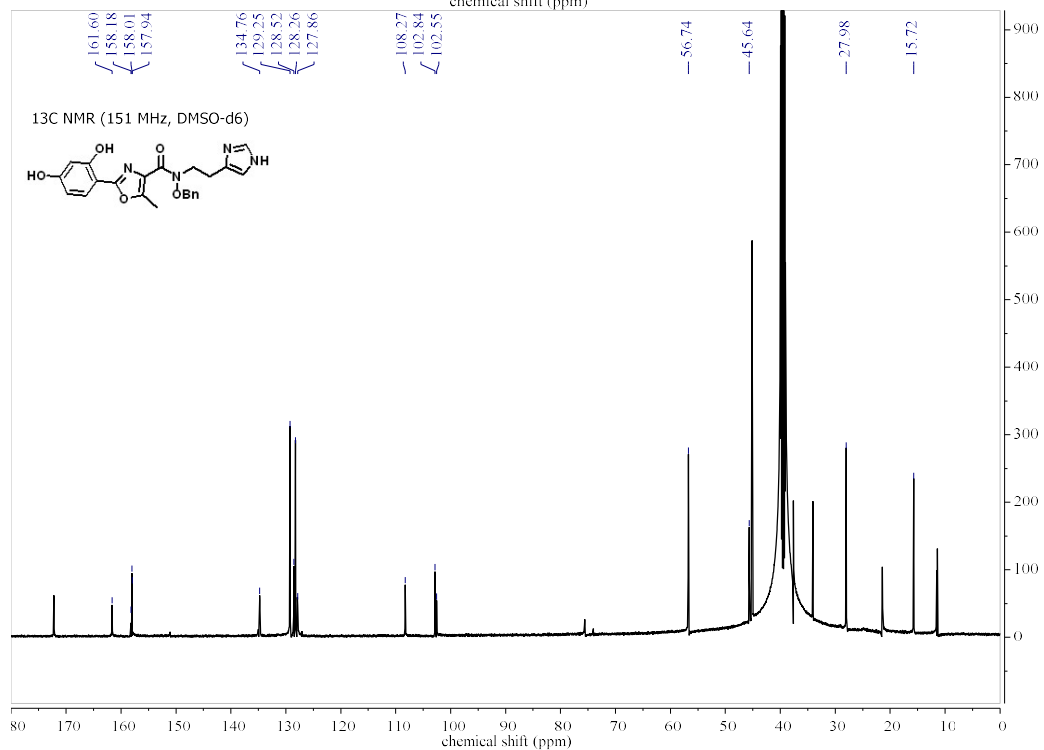
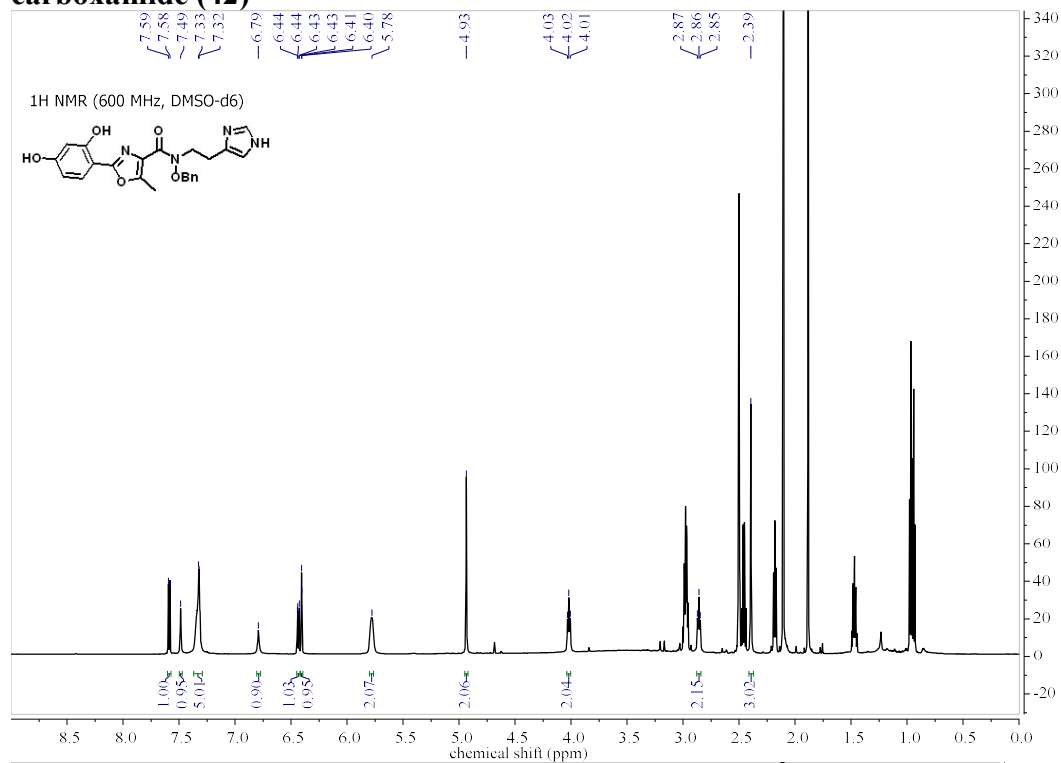


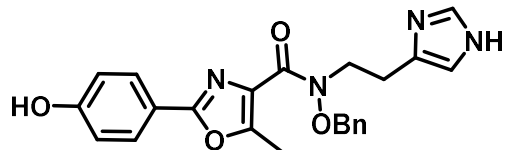
**N-(2-(1H-imidazol-4-yl)ethyl)-N-(benzyloxy)-2-(2,5-dihydroxyphenyl)-5-methyloxazole-4-carboxamide (41)**



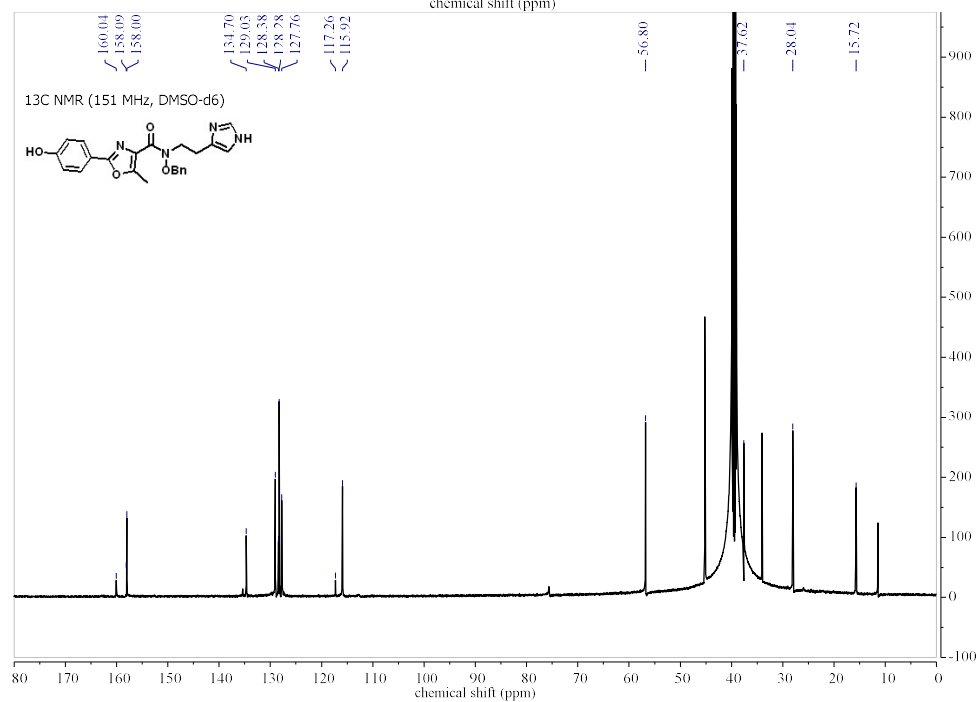
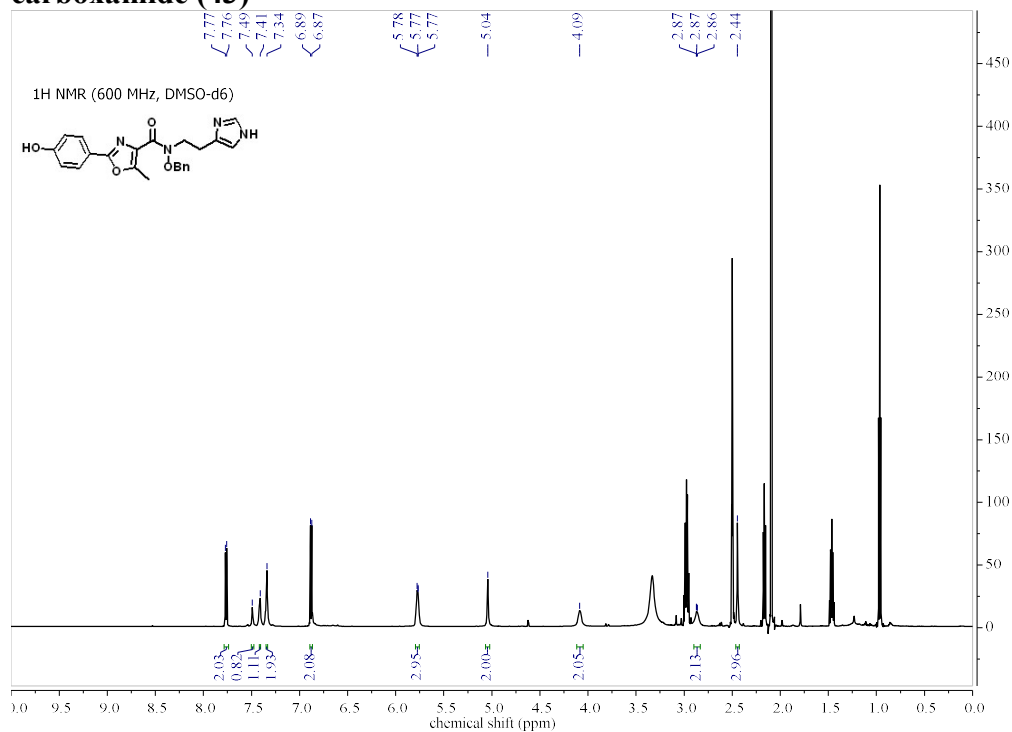


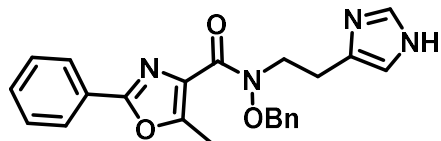
**N-(2-(1H-imidazol-4-yl)ethyl)-N-(benzyloxy)-2-(2,4-dihydroxyphenyl)-5-methyloxazole-4-carboxamide (42)**



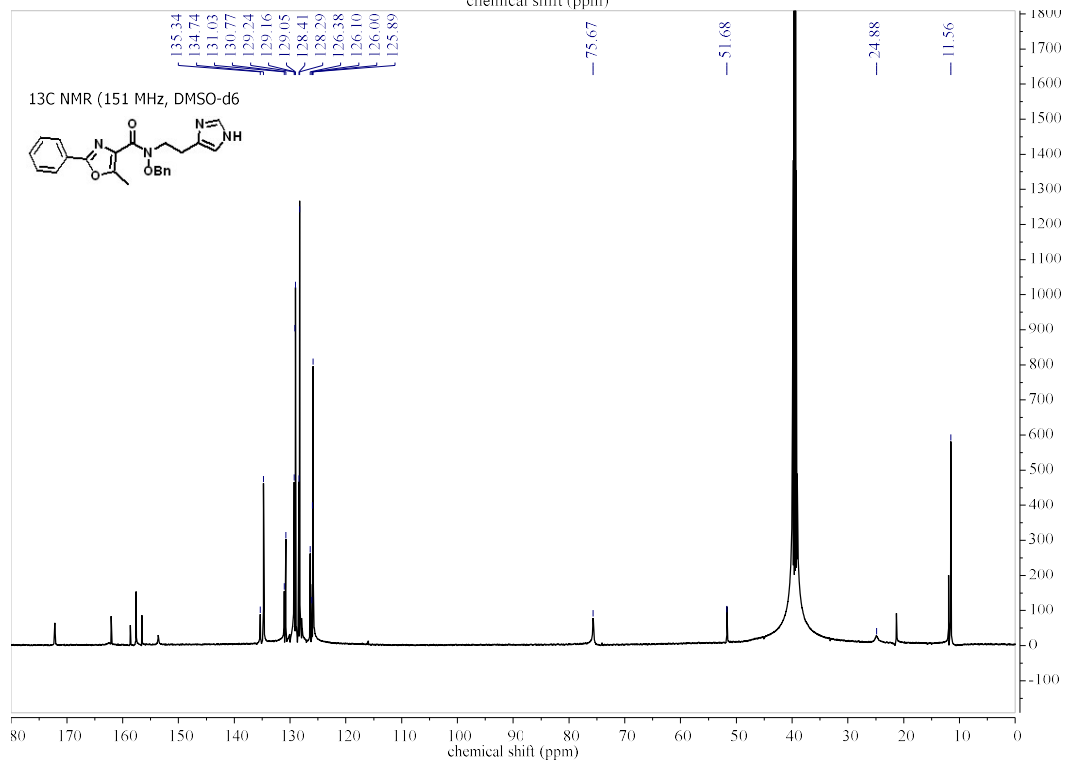
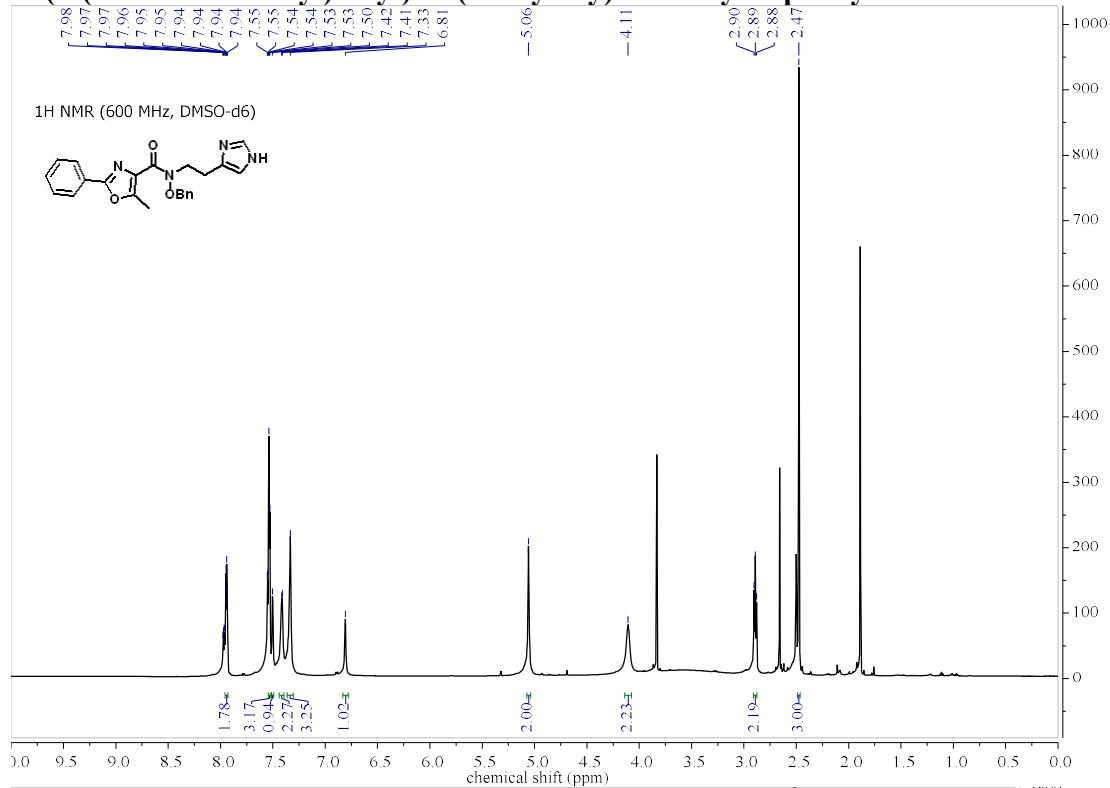


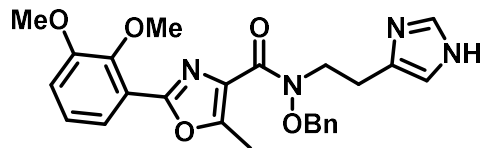
**N-(2-(1H-imidazol-4-yl)ethyl)-N-(benzyloxy)-2-(4-hydroxyphenyl)-5-methyloxazole-4-carboxamide (43)**



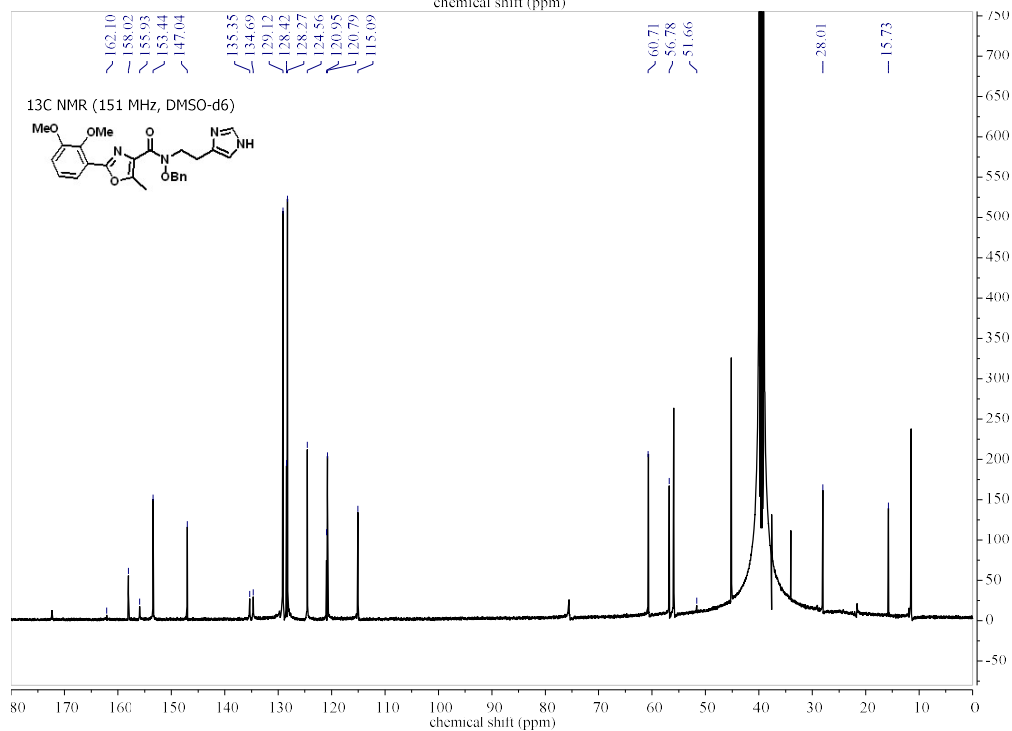
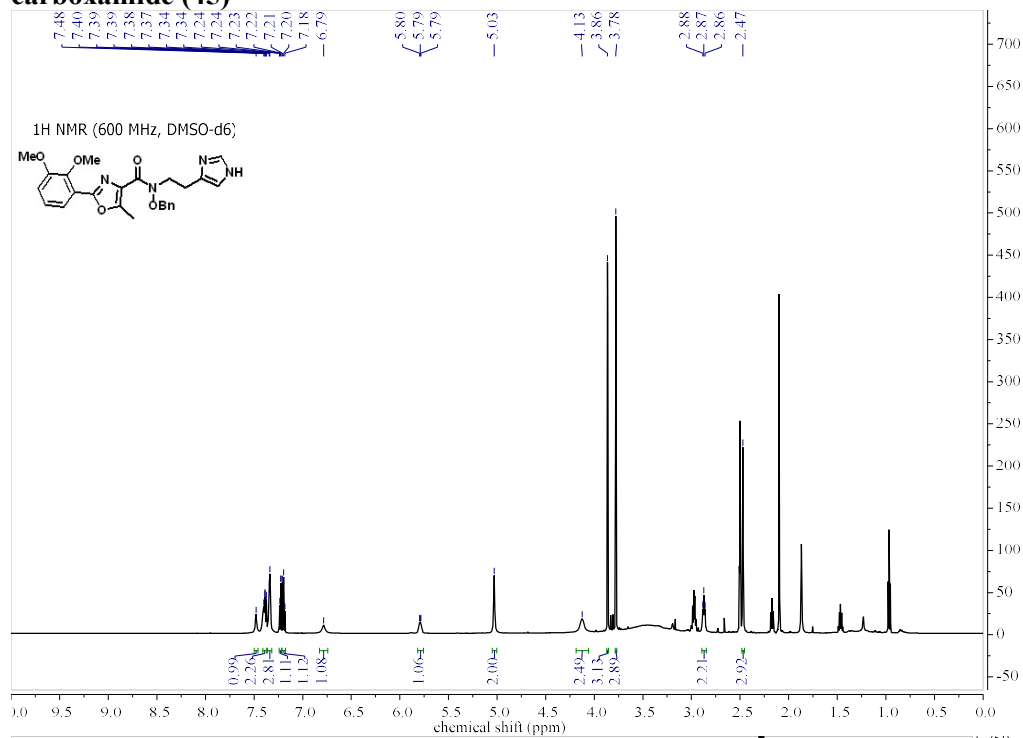


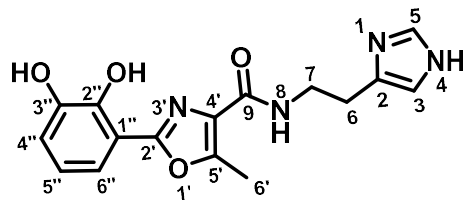
**N-(2-(1H-imidazol-4-yl)ethyl)-N-(benzyloxy)-5-methyl-2-phenyloxazole-4-carboxamide (44)**





**N-(2-(1H-imidazol-4-yl)ethyl)-N-(benzyloxy)-2-(2,3-dimethoxyphenyl)-5-methyloxazole-4-carboxamide (45)**



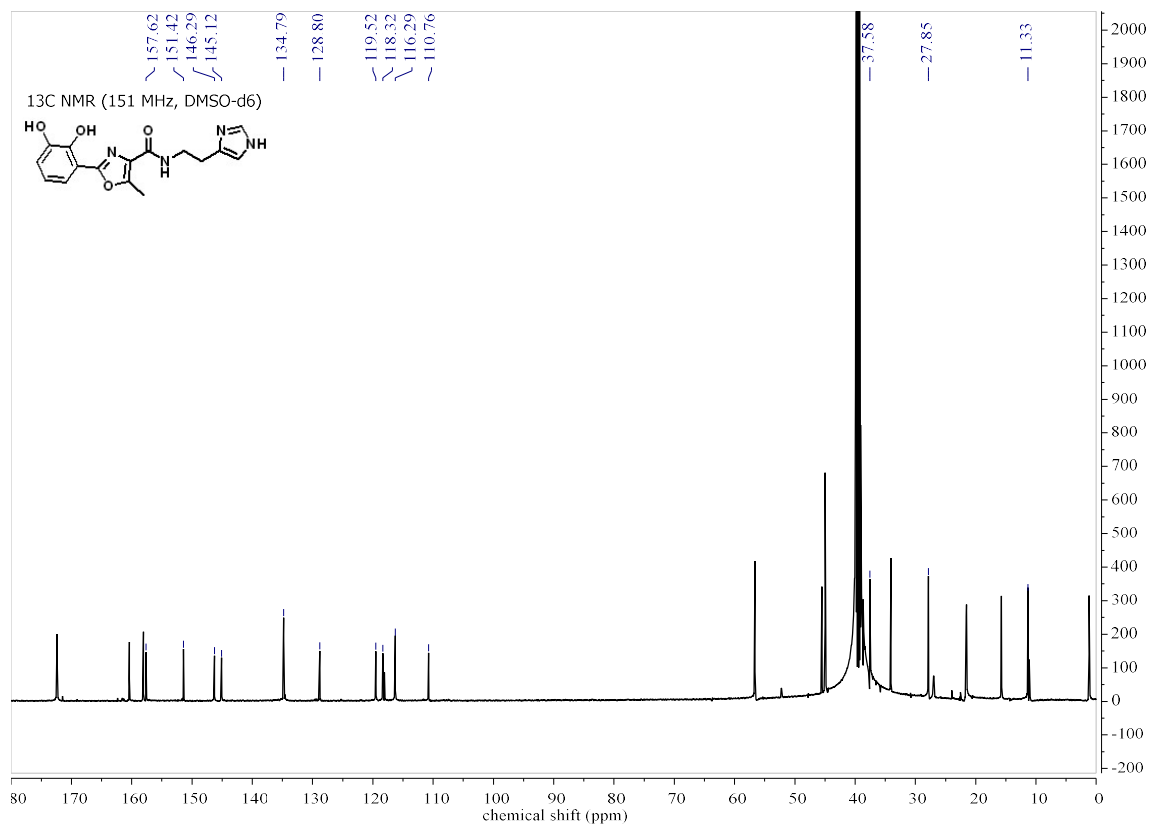
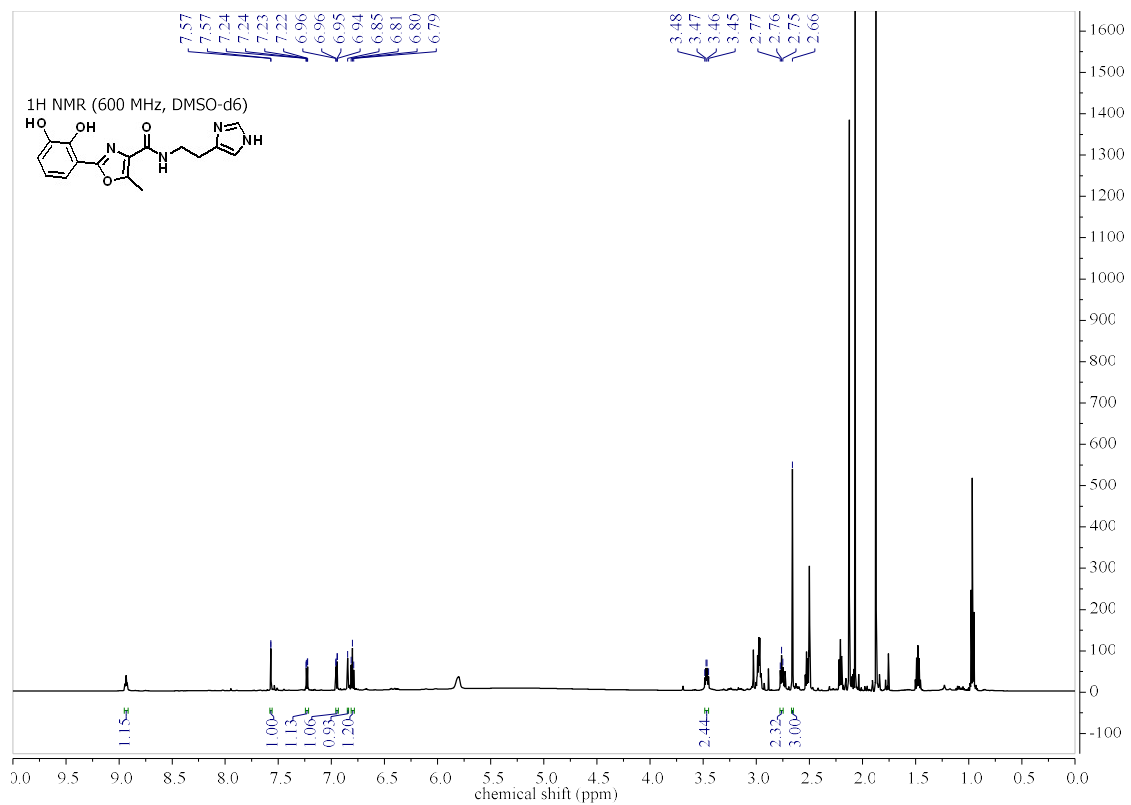


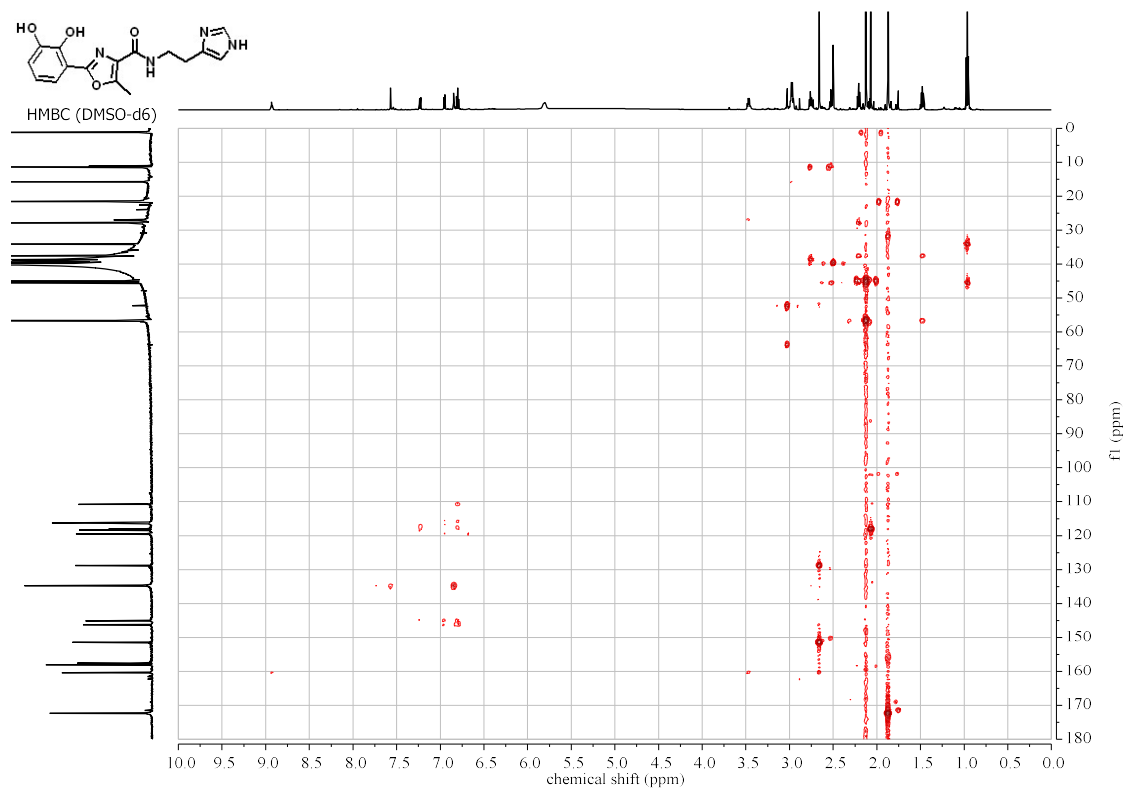
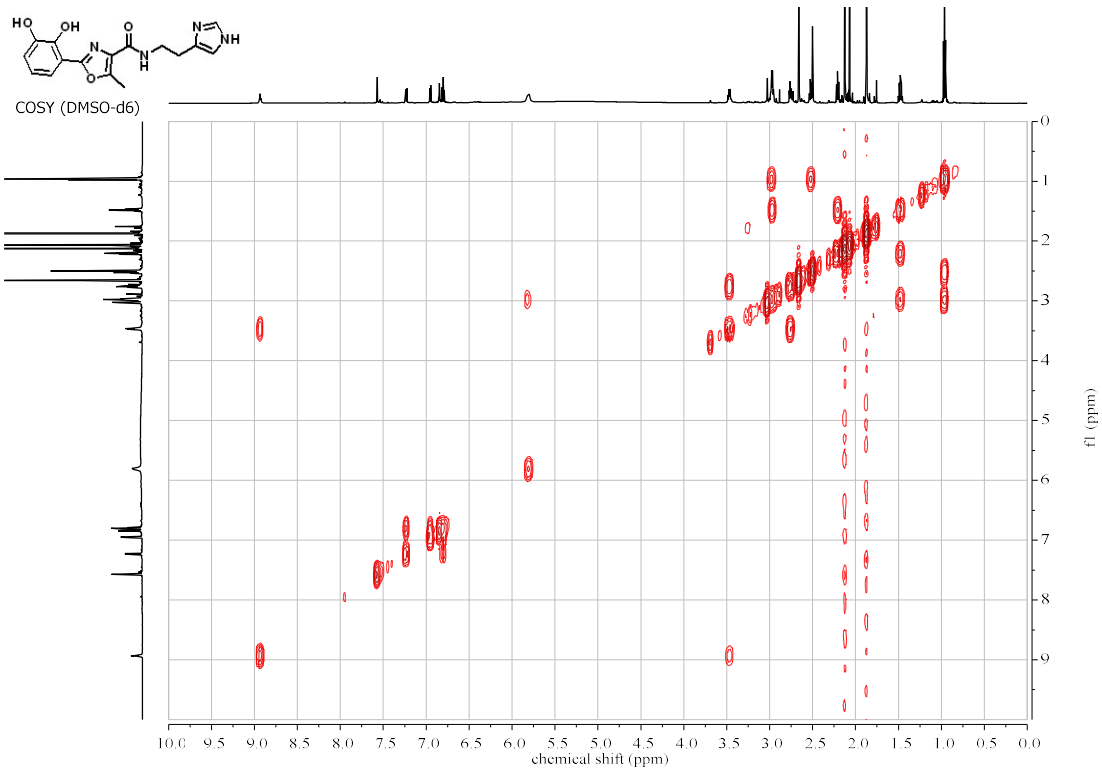
**N-(2-(1H-imidazol-4-yl)ethyl)-2-(2,3-dihydroxyphenyl)-5-methyloxazole-4-carboxamide – 1<sup>1</sup>**

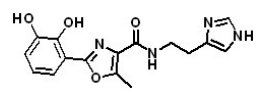
HRMS calcd for C<sub>16</sub>H<sub>17</sub>N<sub>4</sub>O<sub>4</sub> (M + H)<sup>+</sup> 329.1244; found 329.1245

Atom	<sup>13</sup> C (ppm)	<sup>1</sup> H (ppm), Multiplets in Hz	COSY 1H-1H 3 bond	HMBC 1H-13C 2-3 bond	HSQC
2					
3		6.85 (s, 1H)			
5	134.8	7.57 (d, 1H)			5
6	27.9	2.76 (t, 2H)	7	7	6
7	37.6	3.47 (q, 2H)	6		
9					
2'	157.6				
4'	128.8				
5'	151.4				
6'	11.3	2.66 (s, 3H)		5'	6'
1''	110.7				
2''	145.1			4'', 6''	
3''	146.3			5''	
4''	118.3	6.65 (dd, 1H)	5''	2'', 5''	4''
5''	119.5	6.80 (t, 1H)	6''	3'', 4''	5''
6''	116.3	7.23 (dd, 1H)	5''	2', 2'', 4''	6''

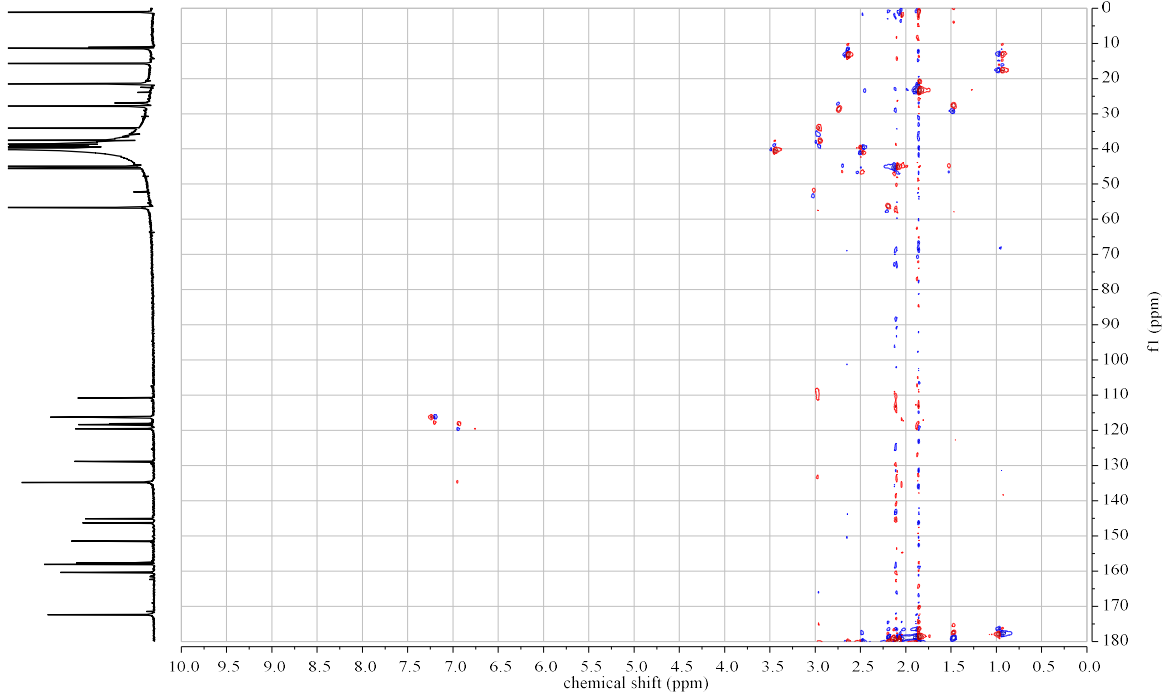




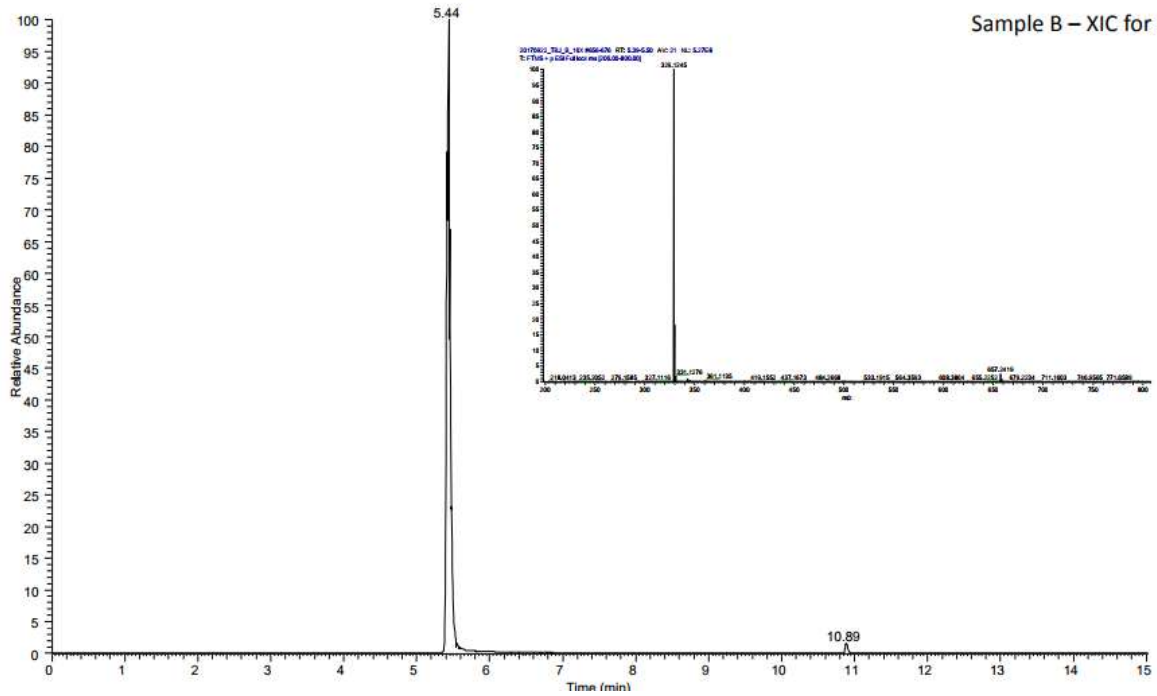
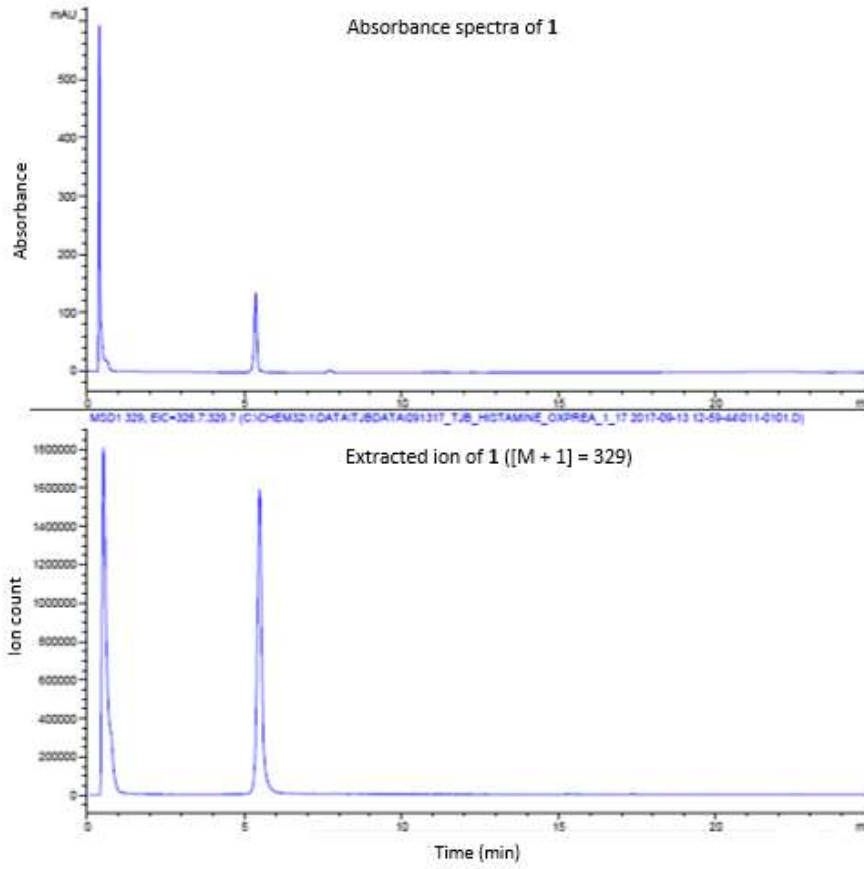


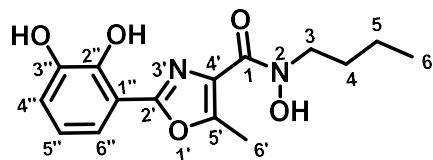


HSQC (DMSO-d6)



LC\_MS and HRMS for 1

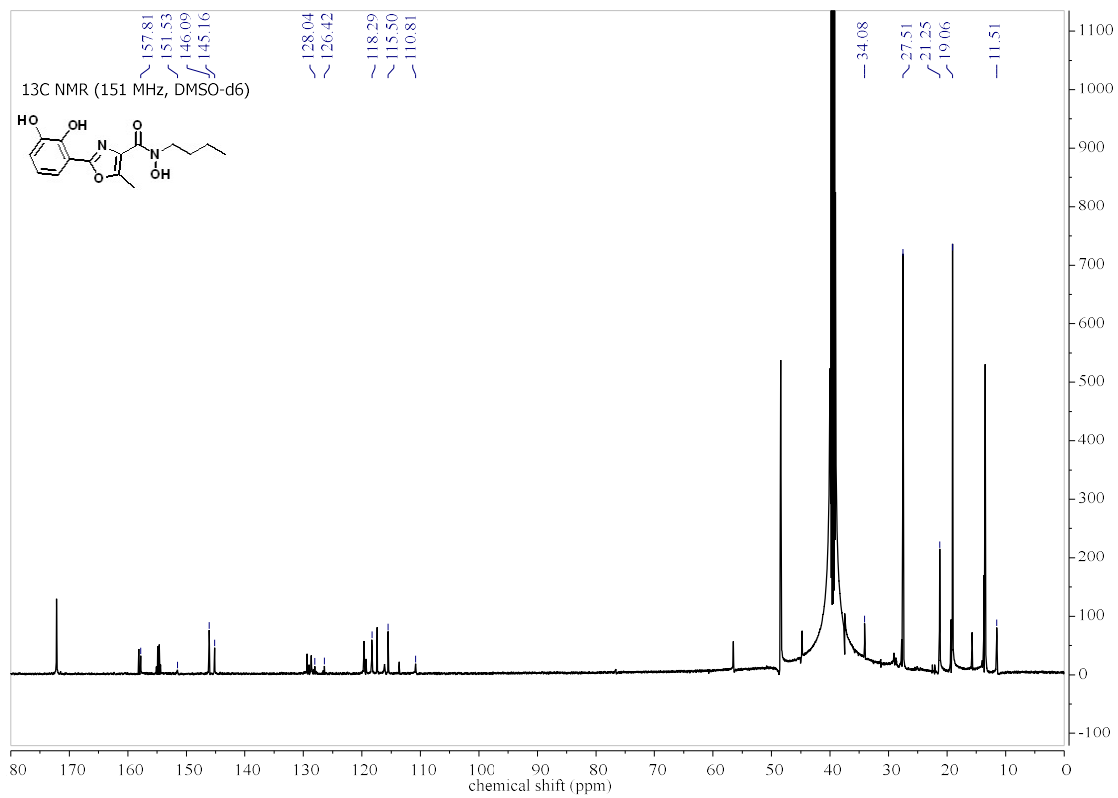
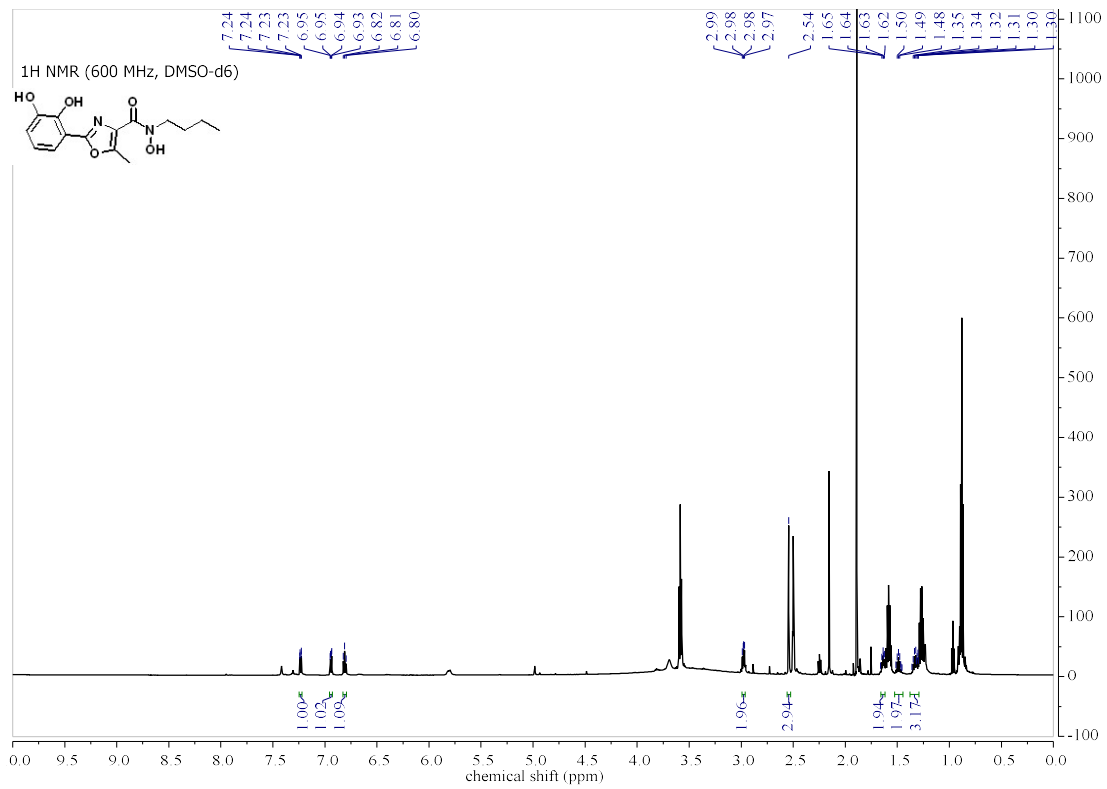


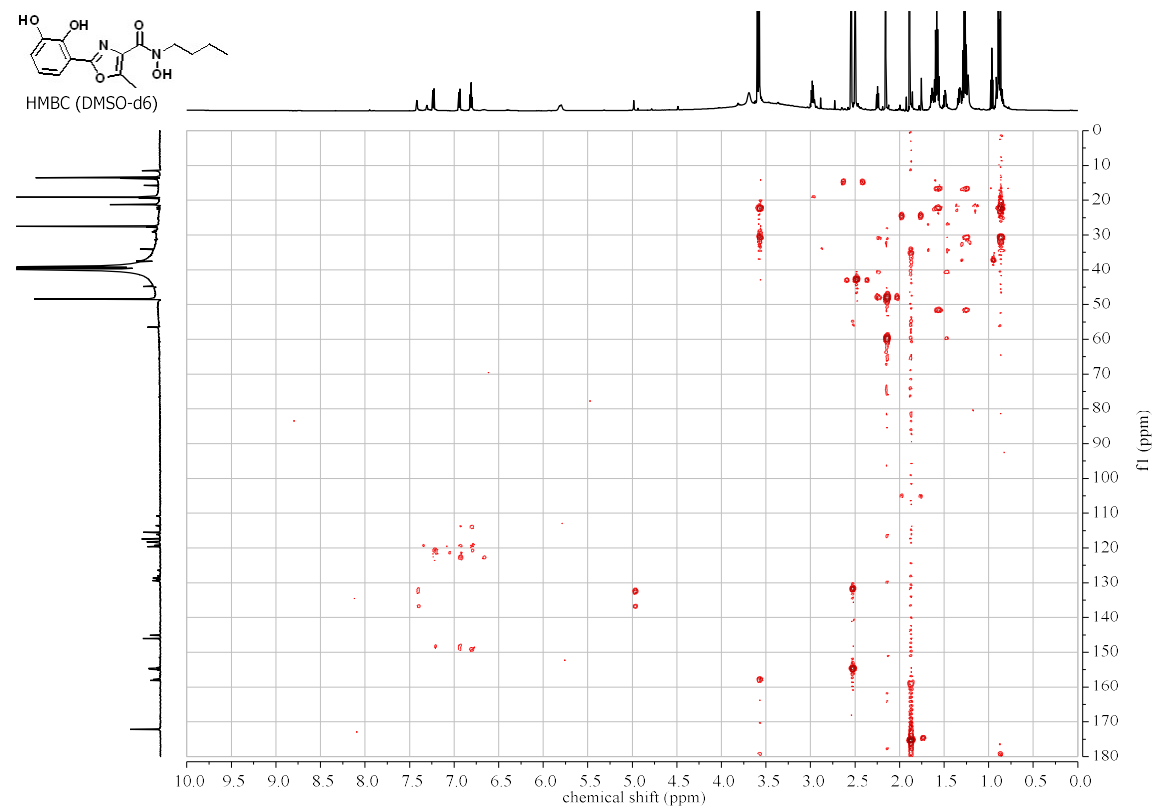
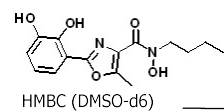
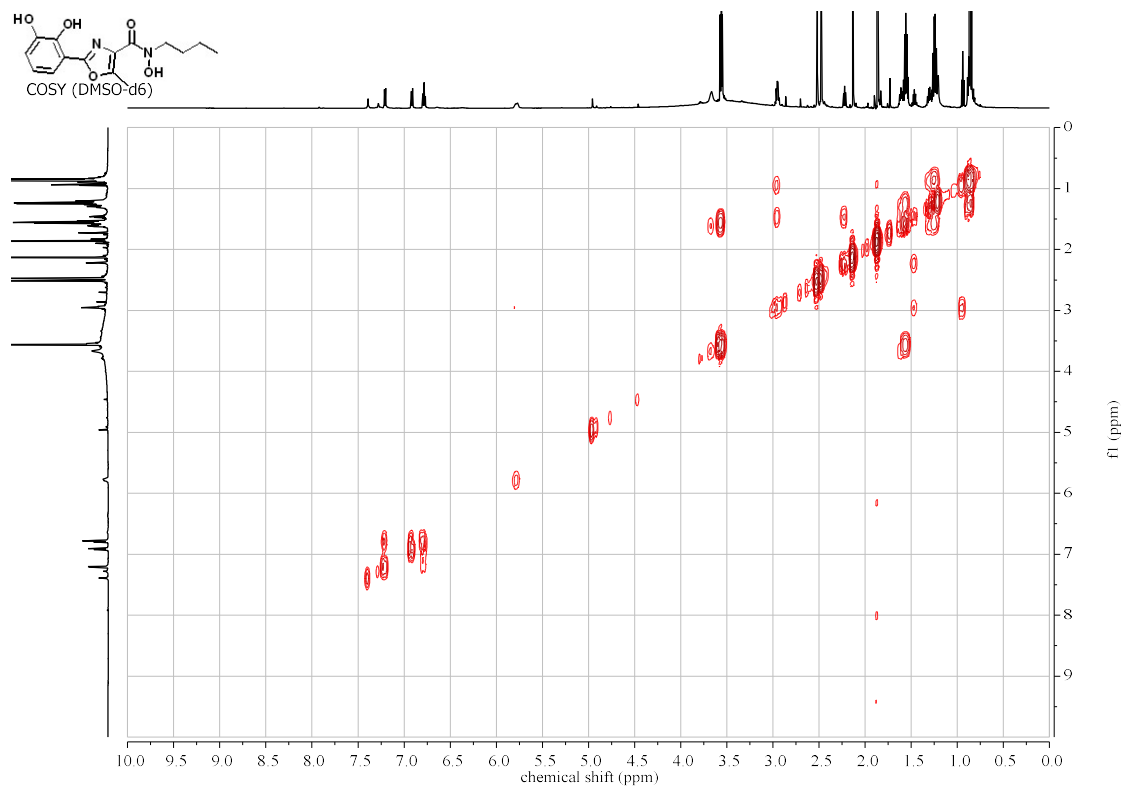
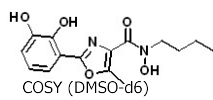


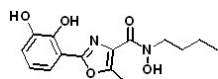
**N-butyl-2-(2,3-dihydroxyphenyl)-N-hydroxy-5-methyloxazole-4-carboxamide – 2**

HRMS calcd for  $C_{15}H_{19}N_2O_5$  ( $M + H$ )<sup>+</sup> 307.1288; found 307.1286

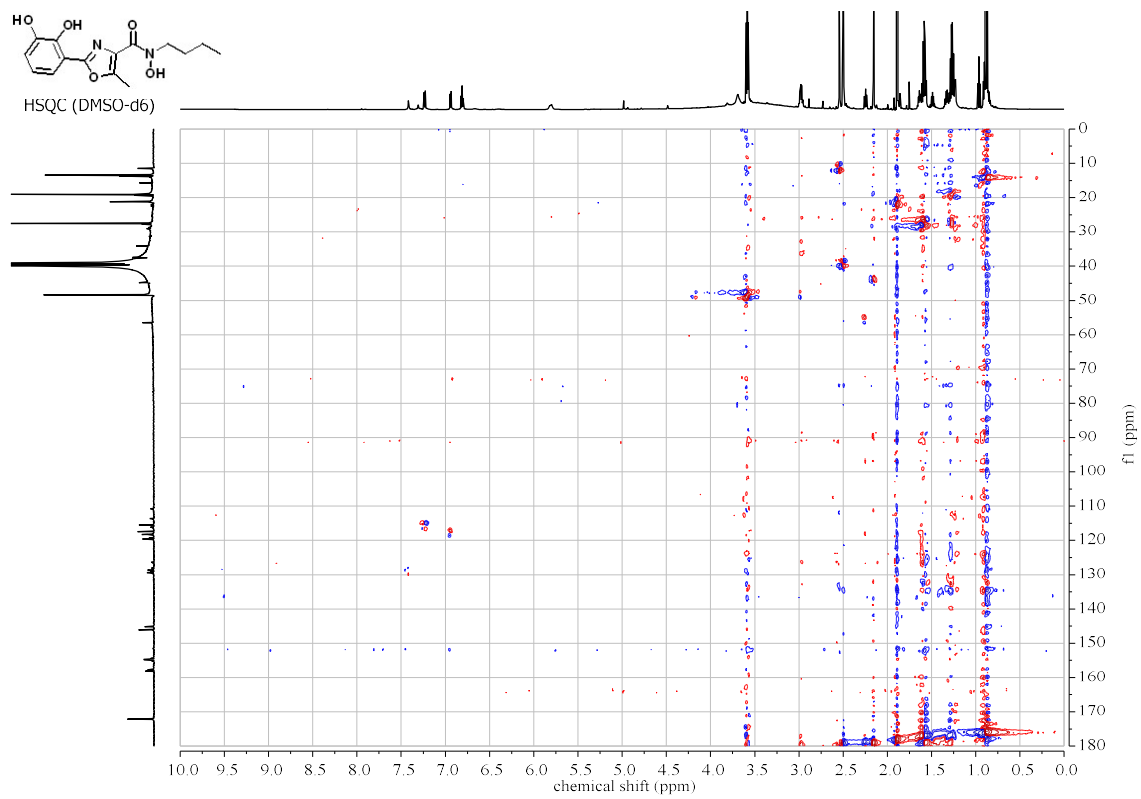
Atom	<sup>13</sup> C (ppm)	<sup>1</sup> H (ppm), Multiplets in Hz	COSY 1H-1H 3 bond	HMBC 1H-13C 2-3 bond	HSQC
1					
2					
3	34.1	2.98 (m, 2H)	4	4	3
4	27.5	1.65 (m, 2H)	3, 5	3, 5	4
5	21.2	1.48 (m, 2H)	4, 6	4, 6	5
6	1.32	1.32 (m, 3H)	5	5	6
2'	157.8				
4'	128.0				
5'	151.5				
6'	11.5	2.54 (s, 3H)		5'	6'
1''	110.8				
2''	145.2			4'', 6''	
3''	146.1			5''	
4''	118.3	6.94 (dd, 1H)	5''	2'', 5''	4''
5''	126.4	6.80 (t, 1H)	6''	3'', 4''	5''
6''	115.5	7.23 (dd, 1H)	5''	2', 2'', 4''	6''





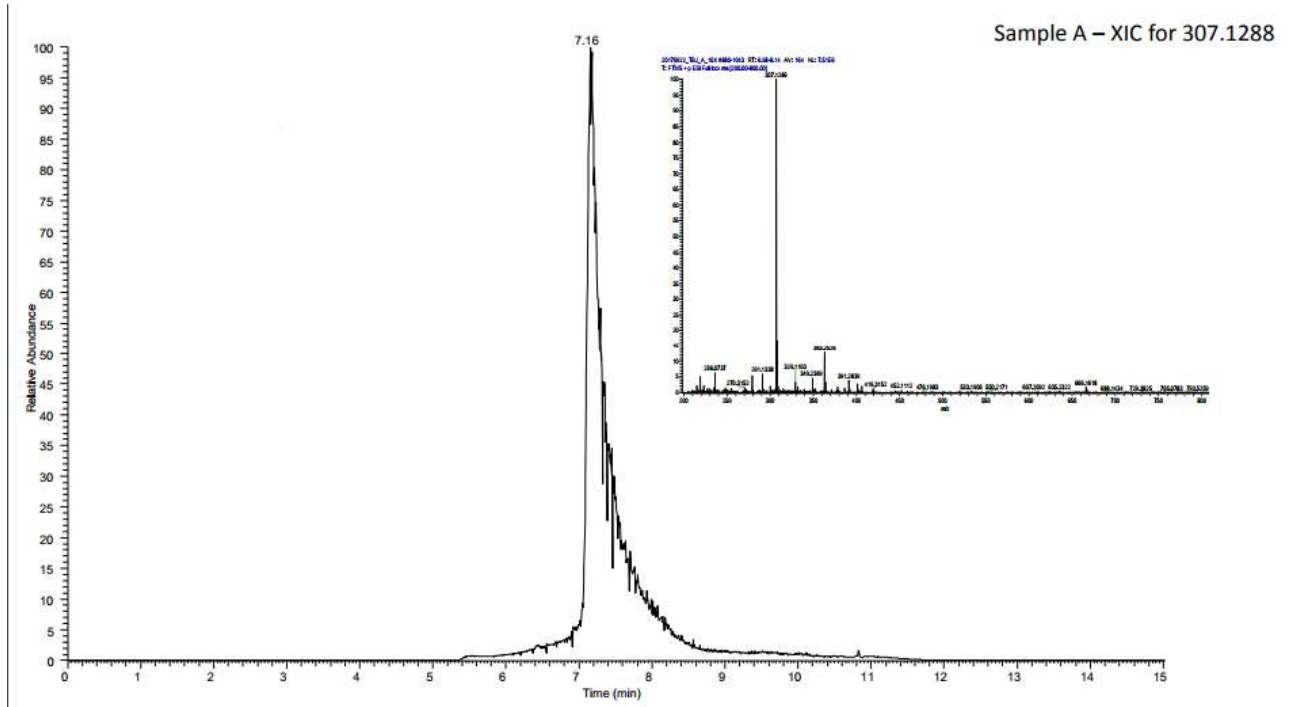
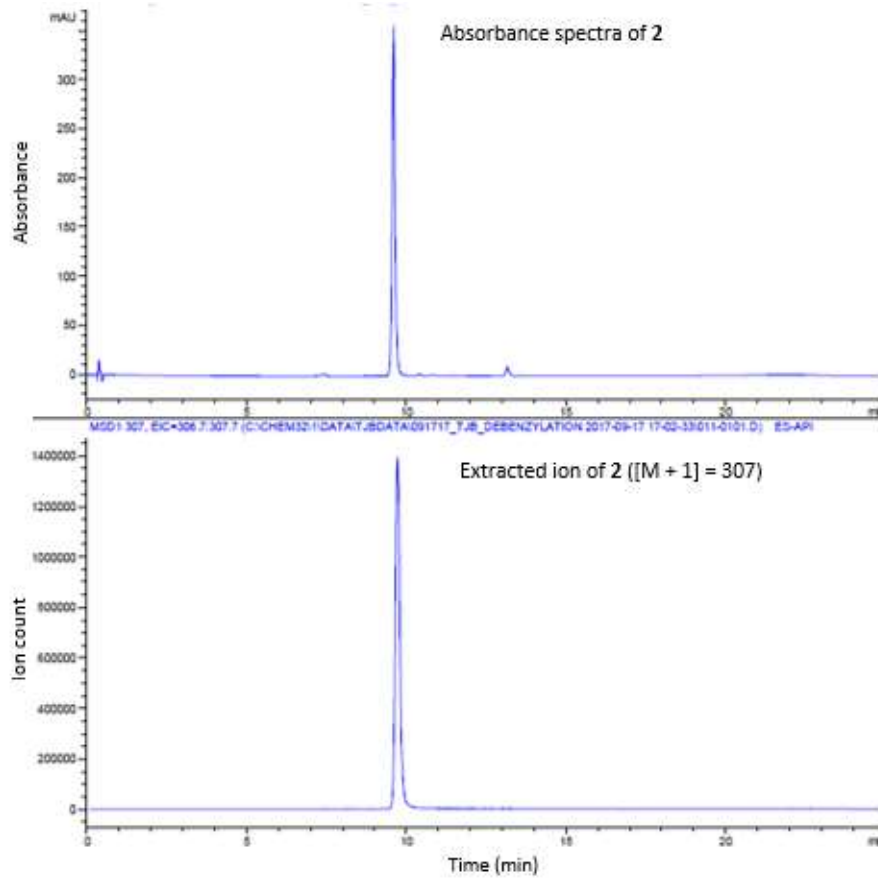


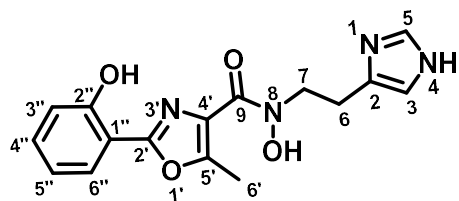
HSQC (DMSO-d6)





LC\_MS and HRMS for 2

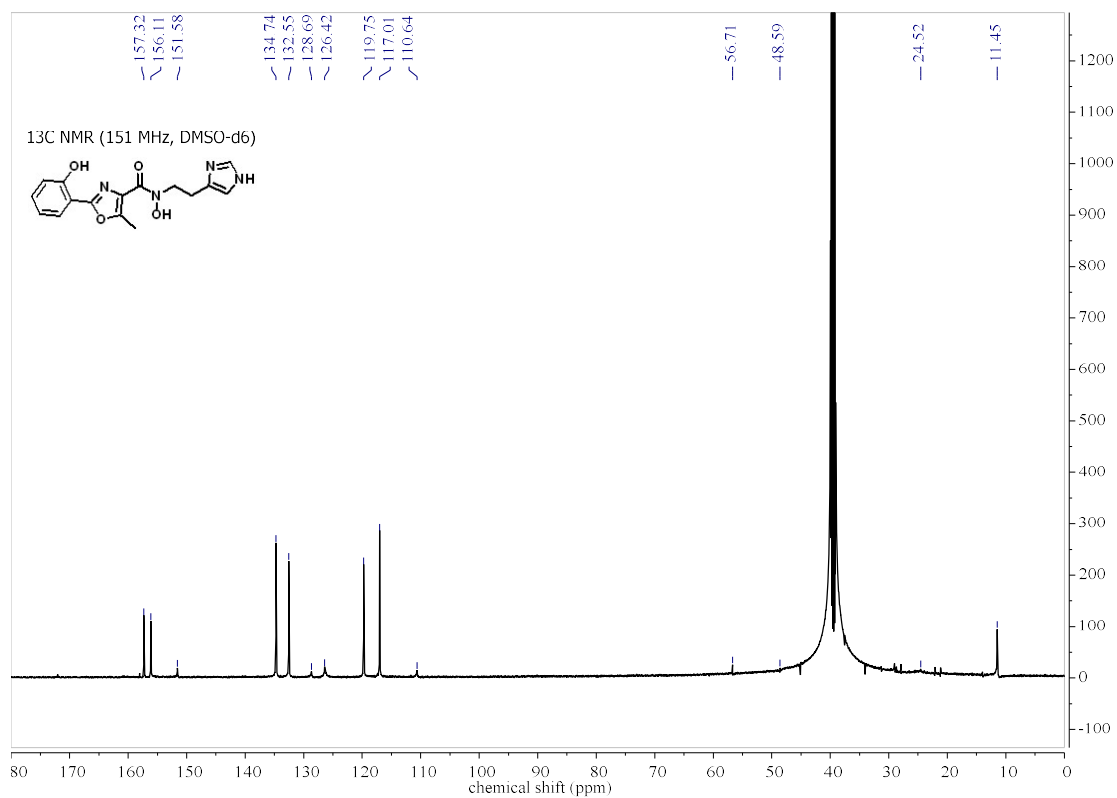
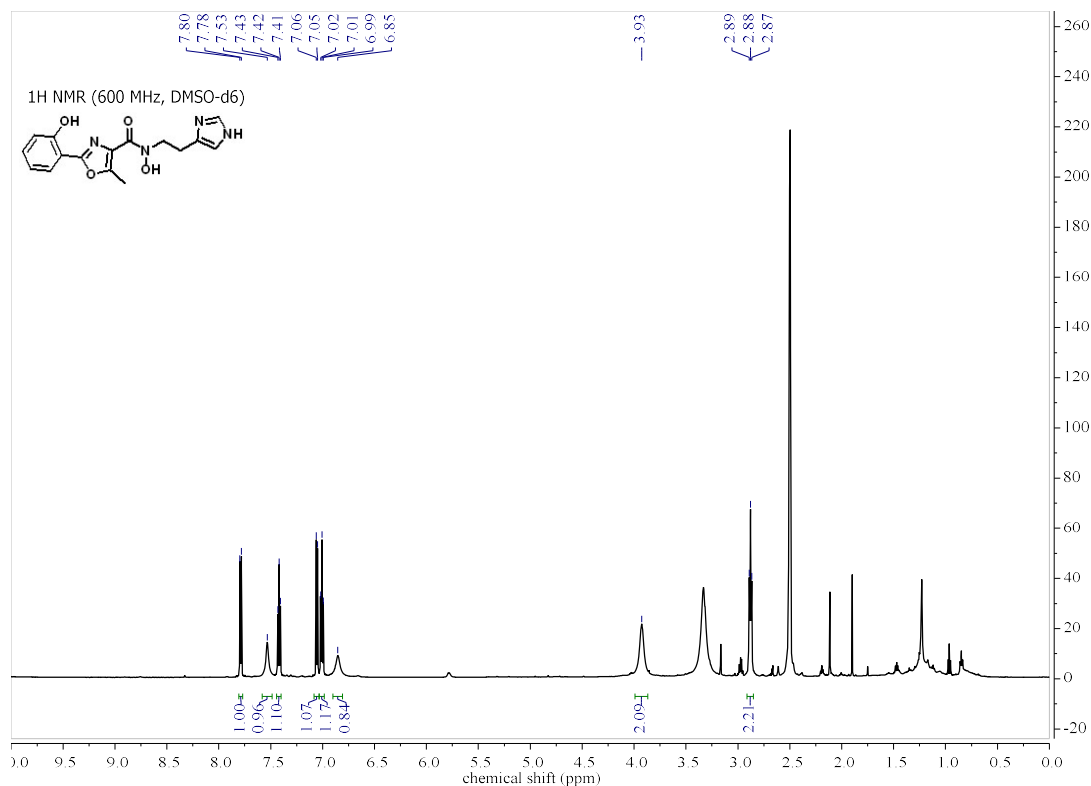


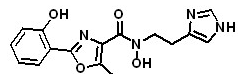


**N-(2-(1H-imidazol-4-yl)ethyl)-N-hydroxy-2-(2-hydroxyphenyl)-5-methyloxazole-4-carboxamide – 3**

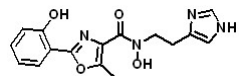
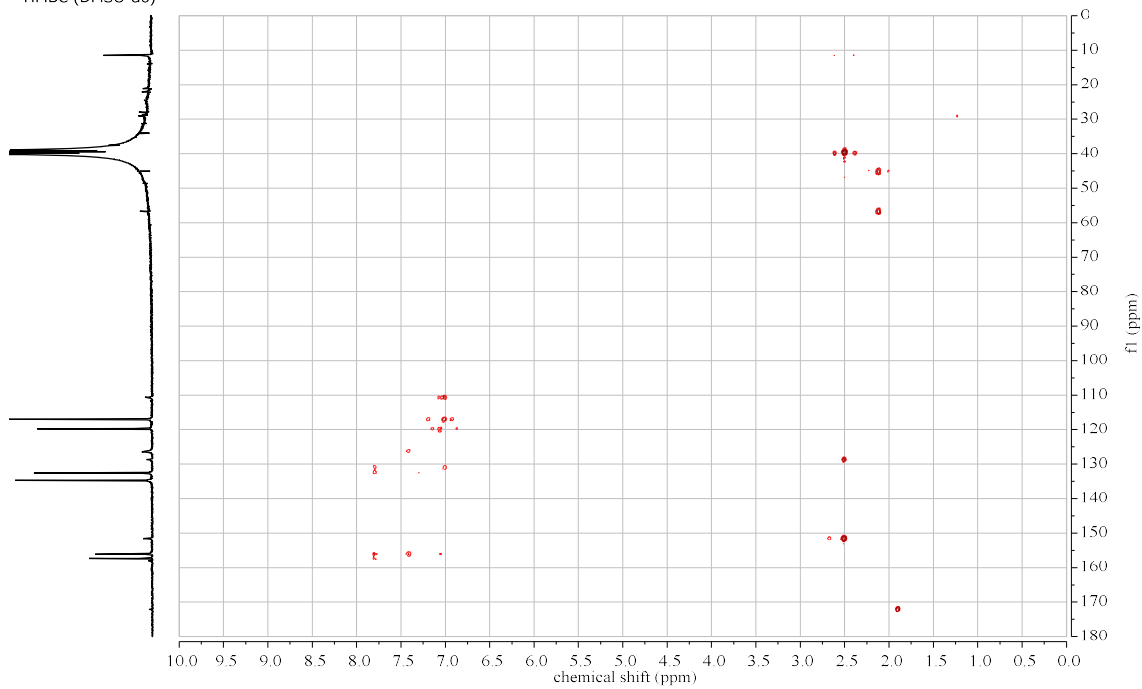
HRMS calcd for  $C_{16}H_{17}N_4O_4$  (M + H)<sup>+</sup> 329.1244; found 329.1241

Atom	<sup>13</sup> C (ppm)	<sup>1</sup> H (ppm), Multiplets in Hz	COSY 1H-1H 3 bond	HMBC 1H-13C 2-3 bond	HSQC
2					
3		6.85 (s, 1H)			
5	134.7	7.54 (s, 1H)			5
6	24.5	2.88 (t, 2H)	7		6
7		3.93 (s(br), 2H)	6		
9					
2'	157.3				
4'	128.7				
5'	151.6				
6'	11.5	2.50 (s, 3H) *under DMSO peak		4', 5'	6'
1''	110.6				
2''	156.1				
3''	117.0	7.05 (d, 2H)	4''	1'', 5'', 2''	3''
4''	132.5	7.42 (t, 1H)	3''	6'', 2''	4''
5''	119.8	7.01 (t, 1H)	4'', 6''	1'', 3'', 6''	3''
6''	126.4	7.79 (d, 1H)	3''	2'', 4'', 2'	6''

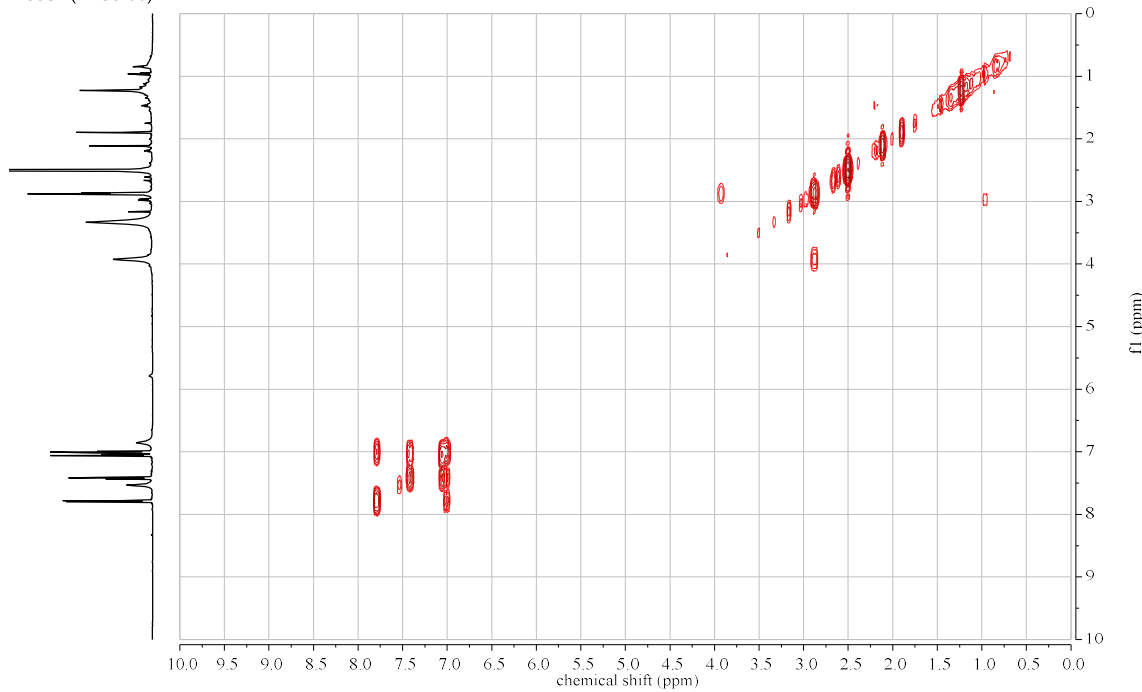


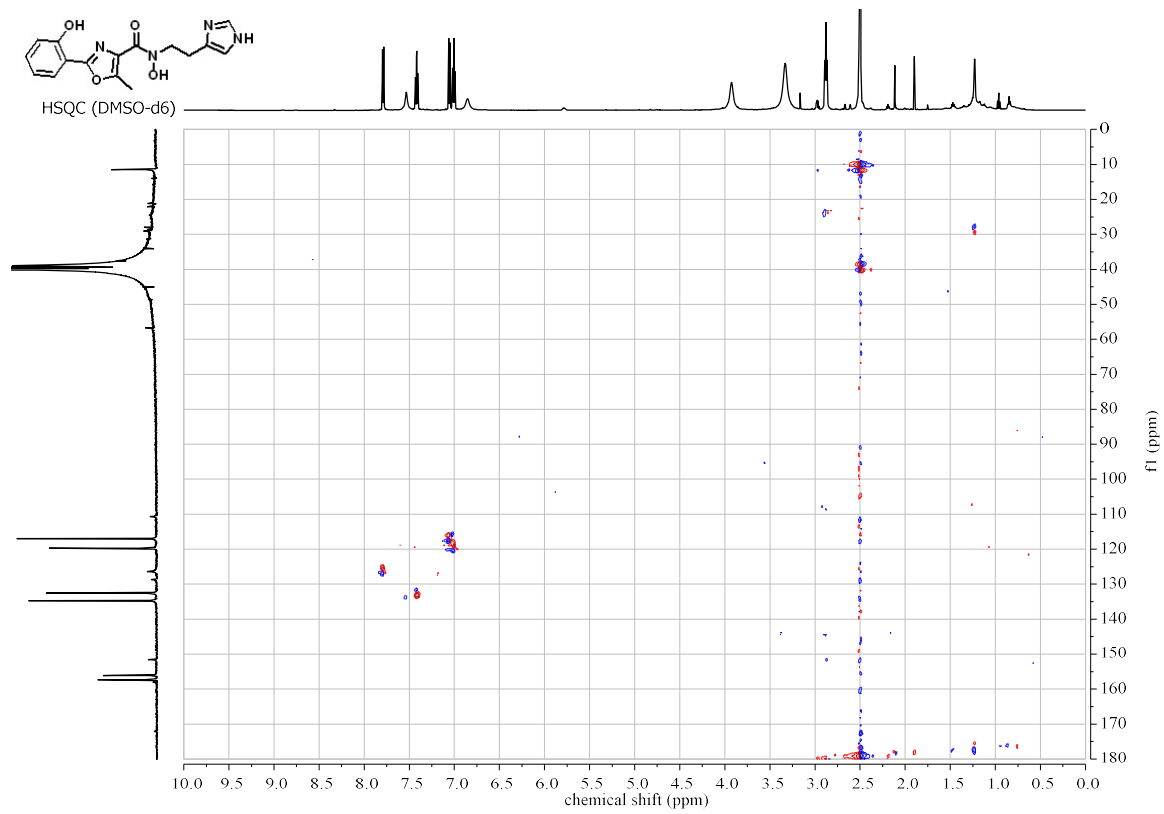


HMBC (DMSO-d6)

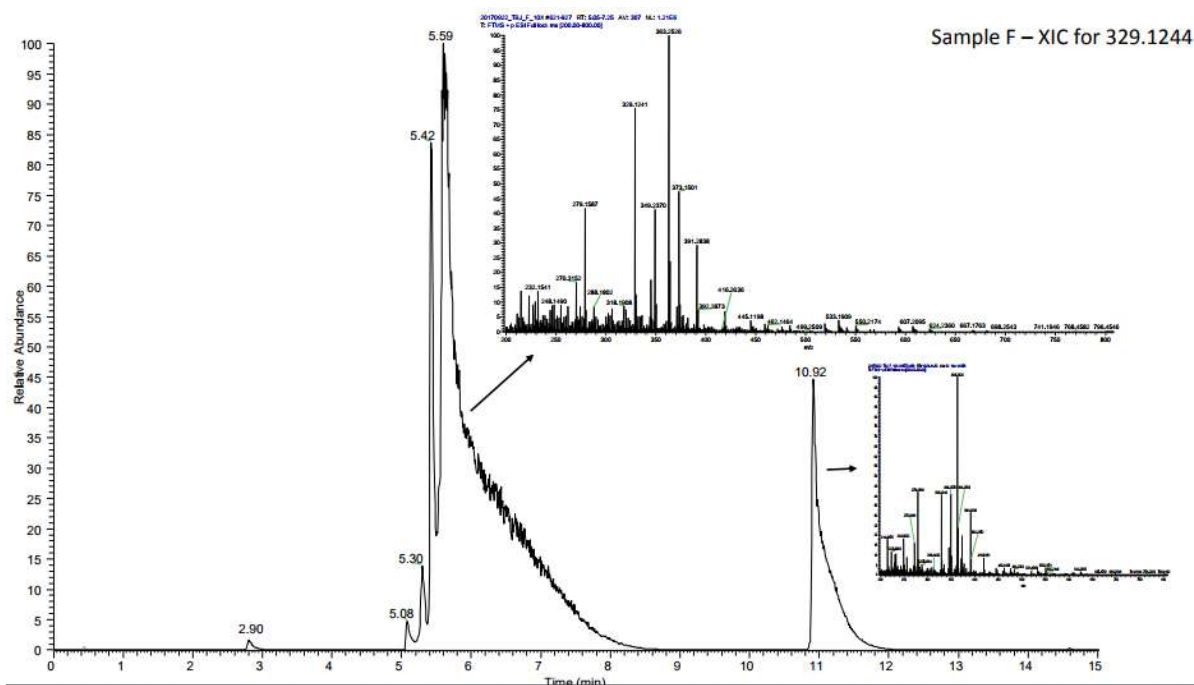
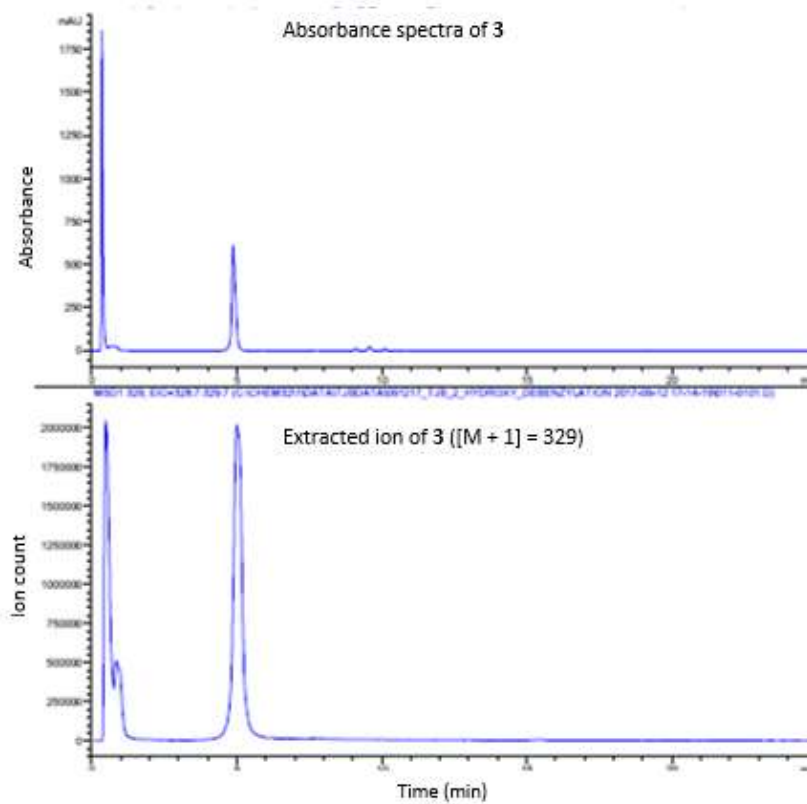


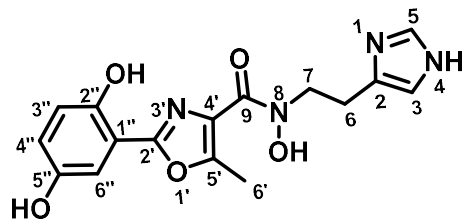
COSY (DMSO-d6)





## LC\_MS and HRMS for 3

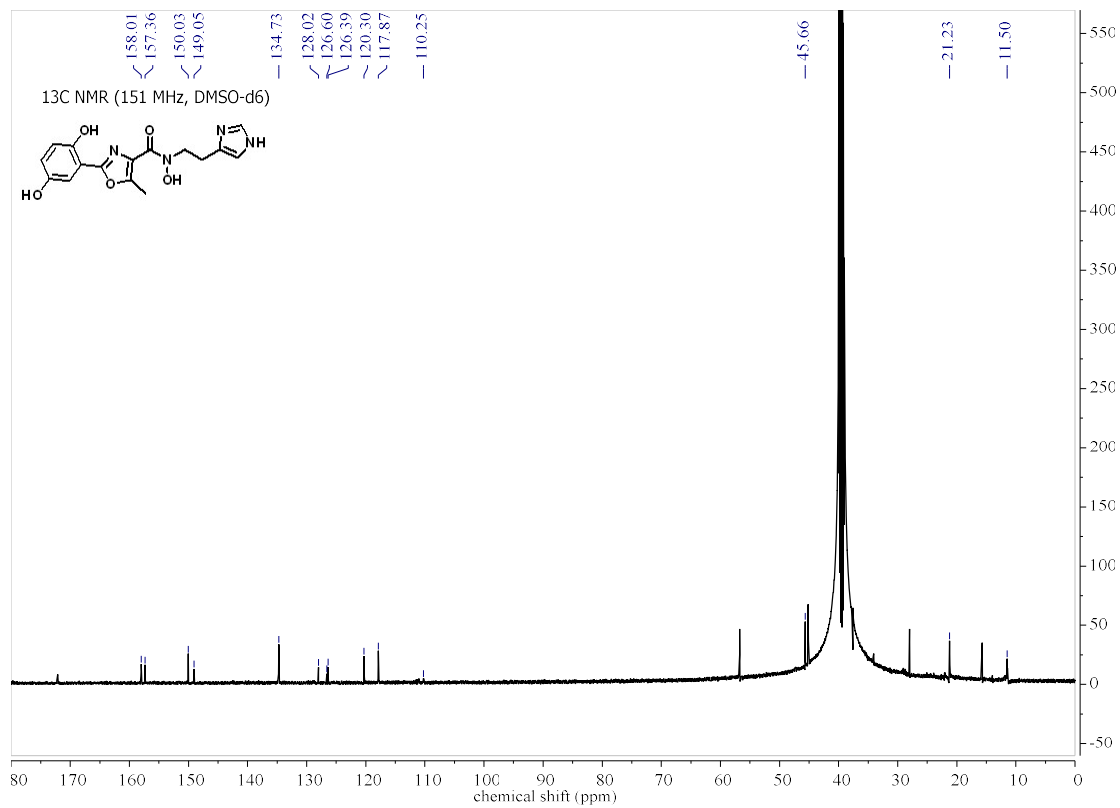
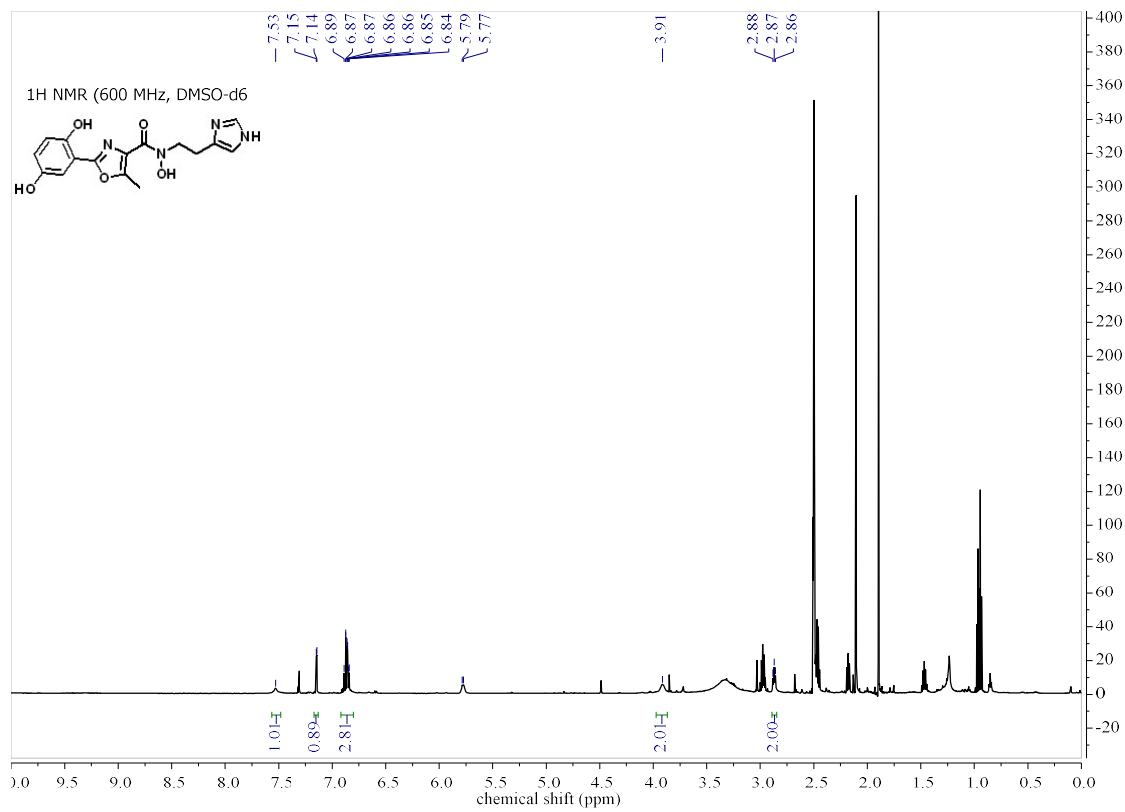




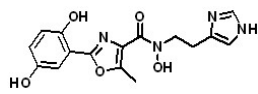
**N-(2-(1H-imidazol-4-yl)ethyl)-2-(2,5-dihydroxyphenyl)-N-hydroxy-5-methyloxazole-4-carboxamide – 4**

HRMS calcd for C<sub>16</sub>H<sub>17</sub>N<sub>4</sub>O<sub>5</sub> (M + H)<sup>+</sup> 345.1193; found 345.1190

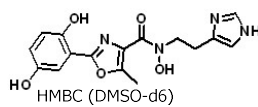
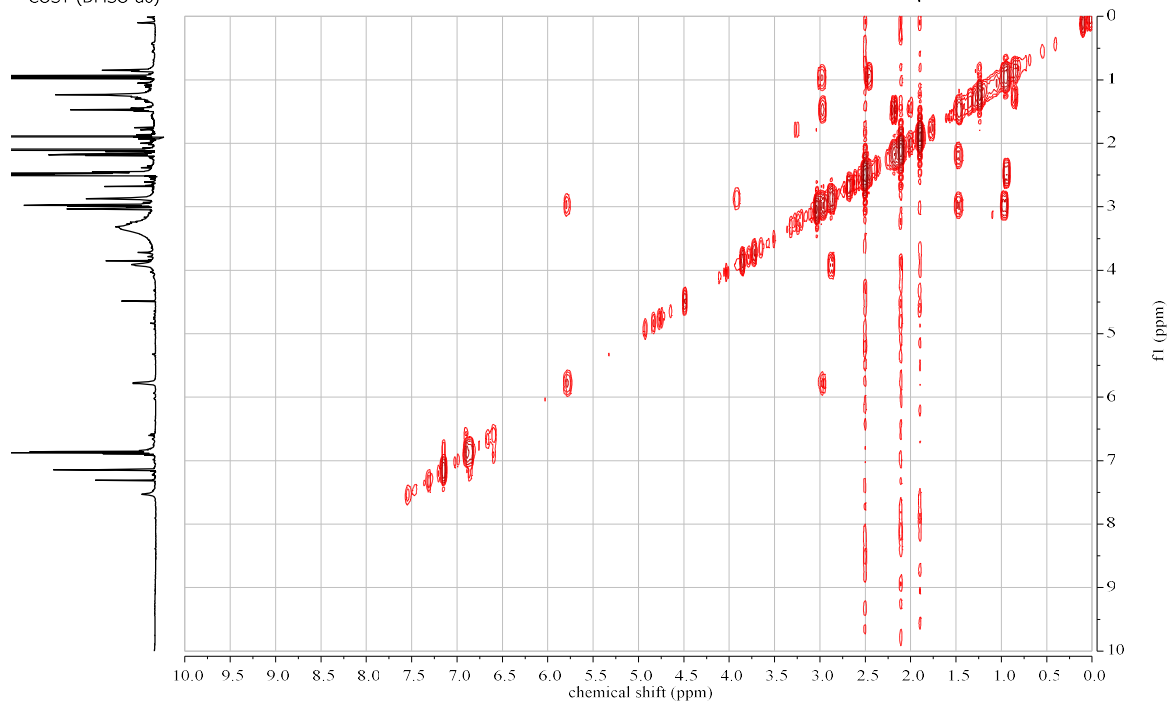
Atom	<sup>13</sup> C (ppm)	<sup>1</sup> H (ppm), Multiplets in Hz	COSY 1H-1H 3 bond	HMBC 1H-13C 2-3 bond	HSQC
2					
3		6.86 (m, 3H)			
5	134.7	7.53 (s, 1H)			5
6	21.2	2.87 (t, 2H)	7	7	6
7	45.7	3.91 (s (br), 2H)	6		
9					
2'	158.2				
4'	128.0				
5'	149.1				
6'	11.5	2.50 (s, 3H) Under DMSO peak		5'	6'
1''	110.2				
2''	126.4				
3''	126.6	6.86 (m, 3H)	4''	2'', 4''	3''
4''	120.3	6.86 (m, 3H)	3''	3''	4''
5''	150.0				
6''	117.9	7.14 (d, 1H)			6''



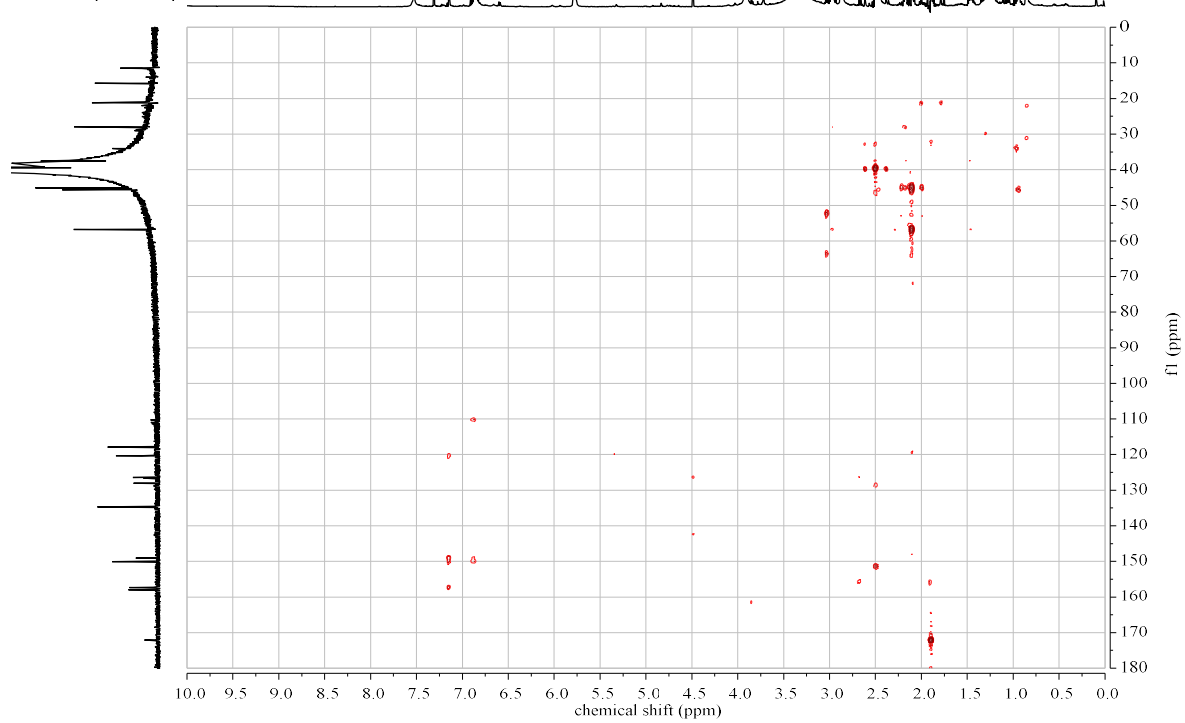


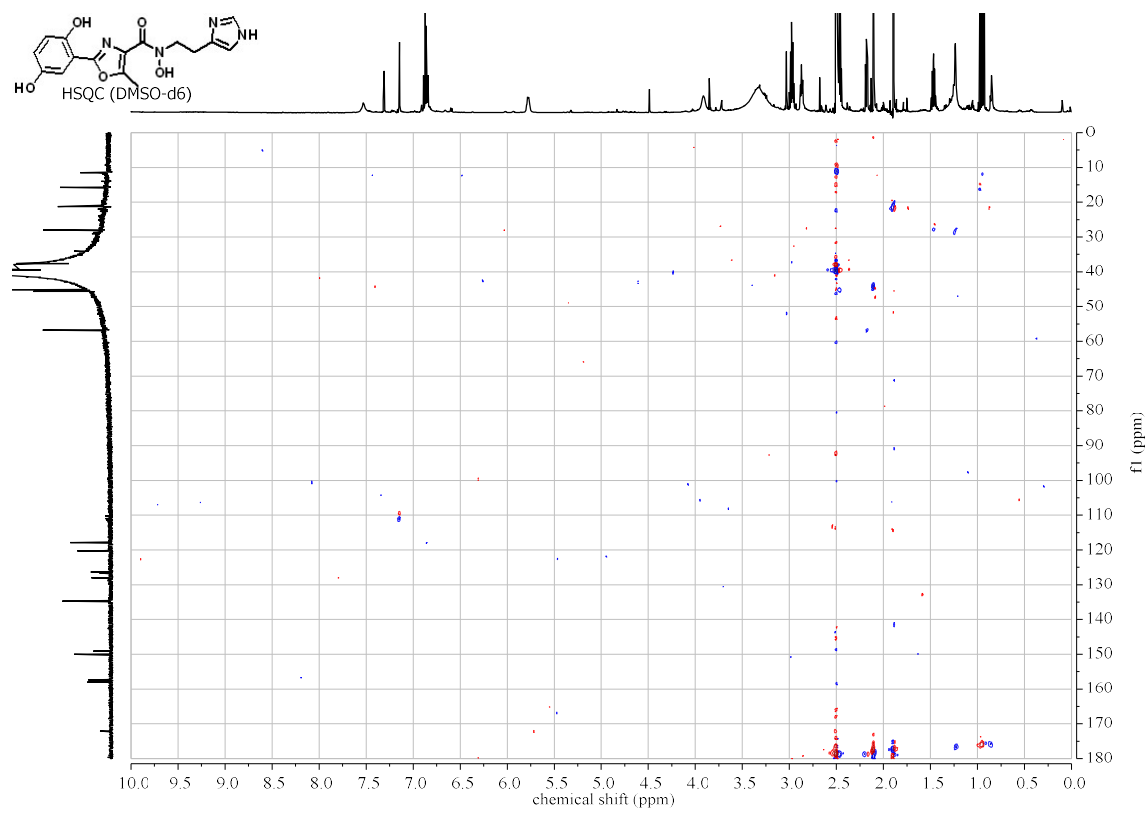
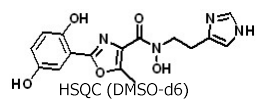


COSY (DMSO-d6)

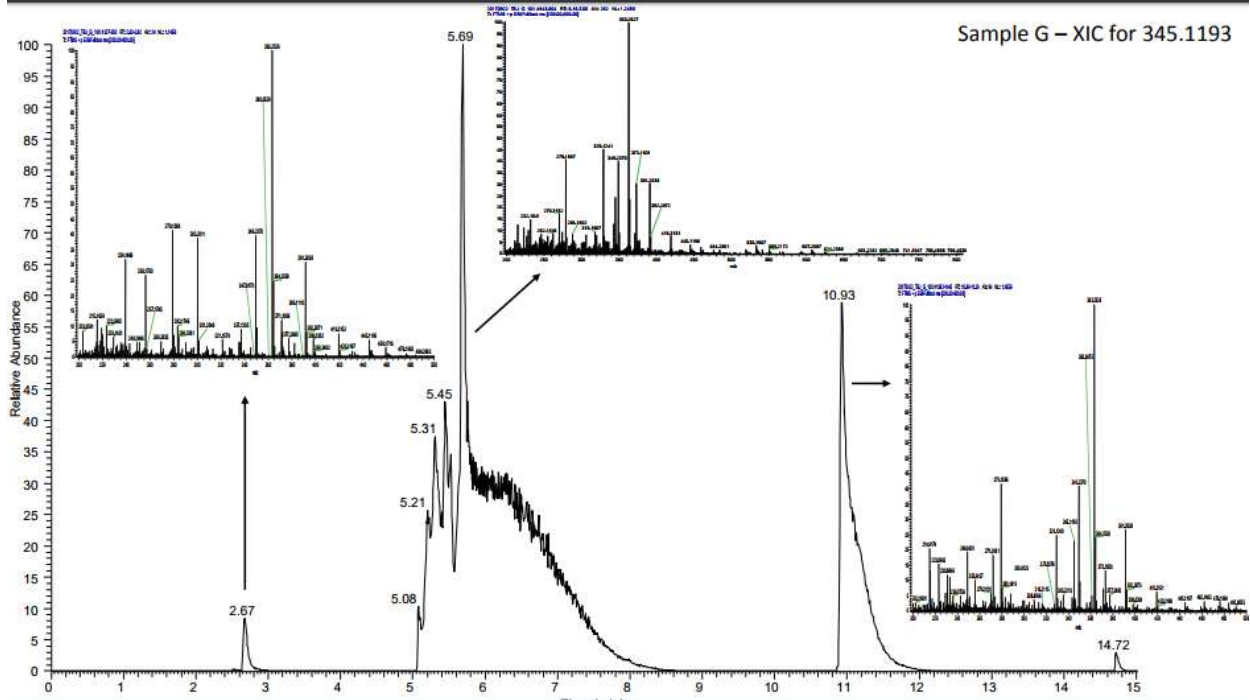
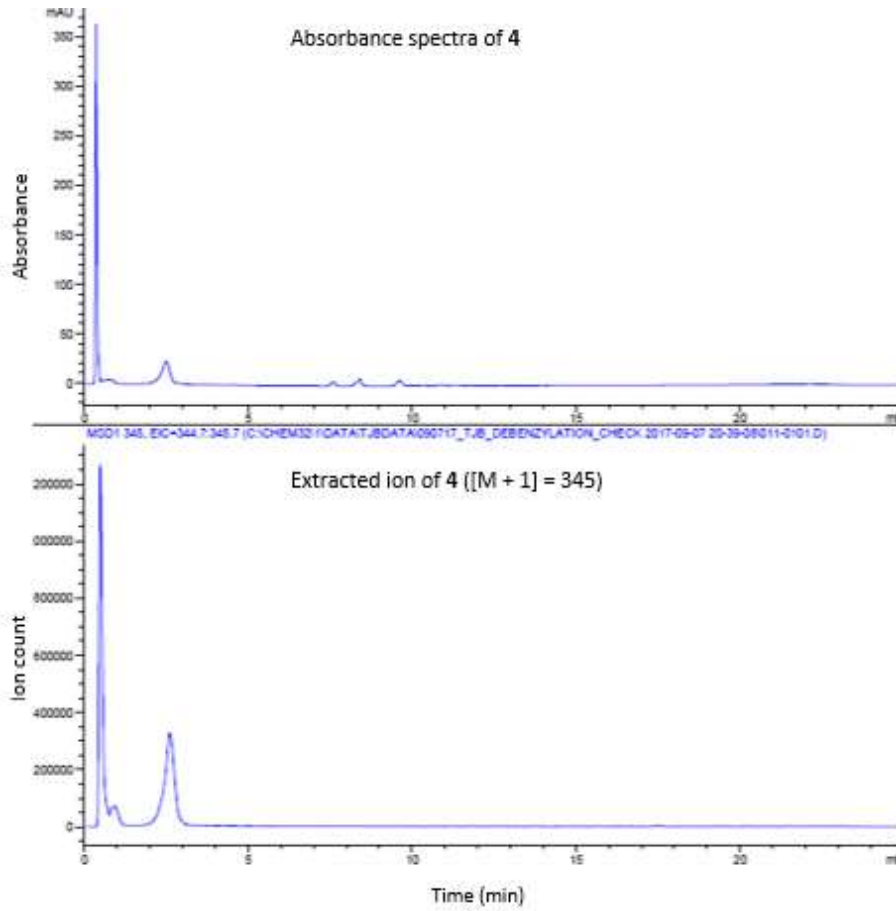


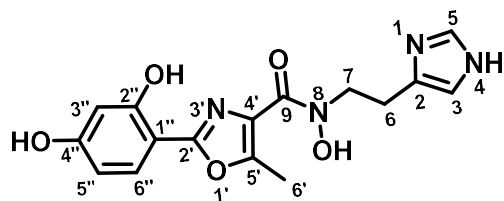
HMBC (DMSO-d6)





LC\_MS and HRMS for 4

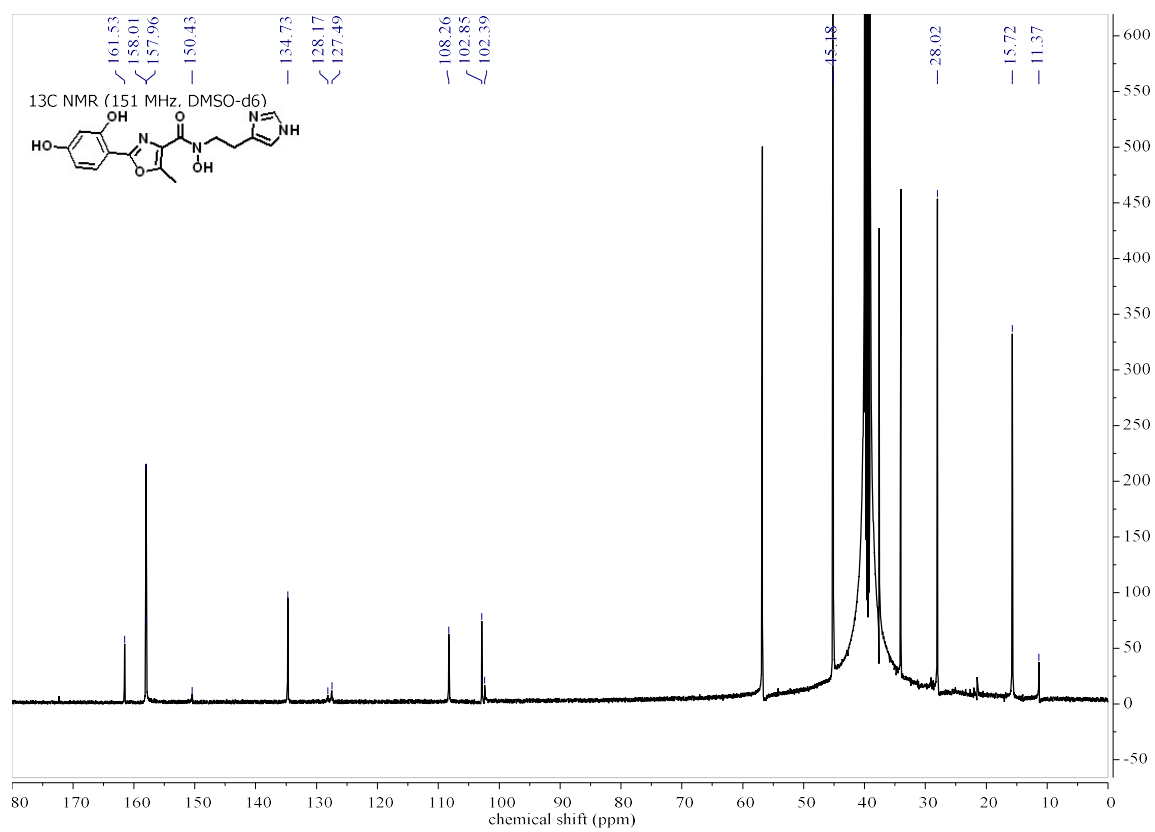
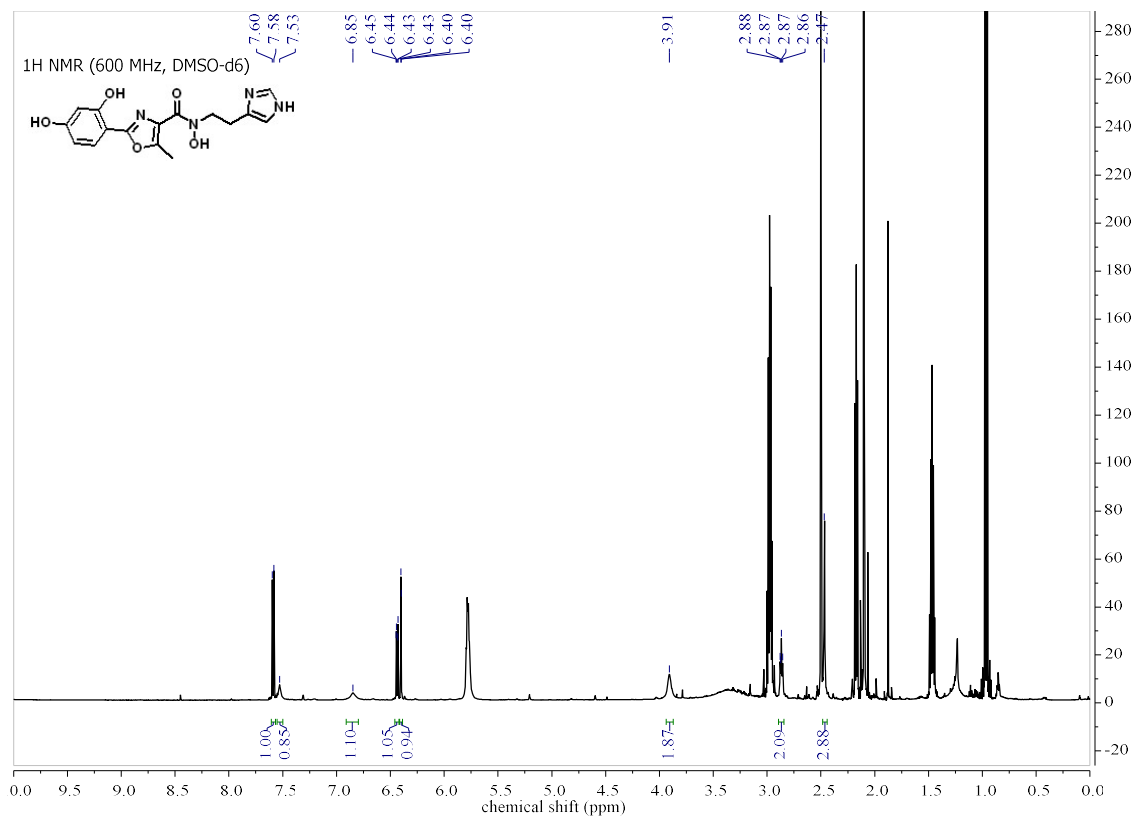


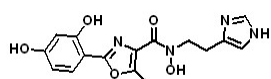


**N-(2-(1H-imidazol-4-yl)ethyl)-2-(2,4-dihydroxyphenyl)-N-hydroxy-5-methyloxazole-4-carboxamide – 5**

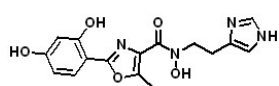
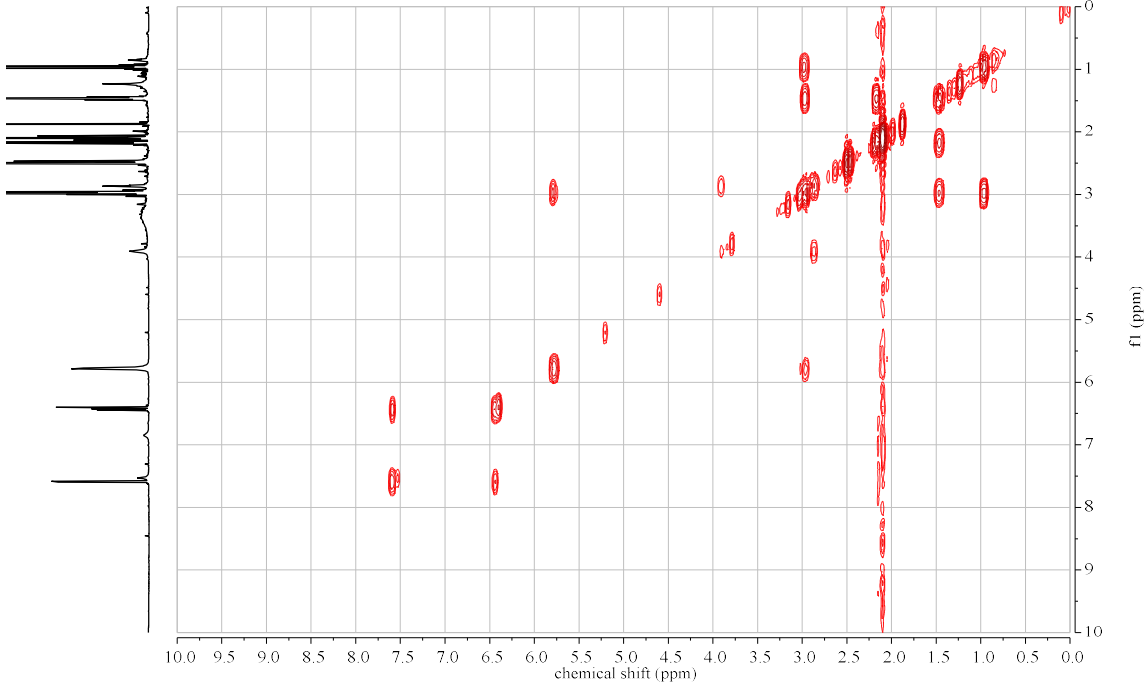
HRMS calcd for C<sub>16</sub>H<sub>17</sub>N<sub>4</sub>O<sub>5</sub> (M + H)<sup>+</sup> 345.1193; found 345.1190

Atom	<sup>13</sup> C (ppm)	<sup>1</sup> H (ppm), Multiplets in Hz	COSY 1H-1H 3 bond	HMBC 1H-13C 2-3 bond	HSQC
2					
3		6.85 (s, 1H)			
5	134.7	7.53 (s, 1H)			4
6	28.0	2.09 (t, 2H)	7	7	6
7	45.2	3.91 (s(br), 2H)	6		
9					
2'	158.0				
4'	128.2				
5'	150.4				
6'	11.4	2.47 (s, 3H)		5'	6'
1''	102.4				
2''	158.0			3''	
3''	102.8	6.40 (d, 1H)		2'', 4''	3''
4''	161.6				
5''	108.3	6.43 (dd, 1H)	6''	6'', 4''	5''
6''	127.5	7.59 (d, 1H)	5''		6''

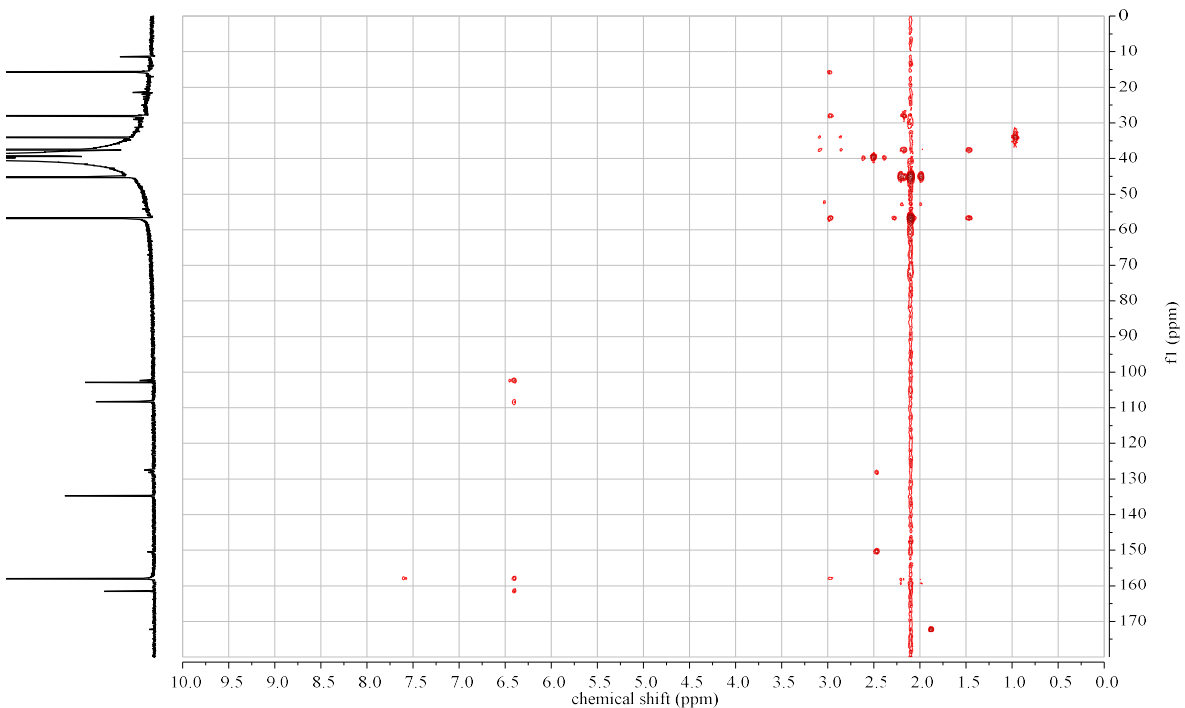


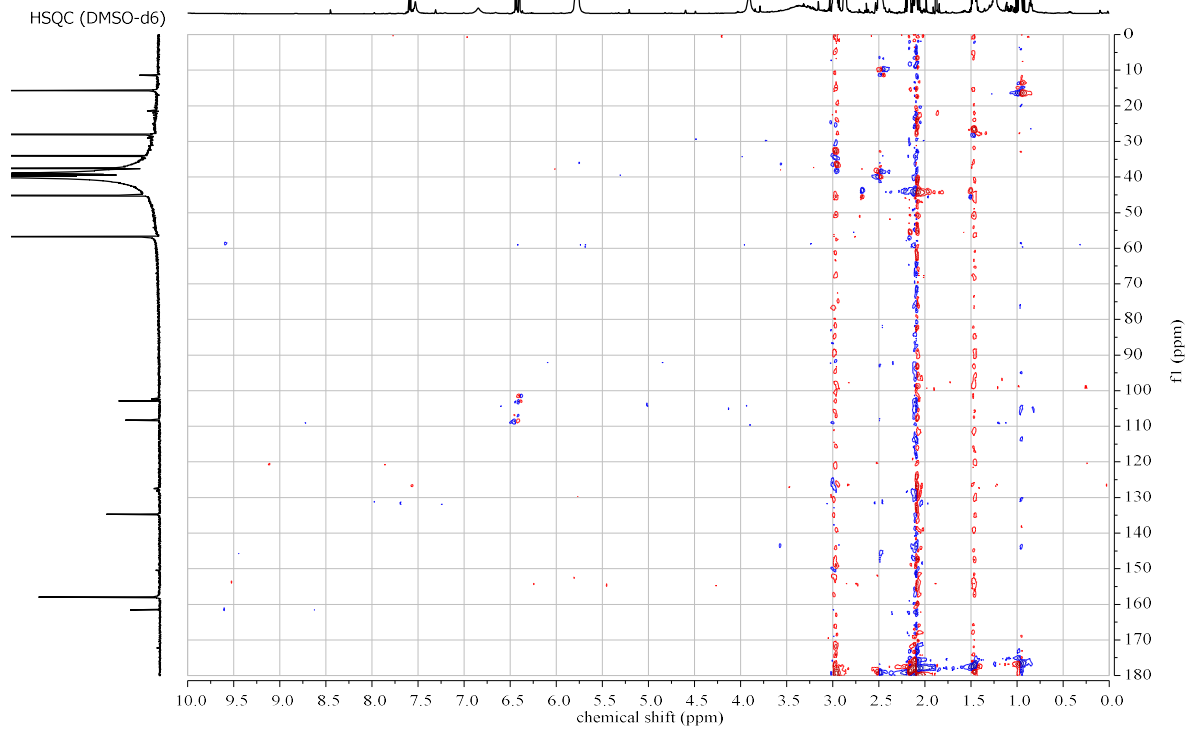
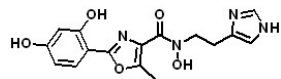


COSY (DMSO-d6)

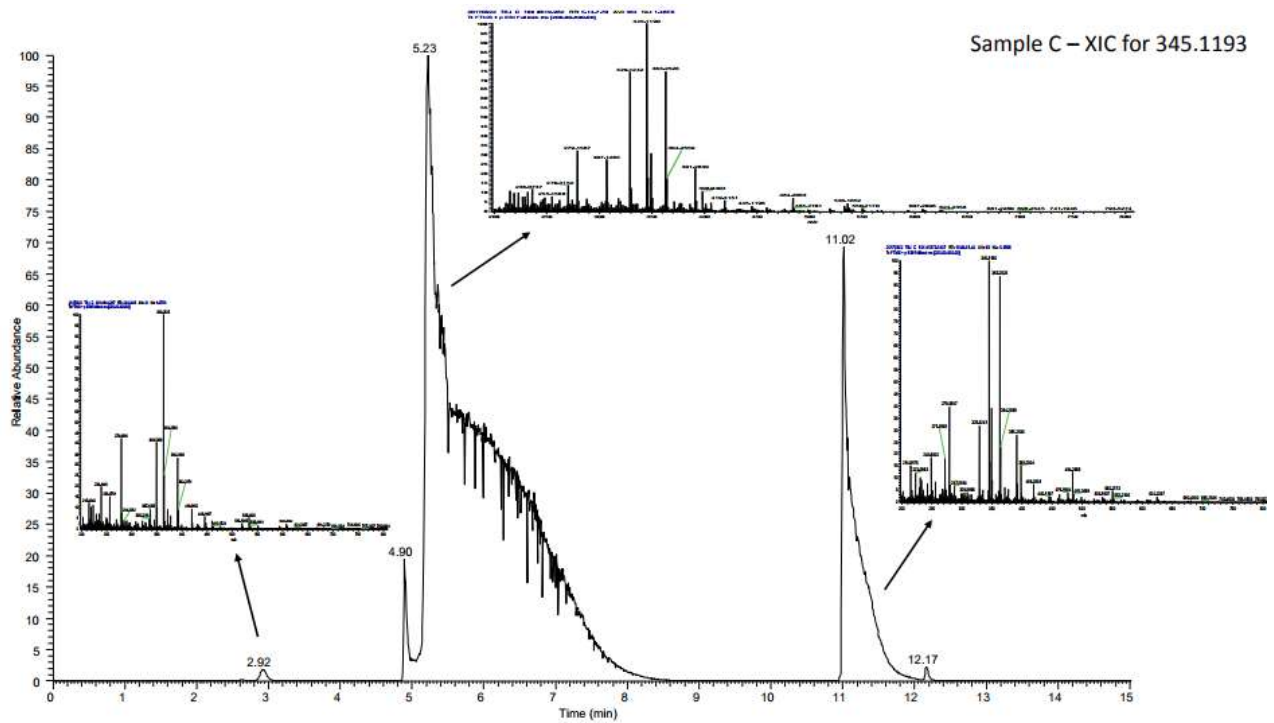
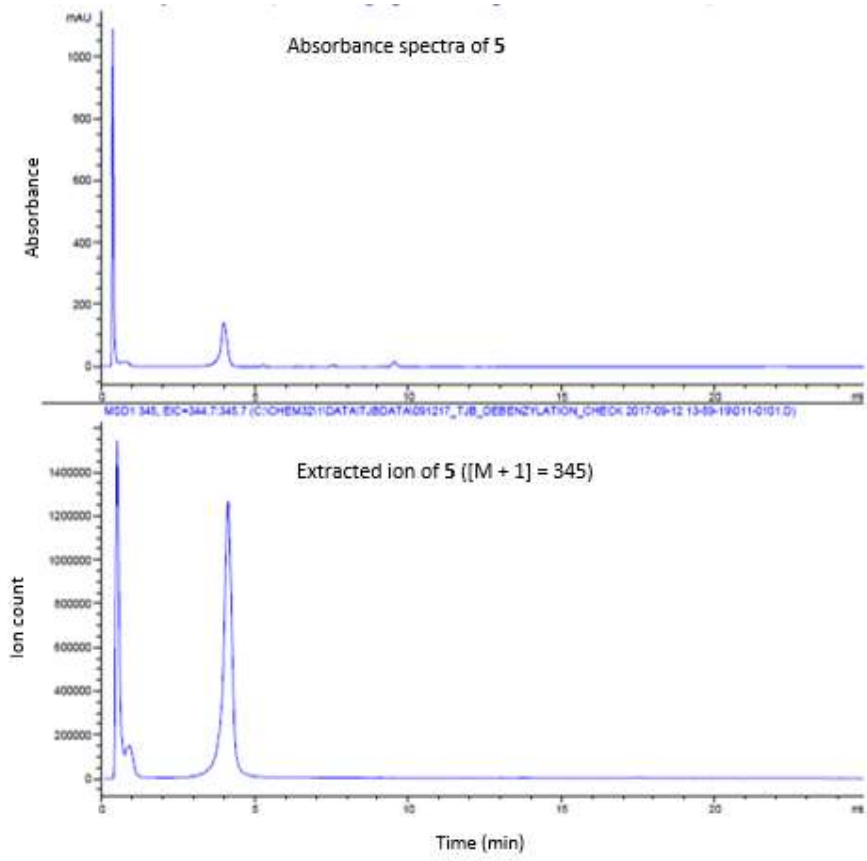


HMBC (DMSO-d6)

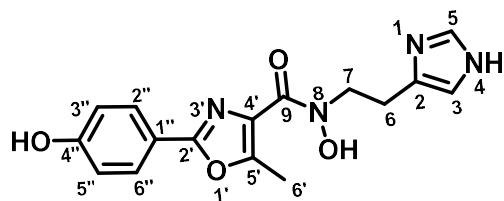




LC\_MS and HRMS for 5



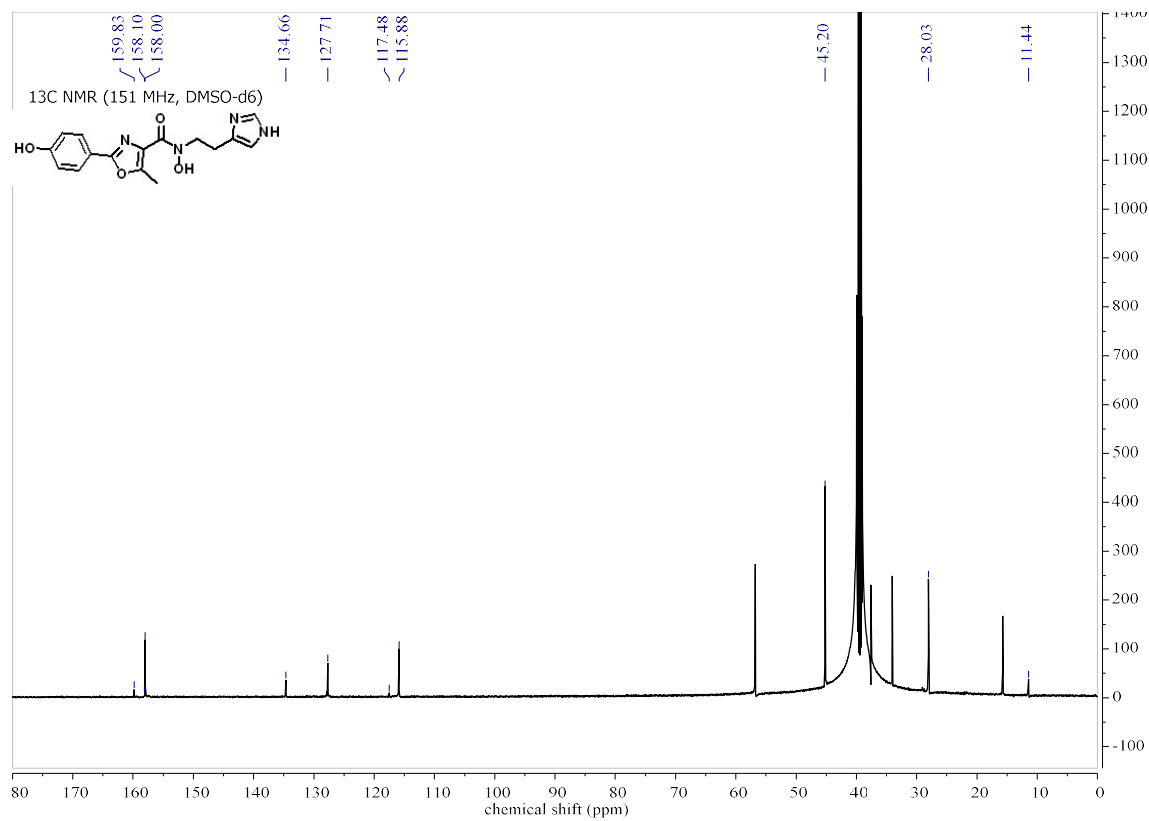
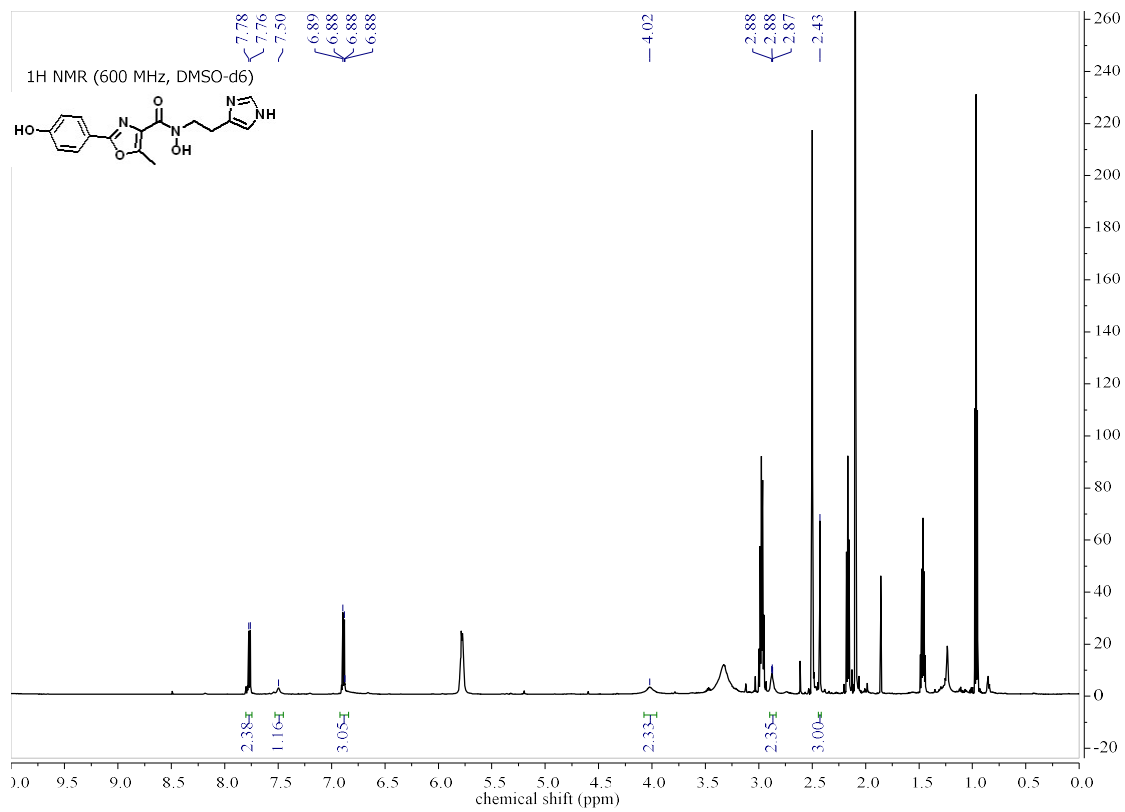


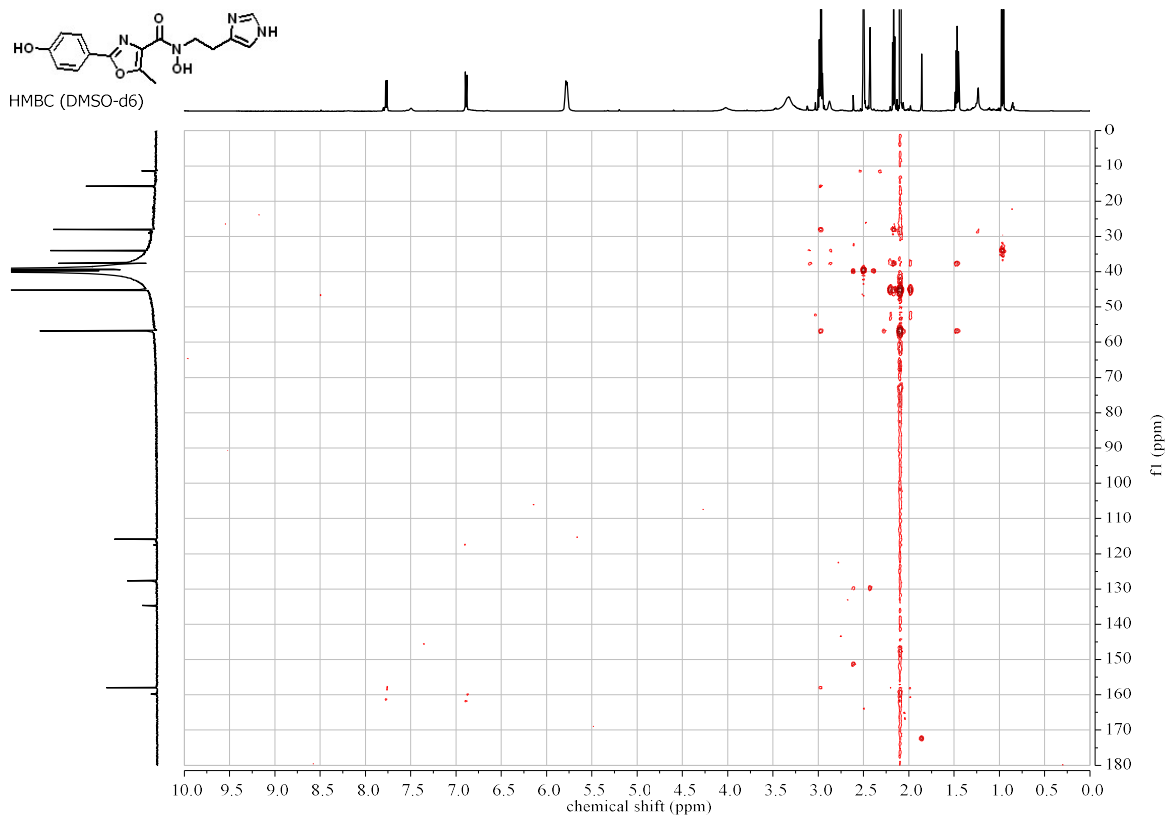
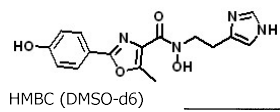
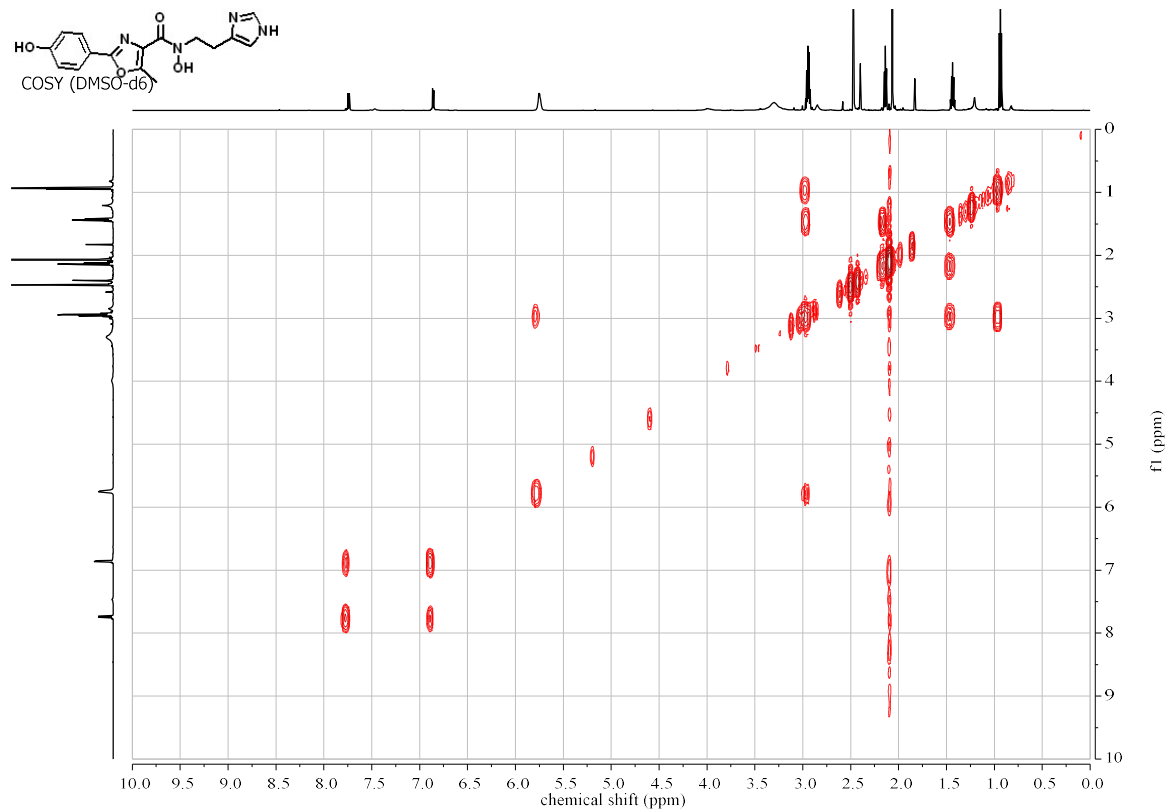
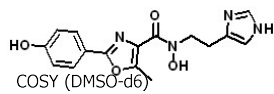


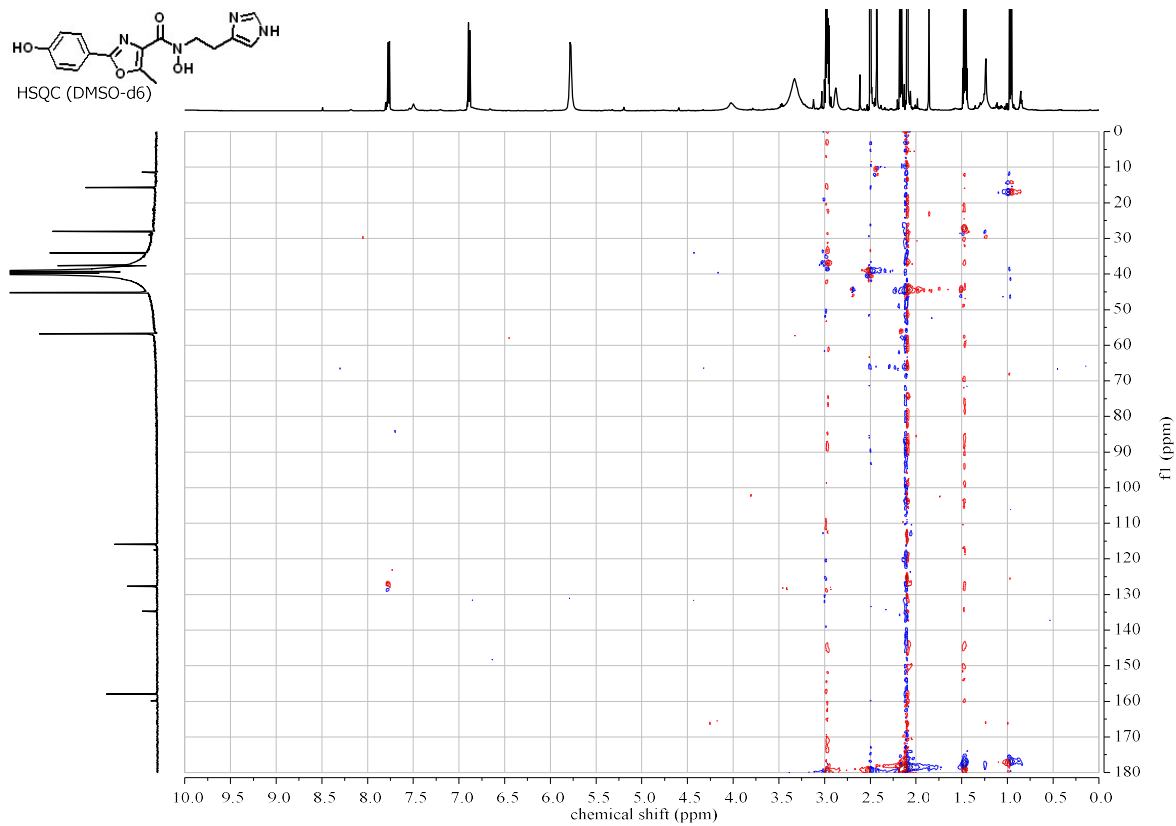
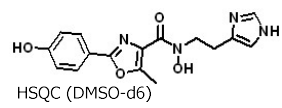
**N-(2-(1H-imidazol-4-yl)ethyl)-N-hydroxy-2-(4-hydroxyphenyl)-5-methyloxazole-4-carboxamide – 6**

HRMS calcd for C<sub>16</sub>H<sub>17</sub>N<sub>4</sub>O<sub>4</sub> (M + H)<sup>+</sup> 329.1244; found 329.1242

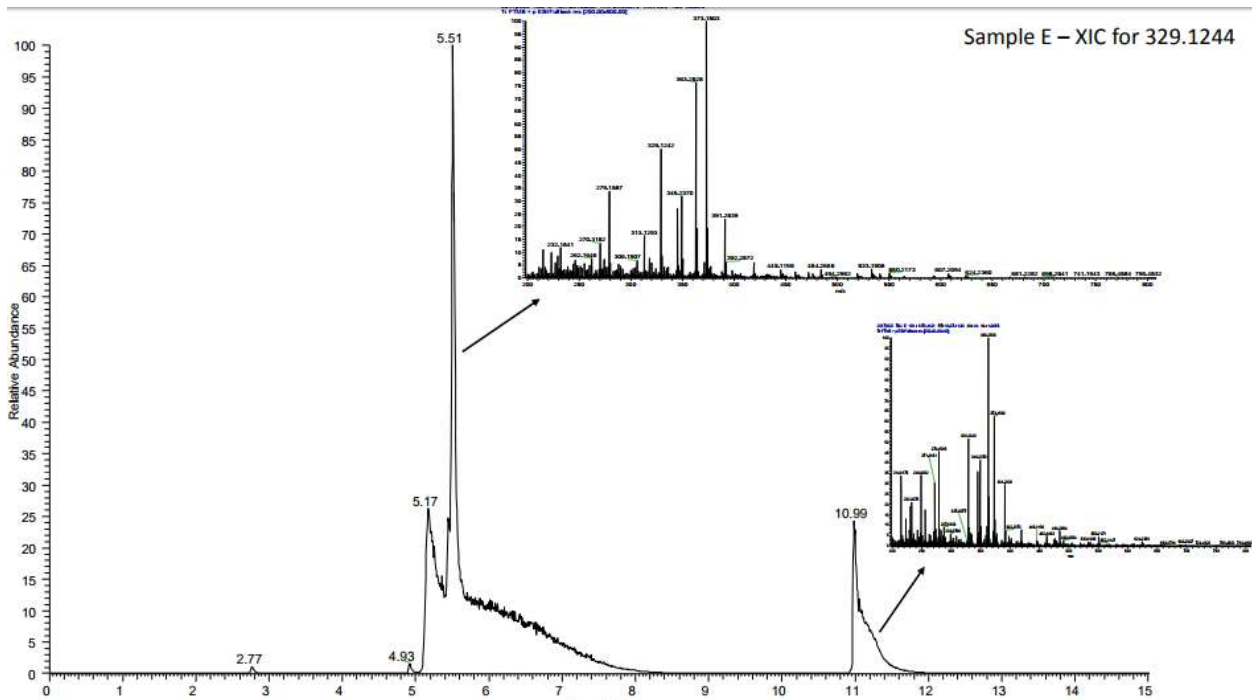
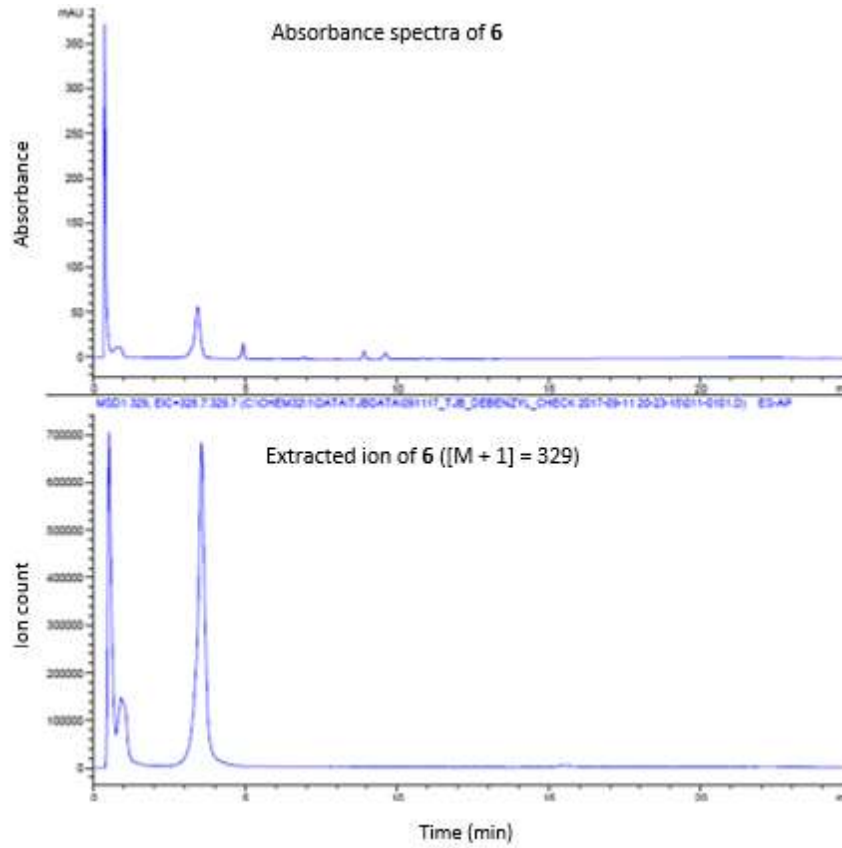
Atom	<sup>13</sup> C (ppm)	<sup>1</sup> H (ppm), Multiplets in Hz	COSY 1H-1H 3 bond	HMBC 1H-13C 2-3 bond	HSQC
2					
3		6.88 (m, 3H)			
5	134.7	7.50 (s, 1H)			5
6	28.0	2.88 (t, 2H)	7	7	6
7	45.2	4.02 (s (br), 2H)	6		
9					
2'	158.0				
4'	127.2				
5'	158.1				
6'	11.4	2.43 (s, 3H)		5'	6'
1''					
2''	117.5	7.77 (d, 2H)	3''	3''	2''
3''	115.9	6.88 (m, 3H)	2''	2''	3''
4''	160.0				
5''	115.9	6.88 (m, 3H)	6''	6''	5''
6''	117.5	7.77 (d, 2H)	5''	5''	6''

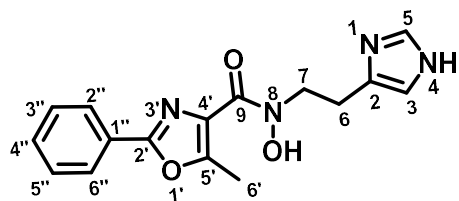






LC\_MS and HRMS for 6

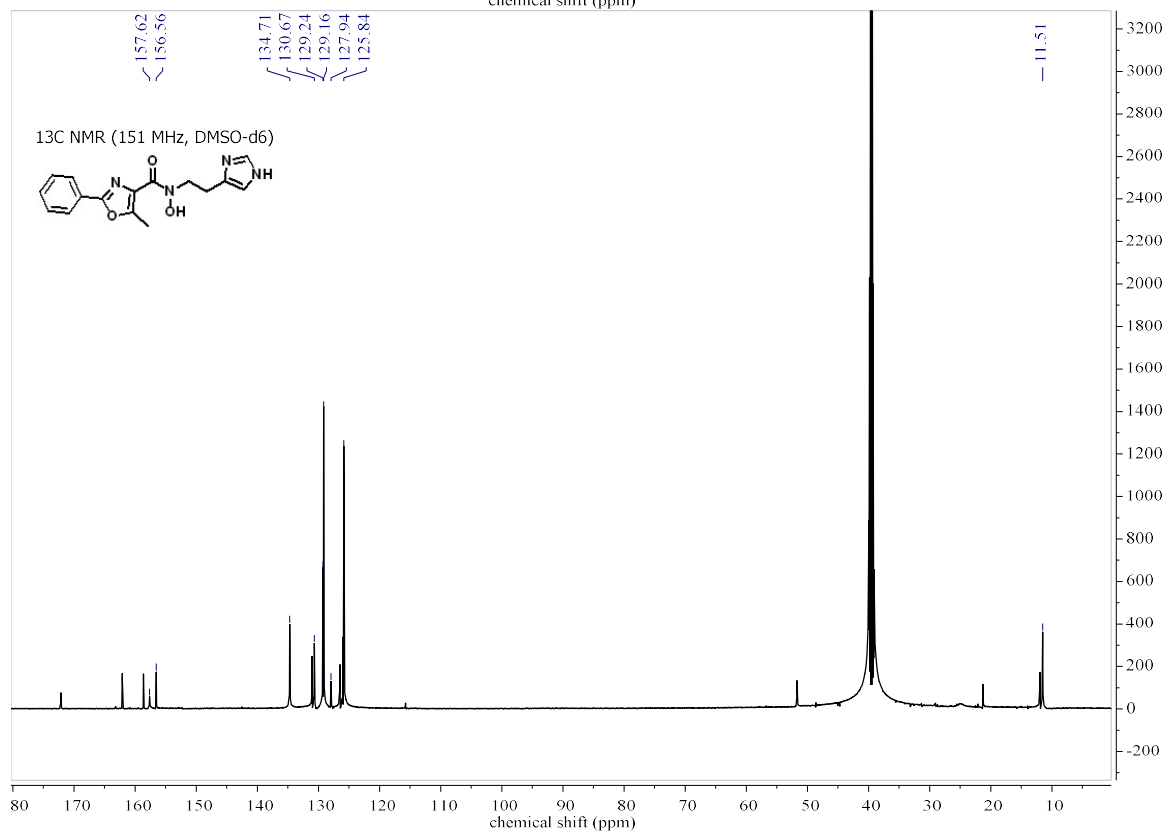
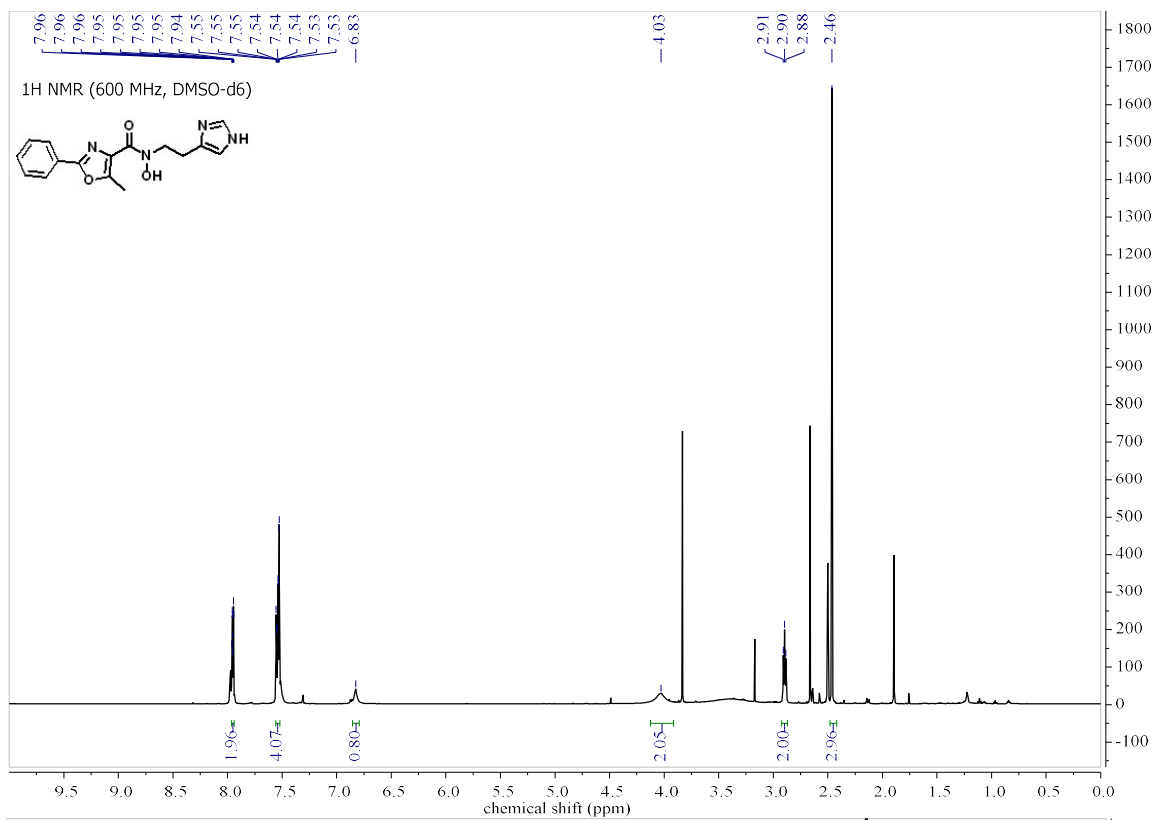


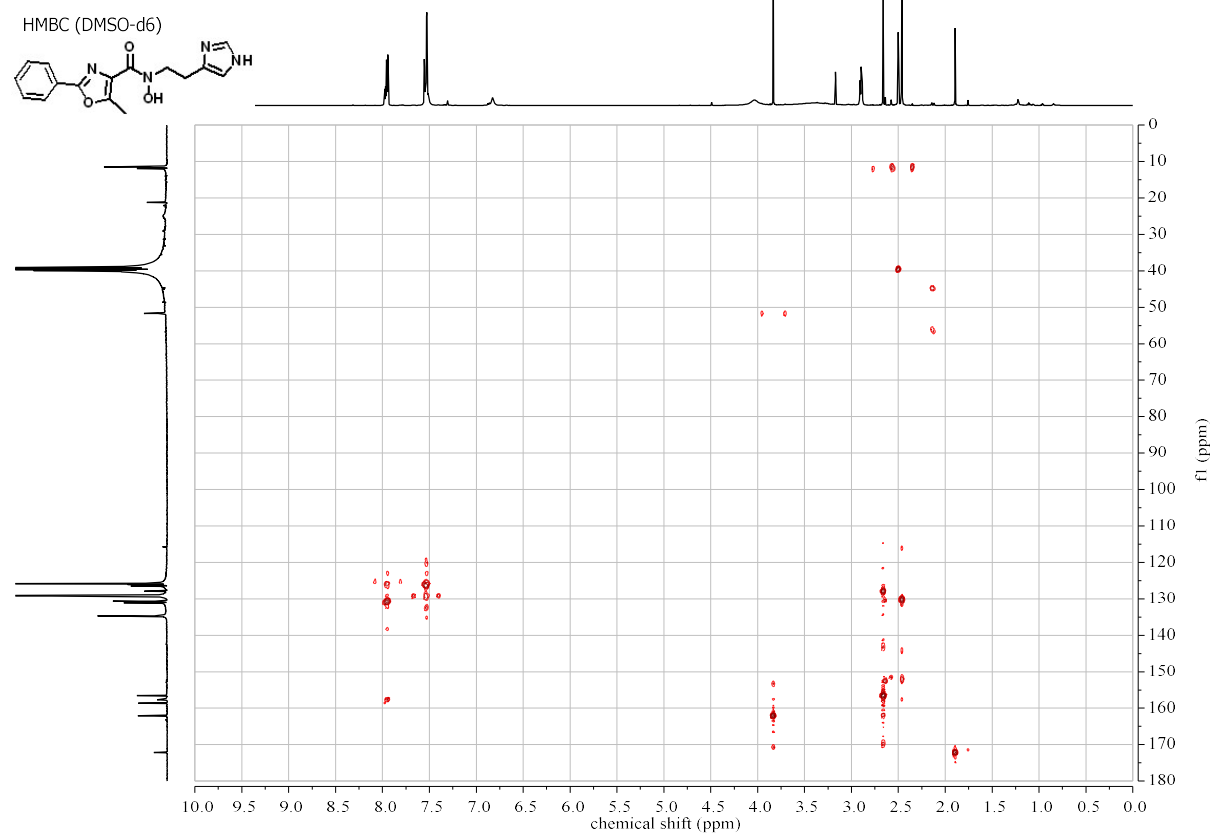
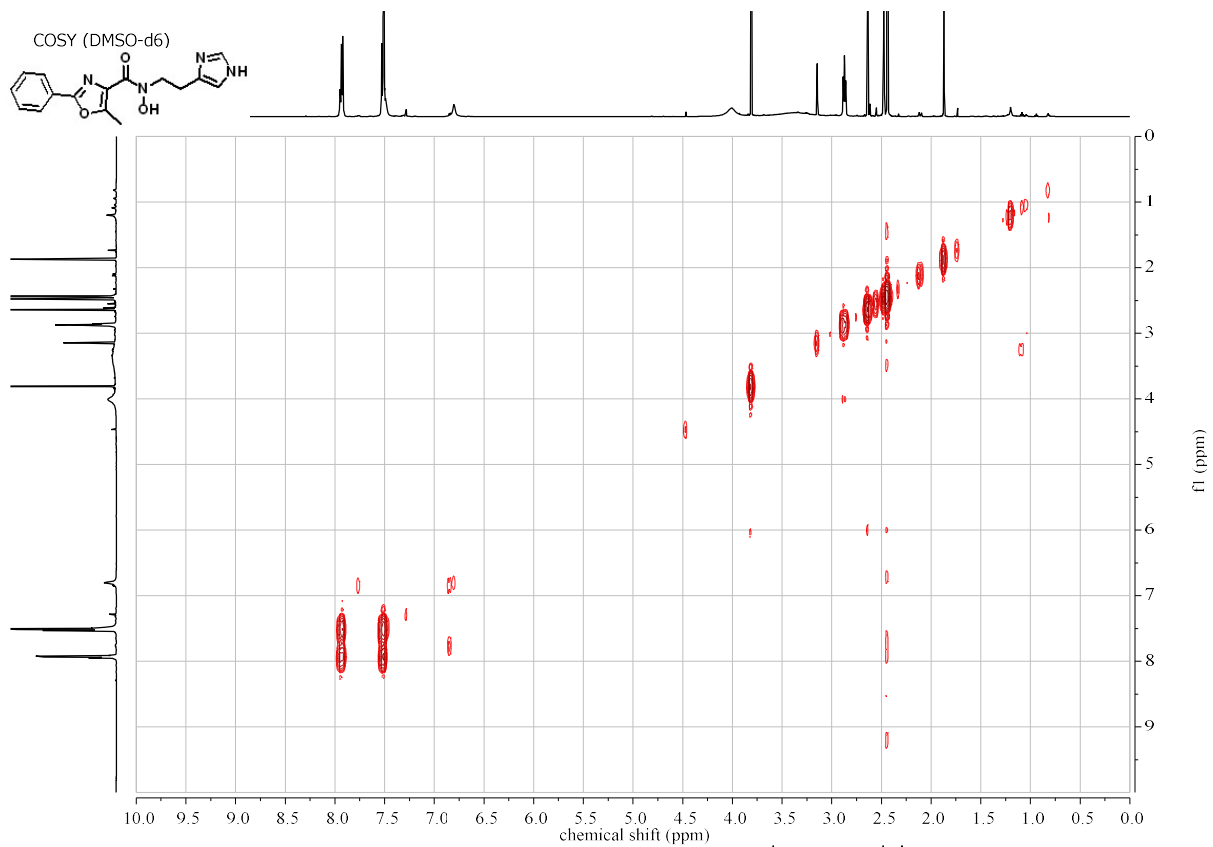


**N-(2-(1H-imidazol-4-yl)ethyl)-N-hydroxy-5-methyl-2-phenyloxazole-4-carboxamide – 7**

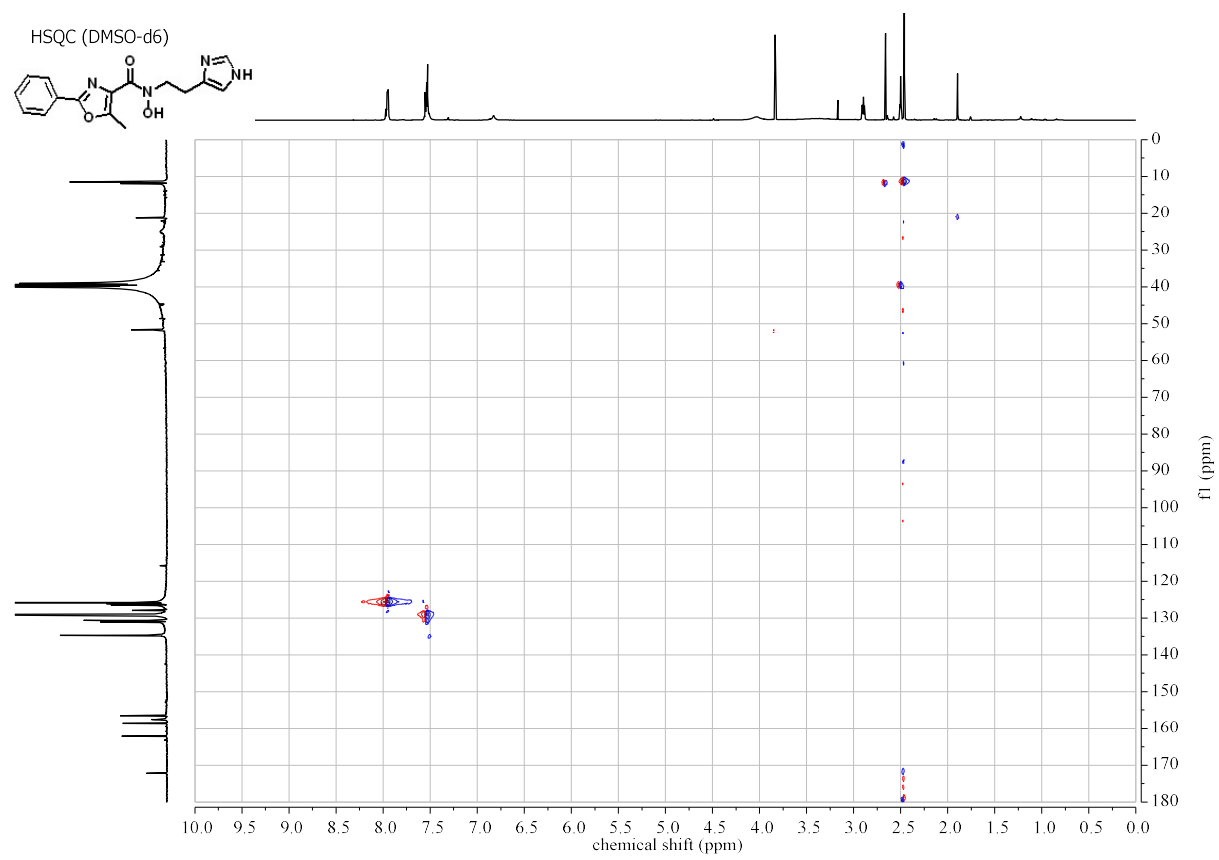
HRMS calcd for  $C_{16}H_{17}N_4O_3$  ( $M + H$ )<sup>+</sup> 313.1295; found 313.1295

Atom	<sup>13</sup> C (ppm)	<sup>1</sup> H (ppm), Multiplets in Hz	COSY 1H-1H 3 bond	HMBC 1H-13C 2-3 bond	HSQC
2					
3		6.80 (s (br), 1H)			
5	134.7	7.54 (m, 4H)			
6		2.89 (t, 2H)	7		6
7		4.02 (s (br), 2H)	6		7
9					
2'	157.7				
4'	127.8				
5'	156.6				
6'	11.52	2.45 (s, 3H)		5'	6'
1''	130.7				
2''	129.2	7.54 (m, 4H)	3''	3'', 4''	2''
3''	125.8	7.95 (m, 2H)	2'', 4''	2'', 4'', 5''	3''
4''	129.3	7.54 (m, 4H)	3'', 5''	2'', 3'', 5'', 6''	4''
5''	125.8	7.95 (m, 2H)	4'', 6''	3'', 4'', 6''	5''
6''	129.2	7.54 (m, 4H)	5''	4'', 5''	6''

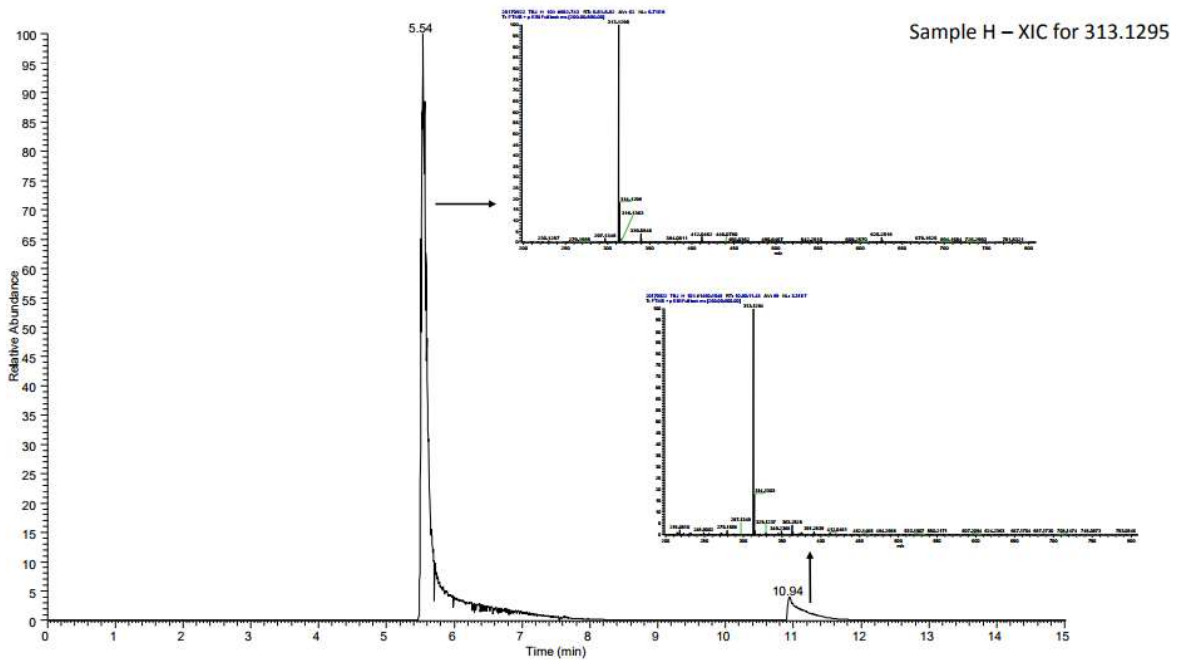
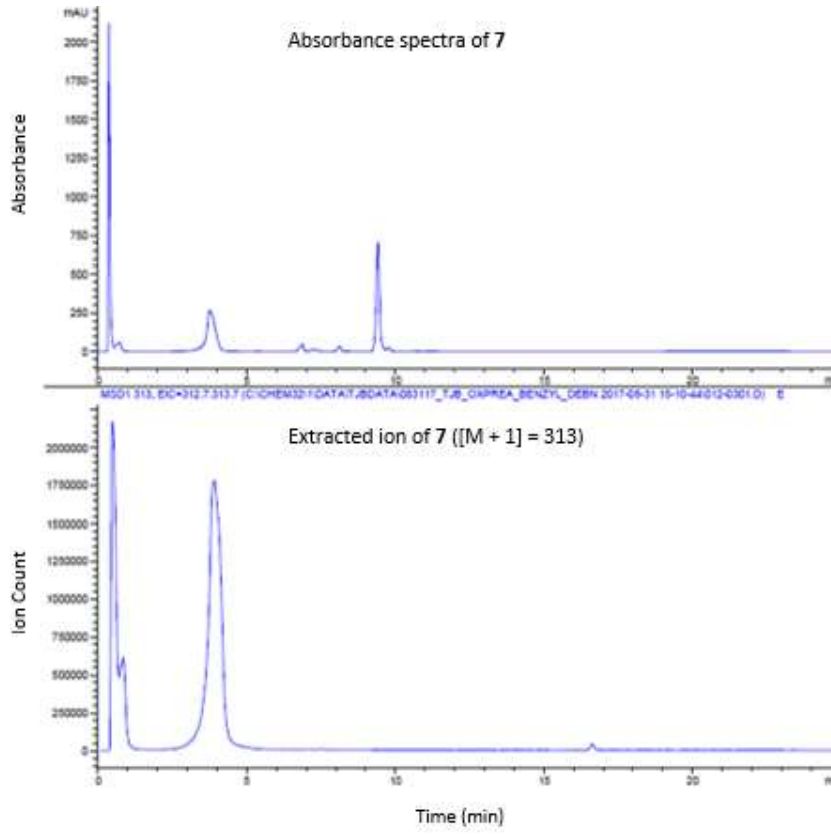


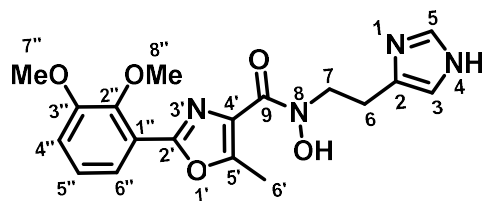






LC\_MS and HRMS for 7

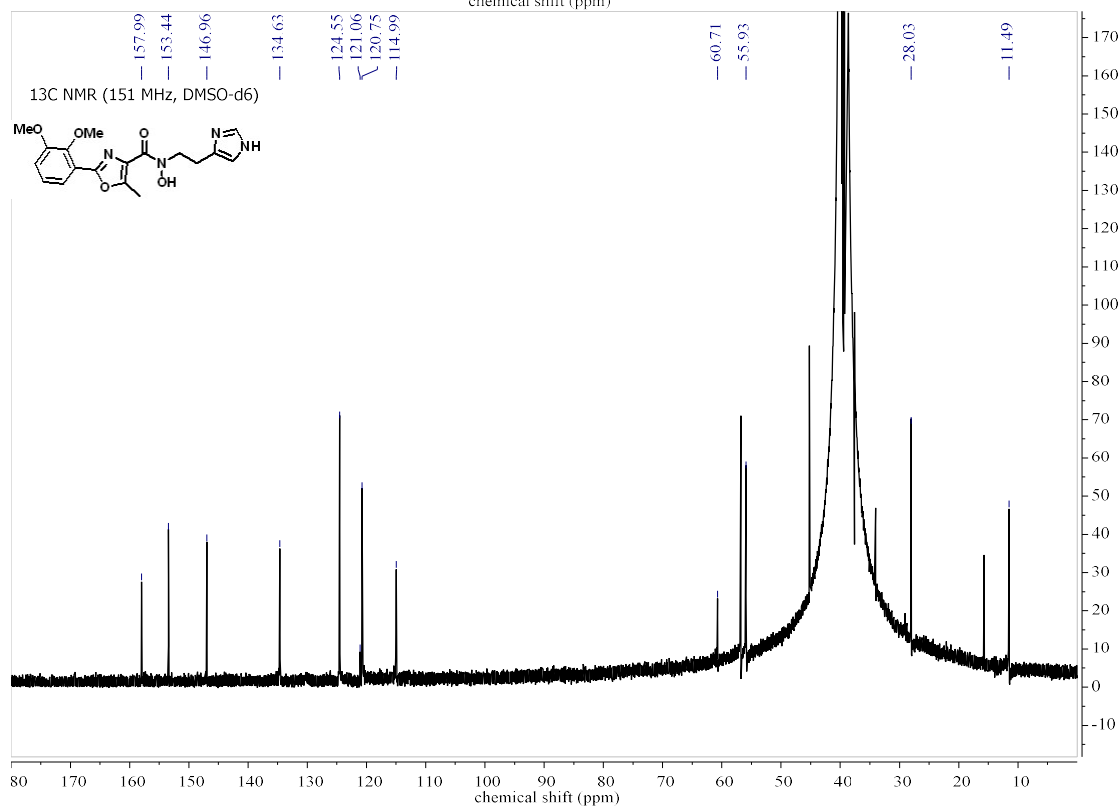
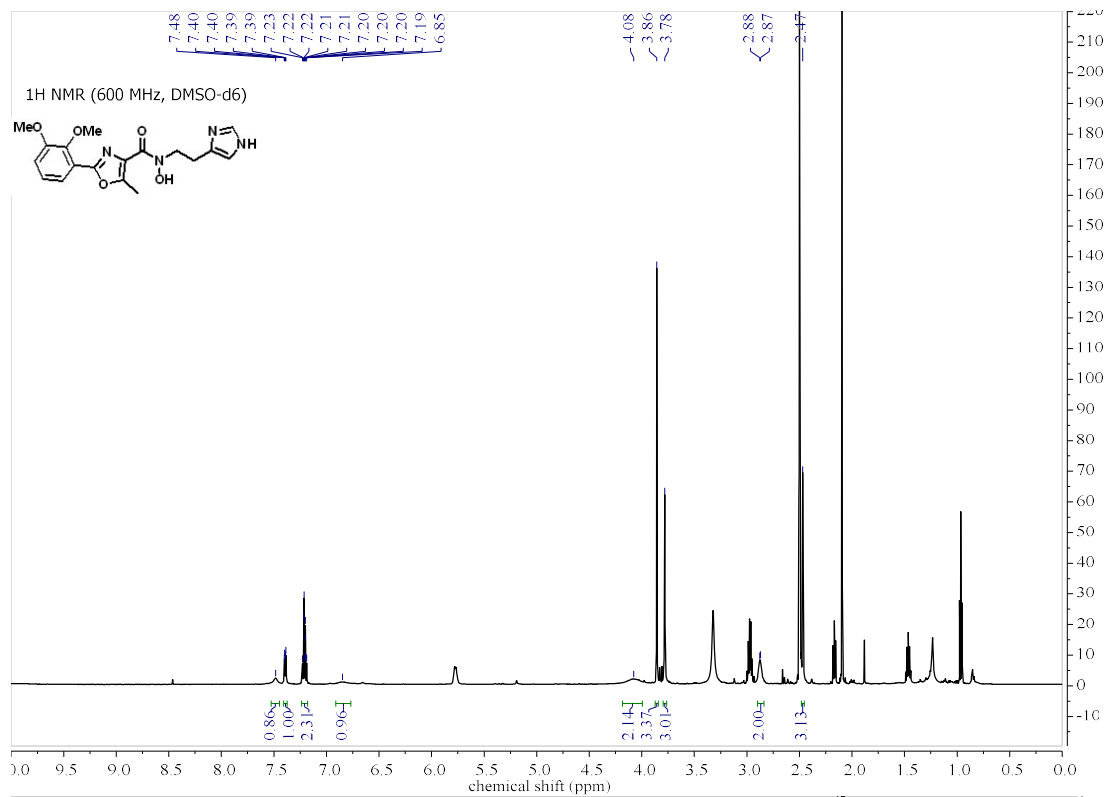


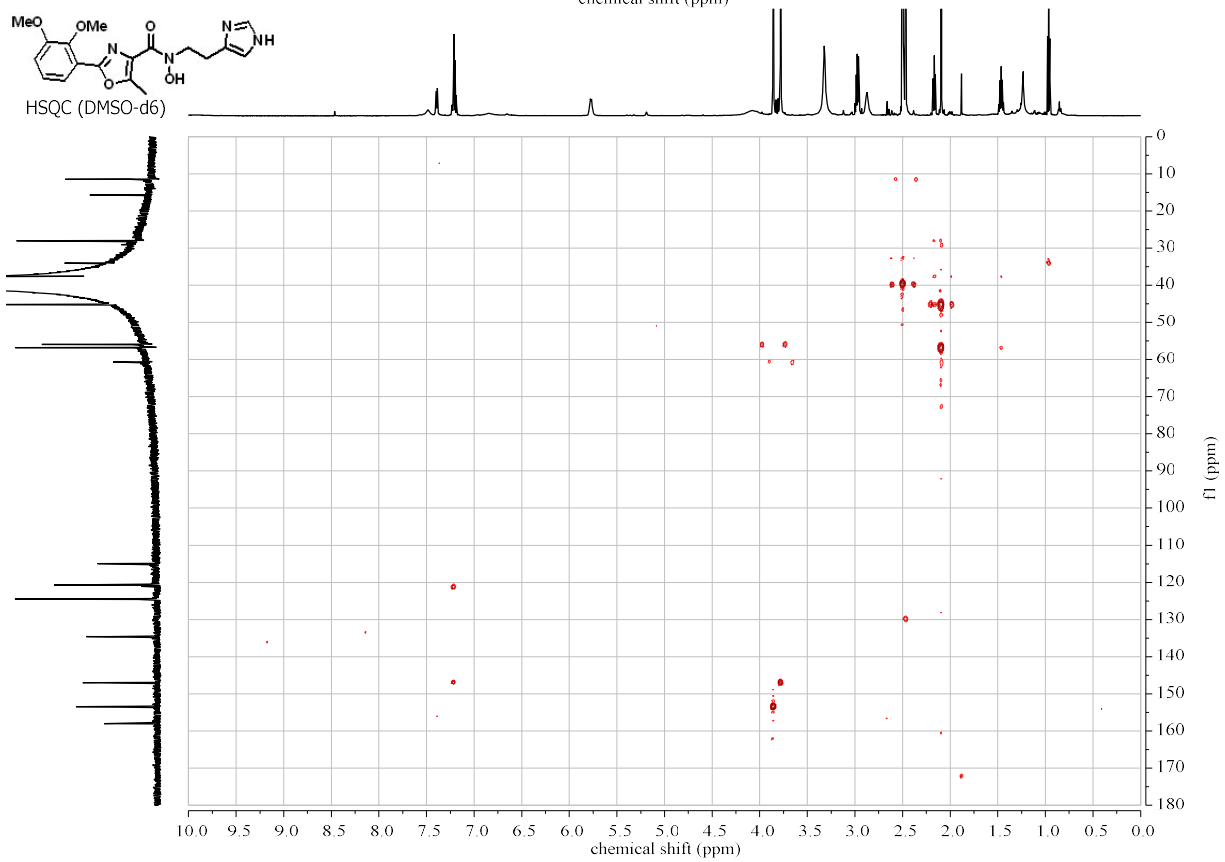
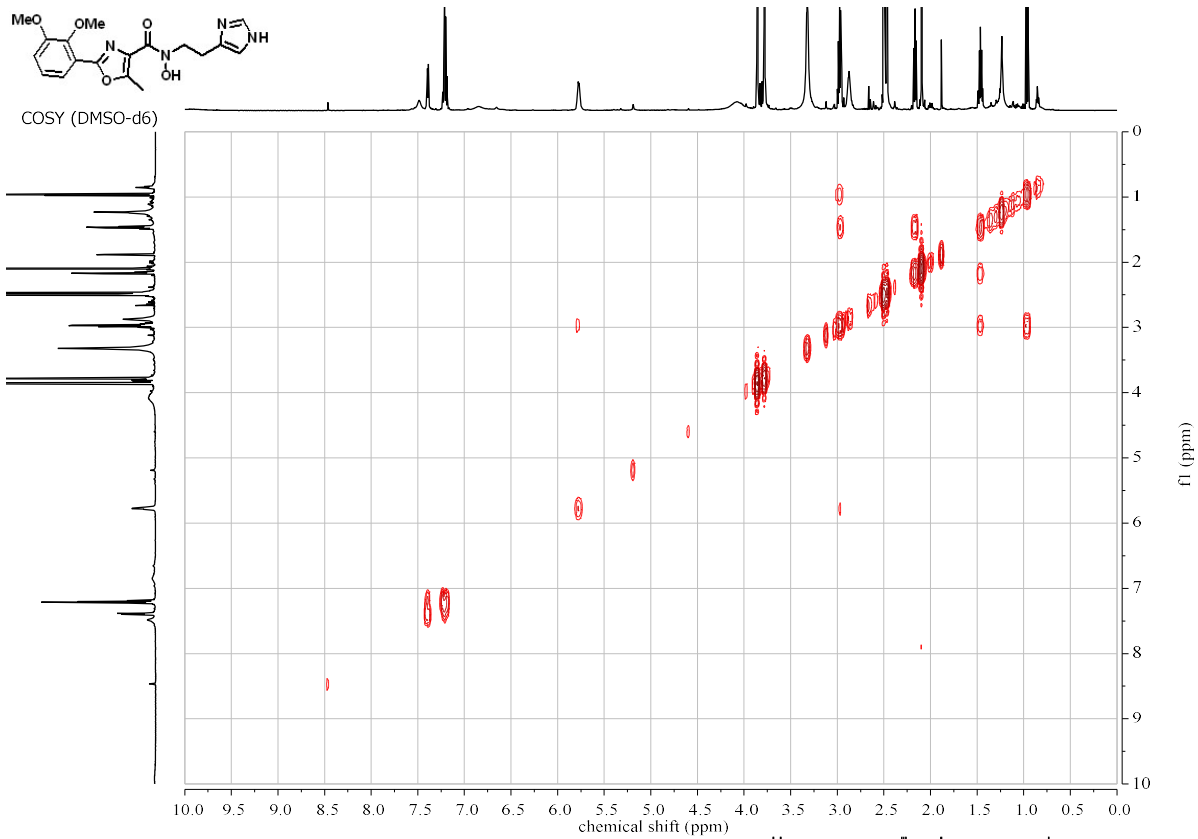


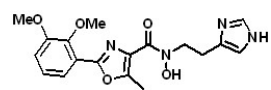
**N-(2-(1H-imidazol-4-yl)ethyl)-2-(2,3-dimethoxyphenyl)-N-hydroxy-5-methyloxazole-4-carboxamide- 8**

HRMS calcd for  $C_{18}H_{21}N_4O_5$  ( $M + H$ )<sup>+</sup> 373.1506; found 373.1502

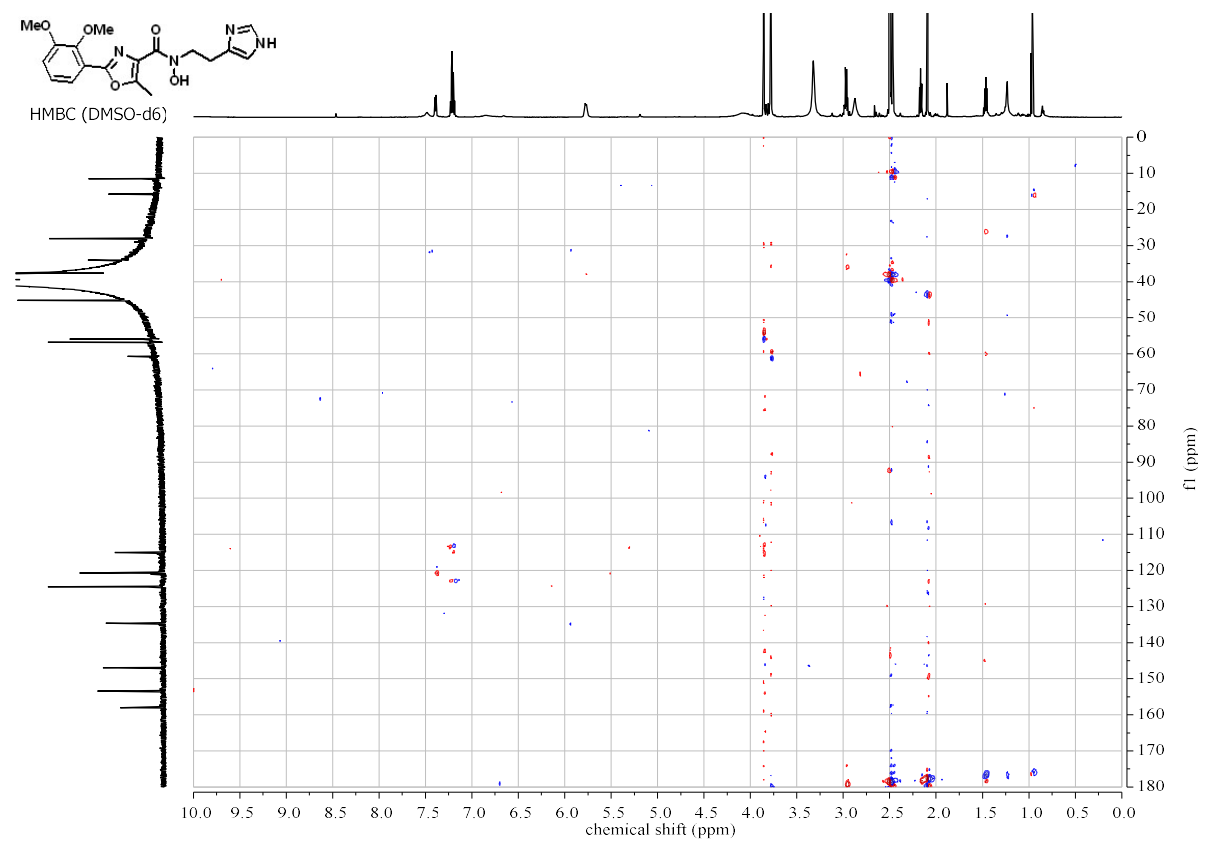
Atom	<sup>13</sup> C (ppm)	<sup>1</sup> H (ppm), Multiplets in Hz	COSY 1H-1H 3 bond	HMBC 1H-13C 2-3 bond	HSQC
2					
3		6.85 (s (br), 1H)			
5	134.6	7.48 (s (br), 1H)			5
6	28.0	2.87 (m, 2H)	7		
7		4.08 (s (br), 2H)	6		
9					
2'	158.0				
4'					
5'					
6'	11.4	2.47 (s, 3H)		5'	6'
1''	121.1				
2''	153.4				
3''	147.0				
4''		7.20 (m, 2H)	5''	5'', 6''	4''
5''	120.8	7.40 (dd, 1H)	6''	4'', 6''	5''
6''	124.6	7.20 (m, 2H)	5''	4'', 5''	6''
7''	60.8	3.78 (s, 3H)		3''	7''
8''	55.8	3.86 (2, 3H)		2''	8''



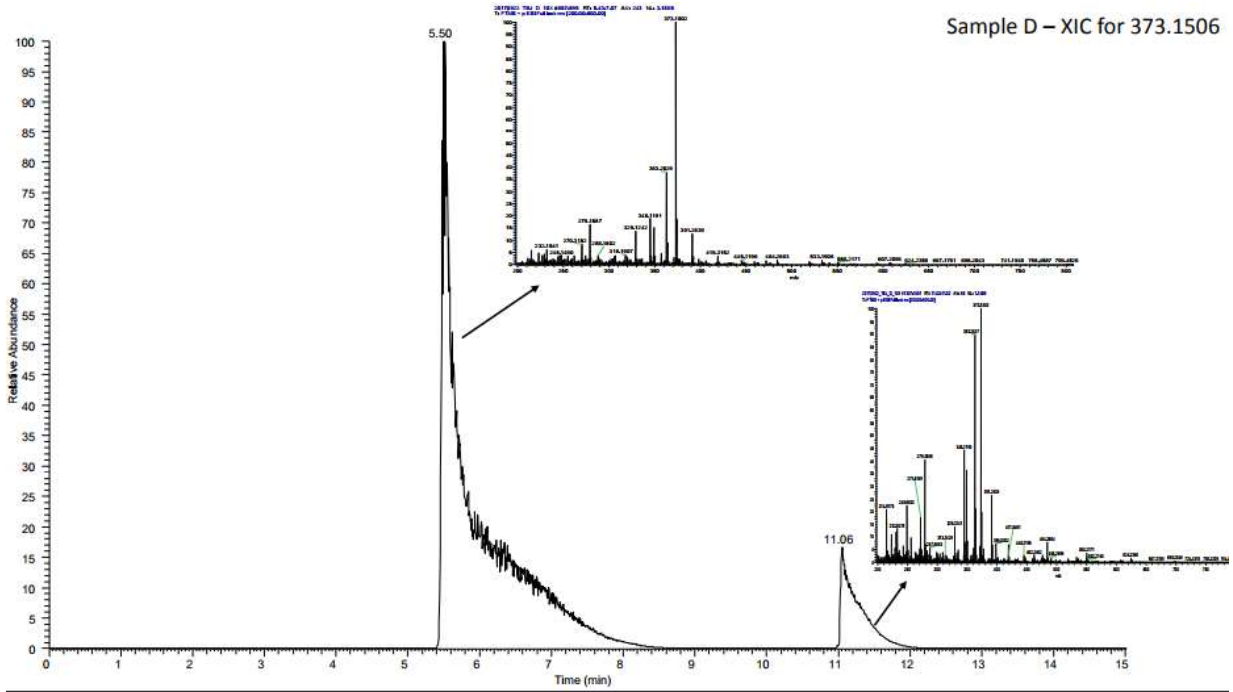
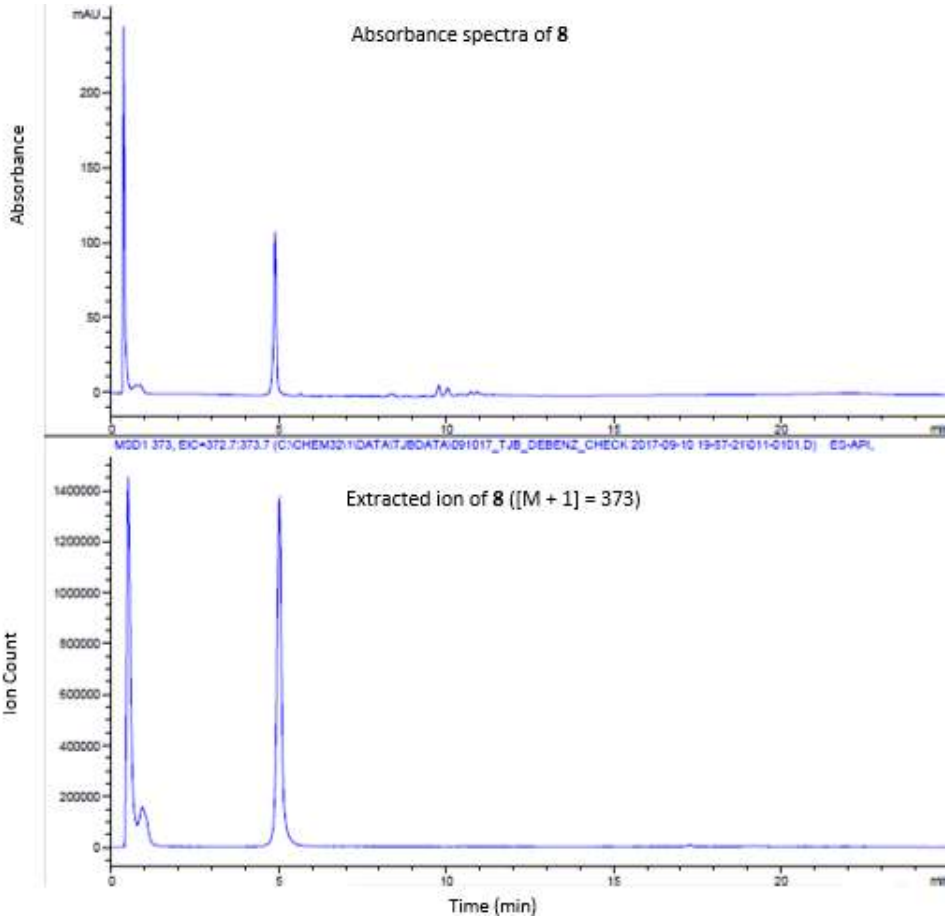




HMBC (DMSO-d6)



LC\_MS and HRMS for 8



## 6.8 References

- [1] Bohac, T. J., Shapiro, J. A., and Wencewicz, T. A. (2017) Rigid Oxazole Acinetobactin Analog Blocks Siderophore Cycling in *Acinetobacter baumannii*, *ACS infectious diseases* 3, 802-806.
- [2] Ohlemacher, S. I., Giblin, D. E., d'Avignon, D. A., Stapleton, A. E., Trautner, B. W., and Henderson, J. P. (2017) Enterobacteria secrete an inhibitor of *Pseudomonas* virulence during clinical bacteriuria, *The Journal of clinical investigation* 127, 4018-4030.
- [3] Shapiro, J. A., and Wencewicz, T. A. (2016) Acinetobactin Isomerization Enables Adaptive Iron Acquisition in *Acinetobacter baumannii* through pH-Triggered Siderophore Swapping, *ACS infectious diseases* 2, 157-168.
- [4] Shapiro, J. A., and Wencewicz, T. A. (2017) Structure-function studies of acinetobactin analogs, *Metallomics : integrated biometal science* 9, 463-470.
- [5] Moynie, L., Serra, I., Scorciapine, M. A., Oueis, E., Page, M. GP., Ceccarelli, M. and Naismith, J. H. (2018) Preacinetobactin not acinetobactin is essential for iron uptake by the BauA transporter of the pathogen *Acinetobacter baumannii*. *eLife* 7, e42270.
- [6] Bailey, D. C., Bohac, T. J., Shapiro, J. A., Giblin, D. E., Wencewicz, T. A., and Gulick, A. M. (2018) Crystal Structure of the Siderophore Binding Protein BauB Bound to an Unusual 2:1 Complex Between Acinetobactin and Ferric Iron, *Biochemistry*.
- [7] Stojiljkovic, I., Kumar, V., Srinivasan, N. (1999). Non-iron metalloporphyrins: potent antibacterial compounds that exploit haem/Hb uptake systems of pathogenic bacteria. *Mol. Microbiol* 31(2), 429-442.



- [8] Banin, E., Lozinski, A., Brady, K. M., Berenshtein, E., Butterfield, P. W., Moshe, M., Chevion, M., Greenberg, E. P., Banin, E. (2008). The potential of desferrioxamine-gallium as an anti-*Pseudomonas* therapeutic agent. *Pro. Natl. Acad Sci USA* 105(43), 16761-16766.
- [9] Graham T.H. (2010). A Direct Synthesis of Oxazoles from Aldehydes *Org. Lett.*, 12, 3614-3617.

## **Chapter 7: Fimsbactin analogs as mimics of the natural Fimsbactin system**

## 7.1 Preface

This chapter was adapted in part with from [Bohac, T. J., Fang, L., Banas, V. S., Giblin, D. E. & Wencewicz, T. A. *manuscript in preparation*] TJB performed the synthesis, characterization and evaluation of the compounds. LF performed all growth and competition studies. VSB assisted in the synthesis of the analogs. DEG performed all DFT calculations. TAW served as principal investigator and oversaw experimental design and completion.

## 7.2 Abstract

Herein, we report the synthesis of three structural and functional Fimsbactin siderophore mimics. We report the growth promotion abilities and iron binding affinities of the three analogs to be comparable to that of natural Fimsbactin A. We determined siderophore charge has little, if any, effect on metal and BauB binding or growth promotion. Through growth recovery and siderophore binding protein, BauB, affinities studies, we observed that the Fimsbactin mimics utilize the siderophore transport pathway and can compete with natural siderophores acinetobactin and Fimsbactin A. Equipped with this knowledge, further mimics and siderophore-antibiotic conjugates can be synthesized to continue to exploit the *A. baumannii* siderophore transport pathways as a Trojan horse strategy for antibiotic delivery.

## 7.3 Introduction

While antibiotic resistance is on the rise for both Gram-negative and Gram-positive pathogens, those infections caused by Gram-negative bacteria are often more difficult to treat.<sup>1</sup> Due to the presence of a second outer cell membrane, many traditional antibiotics that are effective against Gram-positive pathogens fail to permeate the outer membrane of Gram-negative pathogens, rendering them ineffective.<sup>2</sup> Thus, unique strategies for targeted antibiotic delivery are of increasing interest to combat multi-drug resistant Gram-negative infections.<sup>2</sup> In particular,

Trojan horse delivery strategies which employ siderophores as vehicles of antibiotic delivery have gained interest over the past few decades.<sup>2</sup> Siderophore-antibiotic conjugates have shown promise against both Gram-positive and Gram-negative pathogens, and siderophore-antibiotic conjugate Cefiderocol of Shionogi has recently proceeded to phase III clinical trials for the treatment of a range of MDR Gram-negative pathogens.<sup>3</sup>

In particular, our laboratory focuses on the study of one such multi-drug resistant pathogen, *Acinetobacter baumannii*, which produces a cocktail of three siderophores. These siderophores, acinetobactin<sup>4</sup>, Fimsbactin<sup>5</sup> and baumannoferrin<sup>6</sup>, support cell growth through the acquisition of essential metal nutrients. On-going work in our lab has sought to elucidate the mechanisms by which *A. baumannii* siderophores interact and promote growth. Building upon the body of research targeting the biosynthesis and biological function of Acb and Fims, we sought to expand these studies to include synthetically simpler siderophore mimics as probes of the natural system.

Leading in the synthesis, discovery and evaluation of Trojan horse siderophore-antibiotic conjugates, the Miller group synthesized a Fimsbactin structural mimic (Fim analog 1, **2**), containing three bidentate binding moieties consistent with natural Fimsbactin A: two catechols and one hydroxymate moiety (**Figure 7.1**). Unlike the natural system, this structural mimic does not contain any stereo-centers; thus, represents as a synthetically simpler target molecule. To date, numerous antibiotics have been conjugated to this structural mimic, including ciprofloxacin<sup>2,7</sup>, carbacephalosporin,<sup>2</sup> daptomycin,<sup>8</sup> and vancomycin.<sup>9</sup> Interestingly, while both Fimsbactin analog-conjugated carbacephalosporin and daptomycin showed extremely low MIC values (as low as 0.2 $\mu$ M) against *A. baumannii*, conjugates with fluoroquinolones (ciprofloxacin) afford little to no inhibition against *A. baumannii* (MIC >125 $\mu$ M).<sup>2,8</sup> Given that beta-lactam antibiotics target penicillin binding proteins (PBP) located in the periplasm, while fluoroquinolones target DNA

gyrase located in the cytoplasm, the lack of growth inhibition by the Fimsbactin mimic-ciprofloxacin target suggests the Fimsbactin structural mimic fails to reach the cytoplasm of the cell. Correspondingly, it has been hypothesized that the natural Fimsbactin siderophores are reduced in the periplasm of the cell and never reach the cytoplasm. This hypothesis is further supported by the absence of an inner membrane transport protein in the *A. baumannii* Fimsbactin gene cluster.<sup>11</sup> However, the mechanism of action of transport and delivery via Fimsbactin analog antibiotic conjugates still remains unknown. In this regard, we sought to explore if this Fimsbactin analog serves as both a structural analog *and* functional mimic of the natural Fimsbactins, which utilizes the natural Fimsbactin transport pathways that support bacterial virulence. This chapter includes the synthesis and biological study of three structural Fimsbactin mimics (**Figure 7.2**) and evaluates their ability to serve as possible siderophore-like scaffolds for antibiotic delivery.

## 7.4 Results and Discussion

To achieve our established goals, we first synthesized compound **1** in 8 steps starting from commercially available starting materials (**Figure 7.3**)<sup>2</sup>, which, after troc-deprotection, possesses a terminal primary amine for further coupling/diversification. Previous work in our group has highlighted the role of siderophore charge in bacteria siderophore utilization [in particular, of danoxamine analogs of *S. aureus*<sup>9</sup>]. This led us to explore the influence of charge on the structural Fimsbactin mimic system. To this end, we synthesized previously reported Fimsbactin analog 1 (**2**) - negatively charged at neutral pH, Fimsbactin analog 2 (**3**) – neutral charge at neutral pH, and Fimsbactin analog 3 (**4**) – positively charges at neutral pH. Fimsbactin analog 1 (**2**) was obtained in two steps from compound **1** via the removal of the troc-protecting group and addition of succinic anhydride, followed by global benzyl de-protection via hydrogenolysis. Similarly, Fimsbactin analogs 2 and 3 (**3**, **4**) were synthesized via troc-deprotection of compound **1** with activated zinc,

followed by the addition of acetic anhydride or Cbz-beta-alanine-N-hydroxysuccinimide ester, respectively; global benzyl/benzylcarbamate de-protection then affords title compounds **3** and **4**, in good overall yield.

With these analogs in hand, we first sought to investigate the role of siderophore-mimic charge on growth promotion abilities. In both the apo- and holo- forms, all three analogs were seen to promote growth in a dose dependent manner—with higher growth promotion in the holo- form than in the apo- variant (**Figure 7.4, 7.5**). There was no apparent effect of charge on growth promotion, as all three analogs promoted growth at a similar rate. As all three analogs promoted growth in the holo- form, we sought to explore the effect of charge on iron binding affinity in reference to the natural Fimsbactin system. We were excited to find that all three fimbactin analogs bind iron with similar affinities as the natural system ( $\log K_{\text{Fe}} = 27.1$ ) (**Table 7.1**)—with the neutrally charged analog (**3**) possessing a slightly higher binding affinity ( $\log K_{\text{Fe}} = 28.5$ ) than the positively charged analog (**4**) ( $\log K_{\text{Fe}} = 27.3$ ). These results implied that the structural modification of Fimsbactin A to afford simpler analogs—provided the metal-binding functional groups are maintained—allows for the easy generation of viable Fims-like probes.

Due to the similarities in the iron binding and growth promotion of the Fimsbactin analogs to natural Fimsbactin A, we next sought to investigate if the analogs utilize the siderophore transport pathway as a means of gaining outer membrane permeability. To explore this possibility, we synthesized gallium loaded Fimsbactin analog compounds and tested their effect on the whole cell growth of *A. baumannii*. As expected, all three gallium complexes inhibited whole cell growth. Gallium mimics the iron-siderophore contacts but is not reduced in the periplasm or cytosol—therefore inhibiting essential iron acquisition. We next set out to identify if growth could be recovered via the addition of natural siderophore iron complexes, FimFe and AcbFe, which would

indicate that the Ga-Fims analog complexes utilize the siderophore pathway. Indeed, dose-dependent growth recovery was observed with the addition of FimFe and AcbFe, demonstrating that the analogs compete with Fimsbactin and Acb uptake pathways (**Figures 7.6-7.9**). Greater growth recovery was observed in the FimsFe/Fim-Ga competition studies, suggesting direct competition of the analog with Fims-specific transport and illustrating that the Fimsbactin analog are in fact functional, as well as structural, mimics. Fimsbactin analog-Ga competition with Acb is consistent with our previous findings<sup>10</sup> that natural Fims compete with natural Acb, as well, since previous studies have shown that natural Fimsbactin can compete with Acb for periplasmic binding protein, BauB.<sup>11</sup> Thus, to evaluate if the Fimsbactin analogs could also bind BauB, we performed BauB fluorescence quenching assays with both the apo- and holo- forms of each analog (**Table 7.1, Figure 7.10**). BauB-binding was observed for all analog forms and apparent binding affinities were consistent with natural Fimsbactin A, further supporting that the Fimsbactin analogs serve as functional Fimsbactin mimics.

The DFT-computed energy minimized structure of holo-Fimsbactin analog 1 (**2**), was strikingly similar to that of the computed holo-Fimsbactin A structure (**Figure 7.11A and 7.11B**). Both structures bind iron in a hexadentate manner, with the catecholate ligands and hydroxamate ligand occupying the same sites. An overlap of these two structures highlight these commonalities (**Figure 7.11C**). Both these energy-minimized structures contain a tetrahedral center, denoted with a star in **Figure 7.1**; this center forces the geometry of the binding moieties of the Fimsbactin analog to occupy the same 3-dimensional positions as in the natural system, thus providing further evidence of the ability of the analog to mimic natural Fimsbactin A. Moreover, the DFT energy minimized structure of [FimFe]<sup>-</sup> was strikingly similar to the experimentally observed *cis*-[Acb<sub>2</sub>Fe]<sup>-</sup> complexed to BauB.<sup>12</sup> Since the minimized structure of [FimFe]<sup>-</sup> appears to occupy

similar 3-dimensional space as BauB-bound  $[\text{Acb}_2\text{Fe}]^-$  (as depicted in **Figure 7.11**), we hypothesize that the  $[\text{FimsbactinFe}]^-$  analog will also bind BauB in a similar fashion—as the energy minimized structure of the  $[\text{FimsbactinFe}]^-$  analog overlays well with the  $[\text{FimFe}]^-$  structure. These findings are consistent with the ability of the Fimsbactin analogs to compete with both natural Fimsbactin and natural Acb in BauB binding and indicate the viability of the simplified analogs to serve as functional mimics of the natural system. Moreover, the structural simplification of more complex siderophore systems may prove useful in the facile generation of functional siderophore-like probes and new simplified scaffolds for antibiotic-conjugate drug delivery systems. However, it must be noted that the analogs cannot be hydrolyzed. As discussed in chapter 4, the potential ability of the natural Fimsbactin A siderophore to be hydrolyzed to fimsbactin F may play a vital role in the interworking of the Fimsbactin system.

## 7.5 Outlook and Conclusions

In summary, we completed the synthesis of three simplified structural Fimsbactin analogs. Through whole cell growth promotion studies and iron binding assays, we demonstrated that all three analogs promote growth and bind iron in a similar manner as the natural Fimsbactin A siderophore—independent of analog formal charge. Moreover, we determined that all three analogs utilize the siderophore transport pathway through growth recovery competition assays with gallium bound analogs and iron bound Fimsbactin and acinetobactin. In particular, the observed competition between the Fimsbactin analogs and acinetobactin highlights the importance of siderophore competition for periplasmic binding protein, BauB, binding as it relates to growth promotion. BauB binding assays confirmed that the generated Fimsbactin bind BauB with similar affinities as the natural siderophores, Fimsbactin and acinetobactin. Taken collectively, these results suggest that the simplified Fimsbactin analogs serve as both structural and functional



Fimsbactin mimics and may be useful for the generation of “siderophore”-antibiotic conjugates for targeted drug delivery.

## 7.6 Materials and Methods

### *Strains, Materials, and Instrumentation*

Growth studies for the Fimsbactin analogs were conducted using *A. baumannii* ATCC 19606<sup>T</sup> provided by Dr. Luis Actis. Precultures, and 96-well plate *A. baumannii* growth assays were performed in filter-sterilized M9 minimal media. Samples for LC-MS were prepared in 0.45  $\mu$ M PTFE mini-UniPrep vials from Agilent. All preparatory HPLC was performed using a Beckman Coulter SYSTEM GOLD 127P solvent module and 168 detector with a Phenomenex Luna 10u C18(2) 100A column, 250  $\times$  21.20 mm, 10  $\mu$ m with guard column. Prep HPLC was performed with a mobile phase of 5 mM ammonium acetate in (A) water and (B) acetonitrile, and data were processed using 32 Karat software, version 7.0. All LC-MS was performed on an Agilent 6130 quadrupole LC-MS with G1313 autosampler, G1315 diode array detector, and 1200 series solvent module. A Phenomenex Gemini C18 column, 50  $\times$  2 mm, 5  $\mu$ m with guard column was used for all LC-MS separations. LC-MS mobile phases were 0.1% formic acid in (A) water and (B) acetonitrile, and data were processed using G2710 ChemStation software. NMR was performed on a Varian Unity Inova-600 MHz instrument with a cold probe. Bacterial growth studies were performed using polystyrene 96-well plates with polystyrene lids. BauB affinity studies were conducted using a fluorescence cuvette (HellmaAnalytics High Precision Cell cuvette made of Quartz SUPRASIL; light path 10  $\times$  2 mm). Emission spectra were recorded at  $\lambda_{\text{emission}} = 300\text{--}400$  nm using a PerkinElmer LS 55 Luminescence Spectrometer (slit width 10 nm; scan speed 400 nm/min) at  $\lambda_{\text{excitation}} = 280$  nm. Fluorescence intensity at 320 nm was plotted versus substrate

concentration (nM) and apparent  $K_d$  was calculated using nonlinear regression and a one binding site model in GraphPad Prism v7.0b

### ***A. baumannii* Growth Studies in Minimal Media**

M9 minimal media was prepared as described previously.<sup>13,14,15</sup>

#### **Growth studies**

For biological assessment of Fimsbactin analogs under iron-restrictive conditions, stock solutions of 10 mM each analog were prepared in DMSO. A 96-well plate was filled with 50  $\mu$ L of M9 minimal media per well. These stock solution were diluted adding 5  $\mu$ L of 10 mM Fimsbactin analog stock to 195  $\mu$ L of M9 minimal, affording 250  $\mu$ M stock solutions. 50  $\mu$ L the Fimsbactin analog 250  $\mu$ M stock solutions were added to the first row of a 96 well plate. Compound was serially diluted down the plate to 1.95  $\mu$ M. An inoculum was made by adding 100  $\mu$ L of 0.5 McFarland standard (*A. baumannii* ATCC 17978) to 4.0 mL of M9 minimal media supplemented with 350  $\mu$ M 2,2'-dipyridyl. Inoculum (50  $\mu$ L) was added to each well for a final concentration of 175  $\mu$ M 2,2'-dipyridyl and a serial dilution of 62.5-1.95  $\mu$ M Fimsbactin analog. Growth promotion was determined as compared to a control with 175  $\mu$ M 2,2'-dipyridyl, 0  $\mu$ M Fimsbactin analog. All experiments were performed in triplicate.

For the biological evaluation of the  $\text{Fe}^{3+}$ -complex of 250  $\mu$ M stocks of each Fimsbactin analog- $\text{Fe}^{3+}$  were prepared in M9 minimal media. A 96-well plate was filled with 50  $\mu$ L of M9 minimal media per well. Into the first row, 50  $\mu$ L of Fimsbactin analog- $\text{Fe}^{3+}$  stock was added, and rows were serially diluted down to 1.95  $\mu$ M. An inoculum was made by adding 100  $\mu$ L of 0.5 McFarland standard (*A. baumannii* ATCC 17978) to 4.0 mL of M9 minimal media supplemented with 350  $\mu$ M 2,2'-dipyridyl. Inoculum (50  $\mu$ L) was added to each well for a final concentration of 175  $\mu$ M 2,2'-dipyridyl and a serial dilution of 62.5-1.95  $\mu$ M Fimsbactin analog- $\text{Fe}^{3+}$ . Growth

promotion was determined as compared to a control with 175  $\mu\text{M}$  2,2'-dipyridyl, 0  $\mu\text{M}$  Fimsbactin analog- $\text{Fe}^{3+}$ . All experiments were performed in triplicate.

### **Growth studies with Gallium:**

For the biological evaluation of the Ga-complex of 125  $\mu\text{M}$  stocks of each Fimsbactin analog-Ga were prepared in M9 minimal media. A 96-well plate was filled with 50  $\mu\text{L}$  of M9 minimal media per well. Into the first row, 50  $\mu\text{L}$  of Fimsbactin analog-Ga stock was added, and columns were serially diluted down to 0.9765  $\mu\text{M}$ . An inoculum was made by adding 100  $\mu\text{L}$  of 0.5 McFarland standard (*A. baumannii* ATCC 17978) to 4.0 mL of M9 minimal media supplemented with 350  $\mu\text{M}$  2,2'-dipyridyl. Inoculum (50  $\mu\text{L}$ ) was added to each well for a final concentration of 175  $\mu\text{M}$  2,2'-dipyridyl and a serial dilution of 31.25-0.9765  $\mu\text{M}$  Fimsbactin analog-Ga. To all wells in the first 3 columns, 2  $\mu\text{L}$  of 195  $\mu\text{M}$  FimA-Fe was added to afford a final concentrations of 3.9  $\mu\text{M}$  of FimA-Fe. To all the wells in the next 3 columns, 2  $\mu\text{L}$  of 195  $\mu\text{M}$  Acb-Fe was added to afford a final concentrations of 3.9  $\mu\text{M}$  of Acb-Fe. Growth promotion was determined as compared to a control with 175  $\mu\text{M}$  2,2'-dipyridyl, 0  $\mu\text{M}$  Fimsbactin analog-Ga and also compared to an additional control of a 175  $\mu\text{M}$  2,2'-dipyridyl, and a serial dilution of 31.25-0.9765  $\mu\text{M}$  Fimsbactin analog-Ga. All experiments were performed in triplicate.

### ***BauB Fluorescence Quenching Studies***

BauB fluorescence quenching studies were performed as previously reported.<sup>11,12</sup> Briefly, a bead of protein BauB-ss was thawed and diluted to provide a 400 nM stock solution. 300  $\mu\text{L}$  of this 400 nM stock solution was transferred to a fluorescence cuvette. A stock solution of 400 nM protein and 16  $\mu\text{M}$  small molecule was made. An emission spectrum was taken at each concentration as an average of 3 scans. Excitation wavelength of 280 nm, fluorescence observed between 300 and 400 nm. Slit width was set to 10 nm with a scan speed of 400. Fluorescence at

320 nm was tracked as a function of small molecule concentration. All experiments were performed in duplicate as independent trials. Increasing concentrations of small molecule were added without altering protein concentration. Measurements at the following concentrations of small molecule were taken: 0, 106.8, 212.8, 318, 422.4, 684, 1196, 1688, 2644, 3536 nM

### ***DFT Calculations.***

Stable *holo*-siderophore complexes with ferric iron were calculated using density functional theory<sup>16,17</sup> (DFT) in a similar manner as described previously.<sup>12</sup> Monte Carlo/MMFF molecular mechanics/dynamics was used to explore conformer spaces. Initial structure optimization was performed by using the PM3d semi-empirical algorithm (Spartan Linux v10, WaveFunction, Inc.). We employed DFT (Density Functional Theory, Gaussian 09, Gaussian Inc.) for calculations using the PBE0 hybrid functional (PBE1PBE in Gaussian parlance) with basis sets Def2-SVP and Def2-TZVP. Minima were optimized at the level PBE0/Def2-SVP and single-point energies were calculated at level PBE0/Def2-TZVP, with scaled thermal-energy corrections from B3LYP/6-31G(d,p).<sup>18</sup> Solvent-based single-point energies were calculated at the same level using the CPCM polarizable conductor calculation model for water and the Universal Force Field for atomic radii.<sup>19</sup> DFT functionals and basis sets were chosen for efficiency and compatibility with ferric complexes.<sup>20,21,22</sup>

### ***Determination of $K_{Fe}$***

Stock solutions 100  $\mu$ M Fimsbactin analog iron complexes were prepared in 10 mM HEPES buffer and a UV-Vis scan was recorded. Next 120  $\mu$ M EDTA was added and absorbance at 500 nm was measured over 800 minutes. Iron-binding affinity ( $K_{Fe}$ ) was determined using the following calculations.

$$(1) \quad K_L = \frac{[FeL]}{[Fe^{3+}][L]} \quad \text{for the following equilibrium;} \quad [Fe^{3+}] + [L] \rightleftharpoons [FeL]$$

$$(2) \quad K_{FeEDTA} = \frac{[FeEDTA]}{[Fe^{3+}][EDTA]} \quad \text{for the following equilibrium;} \quad [Fe^{3+}] + [EDTA] \rightleftharpoons [FeEDTA]$$

$$(3) \quad K_{Exchange} = \frac{K_L}{K_{FeEDTA}} \quad \text{for the following equilibrium;} \quad [FeEDTA] + [L] \rightleftharpoons [FeL] + [EDTA]$$

$$(4) \quad K_{Exchange} = \frac{[FeL][EDTA]}{[FeEDTA][L]}$$

$$(5) \quad \Delta = \frac{Abs_{FeL} - Abs_{FeL+EDTA}}{\epsilon_L}$$

$$(6) \quad K_L = K_{FeEDTA} \times \frac{[FeL][EDTA]}{[FeEDTA][L]}$$

$$(7) \quad [FeL] = \frac{Abs_{FeL}}{\epsilon_L}$$

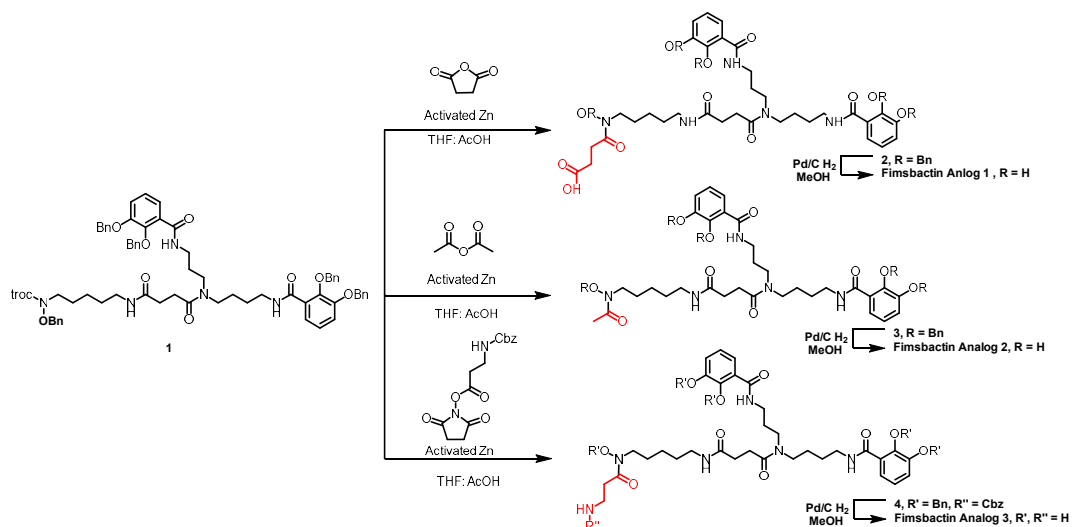
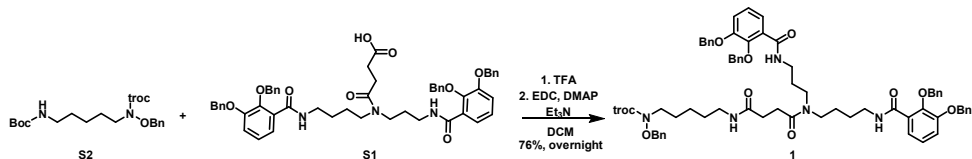
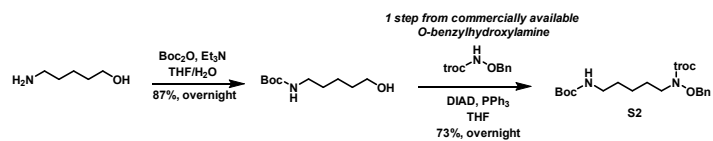
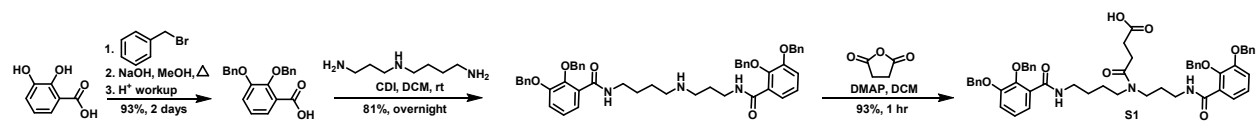
$$(8) \quad [EDTA] = [EDTA]_T - \Delta \quad \text{where} \quad [EDTA]_T = \text{total EDTA added}$$

$$(9) \quad [FeEDTA] = \Delta$$

$$(10) \quad [L] = \Delta$$

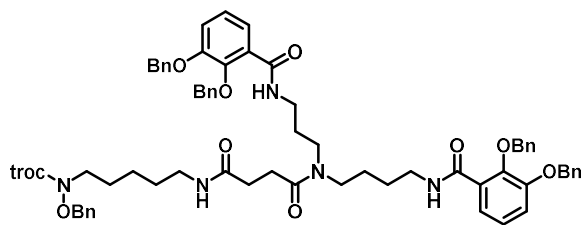
$$(11) \quad K_{Fe} = \text{apparent } K_L$$

## Compound Synthesis

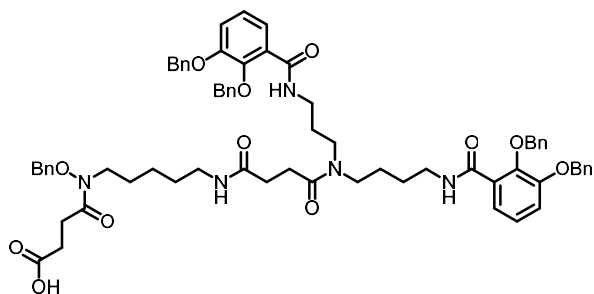


## Synthetic Scheme 1

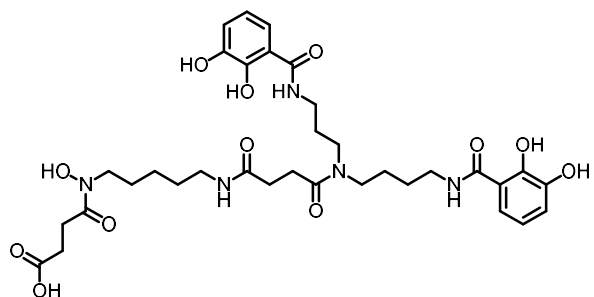
### Synthetic procedures:



**Compound 1** was synthesized and characterized as previously reported by Miller and colleagues following **synthetic scheme 1**.<sup>2</sup> Briefly, 2,3 dihydroxybenzoic acid was benzyl protected with benzylbromide and subsequent saponification afforded 2,3(bisbenzyloxy)benzoic acid (93%, 17.4 grams). An *N,N'*-carbonyldiimidazole (CDI)-mediated coupling reaction of spermidine and 2,3(bisbenzyloxy)benzoic acid afforded *N'**N*<sup>8</sup>-bis(2,3-bis(benzyloxy)benzoyl)spermidine (91%, 6.87 grams). Addition of succinic anhydride in the presence of catalytic DMAP in DCM afforded 4-((4-(2,3-bis(benzyloxy)benzamido)butyl)(3-(2,3-bis(benzyloxy)benzamido)propyl)amino)-4-oxobutanoic acid, **S1** (93%, 3.79 grams). Correspondingly, boc protection of 5-amino-1-pentanol (87%, 15.4 grams) followed by Mitsunobu amination with *N*-troc-*O*-benzyl-hydroxylamine provided 2,2,2-trichloroethyl (benzyloxy)(5-((tert-butoxycarbonyl)amino)pentyl)carbamate, **S2** (73%, 3.96 grams). The free amine of **S2** was synthesized via the removal of boc-protecting group of **S2** by trifluoroacetic acid. Subsequent EDC-mediated coupling with **S1** in the presence of facilitating base, triethyl amine and catalytic DMAP provided compound 1 (76%, 3.86 grams). NMR characterization was consistent previously reports.



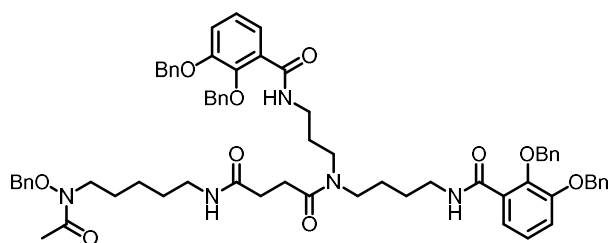
**Benzyl protected - Fimsbactin analog 1** was synthesized and characterized as previously reported.<sup>2</sup> Briefly, activated zinc was added to a stirring solution of compound 1 in a 1:1 mixture of THF:AcOH at room temperature under argon atmosphere. To the stirring reaction mixture was added succinic anhydride, dropwise, slowly. When the reaction was complete (as determined by LC-MS, ~ 3 hours), the mixture was filtered to remove insoluble zinc, and the solvent removed under reduced pressure. The resultant crude oil was dissolved in EtOAc and washed with water (2 times) and brine (2 times), dried over magnesium sulfate, filtered over cotton, and concentrated under reduced pressure. The crude mixture was separated by preparative high performance liquid chromatography (C18-silica, 0B to 95B gradient 17 minutes, 95B to 100B gradient 8 minutes, 5 mM ammonium acetate buffer) to afford benzyl-protected Fimsbactin analog 1 (60 mg) NMR (**Figures 7.13 & 7.14**) analysis was consistent with previous reports.



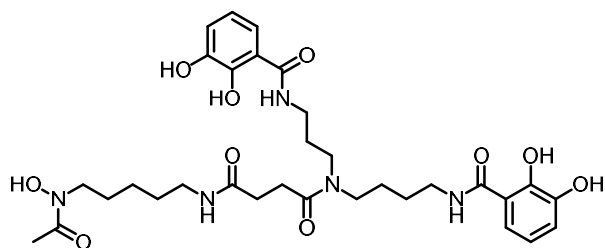
**Fimsbactin Analog 1.** To a stirring solution of benzyl-protected Fimsbactin analog 1 dissolved in MeOH under argon atmosphere was added ~1/10 mass equivalent of 10% Pd/C as a solid in one portion. The flask was purged with H<sub>2</sub>, and the resultant solution stirred under hydrogen atmosphere (1 atm) for approximately 1 hour. Upon confirmation of reaction completion by LC-



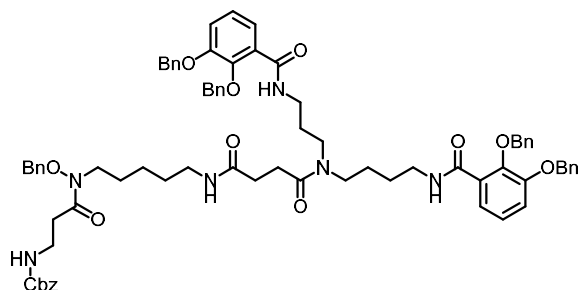
MS (~1 hr), the reaction mixture was filtered to remove insoluble palladium catalyst, and the solution was concentrated under reduced pressure to afford Fimsbactin Analog 1 (10 mg). ESI LC-MS, HR-MS and NMR (**Figures 7.15-7.18**) analysis of Fimsbactin Analog 1 were consistent with previous reports



**Benzyl protected - Fimsbactin analog 2.** Activated zinc (6 mg) was added to a stirring solution of compound **1** (6 mg) in a 1:1 mixture of THF:AcOH at room temperature under argon atmosphere. To the stirring reaction mixture was added acetic anhydride (4.9 mg), slowly. When the reaction was complete (as determined by LC-MS, ~ 3 hours), the mixture was filtered to remove insoluble zinc, and the solvent removed under reduced pressure. The resultant crude oil was dissolved in EtOAc and washed with water (2 times) and brine (2 times), dried over magnesium sulfate, filtered over cotton, and concentrated under reduced pressure. The crude mixture was separated by preparative high performance liquid chromatography (C18-silica, 0B to 95B gradient 17 minutes, 95B to 100B gradient 8 minutes, 5 mM ammonium acetate buffer) to afford compound **3** (6 mg). NMR analysis of benzyl protected Fimsbactin analog **2** are shown in **Figures 7.19 & 7.20**.

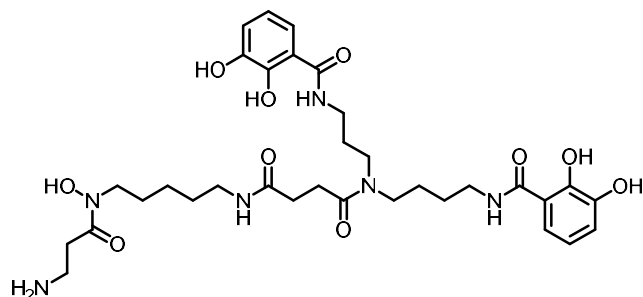


**Fimsbactin Analog 2.** To a stirring solution of compound benzyl protected Fimsbactin analog 2 dissolved in MeOH under argon atmosphere was added  $\sim 1/10$  mass equivalent of 10% Pd/C as a solid in one portion. The flask was purged with H<sub>2</sub>, and the resultant solution stirred under hydrogen atmosphere (1 atm) for approximately 1 hour. Upon confirmation of reaction completion by LC-MS ( $\sim 1$  hr), the reaction mixture was filtered to remove insoluble palladium catalyst, and the solution was concentrated under reduced pressure to afford Fimsbactin Analog 2 (8.6 mg). **Figures 7.21-7.24**



**Benzyl/Cbz protected - Fimsbactin analog 3.** Activated zinc (6 mg) was added to a stirring solution of compound 1 (4.4 mg) in a 1:1 mixture of THF:AcOH at room temperature under argon atmosphere. To the stirring reaction mixture was added Cbz-beta-alanine-N-hydroxysuccinimide ester (113 mg), slowly. When the reaction was complete (as determined by LC-MS,  $\sim 3$  hours), the mixture was filtered to remove insoluble zinc, and the solvent removed under reduced pressure. The resultant crude oil was dissolved in EtOAc and washed with water (2 times) and brine (2 times), dried over magnesium sulfate, filtered over cotton, and concentrated under reduced pressure. The crude mixture was separated by preparative high performance liquid

chromatography (C18-silica, 0B to 95B gradient 17 minutes, 95B to 100B gradient 8 minutes, 5 mM ammonium acetate buffer) to afford Benzyl/Cbz protected - Fimsbactin analog 3 (5 mg). NMR analysis is shown in **Figures 7.25 & 7.26**.



**Fimsbactin Analog 3.** To a stirring solution of Benzyl/Cbz protected - Fimsbactin analog 3 dissolved in MeOH under argon atmosphere was added ~1/10 mass equivalent of 10% Pd/C as a solid in one portion. The flask was purged with H<sub>2</sub>, and the resultant solution stirred under hydrogen atmosphere (1 atm) for approximately 1 hour. Upon confirmation of reaction completion by LC-MS (~1 hr), the reaction mixture was filtered to remove insoluble palladium catalyst, and the solution was concentrated under reduced pressure to afford Fimsbactin Analog 3 (4.2 mg). ). NMR analysis is shown in **Figures 7.27-7.30**.

## 7.7 Figures and Tables

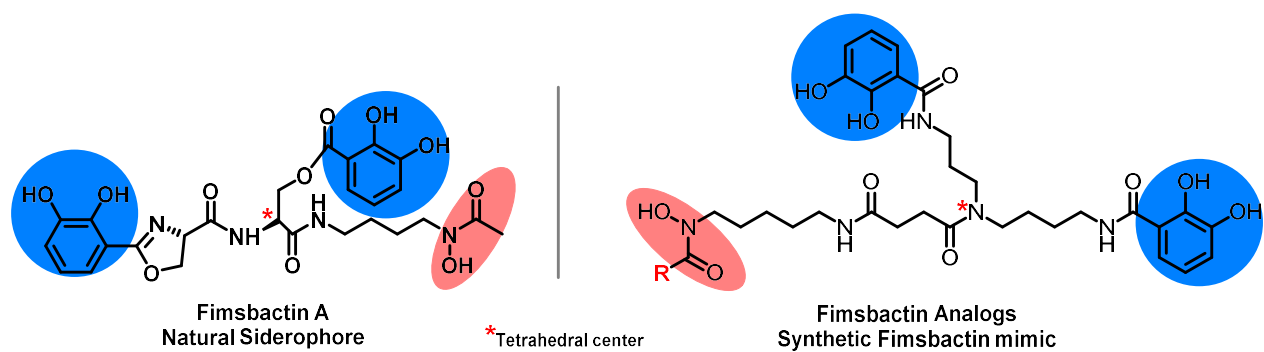


**Figure 7.1:** Natural Fimsbactin A and synthetic Fimsbactin Analogs. Common metal binding moieties are highlighted – catechol (blue) and hydroxamate (red). Each compound contains a similar tetrahedral center denoted with a \*.

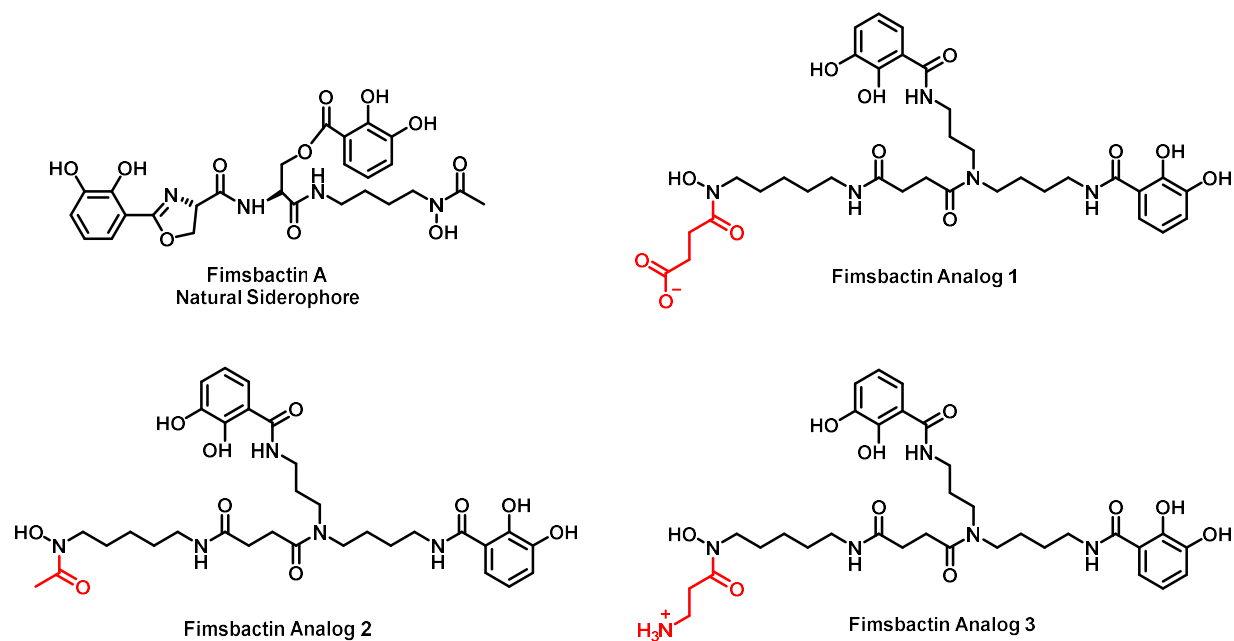


**Figure 7.2:** Naturally produced siderophore Fimsbactin A and three synthetic analogs. Each analog contains a different sidechain substituent which are negatively, neutral and positively charged, respectively, as neutral pH.

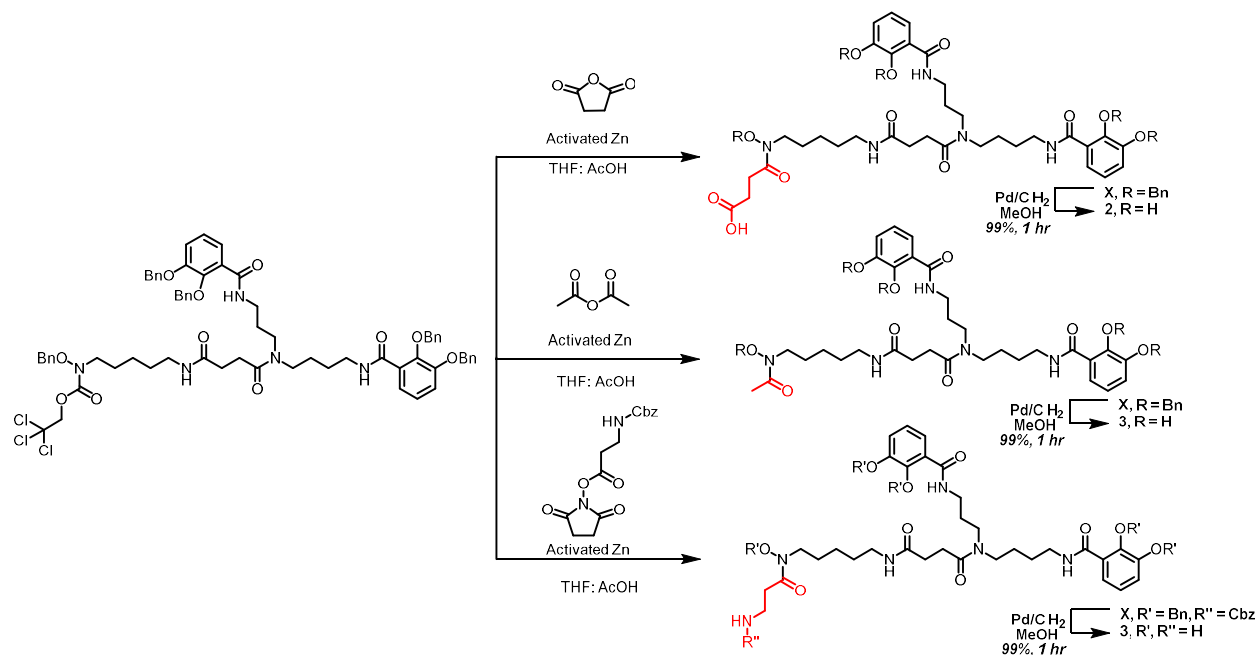


**Figure 7.3:** Three Fimsbactin structural analogs are synthesized via divergent synthesis from common compound 1

Compound	BauB Binding Affinity (apo/holo)	LogK <sub>Fe</sub>
Fimsbactin A <sup>12</sup>	354.8 ± 139.3/ 244.4 ± 93.3	27.1 ± 0.2
Fims analog - 1	393.3 ± 63.3/ 350.3 ± 143.5	27.9 ± 0.1
Fims analog - 2	259.3 ± 55.4/ 215.9 ± 30.3	28.5 ± 0.4
Fims analog - 3	239.4 ± 103.2/ 286.3 ± 106.9	27.3 ± 0.1

**Table 7.1:** Iron affinities and periplasmic siderophore binding protein, BauB, binding affinities for both iron-bound and iron-free Fimsbactin analogs and natural Fimsbactin A.

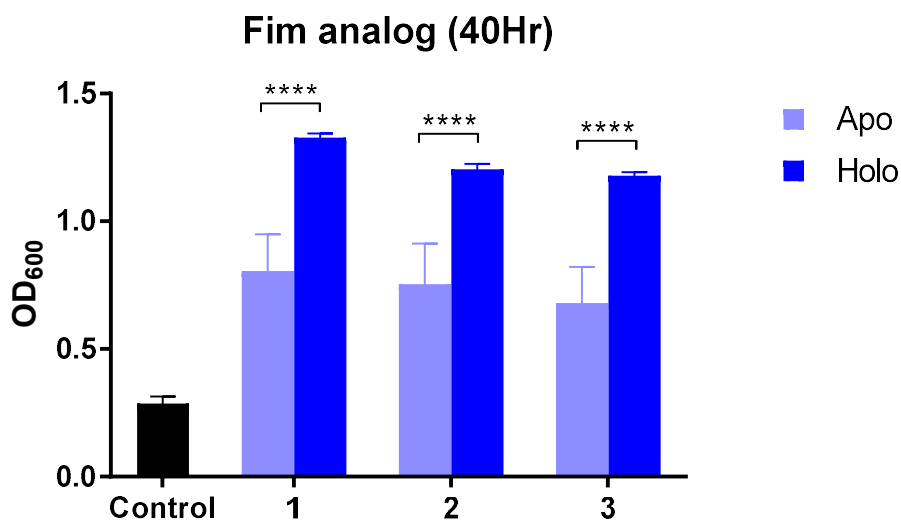


**Figure 7.4:** Influence of *apo*- and *holo*-fimsbactin analogs on *A. baumannii* growth. Bar graphs depict the growth of *A. baumannii* ATCC 17978 determined by measuring the optical density at 600 nm (OD<sub>600</sub>) as a function of time in the presence of 15.625 μM concentration of either the apo- or holo- form of each Fimsbactin analog. Error bars represent standard deviations from the mean for three independent trials. \*\*\*\*p < 0.0001. Full growth curves at variable concentration seen in **Figure 7.5**.

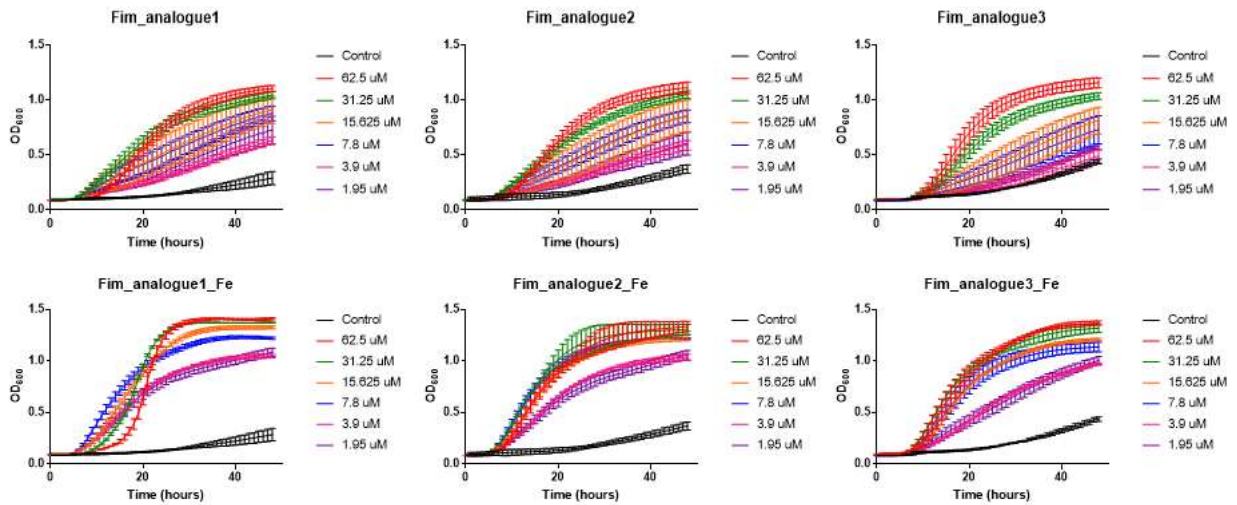
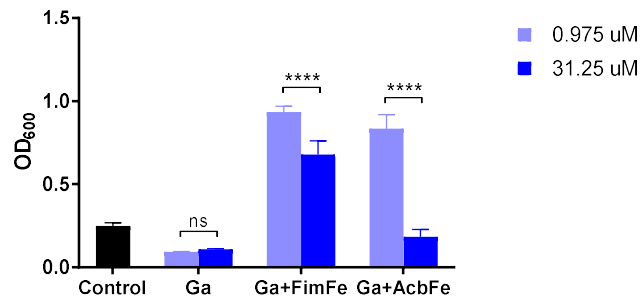
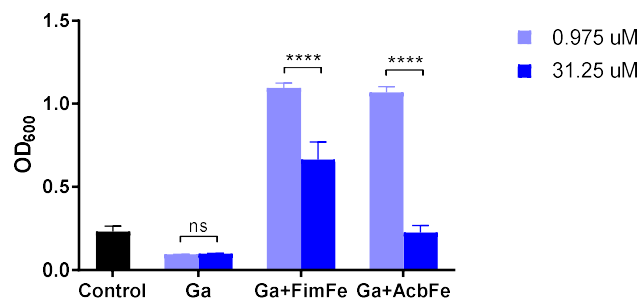


**Figure 7.5:** Influence of *apo*- and *holo*-fimsbactin analogs on *A. baumannii* growth. Line graphs depict the growth of *A. baumannii* ATCC 17978 determined by measuring the optical density at 600 nm ( $OD_{600}$ ) as a function of time in the presence of variable concentration of either the *apo*- or *holo*- form of each Fimsbactin analog. Error bars represent standard deviations from the mean for three independent trials.

Fim analog 1\_Ga with 3.9uM FimFe/AcbFe (40 Hr)



Fim analog 2\_Ga with 3.9uM FimFe/AcbFe (40 Hr)



Fim analog 3\_Ga with 3.9uM FimFe/AcbFe (40 Hr)

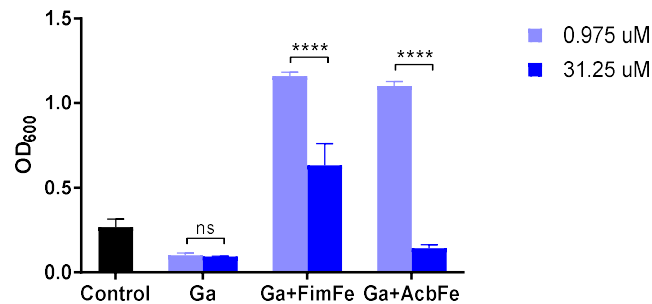


**Figure 7.6:** Growth inhibition by each Fimsbactin analog-Ga complex and the growth recovery of variable Fimsbactin analog-Ga (0.975 $\mu$ M or 31.25 $\mu$ M) and 3.9 $\mu$ M Fimsbactin A-Fe or Acb-Fe. Bar graphs depict the growth of *A. baumannii* ATCC 17978 determined by measuring the optical density at 600 nm (OD<sub>600</sub>) as a function of time. Error bars represent standard deviations from the mean for three independent trials. \*\*\*\*p < 0.0001, ns: non-significant. Full growth curves at variable concentration seen in **Figure 7.7, 7.8** and **7.9**.



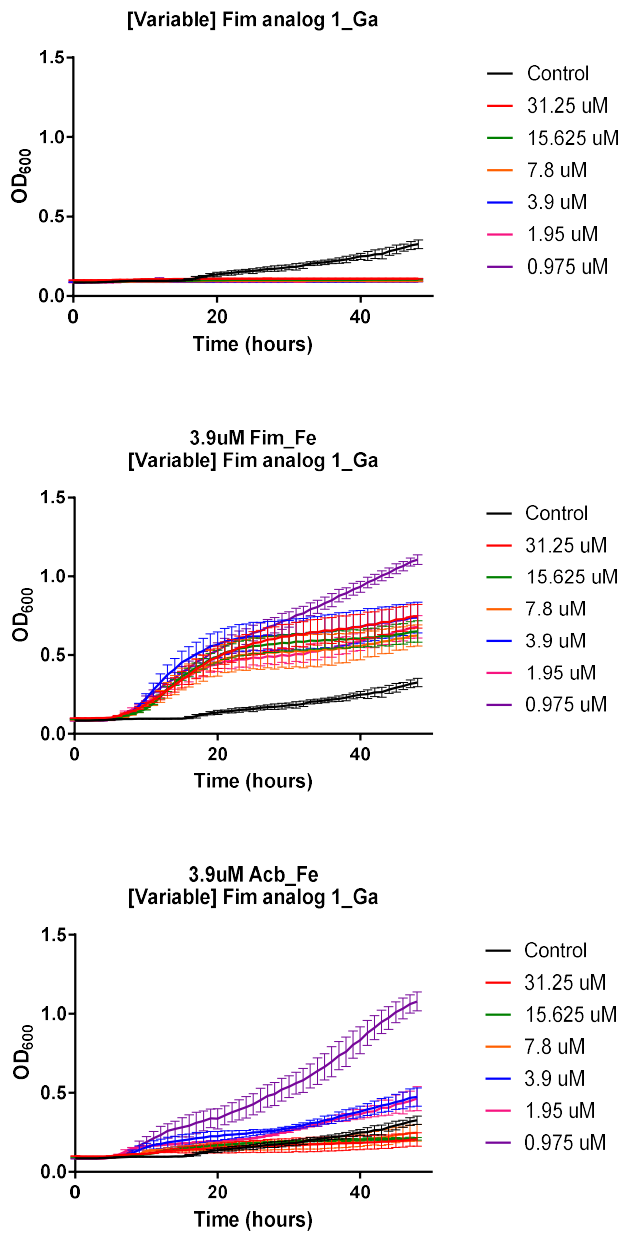


**Figure 7.7:** (a) Dose dependent growth inhibition by Fimsbactin analog 1-Ga complex (b) 3.9 $\mu$ M Fim-Fe and variable Fimsbactin analog 1-Ga complex (c) 3.9 $\mu$ M Acb-Fe and variable Fimsbactin analog 1-Ga complex .Line graphs depict the growth of *A. baumannii* ATCC 17978 determined by measuring the optical density at 600 nm ( $OD_{600}$ ) as a function of time. Error bars represent standard deviations from the mean for three independent trials.

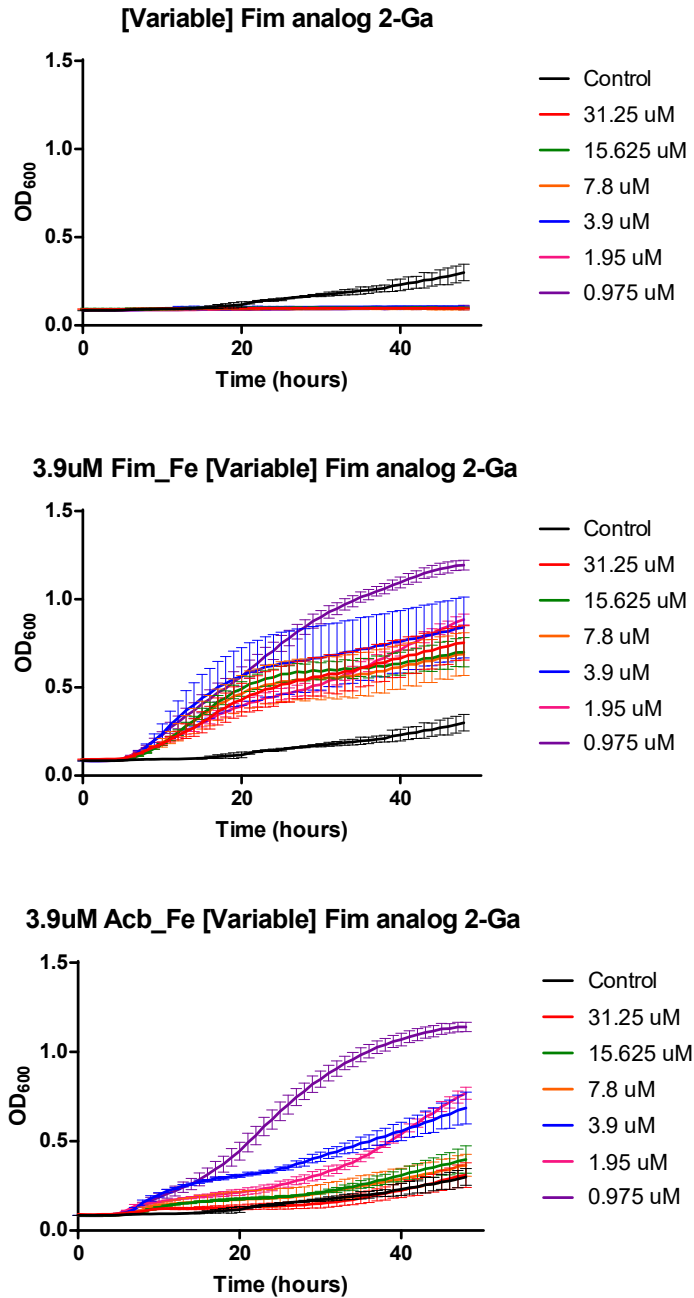


**Figure 7.8:** (a) Dose dependent growth inhibition by Fimsbactin analog 2-Ga complex (b) 3.9 $\mu$ M Fim-Fe and variable Fimsbactin analog 2-Ga complex (c) 3.9 $\mu$ M Acb-Fe and variable Fimsbactin analog 2-Ga complex .Line graphs depict the growth of *A. baumannii* ATCC 17978 determined by measuring the optical density at 600 nm (OD<sub>600</sub>) as a function of time. Error bars represent standard deviations from the mean for three independent trials.

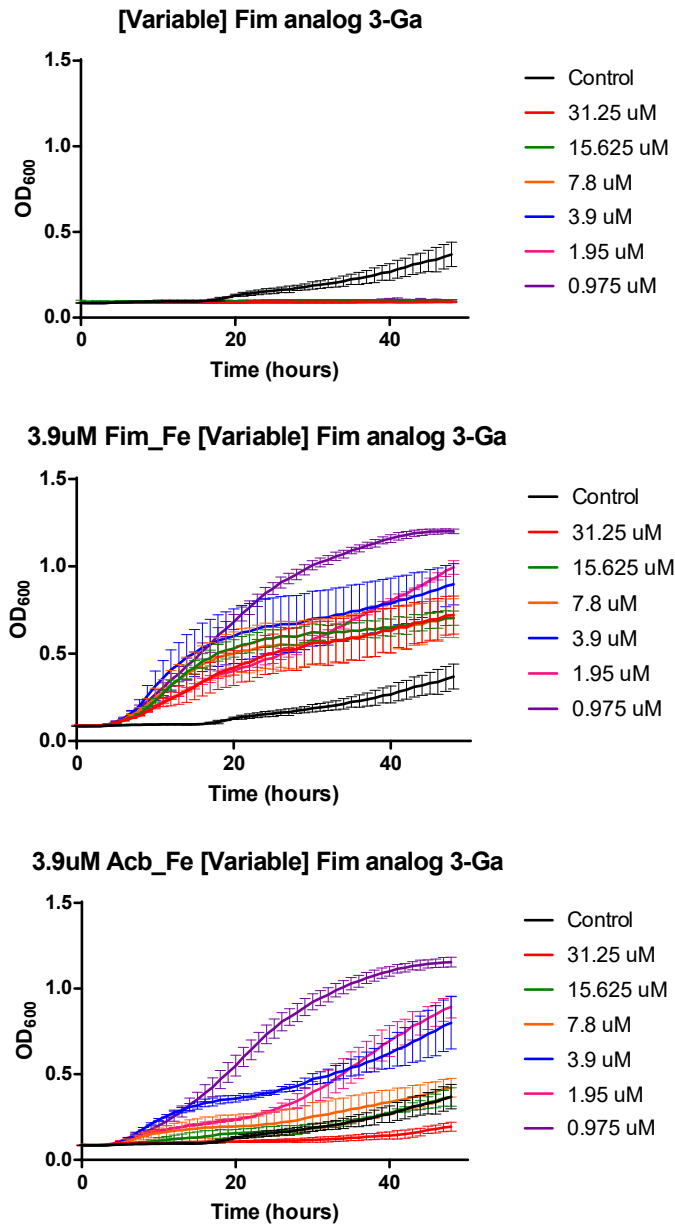


**Figure 7.9:** (a) Dose dependent growth inhibition by Fimsbactin analog 3-Ga complex (b) 3.9 $\mu$ M Fim-Fe and variable Fimsbactin analog 3-Ga complex (c) 3.9 $\mu$ M Acb-Fe and variable Fimsbactin analog 3-Ga complex .Line graphs depict the growth of *A. baumannii* ATCC 17978 determined by measuring the optical density at 600 nm ( $OD_{600}$ ) as a function of time. Error bars represent standard deviations from the mean for three independent trials.

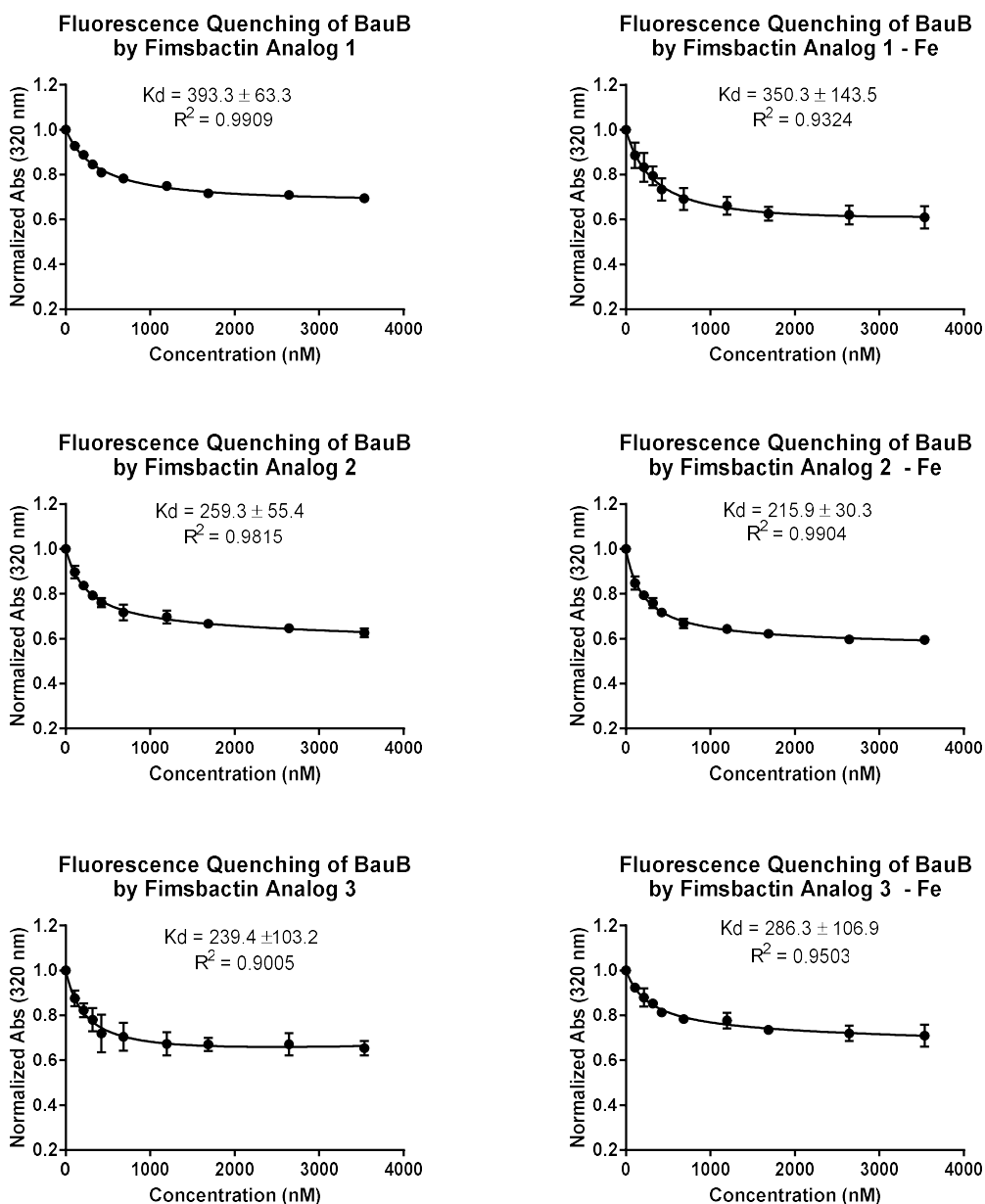


**Figure 7.10:** Fluorescence quenching by Fimsbactin analogs and their respective iron complex of *N*-His<sub>6</sub>-BauB. Graphs depict intrinsic tryptophan fluorescence quenching (y-axis;  $\lambda_{\text{excitation}} = 280$  nm;  $\lambda_{\text{emission}} = 340$  nm) of 400 nM *N*-His<sub>6</sub>-BauB in the presence of variable siderophore concentrations (x-axis). Apparent  $K_d$  values were calculated using a single-binding mode curve-fitting model in GraphPad Prism version 7.0b. Error bars represent standard deviations for two independent trials.

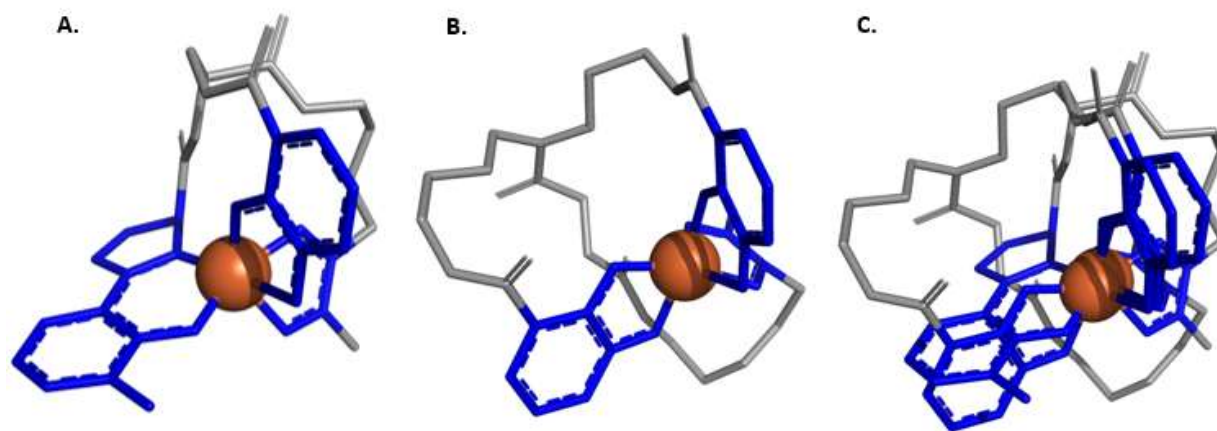


**Figure 7.11:** Structural comparison of FimFe and Fimsbactin analog 1 complexes. DFT calculated structures of the monoanionic (a) 1:1 [FimFe]<sup>-</sup> and (b) 1:1 [Fimsbactin analog 1-Fe]<sup>-</sup> complexes (c) Overlay of both structures highlighting similarity of geometry and placement of ligands.

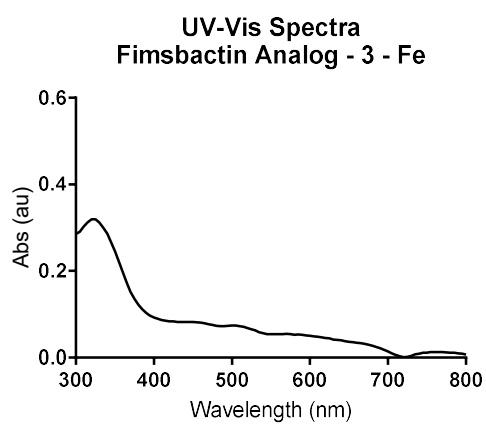
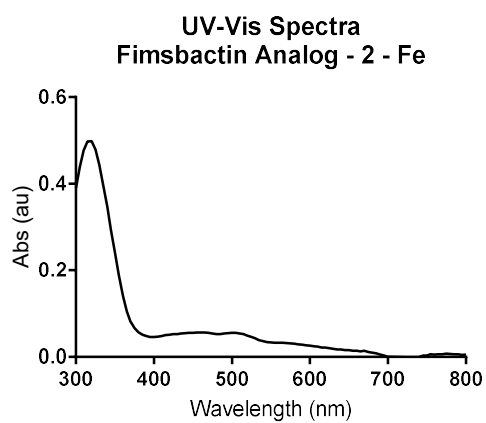
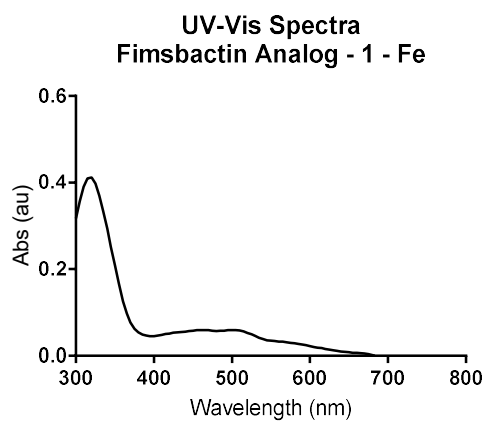


**Figure 7.12:** UV-Vis spectra of Fimsbactin analog 1, 2 and 3 iron complexes

## I. Compound Characterization

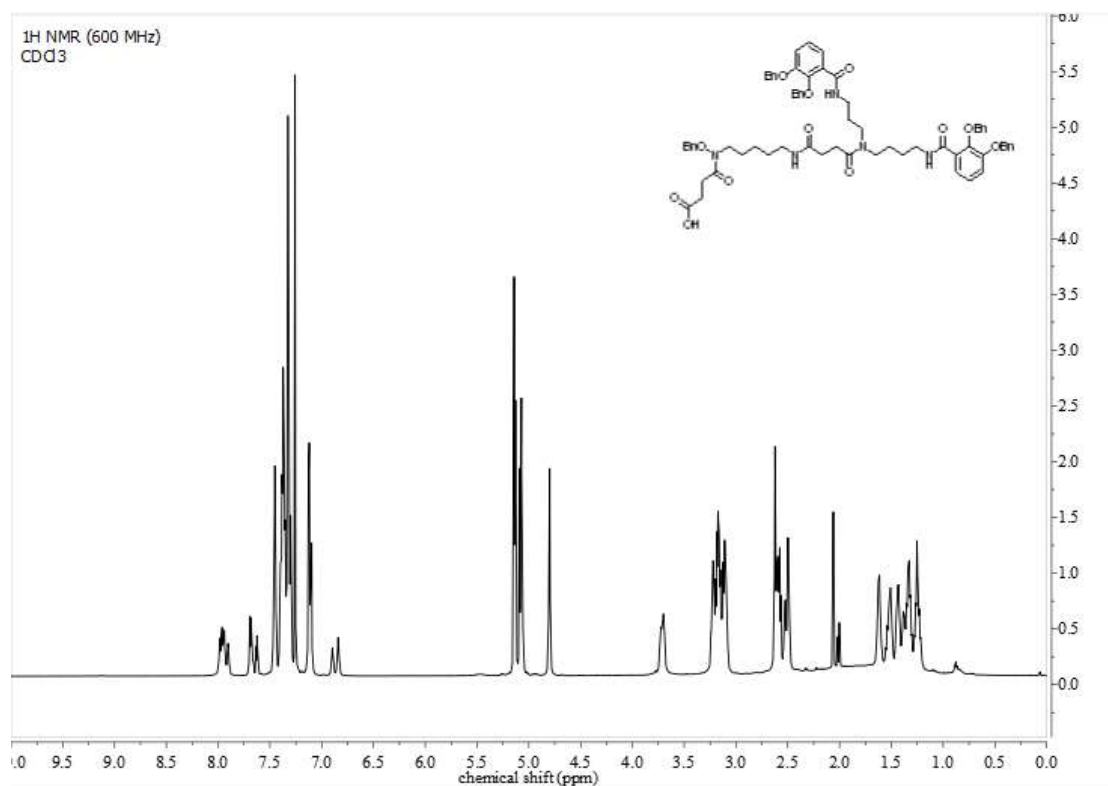


**Figure 7.13.** <sup>1</sup>H-NMR (600 MHz, CDCl<sub>3</sub>) spectrum of benzyl-protected compound 2, Fimsbactin Analog 1. The x-axis is chemical shift given in parts per million (ppm). The y-axis is arbitrary peak intensity.

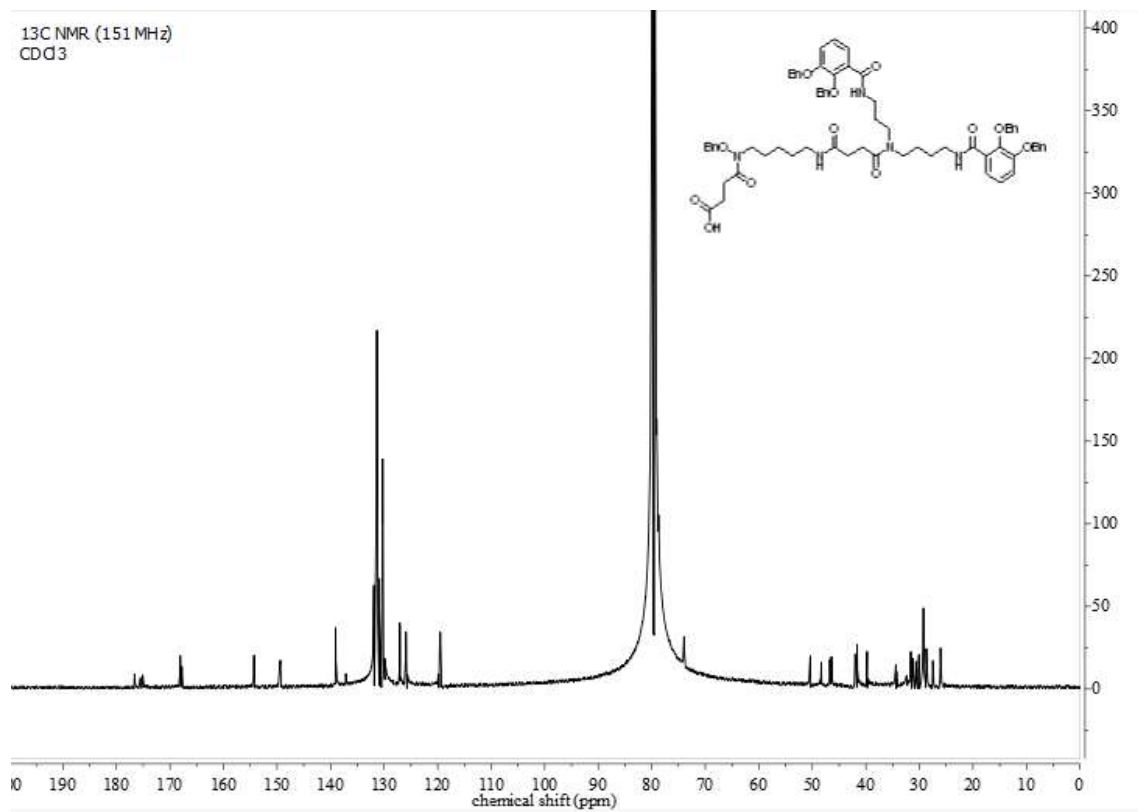


**Figure 7.14.** <sup>13</sup>C-NMR (151 MHz, CDCl<sub>3</sub>) spectrum of benzyl protected compound 2, Fimsbactin Analog 1. The x-axis is chemical shift given in parts per million (ppm). The y-axis is arbitrary peak intensity.



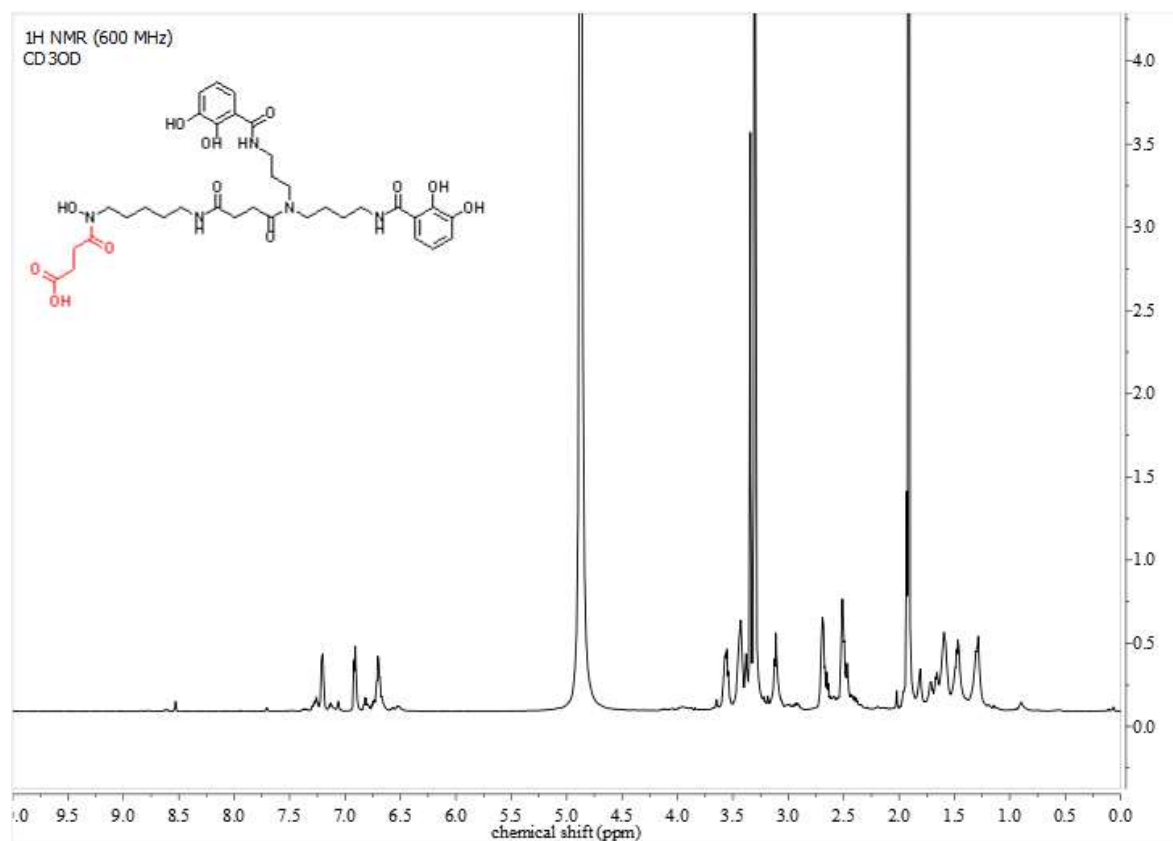


**Figure 7.15.** <sup>1</sup>H-NMR (600 MHz, CD<sub>3</sub>OD) spectrum of compound 2, Fimsbactin Analog 1. The x-axis is chemical shift given in parts per million (ppm). The y-axis is arbitrary peak intensity.

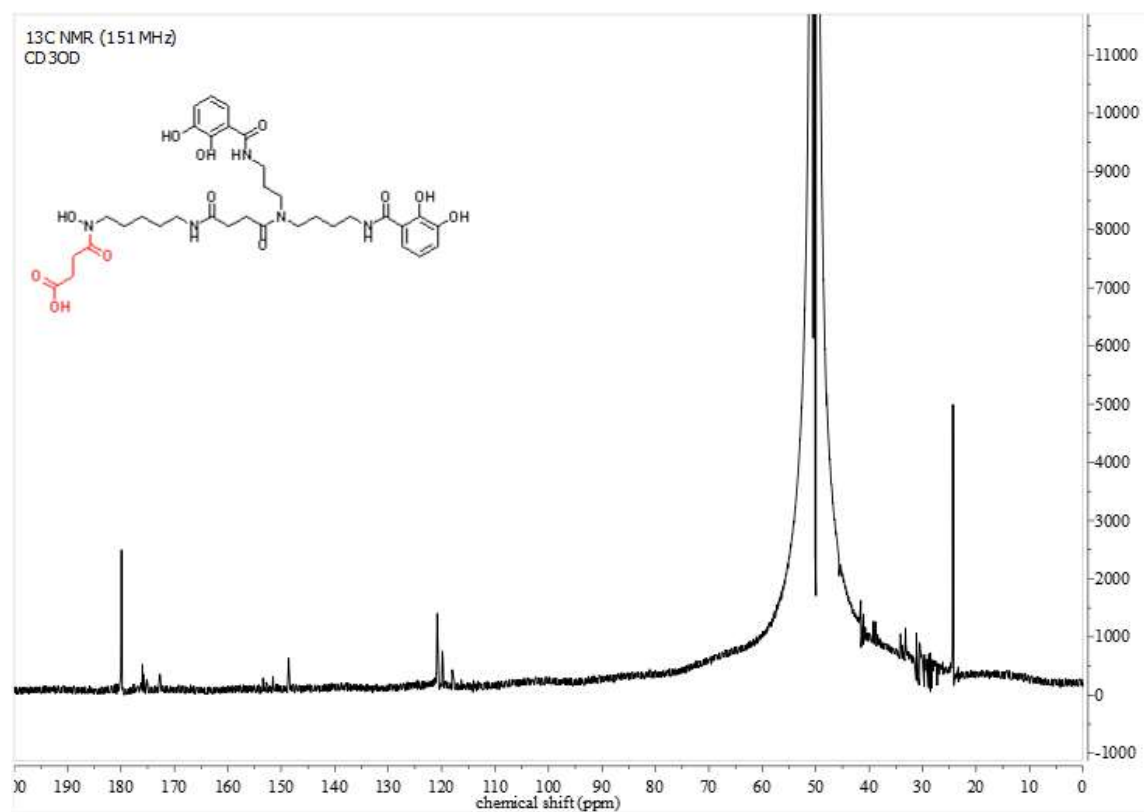


**Figure 7.16.** <sup>13</sup>C-NMR (151 MHz, CD<sub>3</sub>OD) spectrum of compound 2, Fimsbactin Analog 1. The x-axis is chemical shift given in parts per million (ppm). The y-axis is arbitrary peak intensity.

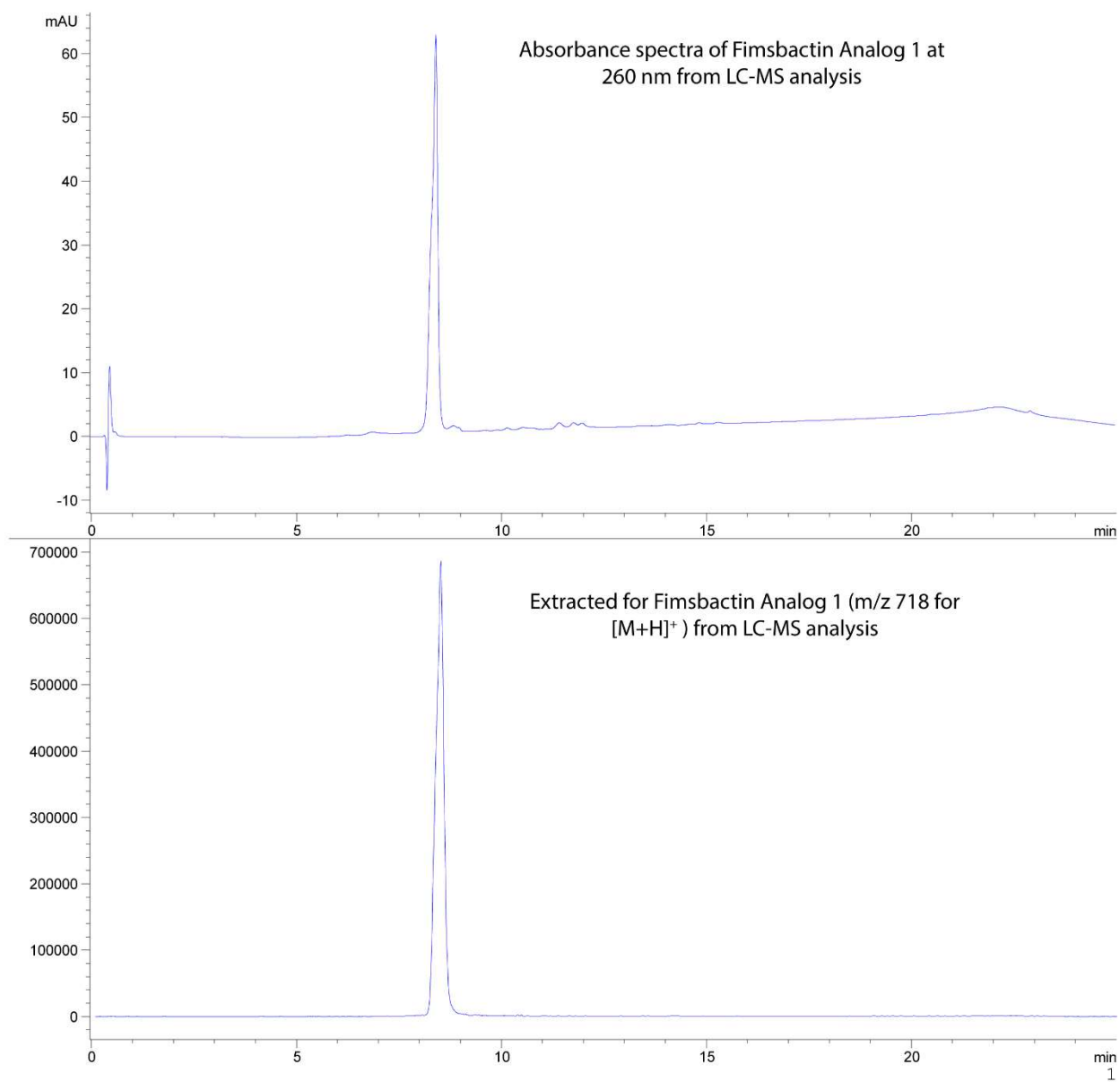


**Figure 7.17.** Diode array optical absorbance detection (DAD) and extracted ion chromatograms (EICs) for fimsbactin analog 1  $[M+H]^+$  ions from LCMS analysis using ESI ionization in positive ion mode. The x-axis represents retention time (min) for all chromatograms.

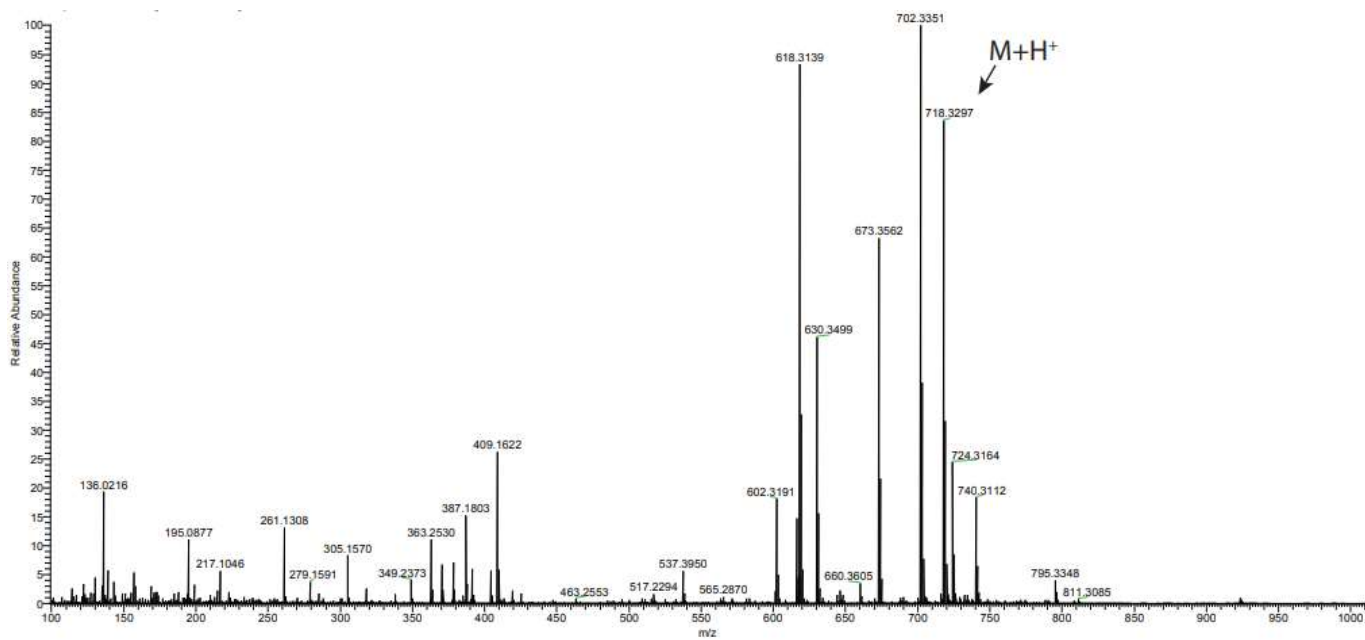


**Figure 7.18.** High-resolution ESI MS (positive ion mode) of Fimsbactin analog 1

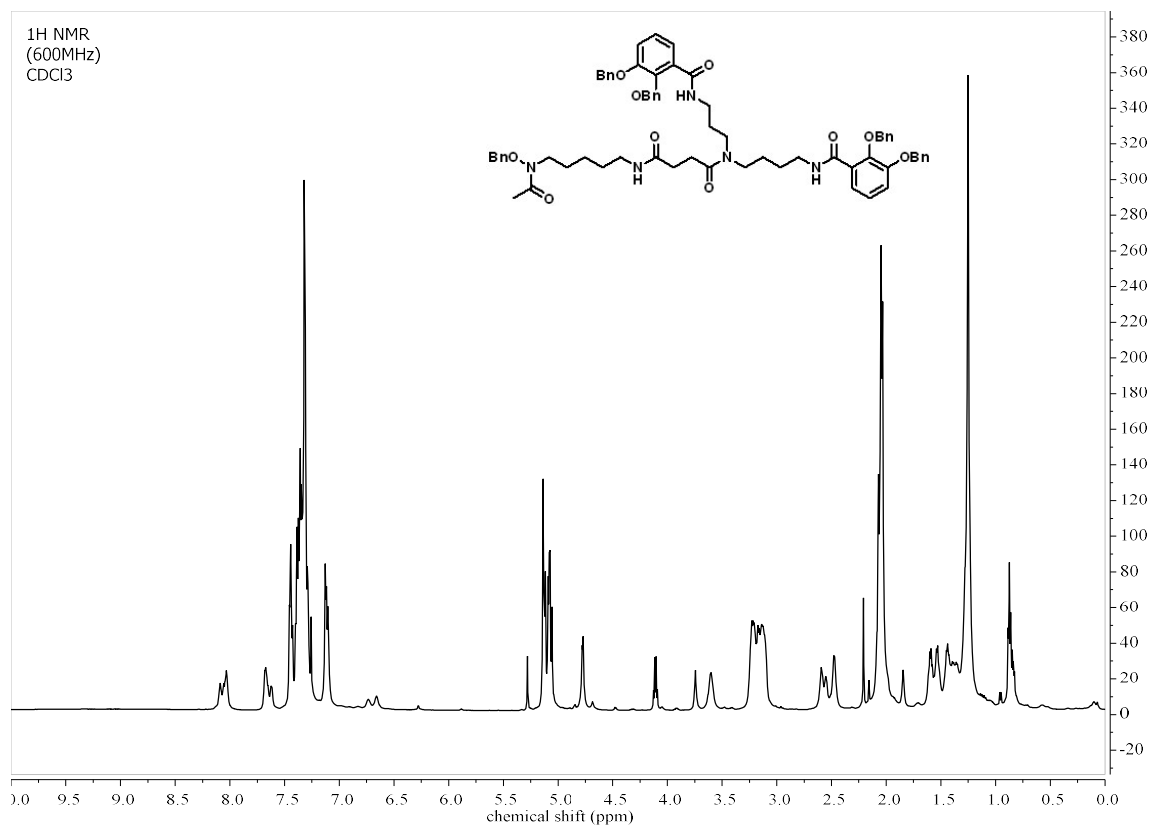


**Figure 7.19.** <sup>1</sup>H-NMR (600 MHz, CDCl<sub>3</sub>) spectrum of benzyl-protected compound 3, Fimsbactin Analog 2. The x-axis is chemical shift given in parts per million (ppm). The y-axis is arbitrary peak intensity.

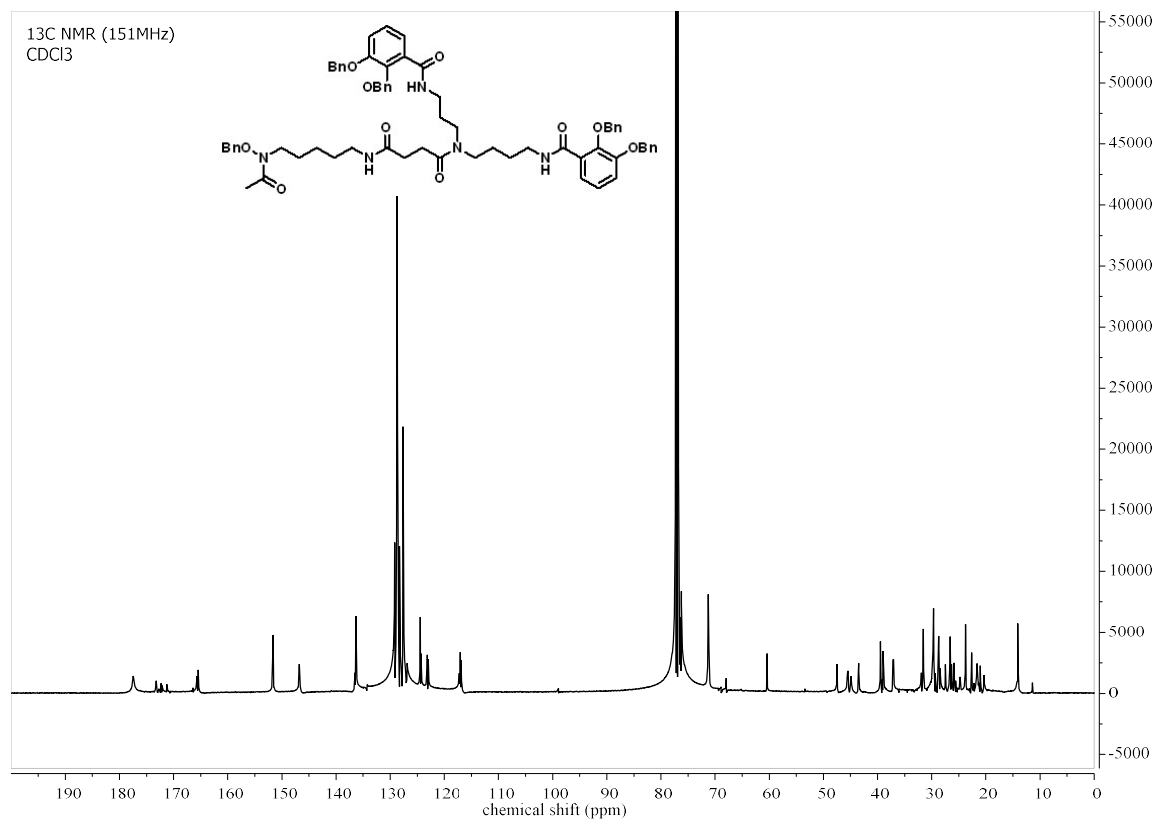


**Figure 7.20.** <sup>13</sup>C-NMR (151 MHz, CDCl<sub>3</sub>) spectrum of benzyl-protected compound 3, Fimsbactin Analog 2. The x-axis is chemical shift given in parts per million (ppm). The y-axis is arbitrary peak intensity.

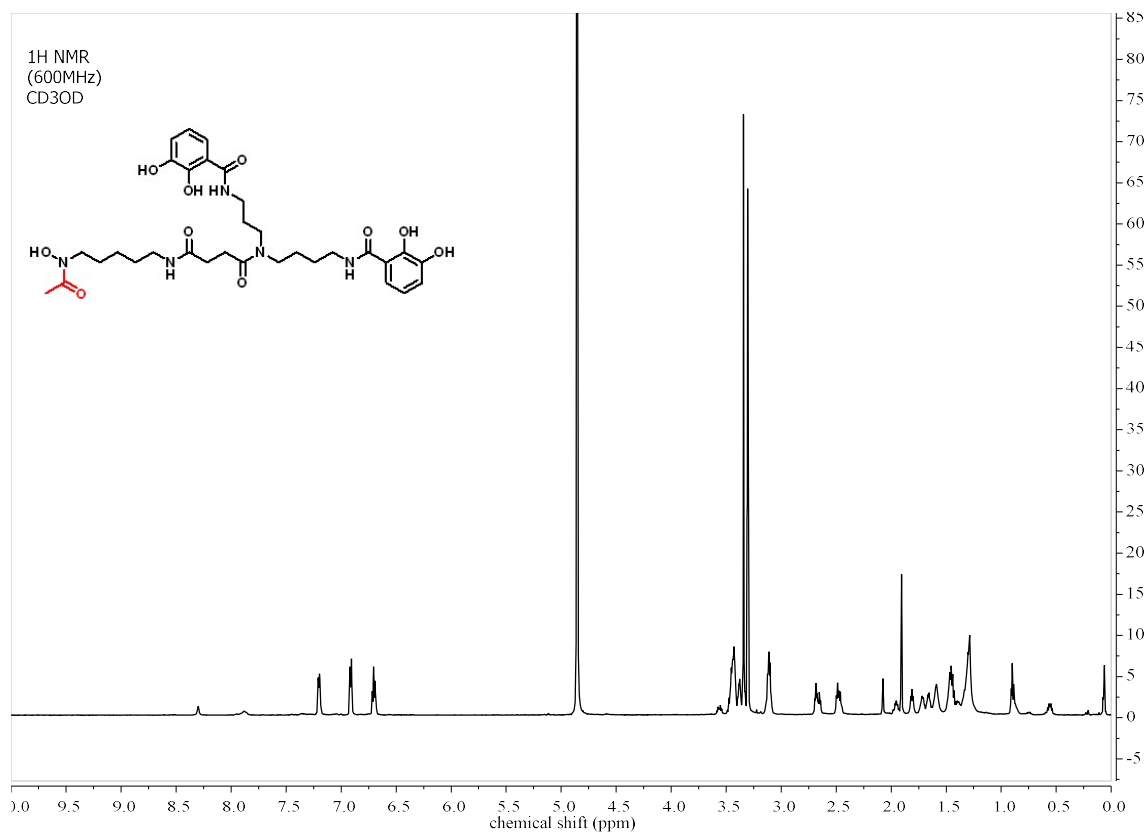


**Figure 7.21.** <sup>1</sup>H-NMR (600 MHz, CD<sub>3</sub>OD) spectrum of compound 3, Fimsbactin Analog 2. The x-axis is chemical shift given in parts per million (ppm). The y-axis is arbitrary peak intensity.

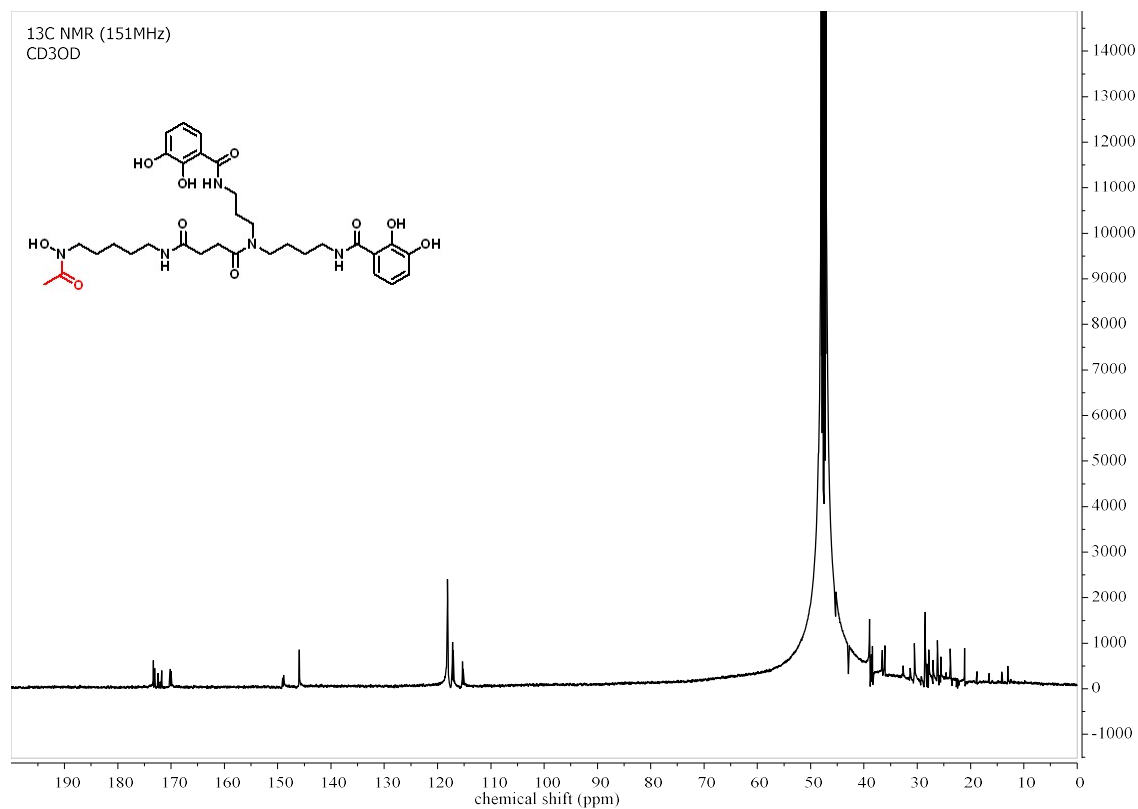


**Figure 7.22.** <sup>13</sup>C-NMR (151 MHz, CD<sub>3</sub>OD) spectrum of compound 3, Fimsbactin Analog 2. The x-axis is chemical shift given in parts per million (ppm). The y-axis is arbitrary peak intensity.



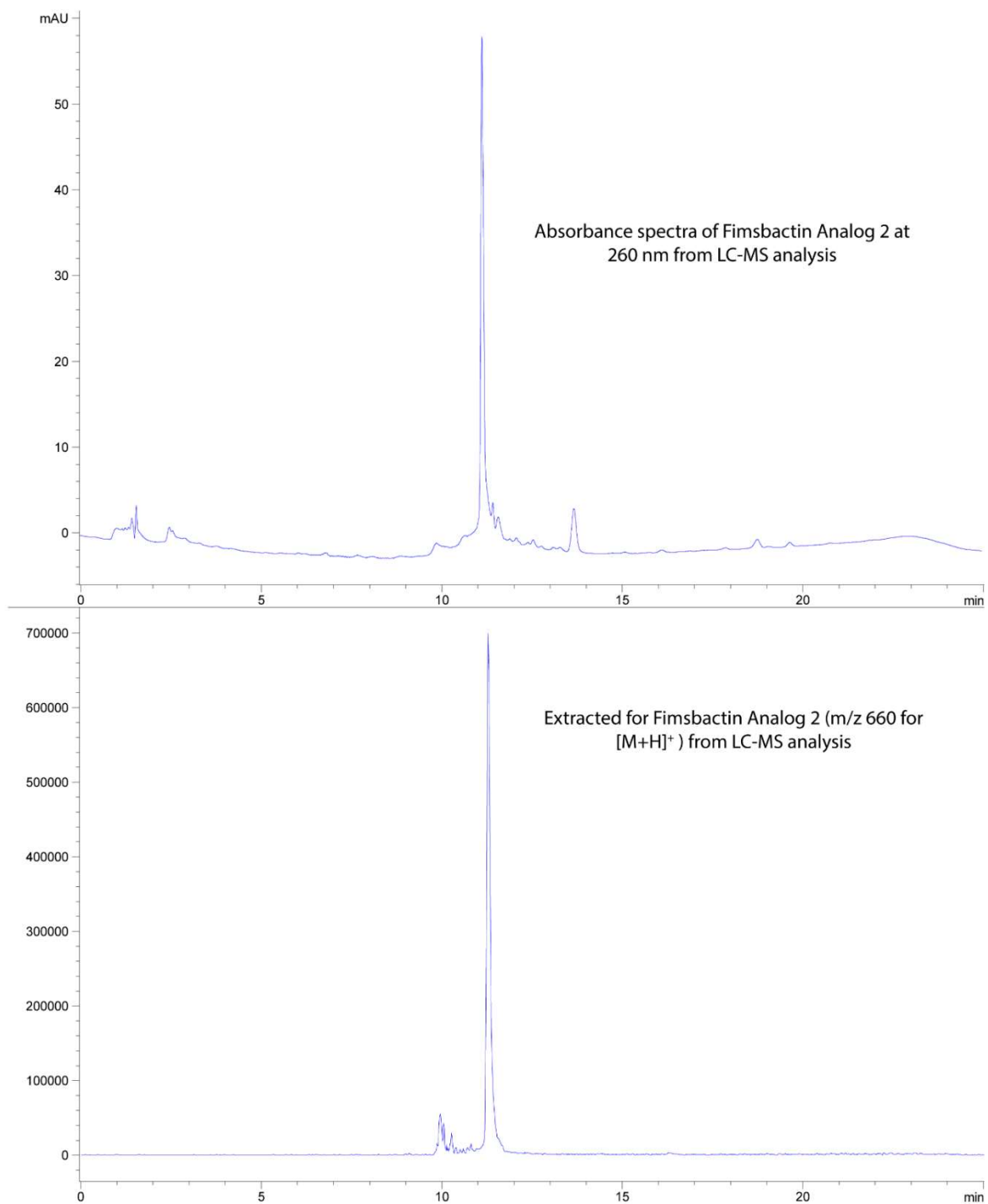


**Figure 7.23.** Diode array optical absorbance detection (DAD) and extracted ion chromatograms (EICs) for fimsbactin analog 2  $[M+H]^+$  ions from LCMS analysis using ESI ionization in positive ion mode. The x-axis represents retention time (min) for all chromatograms.

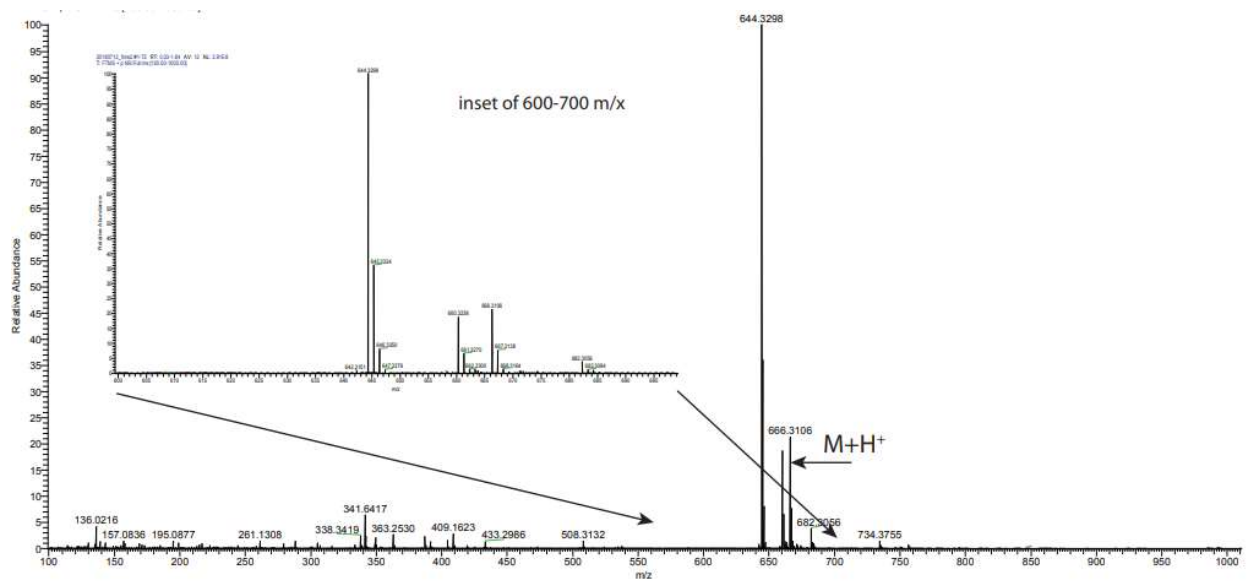


**Figure 7.24.** High-resolution ESI MS (positive ion mode) of Fimsbactin analog 2

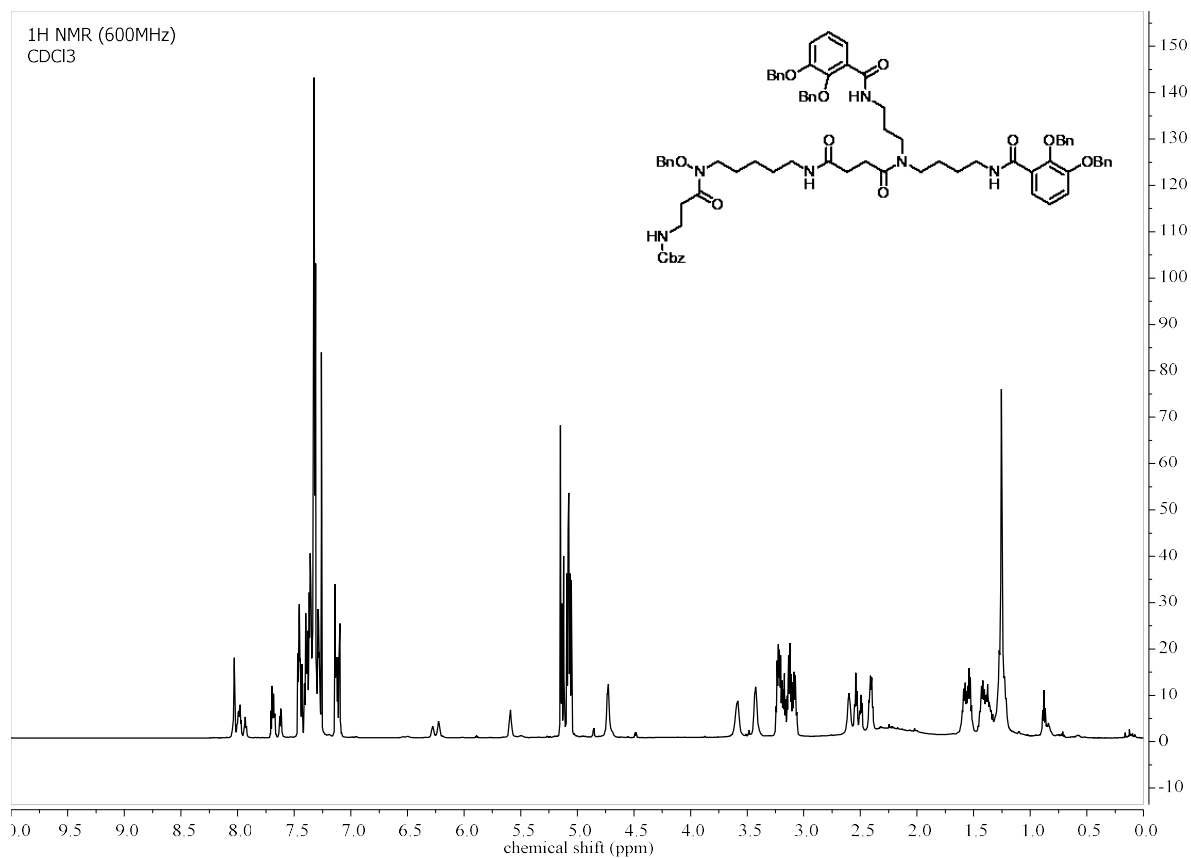


**Figure 7.25.** <sup>1</sup>H-NMR (600 MHz, CDCl<sub>3</sub>) spectrum of benzyl/cbz-protected compound 4, Fimsbactin Analog 3. The x-axis is chemical shift given in parts per million (ppm). The y-axis is arbitrary peak intensity.

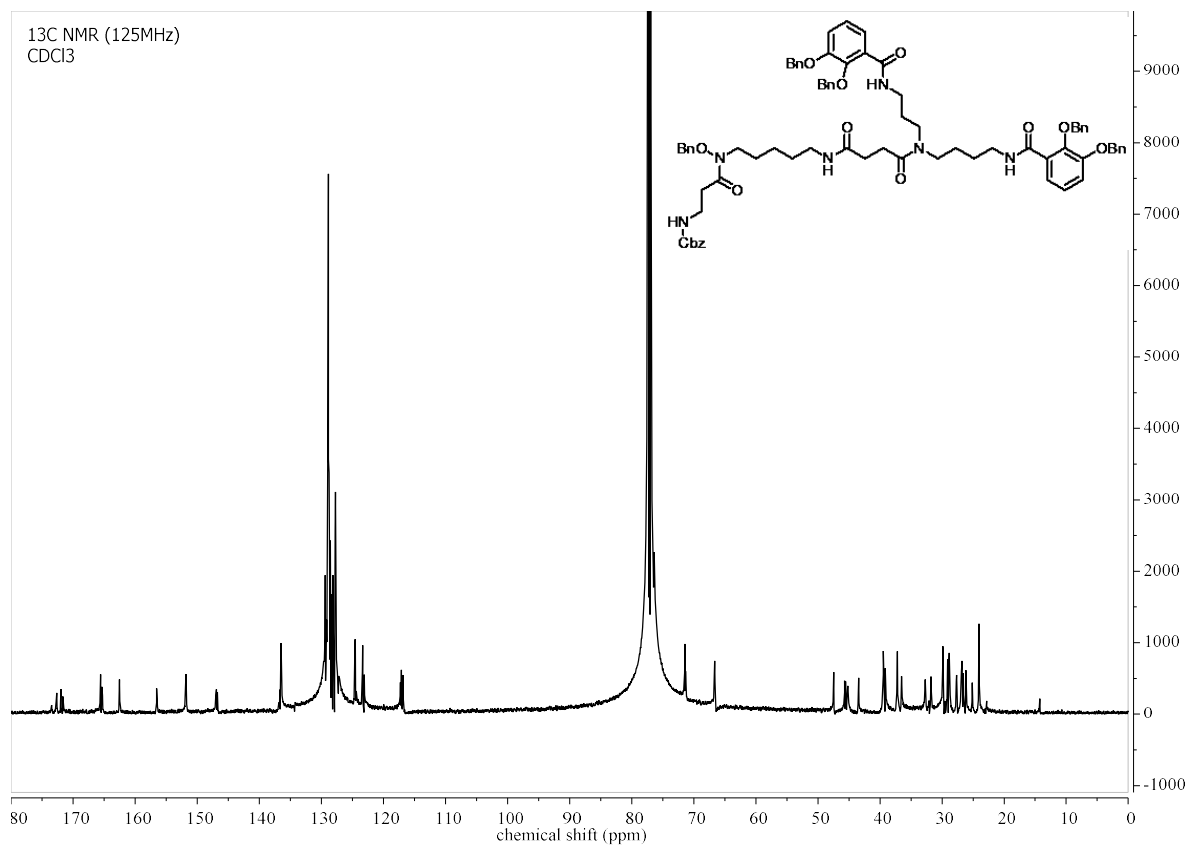


**Figure 7.26.**  $^{13}\text{C}$ -NMR (151 MHz,  $\text{CDCl}_3$ ) spectrum of benzyl/cbz-protected compound 4, Fimsbactin Analog 3. The x-axis is chemical shift given in parts per million (ppm). The y-axis is arbitrary peak intensity.

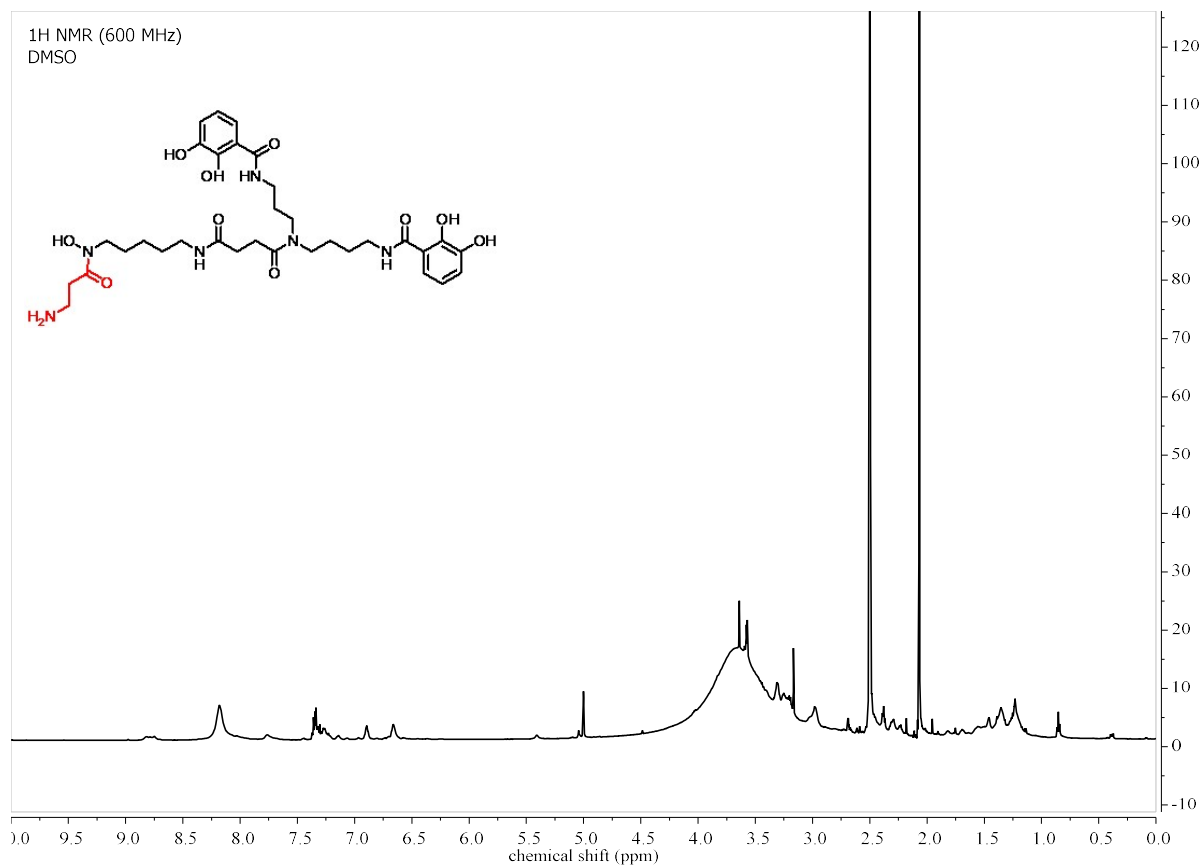


**Figure 7.27.** <sup>1</sup>H-NMR (600 MHz, DMSO-d<sub>6</sub>) spectrum of compound 4, Fimsbactin Analog 3. The x-axis is chemical shift given in parts per million (ppm). The y-axis is arbitrary peak intensity.

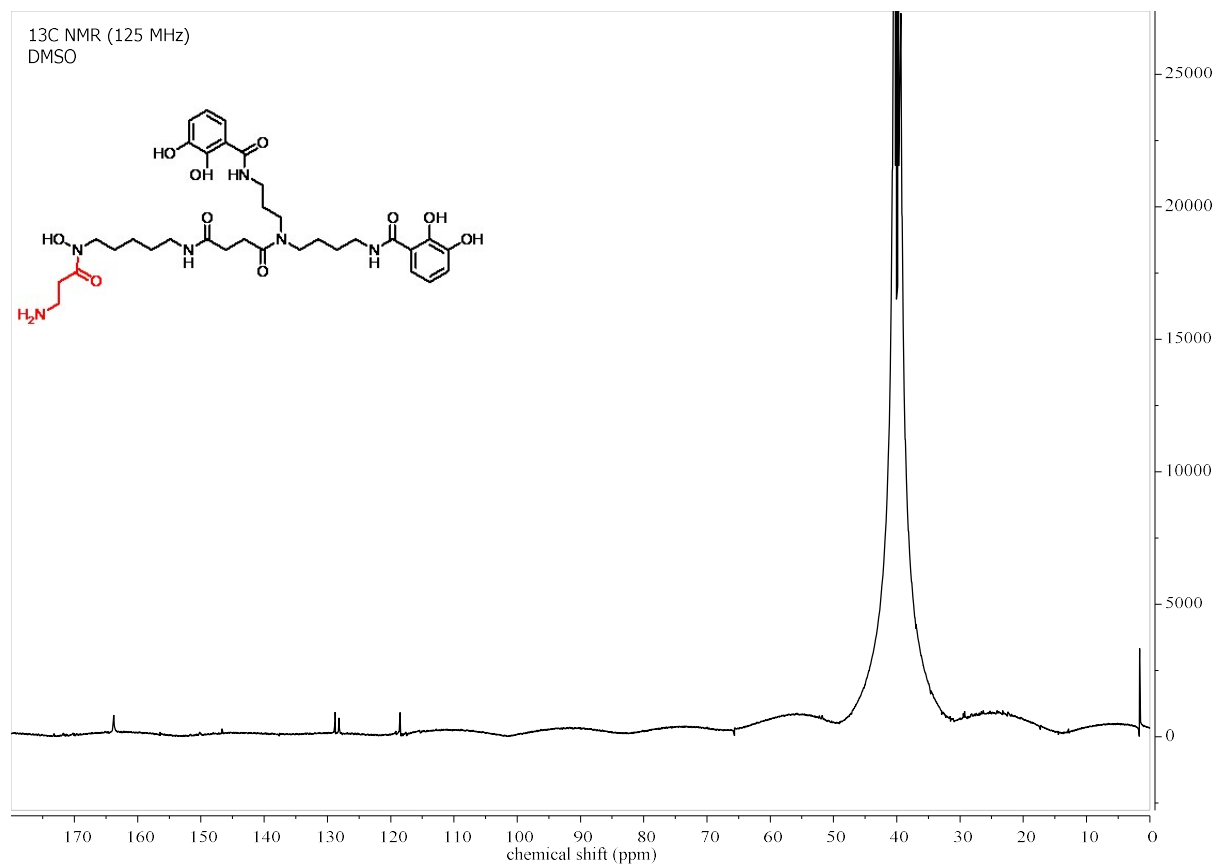


**Figure 7.28.**  $^{13}\text{C}$ -NMR (151 MHz,  $\text{DMSO-d}_6$ ) spectrum of compound 4, Fimsbactin Analog 3.

The x-axis is chemical shift given in parts per million (ppm). The y-axis is arbitrary peak intensity.

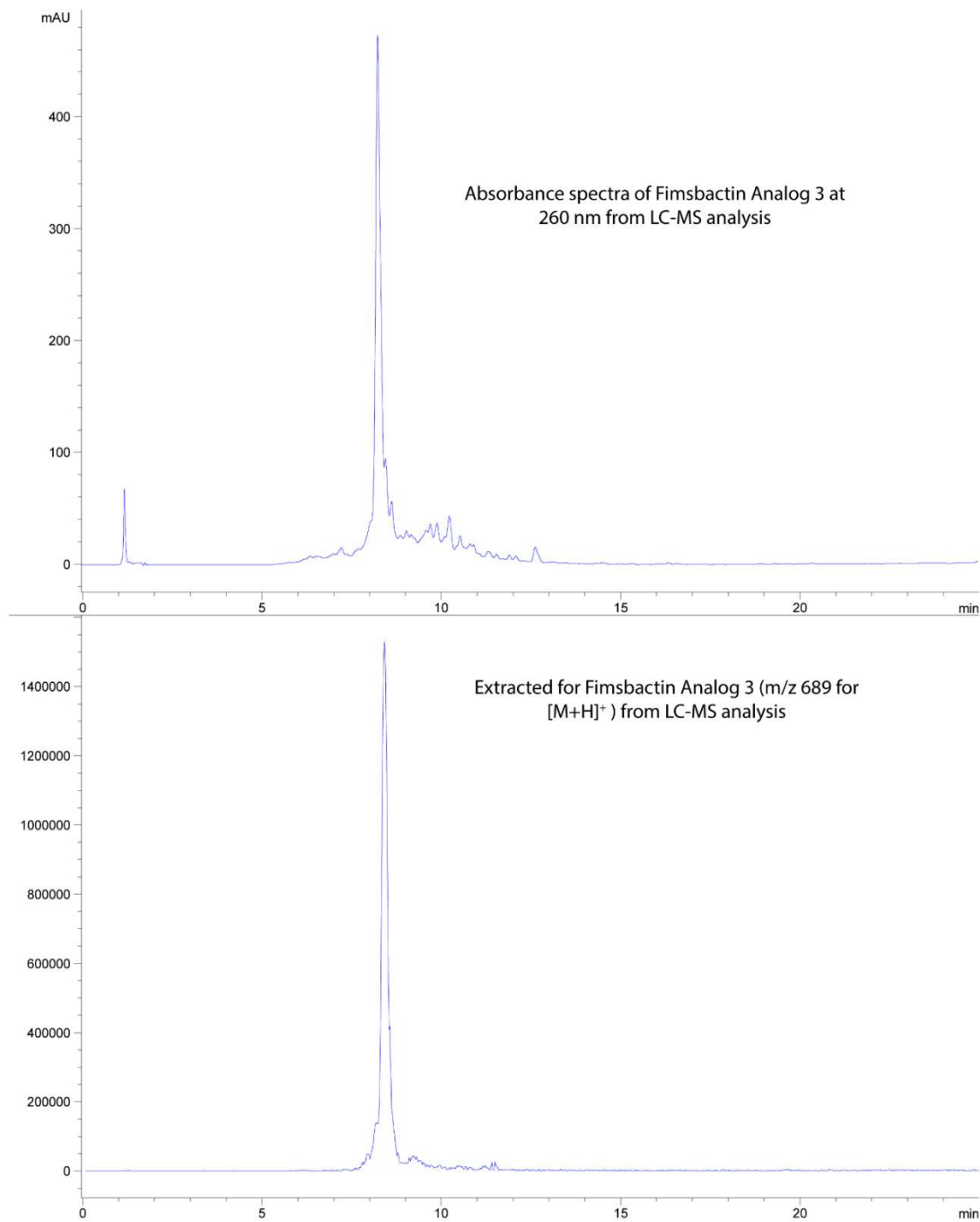


**Figure 7.29.** Diode array optical absorbance detection (DAD) and extracted ion chromatograms (EICs) for fimsbactin analog 3  $[M+H]^+$  ions from LCMS analysis using ESI ionization in positive ion mode. The x-axis represents retention time (min) for all chromatograms.

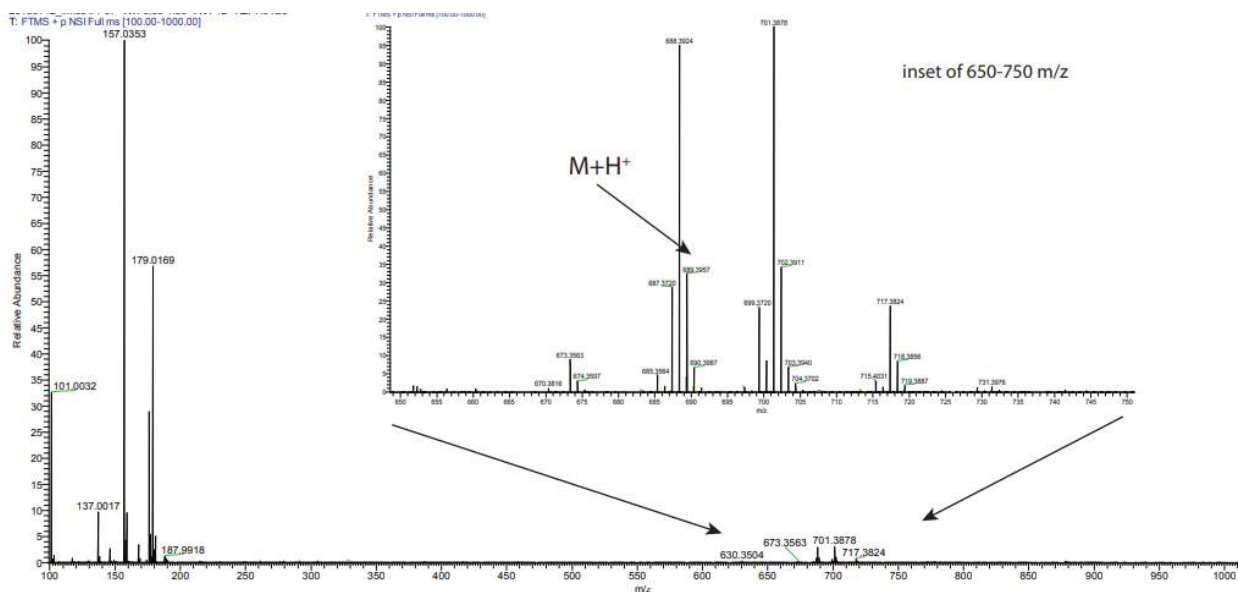


**Figure 7.30.** High-resolution ESI MS (positive ion mode) of Fimsbactin analog 3

## 7.8 References

- [1] Kaplan, M. (2014) The problem with gram-negative bacteria. <http://www.anapsid.org/gramnegative.html>
- [2] Wenciewicz, T. A., Miller, M. J. (2013) Biscatecholate-monohydroxamate mixed ligand siderophore-carbacephalosporin conjugates are selective sideromycin antibiotics that target *Acinetobacter baumannii*. *J. Med. Chem* 56(10), 4044-4052.
- [3] Business Wire. Shionogi to Present Data on Cefiderocol and Baloxavir Marboxil at IDWeek 2018. (2018) <https://www.businesswire.com/news/home/20180927005497/en/Shionogi-Present-Data-Cefiderocol-Baloxavir-Marboxil-IDWeek>
- [4] Yamamoto, S., Okujo, N., and Sakakibara, Y. (1994) Isolation and structure elucidation of acinetobactin, a novel siderophore from *Acinetobacter baumannii*, *Archives of microbiology* 162, 249-254.
- [5] Proschak, A., Lubuta, P., Grun, P., Lohr, F., Wilharm, G., De Berardinis, V., and Bode, H. B. (2013) Structure and biosynthesis of fimsbactins A-F, siderophores from *Acinetobacter*



- baumannii and Acinetobacter baylyi, *Chembiochem : a European journal of chemical biology* 14, 633-638.
- [6] Penwell, W. F., DeGrace, N., Tentarelli, S., Gauthier, L., Gilbert, C. M., Arivett, B. A., Miller, A. A., Durand-Reville, T. F., Joubran, C., and Actis, L. A. (2015) Discovery and Characterization of New Hydroxamate Siderophores, Baumannoferrin A and B, produced by Acinetobacter baumannii, *Chembiochem* 16, 1896-1904.
- [7] Ji, C., Miller, M. J. (2015) Siderophore-fluoroquinolone conjugates containing potential reduction-triggered linkers for drug release: synthesis and antibacterial activity. *Biometals* 28(3), 541-551.
- [8] Ghosh, M., Lin, Y. M., Miller, P. A., Mollmann, U., Boggess, W.C., Miller, M. J. (2018) Siderophore Conjugates of Daptomycin are Potent Inhibitors of Carbapenem Resistant Strains of Acinetobacter baumannii. *ACS Infect Dis* 4, 1529-1535.
- [9] Ghosh, M., Miller, M. J. (1996) Synthesis and In Vitro Antibacterial Activity of Spermidine-Based Mixed Catechol- and Hydroxamate-Containing Siderophore-Vancomycin Conjugates. *Bioorganic & Medicinal Chemistry* 4(1), 43-48.
- [10] Endicott, N. P., Lee, E., and Wencewicz, T. A. (2017) Structural Basis for Xenosiderophore Utilization by the Human Pathogen Staphylococcus aureus, *ACS infectious diseases* 3, 542-553.
- [11] Bohac, T. J., Fang, L., Giblin, D., Wencewicz, T. A. Fimsbactin and Acinetobactin Compete for the Periplasmic Siderophore Binding Protein BauB in Pathogenic Acinetobacter baumannii. *ACS Chemical Biology manuscript accepted. DOI: 10.1021/acsembio.8b01051*

- [12] Bailey, D. C., Bohac, T. J., Shapiro, J. A., Giblin, D. E., Wencewicz, T. A., and Gulick, A. M. (2018) Crystal Structure of the Siderophore Binding Protein BauB Bound to an Unusual 2:1 Complex Between Acinetobactin and Ferric Iron, *Biochemistry*.
- [13] Shapiro, J. A., and Wencewicz, T. A. (2016) Acinetobactin Isomerization Enables Adaptive Iron Acquisition in *Acinetobacter baumannii* through pH-Triggered Siderophore Swapping, *ACS infectious diseases* 2, 157-168.
- [14] Shapiro, J. A., and Wencewicz, T. A. (2017) Structure-function studies of acinetobactin analogs, *Metallomics* 9, 463-470.
- [15] Bohac, T. J., Shapiro, J. A., and Wencewicz, T. A. (2017) Rigid Oxazole Acinetobactin Analog Blocks Siderophore Cycling in *Acinetobacter baumannii*, *ACS infectious diseases* 3, 802-806.
- [16] Shephard, M. J., and Paddon-Row, M. N. (1995) Gas Phase Structure of the Bicyclo[2.2.1]heptane (Norbornane) Cation Radical: A Combined ab Initio MO and Density Functional Study, *The Journal of Physical Chemistry* 99, 3101-3108.
- [17] Zhao, Y., and Truhlar, D. G. (2008) Density functionals with broad applicability in chemistry, *Accounts of chemical research* 41, 157-167.
- [18] Pople, J. A., Scott, A. P., Wong, M. W., and Radom, L. (1993) Scaling Factors for Obtaining Fundamental Vibrational Frequencies and Zero-Point Energies from HF/6-31G\* and MP2/6-31G\* Harmonic Frequencies, *Israel Journal of Chemistry* 33, 345-350.
- [19] Cossi, M., Rega, N., Scalmani, G., and Barone, V. (2003) Energies, structures, and electronic properties of molecules in solution with the C-PCM solvation model, *Journal of Computational Chemistry* 24, 669-681.

- [20] Rydberg, P., and Olsen, L. (2009) The Accuracy of Geometries for Iron Porphyrin Complexes from Density Functional Theory, *The Journal of Physical Chemistry A* 113, 11949-11953.
- [21] Ansbacher, T., Srivastava, H. K., Martin, J. M., and Shurki, A. (2010) Can DFT methods correctly and efficiently predict the coordination number of copper(I) complexes? A case study, *J Comput Chem* 31, 75-83.
- [22] Weigend, F., and Ahlrichs, R. (2005) Balanced basis sets of split valence, triple zeta valence and quadruple zeta valence quality for H to Rn: Design and assessment of accuracy, *Physical Chemistry Chemical Physics* 7, 3297-3305.

## **Chapter 8: Conclusions and Future Directions**

## 8.1 Preface

This chapter was written by T. Bohac. Initial work towards some of the future directions has been conducted by TJB, VSB and LF.

## 8.2 Summary of Dissertation

Taken collectively, this dissertation aims to further expand the fundamental knowledge of pathogenic virulence factors in the hopes of combating the rise in anti-microbial resistance – particularly as it relates to the multi-drug resistant pathogen *A. baumannii*. This dissertation focuses on nutrient acquisition, metal in particular, via small secondary metabolites called siderophores. *A. baumannii* is known to synthesize three classes of siderophores, acinetobactin, Fimsbactin and baumannoferrin. This dissertation is two-part in that it begins with furthering the current knowledge of the natural system and ends with applying this knowledge to the design and synthesis of antimicrobial compounds for potential therapeutic applications.

Chapter one of this dissertation provides an in-depth discussion of iron acquisition in pathogens, as well as an overall of the current knowledge of the siderophores of *A. baumannii*. Chapter two expands upon the knowledge of siderophore acinetobactin, as we discuss a crystal structure of  $\text{Acb}_2\text{Fe}$  bound to periplasmic siderophore binding protein, BauB. We identify key binding residues and interactions and perform fluorescence quenching assays with a panel of acinetobactin and pre-acinetobactin analogs to further probe these key binding interactions.

Chapter three discusses the isolation and characterization of siderophore Fimsbactin A. By performing siderophore competition studies between natural acinetobactin and Fimsbactin A, we were surprised to see an inhibitory effect at high concentrations of Fimsbactin A, demonstrating the importance of concentration and balance in the growth-promoting siderophore cocktail.

Moreover, studies on protein binding and ligand displacement showed that Fimsbactin A can compete with acinetobactin for siderophore transport protein BauB. We proposed that this finding was important in understanding the role of siderophore cocktail biosynthesis and production, as strains containing the Fims biosynthetic gene cluster maintain low concentrations of Fims in infectious conditions. Furthermore, many strains of *A. baumannii* do not contain the Fimsbactin biosynthetic gene cluster but produce high quantities of acinetobactin, thus eliminating any deleterious competition caused by dual production.

Chapter four attempts to examine the seemingly redundancy of multiple siderophores in *A. baumannii*, we isolated and characterized Fimsbactin F and explored additional siderophore combination studies. In addition, we investigated metal preference among natural and synthetic siderophores to explore their role in metal homeostasis.

Chapter five and six explore the ability to induce subtle structural changes through oxidation and aromatization of cyclic moieties to transform a growth promoting siderophore, acinetobactin, into a growth inhibitor “siderophore-like” analog, oxidized acinetobactin. We show iron binding to be crucial for inhibition, and findings support that inhibition occurs through the disruption of the siderophore transport pathway. We highlighted OxPreAcb effectiveness against a panel of CDC multi-drug resistant *A. baumannii* clinical isolates, and concurrent mammalian cytotoxicity studies showed that OxPreAcb was non-cytotoxic, even at high concentrations, making it an ideal candidate for further development in *in vivo* infection models.

Finally, studies presented in Chapter seven examined a currently used Fimsbactin structural mimic and generated 2 new related analogs. We hypothesized that these mimics would serve as effective vehicles for antibiotic drug delivery, through Trojan horse siderophore-antibiotic conjugates, and studies were designed to validate the effectiveness of the structural analogs to

behave in a similar manner to the natural system. In this regard, we were able to confirm that the three Fimsbactin mimics serve as both structural and functional Fimsbactin mimics and that net charge has little to no effect on the ability of each mimic to function as a siderophore. Taken collectively, this work highlights the ability to simplify structurally complex siderophore systems, while maintaining biological viability, and serves as a reference for further development of siderophore probe molecules—particularly in regards to Trojan horse antibiotic delivery.

### 8.3 Future Directions

While this dissertation extended previous work, it also laid the foundation for future work. While there are many many ideas and future directions that stem from the work discussed in this dissertation, herein I will highlight a few areas that I view as interesting and instrumental in the future of this project.

#### *Baumannoferrin synthesis and evaluation*

In order to truly understand the interworking of a siderophore cocktail in *A. baumannii*, the third siderophore, the baumannoferrins, must be synthesized or isolated. While no total synthesis of the baumannoferrins has been reported, synthesis of siderophores containing fragments similar to the baumannoferrins have been reported in the synthesis of staphyloferrin B by Nolan (2015)<sup>1</sup> and in the synthesis of acinetoferrin by Phanstiel (1998).<sup>2</sup> Using similar methods developed in these two works, a proposed total synthesis of the baumannoferrins could be accomplished through the route seen in **Figure 8.1**.

The proposed synthesis commences with isolation of benzyl ester **4** in three steps starting from (*S*)-malic acid **1**, as previously reported by Nolan (2015).<sup>1</sup> Dioxolanone **2** is afforded through the stereoselective acetyl protection of malic acid **1** with trimethylacetaldehyde. Allylation by

allyl bromide, with lithium hexamethyldisilazide (LiHMDS) as facilitating base, provides **3** in moderate yield. Subsequent ring-opening transesterification affords the resulting acid **4**. In turn, amine **7** could be generated from the EDC-mediated coupling of carboxylic acid **5**, derived from 2-oxo-pentanedioic acid.<sup>3</sup> and amino-acid derivative **6**, derived from Bn-protected Boc-protected of 2, 4-diamino-butyric acid.

Coupling of amine **7** with acid **4**, using EDC and Hunig's base, would provide amide **8**. Oxidative cleavage of the terminal olefin of **8** with ruthenium (III) chloride in the presence of sodium periodate would afford terminal carboxylic acid **9**. EDC-mediated coupling of acid **9** with compound *tert*-butyl (3-aminopropyl)(benzyloxy)carbamate **10**, in the presence of facilitating base (N,N-diisopropylethylamine, DIPEA), would generate compound **11**. Subsequent Pd-catalyzed hydrogenation and treatment with TFA would provide hydroxamine **12**. The diversification of baumannoferrin analogs can be achieved at in the final step of the synthesis, where various acid chlorides can be coupled with hydroxamine **12** to provide the corresponding hydroxamides. Through exploration of derivatives, necessity of a double bond in the structure could be probed or additional degrees of unsaturations can be installed to evaluate the importance of tail structural rigidity. Additionally, since it has been hypothesized that the baumannoferrins are able to integrate with the lipid membrane and experience membrane "flip-flop", based upon a "flip-flop" motion observed by structurally similar siderophore acinetoferrin (**Figure 8.2**), we can identify the optimal chain length of the hydrophobic lipid chain through analog synthesis.<sup>4</sup> In the case of the synthesis of baumannoferrin A (**13**), hydroxamine **12** can be treated with 2-decenoyl chloride (derived from 2-decenoic acid) with facilitating base to afford the title product (**13**).

With the baumannoferrins in hand, we could explore structure activity relationships as aforementioned. Further, we could perform biological evaluation of the baumannoferrins through



growth assays, metal binding and affinity studies and protein binding assay. Moreover, with pre-acinetobactin, acintobactin and Fimsbactin already isolated/synthesized, combination studies with all three siderophore classes of *A. baumannii* would allow for a more holistic representation of the natural system.

### ***Further derivatization of OxPreAcb and Click Chemistry***

In Chapters 5 and 6, the synthesis and evaluation of oxidized pre-acinetobactin (OxPreAcb) and analog was discussed in depth. With the strong inhibitory nature of this lead compound, further evaluation and exploration of this compound is merited. While 8 structural analogs of OxPreAcb have been synthesized and evaluated, discussed in Chapter 6, further diversification and SAR of OxPreAcb can be explored around the right hand of the molecule with changes to the imidazole tail (**Figure 8.3**), as this position was seen to be non-crucial for iron binding nor growth inhibition. Further diversification can be explored at the oxazole ring system (**Figure 8.3**), to date no SAR around this system has been explored.

While we have seen that OxPreAcb can interact with BauB and the siderophore transport pathway, further exploration of the mechanism of action of this molecule is desirable. One analog of OxPreAcb that can allow for vast diversification and serve many function is an OxPreAcb alkyne with the alkyne moiety on the right hand side of the molecule in place of the imidazole ring (**Figure 8.4**). This alkyne moiety then can undergo click chemistry with different azide molecules, resulting in formation of a triazole moiety along with attachment of different groups as seen in **Figure 8.4**. One route can use click chemistry with azide-antibiotic groups to observe where the OxPreAcb molecule reaches inside the cell, as well as to observe the inhibitor-antibiotic effect on inhibition. As discussed in Chapter 7, work by many, including Wencewecz et al., highlighted the utility of employing siderophore-antibiotic conjugates as a means of Trojan horse drug delivery.<sup>5</sup>

While a siderophore is innately growth promoting, siderophore-antibiotic conjugates have been seen to reach MIC's as low as 0.2  $\mu$ M against *A. baumannii*<sup>6</sup>; since OxPreAcb in itself is inhibitory, OxPreAcb-antibiotic conjugates serve as an attractive target molecule. Further, following work by Wencewicz et al, through attachment of beta-lactams antibiotics (penicillin binding protein target – periplasm) and fluoroquinolones antibiotics (DNA gyrase target – cytoplasm), we can investigate where the OxPreAcb molecule reaches in the cell based upon MIC values and effectiveness of these two conjugates.<sup>5</sup> In the same vein, click chemistry between the OxPreAcb-alkyne and fluorophore-azides can allow for imaging and cellular localization studies and possible identification of the ultimate intracellular location of the OxPreAcb-fluorophore conjugate.

While we have evidence that OxPreAcb interacts with periplasmic siderophore binding protein, BauB, we can use the OxPreAcb-alkyne molecule to further probe the interactions of OxPreAcb on the protein level. Through bacteria feeding studies, incubation allows the OxPreAcb-alkyne to interact with target proteins, which, after cell lysis and click conjugation with an affinity tag, could be isolated and characterized through MS-MS proteomics.

We have previously showed that OxPreAcb binds to iron in a 2:1 stoichiometry.<sup>7</sup> Synthetically derived OxPreAcb dimers, using click chemistry between the OxPreAcb-alkyne molecule and an OxPreAcb-azide molecule, serve as interesting target compounds. These dimers can be synthesized of various lengths, as well as of various forms of connectivity (head to head, tail to head, etc.). Subsequent iron binding and metal titration studies with the generated dimer library would allow for the determination of metal-ligand stoichiometry—in hopes of identifying a candidate which binds iron in a 1:1 ligand-metal conformation. Such a system would decrease the entropy cost associated with iron binding and enhance the ability of the molecule to outcompete

the natural acinetobactin system. Outcompeting the natural siderophore systems would then provide a means to more potently inhibit the growth of MDR *A. baumannii*.

### ***Extending oxidation to other known siderophores with oxidizable groups***

Previous work by the Henderson group highlighted the ability of nature to synthesize an antimicrobial secondary metabolite, escherichelin, which is structurally similar to a known growth promoting siderophore, pyrochelin.<sup>8</sup> The most noteworthy difference between these two compounds is the degree of unsaturation within the S,N-containing heterocycle, which is a thiazole in escherichelin and a thiazoline in pyrochelin. As discussed in Chapters 5 and 6, our group was able to extend this “oxidation strategy” to the acinetobactin system of *A. baumannii* by synthesizing an oxidized variant of the natural siderophore. This variant, coined OxPreAcb, contained an oxazole in the place of the natural oxazoline and served as a growth inhibitor as opposed to a growth promoter.<sup>7</sup> Pyrochelin and pre-acinetobactin are two of a plethora of known siderophores with oxidizable heterocyclic groups; some of these siderophores include agrobactin, anguibactin, and mycobactin (**Figure 8.5**). With the structural similarity to pre-acinetobactin, anguibactin, produced by the fish pathogen *Vibrio anguillarum*, presents as a suitable target molecule for synthesis and evaluation by our group. Additionally, a recent publication by Abe et al reports the isolation of the hinduchelins A-D.<sup>9</sup> These compounds contain a central oxazole, serving as yet another example of a siderophore-like oxidized system further supporting the incorporation of these motifs in future synthetic strategies to biologically active small molecules.

Our group has been recently working towards the synthesis of both the natural anguibactin siderophore, as well as the oxidized version of the molecule. Unlike pre-acinetobactin, anguibactin is hypothesized to not undergo isomerization to a post-isomerized form (**Figure 8.6**).<sup>10, 11</sup> However, this hypothesis has never been experimentally confirmed in the context of a synthetic

strategy. Thus, our group targeted the synthesis of natural anguibactin in order to evaluate its biological activity and explore its possible pH-dependent isomerization. While current efforts are focused on optimization of the synthesis, initial synthetic efforts commenced with EDC/HOBt mediated coupling of 2,3-dihydroxybenzoic acid and L-cysteine-methyl ester in the presence of facilitating to afford coupled compound **1** (**Figure 8.7**). Compound **1** is then cyclized to afford the corresponding thiazoline-methyl ester **2**. Concurrently, histamine **3** is converted to the corresponding halogenated salt **4** which then through an S<sub>N</sub>2 reaction with *N*-*boc*-*O*-benzyl-amine provides *N*-*boc*-*O*-benzyl-histamine **5**. Thiazoline-methyl ester **2** is then saponified with lithium hydroxide to afford the free acid. Hydrogenation of *N*-*boc*-*O*-benzyl-histamine **5** with palladium on carbon followed by treatment with trifluoroacetic acid provides free amine, *N*-(2-(1H-imidazol-4-yl)ethyl)hydroxylamine, **7**. EDC/HOBt mediated coupling between free acid and free amine in the presence of facilitating bases yields title compound, anguibactin. Interestingly, with HPLC prep purifying the title compound, anguibactin (m/z 348), we observed a new peak appearing over time. This new peak (m/z 332) we hypothesize is in fact due to isomerization of anguibactin, followed by hydrolysis of the newly formed thiocarbonyl forming des-methyl-acinetobactin (**Figure 8.8**). We hypothesize that the isomerization is indeed occurring and due to the subsequent addition of water, may have gone overlooked previously. Future studies are needed to isolate, fully characterize, and monitor isomerization conditions and determine isomerization rates of the anguibactin system.

The synthesis of oxidized anguibactin (OxAng) is also currently being pursued and optimized in our lab. Similarly to the synthesis of OxPreAcb, the synthesis of OxAng commences with a one pot, two-step reaction of coupling 2,3-dihydroxybenzaldehyde and L-cysteine-methyl-ester, cyclization and oxidation by DBU to afford the thiazole-methyl-ester **1** (**Figure 8.9**). As

previously discussed *N*-*boc*-*O*-benzylhydroxyhistamine **4** can be synthesized in 2 steps starting from histamine **2**. Saponification of thiazole-methyl-ester with lithium hydroxide afforded free acid **5** while treatment of doubly protected amine **4** with TFA provides free amine **6**. HATU coupling of acid **5** and amine **6** yields the title compound-benzyl-ester protected **7**, which upon deprotection with boron trichloride and tetra-*n*-butylammonium bromide, affords OxAng **8**.

Upon successful synthesis of both anguibactin and OxAng, biological evaluation of these compounds can explore whether the oxidation of a known siderophore can result in inhibition in a third system. Provided OxAng has an inhibitory effect, this strategy of siderophore oxidization as a potential anti-virulent approach should be optimized and extended as a general strategy of combating multi-drug resistant pathogens.

### ***Fimbactin (A and F) analogs and antibiotic conjugates***

As discussed in chapters 3 and 4, we now have a method for isolating natural Fimsbactin A, as well as natural Fimsbactin F, from *A. baumannii* culture. Isolating these compounds opens the door for numerous derivatization and conjugation chemistry. Using a semi-synthetic approach, isolation of Fimsbactin A and F followed by oxidation of the oxazoline ring, using methods such as the DBU oxidation that was seen to be successful with the OxPreAcb system, might allow for the synthesis of yet another two oxidized siderophore systems (**Figure 8.10**). Further, Fimsbactin F contains an alcohol moiety that can serve as a handle for potential further chemistry (**Figure 8.11**). Like with the OxPreAcb-alkyne system, further diversification can include attachment of fluorophores and/or antibiotics to both investigate the target location of Fimsbactin F inside the cell, as well as serve as a Trojan horse scaffold. Moreover, the alcohol handle on Fimsbactin F may allow for quick diversification through the addition of various acyl chlorides. Addition of a molecule such as 4-chlorobenzoyl chloride can serve as a probe molecule to investigate the

relationship/interconversion, if any, between Fimsbactin A and Fimsbactin F. Synthesizing this analog, feeding it to the bacteria, and then performing HRMS can allow us to detect formation, if any, of the free 4-chlorobenzoic acid. If detected that may indicate that Fimsbactin A is cleaved by an esterase to yield Fimsbactin F.

Fimsbactin A can also be obtained through total synthesis as shown in **Figure 8.12**. Crude final compound was obtained, however there was racemization at the denoted carbon. This synthetic strategy could be optimized to allow for diversification to allow for the synthesis of various fimsbactin analogs.

### ***DFT computational calculations and BauB crystal structures***

With extremely fruitful collaborations with both the Gulick group (State University of New York at Buffalo) and Dr. Daryl Giblin (WUSTL Chemistry), we are currently continuing our efforts to further expand upon on previous work. Efforts continue to crystalize periplasmic siderophore binding protein, BauB, and other siderophore transport proteins with our current panel of natural and synthetic compounds. Further structural evidence and interactions at the protein level will allow for more targeted structure diversification work, as well as provide insight to the inter-workings of the natural siderophore transport pathways. DFT and computational work continues to explore lowest energy confirmation of natural and synthetic compounds, as well as to explore metal interactions and metal complex formations to extend upon our work with various metal titration/preference of various siderophore systems.

## **8.4 Acknowledgements**

I would like to thank Dr. Jeff Lung-Fa Kao and Dr. Manmilan Singh (WUSTL Chemistry) for assistance in obtaining 2D NMR data and instrument trouble shooting. I thank Dr. Bradley

Evans and Dr. Jonathan Mattingly (Danforth Plant and Science Center) for assistance in acquisition of HRMS data on many compounds through the years. A big thanks to Dr. John-Stephen Taylor for allowing me to use his lab space and fluorimeter to perform quenching assays. Dr. Luis Actis (Miami University) for providing us with *A. baumannii* ATCC 19606 t6, t7 and s1 mutants. Dr. Daniel Bailey and Dr. Andrew Gulick (State University of New York at Buffalo) for fruitful collaboration and their efforts in obtaining the pET28bTEV plasmid encoding for *N*-His<sub>6</sub>-BauB. Dr. Daryl Giblin (WUSTL Chemistry) for his efforts in DFT calculations of many of the molecules discussed in this dissertation. Finally, to NSF for the monetary support to fund this research, most of which was supported by NSF CAREER award 1654611 awarded to TAW.

## 8.5 Figures

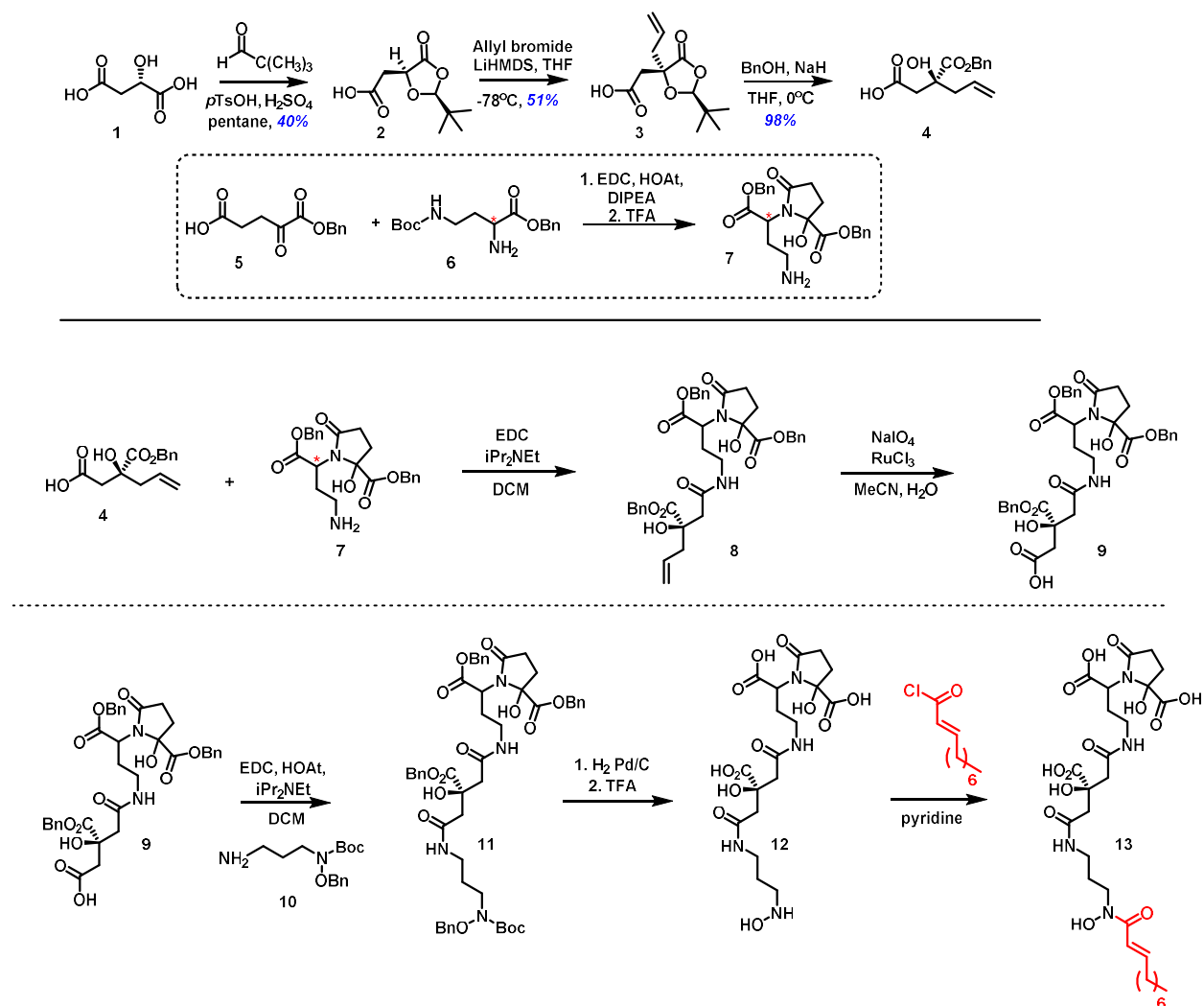


**Figure 8.1.** Proposed synthetic route towards the total synthesis of the baumannoferrins. Highlighted in red shows a site of potential diversification which can allow for rapid derivatization of variable chain length and degrees of unsaturation.



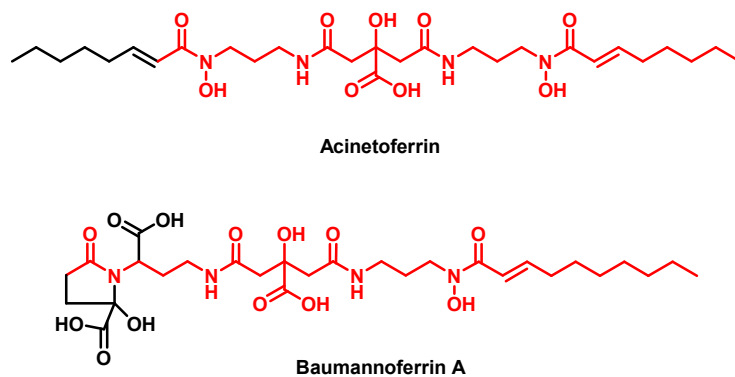


**Figure 8.2.** Structures of Baumannoferrin A and structurally similar Acinetoferrin. Shared structural features are highlighted in red.

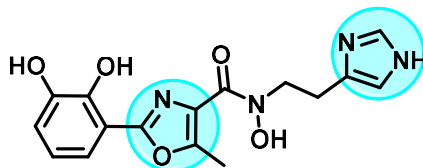


**Figure 8.3.** OxPreAcb structure. Blue circles represent areas for potential site for further diversification.

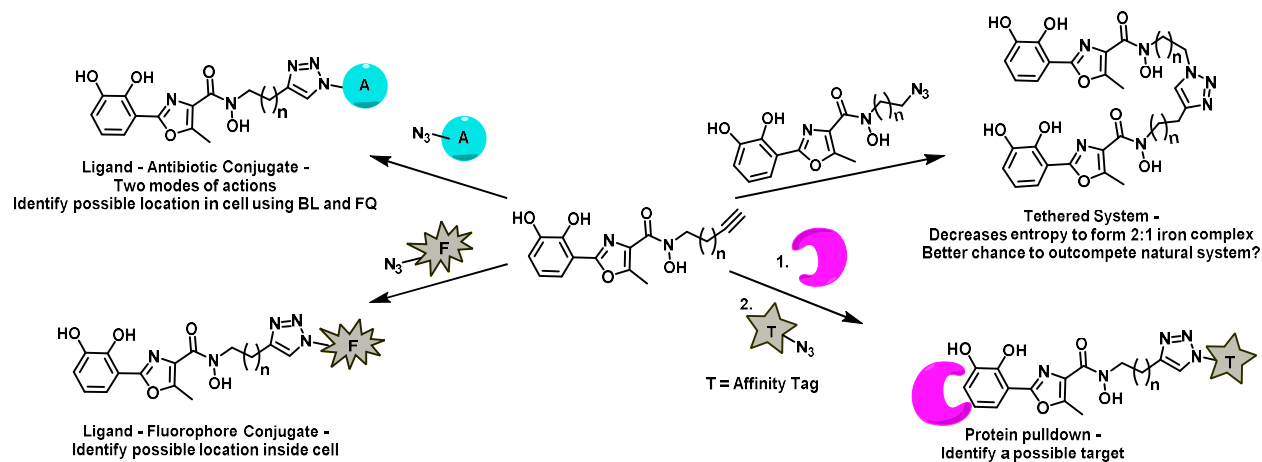


**Figure 8.4.** OxPreAcb-alkyne molecule can allow for rapid functionalization via click chemistry to explore the location of OxPreAcb in the cell, protein the molecule interacts with, potential optimization of the molecule as an inhibition through dimerization and a potential Trojan horse vehicle inhibitor-antibiotic system.

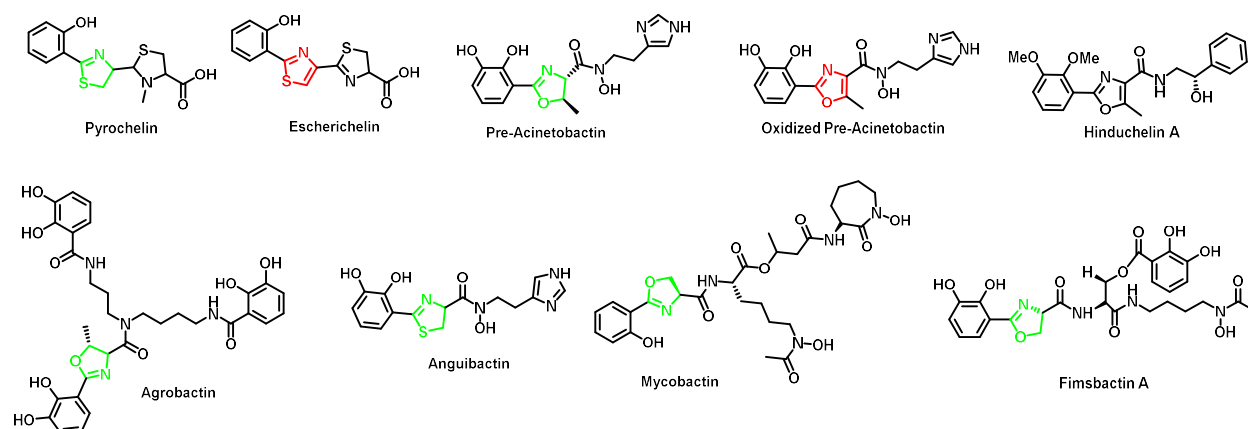


**Figure 8.5.** Structures of siderophores with oxidizable groups highlighted in green. Groups in red denote the two oxidized moiety in “siderophore-like” molecules that have been shown to be inhibitory in their respective pathogens.

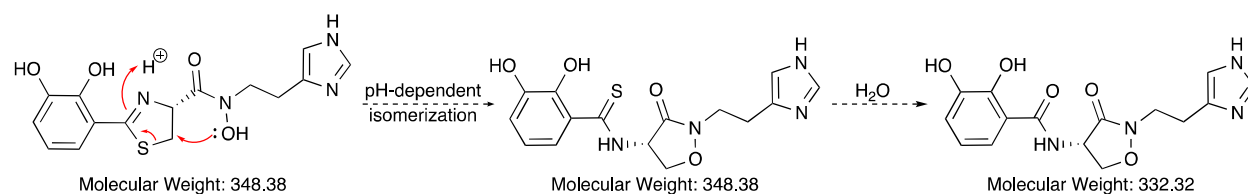


**Figure 8.6.** Anguibactin, a siderophore from *Vibrio anguillarum* is thought to not be able to undergo spontaneous isomerization as is seen in the case of pre-acinetobactin from *A. baumannii* isomerizing to acinetobactin. Initial research by group, however, suggests potential isomerization followed by addition of water to the thiocarbonyl to afford acinetobactin des-methyl.

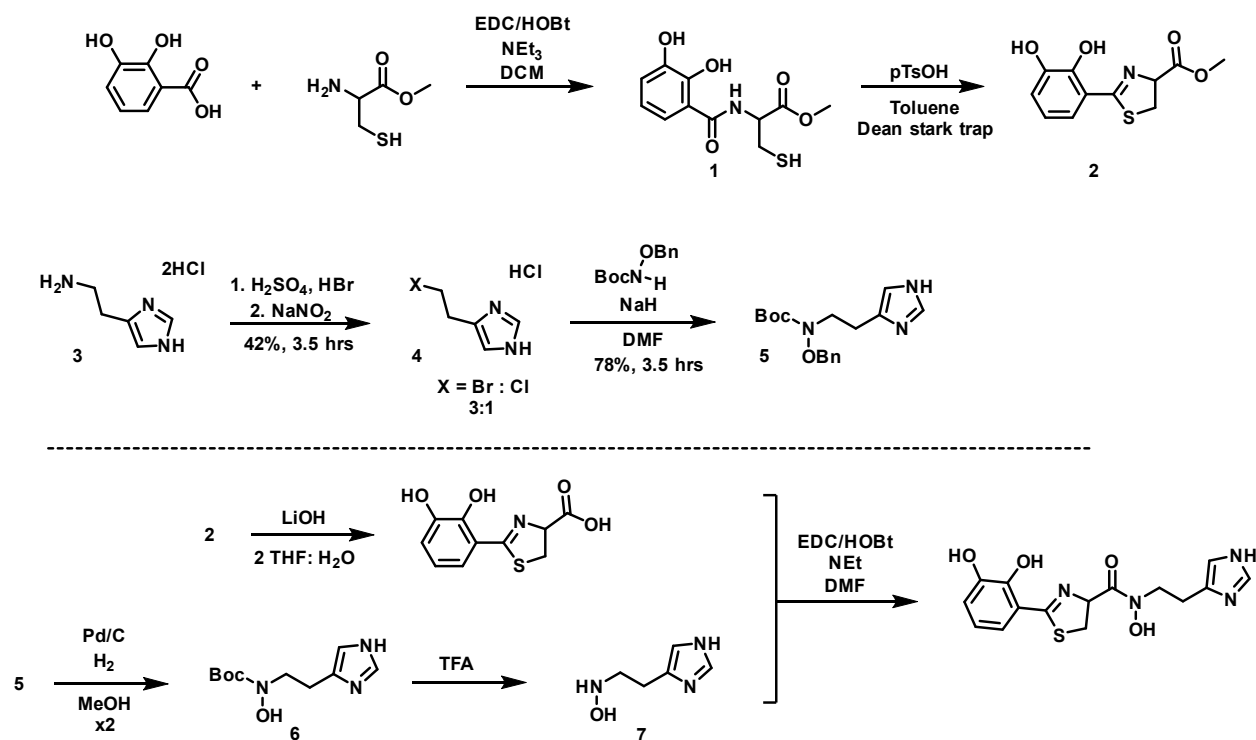


**Figure 8.7.** Synthetic route to the total synthesis of anguibactin

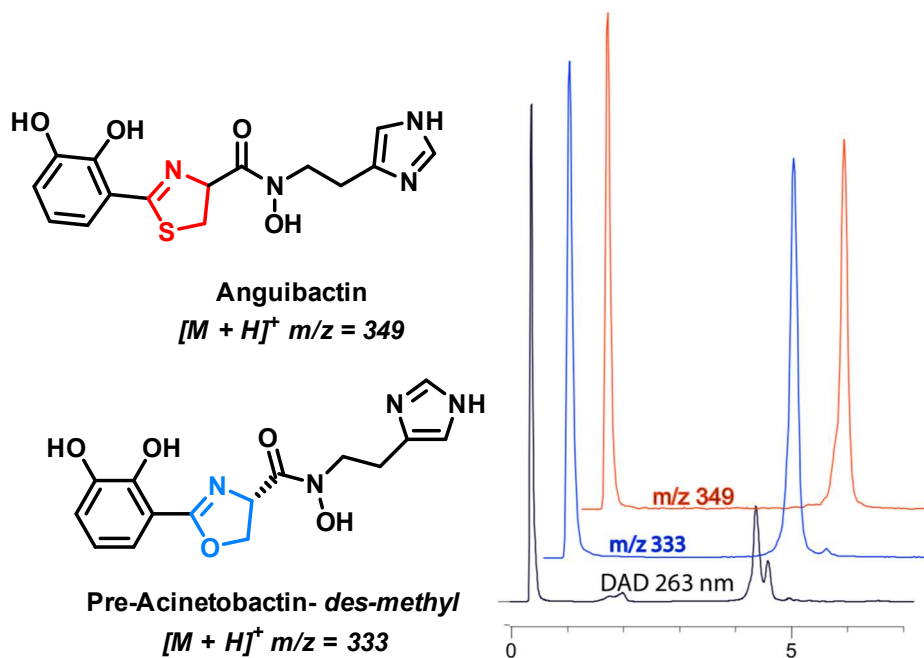


**Figure 8.8.** DAD at 263 nm (black), EIC at  $m/z$  333 (pre-acinetobactin-*des-methyl*, blue), and EIC at  $m/z$  349 (anguibactin, red) chromatographs from LCMS synthesis of HPLC-prep purification of synthetic anguibactin.

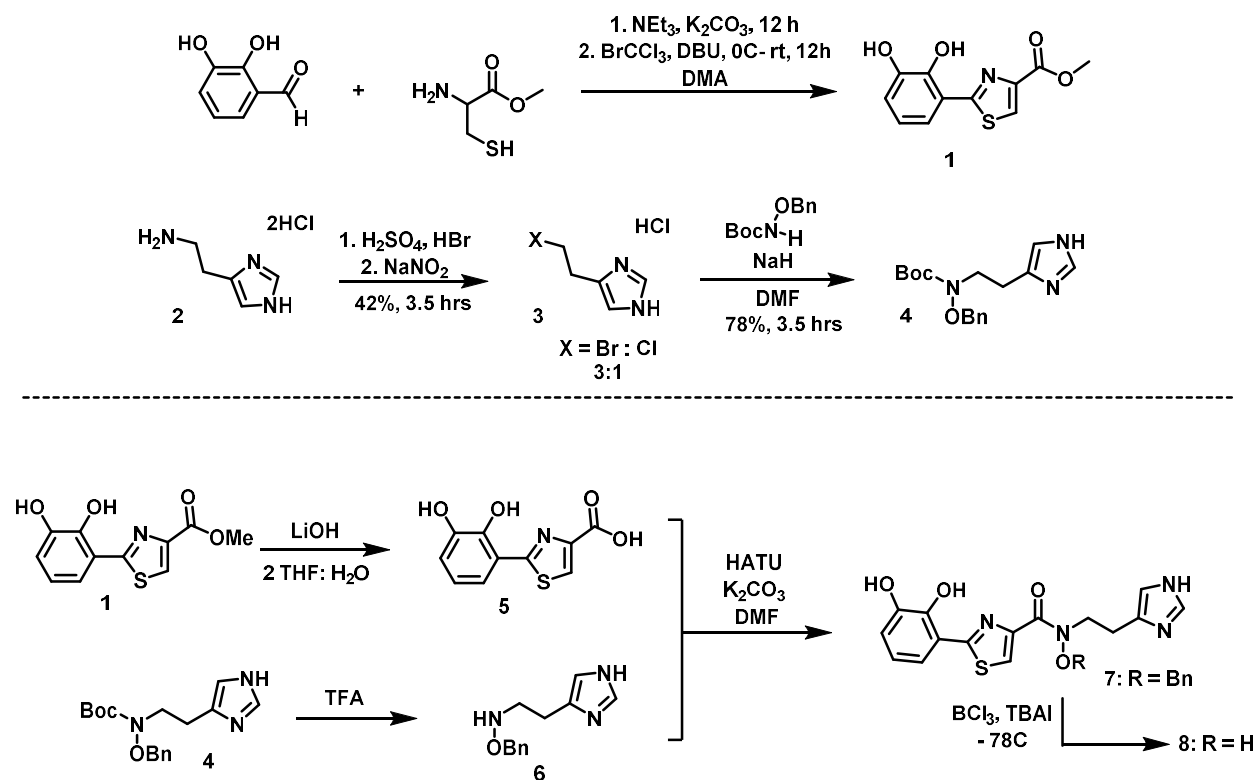


**Figure 8.9.** Synthetic route towards the total synthesis of OxAng

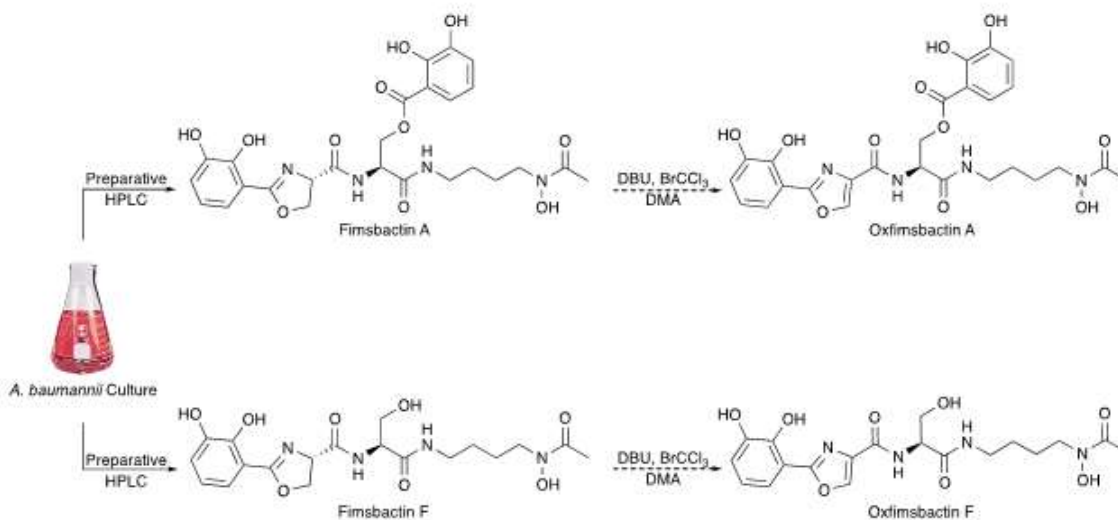


**Figure 8.10.** Potential semi-synthetic route to synthesis of Ox-FimA and Ox-FimF

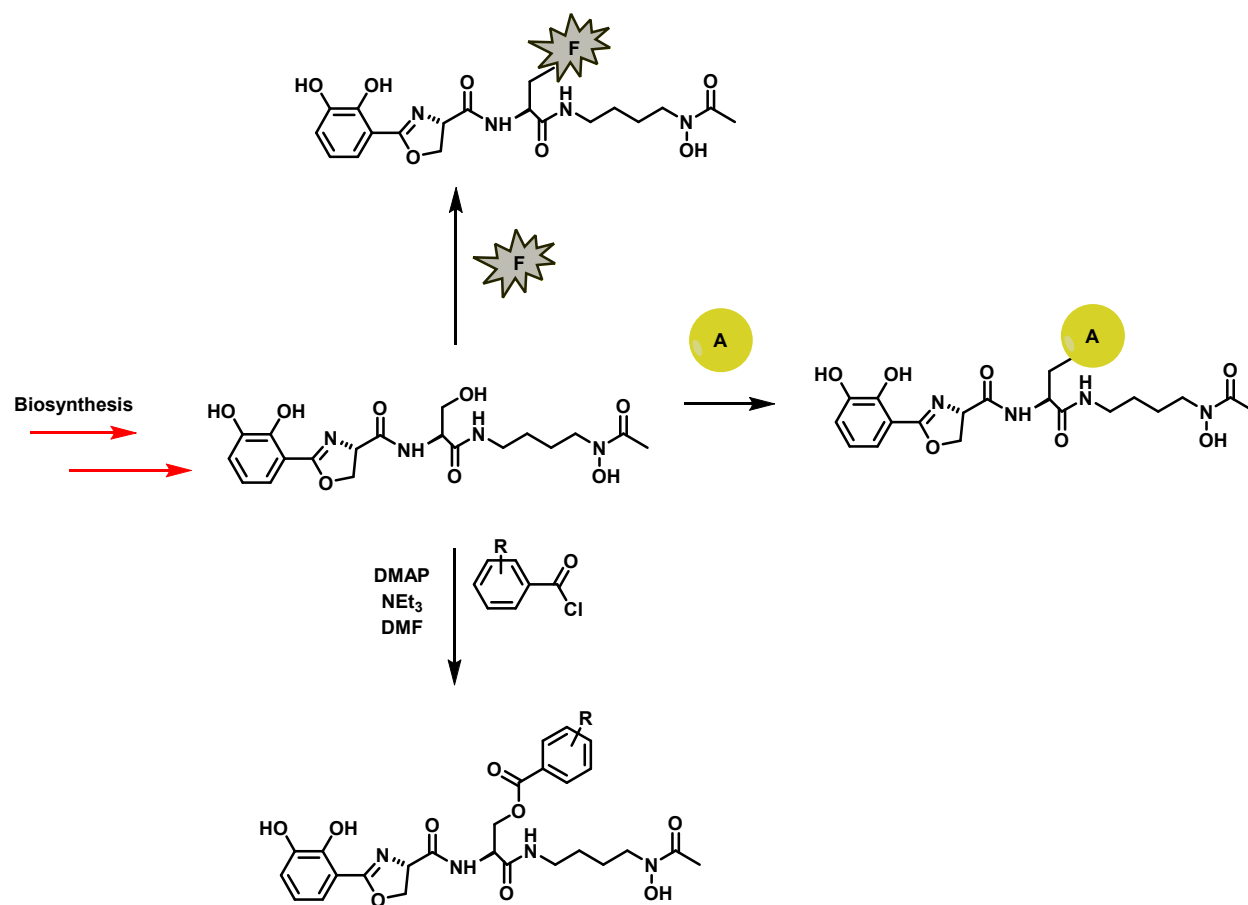


**Figure 8.11.** Potential semi-synthetic approach to the diversification of Fimsbactin F, allowing for fluorophore and antibiotic conjugation as well as rapid synthesis of analogs via derivatization at the alcohol handle.

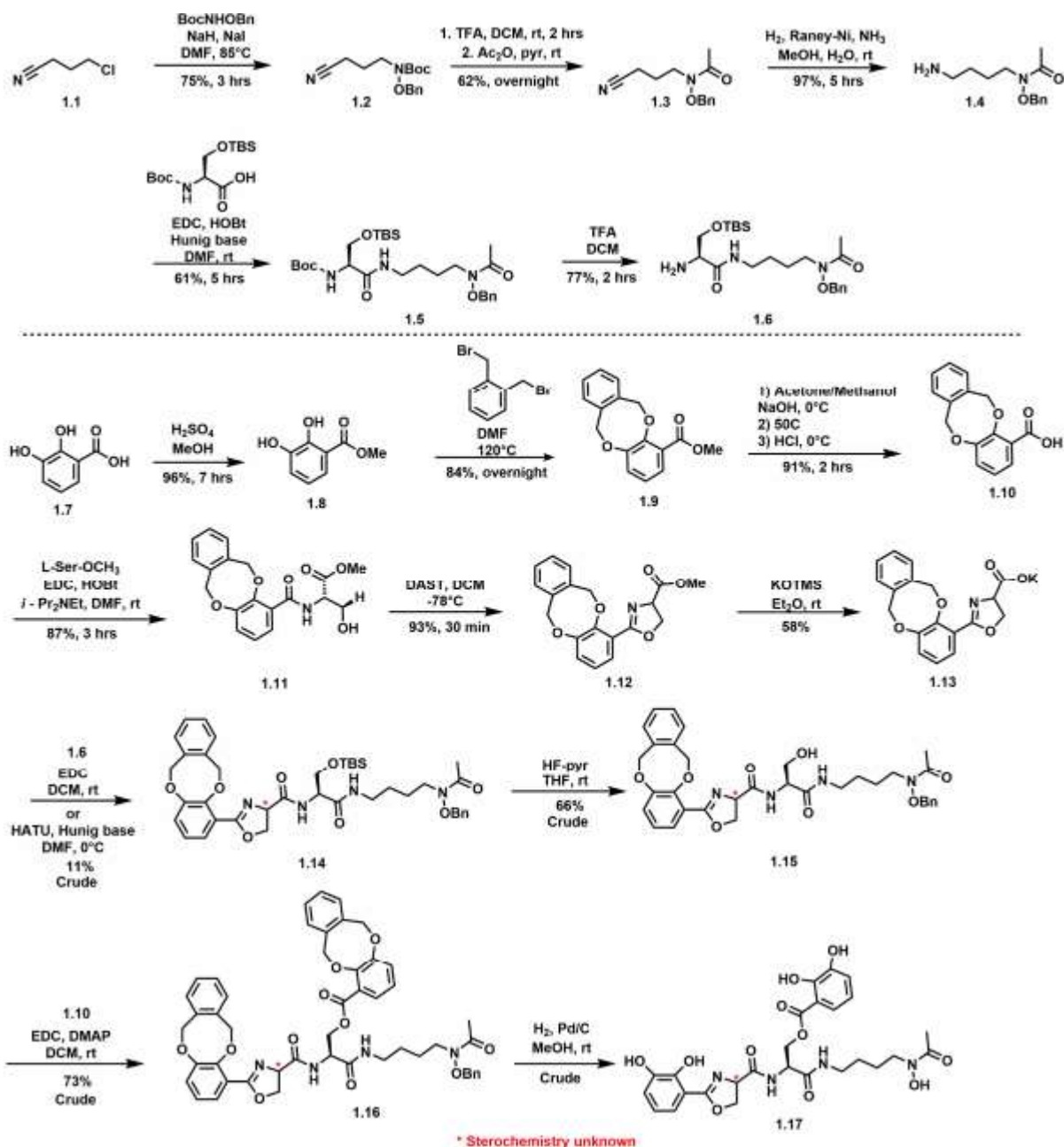


**Figure 8.12.** Synthetic efforts towards the synthesis of Fimsbactin A. Crude compound was obtained but there was racemization of stereochemistry at the denoted carbon. Further optimization is needed.

## 8.6 References

- [1] Madsen, J. L. H.; Johnstone, T. C.; Nolan, E. M., Chemical Synthesis of Staphyloferrin B Affords Insight into the Molecular Structure, Iron Chelation, and Biological Activity of a Polycarboxylate Siderophore Deployed by the Human Pathogen *Staphylococcus aureus*. *Journal of the American Chemical Society* **2015**, 137 (28), 9117-9127.
- [2] Wang, Q. X.; Phanstiel, O., Total Synthesis of Acinetoferrin. *The Journal of Organic Chemistry* **1998**, 63 (5), 1491-1495.
- [3] Choh, N., Morimoto, A., & Noguchi, N. (1989). *U.S. Patent No. EP 0253337 A2*. Washington, DC: U.S. Patent and Trademark Office.
- [4] Luo, M.; Fadeev, E. A.; Groves, J. T., Membrane Dynamics of the Amphiphilic Siderophore, Acinetoferrin. *Journal of the American Chemical Society* **2005**, 127 (6), 1726-1736.
- [5] Wencewicz, T. A., Miller, M. J. (2013) Biscatecholate-monohydroxamate mixed ligand siderophore-carbacephalosporin conjugates are selective sideromycin antibiotics that target *Acinetobacter baumannii*. *J. Med. Chem* 56(10), 4044-4052.
- [6] Ghosh, M., Lin, Y. M., Miller, P. A., Mollmann, U., Boggess, W.C., Miller, M. J. (2018) Siderophore Conjugates of Daptomycin are Potent Inhibitors of Carbapenem Resistant Strains of *Acinetobacter baumannii*. *ACS Infect Dis* 4, 1529-1535.
- [7] Bohac, T. J., Shapiro, J. A., and Wencewicz, T. A. (2017) Rigid Oxazole Acinetobactin Analog Blocks Siderophore Cycling in *Acinetobacter baumannii*, *ACS infectious diseases* 3, 802-806.
- [8] Ohlemacher, S. I., Giblin, D. E., d'Avignon, D. A., Stapleton, A. E., Trautner, B. W., and Henderson, J. P. (2017) Enterobacteria secrete an inhibitor of *Pseudomonas* virulence during clinical bacteriuria, *The Journal of clinical investigation* 127, 4018-4030.

- [9] He, F., Nakamura, H., Hoshino, S., Chin, J.S.F, Yang, L., Zhang H., Hayashi, F., Abe, I. (2018) Hinduchelins A-D, Noncytotoxic Catechol Derivatives from *Streptoalloteichus hindustanus*, *Journal of Natural Products* 81, 1493-1496.
- [10] Shapiro, J. A., and Wencewicz, T. A. (2016) Acinetobactin Isomerization Enables Adaptive Iron Acquisition in *Acinetobacter baumannii* through pH-Triggered Siderophore Swapping, *ACS infectious diseases* 2, 157-168.
- [11] Lee, H., Song, W. Y., Kim, M., Lee, M.W., Kim, S., Park, Y. S., Kwak, K., Oh, M. H., and Kim, H. J. (2018) Synthesis and Characterization of Anguibactin to Reveal Its Competence to Function as a Thermally Stable Surrogate Siderophore for a Gram-Negative Pathogen, *Acinetobacter baumannii Organic Letters* 20, 6476-6479.